UNIVERSIDADE FEDERAL DE SANTA CATARINA
CENTRO TECNOLÓGICO
PROGRAMA DE PÓS-GRADUAÇÃO EM ENGENHARIA ELÉTRICA

Edhuardo Francisco Celli Grabovski

TOWARDS A COMPREHENSIVE CONTROL FRAMEWORK FOR GRID-TIED POWER CONVERTER SYSTEMS

Florianópolis
Dezembro de 2024

Edhuardo Francisco Celli Grabovski

TOWARDS A COMPREHENSIVE CONTROL FRAMEWORK FOR GRID-TIED POWER CONVERTER SYSTEMS

Tese submetida ao Programa de Pós–Graduação em Engenharia Elétrica da Universidade Federal de Santa Catarina para a obtenção do Grau de Doutor em Engenharia Elétrica.
Supervisor: Prof. Samir Ahmad Mussa, Dr.
Co-supervisor: Prof. Marcelo Lobo Heldwein, Dr.

Florianópolis
Dezembro de 2024

Ficha catalográfica gerada por meio de sistema automatizado gerenciado pela BU/UFSC.
Dados inseridos pelo próprio autor.

Grabovski, Edhuardo Francisco Celli
Towards a Comprehensive Control Framework for Grid-Tied Power Converter Systems / Edhuardo Francisco Celli Grabovski ; orientador, Samir Ahmad Mussa, coorientador, Marcelo Lobo Heldwein, 2024.
336 p.

Tese (doutorado) - Universidade Federal de Santa Catarina, Centro Tecnológico, Programa de Pós-Graduação em Engenharia Elétrica, Florianópolis, 2024.

Inclui referências.

1. Engenharia Elétrica. 2. Eletrônica de Potência. 3. Modelagem de Conversores Estáticos. 4. Análise de Estabilidade. 5. Sincronização de Portadoras. I. Mussa, Samir Ahmad. II. Heldwein, Marcelo Lobo. III. Universidade Federal de Santa Catarina. Programa de Pós-Graduação em Engenharia Elétrica. IV. Título.

Edhuardo Francisco Celli Grabovski

TOWARDS A COMPREHENSIVE CONTROL FRAMEWORK FOR GRID-TIED POWER CONVERTER SYSTEMS

O presente trabalho em nível de doutorado foi avaliado e aprovado por banca examinadora composta pelos seguintes membros:

Prof. Humberto Pinheiro, Dr.
Universidade Federal de Santa Maria

Prof. Fernando Luiz Marcelo Antunes, Dr.
Universidade Federal do Ceará

Prof. André Luis Kirsten, Dr.
Universidade Federal de Santa Catarina

Prof. Joabel Moia, Dr.
Instituto Federal de Santa Catarina

Certificamos que esta é a **versão original e final** do trabalho de conclusão que foi julgado adequado para obtenção do título de Mestre em Engenharia Elétrica.

ICP-Edu
Documento assinado digitalmente
Telles Brunelli Lazzarin
Data: 10/12/2024 08:38:12-0300
CPF: ***.400.719-**
Verifique as assinaturas em https://v.ufsc.br

Prof. Telles Brunelli Lazzarin, Dr.
Coordenador do Programa

ICP-Edu
Documento assinado digitalmente
Samir Ahmad Mussa
Data: 06/12/2024 12:59:32-0300
CPF: ***.044.430-**
Verifique as assinaturas em https://v.ufsc.br

Prof. Samir Ahmad Mussa, Dr.
Orientador

Florianópolis
Dezembro de 2024.

À minha família.

Acknowledgements

First and foremost, I would like to express my deepest gratitude to my family. To my parents, Francisco and Mery, and my sister, Giovanna, for their unconditional love, sacrifices, and unwavering support throughout my life. Your encouragement has been my foundation and motivation to always strive for excellence in the most creative and unrestricted ways.

I am deeply grateful to my supervisor, Prof. Samir A. Mussa, for his constant support throughout these years. Your invaluable mentorship, insightful advice, and patience during this research have been indispensable. Your guidance has not only shaped the course of this thesis but also profoundly influenced my academic and professional growth.

I am immensely thankful to my co-supervisor, Prof. Marcelo L. Heldwein, for dedicating your time and making significant contributions throughout the development of this thesis. From the conception of the topic to the weekly meetings and discussions on a wide range of subjects in power electronics, your support has been invaluable. Thank you also for fostering an environment where I could not only carry out my thesis work but also learn about diverse topics. The knowledge I carry forward into my professional life is a direct result of your guidance and dedication throughout this process.

Special thanks to the other professors at INEP–UFSC who contributed to my professional formation: Prof. Arnaldo J. Perin, Prof. André L. Kirsten, Prof. Denizar C. Martins, Prof. Gierri Waltrich, and Prof. Telles B. Lazzarin. I also extend my gratitude to the exceptional lab technician, Dr. Antonio L. S. Pacheco, and to Diogo Duarte for their invaluable support during my time at INEP.

I would also like to express my heartfelt gratitude to the friends and colleagues who shared this journey with me at INEP. Bruno Bertoldi, Gean Souza, Marcos Mocellini, Gustavo Finamor, Thiago Rech, Douglas Sotoriva, Leonardo Bender, Ícaro Albuquerque, Rossano Sotoriva, Marcos Jacoboski, André Lange, Mateus Orige, Ésio dos Santos Filho, Lucas Militão, Gustavo Pereira, Mateo Greidanus, Eduardo Souza, André Furlan, Francisco Viglus, Andreas Corrêa, Lucas Cunico, Júlio Dias, Rodrigo Pinto, Renan Barcelos, Rossano Barcelos, Vinicius Fuerback, Douglas Haupt, Leandro Fisch, Humberto Cardoso, Luiz Gili, Valdecir de Paris, Tailan Orlando, Neilor Dal Pont, Vinicius Fiamoncini, and many others with whom I had the honor of sharing time and knowledge.

This work is dedicated to everyone that has been a part of this journey.

"non est ad astra mollis e terris via"
Seneca the Younger

Resumo

Este estudo apresenta uma exploração abrangente de inversores de fonte de tensão trifásicos conectados à rede, oferecendo uma perspectiva mais ampla em comparação com abordagens existentes. Ele investiga as interações nos sistemas de controle do inversor, indo além das limitações dos métodos atuais do estado da arte. A pesquisa começa analisando modelos de conversores de potência conectados em paralelo, revelando como variações paramétricas impactam as correntes circulantes de média e alta frequência em conexões de corrente contínua compartilhadas e isoladas. O estudo também investiga a eficácia de técnicas de controle. Ele avalia a aplicabilidade do Regulador Linear Quadrático (LQR) e do Controle Robusto com controladores ressonantes para realimentação de estado. Além disso, o desempenho de um Observador de Modo Deslizante Estendido (ESMO) adaptado para sistemas eletrônicos de potência, especialmente conversores em paralelo, é avaliado. Uma estratégia para controle de corrente de eixo zero é proposta com base em princípios de passividade. Modelos de Espaço de Estado Harmônico Não Linear são desenvolvidos, facilitando a análise de Sistemas Não Lineares Invariantes no Tempo. Esse framework permite a exploração de pontos fixos e estabilidade, com foco específico na interação entre controles de potência ativa e reativa, especialmente em condições de rede fraca. O estudo conclui apresentando uma técnica de sincronização de portadora com o objetivo de minimizar correntes circulantes de alta frequência. Essa estratégia integra conceitos previamente estabelecidos, garantindo uma abordagem robusta. Em essência, este trabalho avança na compreensão da operação e controle de inversores de fonte de tensão trifásicos, fornecendo insights valiosos para o progresso de sistemas de energia conectados à rede.

Palavras-chave: Paralelismo de conversores, modelagem de conversores, sincronização de portadoras, correntes de circulação.

Abstract

This study presents a comprehensive exploration of grid-connected Three-Phase Voltage Source Inverters, offering a broader perspective compared to existing approaches. It investigates interactions within inverter control systems, going beyond the limitations of current state-of-the-art methods. The research begins by analyzing models of parallel-connected power converters, revealing how parametric variations impact medium- and high-frequency circulating currents in both shared and isolated dc connections. The study also investigates the efficacy of control techniques. It assesses the applicability of Linear Quadratic Regulator (LQR) and Robust Control with resonant controllers for state-feedback. Additionally, the performance of a Extended Sliding-Mode Observer (ESMO) tailored for power electronic systems, especially paralleled converters, is evaluated. A strategy for zero axis current control is proposed based on passivity principles. Nonlinear Harmonic State-Space models are developed, facilitating the analysis of Nonlinear Time-Invariant Systems. This framework enables the exploration of fixed points and stability, with a specific focus on the interplay between active and reactive power, particularly in weak grid conditions. The study concludes by presenting a carrier synchronization technique aimed at minimizing high-frequency circulating currents. This strategy integrates previously established concepts, ensuring a robust approach. In essence, this work advances the understanding of Three-Phase Voltage Source Inverters' operation and control, providing valuable insights for the progress of grid-connected power systems.

Key-words: Paralleled converters, modelling of power converters, carrier synchronization, circulating currents.

Resumo Expandido

Introdução

O aumento na demanda por conversores estáticos de potência para interfacear diferentes fontes de energia com a rede elétrica, especialmente para aplicações de potências elevadas, criou uma necessidade de projetos otimizados de sistemas empregando tais conversores. Nas últimas décadas, o estado da arte evoluiu em uma maneira ditada por estas tendências, com estimativas de aumento da densidade de potência dobrando a cada dez anos. No entanto, a escala destes sistemas têm demonstrado uma demanda for maior modularidade e reconfigurabilidade, de modo a aumentar a disponibilidade e escalabilidade dos sistemas menciondos.

Tal fato provocou um aumento no estudo sobre conexões série e paralelo de conversores estáticos,, desde a concepção do conceito de geração distribuída e microrredes, abrindo caminho para uma geração descentralizada de energia elétrica, em oposição ao aos legados sistemas centralizados, que exigem sistemas de alta potência e alta tensão. Algumas dessas aplicações são estremamente dependentes na conexão em paralelo de conversores de potência, de forma a atender os requisitos de processamento de energia, e ao mesmo tempo melhorar a disponibilidade e maximizar a eficiência do processo.

O interesse por conexões em paralelo de inversores foi inicialmente desenvolvido para aumentar a confibialidade de sistemas de geração ininterrupta (UPS). A partir daquele momento, os sistemas de controle de conversores em paralelo visando uma conexão perfeita já eram discutidos, com estratégias de controle de *droop* sendo propostos, de forma a emular uma impedância entre os conversores conectados aos chamados sistemas rígidos, como meios de regular o compartilhamento de potência ativa e reativa entre tais conversores. Esta estratégia abriu caminho para uma grande variedade de estratégias de controle, baseada em valores de regime permanente das variáveis elétricas.

Atualmente, os métodos mais comuns para a análise de estabilidade da conexão de conversores são baseadas na teoria do teorema N-ésimo elemento extra, útil para sistemas compostos por redes lineares, provendo restrições à impedância de entrada dos conversores no projeto da estratégia de controle. No entanto, questionamentos podem ser levantados com relação à aplicabilidade de análise de sistemas lineares em sistemas com características fortemente não-lineares. Este fato é mais claro quando operando em condições de rede fraca, em oposição à premissa da estratégia de controle droop com relação à conexão rígida. Portanto, o comportamento de sistemas quando o critério de Middlebrook não é atendido, ou a verificação da validade a aproximação por sistemas lineares ainda não foi matematicamente descrita.

Objetivos

Os objetivos do trabalho podem ser listados como:

- Desenvolvimento de modelos matemáticos generalizados baseados em sistemas po-

lifásicos, formulados a partir de suas representações em esaço de estados no domínio harmônico, levando em consideração variações paramétricas. Este procedimento emprega as transformações lineares de Clarke e Lunze e a teoria do Espaço de Estado Harmônico e modelos politópicos, permitindo a definição de impedâncias de modo comum e diferencial como meios de verificar ressonâncias entre os conversores em paralelo;

- Definição de uma estrutura de modelagem de espaço de estado harmônico baseada na Transformada de Fourier 2-D e sua extensão para o caso multidimensional como meio de simplificar a análise do acoplamento harmônico entre sistemas multifrequenciais;
- Desenvolvimento de um modelo não linear do SRF-PLL no domínio harmônico, que permite a investigação de interações de perda de bloqueio e não lineares entre os laços de controle do inversor e a inspeção de instabilidades e bifurcações devido ao comportamento não linear de sistemas conversores de energia, especialmente sob condições de rede fraca;
- Formulação de um modelo não linear empregando o espaço de estados harmônicos para um sistema solar fotovoltaico com base na temperatura e irradiância das células fotovoltaicas e um conversor de potência para rastreamento do ponto de potência máxima que permite a investigação de interações dinâmicas entre sistemas CA e CC;
- Estudo de técnicas de filtragem adaptativa linear e não linear e proposta de um estimador de frequência baseado na estimativa amplamente linear e um filtro de cancelamento de sinal atrasado adaptativo para operação em condições de rede distorcidas;
- Estudo de técnicas de controle robusto e desigualdades de matriz linear como meios de obter uma estratégia de controle ótima com base na técnica de controle de feedback de estado e proposta de um observador de modo deslizante de perturbação para estimar variáveis de estado ao mesmo tempo em que leva em consideração perturbações devido a erro de modelagem;
- Metodologia para avaliação de estabilidade não linear de sistemas conversores de potência no domínio harmônico sob condições de rede fraca e verificação do comportamento das admitâncias de entrada do sistema conversor de potência para múltiplos pontos de operação com base na abordagem do modelo linear politópico;
- Proposta de uma técnica de sincronização de portadora para mitigar correntes circulantes de alta frequência entre conversores de potência em paralelo e validação das estratégias propostas implementadas em um FPGA e hardware-in-the-loop.

Metodologia

Nos anos recentes, há uma busca por modelos matemáticos mais fiéis, de forma a representar os efeitos das não-linearidades de forma mais precisa. Tal representação pode ser realizada através de mapas de Poincaré ou multiplicadores de Floquet,. Este trabalho visa apresentar uma análise matemática da conexão de conversores com a rede, bem como a conexão de conversores em paralelo. São apresentados ainda modelos de conversores que podem compor um sistema de conversores, bem como auxiliar a interface entre as diversas fontes de energia com a rede elétrica.

São apresentadas estratégias de controle, de forma a garantir o funcionamento adequado dos conversores em um primeiro momento, om suas respectivas implementações e validação utilizando os conversores emulados via *hardware-in-the-loop* (HIL). Tais estratégias são baseadas nas teorias de controle robusto e controle ótimo.

Logo após, são apresentados modelos para a análise de estabilidade, visando a descrição do sistema em espaço de estados harônico (HSS), de forma a obter os pontos de equilíbrio para diferentes pontos de operação. O cálculo dos pontos de equilíbrio, bem como a análise dos autovalores do sistema para os diferentes pontos de operação, demonstram a característica não-linear do sistema, visto que há uma variação considerável dos autovalores do sistema, bem como questionamentos acerca da existência do ponto de equilíbrio para diferentes os diferentes níveis de potência ativa e reativa processados pela interface. Tais modelos são validados utilizando as estratégias de controle propostas em um primeiro momento, com o sistema de conversores também emulado via HIL.

Por fim, é apresentada uma estratégia de sincronização de portadoras, de forma a reduzir as correntes de circulação de alta frequência que existem entre conversores estáticos conectados em paralelo. A minimização é composta por duas etapas, a primeira sendo uma sincrnização de frequência de comutação, seguido por uma estratégia de minimização das correntes circulantes, visando a equalização de fase das portadoras.

Resultados e Discussões

Este trabalho apresentou um estudo sobre questões relacionadas ao controle de sistemas conversores de potência. Em um primeiro momento, os conversores de potência trifásicos foram modelados com a suposição de parâmetros balanceados, e uma regra para modelar conversores trifásicos a partir de sua contraparte monofásica baseada na Transformada de Clarke-Lunze foi empregada. Diferentes modelos foram obtidos como uma nova estrutura para analisar variações paramétricas e o acoplamento de modos aditivos e subtrativos inter e intraconversores. Um estudo sobre possíveis circuitos dc também foi apresentado, com o objetivo de analisar a interconexão entre sistemas dc-ac. Um modelo multifrequencial de conversor de matriz indireta também foi obtido, completando a análise para sistemas conversores de potência ac-ac.

A partir da análise e simulações de sistemas conversores em paralelo, um comportamento não passivo foi observado, embora a análise de um único conversor tenha resultado em um sistema passivo. Isso aconteceu quando a frequência dos filtros do conversor de potência se aproxima da frequência de comutação dos conversores. A ressonância do modo subtrativo, que está relacionada à dinâmica da perturbação, principalmente pelas interações entre filtros, pode servir como base para o projeto de estruturas de amortecimento passivas. Se ignorada ao projetar filtros de saída, a perda em componentes passivos pode ser subestimada e pode resultar em efeitos catastróficos.

O estudo sobre minimização de correntes circulantes de média frequência resultou na proposta de um controlador para manter um comportamento passivo do loop de controle. No entanto, o acoplamento entre os componentes $\alpha\beta$ e a tensão sintetizada do eixo γ por meio de injeção harmônica do eixo zero pode precisar de uma rejeição de perturbação maior para certas frequências, especialmente quando os conversores em paralelo processam diferentes níveis de energia. Portanto, a utilização de controladores ressonantes também foi verificada e um procedimento de projeto foi proposto, com a passividade dependente do amortecimento do controlador. O procedimento proposto foi comparado a outros procedimentos, como LQR e controle robusto. Um observador de modo deslizante estendido foi então empregado como meio de reduzir o número de sensores necessários para a estratégia de controle de feedback de estado completo, resultando em complexidade

adicional para a implementação do controle. Uma estratégia de controle multirressonante junto ao observador de estados foi implementada em um FPGA e validada em Hardware-in-the-loop para verificar o comportamento do sistema ao operar com conversores conectados em paralelo.

A operação de conversores estáticos e efeitos como perda de sincronismo dos algoritmos de sincronismo e acoplamento entre diferentes malhas de controle motivaram o estudo da modelagem da dinâmica do barramento CC e estratégias de sincronismo no modelo, levando à obtenção de um modelo de malha fechada completo que representava todo o sistema. Isso levou à obtenção dos diagramas de bode de rejeição de perturbações e malhas de controle, e permitiu o cálculo da estabilidade global, ou pelo menos a estabilidade local ao ignorar efeitos ao assumir uma rede rígida. Os modelos obtidos podem ser expandidos ainda mais para sistemas de conversores de energia formadores de rede, assumindo uma certa dinâmica que governa a amplitude e a frequência da tensão do ponto de conexão com a rede elétrica.

Uma estratégia para sincronização de portadora também foi proposta, como meio de reduzir as correntes circulantes de alta frequência. No entanto, foi detectado que, embora o sincronismo resolva problemas relacionados a pequenos desvios de frequência de comutação devido a variações paramétricas de cristais de *clock*, o sistema ainda necessita de um método de otimização para atuar na fase das portadoras. O estado da arte atual neste tópico ainda depende de um canal de comunicação para executar a rotina de otimização. Contudo, foi detectado que essas estratégias ainda têm necessidade de melhorias, como meios para aumentar a modularidade e a confiabilidade dos sistemas de conversores estáticos. O método baseado em rede neural apresentou resultados promissores com relação à possibilidade de operar sem um canal de comunicação específico, fato que pode ser expandido para diferentes topologias de conversores.

Considerações Finais

Com o intuito de apresentar uma continuidade do trabalho proposto, pode-se propor contribuições futuras como:

- Verificação dos desvios paramétricos na estabilidade da conexão dos sistemas de conversores estáticos com a rede elétrica, assumindo que a amplitude das correntes de modo subtrativo (ou diferencial) são consideráveis, e que os múltiplos conversores possuem distintos pontos de operação;
- Avaliação da estabilidade da conexão série de conversores estáticos que compõe o sistema, visando estudar o acoplamento da dinâmica das fontes de energia com a rede elétrica, de forma a verificar o efeito de distúrios de geração na estabilidade da conexão;
- Estudo e proposição de diferentes estratégias de controle, visando a mitigação e o amortecimento das correntes de modo subtrativo;
- Modelagem do controle em coordenadas síncronas utilizando a metoologia poposta neste trabalho;
- Implementação de diferentes estruturas de neurônios nos algoritmos de sincronização de portadoras, visando uma melhora no comportamento transitório do sistema.

Palavras-chave: Paralelismo de conversores, modelagem de conversores, sincronização de portadoras, correntes de circulação.

List of Figures

List of Tables

List of abbreviations and acronyms

ac	Alternate Current
dc	Direct Current
AM	Additive-Mode
SM	Subtractive-Mode
RMS	Root-Mean-Square
THD	Total Harmonic Distortion
UPS	Uninterruptible Power Supplies
HSS	Harmonic State-Space
DP	Dynamic Phasor
SMO	Sliding Mode Observer
LTV	Linear Time-Varying
2LVSI	Two-Level Voltage Source Inverter
ESR	Equivalent Series Resistance
FIR	Finite Impulse Response
IIR	Infinite Impulse Response
PLL	Phase-Locked Loop
FLL	Frequency-Locked Loop
PLM	Polytopic Linear Model
LQR	Linear Quadratic Regulator
PWM	Pulse-Width Modulation
LMI	Linear Matrix Inequality
SPWM	Sinusoidal Pulse-Width Modulation
SVM	Space-Vector Modulation

SNR	Signal-to-noise Ratio
DFT	Discrete Fourier Transform
IDFT	Inverse Discrete Fourier Transform
LMS	Least Mean Square
CLMS	Complex Least Mean Square
ACLMS	Augmented Complex Least Mean Square
ACTLS	Augmented Complex Total Least Square
SLE	Strictly-Linear Estimator
WLE	Widely-Linear Estimator
DSC	Delayed-Signal Cancellation
GSPWM	Global Synchronous Pulse-Width Modulation
LSPWM	Local Synchronous Pulse-Width Modulation
GAT	Grid Angle Tracker
CAT	Carrier Angle Tracker
PLL-CS	Phase-Locked Loop Carrier Synchronization
P&O	Perturbation and Observation
ABC	Artificial Bee Colony
ANN	Artificial Neural Networks
FPGA	Field-Programmable Gate Arrays
DSP	Digital Signal Processor
LTI	Linear TIme-Invariant
BIBO	Bounded Input Bounded Output
AR	Autorregressive
MA	Moving Average
ARMA	Autorregressive Moving Average
NAR	Nonlinear Autorregressive
NMA	Nonlinear Moving Average
NARMA	Nonlinear Autorregressive Moving Average
RNN	Recurrent Neural Network
MLP	Multilayer Perceptron

List of symbols

ι	imaginary number
D	Differential operator
$\mathbb{N}$	Set of natural Numbers
$\mathbb{N}_n$	Set of natural numbers lower or equal to n
$\mathbb{Z}$	Set of integer numbers
$\mathbb{R}$	Field of real numbers
$\mathbb{C}$	Field of complex numbers
$\circ$	Function composition operator ($f \circ x := f(x), f \circ g \circ x := f(g(x))$)
$\otimes$	Kronecker product
$\odot$	Hadamard produdct
$\mathbf{T}_{dm}$	Differential mode transformation
$\mathbf{T}_{ll}$	Line-to-line transformation
$\mathbf{T}_{\alpha\beta\gamma}$	Clarke transform
$\mathbf{T}_{\alpha\beta}$	Clarke transform without zero axis component
$\operatorname{diag}(\cdot)$	Block diagonal matrix function
$\operatorname{Im}(\cdot)$	Image of a linear map
$\ker(\cdot)$	Kernel of a linear map
$\operatorname{span}(\cdot)$	Linear span or hull of a set
$\operatorname{eigen}(\cdot)$	Eigenvalues of a matrix
x_i	i^{th} coordinate of vector x
$\mathbf{y}^j$	j^{th} vector of ordinated set y
$(x_i)_{i=1}^n$, $(x_1, \ldots, x_n)$ or $\mathbf{x}$	vector x in terms of its coordinates
$x_{m:n}$	$(x_i)_{i=m}^n$

$y_{j,i}$	i^{th} coordinate of the j^{th} vector of the ordinated set y
$(\mathbf{y}_j)_{i=1}^m$, $(\mathbf{y}_1, \ldots, \mathbf{y}_m)$ or $((y_{1,i})_{i=1}^n, \ldots, (y_{m,i})_{i=1}^n)$	ordinated set of vectors y
$\mathcal{L}(V, W)$	Space of all the linear maps of $V \to W$
$\langle x \rangle_h$	Dynamic phasor of x at harmonic component h
$\mathfrak{R}\{\cdot\}$	Real part of a complex number
$\mathfrak{I}\{\cdot\}$	Imaginary part of a complex number
$\mathbf{I}_n$	$n \times n$ identity matrix
$\mathbf{1}_{m\times n}$	$m \times n$ matrix of ones
$\mathbf{0}_{m\times n}$	$m \times n$ matrix of zeros
$\delta_{i,j}$	Kronecker delta
$\mathbf{A}^+$	Pseudo-inverse of matrix $\mathbf{A}$
$\mathrm{Tr}(\cdot)$	Trace of a matrix
$\exp(\cdot)$	Exponential function
$\succ \mathbf{0}$	Positive definite matrix
$\prec \mathbf{0}$	Negative definite matrix

Contents

Chapter

1 Introduction

1.1 CONTEXTUALIZATION

The increase in demand for power converters to interface different energy resources with the electric grid, especially for higher power applications, created the need for optimized designs of power converter systems. Over the last few decades, the state-of-the-art evolved in a way dictated by these trends, with estimates of the power density roughly doubling every ten years [3, 4]. However, the ever large scale of these systems demonstrates a need for higher modularity and reconfigurability as means to increase the availability and scalability of the afformentioned systems.

There have been an increase in studies on the series and parallel connection since the conception of distributed generation and microgrids as to make way for a more descentralized energy system generation, as opposed to legacy centralized systems, which demanded for high-power, high-voltage power systems. Some of these applications are extremelly dependent on the parallel connection of power converters to meet the energy processing requirements while improving the availability and maximizing the efficiency of the process.

The interest in parallel-connected inverters was first developed to increase the reliability of Uninterruptible Power Supplies (UPS) systems [5]. From that time, the control systems of paralleled converters aiming at a seamless connection was already discussed, with droop control strategies being proposed in [6] as means to emulate an impedance between power converters connected to the so called stiff systems as means of regulating the active and reactive power sharing between parallel-connected converters. This strategy gave way for a wide variety of control strategies based on the steady state values of the electrical quantities, which are reviewed in [7–11].

Currently, the most employed methods for stability analysis of parallel-connected power converters is based on the N-extra element theorem [12], which is useful for linear networks, as it provides simple restrictions on the input impedance of paralleled converters for controller design constraints. However, questions can be raised over the validity of the

analysis for nonlinear systems, as nonlinear dampings that can provide stability, as well as the operation with the presence of limited amplitude limit cycles are not considered due to the limitations of the linear analysis. This fact is more clear when operating at weak grid conditions, as opposed to a stiff grid connection which was the premisse of [6]. Hence, the behaviour of power converters when the Middlebrook's Criteria is not meet is still not fully described.

However, instabilities considering a nonlinear model are discussed in [13], where the nonlinearities of power converters were inserted in the model by means of continuous-discrete models and employing Poincaré maps and Floquet multipliers. That work presents a sliding mode control for the minimization of the circulating currents between converters, with the assumption that there is a central controller that measures all the involved variables. The work in [14] analyzes the bifurcations of the first order with models in the synchronous reference frame while employing a droop control strategy.

In the recent years, there has been an increase in demand for more faithful mathematical models representing such effects, which typically discard the eventual presence of harmonics [15] or take advantage of multiple-frequency averaging models [16] and Dynamic Phasor (DP) or Harmonic State-Space (HSS) approaches [17–19]. These approaches aim to perform and analyze the projection of the infinite-dimensional characteristic of Nonlinear Time-Periodic (NLTP) systems, which are described relating to state and input/disturbance variables expressed in terms of $L^2(\mathcal{P})$ functions with respect to a certain set $\mathcal{P}$, into a finite dimensional time-invariant space which can be complex- or real-valued depending on the adopted approach.

Still on the problem of harmonics, another problem that rises is in the operation of paralleled converters under distorted grid conditions. This problem was first discussed in [20], where a droop control is employed for the compensation of harmonic distortions, although the method is dependent on the real-time measurements of each harmonic component. These harmonics can also be compensated by means of a virtual impedance, which can be seen as a feedforward control of the disturbance. This compensation can be performed via proportional gains, resulting in a resistive impedance, and washout filters, which results in an inductive impedance [14]. However, these strategies are not suitable for higher frequencies, as they present low robustness to measurement noises.

The previous mentioned effects are related to the spectrum in which the control strategy presents a high degree of controllability, which are dependent on the control loops of each converter. However, there can be high-frequency circulating currents between converters due to the asymmetry of the high frequency components generated by the converters [1, 21–24]. In the case of converters with a common dc voltage bus, these effects are more pronounced since the impedance of the subtractive-mode (or differential-mode [25]) components is low when looking at a systemic approach, with the inclusion of a γ-axis circulating currents due to a current path for zero-axis components. These

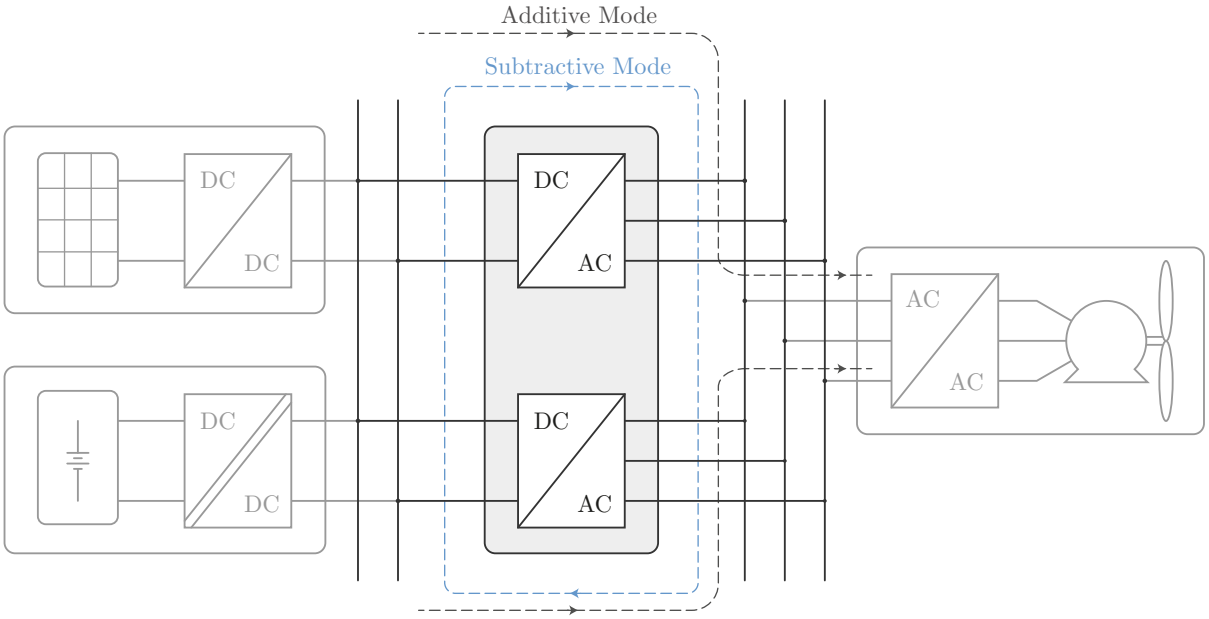

Figure 1.1 – Illustration of additive-mode and subtractive-mode currents in grid-tied power converter systems.

components are illustrated by Figure 1.1. Therefore, the instantaneous voltage differences can create the so called circulating currents, which can be of high-frequency, related to modulation characteristics, and medium-frequency, related to the feedforward action of the third-harmonic injection. Hence we can classify these circulating currents as:

i. Medium-frequency controllable circulating currents: currents mainly generated by parametric differences between power converters, due to a coupling between the subtractive and additive-mode, with the frequency spectrum inside the control bandwith of each inverter;

ii. Medium-frequency uncontrollable circulating currents: currents generated by resonances in loops of the output filter of power converters, and possibly with network elements, such as cables, transformers, which are not controlled, caused mainly by the dynamics of the disturbances;

iii. High-frequency circulating currents: currents generated by the modulation assymetry, which are mainly caused by the differences of modulation schemes, sensors, clock generation and carrier characteristics, such as the switching frequency and carrier phase.

1.2 MOTIVATION

From the modelling aspect, the state-of-the-art still does not present an unified modelling technique for power converters, and the effect of parametric variations of power converters is still not fully known. Linear analysis have been performed, usually based

on impedance analysis, although the validity of such analysis can be questioned, as the dynamic systems present an inherent nonlinear characteristic.

The coupling between synchronization algorithms and the control loops related to the operation of the power converters are not fully explored, and stability analysis based on these linear models can be equivocated.

Hence, the current work aims to present a framework for modelling paralleled connected three-phase dc-ac power converters and the interface between the dc and ac circuits, as means to explore the limits of the linear and nonlinear models to verify the behaviour of the dynamical system for multiple points of operation and under a multitude of transient responses. The models presented in this thesis are based on Nonlinear Harmonic State-Space.

An optimal method for the project of controller gains is also proposed, naturaly developed from the modeling, aiming to shape the impedance values at fixed frequencies, as means of designing a virtual impedance for power converters without a specific control loop. Hence the paralleled connected power converters present harmonic power sharing characteristic, which in turn minimizes subtractive mode components even for different converters, leading to a reduction of the circulating currents.

A nonlinear PLL model based on dynamic phasors was also obtained for the stationary reference frame, coupling the dynamic models of power converters, control loops and the reference generation, with the objective of assessing the system stability, especially under weak grid conditions for multiple points of equilibrium.

After minimizing the effects on medium-frequency circulating currents, a method for synchronizing the carriers via the zero axis was proposed, as means of minimizing the high-frequency circulating currents caused by asynchronous carriers.

The use of such framework can serve as a basis for stability assessment of power converter systems, especially under weak grid conditions. The presented methodology should also improve the robustness of control loops, while also verifying the feasibility and performance of the employed control strategies in a controlled environment while extending its uses for real applications.

1.3 OBJECTIVES

The main contributions of this work can be listed as:

- Development of generalized mathematical nonlinear models based of polyphase systems formulated from their state-space representation in the harmonic domain while taking parametric variations into account. This procedure employs the linear transformations of Clarke and Lunze and Harmonic State-Space theory and polytopic models, enabling the definition of differential- and common-mode impedances as means of verifying resonances between the paralelled converters;

- Definition of a harmonic state-space modeling framework based on the 2-D Fourier Transform and its extension to the multidimensional case as means of simplifying the analysis of the harmonic coupling between multi-frequency systems;
- Development of a nonlinear model of the SRF-PLL in the harmonic domain, which enables the investigation of loss-of-lock and nonlinear interactions between the inverter control loops and the inspection of instabilities and bifurcations due to the nonlinear behaviour of power converter systems, especially under weak grid conditions;
- Formulation of a nonlinear model employing the harmonic state-space for a solar photovoltaic system based on the temperature and irradiance of the photovoltaic cells and a power converter for maximum power point tracking that enables the investigation of dynamic interactions between ac and dc systems;
- Study of linear and nonlinear adaptive filtering techniques and proposal of a frequency estimator based on the widely linear estimation and an adaptive delayed-signal cancellation filter for operation under distorted grid conditions;
- Study of robust control techniques and linear matrix inequalities as means of obtaining an optimal control strategy based on the state-feedback control technique and proposal of a disturbance sliding-mode observer to estimate state-variables while taking into account disturbances due to modeling error;
- Methodology for the nonlinear stability assessment of power converter systems in the harmonic domain under weak grid conditions and verification of the behaviour of the power converter system input admittances for multiple points of operation based on the polytopic linear model approach;
- Proposal of a carrier synchronization technique to mitigate high frequency circulating currents between paralleled power converters and validation of the proposed strategies implemented in a FPGA and hardware-in-the-loop.

The minor contributions can be listed as

- Obtention of a 2-D Fourier Transform-based model for an Indirect Matrix Converter;
- Definition of a time-invariant model for a Three-Phase Series Resonant Converter;
- Study of linear and nonlinear adaptive filtering techniques and proposal of a frequency estimator based on the widely linear estimation and an adaptive delayed-signal cancellation filter for operation under distorted grid conditions.

1.4 METHODOLOGY AND ORGANIZATIONAL STRUCTURE

The present work was divided into four chapters, each approaching a different aspect inherent to the operation of power converter systems or a solution to a problem detected in a previous step, and two appendices.

The first chapter presents a procedure for the obtention of mathematical models for paralleled power converters considering parameter mismatchings and unbalances, as well as models for dc-dc and ac-ac converters.

The second chapter discusses the state-feedback control strategy that is employed, a state estimator to reduce the amount of required sensors.

The third chapter presents a model for reference generation based on a voltage feedback and synchronization algorithms, as well as the stability assessment of grid-connected power converters operating under weak grid conditions.

The fourth chapter presents a method to synchronize the carriers of power converters as means to reduce the circulating currents.

Appendix A demonstrates the implementaiton of a frequency estimator, and discusses further improvements in the accuracy of the estimation.

Appendix B presents a short review on linear adaptive filters and a study on basic concepts related to Artificial Neural Networks.

CHAPTER

2 PRELIMINARIES

In this chapter, we briefly discuss some topics which are relevant to a thorough understanding of the sequel. In a first moment, we aim to define the harmonic-domain variables and basic operations, which are further explored in the following chapters as means of describing more complex nonlinear time-variant dynamic systems with their time invariant counterparts.

2.1 LOCAL AVERAGE VALUE

The average value of a time-variant signal $s \in L^2(\mathbb{C})$ on a time window $h \in \mathbb{R}$ is here defined as

$$\langle s(t) \rangle_0 = \frac{1}{h} \int_{t-h}^{t} s(\tau) \, \mathrm{d}\tau. \tag{2.1}$$

This approach is widely used in power electronics systems to reduce the mathematical complexity of switched systems while sacrificing the model accuracy, with its limitation given by Shannon's Theorem due to the possible aliasing resulting of couplings between the harmonic components of s.

However, this approach does not guarantee that $\langle s \rangle_0$ is time-invariant, due to the possibility of modulating a lower frequency signal as in ac power converter systems. An alternative is to find a system described by $\langle s \rangle := (\langle s \rangle_k)_{k=-\infty}^{\infty}$, with s written as a linear combination of all the harmonic components.

2.2 LINEAR TRANSFORMATIONS

Let V, W two linear spaces spanning over a certain field $\mathbb{F}$. A linear transformation (or linear map) is a mapping $T : V \to W$, with $T \in \mathcal{L}(V, W)$. In this context, we emphasize two important linear maps employed in this work: the **Clarke Transformation**, related to three-phase systems, and the **Lunze Transformation**, related to large scale systems [25].

2.2.1 Clarke Transformation

Let $V \approx W \approx \mathbb{R}^3$ an automorphism of V and W, with $v \in V$ a three-phase vector representing a determined electrical quantity, and let $w \in W$ a three-phase vector in $\alpha\beta\gamma$ coordinates. Let the ordered basis $\mathcal{B}_c$ as the canonical basis employed for the system in *abc* coordinates and $\mathcal{B}_{\alpha\beta\gamma}$ as the ordered basis for the linear space in $\alpha\beta\gamma$ coordinates. The Clarke Transformation consists in finding a basis for V such that $\left\langle \mathcal{B}^k_{\alpha\beta\gamma} \right\rangle = \langle (1,1,1) \rangle$ for the k^{th} basis vector. Therefore, the **Amplitude Invariant Clarke Transformation** is obtained by taking $\mathcal{B}_{\alpha\beta\gamma} = \left(\left(\frac{2}{3}, 0, \frac{1}{3} \right); \left(-\frac{1}{3}, \frac{\sqrt{3}}{3}, \frac{1}{3} \right); \left(-\frac{1}{3}, -\frac{\sqrt{3}}{3}, \frac{1}{3} \right) \right)$ and the **Power Invariant Clarke Transformation** is obtained by applying the Gram-Schmidt process, resulting in $\hat{\mathcal{B}}_{\alpha\beta\gamma} = \left(\left(\frac{2}{\sqrt{6}}, 0, \frac{1}{\sqrt{3}} \right); \left(-\frac{1}{\sqrt{6}}, \frac{1}{\sqrt{2}}, \frac{1}{\sqrt{3}} \right); \left(-\frac{1}{\sqrt{6}}, -\frac{1}{\sqrt{2}}, \frac{1}{\sqrt{3}} \right) \right)$

From this, the transformation matrices for both transformations can be defined as the change of basis matrices from $\mathcal{B}_c$ to $\mathcal{B}_{\alpha\beta\gamma}$ or $\hat{\mathcal{B}}_{\alpha\beta\gamma}$, and expressed by

$$[\mathbf{T}_{\alpha\beta\gamma}] = \frac{1}{3} \begin{bmatrix} 2 & -1 & -1 \\ 0 & \sqrt{3} & -\sqrt{3} \\ 1 & 1 & 1 \end{bmatrix}, \quad \left[\bar{\mathbf{T}}_{\alpha\beta\gamma}\right] = \frac{1}{\sqrt{6}} \begin{bmatrix} 2 & -1 & -1 \\ 0 & \sqrt{3} & -\sqrt{3} \\ \sqrt{2} & \sqrt{2} & \sqrt{2} \end{bmatrix}, \tag{2.2}$$

respectively. In some cases, the analysis of components pertaining to the γ (or zero) axis is suppressed. Thus, we can define a new linear map $\mathbf{T}_{\alpha\beta} : \mathbb{R}^3 \to \mathbb{R}^2$ by making $\ker(\mathbf{T}_{\alpha\beta}) = \langle (1,1,1) \rangle$ such that $w_{1:2}$ is the projection of v on the $\alpha\beta$ plane.

In a more general sense, any linear map $\mathbf{T} \in \mathcal{L}(V, W)$ such that $\ker(\mathbf{T}) = \langle (1, \ldots, 1) \rangle$ is henceforth defined as a subtractive mode transformation, as discussed in the following topic.

2.2.2 Lunze Transformation

Let V and W two n-dimentional linear spaces spanning over a certain field $\mathbb{F}$, such that $\mathcal{B}_v = \mathcal{B}_c$ is a basis for V and $\mathcal{B}_w = (b^i)_{i=1}^n$ such that

$$b^i_j = \begin{cases} \dfrac{\delta_{i,j} n - 1}{n}, & i = 1 \ldots n-1 \\ \dfrac{1}{n}, & i = n. \end{cases},$$

where $\mathbf{I}_l$ is a $l \times l$ identity matrix.

The linear map $\mathbf{L} : V \to W$ is defined as the change of basis from $\mathcal{B}_v$ to $\mathcal{B}_w$, with

the matrix with respect to $\mathbf{L}$ defined as

$$[\mathbf{L}] = \frac{1}{n}\begin{bmatrix} n-1 & -1 & \cdots & -1 & -1 \\ -1 & n-1 & \cdots & -1 & -1 \\ \vdots & \vdots & \ddots & \vdots & \vdots \\ -1 & -1 & \cdots & n-1 & -1 \\ 1 & 1 & \cdots & 1 & 1 \end{bmatrix}. \tag{2.3}$$

From inspection, the linear map $\mathbf{L}$ is not orthonormal. However, the Gram-Schmidt process can be applied to $\mathbf{L}$, resulting in the linear map $\hat{\mathbf{L}}$. Also, the linear space W can be decomposed as a the sum of subtractive and additive modes, as in $W = W_{sm} + W_{am}$, where $W_{am} = \text{span}\left((1, \ldots, 1)\right)$. The subtractive mode can be decomposed into $n-1$ components, as in $W_{sm} = \sum_{i=1}^{n-1} W_{sm,i}$. If W can be written as the direct sum of each differential mode and the common mode component, the system is said to be decoupled.

Most of the times, it is not possible to decouple into n one-dimensional sub-spaces, hence the matrix with respect to the Lunze transformation can be rewritten as

$$[\mathbf{L}] = \frac{1}{n}\begin{bmatrix} (n-1)\mathbf{I}_l & -\mathbf{I}_l & \cdots & -\mathbf{I}_l & -\mathbf{I}_l \\ -\mathbf{I}_l & (n-1)\mathbf{I}_l & \cdots & -\mathbf{I}_l & -\mathbf{I}_l \\ \vdots & \vdots & \ddots & \vdots & \vdots \\ -\mathbf{I}_l & -\mathbf{I}_l & \cdots & (n-1)\mathbf{I}_l & -\mathbf{I}_l \\ \mathbf{I}_l & \mathbf{I}_l & \cdots & \mathbf{I}_l & \mathbf{I}_l \end{bmatrix}, \tag{2.4}$$

aiming to decompose the system into smaller l-dimensional ($l < n$) independent sub-spaces.

This approach is useful for large-scale systems, as to treat a large system into smaller independent (or weakly coupled) systems.

2.2.3 Clarke-Lunze Transformation

We can also define the Clarke transformation matrix for a system with $3N$ components as

$$\mathbf{T}^N_{\alpha\beta\gamma} := \mathbf{I}_N \otimes \mathbf{T}_{\alpha\beta\gamma} \tag{2.5}$$

by applying the Clarke transformation for each group of states in the *abc* axis, where $\otimes$ is the Kronecker product. We can also apply the Lunze transformation matrix for each set of α, β and γ components, with its matrix defined as

$$\mathbf{L}_{N,3} := \mathbf{L}_N \otimes \mathbf{I}_3, \tag{2.6}$$

Thus, we can apply the two transformations, which results in the Lunze-Clarke Transformation, defined as

$$\mathbf{Q}_N := \mathbf{L}_{N,3} \otimes \mathbf{T}_{\alpha\beta\gamma}. \tag{2.7}$$

With this, we have that

$$\mathrm{Im}\left(\mathbf{Q}_N\right) = \{u_{\alpha,am}, \mathbf{u}_{\alpha,sm}, u_{\beta,am}, \mathbf{u}_{\beta,sm}, u_{\gamma,am}, \mathbf{u}_{\gamma,sm}\} \tag{2.8}$$

2.3 DYNAMIC PHASORS AND HARMONIC STATE-SPACE MODELS

2.3.1 Definition of Dynamic Phasors

Let the Lebesgue square integrable functions defined for complex-valued functions be defined by the vector-space

$$L^2(\mathbb{C}) := \left\{ f : \mathbb{C} \to \mathbb{C} : \int_{-\infty}^{\infty} f^* f \ \mathrm{d}t < \infty \right\}. \tag{2.9}$$

Thus, let us define the space $L^2(\mathbb{C}^N)$ for $N \in \mathbb{N}$ as

$$L^2(\mathbb{C}^N) := \left\{ f : \mathbb{C}^N \to \mathbb{C}^N : \int_{-\infty}^{\infty} f^H f \ \mathrm{d}t < \infty \right\}, \tag{2.10}$$

where $(\cdot)^H$ is the Hermitian operator. From this, we can define the inner-product for $f, g \in L^2(\mathbb{C}^N)$ as

$$\langle f, g \rangle := \left(\int_{-\infty}^{\infty} f^H g \ \mathrm{d}t \right)^{\frac{1}{2}}. \tag{2.11}$$

The general idea of the generalized dynamic phasors (DP) and the Harmonic State-Space (HSS) is to treat coefficients of the Fourier Transform of assumed sinusoidal functions to model fast dynamics related to time-periodic systems aiming to obtain time-invariant models. Thus, let a generic time-varying signal $r \in L^2(\mathbb{C})$ be described by

$$r(t) = \sum_{h=-\infty}^{\infty} r_h(t) = \sum_{h=-\infty}^{\infty} \langle r(t) \rangle_h e^{\iota h \theta(t)}, \tag{2.12}$$

where $\iota^2 := -1$ and

$$\theta = \theta_0 + \int_{-\infty}^{t} \omega(\tau) \ \mathrm{d}\tau.$$

Note that if $r \in L^2(\mathbb{R})$, we have that

$$r(t) = 2 \sum_{h=0}^{\infty} \mathfrak{R} \left\{ \langle r(t) \rangle_h e^{\iota h \theta(t)} \right\} \tag{2.13}$$

as $\langle r \rangle_{-h} = \langle r \rangle_h^*, \forall k \in \mathbb{Z}$, which will be mostly true for the cases studied in this thesis. The set $\langle r \rangle$ will be called the set of dynamic phasors of r henceforth.

2.3.2 Linear Time-Variant Models

Let a linear state-space model of a certain dynamic system be described by

$$D_t\mathbf{x} = \mathbf{A}\mathbf{x} + \mathbf{B}\mathbf{u}, \tag{2.14}$$

where D_t is the derivative operator with respect to t, $\mathbf{A} \in \mathbb{R}^{n_x \times n_x}$, $\mathbf{B} \in \mathbb{R}^{n_x \times n_u}$, $\mathbf{x} \in \mathcal{X} \subseteq L^2(\mathbb{R}^{n_x})$ and $\mathbf{u} \in \mathcal{U} \subseteq L^2(\mathbb{R}^{n_u})$, in a manner that

$$\begin{aligned} x_i(t) &:= \sum_{k=-\infty}^{\infty} x_{i,k}(t) = \sum_{k=-\infty}^{\infty} \langle x_i(t) \rangle_k e^{\iota k\theta(t)} \\ u_i(t) &:= \sum_{k=-\infty}^{\infty} u_{i,k}(t) = \sum_{k=-\infty}^{\infty} \langle u_i(t) \rangle_k e^{\iota k\theta(t)}, \end{aligned} \tag{2.15}$$

$\forall i \in \mathbb{N}^{n_x}$, where $\langle x \rangle_k$ is the k^{th} harmonic dynamic phasor for an arbitrary angle

$$\theta := \theta_0 + \int_{-\infty}^{t} \omega(\tau) \mathrm{d}\tau. \tag{2.16}$$

Thus, the HSS model of (2.14) can be written in accordance with

$$\begin{aligned} D_t \langle \mathbf{x} \rangle &= (\mathbf{I}_\infty \otimes \mathbf{A} - \mathbf{G}) \langle \mathbf{x} \rangle + (\mathbf{I}_\infty \otimes \mathbf{B}) \langle \mathbf{u} \rangle \\ \mathbf{G} &:= \operatorname{diag}(\mathbb{Z}) \otimes \iota\omega \mathbf{I}_{n_x}, \end{aligned} \tag{2.17}$$

where $\left\{ \langle \mathbf{x} \rangle \in \ell^2(\mathbb{C}^{n_x}) : \langle \mathbf{x} \rangle = (\langle \mathbf{x} \rangle_k)_{-\infty}^{\infty} \right\}$ is the set of dynamic phasors of $\mathbf{x}$ and $\otimes$ is the tensor product. The HSS model can be truncated for a finite number of harmonics $n_h < \aleph_0$, assuming that the system has a low-pass characteristic when $\omega \to \infty$, as the characteristic polynomial of the HSS system, which is given by

$$\begin{aligned} p(\lambda) &= \det(\lambda \mathbf{I} - (\mathbf{I}_\infty \otimes \mathbf{A} - \mathbf{G})) \\ &= \prod_{k=-\infty}^{\infty} \det((\lambda - \iota k\omega)\mathbf{I} - \mathbf{A}), \end{aligned} \tag{2.18}$$

as $\lambda_k \to \iota k\omega$ for larger values of $|k|$. In this case,

$$\operatorname{span}(D_t\langle \mathbf{x} \rangle) = \bigoplus_{k=-\infty}^{\infty} \operatorname{span}(D_t \langle \mathbf{x} \rangle_k) \approx \bigoplus_{h=-n_h}^{n_h} \operatorname{span}(D_t \langle \mathbf{x} \rangle_k), \tag{2.19}$$

for

$$\mathbf{x} = \sum_{h=-\infty}^{\infty} \langle \mathbf{x} \rangle_h e^{\iota(h\omega t + \theta_0)} \approx \sum_{h=-n_h}^{n_h} \langle \mathbf{x} \rangle_h e^{\iota(h\omega t + \theta_0)}, \tag{2.20}$$

as each frequency subspace is decoupled. From inspection of (2.19), in this case the stability assesment can be performed directly through the computation of the eigenvalues of $\mathbf{A}$

since $\Re\{\lambda\}$ remains unaltered.

The Harmonic State-Space and Dynamic Phasor models are related by the linear map $f : \mathbb{C}^2 \to \mathbb{R}^2$ such that

$$\begin{bmatrix} \Re\{\langle x\rangle_h\} \\ \Im\{\langle x\rangle_h\} \end{bmatrix} = \frac{1}{2}\begin{bmatrix} 1 & 1 \\ \iota & -\iota \end{bmatrix}\begin{bmatrix} \langle x\rangle_{-h} \\ \langle x\rangle_h \end{bmatrix} \tag{2.21}$$

for a certain harmonic component h. Note that f is bijective if x is real-valued, which guarantees the interchangeability between HSS and DP models. From this, we can define a linear map $\boldsymbol{\Psi} : \ell^2(\mathbb{C}) \to \ell^2(\mathbb{R})$ so that $(\Re\{\langle x\rangle\}, \Im\{\langle x\rangle\}) = \boldsymbol{\Psi} \circ \langle x\rangle$, where

$$\boldsymbol{\Psi} = \frac{1}{2}\begin{bmatrix} \mathbf{I} & \mathbf{0} & \mathbf{J} \\ \mathbf{0} & 1 & \mathbf{0} \\ \iota\mathbf{I} & \mathbf{0} & -\iota\mathbf{J} \end{bmatrix} \tag{2.22}$$

and $\mathbf{J}$ is an exchange (or backward identity) matrix. We can also define a linear map $\boldsymbol{\Psi}_n : \ell^2(\mathbb{C}^n) \to \ell^2(\mathbb{R}^n)$ as

$$\boldsymbol{\Psi}_n = \boldsymbol{\Psi} \otimes \mathbf{I}_n, \tag{2.23}$$

leading to $(\Re\{\langle \mathbf{x}\rangle\}, \Im\{\langle \mathbf{x}\rangle\}) = \boldsymbol{\Psi}_{n_x} \circ \langle \mathbf{x}\rangle$.

2.3.3 Polynomial Nonlinear Systems

Let $u, v \in L^2(\mathbb{R})$. From the convolution properties of the Fourier Transform, we can write the multiplication of both signals in the time domain as the convolution in the frequency domain. Since $\langle u\rangle, \langle v\rangle \in \ell^2(\mathbb{C})$, the operation turns into a discrete convolution given by

$$\langle uv\rangle_h = \sum_{j=-\infty}^{\infty} \langle u\rangle_j \langle v\rangle_{h-j} \tag{2.24}$$

for each harmonic component $h \in \mathbb{N}$. We can also employ the **Toeplitz Operator** $\boldsymbol{\Gamma}(\cdot)$ defined by (2.25) as means of solving (2.24), resulting in

$$\boldsymbol{\Gamma} \circ \langle u\rangle = \begin{bmatrix} \langle u\rangle_0 & \langle u\rangle_{-1} & \cdots & \langle u\rangle_{-h} & & & \\ \langle u\rangle_1 & \ddots & \ddots & \ddots & \ddots & & \\ \vdots & \ddots & \langle u\rangle_0 & \langle u\rangle_{-1} & \ddots & \ddots & \\ \langle u\rangle_h & \ddots & \langle u\rangle_1 & \langle u\rangle_0 & \langle u\rangle_{-1} & \ddots & \langle u\rangle_{-h} \\ & \ddots & \ddots & \langle u\rangle_1 & \langle x\rangle_0 & \ddots & \vdots \\ & & \ddots & \ddots & \ddots & \ddots & \langle u\rangle_{-1} \\ & & & \langle u\rangle_h & \cdots & \langle u\rangle_1 & \langle u\rangle_0 \end{bmatrix} \tag{2.25}$$

$$\langle uv \rangle = (\mathbf{\Gamma} \circ \langle u \rangle) \circ \langle v \rangle \,. \tag{2.26}$$

From (2.26), we can write the dynamic phasor for the powers of a signal as

$$\begin{aligned}
\langle u \rangle &= \left(\mathbf{\Gamma}^0 \circ \langle u \rangle\right) \circ \langle u \rangle \\
\left\langle u^2 \right\rangle &= (\mathbf{\Gamma} \circ \langle u \rangle) \circ \langle u \rangle \\
\left\langle u^3 \right\rangle &= (\mathbf{\Gamma} \circ ((\mathbf{\Gamma} \circ \langle u \rangle) \circ \langle u \rangle)) \circ \langle u \rangle = \left(\mathbf{\Gamma}^2 \circ \langle u \rangle\right) \circ \langle u \rangle = (\mathbf{\Gamma} \circ \langle u \rangle)^2 \circ \langle u \rangle \\
\langle u^n \rangle &= \left(\mathbf{\Gamma}^{n-1} \circ \langle u \rangle\right) \circ \langle u \rangle = (\mathbf{\Gamma} \circ \langle u \rangle)^{n-1} \circ \langle u \rangle \,,
\end{aligned} \tag{2.27}$$

which is useful for expressing polynomial dynamical systems. The following discussions present an approximation of more complex systems in terms of polynomial systems.

2.3.4 Exponential Function Model

Let $u, v \in L^2(\mathbb{R})$, defining the signal v as

$$v := \exp(u) \,. \tag{2.28}$$

We can then rewrite v relating to the dc component $\langle u \rangle_0$ as

$$v = \exp(\langle u \rangle_0) \exp(u - \langle u \rangle_0) = \exp(\langle u \rangle_0) \exp(w) \,, \tag{2.29}$$

where $w := u - \langle u \rangle_0$ and $\langle w \rangle = \langle u \rangle|_{\langle u \rangle_0 = 0}$. Thus, (2.29) can be expressed in terms of its Taylor Series expansion centered at $w = 0$ as

$$\exp(u) = \exp(\langle u \rangle_0) \sum_{n=0}^{\infty} \frac{w^n}{n!}. \tag{2.30}$$

Note that for practical models, it might be useful to truncate this series by assuming

$$\exp(u) = \exp(\langle u \rangle_0) \sum_{n=0}^{N} \frac{w^n}{n!}, \quad \forall N \in \mathbb{Z}^+. \tag{2.31}$$

From the previous subsection and (2.30), it is possible to infer that

$$\langle \exp(u) \rangle = e^{\langle u \rangle_0} \left(\hat{h}_0 + \sum_{n=1}^{\infty} \frac{1}{n!} \left(\mathbf{\Gamma}^{n-1} \circ \langle w \rangle\right) \circ \langle w \rangle \right), \tag{2.32}$$

which can be truncated to ease the analysis and computational burden when employing the presented model in a simulation. Figure 2.1 shows the behaviour of the approximation given by (2.32) for an arbitrary signal considering multiple truncation values of the Taylor series to verify the validity of the approximation. The considered phasors are defined in

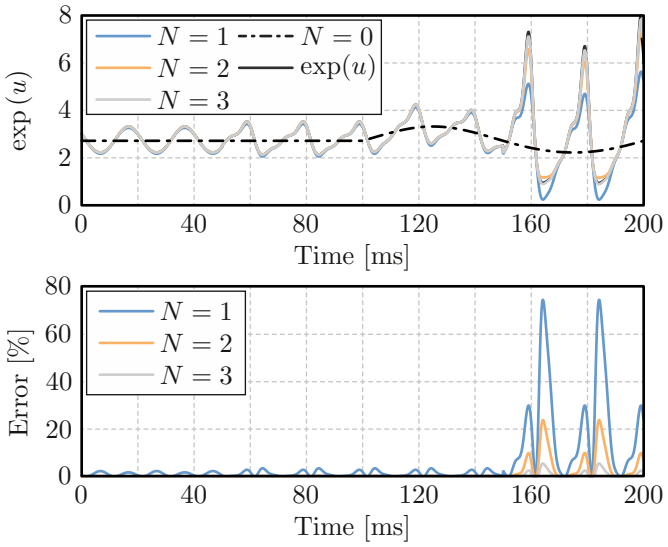

Figure 2.1 – Approximation of the exponential function employing the HSS model truncated at the 9^{th} harmonic for multiple Taylor series truncation values (N) with respect to the signal u with amplitudes given by Table 2.1. The error is defined as the relative error between the real valued function and the projection of the approximation onto the $L^2(\mathbb{R})$ space.

Table 2.1 – Exponential Function Parameters for Model Validation

t [ms]	0–50	50–100	100–150	150–200
$\langle u \rangle_0$	1	1	$1 + 0.2\sin(20\pi t)$	$1 + 0.2\sin(20\pi t)$
$\langle u \rangle_1$	$0.1e^{\iota\frac{\pi}{3}}$	$0.1e^{\iota\frac{\pi}{3}}$	$0.1e^{\iota\frac{\pi}{3}}$	$0.4e^{\iota\frac{\pi}{3}}$
$\langle u \rangle_2$	0	$0.04e^{\iota\frac{\pi}{6}}$	$0.04e^{\iota\frac{\pi}{6}}$	$0.16e^{\iota\frac{\pi}{6}}$
$\langle u \rangle_3$	0	$0.02e^{\iota\frac{\pi}{12}}$	$0.02e^{\iota\frac{\pi}{12}}$	$0.08e^{\iota\frac{\pi}{12}}$
$\langle u \rangle_4$	0	0	0	$0.04e^{\iota\frac{\pi}{6}}$

Table 2.1.

The exponential function serves as a basis for more complex functions, such as trigonometric functions. These can constitute rotations of two-dimensional (2-D) vectors, as in the Park transformation, which is further discussed in the following section.

2.3.5 Division Between Two Real-Valued Signals

Let $u, v \in L^2(\mathbb{R}), v(t) > 0\ \forall t \in \mathbb{R}$. Also, let $\langle v \rangle_0 > 0$ as the dc component of the denominator, resulting in

$$\frac{u}{v} = \frac{u}{\langle v \rangle_0} \frac{1}{1 + \frac{w}{\langle v \rangle_0}}, \tag{2.33}$$

where $w := v - \langle v \rangle_0 \hat{h}_0$. We can then express (2.33) in term of its Taylor Series as

$$\frac{u}{v} = \frac{u}{\langle v \rangle_0} \sum_{n=0}^{\infty} \left(\frac{w}{\langle v \rangle_0} \right)^n, \tag{2.34}$$

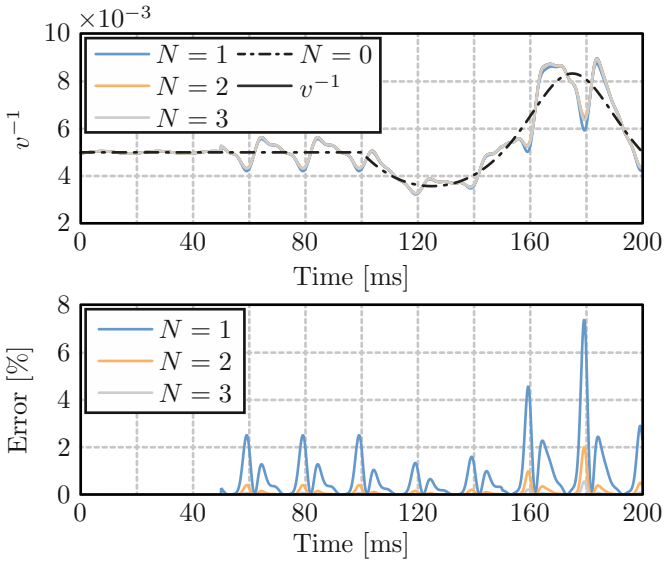

Figure 2.2 – Inverse function HSS model approximation truncated at the 9^{th} harmonic for multiple Taylor series truncation values(N) with respect to the signal v given by Table 2.2. The error is defined as the relative error between the real valued function and the projection of the approximation onto the $L^2(\mathbb{R})$ space.

assuming that $|w| < \langle v \rangle_0$ due to the series region of convergence. Then, from inspection of (2.34), we can define the dynamic phasor of the inverse operator as

$$\left\langle \frac{1}{v} \right\rangle = \frac{\hat{h}_0}{\langle v \rangle_0} + \sum_{n=1}^{\infty} \frac{(-1)^n}{\langle v \rangle_0^{n+1}} \left(\mathbf{\Gamma}^{n-1} \circ \langle w \rangle \right) \circ \langle w \rangle \tag{2.35}$$

and the dynamic phasor of the division between u and v as

$$\boldsymbol{h}_{div}(u, v) := \left\langle \frac{u}{v} \right\rangle = \sum_{n=0}^{\infty} \frac{(-1)^n}{\langle v \rangle_0^{n+1}} \left(\mathbf{\Gamma}^{n} \circ \langle w \rangle \right) \circ \langle u \rangle \,. \tag{2.36}$$

Figures 2.2 and 2.3 demonstrate the behaviour of the proposed approximation for the inverse and division of arbitrary signals, validating the approximation.

2.3.6 Windowed RMS Filter

Let $u \in L^2(\mathbb{R})$. The Windowed Root Mean Square (RMS) Filter consists in calculating the norm of the input signal u for a certain time window $T_w \in \mathbb{R}$, which can be defined by the application $f : L^2(\mathbb{R}) \to L^2(\mathbb{R})$ such that

$$(f \circ u)(t) := \left(\frac{1}{T_w} \int_{t-T_w}^{t} u^2(\tau) \mathrm{d}\tau \right)^{\frac{1}{2}} \tag{2.37}$$

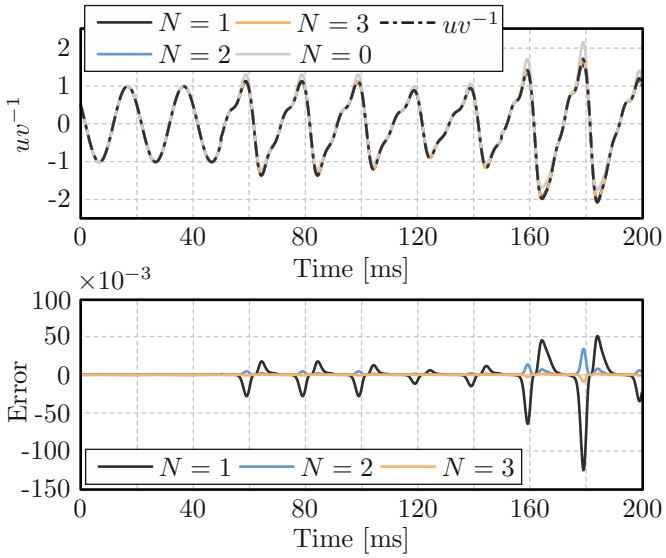

Figure 2.3 – Division of two signals employing the inverse function HSS model approximation truncated at the 9^{th} harmonic for multiple Taylor series truncation values (N) with respect to signals u, v given by Table 2.2. The error is defined as the absolute error between the real valued function and the projection of the approximation onto the $L^2(\mathbb{R})$ space.

Table 2.2 – Parameters for Division Model Validation

t [ms]	0–50	50–100	100–150	150–200
$\langle u \rangle_0$	0	0	$10\sin(20\pi t)$	$10\sin(20\pi t)$
$\langle u \rangle_1$	$100e^{\iota\frac{\pi}{3}}$	$100e^{\iota\frac{\pi}{3}}$	$100e^{\iota\frac{\pi}{3}}$	$100e^{\iota\frac{\pi}{3}}$
$\langle u \rangle_2$	0	$40e^{\iota\frac{\pi}{6}}$	$40e^{\iota\frac{\pi}{6}}$	$40e^{\iota\frac{\pi}{6}}$
$\langle u \rangle_3$	0	$20e^{\iota\frac{\pi}{12}}$	$20e^{\iota\frac{\pi}{12}}$	$0.20e^{\iota\frac{\pi}{12}}$
$\langle u \rangle_4$	0	0	0	$10e^{\iota\frac{\pi}{6}}$
$\langle v \rangle_0$	200	200	$200 + 80\sin(20\pi t)$	$200 + 80\sin(20\pi t)$
$\langle v \rangle_1$	$e^{\iota\frac{\pi}{4}}$	$10e^{\iota\frac{\pi}{4}}$	$10e^{\iota\frac{\pi}{4}}$	$10e^{\iota\frac{\pi}{4}}$
$\langle v \rangle_2$	0	$5e^{\iota\frac{\pi}{6}}$	$5e^{\iota\frac{\pi}{6}}$	$50e^{\iota\frac{\pi}{6}}$
$\langle v \rangle_3$	0	$2.5e^{\iota\frac{\pi}{12}}$	$2.5e^{\iota\frac{\pi}{12}}$	$2.5e^{\iota\frac{\pi}{12}}$
$\langle v \rangle_4$	0	0	0	$e^{\iota\frac{\pi}{6}}$

for a certain time instant $t \in \mathbb{R}$, such that $u(t) = 0,\ \forall t < 0$. From this, we can rewrite (2.37) as

$$\left((f \circ u)(t)\right)^2 = \left((f \circ u)(t - T)\right)^2 + \frac{1}{T_w}\left(\int_{t-T}^{t} u^2(\tau)\mathrm{d}\tau - \int_{t-T-T_w}^{t-T_w} u^2(\tau)\mathrm{d}\tau\right) \tag{2.38}$$

in its recursive form for a given $T \in \mathbb{R} : T_w = NT$ for $N \in \mathbb{N}$. A valid approximation is to let $u(t)$ constant for a time period given by delta, with the assumption that

$$u(t - kT) = u(t - T),\ \forall k \in \mathbb{R} : 0 < k < 1 \tag{2.39}$$

by employing a Zero-Order Holder (ZOH), which is mostly true for discrete-time systems, resulting in

$$\left((f \circ u)(t)\right)^2 = \left((f \circ u)(t-T)\right)^2 + \frac{1}{N}\left(u^2(t) - u^2(t-T_w)\right). \tag{2.40}$$

Since the local RMS filter exhibits a low-pass characteristic, which is attributed to its windowed average nature, we can safely discard its harmonic components while focusing on the dc component as means of avoiding to perform the square root functions. Thus, the dc-component can be expressed as

$$\langle u^2 \rangle_0 = \sum_{k=-\infty}^{\infty} \langle u \rangle_k \langle u \rangle_{-k} = \langle u \rangle^H \langle u \rangle = \langle u \rangle \mathbf{J} \langle u \rangle \tag{2.41}$$

where $\mathbf{J}$ is the reverse identity matrix. Thus, the system dynamic equations given by (2.40) can be approximated by

$$\begin{cases} \mathbf{x} = \mathbf{A}_{\text{ZOH}}\mathbf{x} + \mathbf{B}_{\text{ZOH}} \langle u \rangle \mathbf{J} \langle u \rangle \\ y = \left(\mathbf{C}_{\text{ZOH}}\mathbf{x} + \mathbf{D}_{\text{ZOH}} \langle u \rangle \mathbf{J} \langle u \rangle\right)^{\frac{1}{2}} \end{cases} \tag{2.42}$$

where the set $(\mathbf{A}_{\text{ZOH}}, \mathbf{B}_{\text{ZOH}}, \mathbf{C}_{\text{ZOH}}, \mathbf{D}_{\text{ZOH}})$ can be obtained via the Padé approximation for a time delay of one time window T_w due to the negligence of the time delay T since $T \ll T_w$.

The control of the RMS value can be interpreted as an energy control, where the objective is to regulate the energy of a signal according to a specific norm, in this case the norm defining the $L^2(\mathbb{R}, [0, T_w])$ space. This concept is also discussed in [26] for the capacitor voltage balancing methodology for Modular Multilevel Converters (MMCs) with an infinite window, which in turn solves for an integrator model.

One of the limitations of using the RMS value as a measure of signal amplitude is that it increases when harmonics are present in the signal. Therefore, if the objective is to accurately model the amplitude of a specific harmonic component, more sophisticated methods are required.

To address this, several techniques can be employed. One approach is to use a band-pass pre-filter that selectively allows the desired harmonic frequency band to pass through while attenuating other frequencies. This helps isolate the specific harmonic of interest and facilitates accurate amplitude measurement.

Another method involves utilizing a Phase-Locked Loop (PLL) or Frequency-Locked Loop (FLL) algorithm with voltage estimation. These algorithms track the phase and frequency of the desired harmonic and provide estimates of the harmonic's amplitude based on the acquired voltage information.

Additionally, signal processing algorithms based on the Discrete Fourier Transform

(DFT) can be utilized. The DFT allows decomposition of a signal into its frequency components, providing information about the amplitudes of different harmonics. By employing DFT-based methods, specific harmonic amplitudes can be estimated by analyzing the spectral content of the signal.

The DFT algorithm can be evaluated through the insertion of a ZOH in the same manner as the Windowed RMS filter. Thus, the RDFT of u can be written as

$$\langle u \rangle_1(kT) = \frac{1}{N} \sum_{i=0}^{W-1} u((k-i)T) \exp\left(-\iota \frac{2\pi}{W} \mathrm{rem}(k-i, N)\right) \tag{2.43}$$

for $k \in \mathbb{N}$, which can be rewritten by employing its inherent recursivity as

$$\langle u \rangle_1(kT) = \langle u \rangle_1((k-1)T) + \frac{1}{N} \left(u(kT) - u((k-N-1)T)\right) \exp\left(-\iota \frac{2\pi}{W} \mathrm{rem}(k, N)\right) \tag{2.44}$$

for a window with N samples. The filter output is then defined as

$$y(kT) = |\langle u \rangle_1(kT)| \tag{2.45}$$

In the same manner as the RMS filter, the delay introduced by the dynamic system is given by T_w, which is the same as the fundamental period. An additional moving average filter can be cascaded in case of a small frequency mismatch, increasing the transport delay to two fundamental periods.

2.4 PARK TRANSFORMATION THROUGH A DYNAMIC PHASOR APPROACH

2.4.1 Synchronous Spacial Rotation of a Two-Dimensional Vector

Let $\mathbf{u}_{abc} \in \mathbb{R}^3$ a generic three-phase electrical quantity. Let us also define a complex voltage signal $\bar{u}$, which results from the projection of a three-phase electrical quantity vector onto the $\alpha\beta$ plane through the Clarke Transformation as in

$$\bar{u} := \begin{bmatrix} 1 & e^{-\iota\frac{2}{3}\pi} & e^{\iota\frac{2}{3}\pi} \end{bmatrix} \mathbf{u}_{abc} \tag{2.46}$$

in its complex form, or

$$\mathbf{u} := \left(\Re\left\{\bar{u}\right\}, \Im\left\{\bar{u}\right\}\right) = (u_\alpha, u_\beta) \tag{2.47}$$

in its real form. We can then write $\bar{u} \in L^2(\mathbb{C})$ such that

$$\begin{aligned} \bar{u} &= \sum_{n=-\infty}^{\infty} \langle u_\alpha \rangle_n e^{\iota n\omega t} + \iota \langle u_\beta \rangle_n e^{\iota n\omega t} \\ &= \langle u_\alpha \rangle_0 + \iota \langle u_\beta \rangle_0 + 2 \sum_{n=1}^{\infty} \Re\left\{\langle u_\alpha \rangle_n e^{\iota n\omega t}\right\} + \iota \Re\left\{\langle u_\beta \rangle_n e^{\iota n\omega t}\right\}. \end{aligned} \tag{2.48}$$

Thus, the dynamic phasor of each component can be written as

$$\langle \mathbf{u} \rangle_n = (\langle u_\alpha \rangle_n, \langle u_\beta \rangle_n) \in \ell^2(\mathbb{C}^2), \forall n \in \mathbb{Z}.$$

From this, let us define the the Park transformation as the projection of $\bar{u}$ onto the rotating frame $e^{\iota\theta_\delta}$ as

$$\bar{u}_{dq} := \bar{u}e^{-\iota\theta_\delta} = u_d + \iota u_q, \tag{2.49}$$

where

$$\theta_\delta = \int_0^t \omega \mathrm{d}t + \delta.$$

We can also write $\mathbf{u}_{dq} := (u_d, u_q)$ as a real-valued vector.

$$\begin{aligned}
u_d = \frac{1}{4} \sum_{k=-\infty}^{\infty} \Bigg(& \Big(\Re\left\{\langle u_\alpha \rangle_k\right\} + \Im\left\{\langle u_\beta \rangle_k\right\} \Big) \cos\left((k+1)\omega t + \delta\right) \\
& + \Big(-\Im\left\{\langle u_\alpha \rangle_k\right\} + \Re\left\{\langle u_\beta \rangle_k\right\} \Big) \sin\left((k+1)\omega t + \delta\right) \\
& + \Big(\Re\left\{\langle u_\alpha \rangle_k\right\} - \Im\left\{\langle u_\beta \rangle_k\right\} \Big) \cos\left((k-1)\omega t - \delta\right) \\
& + \Big(\Im\left\{\langle u_\alpha \rangle_k\right\} + \Re\left\{\langle u_\beta \rangle_k\right\} \Big) \sin\left((k-1)\omega t - \delta\right) \Bigg) \\
u_q = \frac{1}{4} \sum_{k=-\infty}^{\infty} \Bigg(& \Big(-\Im\left\{\langle u_\alpha \rangle_k\right\} + \Re\left\{\langle u_\beta \rangle_k\right\} \Big) \cos\left((k+1)\omega t + \delta\right) \\
& + \Big(-\Re\left\{\langle u_\alpha \rangle_k\right\} - \Im\left\{\langle u_\beta \rangle_k\right\} \Big) \sin\left((k+1)\omega t + \delta\right) \\
& + \Big(\Im\left\{\langle u_\alpha \rangle_k\right\} + \Re\left\{\langle u_\beta \rangle_k\right\} \Big) \cos\left((k-1)\omega t - \delta\right) \\
& + \Big(\Re\left\{\langle u_\alpha \rangle_k\right\} - \Im\left\{\langle u_\beta \rangle_k\right\} \Big) \sin\left((k-1)\omega t - \delta\right) \Bigg)
\end{aligned}$$

Hence, the rotation of a complex valued signal solves for (2.50) in the time-domain, which is defined at the top of the following page, and results in two frequency components related to the adjacent harmonics dependent on the positive and negative sequences. Subsequently, we can define two distinct dynamic phasors these adjacent frequencies of the *dq* components as

$$\langle \mathbf{u}_{dq,k} \rangle := (\langle \mathbf{u}_{dq} \rangle_{k+1}, \langle \mathbf{u}_{dq} \rangle_{k-1}) \in \ell^2(\mathbb{C}^4), \forall n \in \mathbb{Z} \tag{2.50}$$

where

$$\langle \mathbf{u}_{dq} \rangle_k := (\langle u_d \rangle_k, \langle u_d \rangle_k) \in \ell^2(\mathbb{C}^2), \forall k \in \mathbb{Z}.$$

Thus, we can define a linear map $\boldsymbol{f} \in \mathcal{L}(\mathbb{C}^2, \mathbb{C}^4)$, such that $\langle \mathbf{u}_{dq,k} \rangle = \boldsymbol{f} \circ \langle \mathbf{u} \rangle_k$ as

$$[\boldsymbol{f}] = \frac{1}{2} \begin{bmatrix} e^{\iota\delta} & -\iota e^{\iota\delta} \\ \iota e^{\iota\delta} & e^{\iota\delta} \\ e^{-\iota\delta} & \iota e^{-\iota\delta} \\ -\iota e^{-\iota\delta} & e^{-\iota\delta} \end{bmatrix}, \tag{2.51}$$

with $\text{rank}(\boldsymbol{f}) = 2$. We can also define the inverse linear map $\boldsymbol{f}^+$ through the Moore-Penrose pseudo-inverse of $\boldsymbol{f}$ as

$$\left[\boldsymbol{f}^+\right] = \frac{1}{2} \begin{bmatrix} e^{-\iota\delta} & -\iota e^{-\iota\delta} & e^{\iota\delta} & \iota e^{\iota\delta} \\ \iota e^{-\iota\delta} & e^{-\iota\delta} & -\iota e^{\iota\delta} & e^{\iota\delta} \end{bmatrix}, \tag{2.52}$$

since $\boldsymbol{f}$ is not bijective. Note that $\boldsymbol{f}^+ = \boldsymbol{f}^H$, i.e., $\boldsymbol{f}$ is a self-adjoint operator.

We can then decompose $\boldsymbol{f}$ into two different components $\boldsymbol{f}_-, \boldsymbol{f}_+ \in \mathcal{L}(\mathbb{C}^2, \mathbb{C}^2)$, the first one restricted to $\langle \mathbf{u}_{dq} \rangle_{n-1}$ and the other restricted to $\langle \mathbf{u}_{dq} \rangle_{n+1}$, defined as

$$[\boldsymbol{f}_+] = \frac{1}{2} \begin{bmatrix} 1 & -\iota \\ \iota & 1 \end{bmatrix} e^{\iota\delta}, \quad [\boldsymbol{f}_-] = \frac{1}{2} \begin{bmatrix} 1 & \iota \\ -\iota & 1 \end{bmatrix} e^{-\iota\delta}, \tag{2.53}$$

which can be called the negative and positive sequence functionals, respectively. We can then write the signal k^{th} harmonic components in dq coordinates as

$$\langle \mathbf{u}_{dq} \rangle_k = \boldsymbol{f}_+ \circ \langle \mathbf{u} \rangle_{k-1} + \boldsymbol{f}_- \circ \langle \mathbf{u} \rangle_{k+1} \tag{2.54}$$

Let us define $\langle \mathbf{u} \rangle := (\langle \mathbf{u} \rangle_k)_{k=-\infty}^{\infty}$ as the set of DPs in $\alpha\beta$ coordinates and $\langle \mathbf{u}_{dq} \rangle := (\langle \mathbf{u}_{dq} \rangle_k)_{k=-\infty}^{\infty}$ the set of DP for dq coordinates. Consequently, we can express the linear map $\boldsymbol{g} \in \mathcal{L}(\ell^2(\mathbb{C}^2), \ell^2(\mathbb{C}^2))$ such that $\langle \mathbf{u}_{dq} \rangle = \boldsymbol{g} \circ \langle \mathbf{u} \rangle$ as

$$[\boldsymbol{g}] = \begin{bmatrix} \ddots & & & & & & & \\ \ddots & f_- & & & & & & \\ \ddots & 0 & f_- & & & & & \\ & f_+ & 0 & f_- & & & & \\ & & f_+ & 0 & f_- & & & \\ & & & f_+ & 0 & f_- & & \\ & & & & \ddots & \ddots & \ddots \end{bmatrix} \tag{2.55}$$

which can be truncated for a given number of harmonics. Note that $\boldsymbol{f}_+ = \boldsymbol{f}_-^*$, thus the

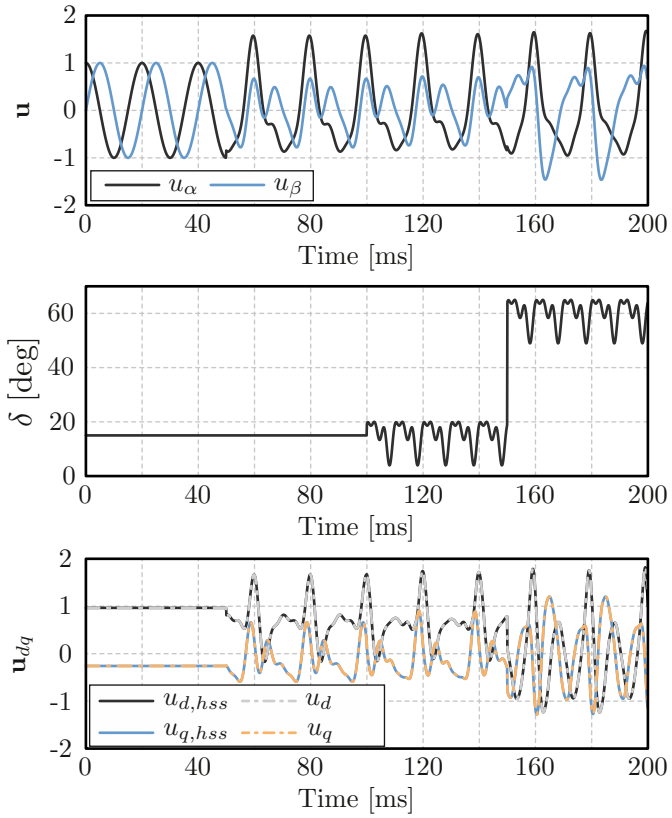

Figure 2.4 – HSS model validation of the spatial rotation of a 2-D time-variant vector $\mathbf{u} = (u_\alpha, u_\beta)$ by the time varying angle $\delta \in L^2(\mathbb{R})$ defined by Table 2.3.

equality given by

$$\langle \mathbf{u}_{dq} \rangle_{-h} = \langle \mathbf{u}_{dq} \rangle_h^* \tag{2.56}$$

is still valid. The linear map $\mathbf{\Psi}_2$ defined in (2.22) can also be employed as means of obtaining a real valued system.

With this, we can write the spacial rotation of a two-dimensional signal in the Harmonic State-Space with respect to an arbitrary angle δ, and consequently the Park transformation, as

$$\begin{aligned} \langle \mathbf{u}_{dq} \rangle &= \boldsymbol{g}(\delta) \circ \langle \mathbf{u} \rangle \\ \langle \mathbf{u} \rangle &= \boldsymbol{g}^H(\delta) \circ \langle \mathbf{u}_{dq} \rangle \,. \end{aligned} \tag{2.57}$$

Figure 2.4 shows a comparison for arbitrary $\mathbf{u}$ and δ using the time-variant and HSS based approaches to compute the Park-transformation with a time-variant angle, which validates the previously described equations.

From (2.54), we can also define the $\boldsymbol{g}_{j,k}, \forall j \in \{d, q\}$ such that

$$\begin{aligned} \langle \mathbf{u}_d \rangle_k &= \frac{1}{2} \begin{bmatrix} e^{\iota\delta} & -\iota e^{\iota\delta} & e^{-\iota\delta} & \iota e^{-\iota\delta} \end{bmatrix} \begin{bmatrix} \langle \mathbf{u} \rangle_{k-1} \\ \langle \mathbf{u} \rangle_{k+1} \end{bmatrix} = \boldsymbol{g}_{d,k} \circ \langle u \rangle \\ \langle \mathbf{u}_q \rangle_k &= \frac{1}{2} \begin{bmatrix} \iota e^{\iota\delta} & e^{\iota\delta} & -\iota e^{-\iota\delta} & e^{-\iota\delta} \end{bmatrix} \begin{bmatrix} \langle \mathbf{u} \rangle_{k-1} \\ \langle \mathbf{u} \rangle_{k+1} \end{bmatrix} = \boldsymbol{g}_{q,k} \circ \langle u \rangle \end{aligned} \tag{2.58}$$

as means of obtaining a single harmonic component.

However, (2.57) still considers a time-variant angle $\delta \in \mathbb{R}$, hence the following subsection aims to obtain a large-signal model in terms of the harmonic components of δ.

2.4.2 Park Transformation Large-Signal HSS Model

Let $\delta \in L^2(\mathbb{R})$ such that

$$\delta := \sum_{k=-\infty}^{\infty} \langle \delta \rangle_k e^{\iota k \omega t} \tag{2.59}$$

be given by the projection of the DPs onto the real plane, which in turn defines

$$\begin{aligned} \bar{\xi} &:= \exp\{-\iota\delta\} \\ &:= \exp\left\{-\iota \sum_{n=-\infty}^{\infty} \langle \delta \rangle_n e^{\iota n \omega t}\right\} \end{aligned} \tag{2.60}$$

as a complex rotation dependent on the dynamic phasor of the angle displacement. We can then apply the procedure adopted in (2.30) to (2.60), which results in

$$\begin{aligned} \bar{\xi} &= \exp\left(-\iota \langle \delta \rangle_0\right) \sum_{n=0}^{\infty} \frac{(\iota w)^n}{n!} \\ &= \sum_{n=0}^{\infty} \exp\left(-\iota\left(\langle \delta \rangle_0 + n\frac{\pi}{2}\right)\right) \frac{w^n}{n!}, \end{aligned} \tag{2.61}$$

Table 2.3 – Parameters for Park Transformation Model Validation

t [ms]	0–50	50–100	100–150	150–200
$\langle u_\alpha \rangle_0$	0	0	$0.05\sin(20\pi t)$	$0.05\sin(20\pi t)$
$\langle u_\alpha \rangle_1$	0.5	0.5	0.5	0.5
$\langle u_\alpha \rangle_2$	0	$0.2e^{\iota\frac{\pi}{6}}$	$0.2e^{\iota\frac{\pi}{6}}$	$0.2e^{\iota\frac{\pi}{6}}$
$\langle u_\alpha \rangle_3$	0	$0.1e^{\iota\frac{\pi}{12}}$	$0.1e^{\iota\frac{\pi}{12}}$	$0.1e^{\iota\frac{\pi}{12}}$
$\langle u_\alpha \rangle_4$	0	0	0	$0.05e^{\iota\frac{\pi}{6}}$
$\langle u_\beta \rangle_0$	0	0	$0.05\sin(20\pi t)$	$0.05\sin(20\pi t)$
$\langle u_\beta \rangle_1$	$0.5e^{-\iota\frac{\pi}{2}}$	$0.2e^{-\iota\frac{2\pi}{5}}$	$0.2e^{-\iota\frac{2\pi}{5}}$	$0.5e^{\iota\frac{\pi}{2}}$
$\langle u_\beta \rangle_2$	0	$0.2e^{\iota\frac{\pi}{6}}$	$0.2e^{\iota\frac{\pi}{6}}$	$0.2e^{\iota\frac{\pi}{6}}$
$\langle u_\beta \rangle_3$	0	$0.1e^{\iota\frac{\pi}{12}}$	$0.1e^{\iota\frac{\pi}{12}}$	$0.1e^{\iota\frac{\pi}{12}}$
$\langle u_\beta \rangle_4$	0	0	0	$0.05e^{\iota\frac{\pi}{6}}$
$\langle \delta \rangle_0$	$\frac{\pi}{12}$	$\frac{\pi}{12}$	$\frac{\pi}{12}$	$\frac{\pi}{3}$
$\langle \delta \rangle_2$	0	0	$\frac{\pi}{72}e^{-\iota\frac{\pi}{2}}$	$\frac{\pi}{72}e^{-\iota\frac{\pi}{2}}$
$\langle \delta \rangle_4$	0	0	$\frac{\pi}{100}e^{-\iota\frac{\pi}{3}}$	$\frac{\pi}{100}e^{-\iota\frac{\pi}{3}}$
$\langle \delta \rangle_6$	0	0	$\frac{\pi}{120}e^{\iota\frac{\pi}{5}}$	$\frac{\pi}{120}e^{\iota\frac{\pi}{5}}$

where $w = \delta - \langle\delta\rangle_0$. Note that each term of the sum corresponds to a rotation of a two dimensional signal, with its formulation given by (2.57). From inspection of (2.32), we can write $\langle \mathbf{u}_{dq} \rangle := \left\langle \bar{u}\bar{\xi} \right\rangle$ as

$$\begin{aligned} \langle \mathbf{u}_{dq} \rangle &= \sum_{n=0}^{\infty} \frac{1}{n!} \left(\left(\mathbf{\Gamma}^n \circ \langle\delta\rangle|_{\langle\delta\rangle_0=0} \right) \otimes \mathbf{I}_2 \right) \circ \\ &\quad \circ \boldsymbol{g} \left(\langle\delta\rangle_0 + n\frac{\pi}{2} \right) \circ \langle u \rangle \\ &=: \boldsymbol{h}_\delta \left(\delta \right) \circ \langle \mathbf{u} \rangle . \end{aligned} \tag{2.62}$$

Since $\langle \mathbf{u}_{dq} \rangle$ concatenates the d and q axis, we can define the linear maps $\mathbf{T}_d, \mathbf{T}_q \in \mathcal{L}(\mathbb{C}^{2n_h}, \mathbb{C}^{n_h})$ as

$$[\mathbf{T}_d] := \mathbf{I}_{n_h} \otimes \begin{bmatrix} 1 & 0 \end{bmatrix}, \quad [\mathbf{T}_q] := \mathbf{I}_{n_h} \otimes \begin{bmatrix} 0 & 1 \end{bmatrix}, \tag{2.63}$$

such that $\langle \mathbf{u}_j \rangle = \mathbf{T}_j \circ \langle \mathbf{u}_{dq} \rangle, \forall j \in \{d, q\}$, which leads to

$$\boldsymbol{h}_j := \mathbf{T}_j \circ \boldsymbol{h}_\delta, \forall j \in \{d, q\} \tag{2.64}$$

as means of directly obtaining each dq-axis component. Note that $\boldsymbol{h}_\delta$ is a self-adjoint operator.

2.4.3 Voltage Controlled Oscillator Model

The Voltage Controlled Oscillator (VCO) model can be directly obtained from the previous equations. From this, we can obtain the set of dynamic phasors of a sinusoidal signal generated from $\left\langle \mathfrak{R}\left\{ e^{\iota\omega t + \delta} \right\} \right\rangle$ for $\delta \in L_2(\mathbb{R})$ by taking

$$\begin{aligned} \langle \cos\left(\omega t + \delta\right) \rangle &= \left(\mathbf{I}_\infty \otimes \begin{bmatrix} 1 & 0 \end{bmatrix} \right) \circ \boldsymbol{h}_d^H(\delta) \circ \hat{h}_0 \\ &=: \boldsymbol{h}_{vco}(\langle\delta\rangle) \end{aligned} \tag{2.65}$$

Note that $\langle \sin\left(\omega t + \delta\right) \rangle = \boldsymbol{h}_{vco}(\langle\delta\rangle - \frac{1}{2}\pi\hat{h}_0)$.

The VCO model can be employed to model the reference generation for a grid connected three-phase converter, with δ being directly generated from the PLL.

Table 2.4 presents the dynamic phasor function approximations described in this work, which will be further explored in the next sections.

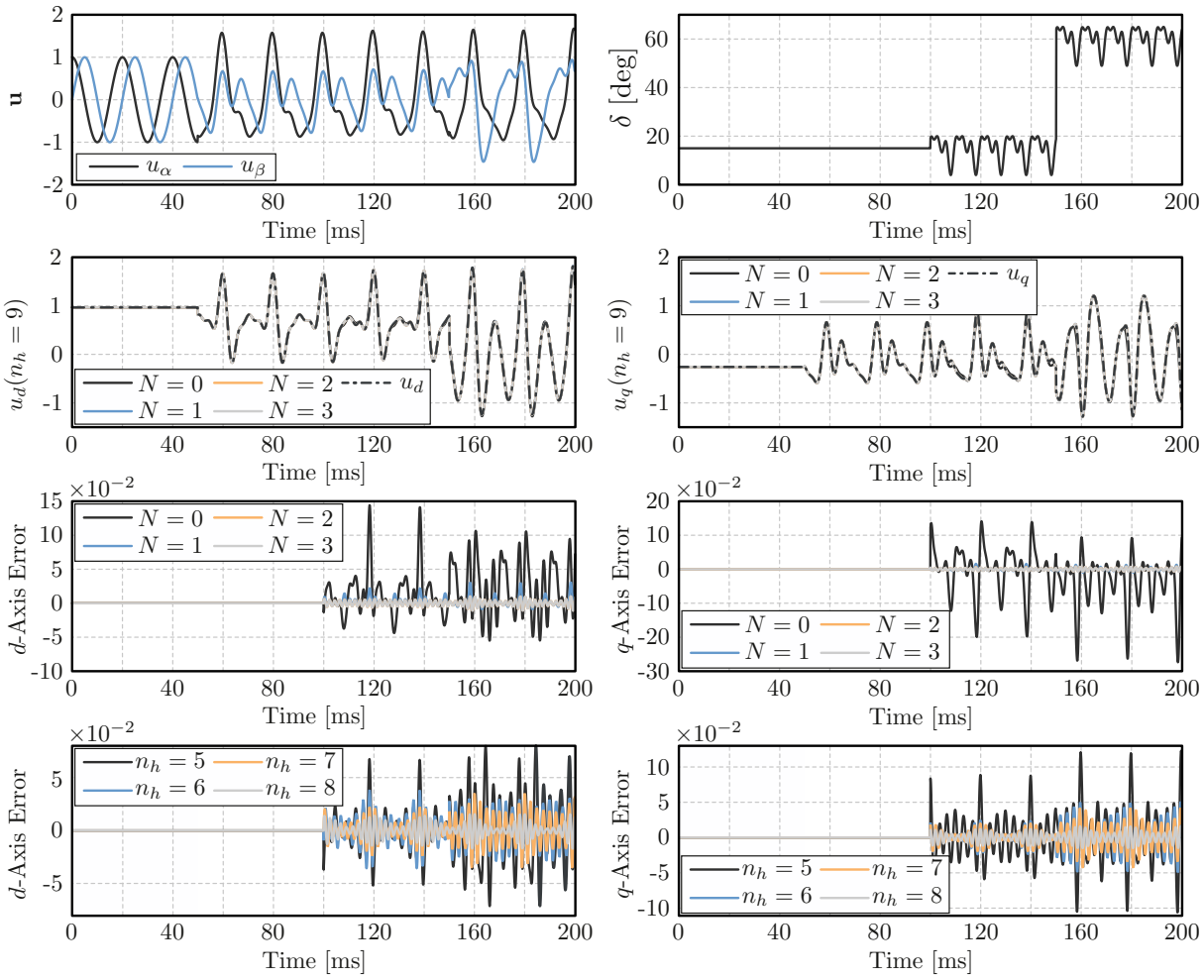

Figure 2.5 – Validation of the harmonic domain-based Park Transformation model for arbitrary signals $\langle \delta \rangle$ and $\langle u \rangle$ with the dynamic phasor amplitudes given in Table 2.3. The error is defined as the absolute error between the real valued function and the projection of the approximation onto the $L^2(\mathbb{R})$ space.

Table 2.4 – Dynamic Phasor Function Approximations

Operation	Symbol	Expression
Multiplication	$\langle uv \rangle$	$(\boldsymbol{\Gamma} \circ \langle u \rangle) \circ \langle v \rangle$
Exponentiation	$\langle u^n \rangle$	$\left(\boldsymbol{\Gamma}^{n-1} \circ \langle u \rangle\right) \circ \langle u \rangle = (\boldsymbol{\Gamma} \circ \cdots \circ (\boldsymbol{\Gamma} \circ \langle u \rangle) \circ \langle u \rangle) \circ \langle u \rangle$
Exponential Function	$\boldsymbol{h}_{\exp}(\langle u \rangle)$	$e^{\langle u \rangle_0} \left(\hat{h}_0 + \sum_{n=1}^{\infty} \frac{1}{n!} \left(\boldsymbol{\Gamma}^{n-1} \circ \langle u \rangle \Big\vert_{\langle u \rangle_0 = 0} \right) \circ \langle u \rangle \Big\vert_{\langle u \rangle_0 = 0} \right)$
Division	$\boldsymbol{h}_{div}(u, v)$	$\sum_{n=0}^{\infty} \frac{(-1)^n}{\langle v \rangle_0^{n+1}} \left(\boldsymbol{\Gamma}^n \circ \langle v \rangle \Big\vert_{\langle v \rangle_0 = 0} \right) \circ \langle u \rangle$
Synchronous Rotation	$\boldsymbol{g}_{\delta}(\langle \delta \rangle_0)$	See (2.53) and (2.55)
Park Transformation	$\boldsymbol{h}_{\delta}(\delta)$	$\sum_{n=0}^{\infty} \frac{1}{n!} \left(\left(\boldsymbol{\Gamma}^n \circ \langle \delta \rangle \vert_{\langle \delta \rangle_0 = 0} \right) \otimes \mathbf{I}_2 \right) \circ \boldsymbol{g}_{\delta} \left(\langle \delta \rangle_0 + n\frac{\pi}{2} \right)$
d-Axis Component	$\boldsymbol{h}_d(\delta)$	$(\mathbf{I}_{N_h} \otimes [1 \quad 0]) \circ \boldsymbol{h}_{\delta}(\delta)$
q-Axis Component	$\boldsymbol{h}_q(\delta)$	$(\mathbf{I}_{N_h} \otimes [0 \quad 1]) \circ \boldsymbol{h}_{\delta}(\delta)$
PLL Feedback	$\boldsymbol{h}_{pll}(\mathbf{u}_{\alpha\beta}, \delta)$	$\boldsymbol{h}_{div} \left(\boldsymbol{h}_q(\delta) \circ \mathbf{u}_{\alpha\beta}, \boldsymbol{h}_d(\delta) \circ \mathbf{u}_{\alpha\beta} \right)$
VCO Signal	$\boldsymbol{h}_{vco}(\langle \delta \rangle)$	$\left(\mathbf{I}_{\infty} \otimes \begin{bmatrix} 1 & 0 \end{bmatrix} \right) \circ \boldsymbol{h}_d^H(\delta) \circ \hat{h}_0$

2.5 MULTI-FREQUENCY MODELS

Let $u \in L^2(\mathbb{C})$ such that

$$u := \sum_{i=-\infty}^{\infty} \sum_{j=-\infty}^{\infty} \langle u \rangle_{i,j} e^{\iota(i\theta_1 + j\theta_2)}, \tag{2.66}$$

a signal described by its Two-Dimensional Fourier Transform, where

$$\theta_k := \theta_{k,0} + \int_{-\infty}^{t} \omega_k(\tau) \mathrm{d}\tau, \quad \forall k \in \{1, 2\}. \tag{2.67}$$

Thus, we can define the matrix associated with the dynamic phasors as

$$[\langle u \rangle] := \begin{bmatrix} \ddots & \vdots & \vdots & \vdots & \iddots \\ \cdots & \langle u \rangle_{-1,-1} & \langle u \rangle_{-1,0} & \langle u \rangle_{-1,1} & \cdots \\ \cdots & \langle u \rangle_{0,-1} & \langle u \rangle_{0,0} & \langle u \rangle_{0,1} & \cdots \\ \cdots & \langle u \rangle_{1,-1} & \langle u \rangle_{1,0} & \langle u \rangle_{1,1} & \cdots \\ \iddots & \vdots & \vdots & \vdots & \ddots \end{bmatrix}, \tag{2.68}$$

and the dynamic phasor vector as

$$\langle u \rangle := \mathrm{vec}\left([\langle u \rangle]\right) = \left(\left(\langle u \rangle_{i,j} \right)_{i=-\infty}^{\infty} \right)_{j=-\infty}^{\infty}. \tag{2.69}$$

To ease the assesment of these signals, it is convenient to truncate the number of harmonics at a fixed number, leading to the subset of harmonics given by $k \in \mathfrak{N}_k \subseteq \mathbb{Z}_{-n_k}^{n_k}, \forall k \in \{1, 2\}$ such that $N_k := \dim(\mathfrak{N}_k) \leq 2n_k + 1, \forall k \in \{1, 2\}$.

Consequently, if we have a state-space system described by

$$D_t \mathbf{x} = \mathbf{A}\mathbf{x} + \mathbf{B}\mathbf{u} \tag{2.70}$$

where $\mathbf{x} \in L^2(\mathcal{X}), \mathcal{X} \subseteq \mathbb{R}^{n_x}$ and $\mathbf{u} \in L^2(\mathcal{U}), \mathcal{U} \subseteq \mathbb{R}^{n_u}$, $\mathbf{A} \in \mathcal{M}(n_x, n_x, \mathbb{R})$ and $\mathbf{B} \in \mathcal{M}(n_x, n_u, \mathbb{R})$, it is possible to rewrite the system in terms of its dynamic phasors as

$$\begin{aligned} D_t \langle \mathbf{x} \rangle &= \left(\mathbf{I}_{N_2} \otimes \left(\mathbf{I}_{N_1} \otimes \mathbf{A} - \mathbf{G}_1\right) - \mathbf{G}_2 \otimes \mathbf{I}_{N_1}\right) \langle \mathbf{x} \rangle + \left(\mathbf{I}_{N_1 N_2} \otimes \mathbf{B}\right) \langle \mathbf{u} \rangle \\ &= \left(\mathbf{I}_{N_1 N_2} \otimes \mathbf{A} - \mathbf{I}_{N_2} \otimes \mathbf{G}_1 - \mathbf{G}_2 \otimes \mathbf{I}_{N_1}\right) \langle \mathbf{x} \rangle + \left(\mathbf{I}_{N_1 N_2} \otimes \mathbf{B}\right) \langle \mathbf{u} \rangle \end{aligned} \tag{2.71}$$

where

$$\mathbf{G}_k = \iota \omega_k \mathrm{diag}\left(\mathfrak{N}_k\right) \otimes \mathbf{I}_{n_x}, \quad \forall k \in \{1, 2\}. \tag{2.72}$$

Let $u, v \in L^2(\mathbb{R})$ signals that can be written in accordance with (2.66), then the multiplication between these two signals can then be described by the convolution of the

harmonic components as given by

$$\langle uv\rangle_{i,j} = \sum_{k_1=-\infty}^{\infty}\sum_{k_2=-\infty}^{\infty} \langle u\rangle_{k_1,k_2}\langle v\rangle_{i-k_1,j-k_2} \tag{2.73}$$

and solves for

$$\langle uv\rangle_{i,j} = \begin{cases} \langle u\rangle_{i,j} = 0,\ \forall j \neq 0, \\ \langle v\rangle_{i,j} = 0,\ \forall i \neq 0, \\ \langle u\rangle_i\langle v\rangle_j,\ \text{else}, \end{cases} \tag{2.74}$$

when u and v are composed by harmonic components with of a specific fundamental frequency. Note that (2.73) can be written as

$$\langle uv\rangle := (\boldsymbol{\Sigma}\circ\langle u\rangle)\circ\langle v\rangle\,, \tag{2.75}$$

where the **Sigma Operator** $\boldsymbol{\Sigma}(\cdot)$ can be defined as

$$\boldsymbol{\Sigma}\circ\langle u\rangle := \begin{bmatrix} \boldsymbol{\Gamma}\circ\langle u\rangle_{0,:} & \boldsymbol{\Gamma}\circ\langle u\rangle_{-1,:} & \cdots & \boldsymbol{\Gamma}\circ\langle u\rangle_{-h_i,:} & & & \\ \boldsymbol{\Gamma}\circ\langle u\rangle_{1,:} & \ddots & \ddots & \ddots & \ddots & & \\ \vdots & \ddots & \boldsymbol{\Gamma}\circ\langle u\rangle_{0,:} & \boldsymbol{\Gamma}\circ\langle u\rangle_{-1,:} & \ddots & \ddots & \\ \boldsymbol{\Gamma}\circ\langle u\rangle_{h_i,:} & \ddots & \boldsymbol{\Gamma}\circ\langle u\rangle_{1,:} & \boldsymbol{\Gamma}\circ\langle u\rangle_{0,:} & \boldsymbol{\Gamma}\circ\langle u\rangle_{-1,:} & \ddots & \boldsymbol{\Gamma}\circ\langle u\rangle_{-h_i,:} \\ & \ddots & \ddots & \boldsymbol{\Gamma}\circ\langle u\rangle_{1,:} & \boldsymbol{\Gamma}\circ\langle u\rangle_{0,:} & \ddots & \vdots \\ & & \ddots & \ddots & \ddots & \ddots & \boldsymbol{\Gamma}\circ\langle u\rangle_{-1,:} \\ & & & \boldsymbol{\Gamma}\circ\langle u\rangle_{h_i,:} & \cdots & \boldsymbol{\Gamma}\circ\langle u\rangle_{1,:} & \boldsymbol{\Gamma}\circ\langle u\rangle_{0,:} \end{bmatrix} \tag{2.76}$$

which decomposes the two dimensional convolution into multiple one-dimensional convolutions. The same methodology can be employed for N-dimensional Fourier Transform models.

The proposed multi-frequency model is not limited to a base frequency as opposed to the one-dimensional approach and can be easily expanded to a multi-dimensional Fourier Transform approach. Applications in power electronics might include motor drives, back-to-back converter and matrix converter models, as further discussed in Chapter 3.

2.6 GENERAL CONCEPTS

For a departure point, consider the following dynamic model

$$D_t\mathbf{x} = \boldsymbol{f}(\mathbf{x},\mathbf{u}),\quad \mathbf{x}(0) = \mathbf{x}_0 \in \mathbb{R}^m,\quad m \in \mathbb{N}, \tag{2.77}$$

where $\mathbf{u} \in U \subseteq \mathbb{R}^n$, $n \in \mathbb{N}$, for the application $\boldsymbol{f} : \mathbb{R}^m \cup U \to \mathbb{R}^m$. We can enunciate a series of concepts which are used henceforth.

Open-loop Control. Let $\mathbf{u}(\cdot) : [0, +\infty) \to U$ for which

$$D_t\mathbf{x}(t) = \boldsymbol{f}(\mathbf{x}(t), \mathbf{u}(t)), \quad t \geq 0, \quad \mathbf{x}(0) = \mathbf{x}_0, \tag{2.78}$$

has a well defined solution.

Closed-loop Control. Let $\boldsymbol{\mathcal{K}} : \mathbb{R}^m \to U$ a mapping such that

$$D_t\mathbf{x}(t) = \boldsymbol{f}\left(\mathbf{x}\left(t\right), \boldsymbol{\mathcal{K}}\left(\mathbf{x}\left(t\right)\right)\right), \quad t \geq 0, \quad x(0) = x_0, \tag{2.79}$$

has a well defined solution. The mapping $\boldsymbol{\mathcal{K}}(\cdot)$ is called feedback and can depend on the time instant t.

Controllability. One says a state $\mathbf{x}_T \in \mathbb{R}^m$ is reachable from $\mathbf{x}_0$ in a time T if $\exists \mathbf{u}(\cdot) : \mathbf{x}(0) = \mathbf{x}_0, \mathbf{x}(T) = \mathbf{x}_T$.

Stabilizability. Assuming that $\exists \bar{\mathbf{x}} \in \mathbb{R}^m, \bar{\mathbf{u}} \in U : \boldsymbol{f}(\bar{\mathbf{x}}, \bar{\mathbf{u}}) = 0$. A mapping $\boldsymbol{\mathcal{K}}(\cdot) : \mathbb{R}^m \to U$ is called stabilizing feedback if $\bar{\mathbf{x}}$ is a stable equilibrium for (2.79).

Observability. In many situations, one observes not $\mathbf{x}(t)$ but $\boldsymbol{g}(\mathbf{x}(t))$, such that

$$\begin{cases} D_t\mathbf{x} = \boldsymbol{f}(\mathbf{x}, \mathbf{u}) \\ \mathbf{y} = \boldsymbol{g}(\mathbf{x}, \mathbf{u}) \end{cases}, \quad \mathbf{x}(0) = \mathbf{x}_0, \tag{2.80}$$

with $\boldsymbol{g}(\cdot)$ as the observation equation. The system is said to be observable if $\exists! \mathbf{y}$ determined by $\boldsymbol{g}(\cdot)$, i.e., $\boldsymbol{g}$ is injective.

Stabilizability of Partially Observable Systems. A constraint on the observation $\mathbf{y}$ such that

$$D_t\mathbf{x} = \boldsymbol{f}(\mathbf{x}, \boldsymbol{\mathcal{K}}(\boldsymbol{g}(\mathbf{x}))). \tag{2.81}$$

The mapping $\boldsymbol{\mathcal{K}}$ is called stabilizing feedback if $\bar{\mathbf{x}}$ is a stable equilibrium for $(\boldsymbol{\mathcal{K}} \circ \boldsymbol{g}) \circ \mathbf{x}$.

Chapter

3

Concepts and Modeling of Paralleled PWM Converters

A first step on the study of power converters is to obtain a mathematical model which represents the figures of merit with accuracy, hence the complexity of the models is dependent on the object of study. Since the focus of this work is to quantify and minimize the circulating currents of a system with parallel connected converters, these models must take into consideration parametric uncertainties and unbalances for medium-frequency circulating currents, and must be valid for a wide frequency range to assertain the characteristics of high-frequency circulating currents.

At a first moment, a methodology to obtain linear models for components' parametric variations is discussed, with the objective of veryfying the need to insert these characteristics into the model, and the estimation of a worst-case scenario, as well as boundaries for parametric variations. The assumption of different parameter values for all the ac-side filter components results in extremely large and complex models.

After that, a unified methodology for obtaining power converter models is demonstrated and applied to two different filter topologies. A first model represent the analysis for an LCL filter for a stand alone operation. The modeling of LCL and a damped LCL filter is then extended for paralleled converters, and some intrisic characteristics of paralleled converter models are then discussed, such as resonances resulting from interactions between the output filters of each converter and their impact on the system stability, as these resonances may lead to an unexpected or unstable behaviour. These models result in Linear Time-Varying (LTV) systems, and can be modeled in the Harmonic Domain by applying the concepts of Chapter 2.

From this, the analysis is extended by inserting the dynamics of the dc bus, with the frequency coupling between the dc and ac stages modeled with techniques based on the Harmonic State-Space (HSS) [17, 27] for a single converter in a first model and then extended for parallel connected converters. The models here presented are left in their non-linear form, although the linearization in this case should be trivial as the equilibrium point for a free duty cycle ratio is well-defined, although the nonlinear characteristic of the feedback mapping commonly adopted by the control structure might demonstrate the

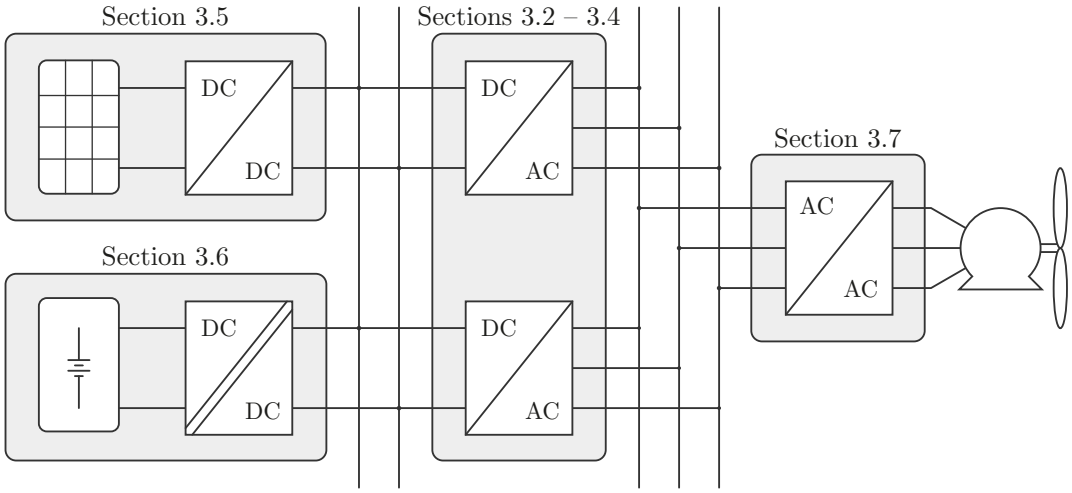

Figure 3.1 – Block diagram of the models presented in this chapter and its respective sections.

presence of multiple equilibrium points.

This section also provides models that focus on dc circuits to showcase the effects of different configurations on the overall system, as illustrated in Figure 3.1. Additionally, a model of an indirect matrix converter is presented, highlighting the multifrequency model ability to generate a time-invariant models considering the time-varying carachteristic of the system with multiple frequencies. These models contribute to a better understanding of the behavior and performance of dc circuits and matrix converters in various applications.

The present analysis adopts the Lunze transformation defined in [25], renaming differential-mode to subtractive-mode and common-mode to additive-mode, since the terminology related to common-mode is often associated with the gamma axis (or zero sequence) components. A more formal definition for the linear maps and concepts employed in this chapter is presented in Chapter 2.

3.1 PASSIVE COMPONENTS

In a first moment, a dynamic model for inductors and capacitors is discussed, aiming to obtain an equivalent circuit from impedance measurements and providing a validation for higher frequency models, since resistance, capacitance and inductance values are frequency dependent.

The method is based on the Vector Fitting algorithm [28], which is a black-box modeling methodology. The analysis is different for inductors and capacitors due to convergence and passivity issues, as discussed in [29]. These estimated models can help obtaining linear models for resistors, inductors and capacitors and their frequency dependence, resulting in a combination of linear damped circuits. Thus, the approximation by a lumped element can represent a worst-case scenario.

From the inspection of the bode diagrams presented in Figure 3.2, which represents the measurement and model approximation of a 300 μH inductor with constructive

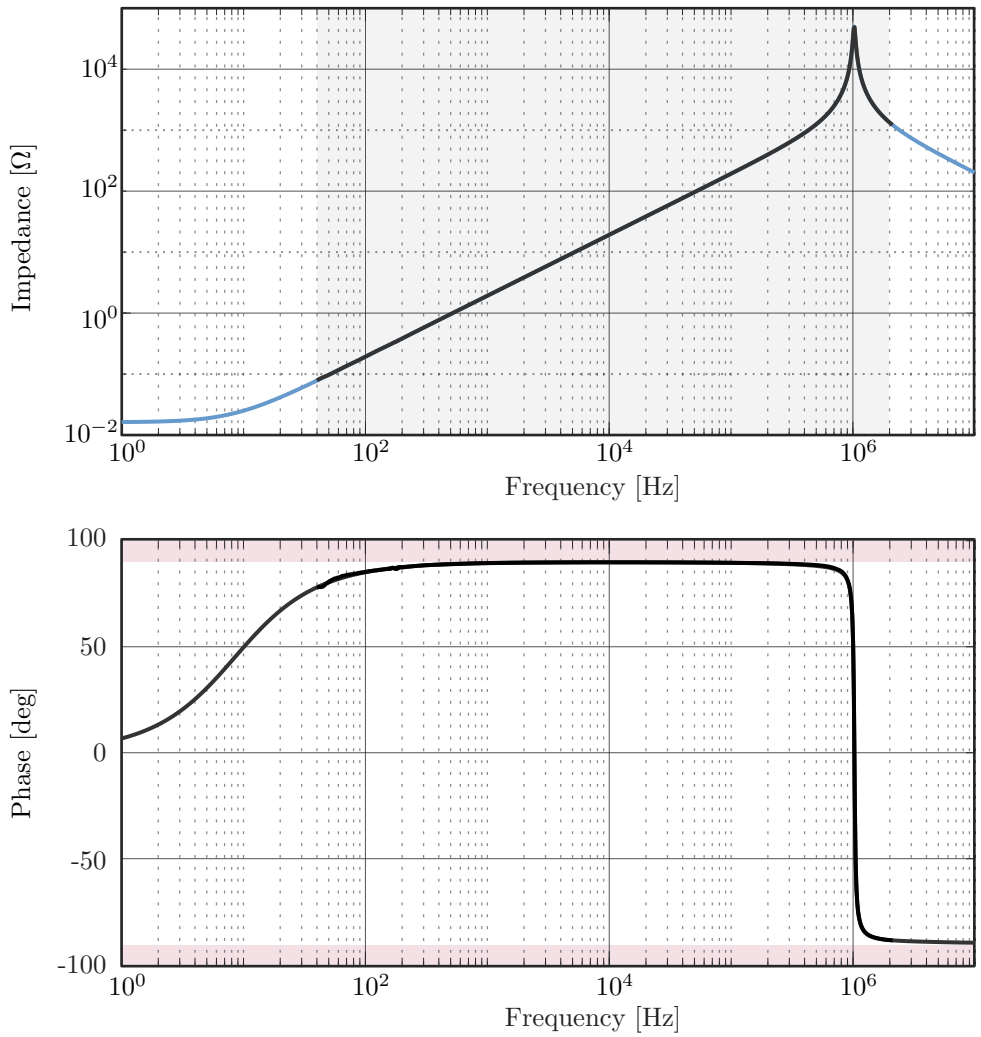

(a)

Figure 3.2 – Comparison between vector fitting (blue) and measurement (black) of a 300 μH inductor, with reference impedance curve based on measurements using an Agilent 4294A Impedance Analyzer, with frequency sweep between 40 Hz – 10 MHz. The fitting was performed using a fourth-order circuit model (a) Impedance.

parameters defined by Table 3.1. The equivalent circuit shown in Fig. 3.3 can be employed when the poles obtained from the vector fitting algorithm are real valued, with paremeters for the discussed inductor given by Table 3.2. Note that the $L_{s,1}$ is extremelly close to the rated inductance value, and the equivalent series resistance can be obtained by taking the

Table 3.1 – Converter Parameters

Specification	**Value**
Core	MS-226060-2
Material	Sendust
Manufactor	KDM
Number of Turns	33

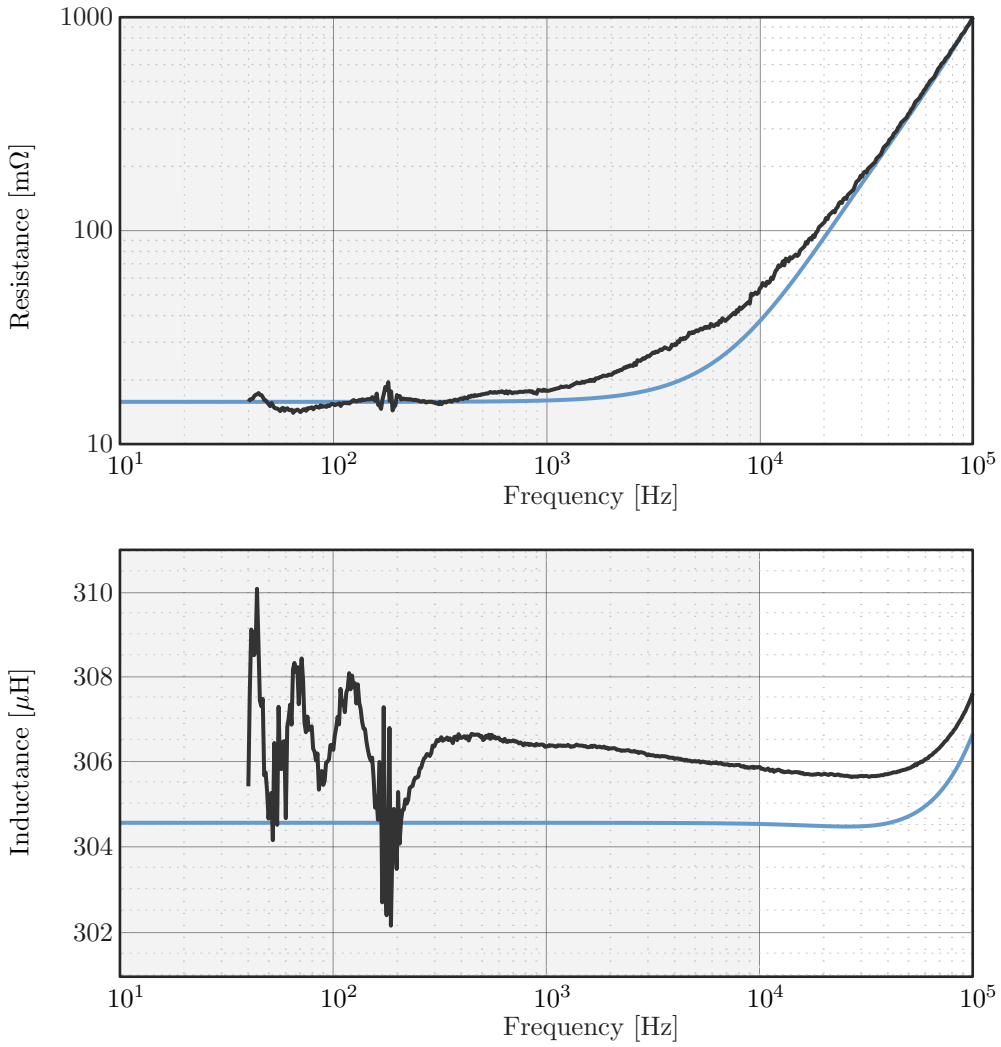

(b)

Figure 3.2 – Comparison between vector fitting (blue) and measurement (black) of a 300 μH inductor, with reference impedance curve based on measurements using an Agilent 4294A Impedance Analyzer, with frequency sweep between 40 Hz – 10 MHz. The fitting was performed using a fourth-order circuit model (b) Resistance and Inductance.

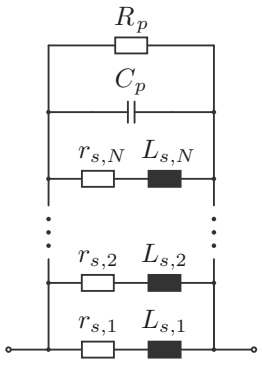

Figure 3.3 – Equivalent circuit of the vector fitting of the admittance of an inductor, assuming all real poles.

parallel of all the resistances.

Table 3.2 – Vector Fitting Equivalent Circuit Parameters

Parameter	**Value**	**Parameter**	**Value**
$L_{s,1}$	304.57 μH	$r_{s,1}$	16.228 mΩ
$L_{s,2}$	2.2676 mH	$r_{s,2}$	11.631 kΩ
$L_{s,3}$	-1.5188 mH	$r_{s,3}$	-16.148 kΩ
$L_{s,4}$	106.41 mH	$r_{s,4}$	25.458 kΩ
C_p	79.954 pH	R_p	31.993 kΩ

We can then conclude that:

- The presented models demonstrate a more damped behaviour in higher frequencies, especially close to the natural resonances of power converter filters, thus the use of simplified models taking into consideration the dc resistance of inductors and capacitors might provide pessimistic scenarios;
- Variations on capacitance and inductance values might shift resonance frequencies, which should be taken into account when designing selective active damping control strategies;
- The stability and stabilization analysis including these models should have better precision, since more realistic characteristics are taken into account, and the more damped characteristic should be taken into account when analyzing the passivity of a control strategy.

3.2 SINGLE CONVERTER MODELS WITH CONSTANT DC-LINK

In a first moment, the Three-phase Two-level Voltage Source Inverter (2LVSI) will be modeled with a constant voltage dc link, as shown in Figure 3.4. This approach is valid for hybrid microgrids, since the dc bus is regulated through the power converters on the dc side, which should present a large inertia. The system model presents a piecewise smooth behaviour, and eventual chaotic behaviours will be disregarded, i.e., the converters are assumed to present an orbital convergence to a steady-state of the switched model [13, 14]. Most of the matricial form of system equations presented in this chapter are suppressed due to the size of each differential equation.

Let a switching function $s_{i,j}$ for each switch $S_{i,j}$ be described by

$$s_{i,j} := \begin{cases} 1, & \text{switch } S_{i,j} \text{ is closed,} \\ 0, & \text{switch } S_{i,j} \text{ is open} \end{cases}, \tag{3.1}$$

with $i \in \{1,2,3\}$ and $j \in \{p,n\}$. Hence, the switching function for each phase can be described as

$$s_i := s_{i,p} - s_{i,n}. \tag{3.2}$$

From inspection, we have that $s_i \in \{-1,1\}$ since p and n are complementary.

3.2.1 Balanced Parameters

Assuming that there is no common-mode current circulation, the system can be modeled as

$$(\mathbf{K}_1 \otimes \mathbf{I}_3)\, D_t\mathbf{x} = (\mathbf{A}_1 \otimes \mathbf{I}_3)\, \mathbf{x} + (\mathbf{B}_1 \otimes \mathbf{T}_{dm})\, \frac{U_{dc}}{2}\mathbf{s} + (\mathbf{E}_1 \otimes \mathbf{T}_{dm})\, \mathbf{w}, \tag{3.3}$$

where $\mathbf{x} := \left((i_{f,i})_{i=1}^{3}, (v_{c,i})_{i=1}^{3}, (i_{l,i})_{i=1}^{3}\right)$, $\mathbf{K}_1 := \operatorname{diag}(L_f, C_c, L_l)$,

$$\mathbf{A}_1 := \begin{bmatrix} -(r_c + r_f) & -1 & r_c \\ 1 & 0 & -1 \\ r_c & 1 & -(r_c + r_w) \end{bmatrix}, \quad \mathbf{B}_1 := \begin{bmatrix} 1 \\ 0 \\ 0 \end{bmatrix}, \quad \mathbf{E}_1 := \begin{bmatrix} 0 \\ 0 \\ -1 \end{bmatrix}, \quad \mathbf{T}_{dm} := \frac{1}{3}\begin{bmatrix} 2 & -1 & -1 \\ -1 & 2 & -1 \\ -1 & -1 & 2 \end{bmatrix}.$$

From inspection, $\ker(\mathbf{T}_{dm}) = \langle (1,1,1) \rangle$, hence the system can be rewritten in $\alpha\beta$ coordinates by applying the similarity transformation $\mathbf{T} := \mathbf{I}_3 \otimes \mathbf{T}_{\alpha\beta\gamma}$ in the linear system

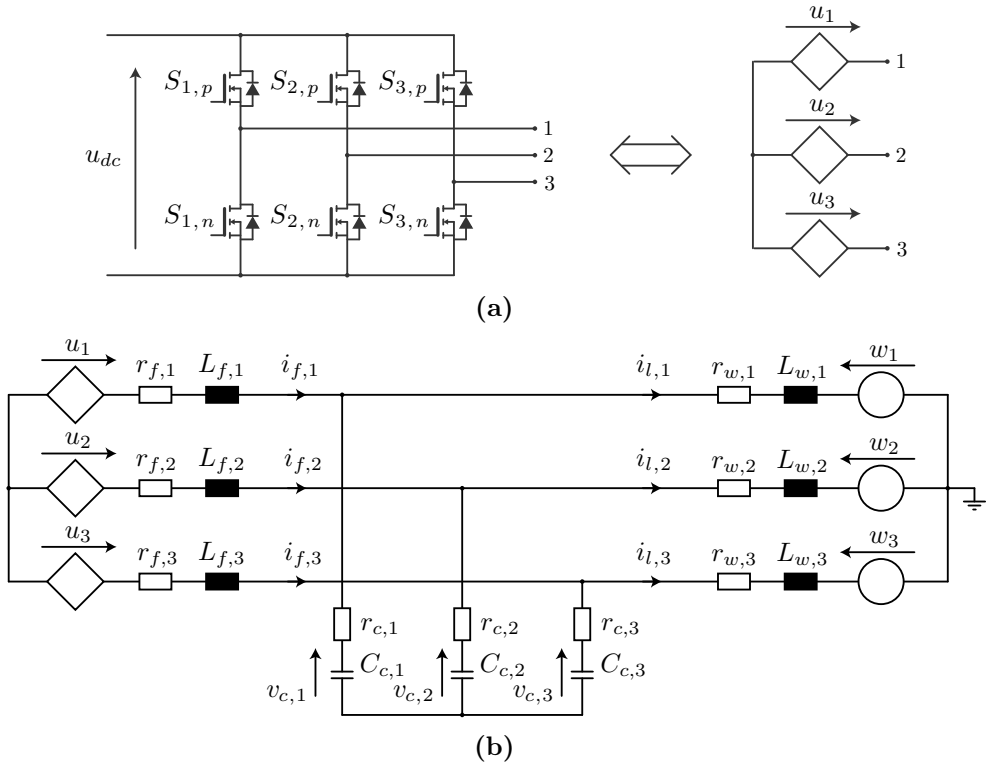

Figure 3.4 – (a) Equivalent circuit model of the Three-Phase Voltage Source Inverter switched model (b) Circuit model of a voltage source converter with constant dc bus employing a LCL filter.

described by (3.3) and the Clarke transformation on the switching function and disturbance, resulting in

$$\begin{aligned}(\mathbf{K}_1 \otimes \mathbf{I}_3)\, D_t \mathbf{x}_{\alpha\beta\gamma} = \mathbf{T}\,(\mathbf{A}_1 \otimes \mathbf{I}_3)\,\mathbf{T}^{-1}\mathbf{x}_{\alpha\beta\gamma} + \mathbf{T}\,(\mathbf{B}_1 \otimes \mathbf{T}_{dm})\,\mathbf{T}^{-1}_{\alpha\beta\gamma}\mathbf{u}_{\alpha\beta\gamma} \\ + \mathbf{T}\,(\mathbf{E}_1 \otimes \mathbf{T}_{dm})\,\mathbf{T}^{-1}_{\alpha\beta\gamma}\mathbf{w}_{\alpha\beta\gamma},\end{aligned} \tag{3.4}$$

which solves for

$$(\mathbf{K}_1 \otimes \mathbf{I}_2)\, D_t \mathbf{x}_{\alpha\beta} = (\mathbf{A}_1 \otimes \mathbf{I}_2)\,\mathbf{x}_{\alpha\beta} + (\mathbf{B}_1 \otimes \mathbf{I}_2)\,\frac{U_{dc}}{2}\mathbf{s}_{\alpha\beta} + (\mathbf{E}_1 \otimes \mathbf{I}_2)\,\mathbf{w}_{\alpha\beta} \tag{3.5}$$

or

$$\mathbf{K}_1 D_t \mathbf{x}_i = \mathbf{A}_1 \mathbf{x}_i + \mathbf{B}_1 \mathbf{u}_i + \mathbf{E}_1 \mathbf{w}_i, \quad \forall i \in \{\alpha, \beta\}, \tag{3.6}$$

where $\mathbf{u} := \frac{1}{2} U_{dc} s$. This approach is only valid for a balanced system, i.e., if the parameter values are the same for the three converter phases, the system can be treated as two single-phase converters in the $\alpha\beta$ axis.

This methodology can be employed for different filter topologies, through the identification of the kernel of the derivative operator D, which in this case is the zero-axis component.

3.2.2 Unbalanced Parameters

Under unbalanced conditions, we consider different values for the parameters of each phase, which accounts for a more general approach. In this case, the $\alpha\beta$ axes are not orthogonal, hence another linear transformation can be obtained through the Gram-Schmidt process if a decoupled system is desired. However, the new transformation is parameter-varying. Since we can write the phase 3 components as a linear combination of phases 1 and 2 components, let us define the line-to-line transformation matrix as

$$\mathbf{T}_{ll} := \begin{bmatrix} 1 & -1 & 0 \\ 0 & 1 & -1 \end{bmatrix} \tag{3.7}$$

The dynamic equations can be written as

$$\begin{cases} \mathbf{T}_{ll}\mathbf{u} = \mathbf{T}_{ll}\,(\mathbf{r}_f \odot \mathbf{i}_f + \mathbf{L}_f \odot D_t \mathbf{i}_f + \mathbf{r}_c \odot \mathbf{C}_c \odot D_t \mathbf{v}_c + \mathbf{v}_c) \\ \mathbf{C}_c \odot D_t \mathbf{v}_c = \mathbf{i}_f - \mathbf{i}_l \\ \mathbf{T}_{ll}\,(\mathbf{r}_c \odot \mathbf{C}_c \odot D_t \mathbf{v}_c + \mathbf{v}_c) = \mathbf{T}_{ll}\,(\mathbf{r}_l \odot \mathbf{i}_f + \mathbf{L}_l \odot D_t \mathbf{i}_l + \mathbf{w}) \end{cases}, \tag{3.8}$$

where $\mathbf{u} := \frac{1}{2} U_{dc} s$ and $\odot$ is the Hadamard product (or element-wise product), which in turn results in a descriptor system, as we can write the states of phase 3 as a linear

combination of phases 1 and 2, according to

$$\begin{aligned} i_3 &= -i_1 - i_2 \\ v_3 &= -\frac{C_1}{C_3} v_1 - \frac{C_2}{C_3} v_2, \end{aligned} \tag{3.9}$$

where i and v are the inductor currents and capacitor voltages, respectively, and C_i is the capacitance associated with the capacitor voltage v_i.

Thus, let us define the state vector as

$$\mathbf{x} := \left((i_{f,i})_{i=1}^{2}, (v_{c,i})_{i=1}^{2}, (i_{l,i})_{i=1}^{2} \right). \tag{3.10}$$

We can write the state-space equation as

$$D_t \mathbf{x} = \mathbf{A}\mathbf{x} + \mathbf{B}\mathbf{u} + \mathbf{E}\mathbf{w}, \tag{3.11}$$

with $\mathbf{x}$ in ab coordinates, since the third phase component was suppressed, and $\mathbf{u}$ and $\mathbf{w}$ in abc coordinates.

A transformation matrix from abc to $\alpha\beta$ coordinates can be defined as

$$\mathbf{T}_i := \mathbf{T}_{\alpha\beta} \begin{bmatrix} 1 & 0 \\ 0 & 1 \\ -1 & -1 \end{bmatrix},$$

for the inductor current states and

$$\mathbf{T}_v := \mathbf{T}_{\alpha\beta} \begin{bmatrix} 1 & 0 \\ 0 & 1 \\ -\dfrac{C_1}{C_3} & -\dfrac{C_2}{C_3} \end{bmatrix}$$

for the capacitor voltage states. Hence we can write a transformation matrix

$$\mathbf{T} := \operatorname{diag}(\mathbf{T}_i, \mathbf{T}_v, \mathbf{T}_i) \tag{3.12}$$

and the dynamic system equation described by (3.8) can then be rewritten as

$$D_t \mathbf{x}_{\alpha\beta} = \underbrace{(\mathbf{I}_3 \otimes \mathbf{T})\, \mathbf{A}\, (\mathbf{I}_3 \otimes \mathbf{T})^{-1}}_{\mathbf{A}_{\alpha\beta}} \mathbf{x}_{\alpha\beta} + \underbrace{(\mathbf{I}_3 \otimes \mathbf{T})\, \mathbf{B}\mathbf{T}_{\alpha\beta\gamma}^{-1}}_{\mathbf{B}_{\alpha\beta\gamma}} \mathbf{u}_{\alpha\beta\gamma} + \underbrace{(\mathbf{I}_3 \otimes \mathbf{T})\, \mathbf{E}\mathbf{T}_{\alpha\beta\gamma}^{-1}}_{\mathbf{E}_{\alpha\beta\gamma}} \mathbf{w}_{\alpha\beta\gamma}. \tag{3.13}$$

From inspection, $\operatorname{span}(\{\mathbf{u}_\gamma, \mathbf{w}_\gamma\}) \in \ker(D_t)$, hence the system can be rewritten with matrices $\mathbf{B}_{\alpha\beta} := \mathbf{B}_{\alpha\beta\gamma}|_{\alpha\beta}$ and $\mathbf{E}_{\alpha\beta} := \mathbf{E}_{\alpha\beta\gamma}|_{\alpha\beta}$.

For both balanced and unbalanced cases, $\ker(D_t) = \operatorname{span}(\{\mathbf{x}_\gamma, \mathbf{u}_\gamma, \mathbf{w}_\gamma\})$. The

following subsection will present models for parallel connected converters. The employed methodology is similar to the one presented for single converters previously discussed.

3.3 PARALLELED CONVERTERS MODELS WITH CONSTANT DC-LINK

From the inspection of (3.4) and (3.13), $\ker(D_t) \subseteq \text{span}(\{\mathbf{x}_\gamma, \mathbf{u}_\gamma, \mathbf{w}_\gamma\})$, which is to be expected as there is no γ-axis components in the circuit illustrated by Figure 3.4. However, the parallel connection of power converters might lead to circulating currents in the γ-axis, resulting in $\ker(D_t) \subset \text{span}(\{\mathbf{x}_\gamma, \mathbf{u}_\gamma, \mathbf{w}_\gamma\})$. From this, the connection of paralleled converters can then be categorized into two different categories, which are defined by the existence of subtractive mode components (or circulation components) γ-axis, which are illustrated by Figure 3.5:

(a) *Isolated dc-link*: The paralleled converters do not share a common dc bus. This configuration is adopted when the interface between different energy sources is done exclusively via the ac side. In this case, $\sum_{j=1}^{N}\sum_{i=1}^{3} i_{f,j,i} = 0$, i.e., $\ker(D_t) = \text{span}(\{\mathbf{x}_\gamma, \mathbf{u}_\gamma, \mathbf{w}_\gamma\})$. In $\alpha\beta\gamma$ coordinates, there is no circulating components in the γ axis between the power converters. However, there will be an additive-mode γ-axis component if there is a current path to the inverter ground, tipically through parasitic elements or EMC filter capacitors;

(b) *Common dc-link*: The paralleled converters share a common dc-link bus. This configuration is present when different converters are employed for the same dc-ac interface, or when the different energy sources are interfaced via the dc side, such as dc and hybrid grids. In this case, $\sum_{j=1}^{N}\sum_{i=1}^{3} i_{f,j,i} \neq 0$, i.e., $\ker(D_t) \subset$

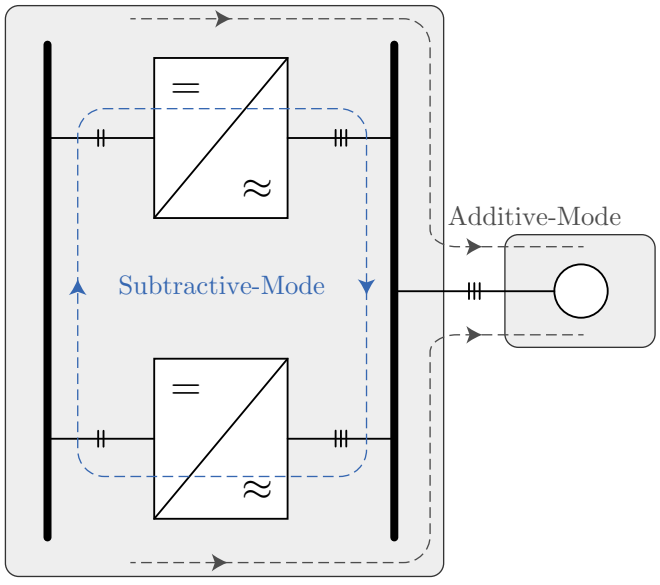

Figure 3.5 – Illustration demonstrating the current path for the subtractive and additive mode components for paralleled connected converters sharing a common dc bus

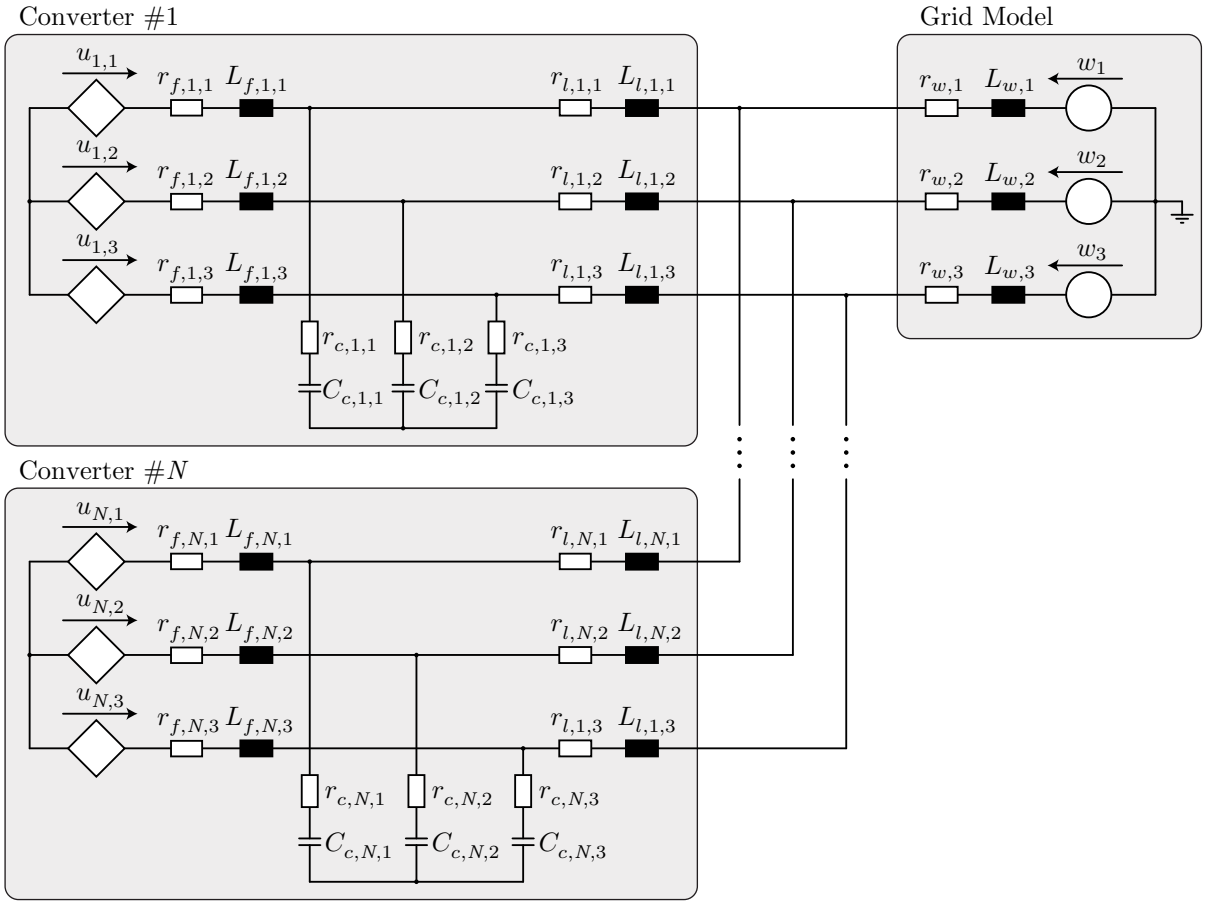

Figure 3.6 – N-paralleled connected Three-phase Voltage Source Inverter model with constant dc link voltage and a LCL output filter.

span $(\{\mathbf{x}_\gamma, \mathbf{u}_\gamma, \mathbf{w}_\gamma\})$. Differently from the previous configuration, there are circulating currents in the γ axis, i.e, $\mathbf{x}_{\gamma,sm} \neq 0$. This category also includes interleaved power converters.

These concepts and its relations to the nature of circulating currents are further explored in the following analysis.

For the ease of notation, the parameters of a converter, such as resistances, inductances and capacitances, are represented as a set of vectors according to

$$\mathbf{b} = (\mathbf{b}_j)_{j=1}^{N} = \left((b_{j,i})_{i=1}^{3}\right)_{j=1}^{N},$$

where the index i represents the phase and j represents the associated converter, hence $\mathbf{b}_j$ is a three-dimensional vector.

3.3.1 Isolated dc-Link Paralleled Converter Models

For a first model, consider the circuit illustrated by Figure 3.6, representing N paralleled connected converters connected at the *point of common coupling* (PCC). Let us

define the state vector $\mathbf{x}$ as

$$\mathbf{x} := (\mathbf{x}_j)_{j=1}^{N}, \tag{3.14}$$

where

$$\mathbf{x}_j := \left((i_{f,j,i})_{i=1}^{2}, (v_{c,j,i})_{i=1}^{2}, (i_{l,j,i})_{i=1}^{2}\right) = \left(\left(x_{1,i}^{j}\right)_{i=1}^{2}, \left(x_{2,i}^{j}\right)_{i=1}^{2}, \left(x_{3,i}^{j}\right)_{i=1}^{2}\right) \tag{3.15}$$

and j refers to the j^{th} paralleled connected converter and i refers to phases 1, 2 and 3 (or a, b and c, respectively). Since there is no γ-axis componentes, we can write the currents of phase 3 components as a linear combination of phases 1 and 2 components, i.e,

$$i_{k,j,3} = -i_{k,j,1} - i_{k,j,2}, \quad \forall j \in \mathbb{N}_N, \forall k \in \{f, l\}$$

and the voltages as

$$v_{k,j,3} = -\frac{C_{k,j,1}}{C_{k,j,3}} v_{k,j,1} - \frac{C_{k,j,2}}{C_{k,j,3}} v_{k,j,2}, \quad \forall j \in \mathbb{N}_N, \forall k \in \{c\}.$$

Also, let the input vector be given by

$$\mathbf{u} := \left((u_{j,i})_{i=1}^{3}\right)_{j=1}^{N}, \tag{3.16}$$

such that $u_{j,i}$ is the i^{th} phase voltage synthesized by the j^{th} converter, where

$$u_{j,i} = \frac{1}{2} U_{dc,j} s_{j,i}, \quad \forall i \in \mathbb{N}_3, j \in \mathbb{N}_N \tag{3.17}$$

where $U_{dc,j}$ is the dc link voltage and $s_{i,j}$ is the i^{th} switching function (or modulation function in case of the averaged model) of the j^{th} converter. Consider also the disturbance vector

$$\mathbf{w} := (w_i)_{i=1}^{3} \tag{3.18}$$

as the grid voltages. Hence, the differential equations for the circuit described by Figure 3.6 can be written as

$$\begin{cases} \mathbf{T}_{ll}\mathbf{u}_j = \mathbf{T}_{ll}\left(\mathbf{r}_{f,j} \odot \mathbf{i}_{f,j} + \mathbf{L}_{f,j} \odot D_t \mathbf{i}_{f,j} + \mathbf{r}_{c,j} \odot \mathbf{C}_{c,j} \odot D_t \mathbf{v}_{c,j} + \mathbf{v}_{c,j}\right) \\ \mathbf{C}_{c,j} \odot D_t \mathbf{v}_{c,j} = \mathbf{i}_{f,j} - \mathbf{i}_{l,j} \\ \mathbf{T}_{ll}\left(\mathbf{r}_{c,j} \odot \mathbf{C}_{c,j} \odot D_t \mathbf{v}_{c,j} + \mathbf{v}_{c,j}\right) = \\ \qquad \mathbf{T}_{ll}\left(\mathbf{r}_{l,j} \odot \mathbf{i}_{f,j} + \mathbf{L}_{l,j} \odot D_t \mathbf{i}_{l,j} + \displaystyle\sum_{k=1}^{N} \left(\mathbf{r}_w \odot \mathbf{i}_{l,k} + \mathbf{L}_w \odot D_t \mathbf{i}_{l,k}\right) + \mathbf{w}\right) \end{cases}, \quad \forall j \in \mathbb{N}_N. \tag{3.19}$$

Note that the obtention of multiple configurations, such as back-to-back systems, can be derived by slightly altering (3.19) as to fit multiple disturbance vectors $\mathbf{w}_j$.

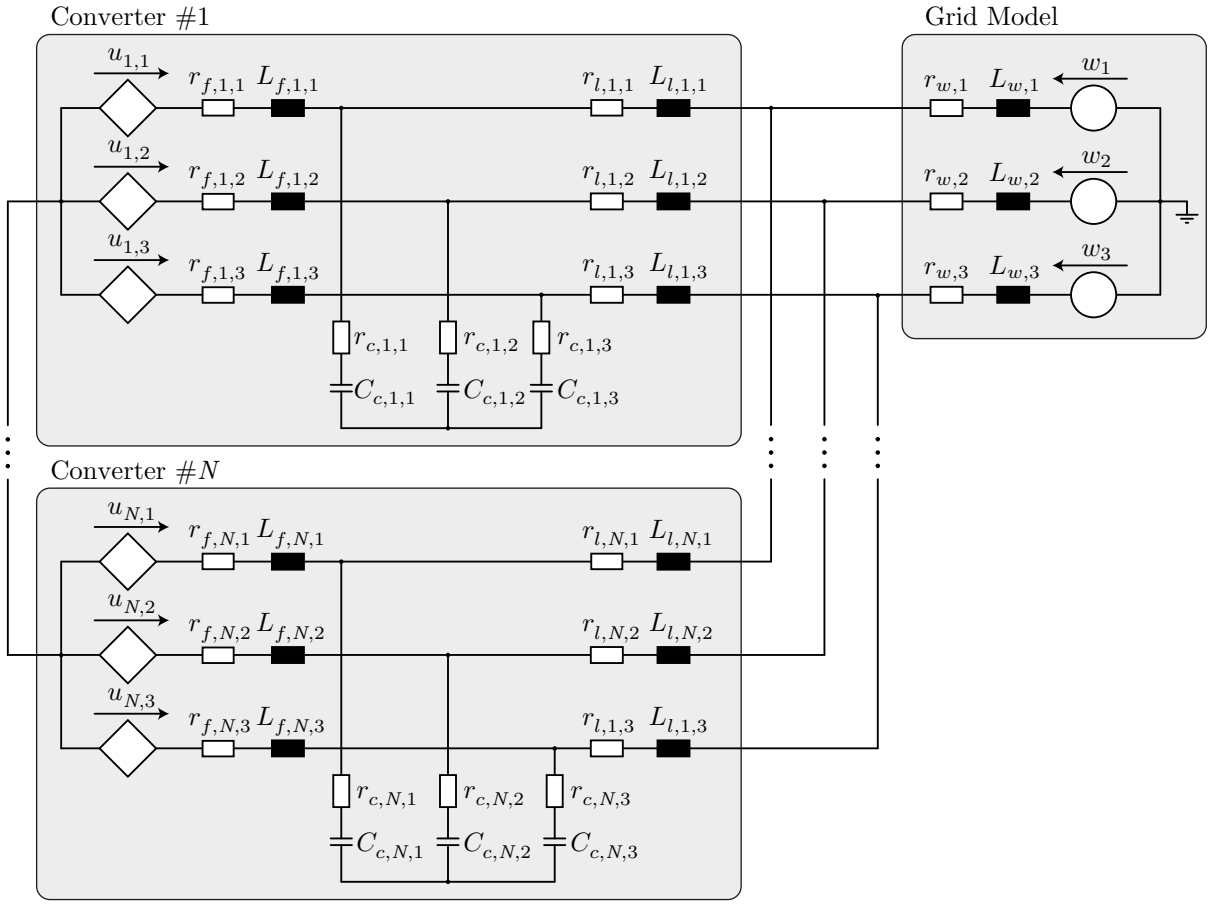

Figure 3.7 – N-paralleled connected Three-phase Voltage Source Inverter model with constant dc link voltage and a LCL output filter.

3.3.2 Common dc-link

3.3.2.1 LCL Filter

An immediate implication is that $\ker(D_t) \supset \text{span}(\{\mathbf{x}_{\gamma,am}\})$, as there is no additive-mode current path connected to the grid, which is not valid for high-frequency components due to a coupling caused by parasitic elements. An illustration of the configuration is presented in Figure 3.7. However, the subtractive-mode currents in the γ-axis do not vanish, as there is a current loop due to the dc bus connection.

From inspection of Figure 3.7, we have that

$$\sum_{j=1}^{N}\sum_{k=1}^{3} i_{f,j,k} = 0,$$

hence we can write an inductor current as a linear combination of the other currents. Thus, let us choose

$$i_{f,1,3} = -\sum_{k=1}^{2} i_{f,1,k} - \sum_{j=2}^{N}\sum_{k=1}^{3} i_{f,j,k}. \tag{3.20}$$

We also have that

$$\sum_{j=1}^{N}\sum_{k=1}^{3} i_{f,j,k} - i_{l,j,k} = 0,$$

which leads to

$$i_{l,1,3} = -\sum_{k=1}^{2} i_{l,1,k} - \sum_{j=2}^{N}\sum_{k=1}^{3} i_{f,j,k} \tag{3.21}$$

and also

$$i_{l,n,3} = \sum_{k=1}^{3} i_{f,n,k} - \sum_{k=1}^{2} i_{l,n,k}, \quad \forall\{n \in \mathbb{N}_N : n \geq 2\}, \tag{3.22}$$

as there is no γ-axis currents flowing through the capacitors. We can also define the grid current vector as a linear combination of the line currents, as in

$$\mathbf{i}_w := \sum_{j=1}^{N} \mathbf{i}_{l,j} \tag{3.23}$$

We can then write the differential equations in the same manner as the previous models according to

$$\begin{cases} \mathbf{T}_{ll}\mathbf{u}_j = \mathbf{T}_{ll}\left(\mathbf{r}_{f,j} \odot \mathbf{i}_{f,j} + \mathbf{L}_{f,j} \odot D_t\mathbf{i}_{f,j} + \mathbf{r}_{j,c} \odot \mathbf{C}_{j,c} \odot D_t\mathbf{v}_{j,c} + \mathbf{v}_{j,c}\right), \quad \forall j \in \mathbb{N}_N \\ u_{j,1} + r_{f,j,1}i_{f,j,1} + r_{l,j,1}i_{l,j,1} + L_{f,j,1}D_t i_{f,j,1} + L_{l,j,1}D_t i_{l,j,1} = \\ \qquad u_{j-1,1} + r_{f,j-1,1}i_{f,j-1,1} + r_{l,j-1,1}i_{l,j-1,1} + L_{f,j-1,1}D_t i_{f,j-1,1} + L_{l,j-1,1}D_t i_{l,j-1,1} \\ \qquad\qquad \forall j \in \mathbb{N} : j \geq 2 \\ \mathbf{C}_{j,c} \odot D_t\mathbf{v}_{j,c} = \mathbf{i}_{f,j} - \mathbf{i}_{l,j}, \quad \forall j \in \mathbb{N}_N \\ \mathbf{T}_{ll}\left(\mathbf{r}_{j,c} \odot \mathbf{C}_{j,c} \odot D_t\mathbf{v}_{j,c} + \mathbf{v}_{j,c}\right) = \\ \qquad \mathbf{T}_{ll}\left(\mathbf{r}_{l,j} \odot \mathbf{i}l, j + \mathbf{r}_{l,j} \odot D_t\mathbf{i}_{l,j} + \mathbf{r}_w \odot \mathbf{i}_w + \mathbf{L}_w \odot D_t\mathbf{i}_w + \mathbf{w}\right), \quad \forall j \in \mathbb{N}_N. \end{cases} \tag{3.24}$$

We can write the state-space equations as a descriptor system. Hence, let us define the state vector $\mathbf{x} \in \mathbb{R}^{9N}$ as

$$\mathbf{x} = \left(\mathbf{x}_j\right)_{j=1}^{N}, \tag{3.25}$$

where

$$\mathbf{x}^j = \left(\left(i_{f,j,i}\right)_{i=1}^{3}, \left(v_{v,c}^{j}\right)_{i=1}^{3}, \left(i_{l,i}^{j}\right)_{i=1}^{3}\right).$$

Thus, we can write the state-space equations as

$$\mathbf{K}D_t\mathbf{x} = \mathbf{A}\mathbf{K}\mathbf{x} + \mathbf{B}\mathbf{u} + \mathbf{E}\mathbf{w}, \tag{3.26}$$

where $\mathbf{A} \in \mathbb{R}^{7N-1\times 7N-1}$, $\mathbf{B} \in \mathbb{R}^{7N-1\times 3N}$, $\mathbf{E} \in \mathbb{R}^{7N-1\times 3}$ and $\mathbf{K} \in \mathbb{R}^{7N-1\times 9N}$ is chosen such

that

$$\mathrm{Im}\left(\mathbf{K}\right) = \mathrm{span}\left(\left\{\left(i_{f,1,i}\right)_{i=1}^{2}, \left(v_{c,i}^{1}\right)_{i=1}^{2}, \left(\left(i_{f,1,i}\right)_{i=1}^{2}, \left(\left(i_{f,j,i}\right)_{i=1}^{3}, \left(v_{c,i}^{j}\right)_{i=1}^{2}, \left(i_{l,i}^{j}\right)_{i=1}^{2}\right)_{j=2}^{N}\right\}\right). \tag{3.27}$$

Note that $\mathbf{B}|_{D_t\mathbf{x}_{\gamma,am}} = \mathbf{0}$ and $\mathbf{E}|_{D_t\mathbf{x}_{\gamma}} = \mathbf{0}$.

We can then apply the Lunze-Clarke Transform, as defined in Chapter 2, resulting in

$$D_t\chi = \mathcal{A}\chi + \mathcal{B}\upsilon + \mathcal{E}\psi, \tag{3.28}$$

where

$$\begin{aligned}
\mathcal{A} &= \left(\mathbf{K}\mathbf{Q}^{-1}\right)^{+}\mathbf{A}\mathbf{K}\mathbf{Q}^{-1}\\
\mathcal{B} &= \left(\mathbf{K}\mathbf{Q}^{-1}\right)^{+}\mathbf{B}\mathbf{Q}_u\\
\mathcal{E} &= \left(\mathbf{K}\mathbf{Q}^{-1}\right)^{+}\mathbf{E}\mathbf{T}_{\alpha\beta\gamma}^{-1}\\
\mathbf{Q} &= \left(\mathbf{L}_N \otimes \mathbf{I}_3\right) \otimes \mathbf{T}_{\alpha\beta\gamma}\\
\mathbf{Q}_u &= \mathbf{T}_{\alpha\beta\gamma}^{-1} \otimes \mathbf{L}_N
\end{aligned}$$

and

$$\begin{aligned}
\chi =& \{i_{f,\alpha,sm}, i_{f,\alpha,am}, i_{f,\beta,sm}, i_{f,\beta,am}, i_{f,\gamma,sm},\\
& v_{c,\alpha,sm}, v_{c,\alpha,am}, v_{c,\beta,sm}, v_{c,\beta,am}, i_{l,\alpha,sm}, i_{l,\alpha,am}, i_{l,\beta,sm}, i_{l,\beta,am}\}\\
\upsilon =& \{u_{\alpha,sm}, u_{\alpha,am}, u_{\beta,sm}, u_{\beta,am}, u_{\gamma,sm}\}\\
\psi =& \{w_\alpha, w_\beta\}
\end{aligned}$$

The matrix $\mathbf{K}$ can be obtained through a simple recursive algorithm. From (3.24), we have that the differential equations are more complex than the parallel-connected case, as the dimension of the differential operator in this case is larger than for the isolated dc bus problem. The dynamic equations for other filter topologies should follow the same procedure, and the following analysis demonstrates the obtention of the dynamic equations for different filter topologies.

3.3.2.2 Damped LCL Filter

The Damped LCL filter presents a damped capacitor and/or inductor, as means to reduce energy variations through the addition of a passive element. In this case, a lossy capacitor was considered, as illustrated in Figure 3.8.

The obtention of the dynamic equations are similar to the LCL filter procedure, with the addition of three states and an extra differential equation. Hence, we can make use of the (3.20), (3.21), (3.22) and (3.23). We can also write the capacitor voltages for phase 3 as a linear combination of phases 1 and 2 as in

$$v_{k,j,3} = -\frac{C_{k,1}}{C_{k,3}}v_{k,j,1} - \frac{C_{k,2}}{C_{k,3}}v_{k,j,2}, \quad \forall j \in \mathbb{N}_N, \forall k \in \{c,d\} \tag{3.29}$$

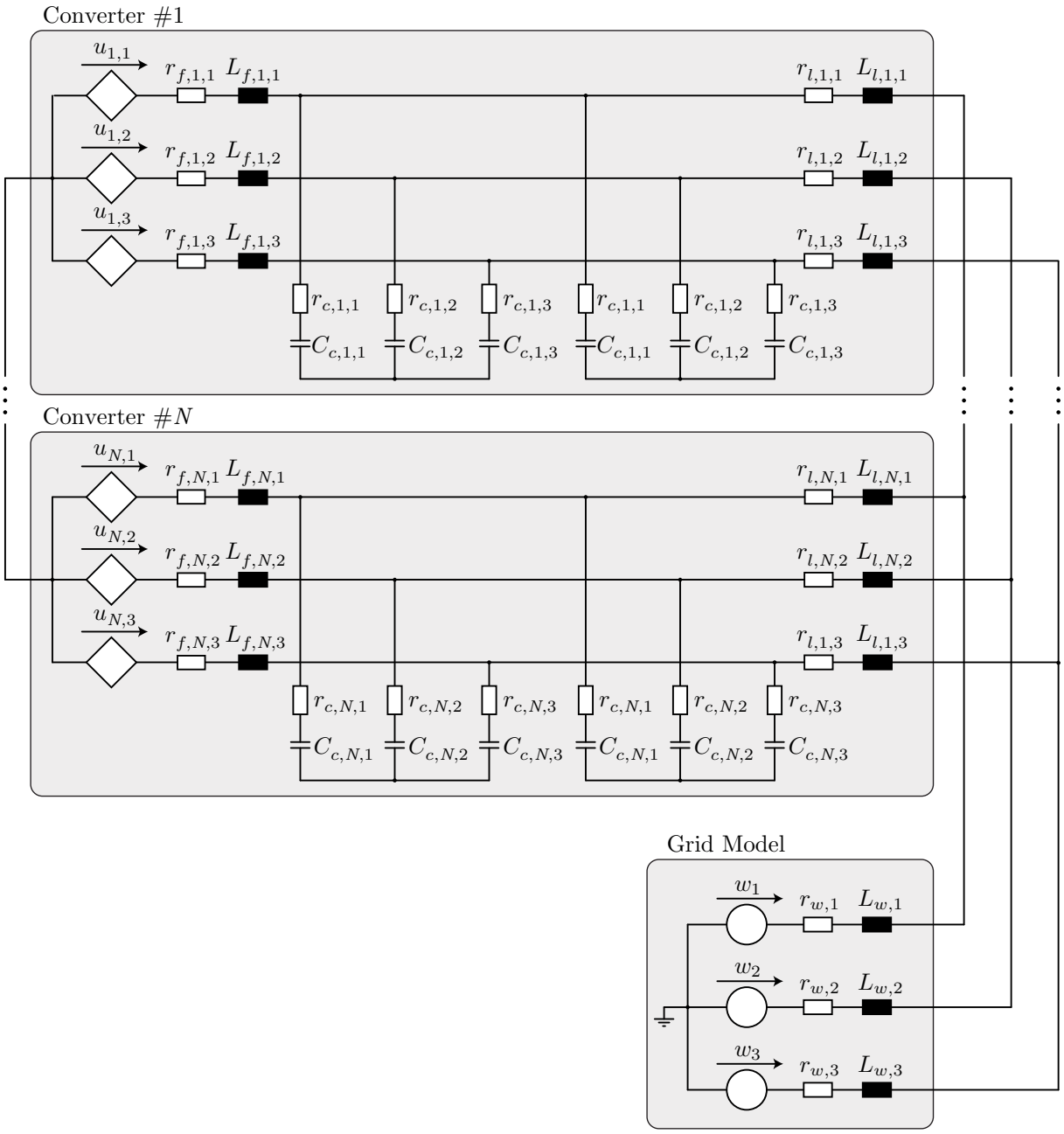

Figure 3.8 – N-paralleled connected Three-phase Voltage Source Inverter model with constant dc link voltage and a damped LCL output filter

From this, we can write the dynamic equations as

$$
\begin{cases}
\mathbf{T}_{ll}\mathbf{u}_j = \mathbf{T}_{ll}\left(\mathbf{r}_{f,j} \odot \mathbf{i}_{f,j} + \mathbf{L}_{f,j} \odot D_t\mathbf{i}_{f,j} + \mathbf{r}_{j,c} \odot \mathbf{C}_{j,c} \odot D_t\mathbf{v}_{j,c} + \mathbf{v}_{j,c}\right), \quad \forall j \in \mathbb{N}_N \\
u_{j,1} + r_{f,j,1}i_{f,j,1} + r_{l,j,1}i_{l,j,1} + L_{f,j,1}D_t i_{f,j,1} + L_{l,j,1}D_t i_{l,j,1} = \\
\qquad u_{j-1,1} + r_{f,j-1,1}i_{f,j-1,1} + r_{l,j-1,1}i_{l,j-1,1} + L_{f,j-1,1}D_t i_{f,j-1,1} + L_{l,j-1,1}D_t i_{l,j-1,1} \\
\qquad\qquad \forall j \in \mathbb{N} : j \geq 2 \\
\mathbf{C}_{j,c} \odot D_t\mathbf{v}_{j,c} + \mathbf{C}_{d,j} \odot D_t\mathbf{v}_{d,j} = \mathbf{i}_{f,j} - \mathbf{i}_{l,j}, \quad \forall j \in \mathbb{N}_N \\
\mathbf{r}_{j,c} \odot \mathbf{C}_{j,c} \odot D_t\mathbf{v}_{j,c} + \mathbf{v}_{j,c} = \mathbf{r}_{d,j} \odot \mathbf{C}_{d,j} \odot D_t\mathbf{v}_{d,j} + \mathbf{v}_{d,j}, \quad \forall j \in \mathbb{N}_N \\
\mathbf{T}_{ll}\left(\mathbf{r}_{j,c} \odot \mathbf{C}_{j,c} \odot D_t\mathbf{v}_{j,c} + \mathbf{v}_{j,c}\right) = \\
\qquad \mathbf{T}_{ll}\left(\mathbf{r}_{l,j} \odot \mathbf{i}l, j + \mathbf{r}_{l,j} \odot D_t\mathbf{i}_{l,j} + \mathbf{r}_w \odot \mathbf{i}_w + \mathbf{L}_w \odot D_t\mathbf{i}_w + \mathbf{w}\right), \quad \forall j \in \mathbb{N}_N.
\end{cases}
\tag{3.30}
$$

Table 3.3 – Converter Parameters

Parameter	Symbol	Value
Inverter Inductance	L_f	150 μH
Inverter Inductor Resistance	r_f	20 mΩ
Filter Capacitance	C_c	19.8 μF
Filter Capacitor Resistance	r_c	10 mΩ
Filter Damped Capacitance	C_d	19.8 μF
Filter Damped Capacitor Resistance	r_d	10m–1 Ω
Line Inductance	L_l	1–10 μH
Line Inductor Resistance	r_l	1 mΩ
Grid Inductance	L_w	50 μH
Grid Inductor Resistance	r_w	50 mΩ

and the same procedure can be adopted to obtain the dynamic system in terms of the subtractive and additive-mode components.

3.3.3 Subtractive-Mode Resonances

The dynamic models previously presented enables a more in-depth analysis of the system. One of the characteristics of this system is a resonance between filters due to a current loop involving $\{\mathbf{C}_{c,1:2}, \mathbf{L}_{l,1:2}\}$ for LCL filters and $\{\mathbf{C}_{c,1:2}, \mathbf{C}_{d,1:2}, \mathbf{L}_{l,1:2}\}$ for two paralleled converters, which is illustrated in Figure 3.9 for a system with parameters defined by Table 3.3. In the case of LCL filters, this resonance is tipically underdamped as the parasitic resistance values of these inductors and capacitors are low.

If the resonance frequencies are higher than the control bandwith of each converter, the only way to dampen the system is through a passive strategy. A solution is to minimize the subtractive-mode voltages by means of carrier synchronization strategies or real-time optimization routines for circulating current minimization. However, the filter parameters must be chosen such that these resonance frequencies are sufficiently far from the switching frequency to avoid instabilities.

Nonetheless, if the resonances are present in the controllable frequency spectrum, the control project must consider the parallel model into account, as opposed to a more descentralized control approach which is tipically employed.

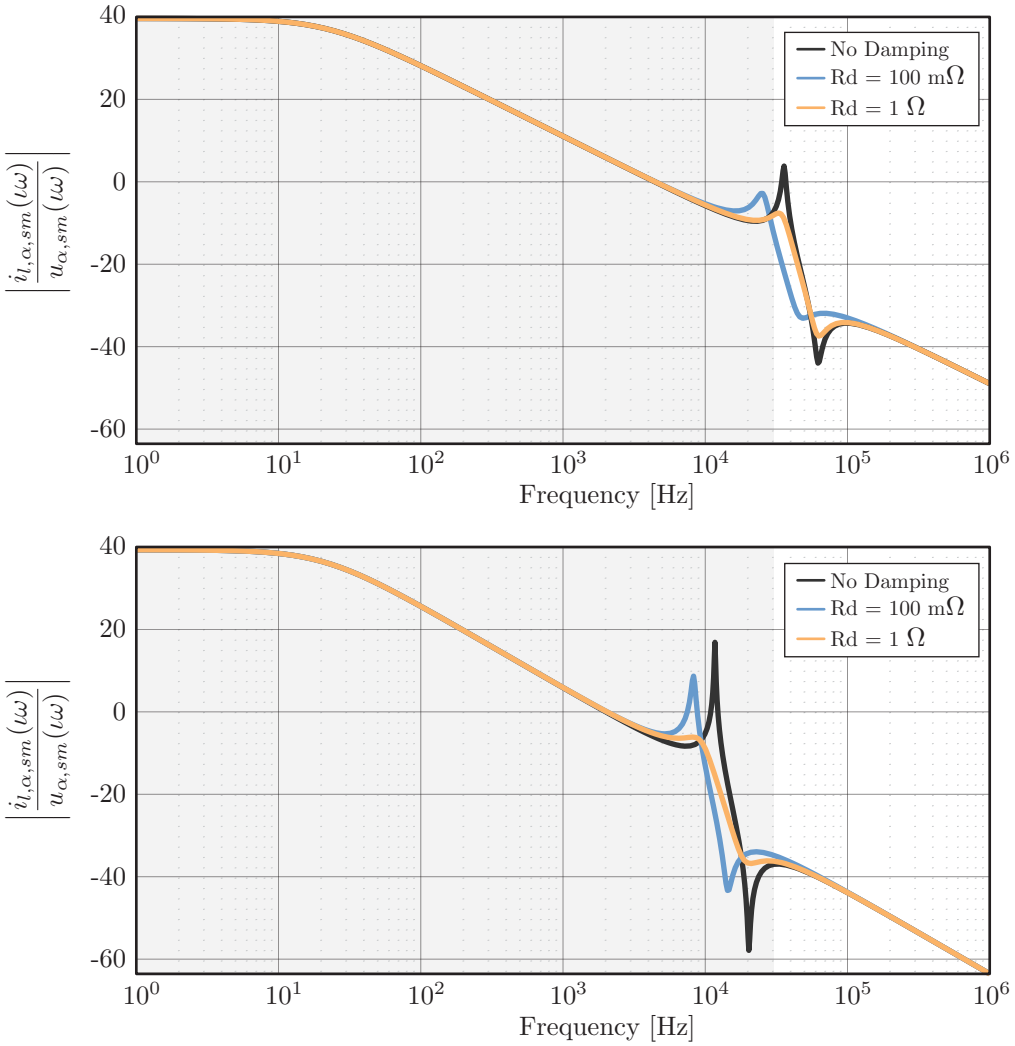

Figure 3.9 – Bode diagram of the subtractive mode line current ($i_{l,sm}$) with respect to the subtractive mode input (u_{sm}) in the α axis, demonstrating a subtractive-mode resonance with different damping resistance values. (a) $L_l = 1$ μH (b) $L_l = 10$ μH. This figure of merit demonstrates a differential-mode resonance, which might lead to instabilities and/or high-amplitude currents, especially when the peak resonance frequency lies close to the switching frequency.

3.4 CONVERTER MODELS WITH VARIABLE DC-LINK

3.4.1 Preliminaries on Dynamic Phasor Definitions

In a first moment, the 2LVSI dc bus was modeled as a constant voltage source U_{dc}, which is valid if the dc bus has a reasonably high inertia, be it due to a large capacitor or by power converters connected to the dc bus, such that $D_t u_{dc}$ approximately vanishes. However, this is not true for systems where dynamics associated with the dc bus are coupled with the converters' control loops, or applications such as solar and wind power systems, especially under weak grid conditions, where the grid impedance is much higher than the input impedance of the power converter system.

The procedure adopted here is similar to the previous case, although a different approach based on the Harmonic State Space (HSS) is employed so that the model presents

an equilibrium point instead of an orbital convergence. Hence a strong assumption can be made that each state variable pertains to the space $L_2(\mathbb{R})$, for a T-periodic orbit of the state vector. For this, let us define the linear map g such that for every state variable $x(t) \in L^2(\mathbb{R})$ the norm L_2 is defined as

$$\|x(t)\|_{L_2}^2 := \int_{-\infty}^{\infty} x^2(\tau)\ \mathrm{d}\tau, \tag{3.31}$$

In this sense, if we have

$$x(t) = X_0 + 2X_1 \cos\left(\omega t + \phi_1\right), \tag{3.32}$$

we have that

$$\begin{aligned} \langle x\rangle_0 &= X_0 \\ \langle x\rangle_1 &= X_1\cos(\phi_1) + \iota X_1 \sin\left(\phi_1\right) \\ \langle x\rangle_{-1} &= X_{-1}\cos(\phi_{-1}) + \iota X_{-1}\sin\left(\phi_{-1}\right) = X_1\cos(\phi_1) - \iota X_1\sin\left(\phi_1\right). \end{aligned} \tag{3.33}$$

such that

$$x(t) = \sum_{k=-1}^{1} \langle x\rangle_k e^{\iota k\omega t}, \tag{3.34}$$

which can be extended for an infinite number of harmonics, as discussed in Chapter 2.

3.4.2 Single Converter Model

From the previously discussed model, it is possible to write

$$\begin{cases} D_t\mathbf{x}_{ac} = \mathbf{A}_{ac}\mathbf{x}_{ac} + \mathbf{B}_{ac}\mathbf{u}_{ac} + \mathbf{E}_{ac}\mathbf{w}_{ac} \\ y_{ac} = \mathbf{C}_{ac}\mathbf{x}_{ac} + \mathbf{D}_{ac}\mathbf{u}_{ac} + \mathbf{F}_{ac}\mathbf{w}_{ac} \end{cases}, \tag{3.35}$$

where y_{ac} is the coupling state between the dc and ac circuits. We can also write a dc system as

$$\begin{cases} D_t\mathbf{x}_{dc} = \mathbf{A}_{dc}\mathbf{x}_{dc} + \mathbf{B}_{dc}i_{dc} + \mathbf{E}_{dc}\mathbf{w}_{dc} \\ y_{dc} = \mathbf{C}_{dc}\mathbf{x}_{dc} + \mathbf{D}_{dc}i_{dc} + \mathbf{F}_{dc}\mathbf{w}_{dc} \end{cases}, \tag{3.36}$$

where y_{dc} is also the coupling state between dc and ac circuits. For simplicity, assume that matrices $\mathbf{C}$ have a single non-null element equal to 1 and that matrices $\mathbf{D}$ and $\mathbf{F}$ vanish. The assumption on $\mathbf{C}$ is weak, as the restrictions were used to guarantee that the model is bilinear with respect to $\mathbf{s}$ and $\mathbf{x}$.

We can write the coupling between ac and dc employing the switching function s in $\alpha\beta$ coordinates for the 2LVSI as

$$\begin{cases} \mathbf{u}_{ac} = \mathbf{T}_{\alpha\beta}^{+}\mathbf{s}\mathbf{C}_{dc}x_{dc} \\ i_{dc} = \mathbf{s}^T\left(\mathbf{T}_{\alpha\beta}^{+}\right)^T\left(\mathbf{T}_{\alpha\beta}^{+}\right)\mathbf{C}_{ac}x_{ac} = \dfrac{3}{2}\mathbf{s}^T\mathbf{C}_{ac}x_{ac} \end{cases} \tag{3.37}$$

Let us consider a dynamic phasor for the fundamental component in the ac side and a dynamic phasor for the dc value and second harmonic. Thus, the coupling signals can be written as

$$\langle \mathbf{u}_{ac,i} \rangle = (\mathbf{\Gamma} \circ \langle y_{dc} \rangle) \circ \langle s_i \rangle = (\mathbf{\Gamma} \circ (\mathbf{I}_\infty \otimes \mathbf{C}_{dc}) \langle x_{dc} \rangle) \circ \langle s_i \rangle \,, \quad \forall i \in \{\alpha, \beta\} \tag{3.38}$$

and

$$\begin{aligned} \langle i_{dc} \rangle &= \frac{3}{4} \left((\mathbf{\Gamma} \circ \langle y_{ac,\alpha} \rangle) \circ \langle s_\alpha \rangle + (\mathbf{\Gamma} \circ \langle y_{ac,\beta} \rangle) \circ \langle s_\beta \rangle \right) \\ &= \frac{3}{4} \left((\mathbf{\Gamma} \circ (\mathbf{I}_\infty \otimes \mathbf{C}_{ac,\alpha}) \langle x_{ac} \rangle) \circ \langle s_\alpha \rangle + (\mathbf{\Gamma} \circ (\mathbf{I}_\infty \otimes \mathbf{C}_{ac,\beta}) \langle x_{ac} \rangle) \circ \langle s_\beta \rangle \right) \end{aligned} \tag{3.39}$$

based on the Toeplitz operator, respecting the previously defined signal norm.

Let the average model of the Voltage Source Inverter shown in Fig. 5.1 be given by

$$\begin{aligned} D_t \mathbf{x}_{dc} &= \mathbf{A}_{dc} \mathbf{x}_{dc} + \mathbf{B}_{dc} \mathbf{u}_{dc} + \mathbf{E}_{dc} \mathbf{w}_{dc}, \\ D_t \mathbf{x}_{ac} &= \mathbf{A}_{ac} \mathbf{x}_{ac} + \mathbf{B}_{ac} \mathbf{u}_{ac} + \mathbf{E}_{ac} \mathbf{w}_{ac}, \end{aligned} \tag{3.40}$$

where $\mathbf{A}_{dc} \in \mathbb{R}^{N_{dc} \times N_{dc}}$, $\mathbf{B}_{dc} \in \mathbb{R}^{N_{dc} \times 1}$ and $\mathbf{E}_{dc} \in \mathbb{R}^{N_{dc} \times 1}$, $\mathbf{A}_{ac} \in \mathbb{R}^{N_{ac} \times N_{ac}}$, $\mathbf{B}_{ac} \in \mathbb{R}^{N_{ac} \times 2}$ and $\mathbf{E}_{ac} \in \mathbb{R}^{N_{ac} \times 2}$, $u_{dc} := \mathbf{d}^T \mathbf{i}_f$, $\mathbf{u}_{ac} := u_{dc} \mathbf{d}$, $\mathbf{d} := (d_\alpha, d_\beta)$, $\mathbf{w} := (w_\alpha, w_\beta)$ and

$$\begin{aligned} \mathbf{x}_{ac} &:= (i_{f,\alpha}, v_{c,\alpha}, v_{d,\alpha}, i_{l,\alpha}, i_{f,\beta}, v_{c,\beta}, v_{d,\beta}, i_{l,\beta}) \\ &:= (\mathbf{x}_{ac,\alpha}, \mathbf{x}_{ac,\beta}). \end{aligned}$$

Assume that

$$\mathbf{d} := \sum_{k=-n_h}^{n_h} \langle \mathbf{d} \rangle_k e^{\iota k \omega t}, \quad \mathbf{w} := \sum_{k=-n_h}^{n_h} \langle \mathbf{w} \rangle_k e^{\iota k \omega t}, \quad u_{dc} := \sum_{k=-n_h}^{n_h} \langle u_{dc} \rangle_k e^{\iota k \omega t}$$

truncated at $n_h \in \mathbb{N}$ harmonics. Let us define the state-space matrices through

$$\begin{aligned} \mathbf{A}_{dc} &:= -\frac{1}{C_{dc} R_{dc}}, \quad \mathbf{B}_{dc} := -\frac{3}{2 C_{dc}}, \quad \mathbf{E}_{dc} := \frac{1}{C_{dc}}, \\ \mathbf{A}_{ac} &:= \mathbf{I}_2 \otimes \mathbf{A}_i, \quad \mathbf{B}_{ac} := \mathbf{I}_2 \otimes \mathbf{B}_i, \quad \mathbf{E}_{ac} := \mathbf{I}_2 \otimes \mathbf{E}_i, \end{aligned} \tag{3.41}$$

assuming a dc bus composed by a current source connected to a dc bus capacitor. The set

$(\mathbf{A}_i, \mathbf{B}_i, \mathbf{E}_i)$ can be defined through

$$\mathbf{A}_i = \begin{bmatrix} -\frac{r_f}{L_f} & -\frac{1}{L_f} & 0 & 0 \\ \frac{r_d(L_f - C_c r_c r_f)}{C_c L_f (r_c + r_d)} & -\frac{C_d L_f L_w r_d - C_c L_f L_w r_c + C_c C_d L_f r_c r_d^2 + C_c C_d L_w r_c r_d^2}{C_c C_d L_f L_w r_d (r_c + r_d)} & -\frac{C_c r_c - C_d r_d}{C_c C_d r_d (r_c + r_d)} & -\frac{r_d (L_w - C_c r_c r_w)}{C_c L_w (r_c + r_d)} \\ 0 & \frac{1}{C_d r_d} & -\frac{1}{C_d r_d} & 0 \\ 0 & \frac{1}{L_w} & 0 & -\frac{1}{L_w} \end{bmatrix}$$

$$\mathbf{B}_i = \begin{bmatrix} \frac{1}{2L_f} & \frac{1 r_c r_d}{2L_f (r_c + r_d)} & 0 & 0 \end{bmatrix}^T, \quad \mathbf{E}_i = \begin{bmatrix} 0 & \frac{r_c r_d}{L_w (r_c + r_d)} & 0 & -\frac{r_w}{L_w} \end{bmatrix}^T \tag{3.42}$$

with the assumption that the converter parameters are balanced, else the methodology presented in this chapter can be employed for model obtention.

We can also define the output matrices with respect to the ac voltages and currents as

$$\mathbf{C}_{v_c} = \mathbf{I}_2 \otimes [0 \quad 1 \quad 0 \quad 0], \quad \mathbf{C}_{i_l} = \mathbf{I}_2 \otimes [0 \quad 0 \quad 0 \quad 1], \tag{3.43}$$

as i_l is the current control process variable and v_c is the voltage measurement used for grid synchronization.

Consequently, the Harmonic State-Space model can be written as

$$\begin{cases} D_t \langle \mathbf{x}_{dc} \rangle = \left(\mathbf{I}_{N_h} \otimes \mathbf{A}_{dc} - \operatorname{diag}\left(\mathbb{Z}_{-n_h}^{n_h} \right) \otimes \iota\omega \mathbf{I}_{N_{dc}} \right) \langle \mathbf{x}_{dc} \rangle + \left(\mathbf{I}_{N_h} \otimes \mathbf{E}_{dc} \right) \langle \mathbf{w}_{dc} \rangle \\ \qquad\qquad + \left(\mathbf{I}_{N_h} \otimes \mathbf{B}_{dc} \right) \begin{bmatrix} \left(\mathbf{\Gamma} \circ \langle i_{f,\alpha} \rangle \right) \circ \langle d_\alpha \rangle \\ \left(\mathbf{\Gamma} \circ \langle i_{f,\beta} \rangle \right) \circ \langle d_\beta \rangle \end{bmatrix} \\ D_t \langle \mathbf{x}_{ac} \rangle = \left(\mathbf{I}_{N_h} \otimes \mathbf{A}_{ac} - \operatorname{diag}\left(\mathbb{Z}_{-n_h}^{n_h} \right) \otimes \iota\omega \mathbf{I}_{N_{ac}} \right) \langle \mathbf{x}_{ac} \rangle + \left(\mathbf{I}_{N_h} \otimes \mathbf{E}_{ac} \right) \langle w_{ac} \rangle \\ \qquad\qquad + \left(\mathbf{I}_{N_h} \otimes \mathbf{B}_{ac} \right) \left(\mathbf{\Gamma} \circ \langle u_{dc} \rangle \right) \left(\mathbf{I}_{N_h} \otimes \mathbf{C}_v \right) \langle \mathbf{d} \rangle . \end{cases} \tag{3.44}$$

3.4.3 Paralleled Converters with Isolated dc-Link

Since the paralleled converter model of the form

$$\begin{bmatrix} D_t \mathbf{x}^1 \\ D_t \mathbf{x}^2 \\ \vdots \\ D_t \mathbf{x}^N \end{bmatrix} = \begin{bmatrix} \mathbf{A}_{1,1} & \mathbf{A}_{1,2} & \cdots & \mathbf{A}_{1,N} \\ \mathbf{A}_{2,1} & \mathbf{A}_{2,2} & \cdots & \mathbf{A}_{2,N} \\ \vdots & \vdots & \ddots & \vdots \\ \mathbf{A}_{2,N} & \mathbf{A}_{2,N} & \cdots & \mathbf{A}_{N,N} \end{bmatrix} \begin{bmatrix} \mathbf{x}_1 \\ \mathbf{x}_2 \\ \vdots \\ \mathbf{x}_N \end{bmatrix} + \begin{bmatrix} \mathbf{B}_1 & \mathbf{0} & \cdots & \mathbf{0} \\ \mathbf{0} & \mathbf{B}_2 & \cdots & \mathbf{0} \\ \vdots & \vdots & \ddots & \vdots \\ \mathbf{0} & \mathbf{0} & \cdots & \mathbf{B}_N \end{bmatrix} \begin{bmatrix} \mathbf{u}_1 \\ \mathbf{u}_2 \\ \vdots \\ \mathbf{u}_N \end{bmatrix} + \begin{bmatrix} \mathbf{E}_1 \\ \mathbf{E}_2 \\ \vdots \\ \mathbf{E}_N \end{bmatrix} \mathbf{w}, \tag{3.45}$$

where $\mathbf{u}_j$ is the voltage synthesized by the j^{th} converter, demonstrates a sparse $\mathbf{B}$ matrix, we can repeat the same procedure for a single converter to couple the dc and ac circuits,

resulting in

$$\begin{bmatrix} D_t\chi_1 \\ D_t\chi_2 \\ \vdots \\ D_t\chi_N \end{bmatrix} = \begin{bmatrix} \mathcal{A}_{1,1}(\upsilon^1) & \mathcal{A}_{1,2} & \cdots & \mathcal{A}_{1,N} \\ \mathcal{A}_{2,1} & \mathcal{A}_{2,2}(\upsilon_2) & \cdots & \mathcal{A}_{2,N} \\ \vdots & \vdots & \ddots & \vdots \\ \mathcal{A}_{N,1} & \mathcal{A}_{N,2} & \cdots & \mathcal{A}_{N,N}(\upsilon_N) \end{bmatrix} \begin{bmatrix} \chi_1 \\ \chi_2 \\ \vdots \\ \chi_N \end{bmatrix} + \begin{bmatrix} \mathcal{E}_1 \\ \mathcal{E}_2 \\ \vdots \\ \mathcal{E}_N \end{bmatrix} \begin{bmatrix} \psi_1 \\ \psi_2 \\ \vdots \\ \psi_N \end{bmatrix}, \tag{3.46}$$

where $\mathcal{A}_{n,n}$ is obtained through the same procedure shown for single converters for $n \in \mathbb{N}_N$, else

$$\mathcal{A}_{n,j} = \begin{bmatrix} \mathbf{0} & \mathbf{0} \\ \mathbf{0} & \mathbf{A}_{n,j} \end{bmatrix}, \quad \forall \{n, \in \mathbb{N}_N : n \neq j\}$$

and

$$\mathcal{E}_n = \mathbf{I}_\infty \otimes \mathbf{E}_n,$$

since the coupling between converters and the switching functions are independent. Note that the number of harmonics can be truncated as means of facilitating the computation process.

3.5 DC BUS MODELS

This section focuses on the discussion of dc circuit models that are relevant to the interface between different energy sources. It begins by examining fundamental models such as current and power sources. The discussion then delves into specific energy sources, including photovoltaic models and battery systems, as well as the dc-dc converters used to interface these various energy sources.

3.5.1 Current Source Model

Let $i_{dc} \in L^2(\mathbb{R})$ a current source, with the dc bus circuit composed by a capacitor with capacitance C_{dc} and a resistor with resistance R_{dc}. The state-space model of the time-variant model can then be expressed as

$$\begin{cases} D_t x_{dc} = -\dfrac{1}{R_{dc}C_{dc}} x_{dc} + \dfrac{1}{C_{dc}}(i_{dc} - \dfrac{3}{2}\mathbf{s}^T\mathbf{i}_f) \\ v_{dc} = x_{dc}. \end{cases} \tag{3.47}$$

with its Harmonic State-Space description given by

$$\begin{cases} D_t \langle x_{dc} \rangle = -\left(\dfrac{1}{R_{dc}C_{dc}}\mathbf{I}_\infty + \iota\omega\mathrm{diag}\,(\mathbb{Z})\right)\langle x_{dc}\rangle + \dfrac{1}{C_{dc}}(\langle i_{dc}\rangle - \langle \psi_{ac}\rangle) \\ \langle v_{dc}\rangle = \langle x_{dc}\rangle\,. \end{cases} \tag{3.48}$$

where $\psi_{ac} \in L^2(\mathbb{R}) : \psi_{ac} := \frac{3}{2}\mathbf{s}^T\mathbf{i}_f$ is the dc circuit output current henceforth, such that

$$\langle \psi_{ac} \rangle = \frac{3}{2C_{dc}} \begin{bmatrix} \mathbf{\Gamma} \circ \langle s_\alpha \rangle & \mathbf{\Gamma} \circ \langle s_\beta \rangle \end{bmatrix} \circ \begin{bmatrix} \langle i_{f,\alpha} \rangle \\ \langle i_{f,\beta} \rangle \end{bmatrix}, \tag{3.49}$$

since the ac current decription is decoupled from the structure of the dc circuit in this chapter, since it only depends on v_{dc}.

3.5.2 Power Source Model

Let $p_{dc} \in L^2(\mathbb{R})$ a time-variant power source. This source can be modeled as a current source, since the voltage over the power source terminals are given by v_{dc}, resulting in

$$i_{dc} = \frac{1}{v_{dc}} p_{dc} = \frac{1}{\mathbf{C}_{dc}\mathbf{x}_{dc}} p_{dc} \tag{3.50}$$

which can be approximated by

$$i_{dc} \approx \frac{1}{\bar{v}_{dc}} p_{dc} - \frac{\bar{p}_{dc}}{\bar{v}_{dc}^2}(v_{dc} - \bar{v}_{dc}) \tag{3.51}$$

considering that the fixed point $\bar{v}_{dc}$ is set by a control loop. A further approximation can be made by taking

$$i_{dc} \approx \frac{1}{\bar{v}_{dc}} p_{dc}, \tag{3.52}$$

which in turn solves for the current source model. However, if we take (3.50), the harmonic state-space model of the current source is given by

$$\langle i_{dc} \rangle = \boldsymbol{h}_{\text{div}}(\langle p_{dc} \rangle, \langle v_{dc} \rangle) = \boldsymbol{h}_{\text{div}}(\langle p_{dc} \rangle, (\mathbf{I}_\infty \otimes \mathbf{C}_{dc}) \langle x_{dc} \rangle), \tag{3.53}$$

which results in

$$\begin{cases} D_t \langle x_{dc} \rangle = -\left(\dfrac{1}{R_{dc}C_{dc}} \mathbf{I}_\infty + \iota\omega \text{diag}(\mathbb{Z}) \right) \langle x_{dc} \rangle \\ \qquad\qquad + \dfrac{1}{C_{dc}} \left(\boldsymbol{h}_{\text{div}}(\langle p_{dc} \rangle, (\mathbf{I}_\infty \otimes \mathbf{C}_{dc}) \langle x_{dc} \rangle) - \langle \psi_{ac} \rangle \right) \\ \langle v_{dc} \rangle = \langle x_{dc} \rangle . \end{cases} \tag{3.54}$$

3.5.3 Photovoltaic Model

The output current of an array formed by $N_s \times N_p$ identic photovoltaic modules be described by the transcendental equation:

$$i_{ar} = \frac{N_p(I_{\text{pvn}} + K_i\Delta T)}{Gn}G - N_p(I_{\text{scn}} + K_i\Delta T)\frac{\exp\left(\dfrac{qR_p(v + i_{ar}R_s)}{N_s^2 ak(T_n + \Delta T)(R_p + R_s)}\right) - 1}{\exp\left(\dfrac{q(V_{\text{ocn}} + K_v\Delta T)}{N_s ak(T_n + \Delta T)}\right) - 1} \tag{3.55}$$

where i_{ar} is the array output current, v_{ar} is the array output voltage, q is the electron charge, k is the Boltzmann constant, a is the diode ideality constant, T_n is the nominal temperature of the $p-n$ junction, ΔT is the temperature variation with respect to T_n, R_p and R_s are the parallel and series resistances of a single cell, G is the irradiance, G_n is the nominal irradiance, I_{scn} is the short-circuit current, V_{ocn} is the open-circuit voltage, and I_{pvn} is the light-generated current at the nominal condition for a single module. Additionally, K_i and K_v represent the open-circuit voltage and short-circuit current temperature coefficients, respectively. Under constant temperature conditions, (3.55) can be simplified, resulting in

$$i_{ar} = k_{\text{pv},1}G + k_{\text{pv},2} - k_{\text{pv},2}\exp\left(k_{\text{pv},3}i_{dc} + k_{\text{pv},4}v_{ar}\right). \tag{3.56}$$

In order to remove the transcendental characteristic, let us introduce a state variable $\xi \in L^2(\mathbb{R})$ such that

$$D_t\xi = 1/\tau_\xi(i_{ar} - \xi) \tag{3.57}$$

as a first-order system with settling-time of approximately $5\tau_\xi$. We can then rewrite (3.55) as

$$\begin{cases} D_t\xi = \dfrac{1}{\tau_\xi}(i_{ar} - \xi) \\ i_{ar} \approx k_{\text{pv},1}G + k_{\text{pv},2} - k_{\text{pv},2}\exp\left(k_{\text{pv},3}\xi + k_{\text{pv},4}v_{ar}\right). \end{cases} \tag{3.58}$$

The Harmonic State-Space model can then be written as

$$\begin{cases} D_t\left\langle\xi\right\rangle = -\left(\dfrac{1}{\tau_\xi}\mathbf{I}_\infty + \iota\omega\text{diag}\left(\mathbb{Z}\right)\right)\left\langle\xi\right\rangle + \dfrac{1}{\tau_\xi}\left\langle i_{ar}\right\rangle \\ \left\langle i_{ar}\right\rangle = (k_{\text{pv},1}G + k_{\text{pv},1})\langle\hat{h}_0\rangle - k_{\text{pv},2}\boldsymbol{h}_{\text{exp}}(k_{\text{pv},3}\left\langle\xi\right\rangle + k_{\text{pv},4}\left\langle v_{ar}\right\rangle), \end{cases} \tag{3.59}$$

where $\boldsymbol{h}_{\text{exp}}$ is defined in Chapter 2.

A large signal model of the MPPT converter can then be applied directly to the set (v_{ar}, i_{ar}) as means of computing i_{dc} in terms of v_{dc}. A first approximation would be to ignore the dynamics of the boost converter, assuming that the energy stored in the magnetic components is much smaller than the energy of the dc bus capacitor. This leads

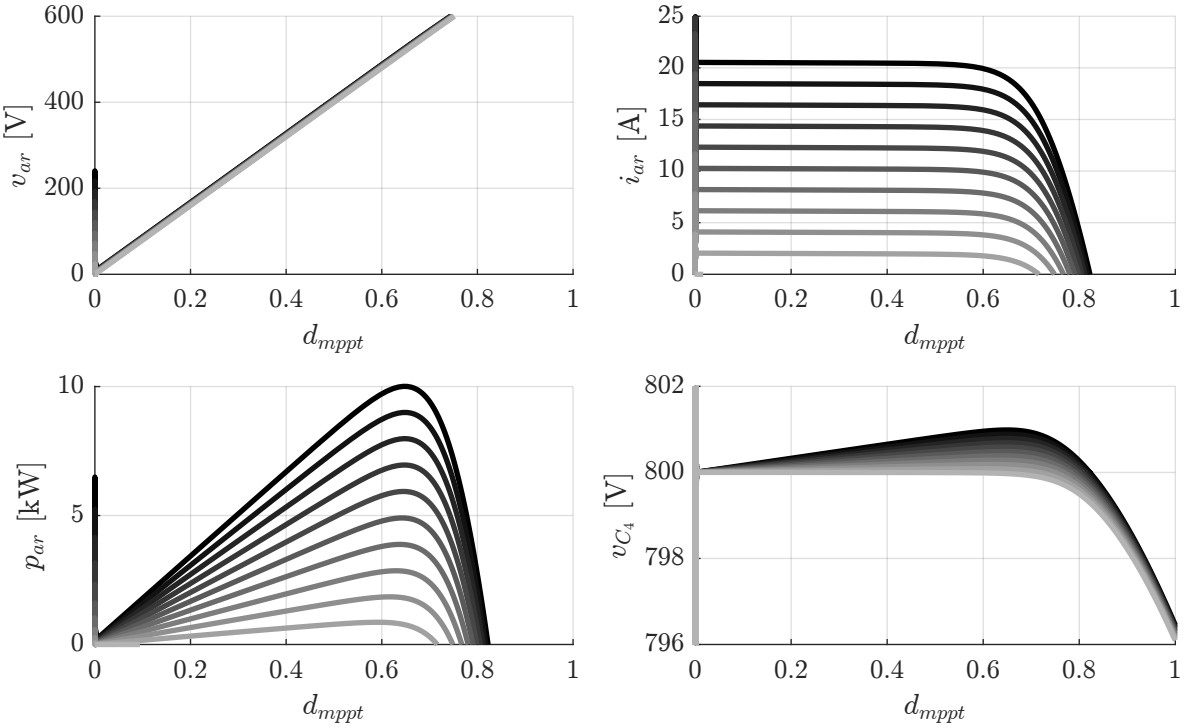

Figure 3.10 – Array of 20 × 2.5 KC200GT Modules characteristic

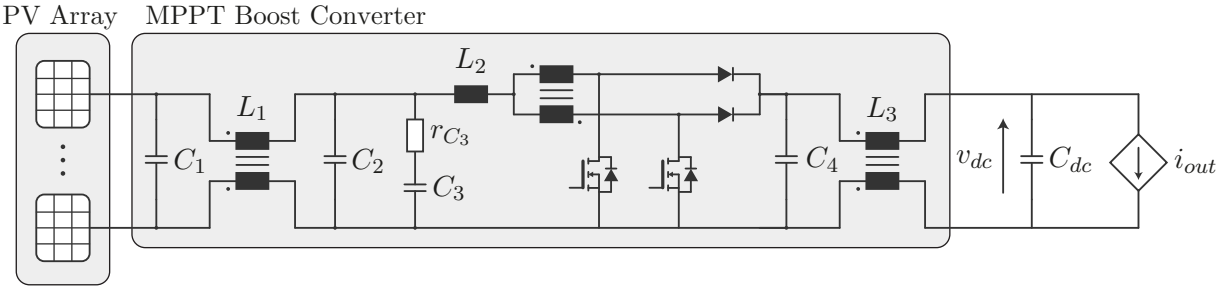

Figure 3.11 – Interleaved Boost Converter for Maximum Power Point Tracking.

to the following Harmonic State-Space equation:

$$\begin{cases} D_t \langle \xi \rangle = -\left(\dfrac{1}{\tau_\xi}\mathbf{I}_\infty + \iota\omega \mathrm{diag}\,(\mathbb{Z})\right)\langle \xi \rangle + \dfrac{1}{\tau_\xi d_{\mathrm{MPPT}}}\langle i_{dc} \rangle \\ \langle i_{dc} \rangle = d_{\mathrm{MPPT}}(k_{\mathrm{pv},1}G + k_{\mathrm{pv},2})\langle \hat{h}_0 \rangle - d_{\mathrm{MPPT}}k_{\mathrm{pv},2}\boldsymbol{h}_{\mathrm{exp}}(k_{\mathrm{pv},3}\langle \xi \rangle + k_{\mathrm{pv},4}d_{\mathrm{MPPT}}\langle v_{dc} \rangle), \end{cases} \tag{3.60}$$

where d_{MPPT} is the complementary switch duty cycle of the boost converter related to the Maximum Power Point Tracking (MPPT) algorithm and $\boldsymbol{h}_{\mathrm{exp}}$ is defined in Chapter 2.

If the dynamic of a boost converter is taken into account, as in [30], we can write the state-space equations of the maximum power point tracker converter differential-mode

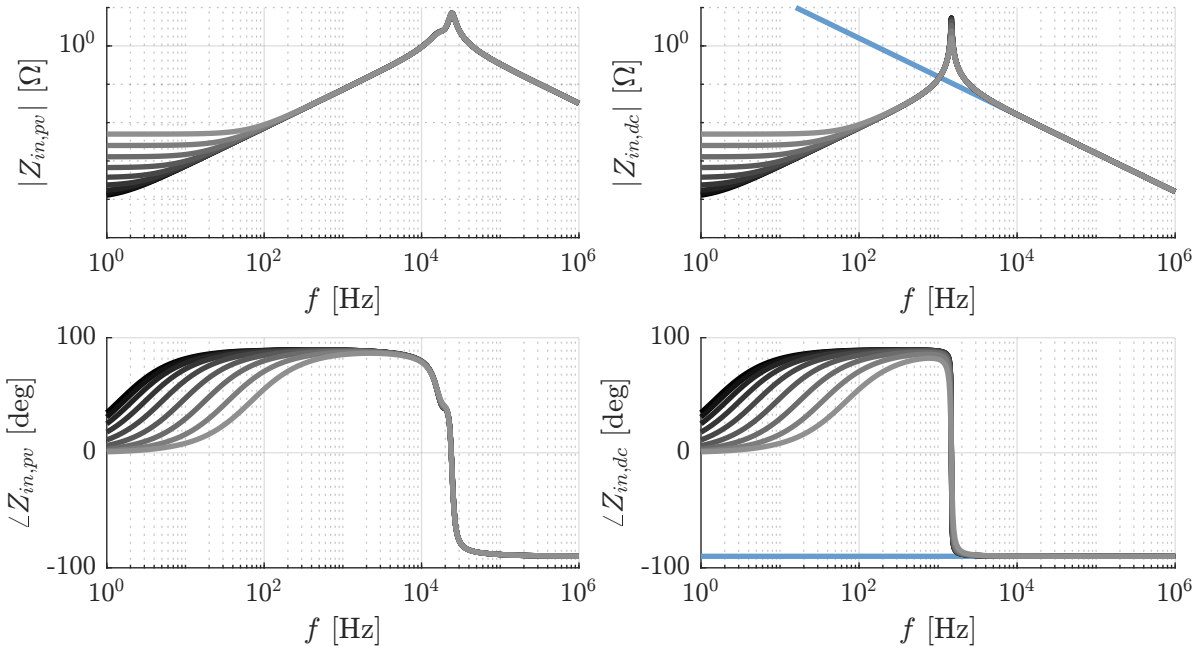

Figure 3.12 – Input impedance of the PV and dc circuit linearized model for multiple dc bus voltages, from 400 V (Black) to 1080 V (Gray).

components illustrated in Figure 3.11 according to

$$\begin{cases} D_t\xi = \dfrac{1}{\tau_\xi}(k_{\text{pv},1}G + k_{\text{pv},2} - k_{\text{pv},2}\exp\left(k_{\text{pv},3}\xi + k_{\text{pv},4}v_{C_1}\right) - \xi) \\ C_1 D_t v_1 = -\dfrac{v_1}{R_p + R_s} - i_{L_1} + \dfrac{R_p}{R_s + R_p}(k_{\text{pv},1}G + k_{\text{pv},2} - k_{\text{pv},2}\exp\left(k_{\text{pv},3}\xi + k_{\text{pv},4}v_{C_1}\right)) \\ v_1 = r_{L_1} i_{L_1} + L_1 D_t i_{L_1} + r_{C_2} C_2 D_t v_{C_2} + v_{C_2} \\ r_{C_2} C_2 D_t v_{C_2} + v_{C_2} = r_{C_3} C_3 D_t v_{C_3} + v_{C_3} \\ C_2 D_t v_{C_2} + C_3 D_t v_{C_3} = i_{L_1} - i_{L_2} \\ r_{C_2} C_2 D_t v_{C_2} + v_{C_2} = r_{L_2} i_{L_2} + L_2 D_t i_{L_2} + d_{\text{MPPT}} v_{C_4} \\ C_4 D_t v_{C_4} = d_{\text{MPPT}} i_{L_2} - i_{L_3} \\ v_{C_4} = r_{L_3} i_{L_3} + L_3 D_t i_{L_3} + v_{dc}, \end{cases} \tag{3.61}$$

with v_{dc} here modeled as an exogenous input. We can then define the input vector $\mathbf{u}_{\text{MPPT}} := (G, d_{\text{MPPT}})$, the state vector $\mathbf{x}_{\text{MPPT}} := \left((i_{L,k})_{k=1}^{3}, (v_{C,k})_{k=1}^{4}, \xi\right)$ and an exogenous input v_{dc} which solves for

$$\begin{cases} D_t \mathbf{x}_{\text{MPPT}} = \boldsymbol{f}_{\text{MPPT}}(\mathbf{x}_{\text{MPPT}}, \mathbf{u}_{\text{MPPT}}, v_{dc}) \\ \qquad i_{dc} = i_{L_3} \end{cases} \tag{3.62}$$

for $\boldsymbol{f}_{\text{MPPT}} : \mathbb{R}^8 \times \mathbb{R}^2 \times \mathbb{R} \to \mathbb{R}^8$.

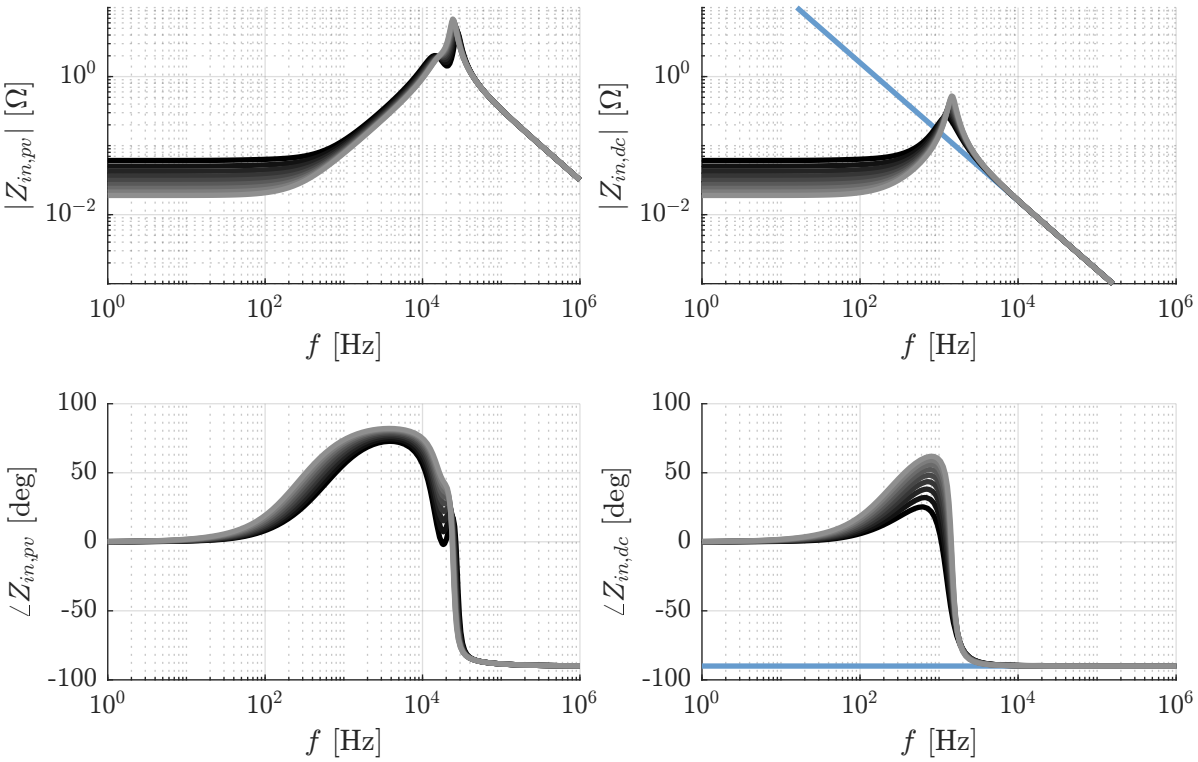

Figure 3.13 – Input impedance of the PV and dc circuit linearized model for multiple dc bus voltages, from 400 V (Black) to 1080 V (Gray), with a closed-loop operation.

Let us consider the Solar Panel Model description with the PV model defined by

$$\mathbf{k}_{\text{pv}} = \left(20.53644950, 2.4562996183 \times 10^{-7}, 2.7711412032 \times 10^{-2}, 5.0988998141 \times 10^{-2}\right), \tag{3.63}$$

which represents a 20×2.5 array of Kyocera KC200GT PV modules. The module curves considering the converter systems for different solar irradiances is shown in Figure 3.10.

We can then linearize Equation 3.61 through the Jacobian matrix of $\boldsymbol{f}_{\text{MPPT}}$ calculated at the fixed point obtained from $\boldsymbol{f}_{\text{MPPT}}(\bar{\mathbf{x}}_{\text{MPPT}}, \bar{\mathbf{u}}_{\text{MPPT}}, \bar{v}_{dc}) = 0$, which solves for

$$D_t\tilde{\mathbf{x}}_{\text{MPPT}} = \tilde{\mathbf{A}}_{\text{MPPT}}\tilde{\mathbf{x}}_{\text{MPPT}} + \tilde{\mathbf{B}}_{\text{MPPT}}\tilde{\mathbf{u}}_{\text{MPPT}} + \tilde{\mathbf{E}}_{\text{MPPT}}\tilde{v}_{dc}. \tag{3.64}$$

We can then analyze the input impedance of the boost converter and the PV array as well as the dc circuit input impedance, taking into account the dc-bus capacitor, as shown in Figure 3.12. Note that the input impedance of the pv array is much smaller than the capacitor impedance at lower frequencies. This can cause unknown effects on the stability of a system, since the impedance presents an resistive/inductive behaviour at lower frequencies.

We can also write $\mathbf{d}_{\text{MPPT}}$ as a feedback system, with the objective of controlling the PV array voltage. In this case, the MPPT occurs on the voltage reference. The system

model for an Integral controller can be written as

$$\begin{cases} D_t\xi = \dfrac{1}{\tau_\xi}(k_{\text{pv},1}G + k_{\text{pv},2} - k_{\text{pv},2}\exp\left(k_{\text{pv},3}\xi + k_{\text{pv},4}v_{C_1}\right) - \xi) \\ C_1 D_t v_1 = -\dfrac{v_1}{R_p + R_s} - i_{L_1} + \dfrac{R_p}{R_s + R_p}(k_{\text{pv},1}G + k_{\text{pv},2} - k_{\text{pv},2}\,\exp\left(k_{\text{pv},3}\xi + k_{\text{pv},4}v_{C_1}\right)) \\ v_1 = r_{L_1} i_{L_1} + L_1 D_t i_{L_1} + r_{C_2} C_2 D_t v_{C_2} + v_{C_2} \\ r_{C_2} C_2 D_t v_{C_2} + v_{C_2} = r_{C_3} C_3 D_t v_{C_3} + v_{C_3} \\ C_2 D_t v_{C_2} + C_3 D_t v_{C_3} = i_{L_1} - i_{L_2} \\ r_{C_2} C_2 D_t v_{C_2} + v_{C_2} = r_{L_2} i_{L_2} + L_2 D_t i_{L_2} + d_{\text{MPPT}} v_{C_4} \\ C_4 D_t v_{C_4} = d_{\text{MPPT}} i_{L_2} - i_{L_3} \\ v_{C_4} = r_{L_3} i_{L_3} + L_3 D_t i_{L_3} + v_{dc} \\ D_t d_{\text{MPPT}} = k_{i,\text{MPPT}}(v_{C_2} - v_{\text{MPPT}}), \end{cases} \tag{3.65}$$

where v_{MPPT} is the PV array voltage reference. The input impedance of the boost converter and PV array operating in closed-loop is shown in Figure 3.13.

The nonlinearity of the PV array can have significant impacts on the behavior of the dc bus. Contrary to the assumption of capacitive behavior, the dc bus tends to exhibit low impedance when operating closer to the maximum power point. This behavior is highly dependent on the operating point and can lead to undesired coupling between dc voltage control loops of power converter systems connected to the dc bus.

Another issue arising from the nonlinear behavior of the PV array is the reduction of average power injection when operating with an oscillating dc bus, as seen in Figure 3.14. This reduction can be attributed to the coupling between harmonic frequencies caused by the exponential function in the PV array model. The presence of these harmonics can affect the overall performance and stability of the power conversion system.

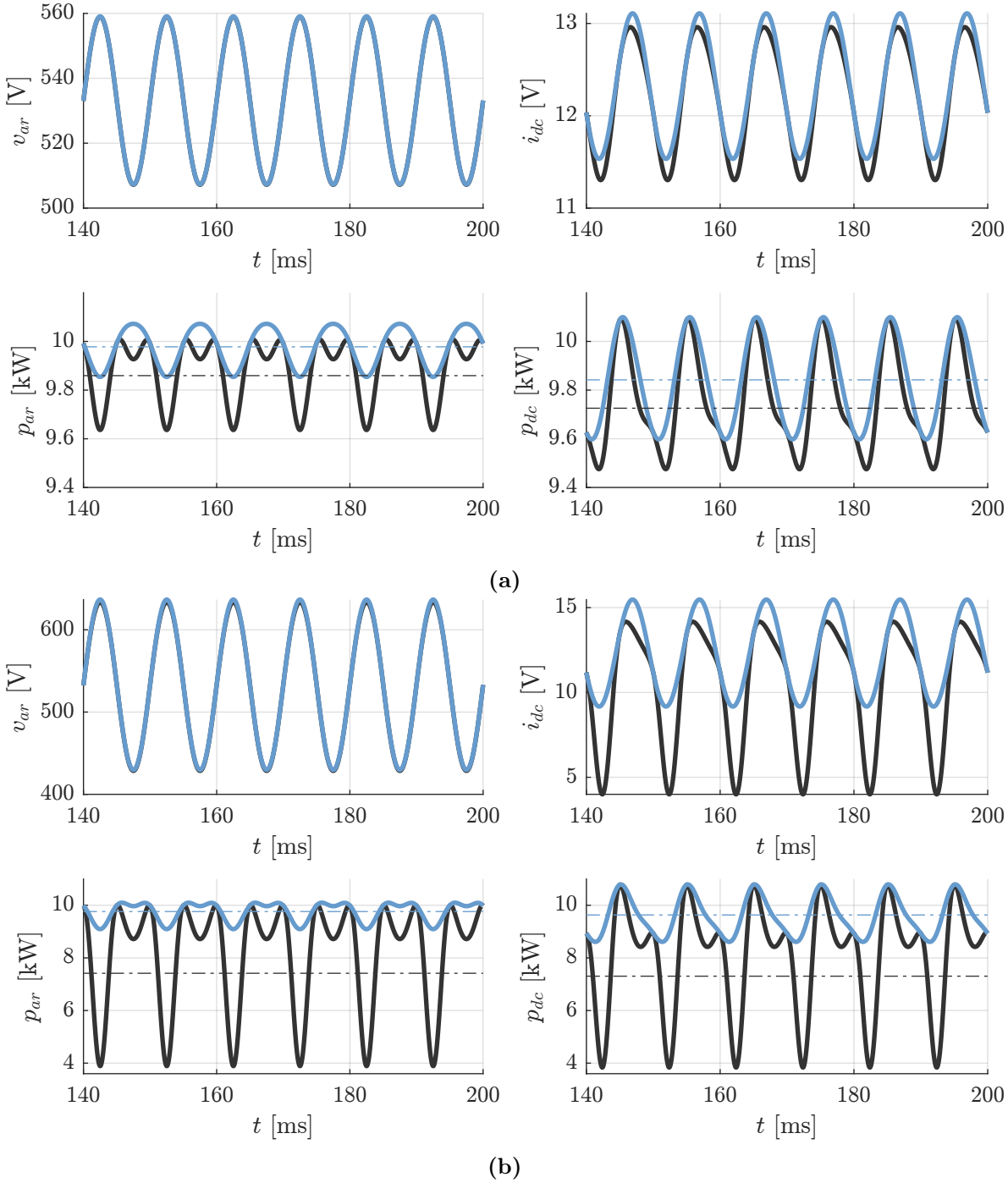

Figure 3.14 – Comparison between linear (blue) and nonlinear (black) Photovoltaic models while operating with an oscillating dc bus. (a) 5% voltage oscillation at 100 Hz (b) 10% voltage oscillation at 100 Hz.

3.6 DC-DC POWER CONVERTERS

The dc bus can also be connected to different power converters, especially for energy storage and backup interface, such as battery systems and supercapacitors. This can be done through dc-dc converters, with a special focus to dc-ac-dc converters, such as resonant converters (series resonant, series-parallel, LLC, etc) and Dual-Active Bridge (DAB) converters. Most of these converters present a similar structure, with changes to the magnetic components design methodology and modulation strategies inherent to each topology.

This section demonstrates an example of a Three-Phase LC resonant converter model, illustrated in Figure 3.15, which employs a similar modeling methodology to the ones previously presented.

3.6.1 Time-Variant Dynamic Model

Let us define the switching function for each converter semiconductor device illustrated in Figure 3.15 as

$$\begin{aligned} s_{i,j,k} &:= \begin{cases} 1, & \text{if the switch is ON,} \\ 0, & \text{else} \end{cases}, \\ &\forall i \in \{1,2\}, j \in \{1,2,3\}, k \in \{p,n\}, \end{aligned} \tag{3.66}$$

where i defines the input and output stages and j is the phase. We can also define a more general switching function given by

$$\begin{aligned} s_{i,j} &:= s_{i,j,p} - s_{i,j,n} \\ &= 2s_{i,j,p} - 1 \end{aligned} \tag{3.67}$$

for $s_{i,j} \in \{-1, 1\}$, assuming that the switches pertaining to the set n are linearly dependent.

From this, we have that the voltage synthesized by each converter arm switching

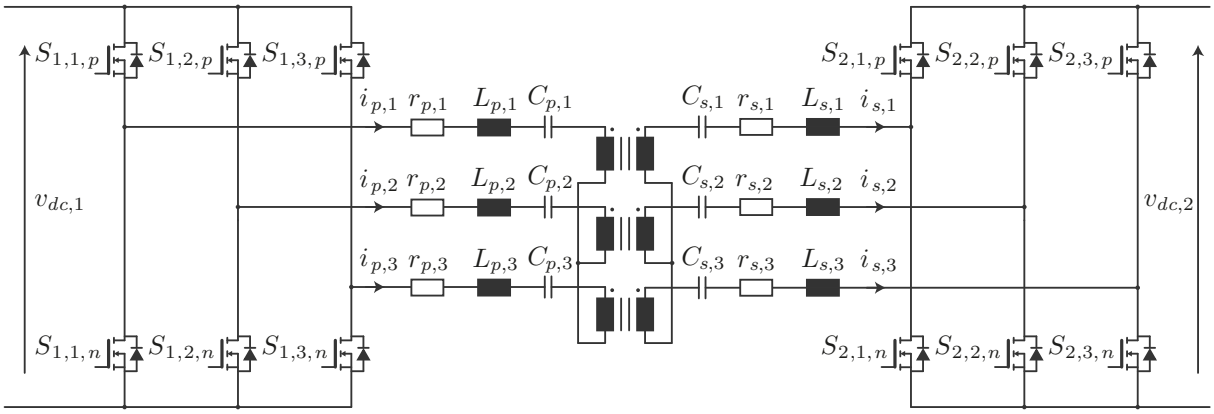

Figure 3.15 – Three-phase LC resonant converter topology.

cell (here named 2L-SC) is given by

$$\mathbf{v_i} := \frac{1}{2} v_{dc,i} \mathbf{s}_i. \tag{3.68}$$

From inspection of the circuit illustrated in Figure 3.15, we can write the transformer currents in phase 3 as a linear combination of the currents in phases 1 and 2, according to

$$i_{j,3} = -i_{j,1} - i_{j,2}, \quad \forall j \in \{p, s\}. \tag{3.69}$$

The capacitor voltages in phase 3 can also be written as a linear combination of phases 1 and 2, such that

$$v_{j,3} = -\frac{C_{j,1}}{C_{j,3}} v_{j,1} - \frac{C_{j,2}}{C_{j,3}} v_{j,2}, \quad \forall j \in \{p, s\}. \tag{3.70}$$

We can also write the transformer voltages as

$$\begin{bmatrix} \mathbf{v}_{t,p} \\ \mathbf{v}_{t,s} \end{bmatrix} = \mathbf{M} D_t \begin{bmatrix} \mathbf{i}_p \\ \mathbf{i}_s \end{bmatrix} = \begin{bmatrix} \mathbf{M}_{pp} & \mathbf{M}_{ps} \\ \mathbf{M}_{ps} & \mathbf{M}_{ss} \end{bmatrix} D_t \begin{bmatrix} \mathbf{i}_p \\ -\mathbf{i}_s \end{bmatrix}, \tag{3.71}$$

where each element of $\mathbf{M} \in \mathbb{R}^{6\times 6}$ can be written as

$$M_{i,j} = \delta_{i,j} L_{i,i} - (1 - \delta_{i,j}) k_{i,j} L_{i,j}, \tag{3.72}$$

where $L_{i,i}$ are the self inductance of each winding, $k_{i,j}$ is the magnetic coupling between windings and $\delta_{i,j}$ is the Kronecker delta. If we assume a balanced three-phase transformer, we can write

$$\begin{gathered} \mathbf{M}_{pp} = \frac{1}{2} \begin{bmatrix} 2L_m & -k_m L_m & -k_m L_m \\ -k_m L_m & 2L_m & -k_m L_m \\ -k_m L_m & -k_m L_m & 2L_m \end{bmatrix} \\ \mathbf{M}_{ps} = \mathbf{M}_{sp} = a\mathbf{M}_{pp}, \quad \mathbf{M}_{ss} = a^2 \mathbf{M}_{pp}, \end{gathered} \tag{3.73}$$

where L_m is the primary-side self-inductance, a is the transformer ratio and k_m is a general magnetic coupling between windings.

Also, we can define employ the phase to line linear map such that

$$\begin{bmatrix} v_{12} \\ v_{23} \end{bmatrix} = \mathbf{T}_{ll} \begin{bmatrix} v_1 \\ v_2 \\ v_3 \end{bmatrix},$$

which will help in the model description. Note that the third line-to-line voltage was suppressed since it is a linear combination of v_{12} and v_{23} due to the three-wire characteristic of the system. From (3.69), (3.70) and (3.7), we can infer that the common-mode current

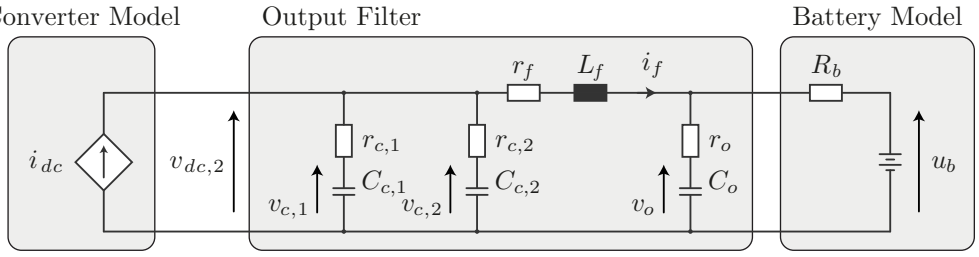

Figure 3.16 – Dc-dc converter output filter connected to a battery, which was modeled as a voltage source and a series resistance.

belongs to the kernel of the linear transformation, i.e., the common-mode current state is non-controllable. This is mostly true, since a zero axis circuit was not modeled. Thus, the dynamic equations of the three-phase circuit in Figure 3.15 can be written as

$$\begin{cases} \dfrac{1}{2}\mathbf{T}_{ll} v_{dc,1} \mathbf{s}_1 = \mathbf{T}_{ll} \left(\mathbf{r}_p \odot \mathbf{i}_p + \mathbf{L}_p \odot D_t \mathbf{i}_p + \mathbf{v}_p + \mathbf{M}_{pp} D_t \mathbf{i}_p \right. \\ \qquad\qquad \left. - \mathbf{M}_{ps} D_t \mathbf{i}_s \right) \\ \mathbf{C}_p \odot D_t \mathbf{v}_p = \mathbf{i}_p \\ \dfrac{1}{2}\mathbf{T}_{ll} v_{dc,2} \mathbf{s}_2 = \mathbf{T}_{ll} \left(-\mathbf{r}_s \odot \mathbf{i}_s - \mathbf{L}_s \odot D_t \mathbf{i}_s - \mathbf{v}_s + \mathbf{M}_{sp} D_t \mathbf{i}_p \right. \\ \qquad\qquad \left. - \mathbf{M}_{ss} D_t \mathbf{i}_s \right) \\ \mathbf{C}_s \odot D_t \mathbf{v}_s = \mathbf{i}_s \end{cases} . \tag{3.74}$$

The output filter illustrated in Figure 3.16 differential equations can be written as

$$\begin{cases} \mathbf{s}_2^T \mathbf{i}_s = i_f + \displaystyle\sum_{j=1}^{2} C_{c,i} D_t v_{c,i} \\ v_{c,1} + r_{c,1} C_{c,1} D_t v_{c,1} = v_{c,2} + r_{c,2} C_{c,2} D_t v_{c,2} \\ v_{c,1} + r_{c,1} C_{c,1} D_t v_{c,1} = r_f i_f + L_f D_t i_f + r_o C_o D_t v_o + v_o \\ i_f = \dfrac{1}{R_b} \left(r_o C_o D_t v_o + v_o - u_b \right) + C_o D_t v_o \end{cases} \tag{3.75}$$

For simplicity, assume that $r_{c,1}$ vanishes, which results in

$$\mathbf{v}_{dc} = \left(u_{dc}, v_{c,1} \right), \tag{3.76}$$

where u_{dc} is the input voltage.

The state vector $\mathbf{x}$ can then be divided into two different components, one related to the resonant converter (subscript r) and the other related to the output filter (subscript f), such that

$$\mathbf{x}' := (\mathbf{x}_r, \mathbf{x}_f), \tag{3.77}$$

where

$$\begin{aligned}\mathbf{x}_r &:= \left((i_{p,j})_{j=1}^2, (v_{p,j})_{j=1}^2, (i_{s,j})_{j=1}^2, (v_{s,j})_{j=1}^2\right)\\ \mathbf{x}_f &:= \left((v_{c,j})_{j=1}^2, i_f, v_o\right).\end{aligned}$$

We can also define the disturbance vector $\mathbf{w}$ as

$$\mathbf{w} := (u_{dc}, u_b). \tag{3.78}$$

Thus, the state-space model can be described by solving (3.74) and (3.75) for $D_t\mathbf{x}'$, which results in

$$\begin{aligned}D_t\mathbf{x}' &= f'(\mathbf{x}', \mathbf{s}, \mathbf{w})\\ &= \mathbf{A}'(\mathbf{s})\mathbf{x}' + \mathbf{E}'(\mathbf{s})\mathbf{w}\end{aligned}, \tag{3.79}$$

where $\mathbf{s} = (\mathbf{s}_1, \mathbf{s}_2)$.

If we assume that the parameters of the resonant converter are balanced, we can decouple the phase components by applying the Clarke transformation, which is defined as

$$\mathbf{T}_{\alpha\beta\gamma} := \frac{1}{3}\begin{bmatrix}2 & -1 & -1\\ 0 & \sqrt{3} & -\sqrt{3}\\ 1 & 1 & 1\end{bmatrix}. \tag{3.80}$$

Even if the parameters are unbalanced, the $\alpha\beta$ components should present a lower coupling.

From (3.80), (3.69) and (3.70), we can define two different linear maps for the resonant converter voltages and currents defined as

$$\begin{aligned}\mathbf{T}_i &:= \begin{bmatrix}\mathbf{I}_2 & \mathbf{0}_{1\times 2}\end{bmatrix}\mathbf{T}_{\alpha\beta\gamma}\begin{bmatrix}\mathbf{I}_2\\ -\mathbf{1}_{1\times 2}\end{bmatrix}\\ \mathbf{T}_{v,j} &:= \begin{bmatrix}\mathbf{I}_2 & \mathbf{0}_{1\times 2}\end{bmatrix}\mathbf{T}_{\alpha\beta\gamma}\begin{bmatrix}\mathbf{I}_2\\ -\frac{C_{j,1}}{C_{j,3}} \quad -\frac{C_{j,2}}{C_{j,3}}\end{bmatrix}, \forall j \in \{p, s\}.\end{aligned} \tag{3.81}$$

We can then define a linear map $\mathbf{T}_r : \mathbb{R}^8 \to \mathbb{R}^8$ as

$$\mathbf{T}_r := \operatorname{diag}(\mathbf{T}_i, \mathbf{T}_{v,p}, \mathbf{T}_i, \mathbf{T}_{v,s}) \tag{3.82}$$

such that

$$\mathbf{x}_c := \mathbf{T}_r\mathbf{x}. \tag{3.83}$$

Let us define the input vector $\mathbf{u}$ as

$$\mathbf{u} := \begin{bmatrix}\mathbf{I}_2 & \mathbf{0}_{1\times 2}\end{bmatrix}\mathbf{T}_{\alpha\beta\gamma}\mathbf{s}. \tag{3.84}$$

and redefine the state vector as

$$\mathbf{x} := (\mathbf{x}_c, \mathbf{x}_f) \tag{3.85}$$

such that

$$\begin{aligned} D_t\mathbf{x} &= f(\mathbf{x}, \mathbf{u}, \mathbf{w}) \\ &= \mathbf{A}(\mathbf{u})\mathbf{x} + \mathbf{E}(\mathbf{u})\mathbf{w}, \end{aligned} \tag{3.86}$$

where

$$\mathbf{A}(\mathbf{u}) := \mathbf{T}_r\mathbf{A}'\left(\mathbf{T}_u\mathbf{u}\right)\mathbf{T}_r^{-1}, \quad \mathbf{E}(\mathbf{u}) := \mathbf{T}_r\mathbf{E}'\left(\mathbf{T}_u\mathbf{u}\right)$$
$$\mathbf{T}_u := \mathbf{I}_2 \otimes \left(\begin{bmatrix}\mathbf{I}_2 & \mathbf{0}_{1\times 2}\end{bmatrix}\mathbf{T}_{\alpha\beta\gamma}^{-1}\right).$$

The system described by (3.86) can be rewritten as

$$\frac{\mathrm{d}}{\mathrm{d}t}\begin{bmatrix}\mathbf{x}_c \\ \mathbf{x}_f\end{bmatrix} = \begin{bmatrix}\mathbf{A}_c & \mathbf{A}_{cf}(\mathbf{u}) \\ \mathbf{A}_{fc}(\mathbf{u}) & \mathbf{A}_f\end{bmatrix}\begin{bmatrix}\mathbf{x}_c \\ \mathbf{x}_f\end{bmatrix} + \begin{bmatrix}\mathbf{E}_c(\mathbf{u}) & \mathbf{0} \\ \mathbf{0} & \mathbf{E}_f\end{bmatrix}\mathbf{w} \tag{3.87}$$

Note that (3.86) and (3.87) represent a time-periodic nonlinear system, as the open-loop system reaches $\mathbf{x}(t) = \mathbf{x}(t-T)$ for a certain input $\{\mathbf{u}(t) \in \mathbb{R}^4 : \mathbf{u}(t) = \mathbf{u}(t-T)\}$ and a constant disturbance $\mathbf{w} \in \mathbb{R}^2$ within a finite period T.

3.6.2 Switching Function Model

Consider the switching function vector $\mathbf{s} = (\mathbf{s}_1, \mathbf{s}_2)$, with each switching function defined by (3.67). We can write the Fourier Series of each switching function according to

$$s_{i,j} := \sum_{k=-\infty}^{\infty} \frac{2}{\pi(2k-1)} \cos\left((2k-1)\omega t - \phi_{i,j}(t)\right), \tag{3.88}$$

where ϕ is related to a certain phase-shift, which can be rewritten as

$$s_{i,j} = \sum_{k=-\infty}^{\infty} \langle s_{i,j}\rangle_k e^{\iota k\omega t}, \tag{3.89}$$

where

$$\langle s_{i,j}\rangle_k = \begin{cases} 0, & k \text{ even} \\ \dfrac{2}{\iota\pi k}\exp\left(-\iota k\phi_{i,j}(t)\right), & k \text{ odd}, \end{cases} \tag{3.90}$$

for a certain phase angle $\phi_{i,j}$. Since the interphase angles are fixed, we can write

$$\boldsymbol{\phi}_1 = \boldsymbol{\theta}_1 + \left(0, \frac{2}{3}\pi, -\frac{2}{3}\pi\right), \quad \boldsymbol{\phi}_2 = \delta\cdot(1,1,1) + \boldsymbol{\theta}_2 + \left(0, \frac{2}{3}\pi, -\frac{2}{3}\pi\right),$$

where $\delta \in (-\pi, \pi)$ is the phase between primary and secondary. We can also assume that $\theta_{1,1} = 0$, i.e., all the angles are referenced to the phase 1 of the first three-phase bridge. Note that δ is tipically employed as the control variable for a SISO control system.

From inspection, we have that

$$\ker(D_t) \subset \operatorname{span}\left(\left(0, 0, \sum_{j=1}^{3} s_{i,j}\right)\right), \quad \forall i \in \{1, 2\}, \tag{3.91}$$

i.e., the common-mode voltage synthesized by each three-phase bridge is orthogonal to the derivative of the state vector. From this, we can ignore the common-mode voltage, considering only the subset spanned by the $\alpha\beta$ components. Thus, we can separate the input vector given by (3.84) as

$$\mathbf{u} = (\mathbf{u}_1, \mathbf{u}_2) = \left((u_{1,j})_{j=1}^{2}, (u_{2,j})_{j=1}^{2}\right), \tag{3.92}$$

with each component given by

$$\begin{aligned}
\langle u_{1,1}\rangle_k &= \frac{2}{3\iota\pi k}\left(2 - e^{-\iota k\left(\theta_{1,2}+\frac{2}{3}\pi\right)} - e^{-\iota k\left(\theta_{1,3}-\frac{2}{3}\pi\right)}\right) \\
\langle u_{1,2}\rangle_k &= \frac{2\sqrt{3}}{3\iota\pi k}\left(e^{-\iota k\left(\theta_{1,2}+\frac{2}{3}\pi\right)} - e^{-\iota k\left(\theta_{1,3}-\frac{2}{3}\pi\right)}\right) \\
\langle u_{2,1}\rangle_k &= \frac{2}{3\iota\pi k}\left(2e^{-\iota k(\delta-\theta_{2,1})} - e^{-\iota k\left(\delta+\theta_{2,2}+\frac{2}{3}\pi\right)}\right. \\
&\qquad\qquad \left. -e^{-\iota k\left(\delta+\theta_{2,3}-\frac{2}{3}\pi\right)}\right) \\
\langle u_{2,2}\rangle_k &= \frac{2\sqrt{3}}{3\iota\pi k}\left(e^{\iota k\left(\delta+\theta_{2,2}-\frac{2}{3}\pi\right)} - e^{\iota k\left(\delta+\theta_{2,3}+\frac{2}{3}\pi\right)}\right),
\end{aligned} \tag{3.93}$$

for all odd k.

If the initial angles $\boldsymbol{\theta}$ vanish, it follows that

$$\langle u_{1,1}\rangle_k = \frac{2}{\iota\pi k} \quad \langle u_{1,2}\rangle_k = \frac{2}{\iota\pi k}e^{-\iota k\frac{\pi}{2}} \quad \langle u_{2,1}\rangle_k = \frac{2}{\iota\pi k}e^{-\iota k\delta} \quad \langle u_{2,2}\rangle_k = -\iota\frac{2}{\pi k}e^{-\iota k\left(\delta+\frac{\pi}{2}\right)}, \tag{3.94}$$

$\forall k \in \{1, 5, 7, 11, 13, 17, \ldots\}$.

3.6.3 Harmonic State-Space Model

From (3.87), we can separate the nonlinear model into two different parts:

- a linear part which results from the dynamics of each circuit;
- a nonlinear part which describes the coupling between the two systems, which has a polynomial characteristic due to the product between input and state vectors.

These be expressed as

$$\begin{aligned}
\dot{\mathbf{x}}_c &= \overbrace{\mathbf{A}_c\mathbf{x}_c}^{\text{linear}} + \overbrace{\mathbf{E}_c(\mathbf{u})\mathbf{w} + \mathbf{A}_{cf}(\mathbf{u})\mathbf{x}_f}^{\text{nonlinear}} \\
\dot{\mathbf{x}}_c &= \overbrace{\mathbf{A}_f\mathbf{x}_f}^{\text{linear}} + \overbrace{\mathbf{E}_f(\mathbf{u})\mathbf{w} + \mathbf{A}_{fc}(\mathbf{u})\mathbf{x}_c}^{\text{nonlinear}}.
\end{aligned} \tag{3.95}$$

The linear part of (3.95) can be expanded to its DP (or HSS) form by employing the same methodology described by Chapter 2. The nonlinear part can be decomposed into smaller systems as means of applying the $\mathbf{\Gamma}$ operator, resulting in

$$\begin{aligned}\mathbf{A}_{cf}\left(\mathbf{u}\right)\mathbf{x}_f &= \sum_{i=1}^{2}\sum_{j=1}^{2}\mathbf{A}_{cf}^{i,j}u_{i,j}\mathbf{x}_f \\ \mathbf{A}_{fc}\left(\mathbf{u}\right)\mathbf{x}_c &= \sum_{i=1}^{2}\sum_{j=1}^{2}\mathbf{A}_{fc}^{i,j}u_{i,j}\mathbf{x}_c\end{aligned} \tag{3.96}$$

where

$$\mathbf{A}_x^{i,j} = \mathbf{A}_x\Big|_{\substack{\mathbf{u}_l = \mathbf{0}, \forall l \neq i \\ u_{i,l} = 0, \forall l \neq i}}, \quad \forall x \in \{cf, fc\}.$$

For a simpler model, we can assume that $\langle \mathbf{x}_c \rangle_h$ vanishes for $h = 0$ and $\langle \mathbf{x}_f \rangle_h$ and $\langle \mathbf{w} \rangle_h$ vanish for $h \neq 0$, assuming purely sinusoidal currents in the resonant tank. This approach is valid when operating sufficiently close to the frequency of resonance of the resonant tank. Thus, we come to the nonlinear model given by

$$D_t\langle \mathbf{x} \rangle = \check{\mathbf{A}}(\delta, \omega)\langle \mathbf{x} \rangle + \check{\mathbf{E}}\langle \mathbf{w} \rangle \tag{3.97}$$

The switching frequency ω in this application can be modeled as a function of the output stages, as it varies with the output power and the output current. Hence, we can write

$$\omega = \Phi(x_{f,1}, x_{f,3}) \tag{3.98}$$

for a certain $\Phi : \mathbb{R}^2 \to \mathbb{R}$, which results from an optimization process to maximize the conversion efficiency and guarantee soft-switching for a wider margin and can present a nonlinear behaviour. If $|\dot{\omega}| \ll \left|\dot{\check{x}}_i\right|, \ \forall \check{x}_i \in \check{\mathbf{x}}$, we can model the switching frequency as a disturbance while neglecting its dynamics as means of asserting the stability. Note that, ideally, the frequency update must be decoupled from the dynamics of outer-loop controllers.

3.6.4 Numerical Example

Let a Three-phase LC Resonant Converter with parameters given by Table 3.4. The model validation is shown in Figure 3.17 for multiple points of operation. The nonlinear harmonic state-space model was simulated through a forward euler method, while the power converter was simulated using MATLAB/Simulink. The input impedance of the resonant converter can be written as

$$Z_{in}(s) = \frac{\langle v_{dc,1} \rangle_0(s)}{i_{dc,1}(s)}, \tag{3.99}$$

Table 3.4 – Three-Phase LC Resonant Converter Parameters

Description	**Parameter**	**Value**
Transformer Self-Inductance	$(M_{i,i})_{i=1}^{3}$	777.6 μH
Transformer turns ratio	a	0.666667
Transformer Coupling Factor	k_m	0.99
Primary Side Series Connected Inductance	L_p	22.224 μH
Primary Side Resistance	r_p	110 mΩ
Primary Side Capacitance	C_p	330 μF
Secondary Side Series Connected Inductance	L_s	0.1 μH
Secondary Side Resistance	r_s	50 mΩ
Secondary Side Capacitance	C_s	2500 μF
Filter Capacitance	$C_{o,1}$	8 μF
Filter Capacitor ESR	$r_{o,1}$	0 Ω
Filter Damped Capacitance	$C_{o,2}$	8 μF
Filter Damped Capacitor Resistance	$r_{o,2}$	2.7 Ω
Output Capacitance	$C_{o,3}$	4.5 μF
Output Capacitor ESR	$r_{o,3}$	0 Ω
Filter Inductance	L_f	2 μH
Filter Inductor Resistance	r_f	2 mΩ
Battery Resistance	R_b	300 mΩ

where

$$\langle i_{dc,1} \rangle = \sum_{n \in \{\alpha\beta\}} (\mathbf{\Gamma} \circ \langle s_{1,n} \rangle) \circ \langle i_{p,n} \rangle \,. \tag{3.100}$$

A bode diagram of the input impedance for multiple points of operation in shown in Figure 3.18.

Figure 3.19 shows the Bode diagram of the filter current to the control signal transfer function for two different battery voltages. Note that the lower the switching frequency, the lower the frequency of the first resonance, which is a reflex of the resonant tank resonance. The variation of the gain with the phase-shift presents a relationship varying approximately with

$$H(s, \bar{\delta}) \approx H(s, 0) \sin \bar{\delta}, \tag{3.101}$$

where $H(s, \bar{\delta})$ is the transfer function pertaining to the uncertainty model set.

The multifrequency modeling approach, as discussed in Chapter 2, can be utilized to accurately model the grid frequency harmonics in power converter systems. However, upon analyzing the results shown in Figure 3.19, it can be observed that the power

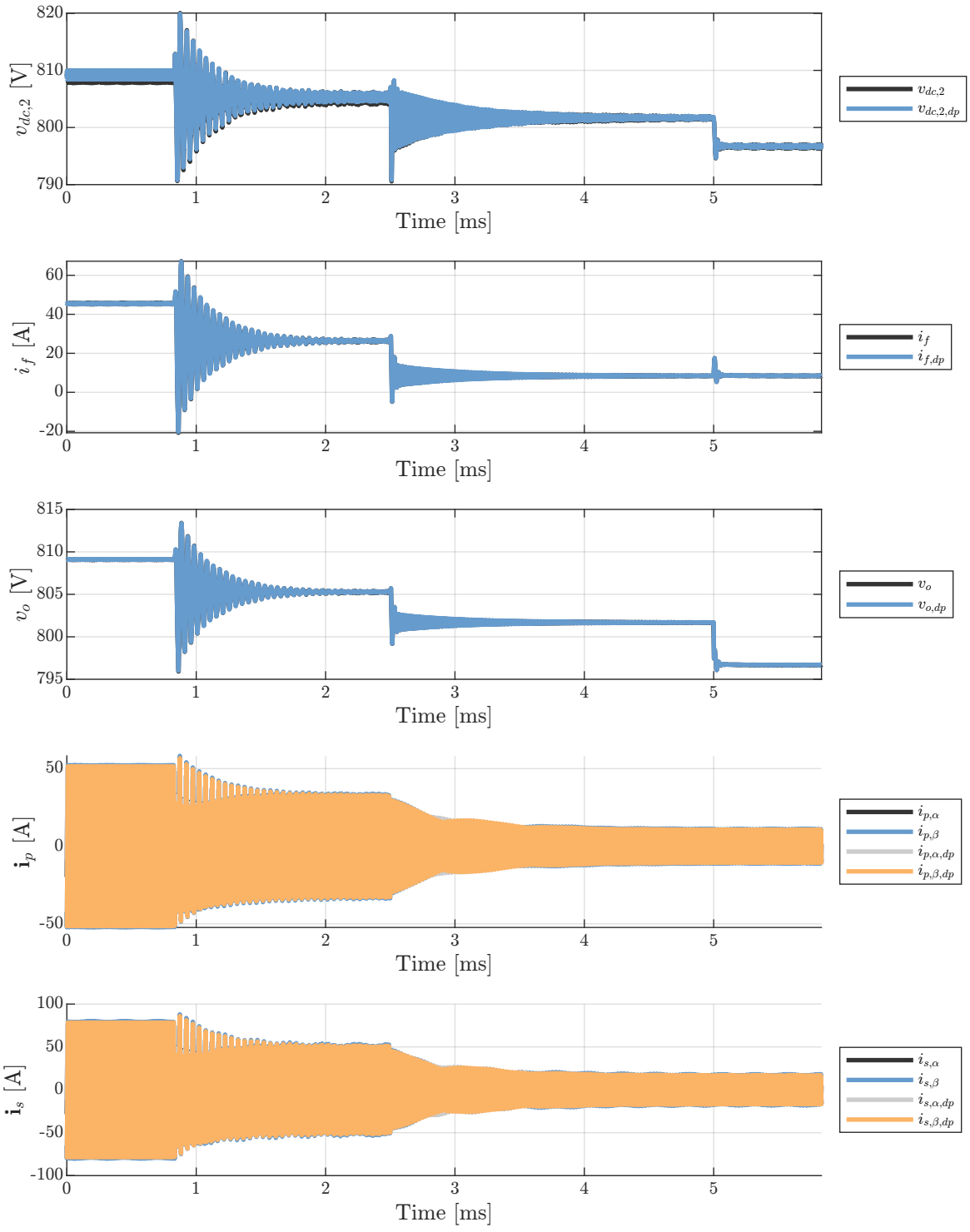

(a)

Figure 3.17 – Nonlinear model validation (a) for (b) Phase angle step from 60° to 30°. (c) Frequency step from 60 kHz to 120 kHz. (d) Output voltage step from 800 V to 795 V. (e) Steady-state operation.

converter predominantly acts as a gain across the majority of the frequency range relevant to grid-connected converters.

This behavior indicates that the power converter amplifies or passes through the

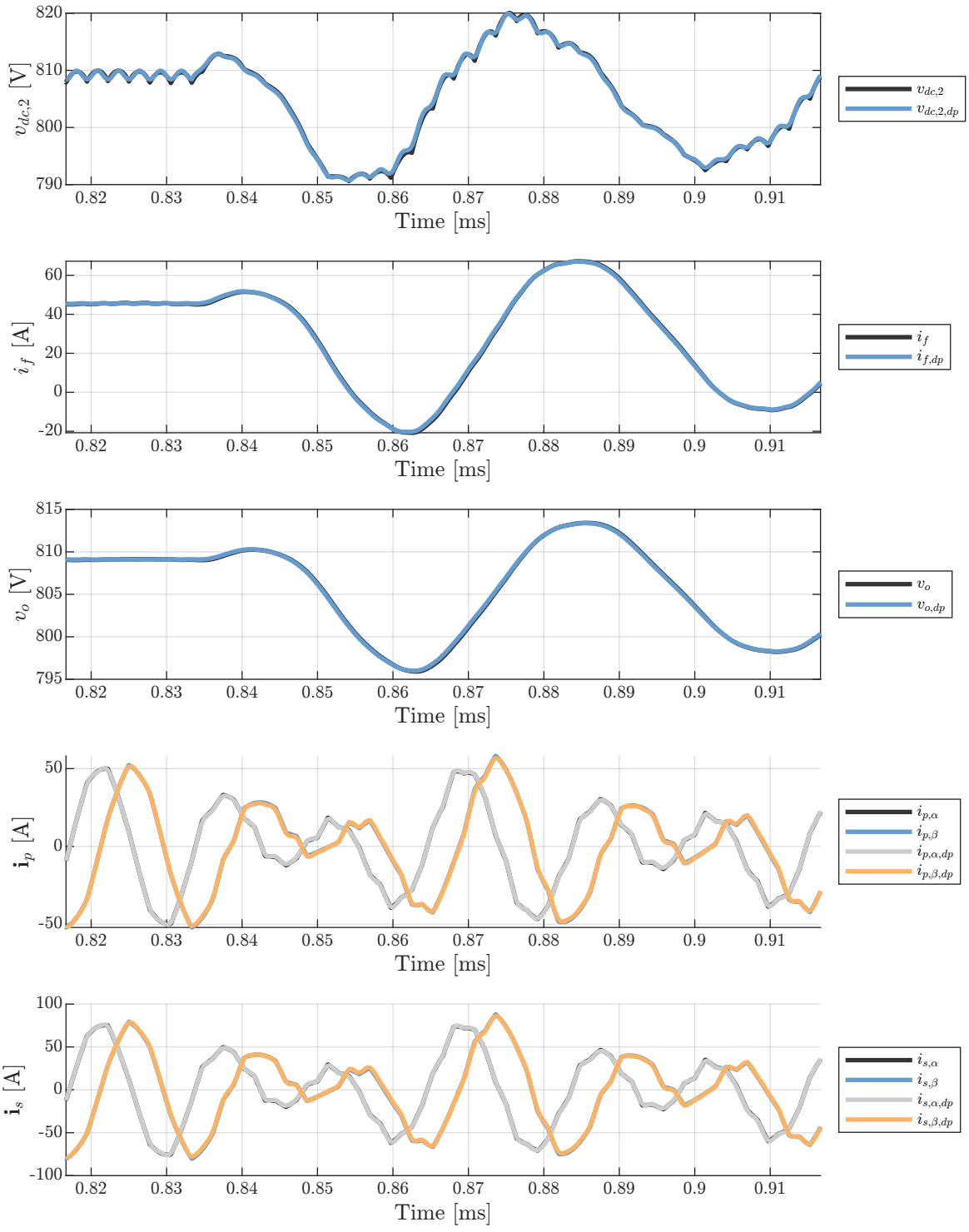

(b)

Figure 3.17 – Nonlinear model validation (a) for (b) Phase angle step from 60° to 30°. (c) Frequency step from 60 kHz to 120 kHz. (d) Output voltage step from 800 V to 795 V. (e) Steady-state operation.

grid frequency harmonics rather than actively attenuating or suppressing them. As a result, the power converter system can contribute to the propagation of these harmonics in the grid rather than mitigating their presence.

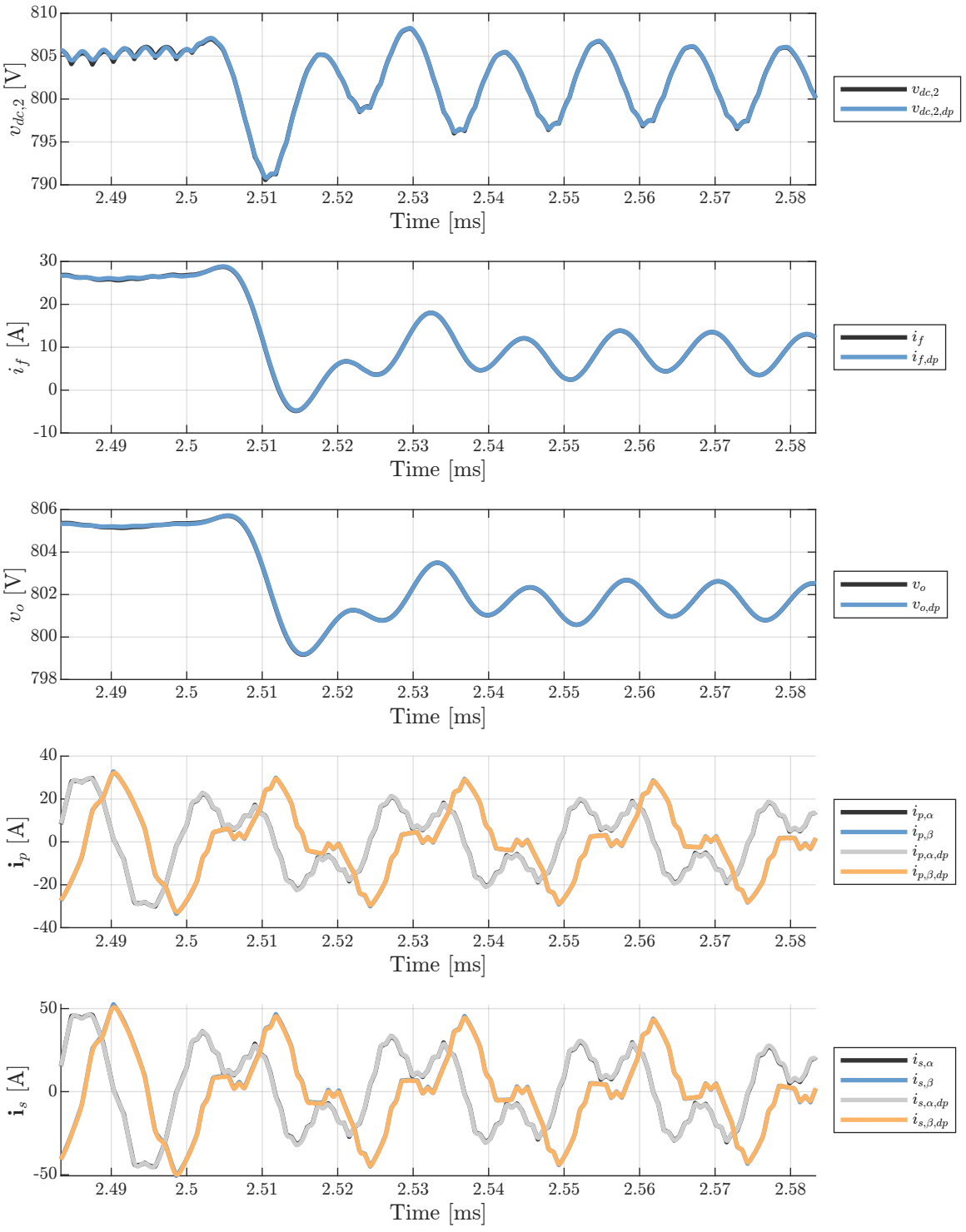

(c)

Figure 3.17 – Nonlinear model validation (a) for (b) Phase angle step from 60° to 30°. (c) Frequency step from 60 kHz to 120 kHz. (d) Output voltage step from 800 V to 795 V. (e) Steady-state operation.

Understanding the gain behavior of the dc-dc converters across different frequency components is crucial for harmonic analysis and control design. Proper measures and strategies need to be implemented to ensure the effective management and reduction of

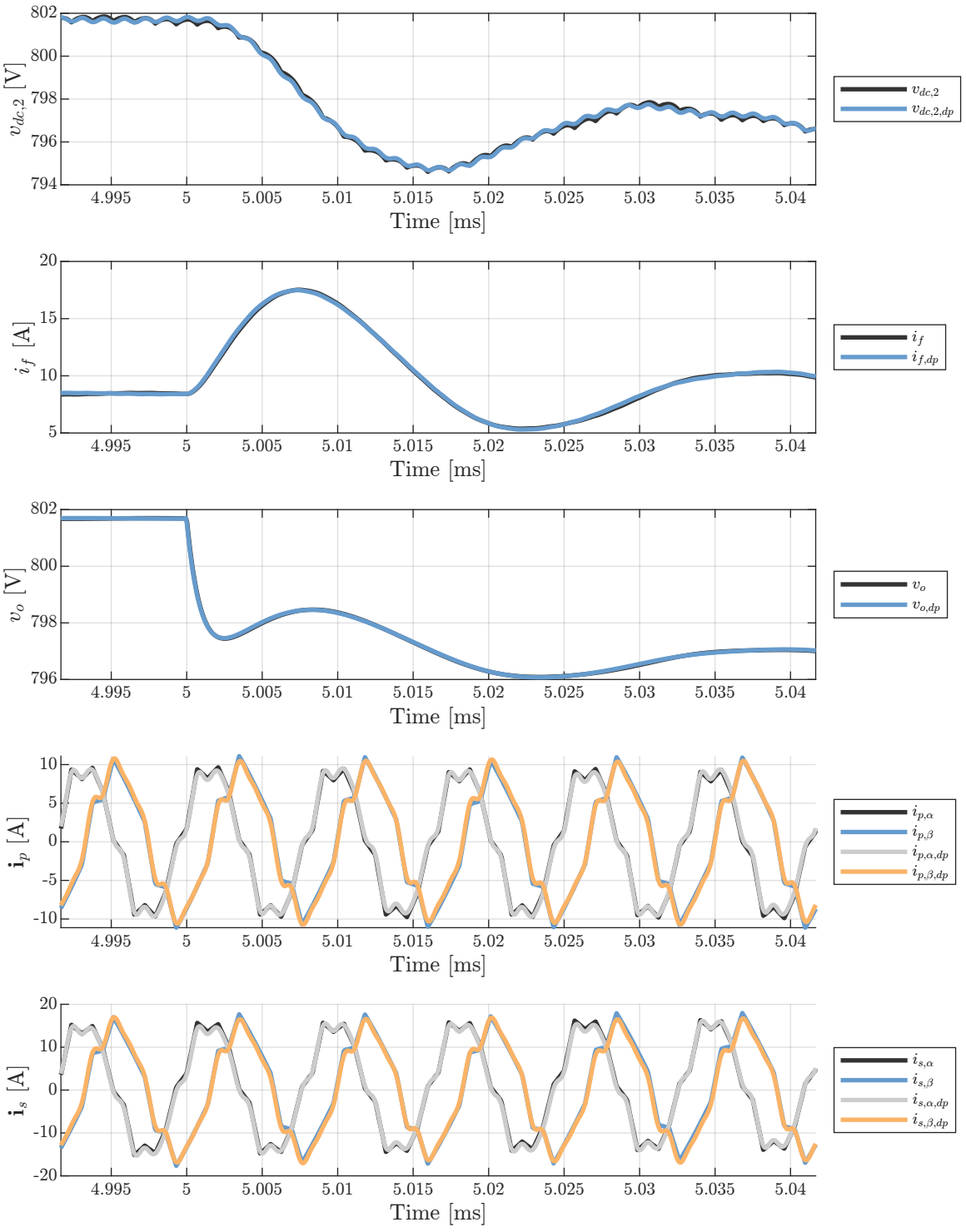

(d)

Figure 3.17 – Nonlinear model validation (a) for (b) Phase angle step from 60° to 30°. (c) Frequency step from 60 kHz to 120 kHz. (d) Output voltage step from 800 V to 795 V. (e) Steady-state operation.

grid frequency harmonics at the output of these power converters as means fo mitigating voltage oscillation across the entire system.

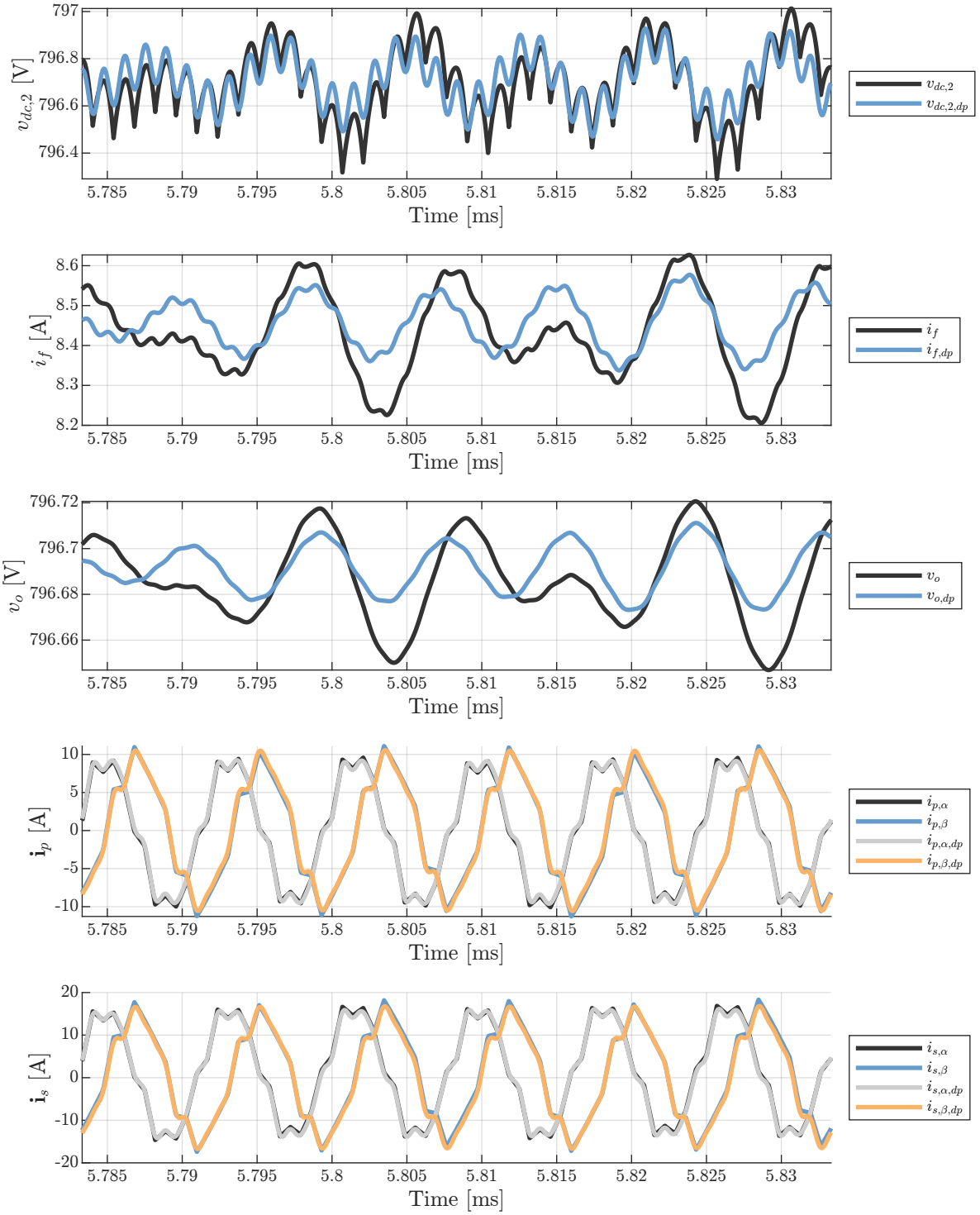

(e)

Figure 3.17 – Nonlinear model validation (a) for (b) Phase angle step from 60° to 30°. (c) Frequency step from 60 kHz to 120 kHz. (d) Output voltage step from 800 V to 795 V. (e) Steady-state operation.

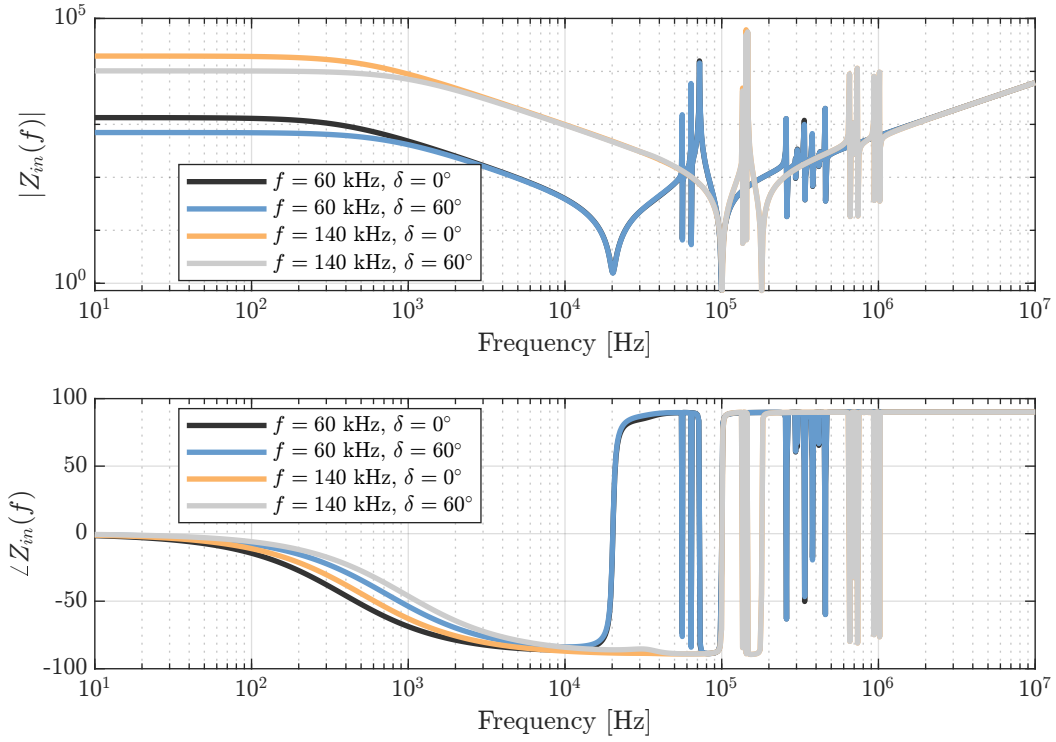

Figure 3.18 – Three-Phase LC Resonant converter input impedance for multiple points of operation.

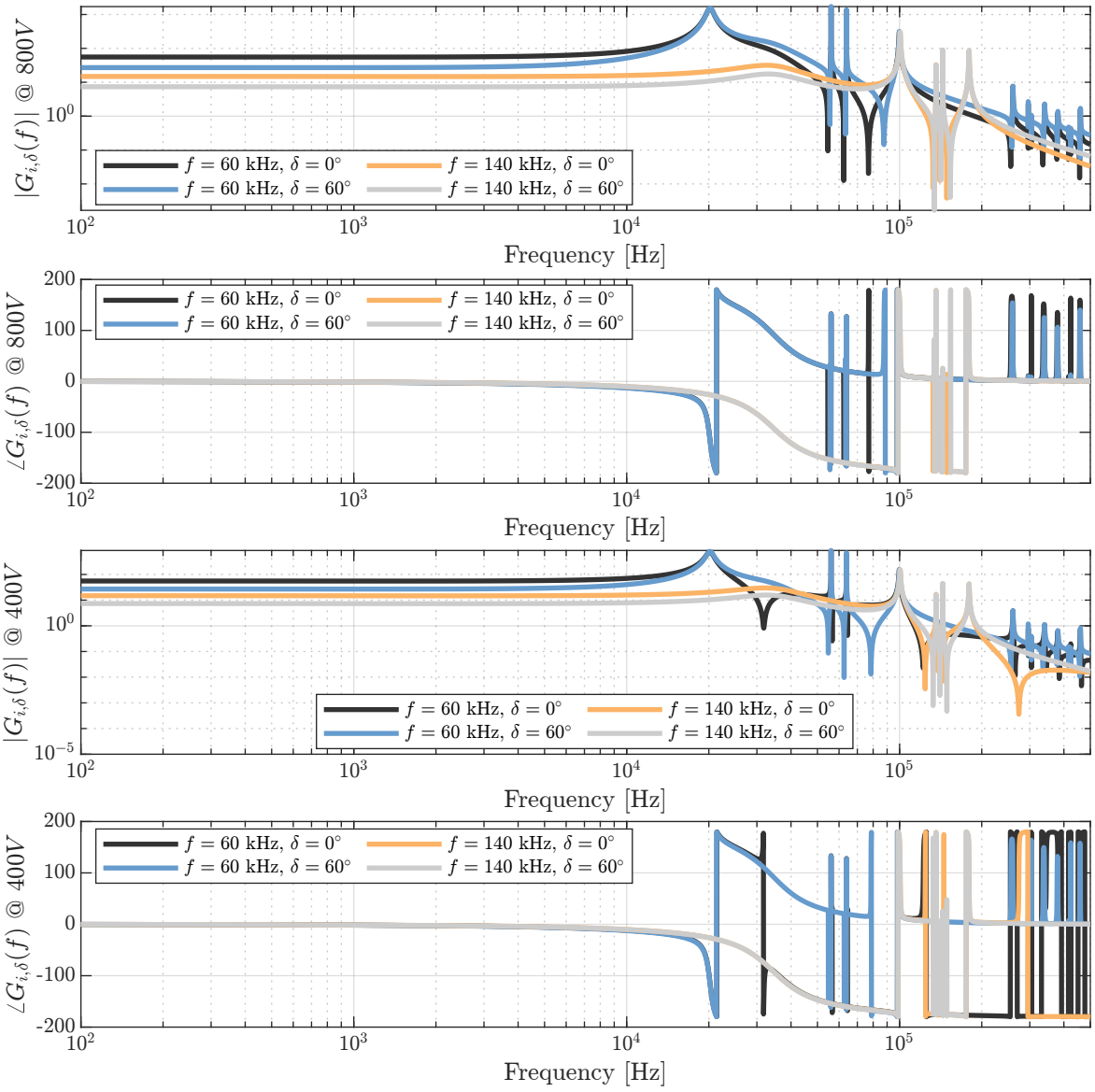

Figure 3.19 – Bode diagram of the output filter current i_f by the control signal δ for $u_b = 800V$ and $u_b = 400V$.

3.7 MATRIX CONVERTER

The matrix converter is a static power converter capable of directly processing ac electric quantities between two distinct ac systems without an intermediary dc stage. The main advantages of such topologies are increased energy conversion efficiency, reduced weight and volume of the power converter, while maintaining the ability to drain and inject sinusoidal currents for both ac systems. According to [31], the most desired characteristics of a static power converter interfacing ac voltages and currents (ac-dc-ac, ac-dc-dc-ac, ac-ac) are as follows:

- Low-cost and compact power circuit;
- Synthesis of output voltage with arbitrary voltage and frequency;
- Input and output currents in sinusoidal format, i.e., with low harmonic distortion;
- Operation with a high power factor for any load condition;
- Bidirectional power flux and regeneration capabilities.

The Indirect Matrix Converter (IMC) topology illustrated in Figure 3.20 has various possible implementations: the traditional IMC [32, 33], the Sparse Matrix Converter [32], the Very Sparse Matrix Converter (VSMC) [34], and the Ultra Sparse Matrix Converter (USMC) [35]. The IMC has the same number of switches as the Conventional Matrix Converter (CMC), while the VSMC uses a different switch configuration that reduces the number of switches. The SMC and USMC have simpler implementations, substituting some switches with diodes, but sacrificing the ability to operate with bidirectional power flux. One of the greatest challenges of this topology is the control of switch commands and power-flow structure, as well as ensuring converter synchronization.

This section presents a mathematical analysis of the IMC based on [36], which can be extended to other matrix converter topologies, while considering the harmonics of both ac stages as an application of the multifrequency models discussed in Chapter 2.

3.7.1 Time-Variant Model

In this section, a dynamic switched model for the indirect matrix converter is presented. This model consider ideal switches which presents two distinct states: enabled and disabled. The subscript 1 henceforth denotes variables pertaining to the rectifier stage, and the subscript 2 to variables belonging to the inverter stage, i.e., $\mathbf{x}_1 := (x_{1,j})_{j=1}^{3}$ are the three-phase electrical quantities pertaining to the rectifier stage and $\mathbf{x}_2 := (x_{2,j})_{j=1}^{3}$ are the quantities pertaining to the inverter stage.

The IMC model has twelve ideal switches. According to the switched model based on Fig. 3.20, a switching function $s_{i,j}$ can be expressed for the state of each switch S_{ij}, as

described by

$$S_{i,j,k} := \begin{cases} 1, & \text{if switch } s_{i,j,k} \text{is ON,} \\ 0, & \text{else,} \end{cases}, \quad \forall i \in \{1,2\}, j \in \{1,2,3\}, k \in \{p,n\}, \tag{3.102}$$

such that $s_{i,j} := S_{i,j,p} - S_{i,j,n}$.

Consequently, the virtual dc bus electrical quantities can be modeled as

$$u_{dc} := \mathbf{s}_1^T \mathbf{v}_1, \quad i_{dc} := \mathbf{s}_2^T \mathbf{v}_2. \tag{3.103}$$

Similarly, the inverter and rectifier stage voltages and currents can be expressed as

$$\begin{aligned} \mathbf{v}_2 &:= \mathbf{s}_2 \mathbf{u}_{dc} = \mathbf{s}_2 \mathbf{s}_1^T \mathbf{v}_1, \\ \mathbf{i}_1 &:= \mathbf{s}_1 \mathbf{i}_{dc} = \mathbf{s}_1 \mathbf{s}_2^T \mathbf{i}_2. \end{aligned} \tag{3.104}$$

This combination results in a switched transformation matrix for the Indirect Matrix Converter which resembles the CMC, directly coupling the voltage and current at both stages, defined as

$$\mathbf{T}_M := \mathbf{s}_2 \mathbf{s}_1^T = \begin{bmatrix} s_{1,1}s_{2,1} & s_{1,2}s_{2,1} & s_{1,3}s_{2,1} \\ s_{1,1}s_{2,2} & s_{1,2}s_{2,2} & s_{1,3}s_{2,2} \\ s_{1,1}s_{2,3} & s_{1,2}s_{2,3} & s_{1,3}s_{2,3} \end{bmatrix}. \tag{3.105}$$

The model can then be divided between the rectifier and inverter stages. Since equations (3.104) and (3.105) describe a relationship between the two stages, it is possible to simplify the switched model shown in Fig. 3.20 using controlled voltage and current sources, as illustrated in Fig. 3.21.

Therefore, the system can be described by two separate state-space representations.

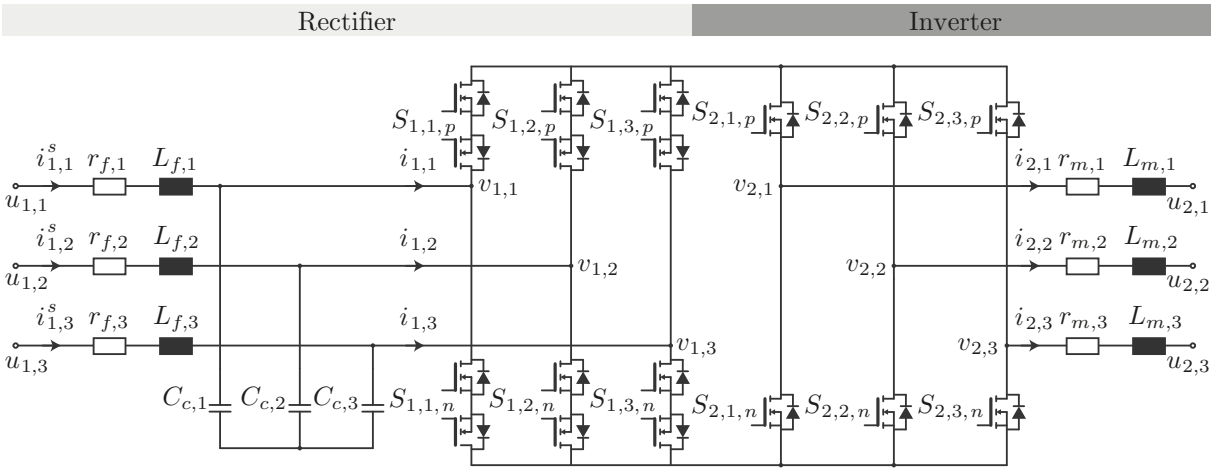

Figure 3.20 – Inverse matrix converter, composed of eighteen switches as well as filtering elements. The *high-side* voltage is defined by $\{u_{1,1}, u_{1,2}, u_{1,3}\}$ and the *low-side* voltage is defined by $\{u_{2,1}, u_{2,2}, u_{2,3}\}$.

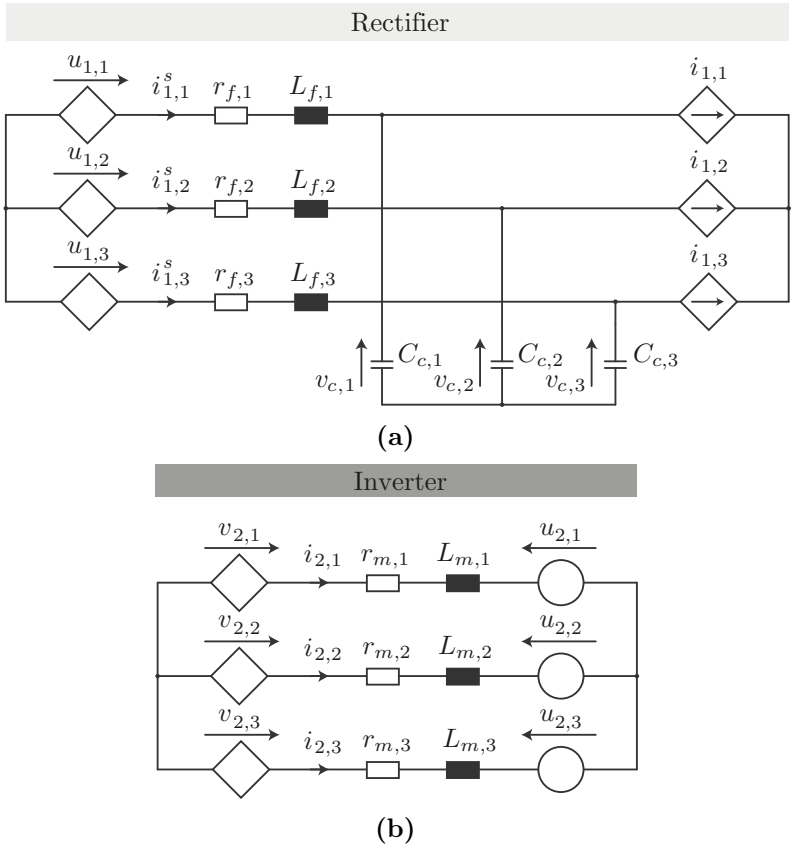

Figure 3.21 – (a) Rectifier (b) Inverter switched model circuit. The switched transformation matrix describes the coupling between both rectifier and inverter stages.

The output voltage vector $\mathbf{u}_2$ can be described according to the different load characteristics. For example, if a motor is connected to the inverter stage, its voltage equations can be coupled into the model. For a resistive load, the resistance value can be grouped with R_m and the voltage vector $\mathbf{u}_2$ is null valued.

Since the rectifier stage voltage vector $\mathbf{u}_1$ and the inverter stage current vector $\mathbf{i}_2$ present a linear dependent state, two new switching matrices can be defined according to

$$\begin{aligned}
\mathbf{T}_1 &:= \begin{bmatrix} s_{1,1}s_{2,1} - s_{3,1}s_{2,1} & s_{2,1}s_{2,1} - s_{3,1}s_{2,1} \\ s_{1,1}s_{2,2} - s_{3,1}s_{2,2} & s_{2,1}s_{2,2} - s_{3,1}s_{2,2} \\ s_{1,1}s_{2,3} - s_{3,1}s_{2,3} & s_{2,1}s_{2,3} - s_{3,1}s_{2,3} \end{bmatrix}, \\
\mathbf{T}_2 &:= \begin{bmatrix} s_{1,1}s_{2,1} - s_{1,1}s_{2,3} & s_{1,1}s_{2,2} - s_{1,1}s_{2,3} \\ s_{1,2}s_{2,1} - s_{1,2}s_{2,3} & s_{1,2}s_{2,2} - s_{1,2}s_{2,3} \end{bmatrix}
\end{aligned} \tag{3.106}$$

such that $\mathbf{v}_2 := \mathbf{T}_1\mathbf{v}_{1,1:2}$ and $\mathbf{i}_{1,1:2} := \mathbf{T}_2\mathbf{i}_{2,1:2}$.

The rectifier voltage v_3 and inverter current $i_{L_m,3}$ can be expressed as a linear combination of the expressed vectors, hence the suppression in the new set of equations.

The circuit equations can be written as

$$\begin{cases} \mathbf{T}_{ll}\left(\mathbf{u}_1 - \mathbf{R}_f\mathbf{i}^s - \mathbf{L}_f D_t\mathbf{i}^s - \mathbf{v}_1\right) = \mathbf{0} \\ D_t\mathbf{v}_{1,1:2} = \mathbf{i}^s_{1,1:2} - \mathbf{T}_2\mathbf{i}_{2,1:2} \\ \mathbf{T}_{ll}\left(\mathbf{T}_1\mathbf{v}_{1,1:2} - \mathbf{R}_m\mathbf{i}_2 - \mathbf{L}_m D_t\mathbf{i}_2 - \mathbf{u}_2\right) = \mathbf{0} \end{cases} \tag{3.107}$$

We can define the state vector as $\mathbf{x} := (\mathbf{i}_{1,1:2}, \mathbf{v}_{1,1:2}, \mathbf{i}_{2,1:2})$, such that

$$D_t\mathbf{x} = \begin{bmatrix} -\frac{R_f}{L_f}\mathbf{I}_2 & -\frac{1}{L_f}\mathbf{I}_2 & \mathbf{0}_2 \\ \frac{1}{C_f}\mathbf{I}_2 & \mathbf{O}_2 & -\frac{1}{C_f}\mathbf{Q}_2 \\ \mathbf{0}_2 & \frac{1}{3L_m}\mathbf{Q}_1 & -\frac{R_m}{L_m} \end{bmatrix}\mathbf{x} + \begin{bmatrix} \frac{1}{L_f}\mathbf{T}_{dm} & \mathbf{0}_2 \\ \mathbf{0}_2 & \mathbf{0}_2 \\ \mathbf{0}_2 & \frac{1}{L_m}\mathbf{T}_{dm} \end{bmatrix}\begin{bmatrix} \mathbf{u}_1 \\ \mathbf{u}_2 \end{bmatrix}, \tag{3.108}$$

where

$$\begin{aligned} \mathbf{Q}_1 &:= \begin{bmatrix} (s_{1,1}-s_{1,3})(2s_{2,1}-s_{2,2}-s_{2,3}) & (s_{1,2}-s_{2,3})(2s_{2,1}-s_{2,2}-s_{2,3}) \\ (s_{1,1}-s_{1,3})(2s_{2,2}-s_{2,1}-s_{2,3}) & (s_{1,2}-s_{1,3})(2s_{2,2}-s_{2,1}-s_{2,3}) \end{bmatrix} \\ \mathbf{Q}_2 &:= \begin{bmatrix} s_{1,1}s_{2,1}-s_{1,1}s_{2,3} & s_{1,1}s_{2,2}-s_{1,1}s_{2,3} \\ s_{1,2}s_{2,1}-s_{1,2}s_{2,3} & s_{1,2}s_{2,2}-s_{1,2}s_{2,3} \end{bmatrix} \\ \mathbf{T}_{dm} &:= \frac{1}{3}\begin{bmatrix} 2 & -1 & -1 \\ -1 & 2 & -1 \end{bmatrix}. \end{aligned} \tag{3.109}$$

We can also apply the Clarke Transformation to (3.108) and (3.109) while ignoring the γ-axis component, which results in

$$D_t\mathbf{x} = \begin{bmatrix} -\frac{R_f}{L_f}\mathbf{I}_2 & -\frac{1}{L_f}\mathbf{I}_2 & \mathbf{0}_2 \\ \frac{1}{C_f}\mathbf{I}_2 & \mathbf{O}_2 & -\frac{3}{2C_f}\mathbf{Q}_M^T \\ \mathbf{0}_2 & \frac{3}{2L_m}\mathbf{Q}_M & -\frac{R_m}{L_m} \end{bmatrix}\mathbf{x} + \begin{bmatrix} \frac{1}{L_f}\mathbf{I}_2 & \mathbf{0}_2 \\ \mathbf{0}_2 & \mathbf{0}_2 \\ \mathbf{0}_2 & \frac{1}{L_m}\mathbf{I}_2 \end{bmatrix}\begin{bmatrix} \mathbf{u}_1 \\ \mathbf{u}_2 \end{bmatrix}, \tag{3.110}$$

where

$$\mathbf{Q}_M := \mathbf{s}_{2,\alpha\beta}\mathbf{s}^T_{1,\alpha\beta}, \tag{3.111}$$

here defined as the Matrix Converter switched transformation matrix in the $\alpha\beta$-axis. The switching function averaged value for a switching period under open-loop operation can be defined as

$$\bar{s}_{1,\alpha\beta} := \exp\left(\iota\omega_1 t + \varphi_1\right), \quad \bar{s}_{2,\alpha\beta} := \frac{2}{3}m\,\exp\left(\iota\omega_1 t + \varphi_2\right),\ \forall m \in \left[0, \frac{\sqrt{3}}{2}\right] \tag{3.112}$$

in the complex domain, where m is the modulation index defining the ratio between

rectifier and inverter as in

$$m := \frac{|\bar{v}_2|}{|\bar{v}_1|}. \tag{3.113}$$

3.7.2 Harmonic State-Space Model

We can rewrite (3.110) in term of the switched transformation matrix as

$$\begin{cases} D_t\mathbf{x}_1 = \mathbf{A}_{1,1}\mathbf{x}_1 + \mathbf{E}_1\mathbf{u} + \mathbf{B}_1\mathbf{Q}_M^T\mathbf{x} = \mathbf{A}_{1,1}\mathbf{x}_1 + \mathbf{E}_1\mathbf{u} + \mathbf{B}_1\mathbf{i}_1 \\ D_t\mathbf{x}_2 = \mathbf{A}_{2,2}\mathbf{x}_1 + \mathbf{E}_2\mathbf{u} + \mathbf{B}_2\mathbf{Q}_M\mathbf{x} = \mathbf{A}_{2,2}\mathbf{x}_1 + \mathbf{E}_2\mathbf{u} + \mathbf{B}_2\mathbf{v}_2 \end{cases} \tag{3.114}$$

with an isolated nonlinear term dependent on the switching functions. We can then define two different output matrices such that

$$\mathbf{v}_1 = \mathbf{C}_v\mathbf{x} = \begin{bmatrix} \mathbf{C}_{v,\alpha} \\ \mathbf{C}_{v,\beta} \end{bmatrix}, \quad \mathbf{i}_2 = \mathbf{C}_i\mathbf{x} = \begin{bmatrix} \mathbf{C}_{i,\alpha} \\ \mathbf{C}_{i,\beta} \end{bmatrix}. \tag{3.115}$$

From this, we can write the dynamic phasors of the inverter synthesized voltage as

$$\begin{aligned} \langle v_{2,\alpha}\rangle &= (\boldsymbol{\Sigma} \circ ((\boldsymbol{\Sigma} \circ \langle s_{1,\alpha}\rangle) \circ \langle s_{2,\alpha}\rangle)) \circ ((\mathbf{I}_\infty \otimes \mathbf{C}_{v,\alpha}) \langle \mathbf{x}\rangle) \\ &\quad + (\boldsymbol{\Sigma} \circ ((\boldsymbol{\Sigma} \circ \langle s_{1,\alpha}\rangle) \circ \langle s_{2,\beta}\rangle)) \circ ((\mathbf{I}_\infty \otimes \mathbf{C}_{v,\beta}) \langle \mathbf{x}\rangle) \\ \langle v_{2,\beta}\rangle &= (\boldsymbol{\Sigma} \circ ((\boldsymbol{\Sigma} \circ \langle s_{1,\beta}\rangle) \circ \langle s_{2,\alpha}\rangle)) \circ ((\mathbf{I}_\infty \otimes \mathbf{C}_{v,\alpha}) \langle \mathbf{x}\rangle) \\ &\quad + (\boldsymbol{\Sigma} \circ ((\boldsymbol{\Sigma} \circ \langle s_{1,\beta}\rangle) \circ \langle s_{2,\beta}\rangle)) \circ ((\mathbf{I}_\infty \otimes \mathbf{C}_{v,\beta}) \langle \mathbf{x}\rangle) \end{aligned} \tag{3.116}$$

and the rectifier synthesized current as

$$\begin{aligned} \langle i_{1,\alpha}\rangle &= (\boldsymbol{\Sigma} \circ ((\boldsymbol{\Sigma} \circ \langle s_{1,\alpha}\rangle) \circ \langle s_{2,\alpha}\rangle)) \circ ((\mathbf{I}_\infty \otimes \mathbf{C}_{i,\alpha}) \langle \mathbf{x}\rangle) \\ &\quad + (\boldsymbol{\Sigma} \circ ((\boldsymbol{\Sigma} \circ \langle s_{1,\beta}\rangle) \circ \langle s_{2,\alpha}\rangle)) \circ ((\mathbf{I}_\infty \otimes \mathbf{C}_{i,\beta}) \langle \mathbf{x}\rangle) \\ \langle i_{1,\beta}\rangle &= (\boldsymbol{\Sigma} \circ ((\boldsymbol{\Sigma} \circ \langle s_{1,\alpha}\rangle) \circ \langle s_{2,\beta}\rangle)) \circ ((\mathbf{I}_\infty \otimes \mathbf{C}_{i,\alpha}) \langle \mathbf{x}\rangle) \\ &\quad + (\boldsymbol{\Sigma} \circ ((\boldsymbol{\Sigma} \circ \langle s_{1,\beta}\rangle) \circ \langle s_{2,\beta}\rangle)) \circ ((\mathbf{I}_\infty \otimes \mathbf{C}_{i,\beta}) \langle \mathbf{x}\rangle), \end{aligned} \tag{3.117}$$

where $\boldsymbol{\Sigma}$ is the sigma operator analog to the Toeplitz operator for multifrequency models defined in Chapter 2.

Consequently, we can write the Multifrequency Harmonic State-Space model of

the Indirect Matrix Converter as

$$\begin{cases} D_t \langle \mathbf{x}_1 \rangle = (\mathbf{I}_{N_2} \otimes (\mathbf{I}_{N_1} \otimes \mathbf{A}_{1,1} - \mathbf{G}_{1,1}) - \mathbf{G}_{1,2} \otimes \mathbf{I}_{N_1}) \langle \mathbf{x} \rangle + (\mathbf{I}_{N_1 N_2} \otimes \mathbf{E}_1) \langle \mathbf{u} \rangle \\ \quad + (\mathbf{I}_{N_1 N_2} \otimes \mathbf{B}_{1,\alpha}) (\mathbf{\Sigma} \circ ((\mathbf{\Sigma} \circ \langle s_{1,\alpha} \rangle) \circ \langle s_{2,\alpha} \rangle)) \circ ((\mathbf{I}_{N_1 N_2} \otimes \mathbf{C}_{i,\alpha}) \langle \mathbf{x} \rangle) \\ \quad + (\mathbf{I}_{N_1 N_2} \otimes \mathbf{B}_{1,\alpha}) (\mathbf{\Sigma} \circ ((\mathbf{\Sigma} \circ \langle s_{1,\beta} \rangle) \circ \langle s_{2,\alpha} \rangle)) \circ ((\mathbf{I}_{N_1 N_2} \otimes \mathbf{C}_{i,\beta}) \langle \mathbf{x} \rangle) \\ \quad + (\mathbf{I}_{N_1 N_2} \otimes \mathbf{B}_{1,\beta}) (\mathbf{\Sigma} \circ ((\mathbf{\Sigma} \circ \langle s_{1,\alpha} \rangle) \circ \langle s_{2,\beta} \rangle)) \circ ((\mathbf{I}_{N_1 N_2} \otimes \mathbf{C}_{i,\alpha}) \langle \mathbf{x} \rangle) \\ \quad + (\mathbf{I}_{N_1 N_2} \otimes \mathbf{B}_{1,\beta}) (\mathbf{\Sigma} \circ ((\mathbf{\Sigma} \circ \langle s_{1,\beta} \rangle) \circ \langle s_{2,\beta} \rangle)) \circ ((\mathbf{I}_{N_1 N_2} \otimes \mathbf{C}_{i,\beta}) \langle \mathbf{x} \rangle) \\ D_t \langle \mathbf{x}_2 \rangle = (\mathbf{I}_{N_2} \otimes (\mathbf{I}_{N_1} \otimes \mathbf{A}_{2,2} - \mathbf{G}_{2,1}) - \mathbf{G}_{2,2} \otimes \mathbf{I}_{N_1}) \langle \mathbf{x} \rangle + (\mathbf{I}_{N_1 N_2} \otimes \mathbf{E}_2) \langle \mathbf{u} \rangle \\ \quad + (\mathbf{I}_{N_1 N_2} \otimes \mathbf{B}_{2,\alpha}) (\mathbf{\Sigma} \circ ((\mathbf{\Sigma} \circ \langle s_{1,\alpha} \rangle) \circ \langle s_{2,\alpha} \rangle)) \circ ((\mathbf{I}_{N_1 N_2} \otimes \mathbf{C}_{v,\alpha}) \langle \mathbf{x} \rangle) \\ \quad + (\mathbf{I}_{N_1 N_2} \otimes \mathbf{B}_{2,\alpha}) (\mathbf{\Sigma} \circ ((\mathbf{\Sigma} \circ \langle s_{1,\alpha} \rangle) \circ \langle s_{2,\beta} \rangle)) \circ ((\mathbf{I}_{N_1 N_2} \otimes \mathbf{C}_{v,\beta}) \langle \mathbf{x} \rangle) \\ \quad + (\mathbf{I}_{N_1 N_2} \otimes \mathbf{B}_{2,\beta}) (\mathbf{\Sigma} \circ ((\mathbf{\Sigma} \circ \langle s_{1,\beta} \rangle) \circ \langle s_{2,\alpha} \rangle)) \circ ((\mathbf{I}_{N_1 N_2} \otimes \mathbf{C}_{v,\alpha}) \langle \mathbf{x} \rangle) \\ \quad + (\mathbf{I}_{N_1 N_2} \otimes \mathbf{B}_{2,\beta}) (\mathbf{\Sigma} \circ ((\mathbf{\Sigma} \circ \langle s_{1,\beta} \rangle) \circ \langle s_{2,\beta} \rangle)) \circ ((\mathbf{I}_{N_1 N_2} \otimes \mathbf{C}_{v,\beta}) \langle \mathbf{x} \rangle) \end{cases} \tag{3.118}$$

assuming that the model was truncated for N_1 harmonics in the rectfier stage and N_2 harmonics in the inverter stage. Figure 3.22 demonstrates a comparison between the time-variant model and the harmonic state-space model reconstructed states simulated using the ode45 solver from MATLAB. The Harmonic State-Space models were obtained by truncating the model at the 3$^{\text{rd}}$ harmonic for both frequencies, resulting in a nonlinear model with 296 states.

A comparison between the eigenvalues of the decoupled system and the HSS linearized model considering up to the 2$^{\text{nd}}$ harmonics is presented in Figure 3.23. Note that the coupling between inverter and rectifier stages dampen the eigenvalues related to the rectifier stage.

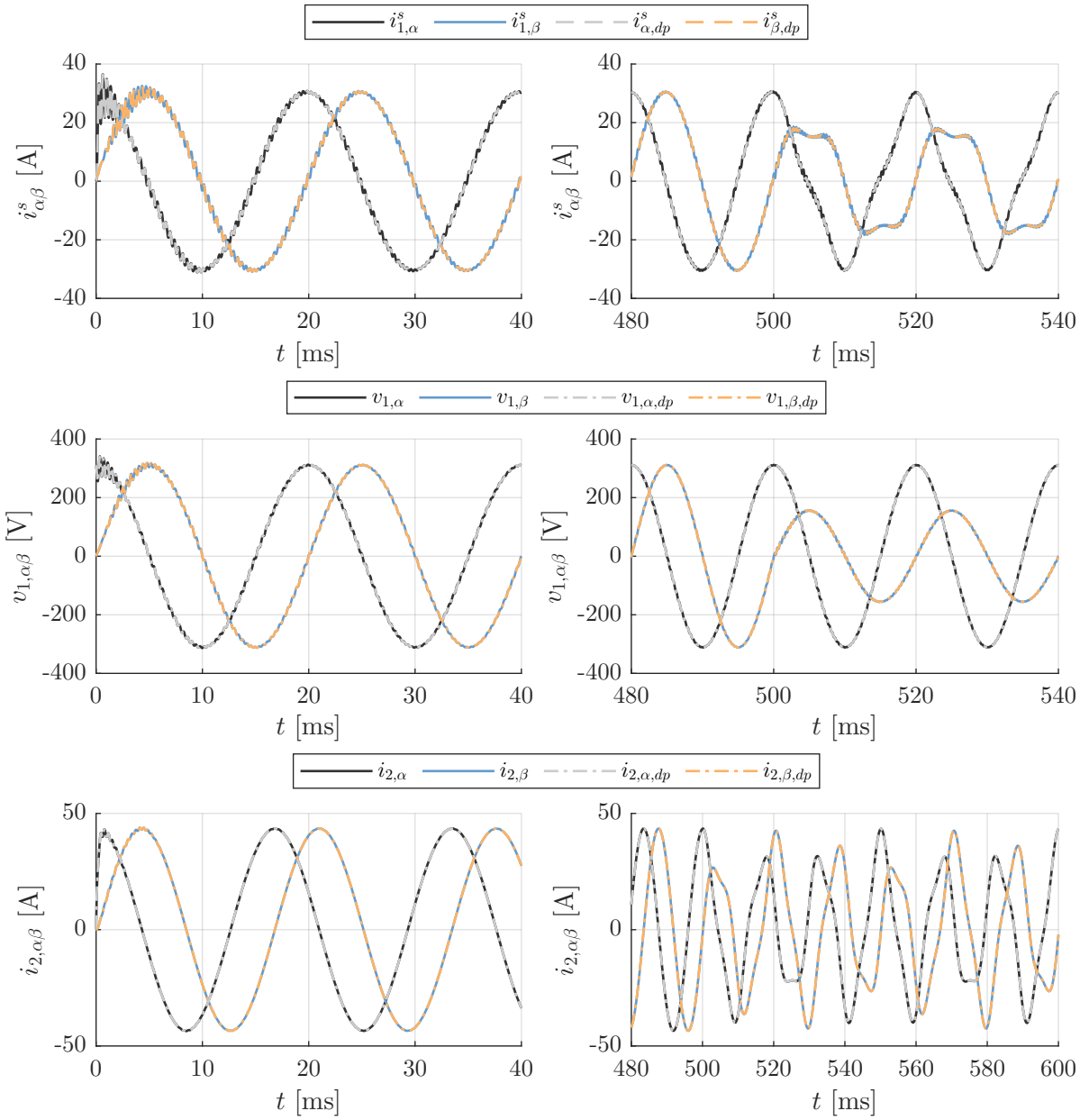

Figure 3.22 – Multifrequency Harmonic State-Space Model of an Indirect Matrix Converter validation, where bold lines are the simulation of the time-variant averaged model and the dashed lines are the state-variables reconstructed in the time-domain.

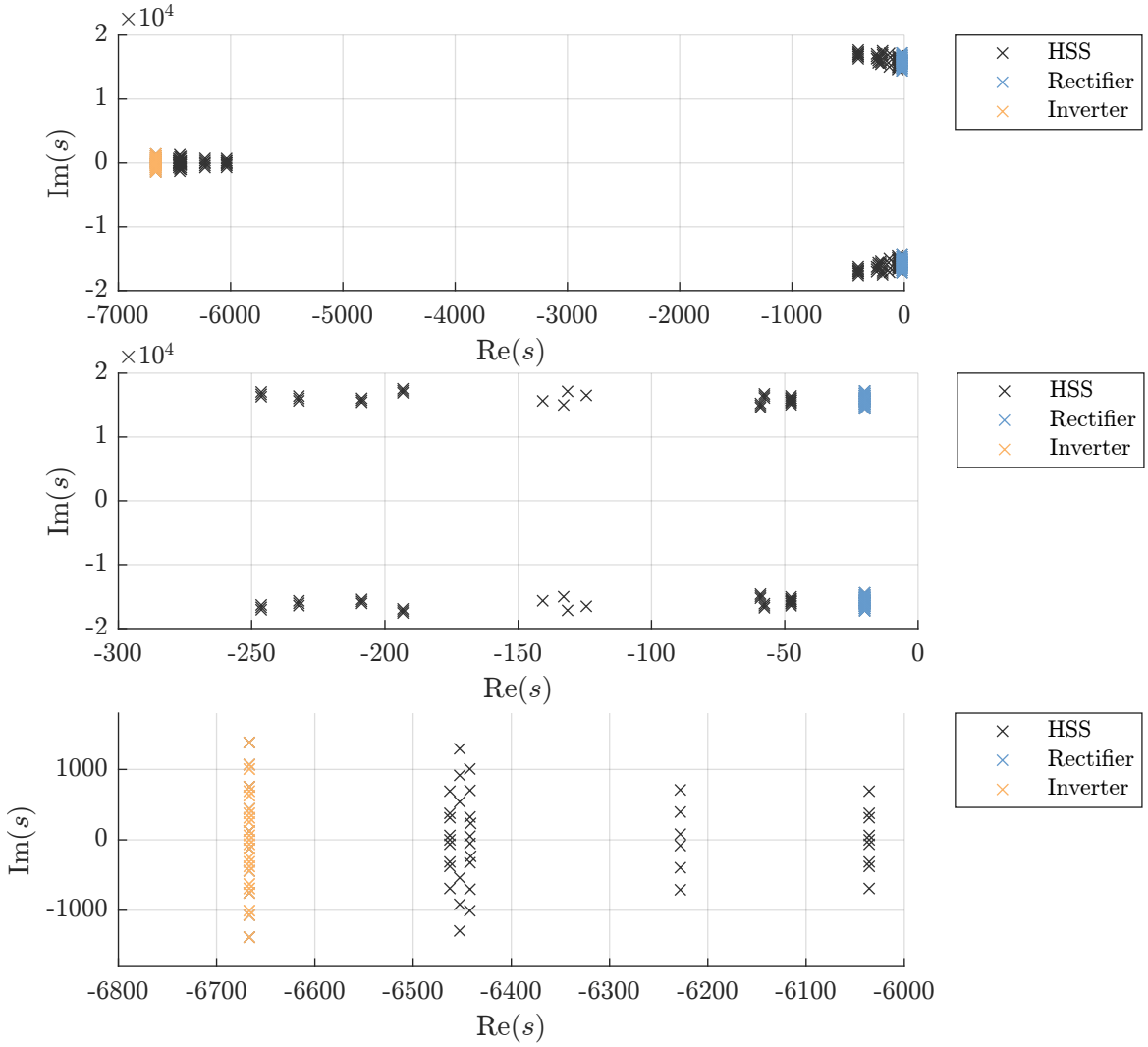

Figure 3.23 – Comparison between the eigenvalues of the linearized HSS Matrix Converter model and the decoupled model HSS model, which assumes that $\mathbf{Q}_M$ vanishes.

3.8 REMARKS

A method for the automated obtention of power converter models based on their dynamic equations was demonstrated. The intrinsic characteristics and parasitic components models were not taken into account. These effects can include the passive components' frequency dependency, parasitic capacitances to ground and nonlinear behaviours, such as the inductance dependency with the current, and were ignored not to hinder the conditioning of the state-space matrices. The model is tipically well-behaved for frequencies up to 100 kHz for low-voltage and low-power converters. After this frequency, these additional characteristics must be modeled with the addition of a more complete EMC filter components model.

The models presented in this chapter can be written to have the system frequency as an input by means of some mathematical manipulations. The next chapter demonstrates frequency dependent control strategies that can be directly coupled with the models presented in this chapter. These frequency dependent models are useful for the analysis of weak grid systems, as certain control strategies tend to lose the synchronism with the eletric grid.

Models of possible dc-connected circuits were also presented as examples of the application of the modeling methodologies described in Chapter 2. The discussions included models with current and power sources and their relationship. In the initial discussions, it was shown that the dc current source can be considered as an approximation of the power source when the dc voltage disturbances are sufficiently low.

Models of photovoltaic panels were also examined to investigate the behavior of the input impedance of the PV array and the dc bus capacitor. It was observed that when operating with a boost dc-dc converter for maximum power point tracking, the impedance becomes low. This low impedance can potentially impact the operation of the interface with the ac grid.

A harmonic state-space model of a three-phase resonant converter was presented to analyze the dynamics of its input-output characteristic. By examining the bode diagrams of linearized models, it was observed that the power converters generally exhibit voltage gain behavior across the frequency range of interest. However, caution is required when operating near the resonant frequency of the resonant tank, as it can introduce underdamped characteristics.

Finally, a Multifrequency Harmonic-State Space model of an Indirect Matrix Converter was presented, showcasing a direct application of the modeling technique. The HSS model demonstrated a high level of accuracy in capturing the system dynamics. However, it is important to note that the model complexity increases due to the inclusion of nonlinearities to account for the coupling between frequencies in the two-dimensional Fourier transform.

Chapter

4

Current Control of Power Converter Systems

One of the challenges of modern power converter systems is to ensure stability, while optimally satisfying constraints of cost, volume, efficiency and robustness [3, 4]. The optimal design of control strategies is able to improve the robustness, while minimizing the power density, as inadequate control strategies often demand for additional passive structures to ensure an adequate behaviour.

The previous chapter presented an analysis of the mathematical state-space models for power converters for different output filter structures, which enables a control design considering parametric variations and a more thorough stability analysis for parallel-connected systems.

In general, an optimal interface between two different energy sources is able to reject disturbances using the least amount of energy. Since this interface does not limit the characteristics of the sources and loads, nonlinear behaviours are expected, which in turn impacts the power quality in the form of harmonics. Low- and medium-voltage systems are especially affected by these characteristics. In the present state-of-the-art, three different control strategies are mostly proposed as solutions to improve robustness: repetitive controllers, resonant controllers and grid-voltage feedforward schemes.

Repetitive controllers consists in the insertion of a FIR filter in the control loop, compensating the multiple frequencies of the first resonance [37–41]. However, they might amplify undesirable harmonic high-frequency harmonic components, must be adequately damped as to improve the system passivity and do not offer a satisfying performance due to the inherent performance of FIR filters, hence another paralleled structure must be employed to ensure robustness for frequencies other than the tunned ones.

The methods based on feedforward cancellation of disturbances are based on measurements of the disturbance [42–45]. However, the disturbance measurement is contaminated by the output inductor voltage, which can be noisy if the inductors are small. Also, the subtractive-mode resonance components can couple in this measurement. Therefore, the frequency bandwidth for direct feedforward cancellation is limited by the SNR of the disturbance measurement. A solution to this is through the use of disturbance

estimators [46], which might be an interesting object of study.

A third strategy is through the use of resonant controllers, also based on the internal model principle [47, 48]. More precisely, if we consider the HSS, each resonant controller behaves as an integrator if there is no damping factor, otherwise it behaves as a low-pass filter with the dc gain given by the damping factor. These controllers can be implemented in synchronous coordinates, such as in [49–51], or stationary coordinates [52–54]. Since the dimension of each resonant controller is equal to two, the number of degrees of freedom is equal to four, if we take into account the resonance frequency, which is usually adaptive in grid-tied applications.

Another issue in power converters is the active damping strategies as a way to ensure a more robust operation. Different techniques are presented in the literature, as presented in [55], but can be resumed into a full or partial state-feedback, with or without a controller structure, such that the L_2-gain of the system is minimized, hence robust control techniques are the most suitable for an optimal (or suboptimal, if subject to performance constraints) damping. Thus, state-feedback strategies can have an inherent active damping characteristic depending on the controllability and stabilizability and the measurements' SNR. An alternative to the use of measurements is through state estimation, although the estimation must have a fast response to dampen higher frequency resonances. The sliding-mode observer is contemplated as means to perform a fast state estimation while avoiding the peaking effect of linear observers through the saturation of the error input [56].

The control strategy is validated through a FPGA-based implementation of the proposed control strategies. The paralleled power converters were emulated by a Opal OP5700 hardware-in-the loop with the emulation time scaled by a factor of 100. This ensured a meticulous representation of the system's inherent switched behavior.

4.1 CURRENT-CONTROL STATE FEEDBACK

Let a continuous-time system be described by

$$\begin{aligned} \dot{\mathbf{x}} &= \boldsymbol{f}(\mathbf{x}, \mathbf{u}, \mathbf{w}) \\ \mathbf{y} &= \boldsymbol{g}(\mathbf{x}, \mathbf{u}, \mathbf{w}), \end{aligned} \tag{4.1}$$

where $\mathbf{x} \in \mathbb{R}^{n_x}$ is the state vector, $\mathbf{u} \in \mathbb{R}^{n_u}$ is the system input vector and $\mathbf{w} \in \mathbb{R}^{n_w}$ is the disturbance vector. From Chapter 3, we have that a Three-Phase VSI with a damped LCL output filter can be modeled as two decoupled single-phase systems,

$$\begin{cases} \dot{\mathbf{x}} = \mathbf{A}(\lambda)\mathbf{x} + \mathbf{B}(\lambda)\mathbf{u} + \mathbf{E}(\lambda)\mathbf{w} \\ \mathbf{y} = \mathbf{C}(\lambda)\mathbf{x} + \mathbf{D}(\lambda)\mathbf{u} + \mathbf{F}(\lambda)\mathbf{w} \end{cases}, \tag{4.2}$$

where

$$\mathbf{x} = (i_f, v_c, i_l)$$
$$\mathbf{u} = \frac{U_{dc}}{2} d$$
$$\mathbf{w} = u_{grid}$$

and $\boldsymbol{\lambda} \in \mathbb{R}^{n_\lambda}$ is the parameter uncertainty vector, assuming – but not limited to – that the converter parameters are balanced, thus the α- and β-axis components are orthogonal, as means to simplify the control project. However, the control evaluation, as well as subsequent stability analysis, can and should consider the complete models discussed in the previous chapter so as to evaluate parametric unbalances.

From (4.2), we can employ the Polytopic Linear Model (PLM) [57, 58] approach to find a set of linearized models with respect to $\boldsymbol{\lambda}$ such that

$$\begin{cases} \dot{\mathbf{x}} = \sum_{j=1}^{n_\lambda} p_j(\mathbf{x}, \mathbf{u}, \mathbf{w}) \left(\mathbf{A}_j \mathbf{x} + \mathbf{B}_j \mathbf{u} + \mathbf{E}_j \mathbf{w} + \mathbf{a}_j \right), \\ \mathbf{y} = \sum_{j=1}^{n_\lambda} p_j(\mathbf{x}, \mathbf{u}, \mathbf{w}) \left(\mathbf{C}_j \mathbf{x} + \mathbf{D}_j \mathbf{u} + \mathbf{F}_j \mathbf{w} + \mathbf{c}_j \right) \end{cases}, \tag{4.3}$$

where

$$\begin{aligned} \mathbf{A}_j &= \mathbf{J}_{\mathbf{x}}(f(\mathbf{x}, \mathbf{u}, \mathbf{w}, \boldsymbol{\lambda}))|_{\boldsymbol{\lambda}=\boldsymbol{\lambda}^j} \\ \mathbf{B}_j &= \mathbf{J}_{\mathbf{u}}(f(\mathbf{x}, \mathbf{u}, \mathbf{w}, \boldsymbol{\lambda}))|_{\boldsymbol{\lambda}=\boldsymbol{\lambda}^j} \\ \mathbf{E}_j &= \mathbf{J}_{\mathbf{w}}(f(\mathbf{x}, \mathbf{u}, \mathbf{w}, \boldsymbol{\lambda}))|_{\boldsymbol{\lambda}=\boldsymbol{\lambda}^j} , \end{aligned}$$

$\mathbf{J}$ is the Jacobian matrix and p is a scheduling function where $\sum_{j=1}^{n_\lambda} p_j = 1$, as to obtain the Uncertainty Model Set $\mathcal{M}$ defined as

$$\mathcal{M}\left(\{\mathbf{A}_i, \mathbf{B}_i, \mathbf{E}_i, \mathbf{a}_i, \mathbf{C}_i, \mathbf{D}_i, \mathbf{F}_i, \mathbf{c}_i\}\right) := \left\{ (\text{PLM}) \,\middle|\, \sum_{j=1}^{n_\lambda} p_j = 1,\ p_j \geq 0 \right\} \tag{4.4}$$

These uncertainties can appear due to many different reasons, such as the inductance and capacitance variation with the current and voltage, respectively, and modeling errors related to the grid model. We can then define $\mathcal{M}_o \in \text{span}(\mathcal{M})$ related to the optimal state-space model which minimizes a certain system norm with respect to all the model vertex, then linearize the system with respect to the rated disturbance vector $\boldsymbol{\lambda}_o$ according to

$$\begin{aligned} D_t \mathbf{x} &= \mathbf{A}_o \mathbf{x} + \mathbf{B}_o \mathbf{u} + \mathbf{E}_o \mathbf{w} + \boldsymbol{\Lambda}_{\mathbf{x}}(\boldsymbol{\lambda} - \boldsymbol{\lambda}_o) \\ \mathbf{y} &= \mathbf{C}_o \mathbf{x} + \mathbf{D}_o \mathbf{u} + \mathbf{F}_o \mathbf{w} + \boldsymbol{\Lambda}_{\mathbf{y}}(\boldsymbol{\lambda} - \boldsymbol{\lambda}_o), \end{aligned} \tag{4.5}$$

assuming that the set $\{\mathbf{a}_o, \mathbf{c}_o\}$ vanish.

Therefore, we can find a feedforward control action $\mathbf{u}_o$ such that

$$\mathbf{B}_o \mathbf{u}_o + \boldsymbol{\Lambda}_{\mathbf{x}}(\boldsymbol{\lambda} - \boldsymbol{\lambda}_o) = \mathbf{0} \tag{4.6}$$

as means of minimizing the influence of the known parameter variations on the eigenvalues of the system, which in turn results in

$$\mathbf{u}_o := -\mathbf{B}_o^{+}\boldsymbol{\Lambda}_{\mathbf{x}}(\boldsymbol{\lambda} - \boldsymbol{\lambda}_o), \tag{4.7}$$

granted that

$$\boldsymbol{\lambda} := \boldsymbol{h}_{\lambda}(\mathbf{x}, \mathbf{u}, \mathbf{w}), \tag{4.8}$$

where $\boldsymbol{h}_{\lambda}$ is a certain function that describes the behaviour of the uncertainties with the system inputs and states. Note that (4.8) can present a transcendental solution, hence an estimate of $\{\mathbf{u}, \mathbf{w}\}$ can be employed, although additional analysis might be required to assert the stability of the control strategy.

4.1.1 State-Feedback Control Structure

Let a system be described by

$$\begin{cases} D_t\boldsymbol{\chi} = \mathbf{A}_{\chi}\boldsymbol{\chi} + \mathbf{B}_{\chi}\mathbf{u}_{\chi} + \mathbf{E}_{\chi}\mathbf{w}_{\chi} \\ \mathbf{y}_{\chi} = \mathbf{C}_{\chi}\boldsymbol{\chi} + \mathbf{D}_{\chi}\mathbf{u}_{\chi} + \mathbf{F}_{\chi}\mathbf{w}_{\chi} \end{cases}. \tag{4.9}$$

Also, let the controller dynamic equations be described by

$$\begin{cases} D_t\boldsymbol{\xi} = \mathbf{A}_{\xi}\boldsymbol{\xi} + \mathbf{B}_{\xi}\mathbf{u}_{\xi} \\ \mathbf{y}_{\xi} = \mathbf{C}_{\xi}\boldsymbol{\xi} + \mathbf{D}_{\xi}\mathbf{u}_{\xi} \end{cases}, \tag{4.10}$$

where

$$\mathbf{u}_{\xi} := \mathbf{r} - \mathbf{y}_{\chi}.$$

Hence, we can write the closed loop system state-space equation as

$$D_t \begin{bmatrix} \boldsymbol{\chi} \\ \boldsymbol{\xi} \end{bmatrix} = \begin{bmatrix} \mathbf{A}_{\chi} + \mathbf{B}_{\chi}\left(\mathbf{K}_{\chi} - \mathbf{C}_{\chi}\mathbf{D}_{\xi}\right)\mathbf{Q} & \mathbf{B}_{\chi}\mathbf{C}_{\xi}\mathbf{Q} \\ -\mathbf{B}_{\xi}\left(\mathbf{C}\chi + \mathbf{D}_{\chi}\mathbf{K}_{\chi}\right)\mathbf{Q} & \mathbf{A}_{\xi} - \mathbf{B}_{\xi}\mathbf{C}_{\xi}\mathbf{D}_{\chi}\mathbf{Q} \end{bmatrix} \begin{bmatrix} \boldsymbol{\chi} \\ \boldsymbol{\xi} \end{bmatrix} + \begin{bmatrix} \mathbf{B}_{\chi}\mathbf{D}_{\xi}\mathbf{Q} \\ \mathbf{B}_{\xi}\mathbf{Q} \end{bmatrix} \mathbf{r} + \begin{bmatrix} \mathbf{E}_{\chi} \\ \mathbf{0} \end{bmatrix} \mathbf{w}, \tag{4.11}$$

where

$$\mathbf{Q} = \left(\mathbf{I} + \mathbf{D}_{\chi}\mathbf{D}_{\xi}\right)^{-1},$$

when considering a null feedforward matrix for disturbances $\mathbf{w}_{\chi}$ and a non-null feedforward for input $\mathbf{u}_{\chi}$. If $\mathbf{D}_{\chi}$ vanishes, we have that

$$D_t \begin{bmatrix} \boldsymbol{\chi} \\ \boldsymbol{\xi} \end{bmatrix} = \begin{bmatrix} \mathbf{A}_{\chi} + \mathbf{B}_{\chi}\left(\mathbf{K}_{\chi} - \mathbf{C}_{\chi}\mathbf{D}_{\xi}\right) & \mathbf{B}_{\chi}\mathbf{C}_{\xi} \\ -\mathbf{B}_{\xi}\mathbf{C}\chi & \mathbf{A}_{\xi} \end{bmatrix} \begin{bmatrix} \boldsymbol{\chi} \\ \boldsymbol{\xi} \end{bmatrix} + \begin{bmatrix} \mathbf{B}_{\chi}\mathbf{D}_{\xi} \\ \mathbf{B}_{\xi} \end{bmatrix} \mathbf{r} + \begin{bmatrix} \mathbf{E}_{\chi} \\ \mathbf{0} \end{bmatrix} \mathbf{w}, \tag{4.12}$$

Notice that it is possible to write closed-loop system in the discrete form in the same way

as (4.11), as $\mathbf{D}_\chi$ might not vanish depending on the discretization method. Also, from (4.12), we can group the controller system feed-forward action and the state-feedback gain into the gain $\mathbf{K}_\chi$ without altering the eigenvalues of the state matrix.

4.1.2 Proportional-Integral Controller

For a SISO control system, we can write the controller system matrices as

$$\mathbf{A}_\xi = 0, \quad \mathbf{B}_\xi = 1, \quad \mathbf{C}_\xi = K_i, \quad \mathbf{D}_\xi = K_p, \tag{4.13}$$

which can be expanded in case of MIMO systems as

$$\mathbf{A}_\xi = \mathbf{0}, \quad \mathbf{B}_\xi = \mathbf{I}, \quad \mathbf{C}_\xi = \operatorname{diag}(\mathbf{K}_i), \quad \mathbf{D}_\xi = \operatorname{diag}(\mathbf{K}_d) \tag{4.14}$$

for a 1DOF-PI controller, which assumes that the control input signal is the error, resulting in

$$\begin{cases} D_t\mathbf{x}_\xi = \mathbf{A}_\xi\mathbf{x}_\xi + \mathbf{B}_\xi\mathbf{e}_\xi = \mathbf{A}_\xi\mathbf{x}_\xi + \mathbf{B}_\xi\mathbf{r} - \mathbf{B}_\xi\mathbf{y} \\ \mathbf{y}_\xi = \mathbf{C}_\xi\mathbf{x}_\xi + \mathbf{D}_\xi\mathbf{e}_\xi = \mathbf{C}_\xi\mathbf{x}_\xi + \mathbf{D}_\xi\mathbf{r} - \mathbf{D}_\xi\mathbf{y}. \end{cases} \tag{4.15}$$

Note that the feedforward action of the reference in the control output $\mathbf{y}_\xi$ can excite resonances on the controlled system, accounting for a reduction of robustness and leading to a larger signal overshoot. Therefore, a 2DOF-PI controller can be employed by multiplying the feedforward action by a constant $\eta \in \mathbb{R}$ in accordance with

$$\begin{cases} D_t\mathbf{x}_\xi = \mathbf{A}_\xi\mathbf{x}_\xi + \mathbf{B}_\xi\mathbf{r} - \mathbf{B}_\xi\mathbf{y} \\ \mathbf{y}_\xi = \mathbf{C}_\xi\mathbf{x}_\xi + \eta\mathbf{D}_\xi\mathbf{r} - \mathbf{D}_\xi\mathbf{y}. \end{cases} \tag{4.16}$$

4.1.3 Resonant Controller

Assuming a SISO control system, we can write the controller system state-space matrices for a resonant controller as

$$\mathbf{A}_\xi(\omega_r) = \begin{bmatrix} 0 & \omega_r \\ -\omega_r & -2\zeta_r\omega_r \end{bmatrix}, \ \mathbf{B}_\xi(\omega_r) = \begin{bmatrix} 0 \\ \omega_r \end{bmatrix}, \ \mathbf{C}_\xi(\omega_r) = \mathbf{K}_r, \ \mathbf{D}_\xi(\omega_r) = 0. \tag{4.17}$$

Note that the employed resonant controller does not have an infinite gain at the resonance frequency ω_r due to the damping factor ζ_r, leading to a steady-state error. The choice of ζ_r is directly related to the passivity of a closed-loop system. Hence, each resonant controller has four degrees of freedom.

We can consider ω_r as the output of a dynamic system that follows the equation

$$\boldsymbol{h}_w(\dot{\omega}_w, \omega_w, \omega_r) = 0. \tag{4.18}$$

This equation holds true for adaptive resonant controllers, where the frequency is typically estimated using an estimation algorithm. For simplicity, let's assume that $\omega_r := \bar{\omega}_r$, $\bar{\omega}_r \in \mathbb{R}$ initially.

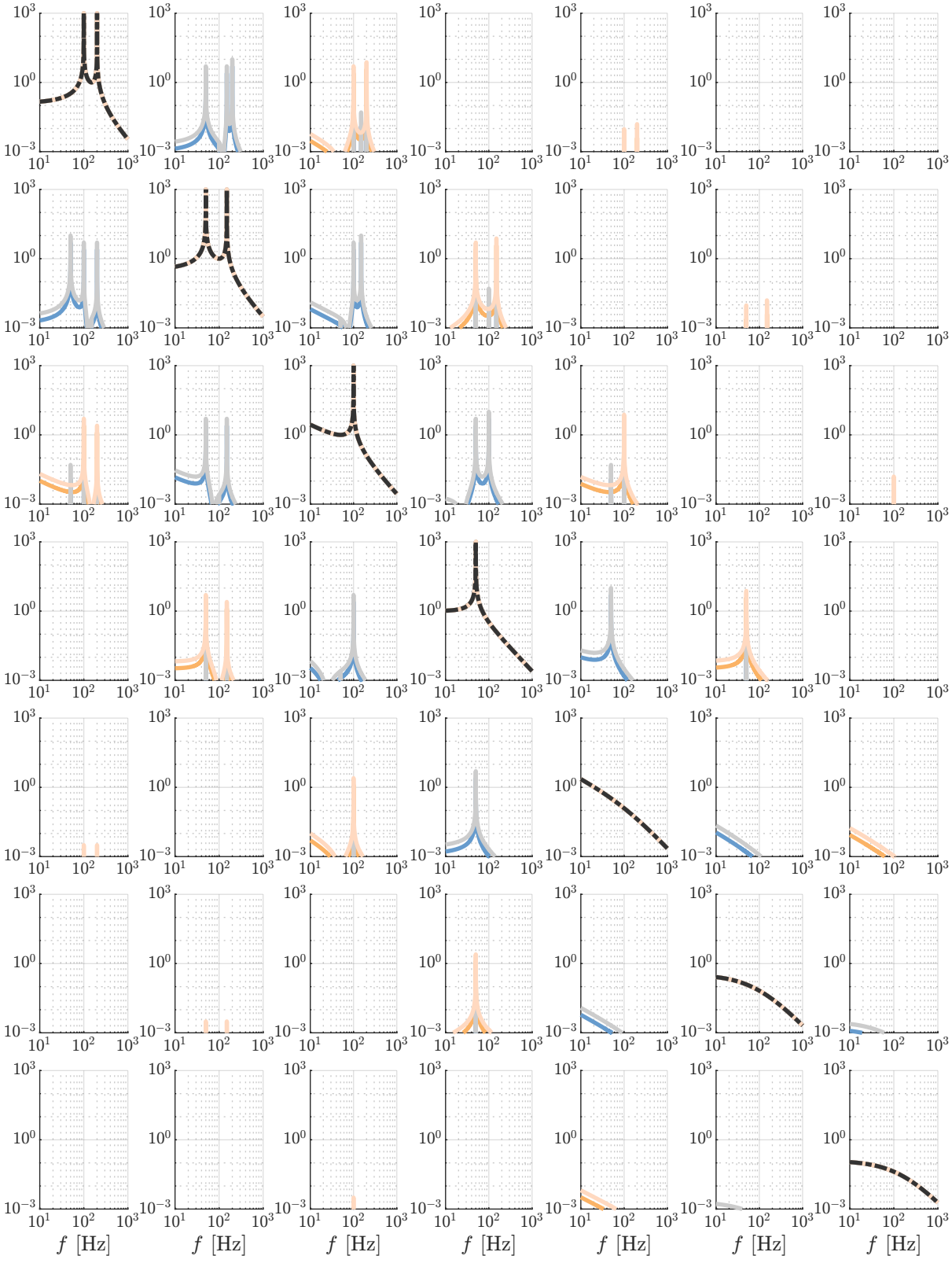

(a) $\frac{\langle x_1 \rangle_k}{\langle u \rangle_k}, \forall k \in \mathbb{Z}^3_{-3}$

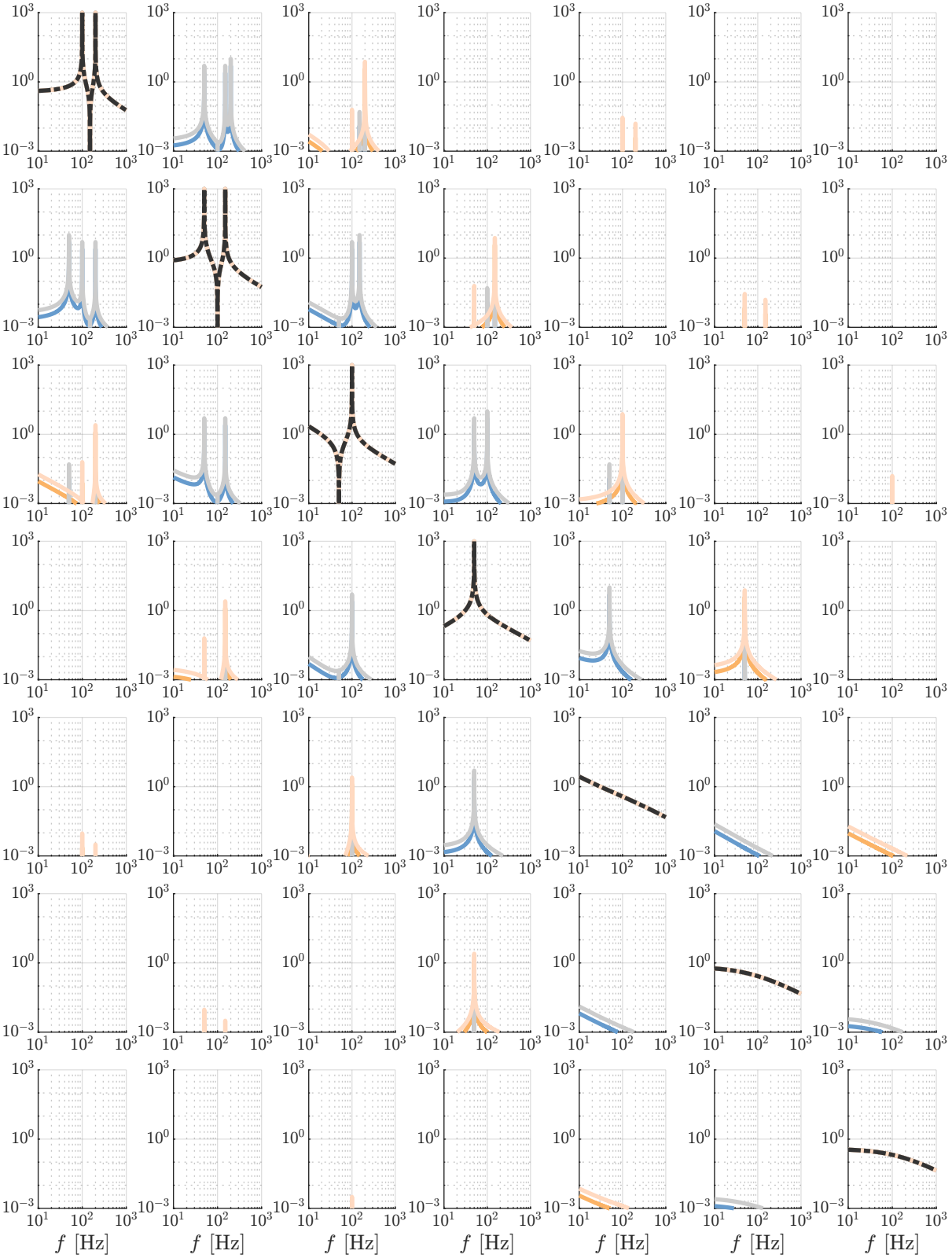

(b) $\frac{\langle x_2 \rangle_k}{\langle u \rangle_k}, \forall k \in \mathbb{Z}^3_{-3}$

Figure 4.1 – Bode Diagrams of the Harmonic State-Space Transfer Functions of the linearized systems for $f_r = 50$ Hz (dashed black) with 0.5% amplitude sinusoidal disturbances with frequencies of 50 Hz (blue) and 100 Hz (orange) and 1% amplitude for frequencies 50 Hz (Gray) and 100 Hz (Peach).

The harmonic state-space description of the resonant controller is given by

$$D_t \begin{bmatrix} \langle \xi_1 \rangle \\ \langle \xi_2 \rangle \end{bmatrix} = \begin{bmatrix} -\iota\omega_w \mathrm{diag}\left(\mathfrak{H}\right) & \bar{\omega}_r \mathbf{I} \\ -\bar{\omega}_r \mathbf{I} & -2\zeta_r \bar{\omega}_r \mathbf{I} - \iota\omega_w \mathrm{diag}\left(\mathfrak{H}\right) \end{bmatrix} \begin{bmatrix} \langle \xi_1 \rangle \\ \langle \xi_2 \rangle \end{bmatrix} + \begin{bmatrix} \mathbf{0} \\ \bar{\omega}_r \mathbf{I} \end{bmatrix} \langle u_\xi \rangle \,, \tag{4.19}$$

where $\mathfrak{H} \in \mathbb{Z}$ is the set of harmonics. By considering $\omega_r \in L^2$, we can obtain a more general equation expressed as

$$D_t \begin{bmatrix} \langle \xi_1 \rangle \\ \langle \xi_2 \rangle \end{bmatrix} = \begin{bmatrix} -\iota\omega_w \mathrm{diag}\left(\mathfrak{H}\right) & \mathbf{\Gamma} \circ \langle \omega_r \rangle \\ -\mathbf{\Gamma} \circ \langle \omega_r \rangle & -2\zeta_r \mathbf{\Gamma} \circ \langle \omega_r \rangle - \iota\omega_w \mathrm{diag}\left(\mathfrak{H}\right) \end{bmatrix} \begin{bmatrix} \langle \xi_1 \rangle \\ \langle \xi_2 \rangle \end{bmatrix} + \begin{bmatrix} \mathbf{0} \\ \mathbf{\Gamma} \circ \langle \omega_r \rangle \end{bmatrix} \langle u_\xi \rangle \,, \tag{4.20}$$

Note that if $\langle \omega_r \rangle_i = \delta_{i,0} \bar{\omega}_r, \ \forall i \in \mathbb{N}$, (4.20) solves for (4.19).

It is also possible to linearize the controller HSS model for a given frequency as means of verifying the effects of the frequency variation on the ability to accurately reject disturbances on the synthonized frequency. From inspection of Figure 4.1, there can be a considerable coupling between frequencies, especially for lower frequency disturbances.

4.1.4 Multi-Resonant Controller

A multi-resonant controller can be obtained by taking n_r parallel resonant controllers with added outputs, resulting in

$$\begin{aligned} \mathbf{A}_\xi(\omega, \zeta) &= \begin{bmatrix} 0 & \omega_1 & 0 & 0 & \cdots & 0 & 0 \\ -\omega_1 & -2\zeta_1\omega_1 & 0 & 0 & \cdots & 0 & 0 \\ 0 & 0 & 0 & \omega_2 & \cdots & 0 & 0 \\ 0 & 0 & -\omega_2 & -2\zeta_2\omega_2 & \cdots & 0 & 0 \\ \vdots & \vdots & \vdots & \vdots & \ddots & \vdots & \vdots \\ 0 & 0 & 0 & 0 & \cdots & 0 & \omega_{n_r} \\ 0 & 0 & 0 & 0 & \cdots & -\omega_{n_r} & -2\zeta_{n_r}\omega_{n_r} \end{bmatrix}. \\ \mathbf{B}_\xi(\omega, \zeta) &= \begin{bmatrix} 0 & 2\zeta_1\omega_1 & 0 & 2\zeta_2\omega_2 & \cdots & 0 & 2\zeta_{n_r}\omega n_r \end{bmatrix}^T \\ \mathbf{C}_\xi &= \begin{bmatrix} \mathbf{K}_r^1 & \mathbf{K}_r^2 & \cdots & \mathbf{K}_r^{n_r} \end{bmatrix} \\ \mathbf{D}_\xi &= 0 \end{aligned} \tag{4.21}$$

The same procedure for the frequency modeling can be adopted in the representation of the multi-resonant controller, since the paralleled controllers are decoupled.

4.1.5 Discretization

From a control design point-of-view, a discrete-time model description is better suited for a digital implementation. Hence we can apply the mapping

$$\begin{cases} \mathbf{x}(k+1) = \mathbf{\Phi}\mathbf{x}(k) + \mathbf{\Gamma}\mathbf{u}(k) + \mathbf{\Xi}\mathbf{w}(k) \\ \mathbf{y}(k) = \mathbf{C}\mathbf{x}(k) + \mathbf{D}\mathbf{u}(k) \end{cases}, \tag{4.22}$$

where

$$\begin{aligned} \mathbf{\Phi} &= \exp\left(\mathbf{A}h\right) \\ \mathbf{\Gamma} &= \int_0^h \exp\left(\mathbf{A}t\right)\mathbf{B}\ dt = \mathbf{A}^{-1}\left(\mathbf{\Phi} - \mathbf{I}\right)\mathbf{B} \\ \mathbf{\Xi} &= \int_0^h \exp\left(\mathbf{A}t\right)\mathbf{E}\ dt = \mathbf{A}^{-1}\left(\mathbf{\Phi} - \mathbf{I}\right)\mathbf{E} \end{aligned}$$

for $t = kh$, where h is the sampling time and assuming that the state-matrix $\mathbf{A}$ is non-singular. It is worth noting that in this mapping, a zero-order holder is adopted for the disturbance $\mathbf{w}$, which is not ideal as $\mathbf{w}$ is a continuous-time disturbance. Some of the impacts of this discretization will be visible in future discussions when the input impedance is analyzed.

When discretizing resonant controllers, the eigenvalues of the state matrix should be the same, hence the method of choice can be viewed as a feedforward action given by the matrix $\mathbf{D}_\xi$, which is equivalent as an increment in the state-feedback gain $\mathbf{K}_\chi$ in the same way as the controller's proportional action. The zero-order hold already inserts a transport delay of a sampling time, which we can assume is related to the PWM modulation. However, we can also take into account the transport delay inserted by the computational time, according to

$$\begin{bmatrix} \chi(k+1) \\ \mathbf{u}_\chi(k) \end{bmatrix} = \begin{bmatrix} \mathbf{\Phi}_\chi & \mathbf{\Gamma}_\chi \\ \mathbf{0} & \mathbf{0} \end{bmatrix} \begin{bmatrix} \chi(k) \\ u_\chi(k-1) \end{bmatrix} + \begin{bmatrix} \mathbf{0} \\ \mathbf{I} \end{bmatrix} \mathbf{u}_\chi(k) + \begin{bmatrix} \mathbf{\Xi} \\ \mathbf{0} \end{bmatrix} \mathbf{w}_\chi(k). \tag{4.23}$$

The delayed control input can also be fed back into the control input u_χ.

The resonant controllers in Equation 4.17 can also be discretized by employing the same methodology, leading to

$$\begin{aligned} \mathbf{\Phi}_{\xi,1,1} &= \frac{\exp(-h\omega\zeta)\left(\zeta\sinh\left(h\omega(\zeta^2-1)^{1/2}\right) + \cosh\left(h\omega(\zeta^2-1)^{1/2}\right)(\zeta^2-1)^{1/2}\right)}{(\zeta^2-1)^{1/2}} \\ \mathbf{\Phi}_{\xi,1,2} &= \frac{\sinh\left(h\omega(\zeta^2-1)^{1/2}\right)\exp(-h\omega\zeta)}{(\zeta^2-1)^{1/2}} \\ \mathbf{\Phi}_{\xi,2,1} &= -\frac{\sinh\left(h\omega(\zeta^2-1)^{1/2}\right)\exp(-h\omega\zeta)}{(\zeta^2-1)^{1/2}} \\ \mathbf{\Phi}_{\xi,2,2} &= -\frac{\exp(-h\omega\zeta)\left(\zeta\sinh\left(h\omega(\zeta^2-1)^{1/2}\right) - \cosh\left(h\omega(\zeta^2-1)^{1/2}\right)(\zeta^2-1)^{1/2}\right)}{(\zeta^2-1)^{1/2}} \end{aligned} \tag{4.24}$$

which simplifies for

$$\mathbf{\Phi}_{\xi} = \begin{bmatrix} \cos h\omega & \sin h\omega \\ -\sin h\omega & \cos h\omega \end{bmatrix} \tag{4.25}$$

when ζ vanishes. To simplify the calculations, the coefficients of (4.24) can be computed via quadratic interpolation for practical implementation.

4.1.6 Controller Design

4.1.6.1 Linear Quadratic Regulator

The gain matrix can be calculated via pole placement, which can be quite difficult due to the total number of eigenvalues of the closed-loop system matrix. We can employ the Linear Quadratic Regulator (LQR) as to minimize the quadratic cost function

$$J(\mathbf{u}) = \sum_{k=1}^{\infty} \mathbf{x}^T(k)\mathbf{Q}\mathbf{x}(k) + \mathbf{u}^T(k)\mathbf{R}\mathbf{u}(k) + 2\mathbf{x}^T(k)\mathbf{N}\mathbf{u}(k) \tag{4.26}$$

over an infinite horizon [59]. However, this approach is dependent on a choice of $\mathbf{Q}$, $\mathbf{R}$ and $\mathbf{N}$, which require previous knowledge of the system behaviour or a good initial guess.

4.1.6.2 Robust Control

An optimal approach, considering disturbance rejection and robustness against parametric variations, is to utilize robust control techniques. Hence, let us explore the application of robust control methods. Let

$$\mathbf{q} := \mathbf{C}_q\mathbf{x} + \mathbf{F}_q\mathbf{w} \tag{4.27}$$

as the variable of interest for the robust analysis. Also, let

$$G_{qw}(\sigma) = \frac{Q(\sigma)}{W(\sigma)} \tag{4.28}$$

as the frequency response of the system G_{qw}, where σ is equal s or z for continuous or discrete-time systems, respectively.

Definition 1 ($\mathcal{H}_2$-norm).

The norm $\mathcal{H}_2$ of the operator input/output is defined as

$$\|G_{qw}(s)\|_2 = \sqrt{\int_0^{\infty} \mathrm{Tr}\left(g_{qw}^T(t)g_{qw}(t)\right) \mathrm{d}t} \tag{4.29}$$

which coincides with the L^2-norm of a system for continuous-time systems or

$$\|G_{qw}(z)\|_2 = \sqrt{\sum_{k=0}^{\infty} \mathrm{Tr}\left(g_{qw}^T(k) g_{qw}(k)\right)} \tag{4.30}$$

which coincides with the ℓ^2-norm for discrete-time systems.

Definition 2 ($\mathcal{H}_\infty$-norm).

The norm $\mathcal{H}_\infty$ of the operator input/output is defined as

$$\|G_{qw}(s)\|_\infty = \sup_{\|w(t)\|_2 \neq 0} \frac{\|\mathbf{q}(t)\|_2}{\|\mathbf{w}(t)\|_2} \tag{4.31}$$

for continuous-time systems or

$$\|G_{qw}(z)\|_\infty = \sup_{\|w(k)\|_2 \neq 0} \frac{\|\mathbf{q}(k)\|_2}{\|\mathbf{w}(k)\|_2} \tag{4.32}$$

for discrete-time systems.

Problem 1. Consider a system described by the dynamic equations

$$\dot{\mathbf{x}} = f(\mathbf{x}, \mathbf{u}, \mathbf{w}) \tag{4.33}$$

The objective is to design the feedback $\mathbf{u} = \boldsymbol{\mathcal{K}}(\mathbf{x})$ given by

$$\boldsymbol{\mathcal{K}}(\mathbf{x}) = \mathbf{K}\mathbf{x} = \begin{bmatrix} \mathbf{K}_x & \mathbf{K}_u & \mathbf{K}_\xi \end{bmatrix} \begin{bmatrix} \chi(k) \\ \mathbf{u}_\chi(k-1) \\ \xi(k) \end{bmatrix} \tag{4.34}$$

such that the map $\boldsymbol{\mathcal{K}}(\cdot)$ is a stabilizing feedback for x and presents the following characteristics:

i. Minimizes an upper bound on the L_2-gain of the input-to-output operator with respect to the disturbance $\mathbf{w}(k)$ to the performance signal $\mathbf{q}(k)$, which translates to the $\|G_{qw}\|_\infty$ for linear systems. Thus, we aim to minimize the scalar γ such that

$$\|G_{qw}\|_\infty \leq \gamma. \tag{4.35}$$

ii. The eigenvalues of the state matrix of the closed-loop system pertain to a region $\mathcal{D} \in \mathbb{C}$.

iii. The rate of convergence of the state trajectory is bounded by a constant r.

Thus, the design specification can be described in the Linear Matrix Inequalities (LMI) framework by means of the modified Lyapunov inequalities [52, 54, 60, 61]. Hence,

an upper-bound on the L_2-gain can determined by minimizing a constant γ such that

$$\exists v(\mathbf{x}) > 0 : r\Delta v(\mathbf{x}) + \frac{1}{\gamma}\mathbf{q}^T\mathbf{q} - \gamma\mathbf{w}^T\mathbf{w} < 0 \tag{4.36}$$

for a certain Lyapunov functional $v(\mathbf{x})$, where

$$\Delta v(\mathbf{x}) = v\left(\mathbf{x}(k+1)\right) - v\left(\mathbf{x}(k)\right).$$

We can consider the quadratic function

$$v(\mathbf{x}) = \mathbf{x}^T\mathbf{P}\mathbf{x} \tag{4.37}$$

as a Lyapunov function candidate, where $\mathbf{P} = \mathbf{P}^T \succ \mathbf{0}$ is to be determined. We can then rewrite the inequality given by (4.36) as the bilinear form

$$\begin{bmatrix} x(k) \\ w(k) \end{bmatrix}^T \begin{bmatrix} \hat{\mathbf{\Phi}}^T r\mathbf{P}\hat{\mathbf{\Phi}} - r\mathbf{P} + \frac{1}{\gamma}\hat{\mathbf{C}}_q^T\hat{\mathbf{C}}_q & \hat{\mathbf{\Phi}}^T\mathbf{P}\hat{\mathbf{\Xi}} \\ * & \hat{\mathbf{\Xi}}^T\mathbf{P}\hat{\mathbf{\Xi}} - \gamma\mathbf{I} \end{bmatrix} \begin{bmatrix} x(k) \\ w(k) \end{bmatrix} < 0, \tag{4.38}$$

where

$$\begin{cases} \hat{\mathbf{\Phi}} = \mathbf{\Phi} + \mathbf{\Gamma}\mathbf{K} \\ \hat{\mathbf{C}}_q = \mathbf{C}_q + \mathbf{D}_{qu}\mathbf{K} \end{cases},$$

which is convex if the gain matrix $\mathbf{K}$ is given, solving for a negative-definite bilinear form.

For convergence purposes, we can work with the dual optimization problem by defining $\mathbf{Q} = \mathbf{P}^{-1}$ and using the parametrization $\mathbf{L} = \mathbf{K}$, and we can write the optimization problem as

$$\begin{aligned} \min_{\mathbf{Q},\mathbf{L}} \quad & \gamma \\ \text{s.t.} \quad & \begin{bmatrix} -r\mathbf{Q} & \mathbf{0} & \mathbf{\Phi}\mathbf{Q} + \mathbf{\Gamma}\mathbf{L} & \mathbf{\Xi} \\ \star & -\gamma\mathbf{I} & \mathbf{C}_q\mathbf{Q} + \mathbf{D}_q\mathbf{L} & \mathbf{F}_q \\ \star & \star & -r\mathbf{Q} & \mathbf{0} \\ \star & \star & \star & -\gamma\mathbf{I} \end{bmatrix} \prec \mathbf{0}, \quad \forall \{\mathbf{\Phi}, \mathbf{\Gamma}, \mathbf{\Xi}, \mathbf{C}_q, \mathbf{D}_q, \mathbf{F}_q\} \in \mathcal{M} \end{aligned} \tag{4.39}$$

for the Uncertainty Model Set $\mathcal{M}$.

We can can define $\mathcal{D} \in \mathbb{C}$ as a LMI region if there are matrices $\mathbf{\Lambda}$ and $\mathbf{M}$ such that

$$\mathcal{D} := \left\{ z \in \mathbb{C} : \mathbf{\Lambda} + \mathbf{M}z + \mathbf{M}^T z^* < 0 \right\}. \tag{4.40}$$

Thus, we can use the constraint

$$\mathbf{\Lambda} \otimes \mathbf{Q} + \mathbf{M} \otimes \mathrm{He}\left(\mathbf{Q}, \mathbf{L}\right) + \mathbf{M}^T \otimes \mathrm{He}\left(\mathbf{Q}, \mathbf{L}\right)^T \prec \mathbf{0}, \quad \forall \ \{\mathbf{\Phi}, \mathbf{\Gamma}\} \in \mathcal{M}, \tag{4.41}$$

where

$$\mathrm{He}\left(\mathbf{Q},\mathbf{L}\right)=\mathbf{\Phi Q}+\mathbf{\Gamma L},$$

to ensure that eigen $\left(\hat{\mathbf{\Phi}}\right)\in\mathcal{D}$.

4.1.6.3 Input Impedance Shaping

In some cases, the condition that the response of a system for a certain disturbance is bounded is not enough to guarantee a certain desired behaviour. Such is the case of paralleled converters, the operation while maintaining a passive behaviour is important for an adequate performance, as shown in [62–64].

Hence, if we consider the system described by (4.2) and a certain linearizing feedback map $\mathbf{u}=\mathcal{K}(x)$, we can write the passivity equation [65] of the power converter system as

$$\mathbf{w}^T\mathbf{C}_i\mathbf{x}\geq 0. \tag{4.42}$$

Note that the system is considered loss-less when $w\to 0$ or $\mathbf{C}_i x\to 0$. If the system satifies

$$\mathbf{w}^T\mathbf{C}_i\mathbf{x}\geq \epsilon\mathbf{w}^T\mathbf{w}, \tag{4.43}$$

we consider that the system has an excess of passivity if $\epsilon>0$ or a shortage of passivity if $\epsilon<0$, or

$$\mathbf{w}^T\mathbf{C}_i\mathbf{x}\geq \delta\mathbf{x}^T\mathbf{C}_i^T\mathbf{C}_i\mathbf{x}, \tag{4.44}$$

we consider that the system has an excess of passivity if $\delta>0$ or a shortage of passivity if $\delta<0$.

Since there is no direct control over the disturbance $\mathbf{w}$, we can only alter the passivity of a system by altering the system response with respect to the control action, i.e., altering the mapping $\mathcal{K}(\cdot)$.

We can write the input admittance and impedance of the system as

$$\begin{aligned} Y_{wi}(s)&=-\frac{\mathbf{C}_i\left(s\mathbf{I}-\mathbf{A}\right)^{-1}\mathbf{E}}{W(s)}\\ Z_{wi}(s)&=\frac{1}{Y_{wi}(s)}\end{aligned}, \tag{4.45}$$

where $|Y_{wi}(\iota\omega)|$ correlates to the L_2-gain. Hence, if we have a general idea of $|W(\iota\omega)|$, we can design the controller such that $|Y_{wi}(\iota\omega_r)|<Y_{min}$ for a certain frequency ω_r, which is the main idea of resonant controllers.

We can then rewrite the passivity condition described by (4.42) as

$$Y_{wi}(\iota\omega)>0,\quad \forall\omega\in\mathbb{R} \tag{4.46}$$

in the frequency domain. Thus, we can define the passivity condition as

$$\Re\left\{Y_{wi}(\iota\omega)\right\} > 0, \quad \forall\omega \in \mathbb{R}. \tag{4.47}$$

However, if we consider the case of parallel converters with LCL filters, the point of common coupling is not necessarily on the grid voltage $\mathbf{w}$. An idea for asserting the passivity is to verify the passivity at the filter capacitor, as in

$$\mathbf{C}_v\mathbf{x}\mathbf{C}_i\mathbf{x} > 0, \tag{4.48}$$

which represents the worst-case scenario.

From this, we can redefine the input admittance and impedance as

$$\begin{aligned} Y_{vi}(s) &= -\frac{\mathbf{C}_i\left(s\mathbf{I}-\mathbf{A}\right)^{-1}\mathbf{E}}{\mathbf{C}_v\left(s\mathbf{I}-\mathbf{A}\right)^{-1}\mathbf{E}}, \\ Z_{vi}(s) &= \frac{1}{Y_{vi}(s)} \end{aligned} \tag{4.49}$$

In this sense, we have two different scenarios for an appropriate choice of variable to control:

- If the closed-loop input impedance absolute value is higher than the grid impedance, we can use the grid current as the controller input with enough robustness;
- If the closed-loop input impedance absolute value is lower or in the same order as the grid impedance, it is more difficult to control the grid current as the system tends to be uncontrollable, hence a more appropriate choice of variable to control would be the inverter current on the first inductor, as is the case with weak grid conditions, or with LC filters, where the second inductor is usually a common-mode choke or a transformer dispersion.

One common practice is the use of virtual impedance control loops, which aim to shape the $Z_{vi}(s)$ through feed-forward control strategies. However, the reference tracking error should be higher than the measured current resolution, as to avoid issues with quantization noise, and higher than the inherent reference feedback tracking error, which for sinusoidal systems is given by the resonant controller damping ζ_r. A virtual impedance is tipically inserted in grid-following converters as means to compensate for the reactive power processed by the magnetic components of the output filter.

It is possible to alter the input impedance amplitude and angle via the resonant controllers parameters. The proposal for such is described through the following procedure:

i. Design the controller gains via one of the previous methods (LQR or Robust Control). In this stage, it is possible to suppress the resonant controllers if the final resonant gain leads to a small dc gain;

ii. Perform a nonlinear optimization to minimize the phase error of the input impedance for the resonant controller frequencies with respect to a reference angle vector $\boldsymbol{\varphi}_r^*$, which is null-valued when a resistive behaviour is desired, according to

$$\begin{aligned} \min_{\mathbf{K},\boldsymbol{\zeta}_r,\boldsymbol{\omega}_r} \quad & \left(\angle Z_{vi}(\boldsymbol{\omega}_r^*) - \boldsymbol{\varphi}_r^*\right)^T \left(\angle Z_{vi}(\boldsymbol{\omega}_r^*) - \boldsymbol{\varphi}_r^*\right). \\ \text{s.t.} \quad & |\boldsymbol{\omega}_r - \boldsymbol{\omega}_r| < \Delta\boldsymbol{\omega}_r \\ & |\mathbf{K} - \mathbf{K}_0| < \Delta\mathbf{K} \\ & \Re\left\{\text{eigen}\left(\mathbf{A} + \mathbf{BK}\right)\right\} < \mathbf{0}, \quad \text{for continuous-time systems} \\ & \left|\text{eigen}\left(\boldsymbol{\Phi} + \boldsymbol{\Gamma}\mathbf{K}\right)\right| < \mathbf{1}, \quad \text{for discrete-time systems} \end{aligned} \tag{4.50}$$

In this case, we want a Local Minimum of the optimization function, remaining in an operating point closer to the optimally calculated in (i).

iii. Redesign the damping factor $\boldsymbol{\zeta}_r$ to obtain a passive system if the new system is not passive. This step is important due to the phase behaviour of resonant controllers, as the system tends to be more passive for higher values of the damping factor ζ_r.

If the phase reference is set to zero and if the frequencies of the resonant controllers are set as the rated frequency vector, it was observed that the procedure is more likely to result in a passive system. It is also possible to employ $\boldsymbol{\varphi}_r^*$ as a slack variable to improve the convexity of the optimization problem. Figure 4.2 shows the bode diagram of the input impedance for the procedure and a comparison with the gains obtained with the LQR formulation for strong grid conditions. The procedure was performed using the Artelys Knitro optimization software, which is based on a nonlinear interior point algorithm.

The LQR technique proved not to be passive at the resonance frequency, resulting from a poor choice of $\mathbf{Q}$ and $\mathbf{R}$. However, this was solved by applying the Impedance Shaping algorithm, which improved the passivity range of the system. Note that the last resonant controller presents a non-passive behaviour, although this can be easily solved by raising the damping factor value of the resonant controller at the 950 Hz frequency.

From the Bode diagram, we can infer that the LMI region $\mathcal{D}$ was assumed to be too conservative with respect to the dynamic behaviour, hence a redesign might be necessary, as the proportional action should be higher as to lower the $\|G_{iw}(\omega)\|_2$.

A comparison between the output current and the inverter current control with respect to the input impedance is shown in Figure 4.3. The grid current control proved to be more robust if compared to the inverter current control. However, the input impedance is mostly capacitive, hence the Impedance Shaping procedure or a virtual impedance control loop might be necessary if a resistive or inductive input impedance is desired.

We can also observe the modeling error due to the disturbance's zero-order hold model, which generates error at higher frequencies, since the phase was expected to be almost purely capacitive for the open-loop model. This error is more noticeable for the

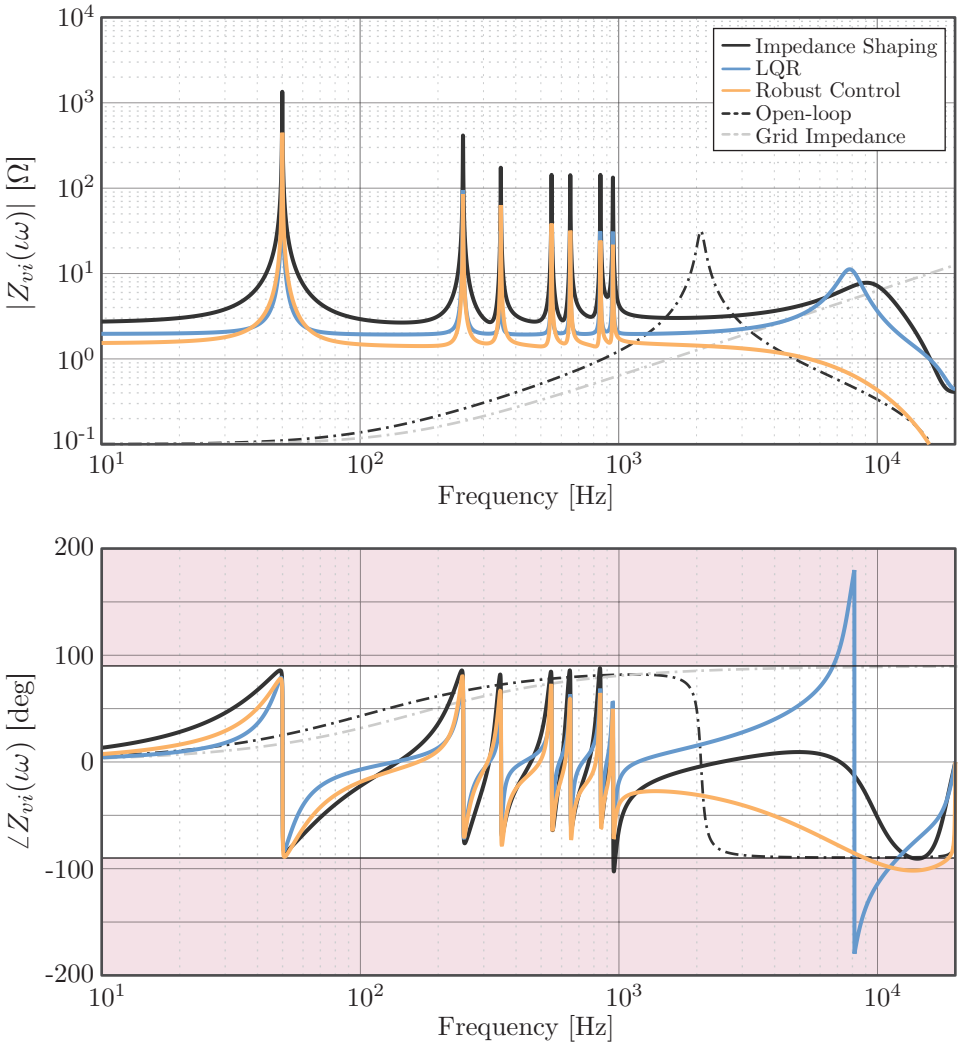

Figure 4.2 – Closed-loop input impedance of the state-feedback control for three different methodologies: LQR, Robust Control and Impedance Shaping.

γ-axis input impedance, as discussed in the next section.

One of the difficulties that the state-feedback technique introduces is the need for a measurement or estimation of all the modeled states, which is discussed in subsection 4.3.1.

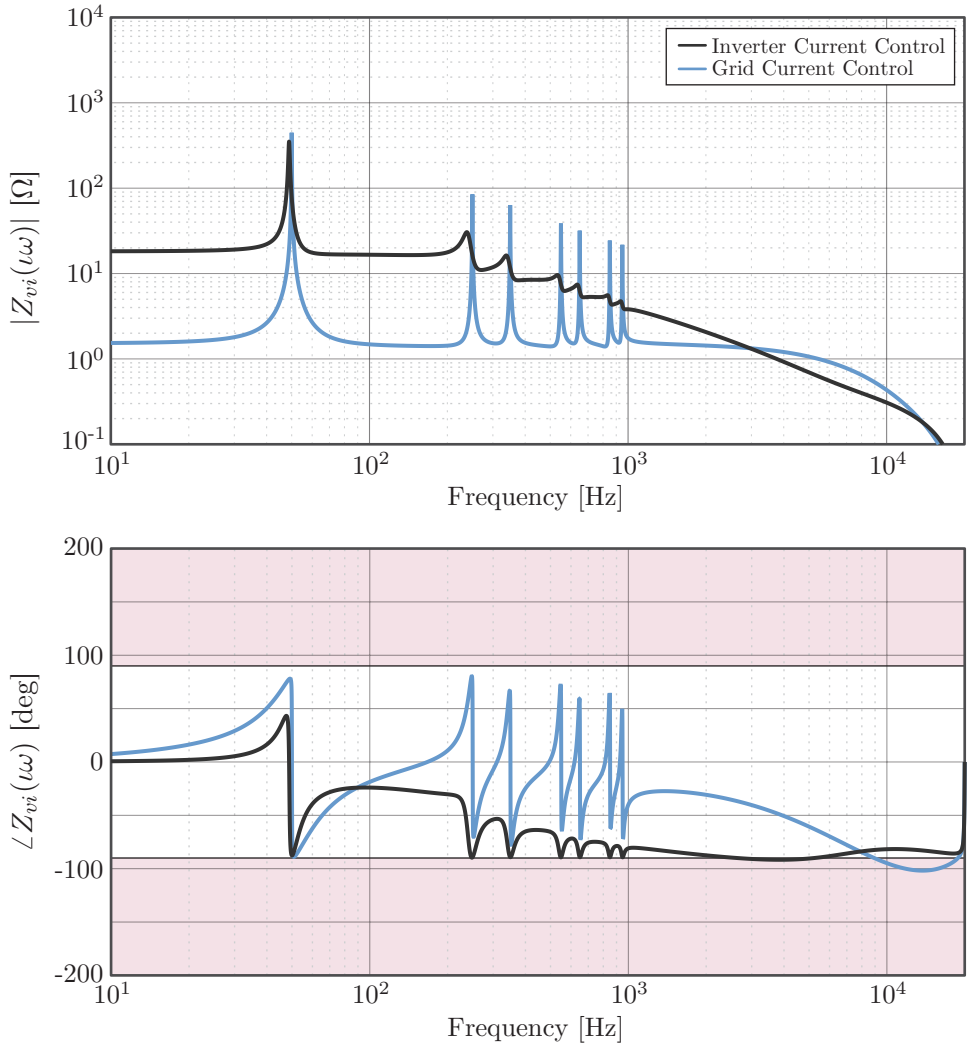

Figure 4.3 – Comparison of the closed-loop input impedance of the state-feedback control employing robust control for Grid Current Control and Inverter Current Control.

4.2 γ-AXIS CURRENT CONTROL

From Chapter 3, we can observe that a γ-axis current loop is present in parallel-connected power converters sharing the same dc bus if there is no transformer before the point of common coupling. One of the characteristics of this loop is the low-impedance when not employing a large common-mode choke, which is given mainly by the series connection of the inductances in the loop, paralleled due to the connection of each phase. Assuming that there is no unbalance, which couples the $\alpha\beta$ axis with the γ axis, we can write the system for N parallel converters as

$$D_t \mathbf{x}_{\gamma,sm} = \mathbf{A}_{\gamma,sm}\mathbf{x}_{\gamma,sm} + \mathbf{B}_{\gamma,sm}\mathbf{u}_{\gamma}, \tag{4.51}$$

where $\mathbf{x}_{\gamma,sm} \in \mathbb{R}^{N-1}$ are the subtractive-mode γ-axis currents and $\mathbf{u}_\gamma \in \mathbb{R}^N$ are the inverter γ-axis voltages synthesized by each converter. Note that we can write

$$\ker\left(D_t\right) = \operatorname{span}\left(\mathbf{1}_N\right),$$

hence $f : \operatorname{span}\left(\mathbf{u}_\gamma\right) \to \operatorname{span}\left(\mathbf{x}_{\gamma,sm}\right)$ is not injective, i.e, we have different combinations of input voltages which might lead to the same subtractive-mode current point of equilibrium. More specifically, the kernel of the linear transformation is given by the additive-mode, as previously discussed.

If we consider that each inverter does not synthesize a common-mode voltage dependent on the levels of the $\alpha\beta$ components, which is the case for the Sinusoidal Pulse-Width Modulation (SPWM), which sacrifices the maximum admissible modulation index, then there is no coupling between common- and differential-mode axis. However, most applications make use of a zero-axis signal injection as means of working with a lower voltage dc bus. Hence, we can rewrite (4.51) as

$$\dot{\mathbf{x}}_{\gamma,sm} = \mathbf{A}_{\gamma,sm}\mathbf{x}_{\gamma,sm} + \mathbf{B}_{\gamma,sm}\boldsymbol{g}(\mathbf{u}_{\alpha\beta}), \tag{4.52}$$

where $\boldsymbol{g}(\mathbf{u}) = (g_i(\mathbf{u}_i))_{i=1}^N$, for a certain mapping $g_i : \mathbb{R}^2 \to \mathbb{R}$ related to the common-mode voltage synthesized by a certain modulation scheme for the i^{th} converter, which is nonlinear in most cases.

Since we cannot guarantee that all the converters will process the same energy, the point of equilibrium of the γ-axis currents might reach prohibitive values, hence a control strategy is necessary to artificially increase the current-loop impedance. Therefore, we can adopt the mapping $h_i : \mathbb{R}^3 \to \mathbb{R}$ such that

$$h_i\left(u_{\alpha\beta}, u_{i,\gamma,\text{ctrl}}\right) = g_i\left(\mathbf{u}_{i,\alpha\beta}\right) + u_{i,\gamma,\text{ctrl}}, \tag{4.53}$$

where the control input is defined as

$$u_{i,\gamma,\text{ctrl}} := \mathcal{K}_i(\mathbf{x}_{i,\gamma}, \xi_{i,\gamma}).$$

In the case of the Space Vector Modulation, we can utilize the scheme proposed by [66], where a zero-axis signal is injected by altering the sampling times of zero vectors.

Thus, let us define the gh-transformation $\mathbf{T}_{gh} \in \mathfrak{L}(\mathbb{R}^2)$ by rotating the β-axis by 30° for the Fast-SVM algorithm, such that

$$\mathbf{T}_{gh} := \frac{1}{4}\begin{bmatrix} 3 & -\sqrt{3} \\ 0 & 2\sqrt{3} \end{bmatrix}. \tag{4.54}$$

We can then define

$$\mathbf{m}_{gh} := \begin{bmatrix} 1 & 0 \\ 0 & 1 \\ 1 & 1 \end{bmatrix} \mathbf{T}_{gh}\mathbf{u}_{\alpha\beta} = \frac{1}{4}\begin{bmatrix} 3 & -\sqrt{3} \\ 0 & 2\sqrt{3} \\ 3 & \sqrt{3} \end{bmatrix} \mathbf{u}_{\alpha\beta}. \tag{4.55}$$

The sextant detection can then be performed by the sign of each of the components of m_{gh} in accordance with

$$\text{sextant} := \begin{cases} 1, & \text{when sign}\,(\mathbf{m}_{gh}) = (+1,+1,+1), \\ 2, & \text{when sign}\,(\mathbf{m}_{gh}) = (-1,+1,+1), \\ 3, & \text{when sign}\,(\mathbf{m}_{gh}) = (-1,+1,-1), \\ 4, & \text{when sign}\,(\mathbf{m}_{gh}) = (-1,-1,+1), \\ 5, & \text{when sign}\,(\mathbf{m}_{gh}) = (+1,-1,-1), \\ 6, & \text{when sign}\,(\mathbf{m}_{gh}) = (+1,-1,+1). \end{cases} \tag{4.56}$$

The duty ratios of each non-null vector can then be described by

$$\mathbf{d}_{\text{SVM,1:2}} := \begin{cases} (m_{gh,1}, m_{gh,2}), & \text{when sextant} = 1, \\ (-m_{gh,1}, m_{gh,3}), & \text{when sextant} = 2, \\ (m_{gh,2}, -m_{gh,3}), & \text{when sextant} = 3, \\ (-m_{gh,2}, -m_{gh,1}), & \text{when sextant} = 4, \\ (-m_{gh,3}, m_{gh,1}), & \text{when sextant} = 5, \\ (m_{gh,3}, -m_{gh,2}), & \text{when sextant} = 6. \end{cases} \tag{4.57}$$

The remaining time, described by

$$d_{\text{SVM,0}} := 1 - d_{\text{SVM,1}} - d_{\text{SVM,2}}, \tag{4.58}$$

can then be allocated to apply the null-vector. In the 2LVSI converter, there are two possiibilities for applying the null-vector, one with a positive valued γ-axis component and one with a negative valued γ-axis component, here denoted as $\mathbf{s}_{0,p}$ and $\mathbf{s}_{0,n}$. The traditional SVM modulation scheme applies the positive and negative valued gamma-axis components with the same ratio, however it is possible to modulate a signal by setting the application duty ratios of each component as

$$\begin{aligned} d_{\text{SVM,0},p} &= \left(\frac{1}{2} + \eta_\gamma\right) d_{\text{SVM,0}} \\ d_{\text{SVM,0},n} &= \left(\frac{1}{2} + \eta_\gamma\right) d_{\text{SVM,0}}, \end{aligned} \tag{4.59}$$

which in turn modulates a signal given by η_γ in the γ-axis. For carrier-based modulation strategies, the control signal can be injected directly to the modulating signals by adding η_γ to the components of each phase.

Thus, we can rewrite the system equations given by (4.51) as

$$\dot{\mathbf{x}}_{\gamma,sm} = \mathbf{A}_{\gamma,sm}\mathbf{x}_{\gamma,sm} + \mathbf{B}_{\gamma,sm}\mathbf{u}_{\gamma,\text{ctrl}} + \mathbf{B}_{\gamma,sm}\boldsymbol{g}\left(\mathbf{u}_{\alpha\beta}\right). \tag{4.60}$$

Previously, we assumed that the γ-axis is decoupled, i.e., $\mathbf{u}_{\alpha\beta} \perp \mathbf{x}_{\gamma,sm}$, hence we can rewrite (4.60) as

$$\dot{\mathbf{x}}_{\gamma,sm} = \mathbf{A}_{\gamma,sm}\mathbf{x}_{\gamma,sm} + \mathbf{B}_{\gamma,sm}\mathbf{u}_{\gamma,\text{ctrl}} + \mathbf{B}_{\gamma,sm}\mathbf{w}_{\text{ff}}. \tag{4.61}$$

However, we cannot measure the subtractive-mode currents to control a decoupled system, hence some mathematical manipulations are needed to express (4.61) in terms of the controlled variables.

Let the subtractive-mode Lunze transformation be given by

$$\mathbf{L}_{sm} := \frac{1}{N}\begin{bmatrix} N-1 & -1 & \cdots & -1 & -1 \\ -1 & N-1 & \cdots & -1 & -1 \\ \vdots & \vdots & \ddots & \vdots & \vdots \\ -1 & -1 & \cdots & N-1 & -1 \end{bmatrix}, \tag{4.62}$$

hence we can write the descriptor system as

$$\mathbf{L}_{sm}\dot{\mathbf{x}}_\gamma = \mathbf{A}_{\gamma,sm}\mathbf{L}_{sm}\mathbf{x}_\gamma + \mathbf{B}_{\gamma,sm}\mathbf{u}_{\gamma,\text{ctrl}} + \mathbf{B}_{\gamma,sm}\mathbf{w}_{\text{ff}}, \tag{4.63}$$

where $\mathbf{x}_\gamma \in \mathbb{R}^N$ are the converters' γ-axis current vector. The system can be rewritten as

$$\dot{\mathbf{x}}_\gamma = \mathbf{L}_{sm}^{+}\mathbf{A}_{\gamma,sm}\mathbf{L}_{sm}\mathbf{x}_\gamma + \mathbf{L}_{sm}^{+}\mathbf{B}_{\gamma,sm}\mathbf{u}_{\gamma,\text{ctrl}} + \mathbf{L}_{sm}^{+}\mathbf{B}_{\gamma,sm}\mathbf{w}_{\text{ff}} \tag{4.64}$$

For a single converter, we can write

$$\dot{\mathbf{x}}_{1,\gamma} = \mathbf{A}_{1,\gamma,1}\mathbf{x}_{1,\gamma} + \mathbf{B}_{1,\gamma}u_{1,\gamma,\text{ctrl}} + \mathbf{B}_{1,\gamma}w1,\text{ff} + \mathbf{E}_{1,\gamma}\mathbf{w}_{1,\gamma}, \tag{4.65}$$

where

$$\mathbf{w}_{1,\gamma} = \left(\left(x_{n,\gamma}\right)_{n=2}^{N}, \left(u_{n,\gamma,\text{ff}}\right)_{n=2}^{N}, \left(u_{n,\gamma,\text{ctrl}}\right)_{n=2}^{N}\right) \tag{4.66}$$

and

$$\begin{aligned} \mathbf{A}_\gamma &= \mathbf{L}_{sm}^{+}\mathbf{A}_{\gamma,sm}\mathbf{L}_{sm} \\ \mathbf{B}_\gamma &= \mathbf{L}_{sm}^{+}\mathbf{B}_{\gamma,sm} \end{aligned}.$$

The system can be discretized in the same way as (4.23) while taking into account

the computational delay, resulting in the system

$$\chi(k+1) = \mathbf{\Phi}_\chi \chi(k) + \mathbf{\Gamma}_\chi \upsilon_\chi(k-1) + \mathbf{\Gamma}_{\chi,\mathrm{ff}} w_{\mathrm{ff}}(k) + \mathbf{\Xi} w_\gamma^1(k). \tag{4.67}$$

In this case, it is not desirable for the circulating current to vanish, as this action would lead to a control action that would cancel the SVM feedforward. Also, the state can be extremelly noisy, due to the high-frequency circulating currents, hence the control bandwidth is limited.

Thus, we can define a mapping $\mathcal{K}(\chi) = \mathbf{K}\chi(k)$ via the LQR procedure or via Robust Control, as discussed in the previous section. In this case, the figure of merit is the input admittance with respect to $w_{1,\gamma}$, which should be small enough as to minimize the current circulation and high enough so that the feedforward action is not hindered. It was observed that an integral controller action makes it difficult to make the system passive, due to the large bandwidth required by the injection of harmonic components at higher frequencies by the modulation scheme. The input impedance with respect to the γ-axis disturbance voltage w is shown in Figure 4.4, with the open-loop and closed-loop responses, demonstrating a passive characteristic of the control loop for two different control strategies. If the disturbance rejection is not sufficient, a resonant controller can also be employed as a way to increase the input impedance at certain frequencies.

This procedure must be repeated for all the parallel-connected converters, and the same input impedance can be adopted as to more evenly distribute the γ-axis subtractive-mode currents.

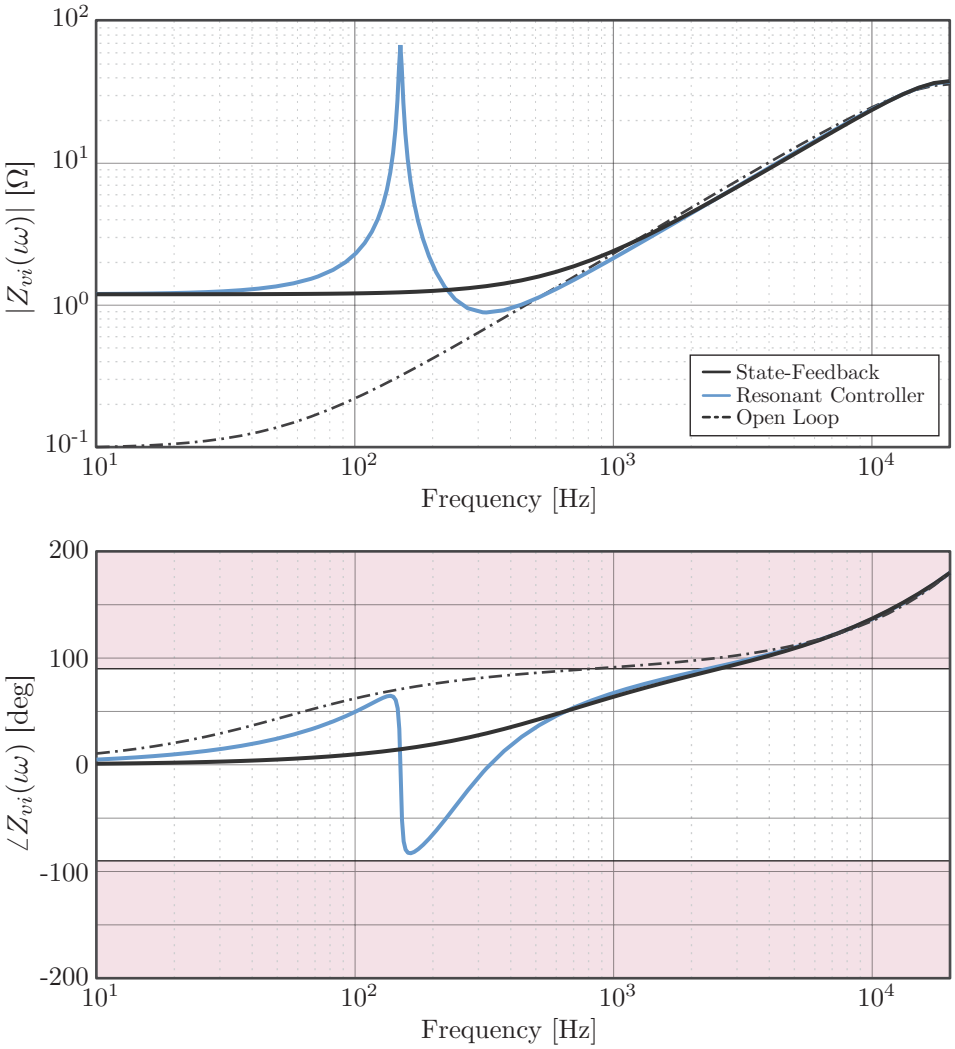

Figure 4.4 – γ-axis input impedance for two different control strategies: state-feedback and state-feedback with resonant controller at the third harmonic.

4.3 STATE OBSERVERS

One of the problems generated by a full state-feedback control strategy is the need to measure all the states of a power converter. If another filter topology discussed in Chapter 3 employing a passive damping structure, we would need still need to measure all the states.

One solution is through output-feedback, where we can add constraints to the optimization routine for the calculation of the state-feedback gains such that the gains for the non-measured states vanish, although this limits the pole placement as we would not have freedom over all the system eigenvalues. Another solution is through the use of state observers, granted that the observability function is injective. However, the dynamics inserted by the state estimation is critical, especially if a wide control bandwidth is desired, adding the difficulty to separating the dynamics of a linear state observer and the controlled system. This also leads to high observer gains, which in turn amplifies the peaking effect.

Therefore, this work presents an alternative for state-estimation based on a Sliding-

Mode Observer.

4.3.1 Sliding Mode Observer

Let a dynamic system be described by

$$\begin{cases} \sigma\mathbf{x} = \mathbf{A}\mathbf{x} + \mathbf{B}\mathbf{u} + \mathbf{E}\mathbf{w} \\ \mathbf{y} = \mathbf{C}\mathbf{x} + \mathbf{D}\mathbf{u} + \mathbf{F}\mathbf{w} \end{cases}, \quad \forall\sigma = s \text{ or } z \tag{4.68}$$

Hence, according to [67], we can design a state observer of the form

$$\sigma\hat{\mathbf{x}} = \mathbf{A}\hat{\mathbf{x}} + \mathbf{B}\hat{\mathbf{u}} + \mathbf{L}\text{sign}\left(\mathbf{y} - \mathbf{C}\hat{\mathbf{x}}\right), \tag{4.69}$$

which differs from the Luenberger observer by the choice of the discontinuous function $\text{sign}\left(\cdot\right)$. Under a suitable choice of the gain $\mathbf{L}$, the sliding occurs on the manifold $\mathbf{C}\hat{\mathbf{x}} - \mathbf{y} = 0$, i.e., the state observer becomes a reduced order observer.

Hence, assume that $\exists\mathbf{T} : \mathbf{T}x = (\mathbf{y}, \mathbf{v})$, such that

$$\begin{aligned} \mathcal{A} &= \mathbf{T}\mathbf{A}\mathbf{T}^{-}1 \\ \mathcal{B} &= \mathbf{T}\mathbf{B} \\ \mathcal{E} &= \mathbf{T}\mathbf{E} \end{aligned} .$$

We can then write

$$\begin{cases} \sigma\mathbf{y} = \mathcal{A}_{1,1}\mathbf{y} + \mathcal{A}_{1,2}\mathbf{v} + \mathcal{B}_1\mathbf{u} + \mathcal{E}_1\mathbf{w} \\ \sigma\mathbf{v} = \mathcal{A}_{2,1}\mathbf{y} + \mathcal{B}_{2,2}\mathbf{v} + \mathcal{B}_2\mathbf{u} + \mathcal{E}_2\mathbf{w} \end{cases}. \tag{4.70}$$

The corresponding SMO for the first subsystem is given by

$$\sigma\hat{\mathbf{y}} = \mathcal{A}_{1,1}\hat{\mathbf{y}} + \mathcal{A}_{1,2}\hat{\mathbf{v}} + \mathcal{B}_1\mathbf{u} + \mathcal{E}_1\hat{\mathbf{w}} + \mathbf{L}_1\text{sign}\left(\mathbf{y} - \hat{\mathbf{y}}\right) \tag{4.71}$$

with the error system described by

$$\sigma\mathbf{e}_y = \mathcal{A}_{1,1}\mathbf{e}_y + \mathcal{A}_{1,2}\mathbf{e}_v + \mathcal{E}_1\left(\mathbf{w} - \hat{\mathbf{w}}\right) - \mathbf{L}_1\text{sign}\left(\mathbf{e}_y\right), \tag{4.72}$$

where $\hat{\mathbf{w}}$ is an estimate of $\mathbf{w}$, as sometimes it is not possible to measure the disturbance. Hence we can choose $\mathbf{L}_1$ such that the sliding occurs along the manifold $\mathbf{e}_y = 0$.

For the second part of the system, we can use the observer equation of the form

$$\sigma\hat{\mathbf{v}} = \mathcal{A}_{2,1}\mathbf{y} + \mathcal{A}_{2,2}\hat{\mathbf{v}} + \mathcal{B}_2\mathbf{u} + \mathcal{E}_2\mathbf{w} + \mathbf{L}_2\mathbf{L}_1\text{sign}\left(\mathbf{y} - \hat{\mathbf{y}}\right), \tag{4.73}$$

with the error equation given by

$$\sigma\mathbf{e}_v = \mathcal{A}_{2,2}\mathbf{e}_v + \mathcal{E}_2(\mathbf{w} - \hat{\mathbf{w}}) - \mathbf{L}_2\mathbf{L}_1\text{sign}\left(\mathbf{e}_y\right). \tag{4.74}$$

If we assume that $\sigma\mathbf{e}_y = \mathbf{e}_y = 0$ and (4.72), we have that

$$\mathbf{L}_1 \text{sign}\left(\mathbf{e}_y\right) = \mathcal{A}_{1,2}\mathbf{e}_v + \mathcal{E}_1\left(\mathbf{w} - \hat{\mathbf{w}}\right). \tag{4.75}$$

We can substitute (4.75) into (4.74), resulting in

$$\sigma\mathbf{e}_v = \left(\mathcal{A}_{2,2} - \mathcal{A}_{1,2}\right)\mathbf{e}_y + \left(\mathcal{E}_2 - \mathbf{L}_2\mathcal{E}_1\right)\left(\mathbf{w} - \hat{\mathbf{w}}\right), \tag{4.76}$$

hence $\mathbf{L}_2$ must be chosen with caution so that the estimated system is stable with the desired rate of convergence while minimizing the disturbance influence on the estimation.

One of the drawbacks of the SMO is that it introduces chattering at frequencies close to the update frequency, which can instabilize a system due to non-modeled high-frequency dynamics, with a special care for subtractive mode resonances. The SNR ratio of the estimation can be much lower than the switching noise in power electronic systems, depending on the estimated state.

The chattering effect is less problematic when the load, in this case the grid, is capable of absorbing its energy. This helps minimize the energy stored in the filter components, resulting in reduced current oscillations. However, when operating under grid conditions, the chattering effect leads to significantly higher current oscillations. Therefore, there is a need for strategies to mitigate this issue.

Power converter systems often encounter uncertainties, particularly in relation to the grid model. Therefore, addressing this issue becomes crucial. The following subsection presents a solution to mitigate the impact of such uncertainties as well as the chattering effect.

4.3.2 Extended Sliding Mode Observer

An Extended State Observer (ESO) is a type of observer that estimates states that are not measured in the system, employed in situations where the system dynamics include disturbances and uncertainties, or unmeasured states that need to be estimated accurately.

The key idea behind an ESO is to design a dynamic observer which presents a compensation for disturbances and uncertainties to the unmeasured states estimates. It tipically involves augmenting the system with additional states together with an observer. The observer gains are then selected to minimize the estimation error between the actual states and the estimated states. Grid-connected power converters require compensation to eliminate modeling errors caused by unknown grid parameters and variations in converter parameters with electrical and physical quantities (e.g., inductance with current and temperature).

Let $\mathbf{w}$ the system disturbance vector. It is safe to assume that $D_t\mathbf{w} < \mathfrak{N}_0$, i.e., the first derivative of the disturbance is bounded. Also, let $\psi \in \mathcal{C}^0(\mathbb{R})$ a nonlinear monotonic

function such that $\lim_{x\to\pm\infty}\psi(x)=\pm 1$, and let $\Psi\in\mathcal{C}^0(\mathbb{R}^m):\Psi_n(\mathbf{x})=\psi(x_n),\ \forall\mathbf{x}\in\mathbb{R}^m$.

The Extended Sliding Mode Observer (ESMO) can be written as

$$\begin{cases}\sigma\hat{\mathbf{y}}=\mathcal{A}_{1,1}\mathbf{y}+\mathcal{A}_{1,2}\hat{\mathbf{v}}+\mathcal{B}_1\mathbf{u}+\mathcal{E}_1(\hat{\mathbf{w}}+\hat{\mathbf{w}}_{\text{ff}})+\mathbf{L}_1\Psi(\mathbf{y}-\hat{\mathbf{y}})\\ \sigma\hat{\mathbf{v}}=\mathcal{A}_{2,1}\hat{\mathbf{y}}+\mathcal{A}_{2,2}\hat{\mathbf{v}}+\mathcal{B}_2\mathbf{u}+\mathcal{E}_2(\hat{\mathbf{w}}+\hat{\mathbf{w}}_{\text{ff}})+\mathbf{L}_2\Psi(\mathbf{y}-\hat{\mathbf{y}})\\ \sigma\hat{\mathbf{w}}=\mathbf{L}_3\Psi(\mathbf{y}-\hat{\mathbf{y}}),\end{cases}\tag{4.77}$$

where $\hat{\mathbf{w}}_{\text{ff}}$ is a feedforward compensation to minimize the energy of the augmented states estimates. If we let $\mathbf{w}$ as the grid voltage, the filter capacitor voltage can be employed.

Note that for a small error the system turns into a Luenberger observer depending on the choice of ψ. In this case, let $\psi(\cdot):=\tanh(\cdot)$, which presents a saturated characteristic for signals with higher amplitude and a close to linear characteristic for signals with smaller amplitudes, with an addition that $\psi\in\mathcal{C}^\infty(\mathbb{R})$. For both observers, robust control techniques or the LQR can be employed to calculate the gains.

4.4 SIMULATIONS

A system with two parallel connected converters was simulated to verify the performance of the estimator and the state-feedback strategy, as well as the behaviour or circulating currents while operating with in-phase and phase-opposed carriers, which represents the best and worst-case scenarios. Converter #1 employs a SMO to estimate the inverter current, which was chosen due to the higher difficulty to estimate due to the transport delay between the measured states and the estimated state. A γ-axis current control strategy was employed by the second converter to minimize the circulation of medium frequency currents, as both converters do not process the same energy levels. The scenario chosen for the simulation is shown in Table 4.1.

4.4.1 In-phase Carriers

The simulations illustrated by Figure 4.5, Figure 4.6 and Figure 4.7 presents the converter states. From this, we can infer that the SMO presented an adequate estimate of the inverter current, as seen in Figure 4.8, and the state-feedback control presented a dynamic of approximately one grid cycle.

We can make use of the Clarke-Lunze transform as to inspect the circulating currents, as shown in Figure 4.9. From this, we can conclude that there is no significant γ-axis current circulation, as the carriers are in-phase and the γ-axis controller maintains a low current amplitude even when processing different energy levels if compared to Figure 4.10, where the γ-axis is uncontrolled.

A high-frequency current with significant amplitude was observed in the filter capacitor subtractive-mode voltage, which is generated by the chattering of the sliding-mode observer. The frequency is close to the subtractive-mode resonance of the output

Table 4.1 – Converter Parameters for Simulation

Parameter	**Symbol**	**Value**
dc Bus Voltage	U_{dc}	400 V
Inverter Inductance	L_f	150 μH
Inverter Inductor Resistance	r_f	20 mΩ
Filter Capacitance	C_c	19.8 μF
Filter Capacitor Resistance	r_c	10 mΩ
Filter Damped Capacitance	C_d	19.8 μF
Filter Damped Capacitor Resistance	r_d	100mΩ
Line Inductance	L_l	10 μH
Line Inductor Resistance	r_l	1 mΩ
Grid Inductance	L_w	50 μH
Grid Inductor Resistance	r_w	50 mΩ
Switching Frequency	f_s	25 kHz

capacitors and inductors and is generally underdamped. These harmonic components are not controllable, and the stability will depend on parasitic resistances for damping. However, the addition of a damping circuit, which was discussed in Chapter 3 is always necessary to guarantee an adequate damping for uncontrollable frequency components.

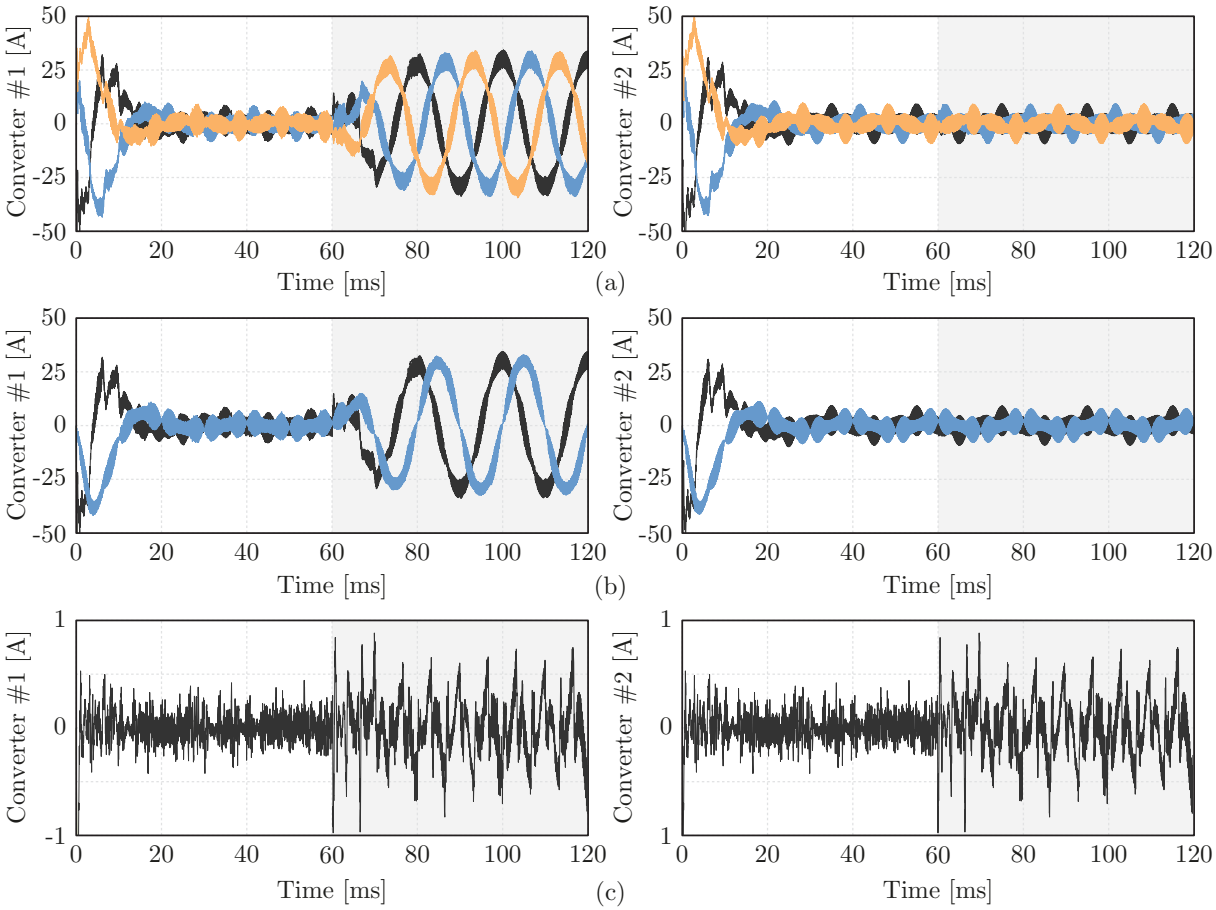

Figure 4.5 – Inverter current of a paralleled converter system with current state-feedback control and γ-axis current control with in-phase carriers. Converter #1 estimates the inverter current via SMO. (a) *abc* coordinates (b) $\alpha\beta$ coordinates (c) γ axis current.

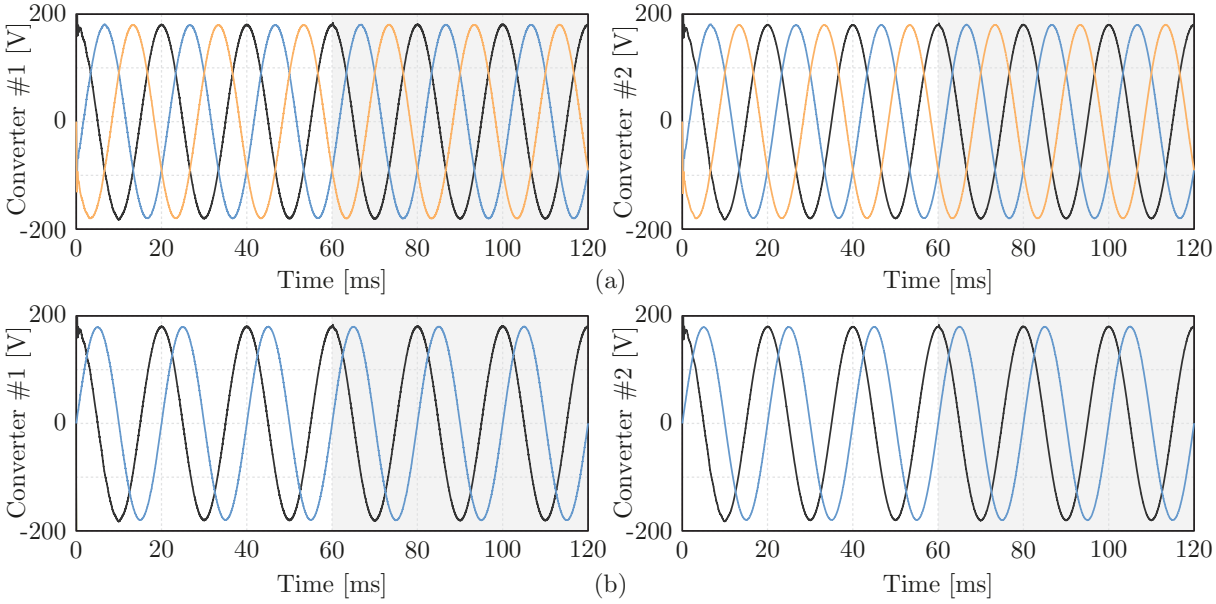

Figure 4.6 – Filter capacitor voltages of a paralleled converter system with current state-feedback control and γ-axis current control with in-phase carriers. Converter #1 estimates the inverter current via SMO. (a) *abc* coordinates (b) $\alpha\beta$ coordinates.

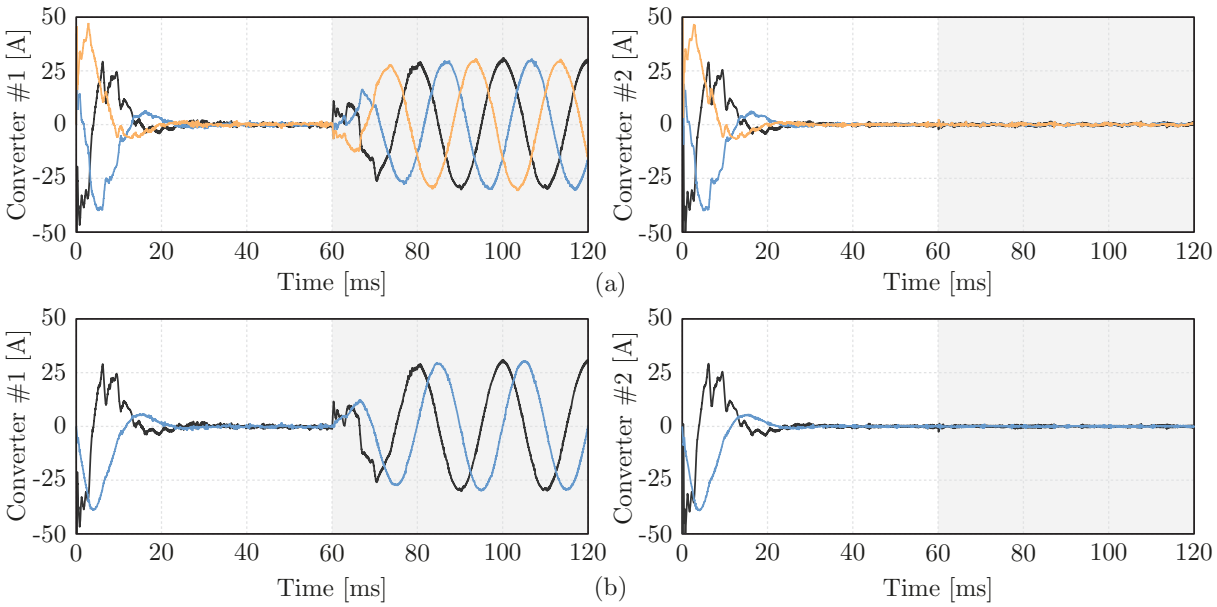

Figure 4.7 – Grid currents of a paralleled converter system with current state-feedback control and γ-axis current control with in-phase carriers. Converter #1 estimates the inverter current via SMO. (a) *abc* coordinates (b) $\alpha\beta$ coordinates.

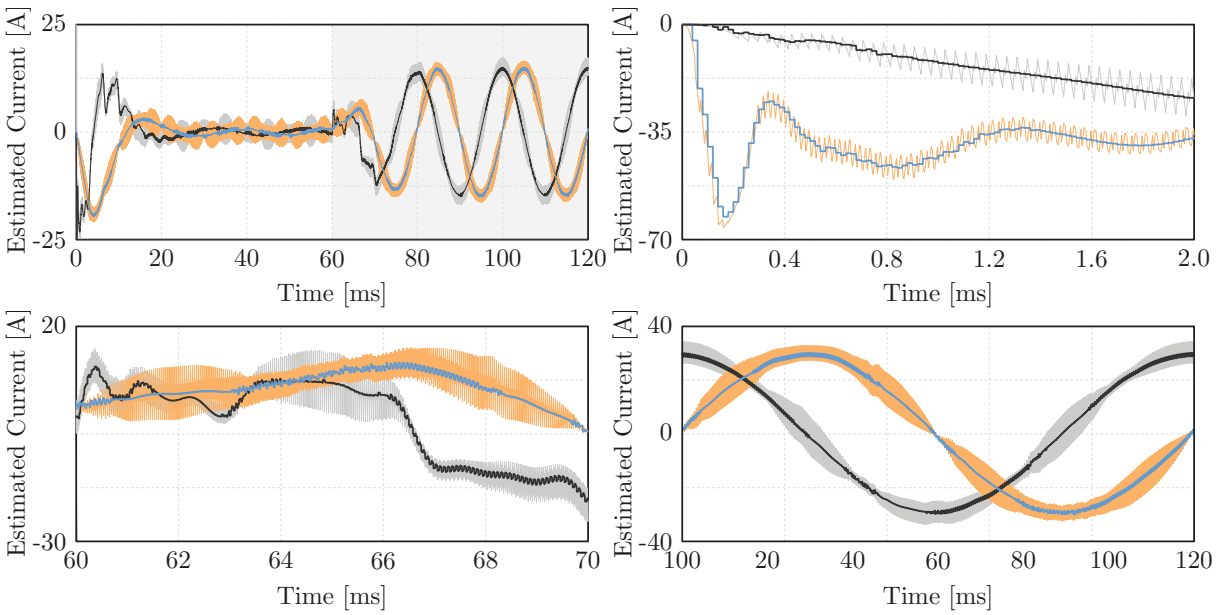

Figure 4.8 – Sliding-mode observer behaviour for the inverter current for different time-stamps, demonstrating the dynamic behaviour of the estimation.

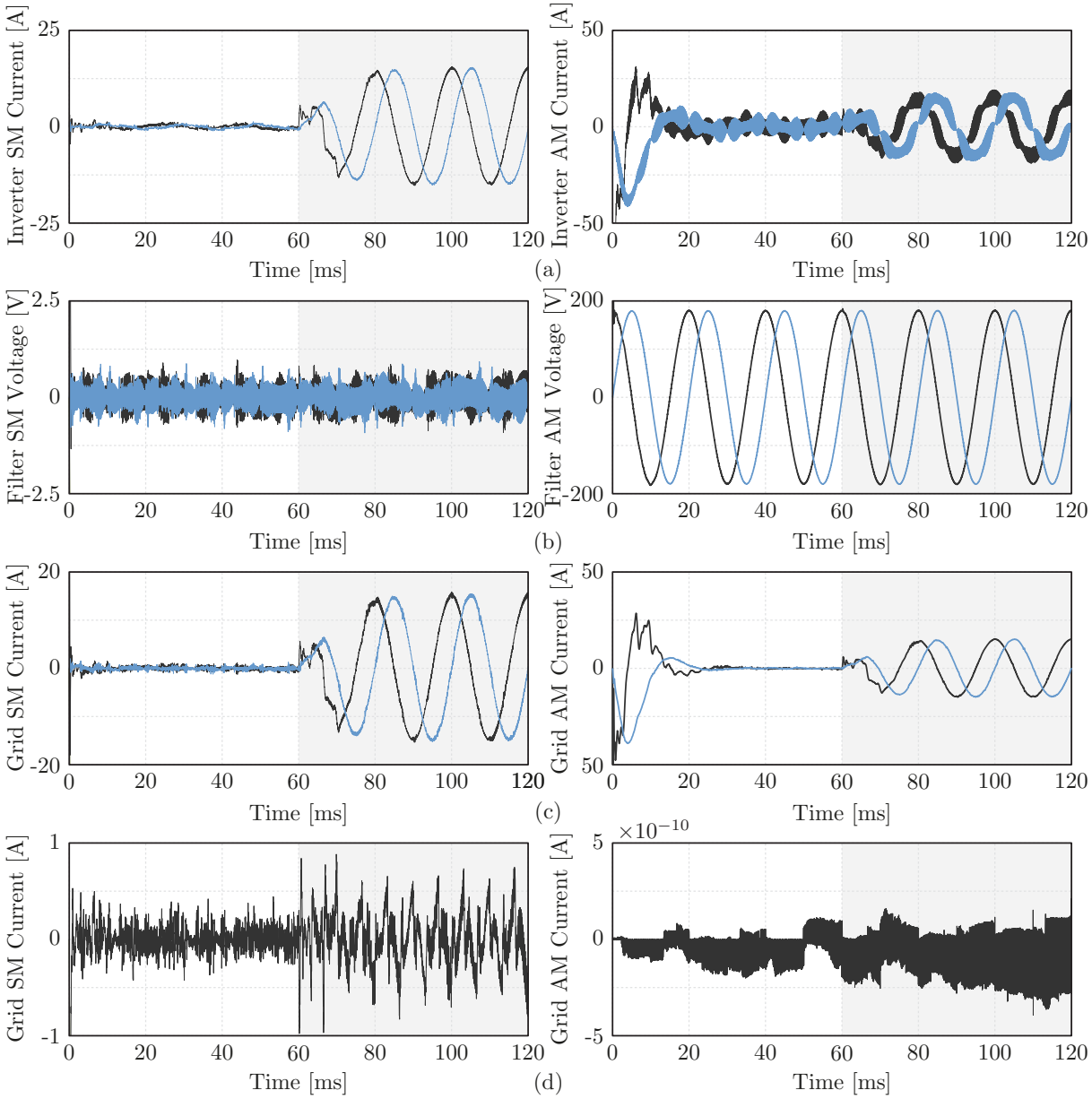

Figure 4.9 – Clarke-Lunze transformation of the states of a paralleled converter system with current state-feedback control, γ-axis current control and in-phase carriers. (a) Inverter current $\alpha\beta$ (b) Filter capacitor $\alpha\beta$ (c) Grid current $\alpha\beta$ (d) γ-axis current subtractive- and additive-mode components

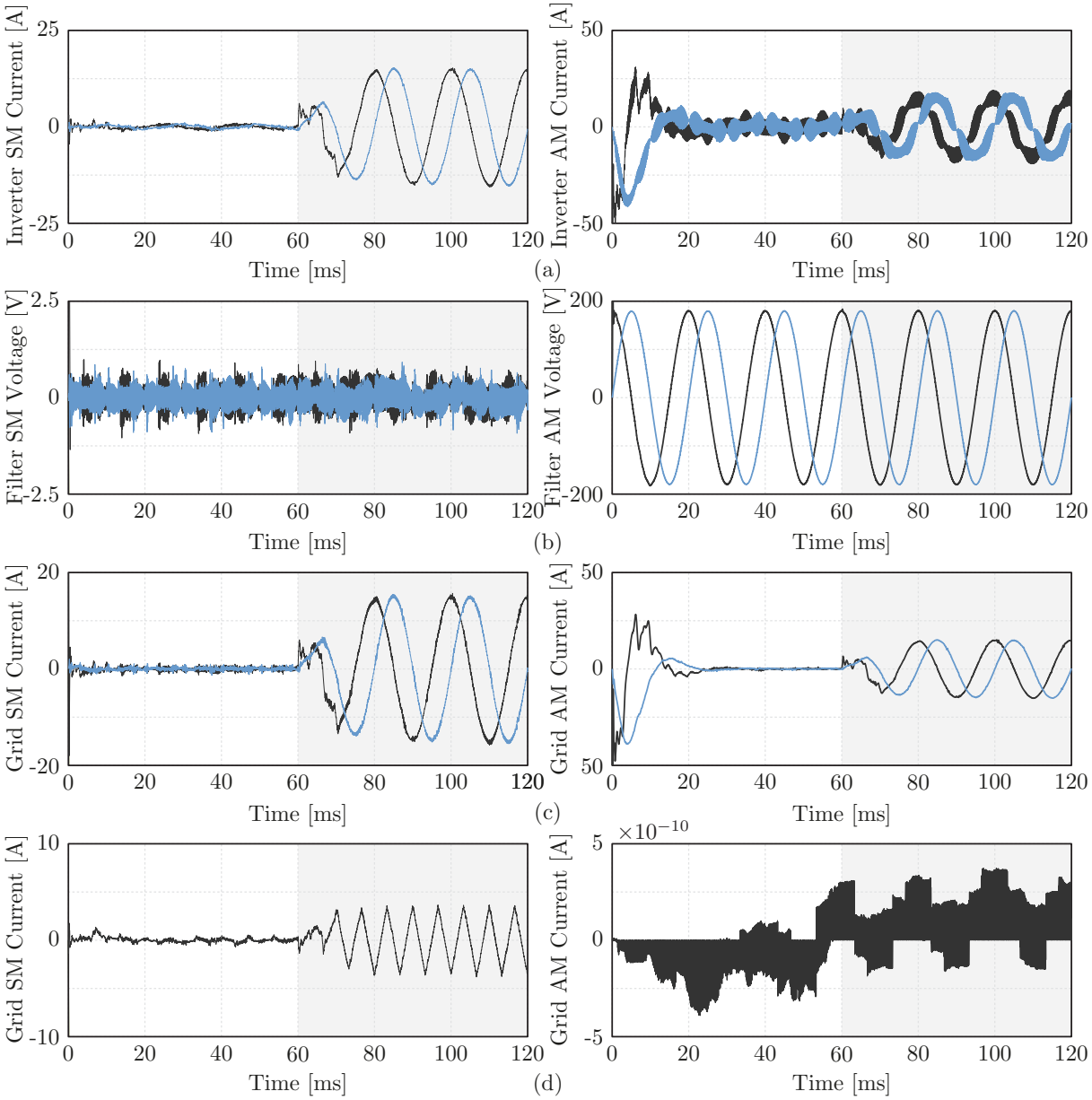

Figure 4.10 – Clarke-Lunze transformation of the states of a paralleled converter system with current state-feedback control, in-phase carriers and without the γ-axis current control. (a) Inverter current $\alpha\beta$ (b) Filter capacitor $\alpha\beta$ (c) Grid current $\alpha\beta$ (d) γ-axis current $\alpha\beta$ subtractive- and additive-mode components

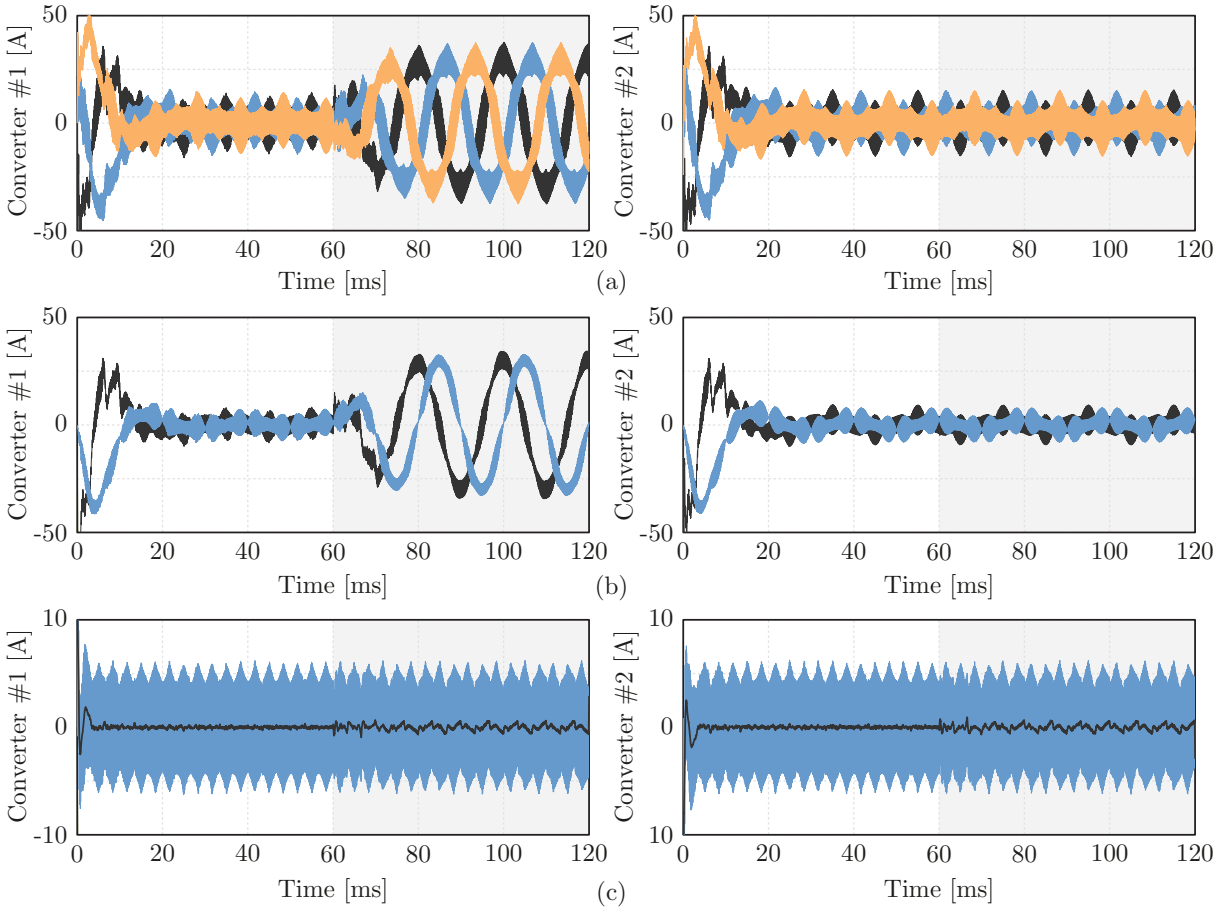

Figure 4.11 – Inverter current of a paralleled converter system with current state-feedback control and γ-axis current control with opposite-phase carriers. Converter #1 estimates the inverter current via SMO. (a) *abc* coordinates (b) $\alpha\beta$ coordinates (c) γ axis current.

4.4.2 Out-of-phase Carriers

The simulations illustrated in Figure 4.11, Figure 4.12 and Figure 4.13 presents the converter states. From this, we can infer that the SMO presented an adequate estimate of the inverter current, as illustrated in Figure 4.14 even under a noisy environment, and the state-feedback control presented a dynamic of approximately one grid cycle. However, Figure 4.15 demonstrates that in this case, the γ-axis current components have a higher amplitude at frequencies close to the switching frequency. However, the average-value of the γ-axis current is the same as the non controlled in-phase carriers.

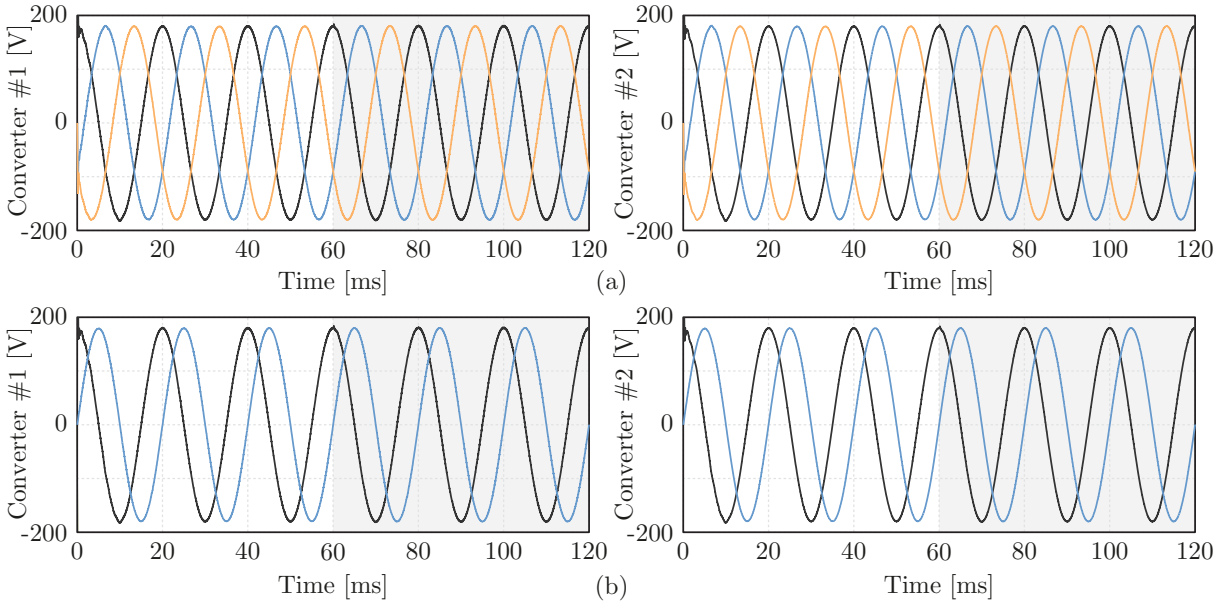

Figure 4.12 – Filter capacitor voltages of a paralleled converter system with current state-feedback control and γ-axis current control with opposite-phase carriers. Converter #1 estimates the inverter current via SMO. (a) *abc* coordinates (b) $\alpha\beta$ coordinates.

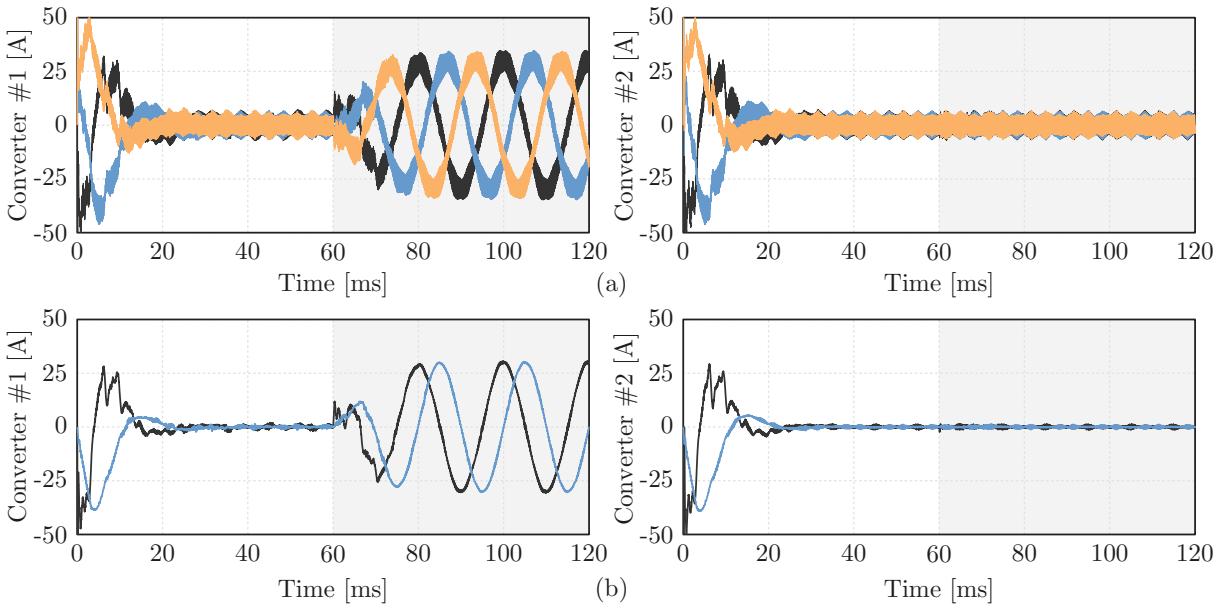

Figure 4.13 – Grid currents of a paralleled converter system with current state-feedback control and γ-axis current control with opposite-phase carriers. Converter #1 estimates the inverter current via SMO. (a) *abc* coordinates (b) $\alpha\beta$ coordinates.

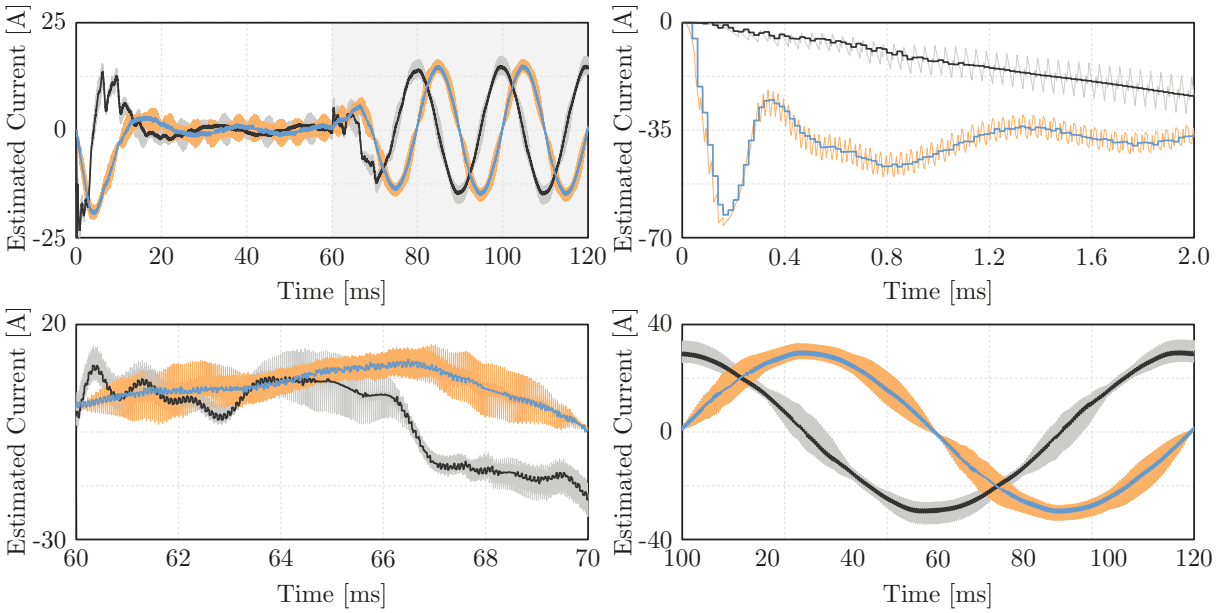

Figure 4.14 – Sliding-mode observer behaviour for the inverter current for different time-stamps with opposite-phase carriers, demonstrating the dynamic behaviour of the estimation under noisy environments.

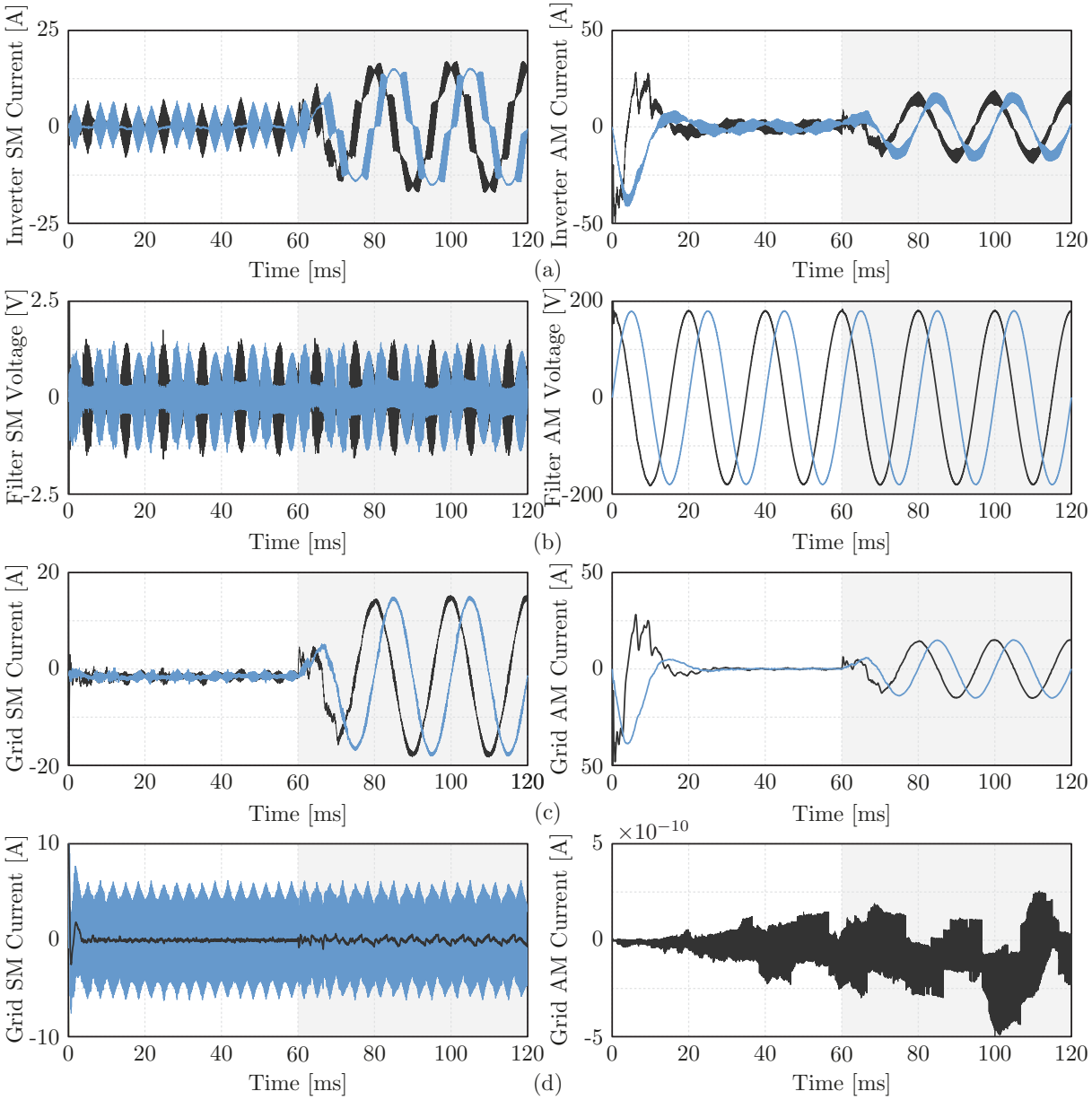

Figure 4.15 – Clarke-Lunze transformation of the states of a paralleled converter system with current state-feedback control, γ-axis current control and opposite-phase carriers. (a) Inverter current $\alpha\beta$ (b) Filter capacitor $\alpha\beta$ (c) Grid current $\alpha\beta$ (d) γ-axis current subtractive- and additive-mode components.

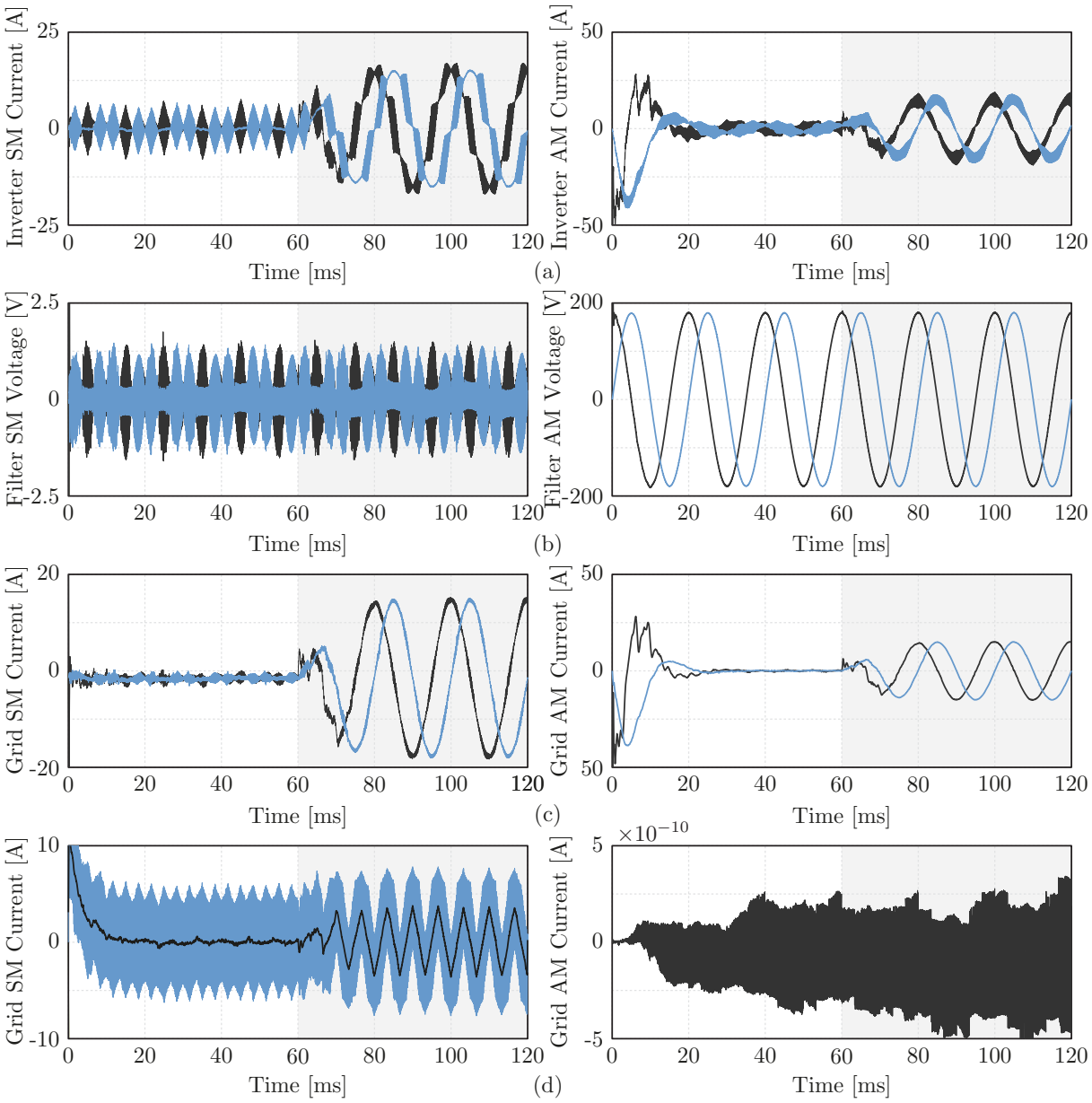

Figure 4.16 – Clarke-Lunze transformation of the states of a paralleled converter system with current state-feedback control, opposite-phase carriers and without and the γ-axis current control. (a) Inverter current $\alpha\beta$ (b) Filter capacitor $\alpha\beta$ (c) Grid current $\alpha\beta$ (d) γ-axis current subtractive- and additive-mode components.

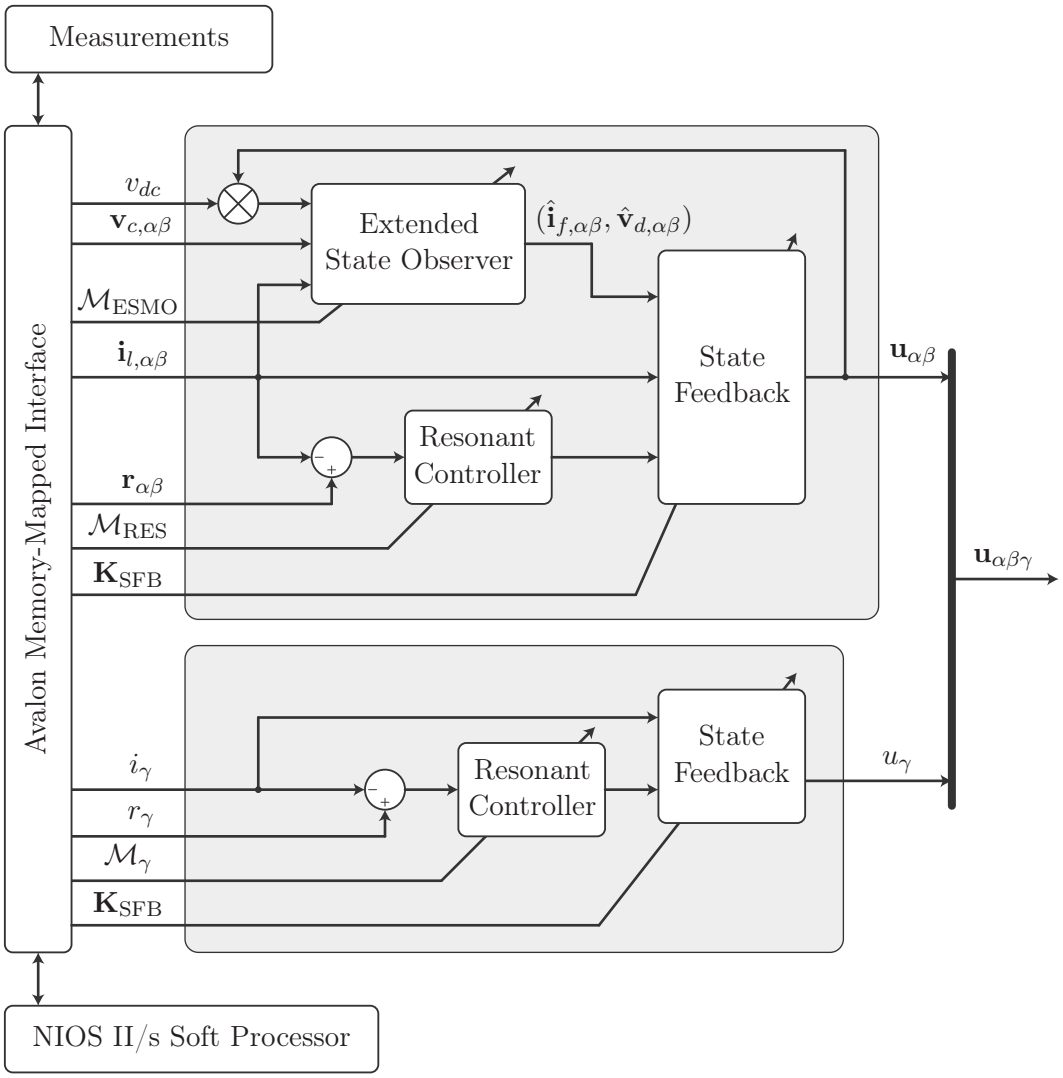

Figure 4.17 – Block diagram of the current control strategy FPGA implementation.

4.5 IMPLEMENTATION

This section aims to provide a clear explanation of the concepts utilized in the FPGA implementation of the proposed current control technique. The FPGA choice was made based on the number of operations required, improving the feasibility of the strategy implementation. The present strategy can be divided into five main structures:

- $\alpha\beta$-axis Resonant Controller;
- $\alpha\beta$-axis State-Feedback;
- $\alpha\beta$-axis Extended Sliding Mode Observer;
- γ-axis Controller;
- Microprocessor–FPGA Memory Mapped Interface.

A block diagram illustrating the implementation of the proposed strategy is shown in Figure 4.17. To configure the resonant controllers, state observers, and feedback gains, a NIOS II/s soft-processor was implemented.

The integration of the NIOS II/s soft-processor provides convenient and flexible control parameter adjustments, significantly enhancing the overall flexibility of the current control technique. This capability extends beyond the current control itself and allows for the implementation of supervisory control loops, such as Phase-Locked Loops and dc Bus voltage control. These supervisory control loops typically do not have strict real-time constraints compared to the current control, and therefore can be effectively implemented using the soft-processor. This further contributes to the versatility and adaptability of the overall control system.

To optimize the utilization of resources, a single structure was adopted for both the α and β axes in the current control implementation. This was achieved by multiplexing the input of the algorithm, which is selected based on a flag generated within the algorithm's behavior.

The upcoming subsections will provide a detailed explanation of the implementation process of the $\alpha\beta$-axis control, shedding light on various aspects of the strategy and its implementation. Details concerning the γ-axis implementation are further discussed in Chapter 6.

4.5.1 $\alpha\beta$-Axis Resonant Controller and State Feedback

In the $\alpha\beta$-axis controller strategy, a Finite State-Machine (FSM) consisting of five states was implemented to manage the sequential behavior of the algorithm. The states in the FSM are as follows:

- st.Idle: In this state, the controller waits for an interruption signal from the main Finite-State Machine;
- st.Load: This state is responsible for loading the controller matrix constants registers with the values stored in the Avalon Memory-Mapped Interface. Additionally, it loads the input register with the error signal from either the α or β axis, based on the chosen configuration.
- st.Calc: The FSM transitions to this state to execute the multiply and accumulate algorithm for the selected axis, determined by a specific flag.
- st.Updt: Once the calculation is completed, the FSM moves to this state. Here, it updates the stored state-vector with the output from the previous state. It then returns to st.Load state and increments the flag, either setting the algorithm for β calculation or transitioning to st.Wait if the flag was previously set.
- st.Wait: In this state, the FSM waits for the deassertion of the start signal.

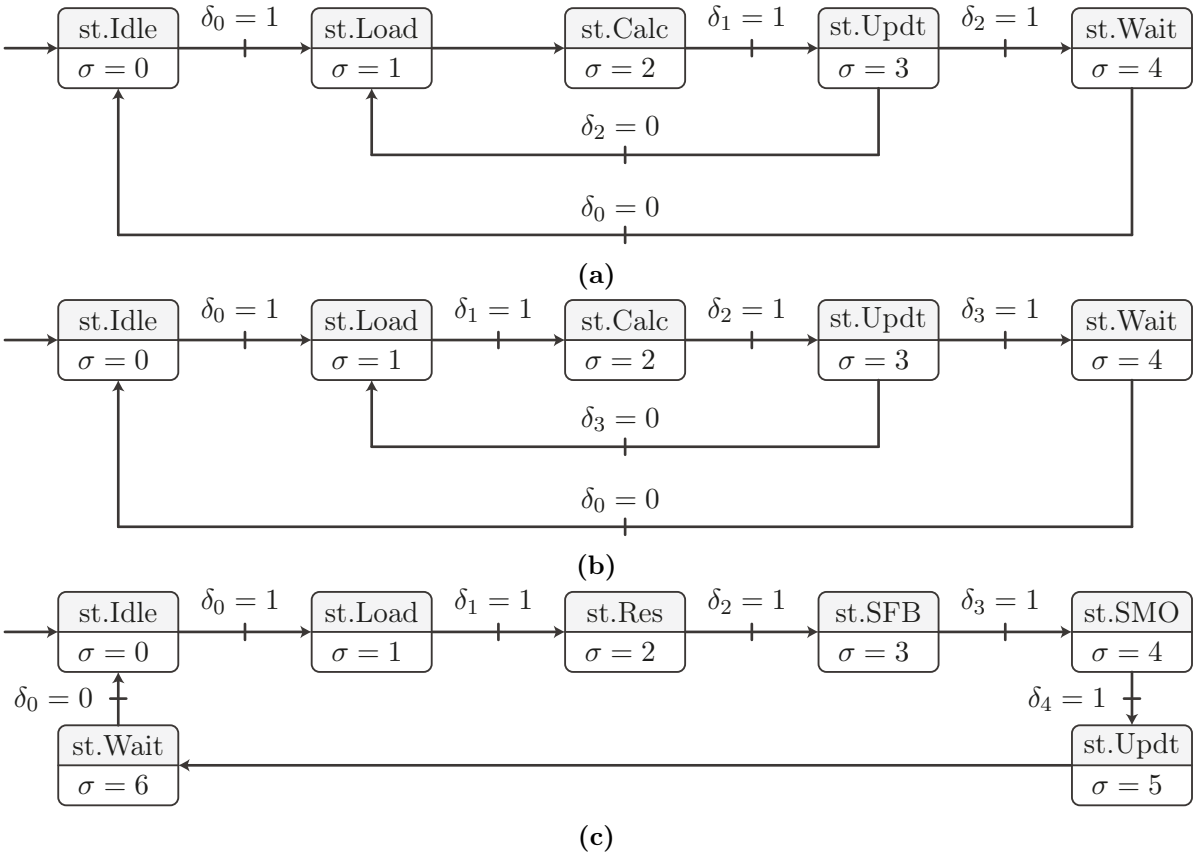

Figure 4.18 – Finite State Machines of the current control strategy, where δ are the inputs related to the end of execution of each algorithm and σ are the outputs in one-hot encoding. (a) $\alpha\beta$-axis Resonant Controller and State Feedback (b) $\alpha\beta$-axis Extended Sliding Mode Observer (c) Control Algorithm.

The FSM behaviour is depicted in Figure 4.18.a, where δ_0 is the start signal, δ_1 is the multiplication and accumulation algorithm end flag, δ_2 is the $\alpha\beta$-axis selection flag, which is incremented in the st.Updt state, and σ is the FSM output signal in one-hot encoding.

The Finite State Machine for the State Feedback component of the FPGA implementation is identical to the resonant controller FSM. The main difference lies in the multiply and accumulate algorithm, as the state gain matrix has only one row for a single axis.

4.5.2 $\alpha\beta$-Axis Extended Sliding Mode Observer

The structure of the $\alpha\beta$-axis Extended Sliding Mode Observer (ESMO) in the FPGA implementation closely resembles the Resonant Controller and State Feedback FSMs. However, there are some alterations in the st.Load state to accommodate the specific requirements of the ESMO.

In the ESMO, a single Look-Up Table (LUT) is implemented to calculate the $\tanh(\cdot)$ function. The input to the LUT is multiplexed based on the state of the control signal σ, which controls the enable signal of the LUT. This allows for the calculation of the nonlinear function of the error signal.

After the error signal is processed by the LUT, the FSM waits for the completion of the calculation of the nonlinear function. Once the calculation is finished, the resulting value serves as an input to the control algorithm described in Equation (4.77). This structure enables the FPGA implementation to incorporate the $\alpha\beta$-axis ESMO, which enhances the estimation of system states based on the error signal and the calculated nonlinear function. A detailed block diagram of the FSM is shown in Figure 4.18.b.

4.5.3 Microprocessor–FPGA Memory Mapped Interface

The Memory-Mapped Interface plays a crucial role in the current control FPGA implementation. It serves as the main entity responsible for communication and data transfer between different processor and entities within the system.

The interface consists of several components, including four read-only interfaces, one write-only and one read-write interface. The read-only interfaces are dedicated to accessing the $\alpha\beta$ controller constants, state feedback gains, the Extended Sliding-Mode Observer constants, and the γ controller and state-feedback constants and gains. The write-only interface is responsible for the measurement data such as currents and voltages, allow the microprocessor to retrieve the necessary parameters and information required for supervisory control algorithms.

Additionally, the read-write interface was specifically designed for converter configuration. This interface enables the FPGA to receive configuration commands and settings that control the behavior and operation of the power converter, such as open- and closed-loop operations, enable and disable of the PWM pulses, and configurations related to the carrier synchronization strategies discussed in Chapter 6.

The block diagram control strategy is illustrated in Figure 4.18.c. Note that the FSM receives the δ signals such as the start signal from the PWM modulator (δ_0), the end of ADC acquisition flag (δ_1), and flags associated with specific control algorithms, including the resonant converter algorithm (δ_2), the state-feedback algorithm (δ_3), and the Extended Sliding-Mode Observer (ESMO) algorithm (δ_4). The signal σ is responsible for initiating each of the algorithms mentioned earlier.

The resource utilization for the implementation in a Cyclone V 5CSEMA4U23C6 FPGA is presented in the Analysis and Synthesis compilation report, as shown in Table 4.2. It is important to note that these values were obtained from the final compilation report for two control strategies implemented in the same FPGA, and the optimization was set to Performance.

Table 4.2 – Resource Utilization by Entity after Analysis and Synthesis: Current Control Strategy and NIOS II/s Processor.

Hierarchy Node	Comb. ALUTs	Dedicated Regs.	Block Memory Bits	DSP Blocks
Meas. Interface	39	156	0	1
$\alpha\beta$ Res. Ctrl.	989	1803	0	9
$\alpha\beta$ State Fb.	590	121	0	1
$\alpha\beta$ ESMO	668	641	0	1
Sigmoid LUT	66	13	90112	0
γ Ctrl.	240	174	0	2
Others	543	4247	0	0

Table 4.3 – Converter Parameters for Hardware-in-the-Loop Validation

Parameter	**Symbol**	**Value**
dc Bus Voltage	U_{dc}	800 V
Switching Frequency	f_s	36 kHz
dc Bus Capacitance	C_{dc}	2 μF
Inverter Inductance	L_f	300 μH
Inverter Inductor Resistance	r_f	15 mΩ
Filter Capacitance	C_c	12 μF
Filter Capacitor Resistance	r_c	100 $\mu\Omega$
Filter Damped Capacitance	C_d	12 μF
Filter Damped Capacitor Resistance	r_d	2 Ω
Line Inductance	L_l	1 μH
Line Inductor Resistance	r_l	30 mΩ
Grid Inductance	L_w	11.25 mH
Grid Inductor Resistance	r_w	500 mΩ
Grid Short Circuit Ratio	SCR	approx. 1.5 (20 MVA, 380 V)

4.6 EXPERIMENTAL RESULTS

This section presents the experimental results from the implementation of the proposed current control technique. These results provide insights into the performance and effectiveness of the control strategy under real-world operating conditions. The system constants were chosen according to Table 4.3, with state-feedback gains for the $\alpha\beta$-axis controller given by Table 4.4, state-feedback for the γ-axis controller given by Table 4.5, dc voltage controller parameters given by Table 4.6 and ac voltag controller parameters given by Table 4.7. For more details with respect to the dc and ac bus voltage control strategy refer to Chapter 5.

The Extended Sliding Mode observer system was obtained from the real system by

Table 4.4 – $\alpha\beta$ Controller Parameters for Hardware-in-the-Loop Validation

Parameter	**Symbol**	**Value**
Inverter Current Feedback Gain	$k_{x,1}$	-0.006419181823730
Capacitor Voltage Feedback Gain	$k_{x,2}$	-0.000748634338379
Damped Capacitor Voltage Feedback Gain	$k_{x,3}$	-0.000424385070801
Line Current Feedback Gain	$k_{x,4}$	-0.017139434814453
Control Output Feedback Gain	k_u	-0.109508514404297
Resonant Controller Gains	$k_{r,1,1}$	0.000125885009766
	$k_{r,1,2}$	0.012179374694824
	$k_{r,5,1}$	-0.001226425170898
	$k_{r,5,2}$	0.006189346313477
	$k_{r,7,1}$	0.000177383422852
	$k_{r,7,2}$	0.004310607910156
	$k_{r,11,1}$	-0.000677108764648
	$k_{r,11,2}$	0.002379417419434
	$k_{r,13,1}$	-0.000164031982422
	$k_{r,13,2}$	0.001978874206543
	$k_{r,17,1}$	-0.000482559204102
	$k_{r,17,2}$	0.001257896423340
	$k_{r,19,1}$	-0.000210762023926
	$k_{r,19,2}$	0.001111984252930

Table 4.5 – γ Controller Parameters for Hardware-in-the-Loop Validation

Parameter	**Symbol**	**Value**
Inverter Current Feedback Gain	$k_{\gamma,x,1}$	-0.000900268554688
Control Output Feedback Gain	$k_{\gamma,x,2}$	-0.048919677734375
Resonant Controller Frequency (Sync.)	$\omega_{\gamma,r}$	200 Hz
Resonant Controller Damping	$\xi_{\gamma,r}$	10^{-3}
Resonant Controller Gains	$k_{\gamma,r,1}$	0
	$k_{\gamma,r,2}$	0.001373291015625

Table 4.6 – dc Bus Controller Parameters for Hardware-in-the-Loop Validation

Parameter	**Symbol**	**Value**
Proportional Gain	$k_{p,dc}$	-48
Integral Gain	$k_{i,dc}$	-405
Feedforward Ratio	$\eta_{p,dc}$	0.9

performing the Euler discretization method, so that

$$\exp\left(\mathbf{A}h\right) \approx \mathbf{I} + \mathbf{A}h, \tag{4.78}$$

Table 4.7 – ac Bus Controller Parameters for Hardware-in-the-Loop Validation

Parameter	**Symbol**	**Value**
Proportional Gain	$k_{p,q}$	20
Integral Gain	$k_{p,q}$	100
RDFT Length	N_{DFT}	1440
MAF Length	N_{MAF}	1440

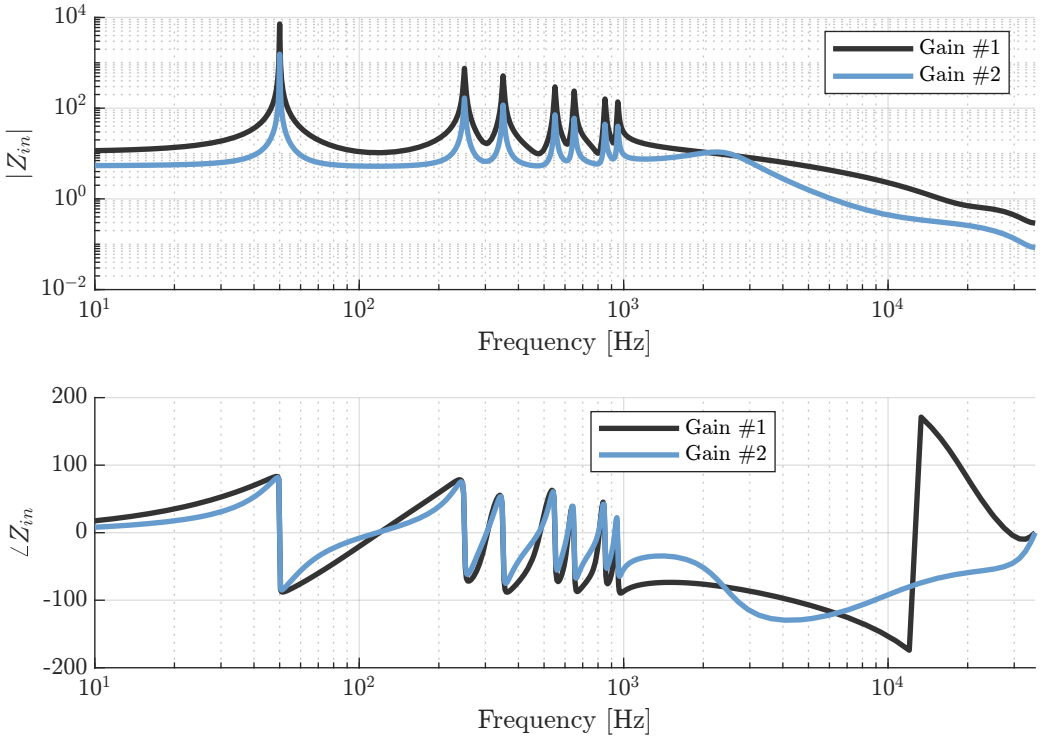

Figure 4.19 – Bode Diagram of the converter input impedance.

and the grid impedance was chosen as

$$Z_{w,\text{ESMO}} := \frac{1}{2} Z_w \tag{4.79}$$

with the objective of inserting a modeling error to be compensated by the disturbance observer.

The controller gains were obtained through the input impedance shaping algorithm for the first two resonances with preliminary gains calculated via an $\mathcal{H}_\infty/\mathcal{D}$ control. The Figure 4.19 shows a bode diagram of the input impedance for both calculated gains. The set of gains #2 was chosen for this chapter.

The Figure 4.20 shows the operation of the paralleled-connected converters sharing the same dc-bus, with an overview of the test presented in Figure 4.20.a. The following figures show details with respect to each disturbance and the system subsequent response.

The test was performed employing an OPAL-RT 5700 hardware-in-the-loop to emulate the power converters, with the control strategy implemented in a FPGA connected

to the OPAL RT digital I/Os. The measurements were internally modulated to the OPAL-RT using a resolution of a signed 16-bit number, with a full scale of 64 A for current measurements and 1024 V for voltage measurements. The communication between the OPAL-RT and the FPGA consisted of a 24-Channel Serial Peripheral Interface (SPI).

The time constants were scaled by a factor of 100, which enabled an accurate representation of the switched characteristic of power converters. The circuit was emulated employing the eHS Power Electronics Toolbox with a time-step of 1 μs, resulting in an effective time-step of 10 ns, coinciding with the clock period of the FPGA. This enabled the minimization of noise due to quantization of the PWM modulator while mitigating aliasing occuring in large simulation, as well as the numerical transients generated by the Pejovic model [68].

The Extended Sliding-Mode Observer variables were obtained direclty from the Nios II JTAG/UART interface with a sampling frequency of 72 Hz, resulting in an effective sampling frequency of 7.2 kHz. Aliasing was observed in some variables due to the switched characteristic of the estimator variables, especially in the Disturbance Observer state variable which demonstrates a higher gain.

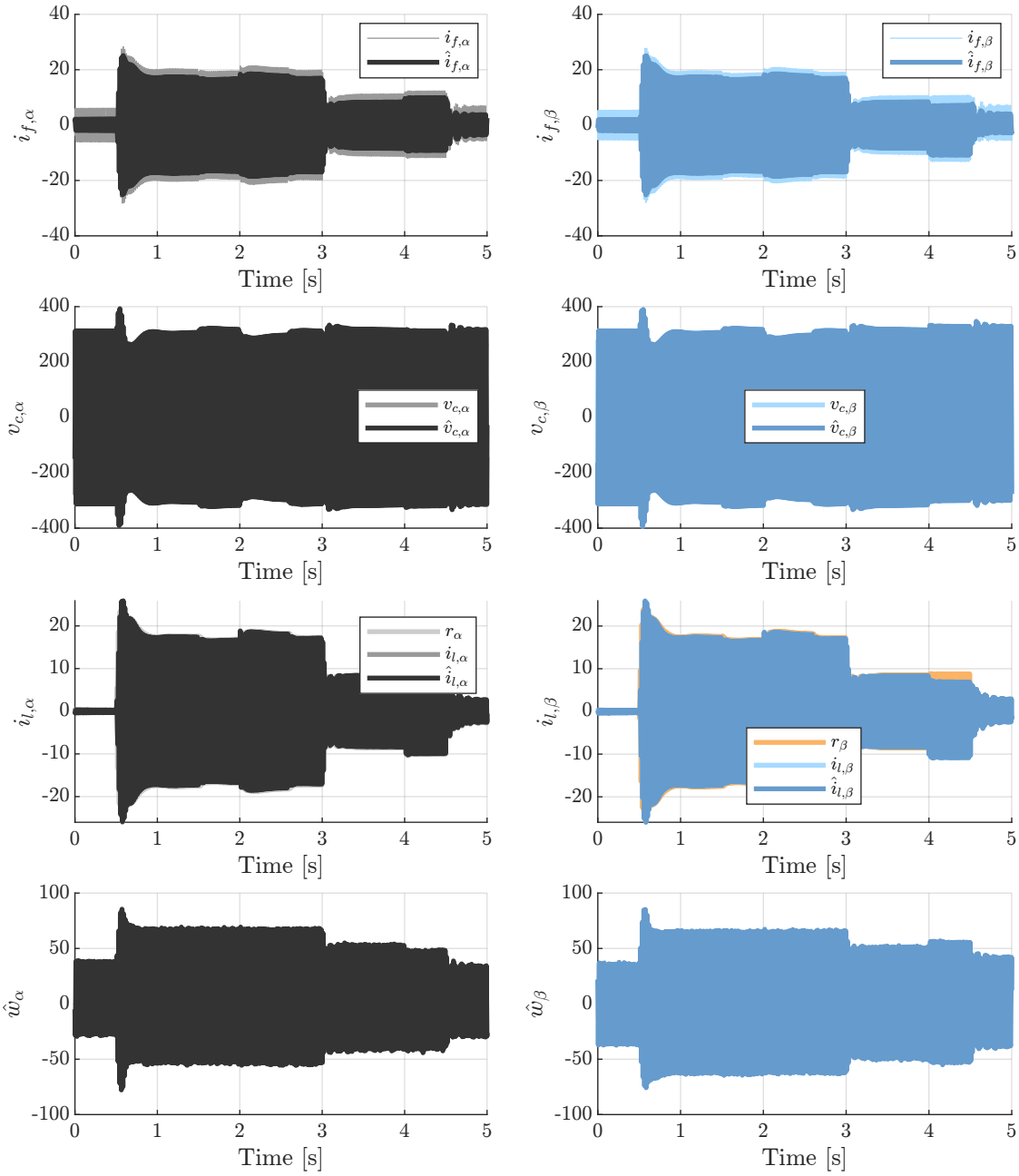

(a) Validation overview.

Figure 4.20 – FPGA-based implementation of the Resonant Controller State-Feedback with Extended Sliding-Mode Observer hardware-in-the-loop validation. The hardware-in-the-loop implementation downscaled the time-constants by a factor of 100, as means of accurately representing the switched characteristic of power converters.

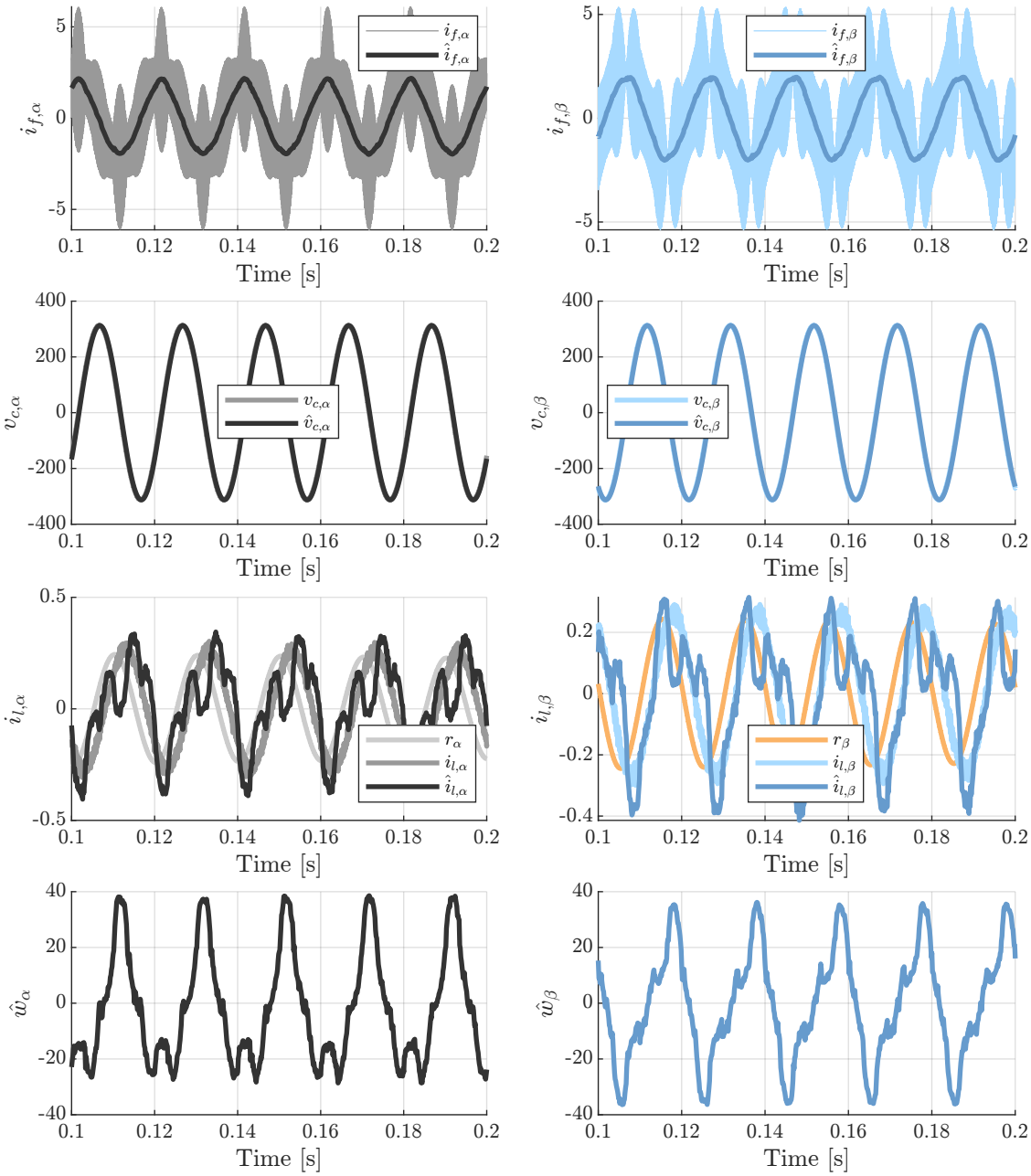

(b) No dc bus power injection.

Figure 4.20 – FPGA-based implementation of the Resonant Controller State-Feedback with Extended Sliding-Mode Observer hardware-in-the-loop validation. The hardware-in-the-loop implementation downscaled the time-constants by a factor of 100, as means of accurately representing the switched characteristic of power converters.

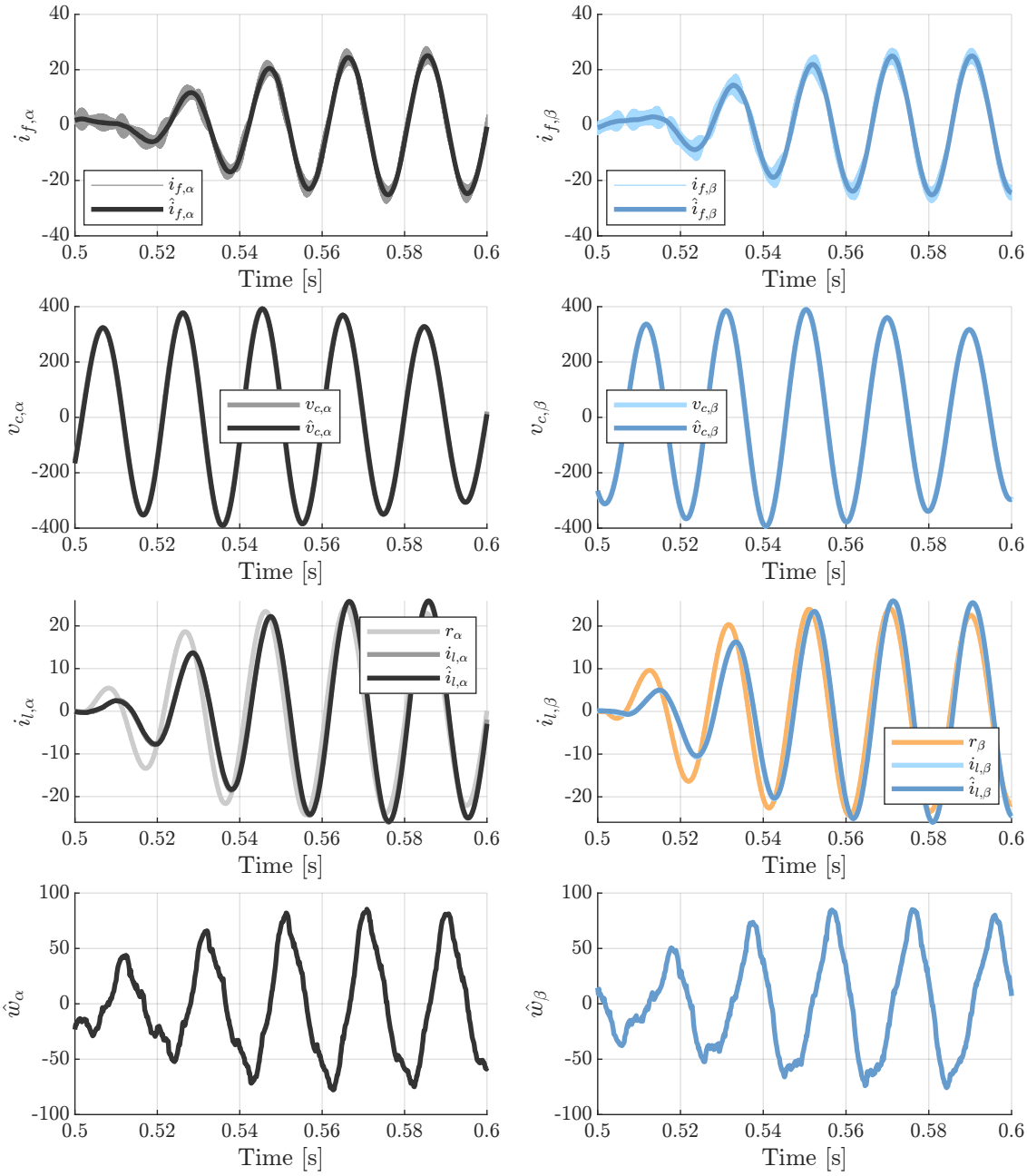

(c) 16 kW power step.

Figure 4.20 – FPGA-based implementation of the Resonant Controller State-Feedback with Extended Sliding-Mode Observer hardware-in-the-loop validation. The hardware-in-the-loop implementation downscaled the time-constants by a factor of 100, as means of accurately representing the switched characteristic of power converters.

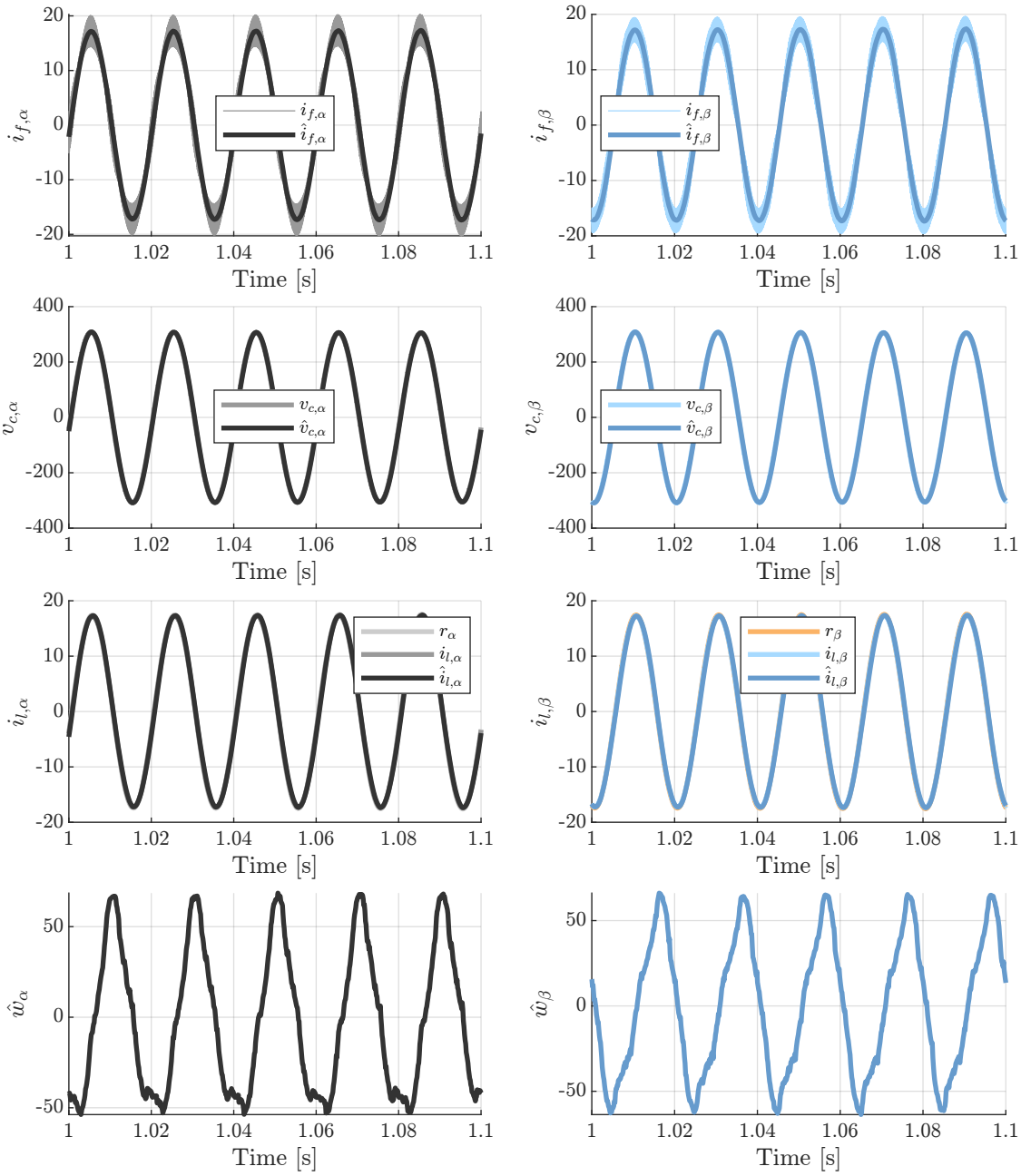

(d) 16 kW dc bus power injection.

Figure 4.20 – FPGA-based implementation of the Resonant Controller State-Feedback with Extended Sliding-Mode Observer hardware-in-the-loop validation. The hardware-in-the-loop implementation downscaled the time-constants by a factor of 100, as means of accurately representing the switched characteristic of power converters.

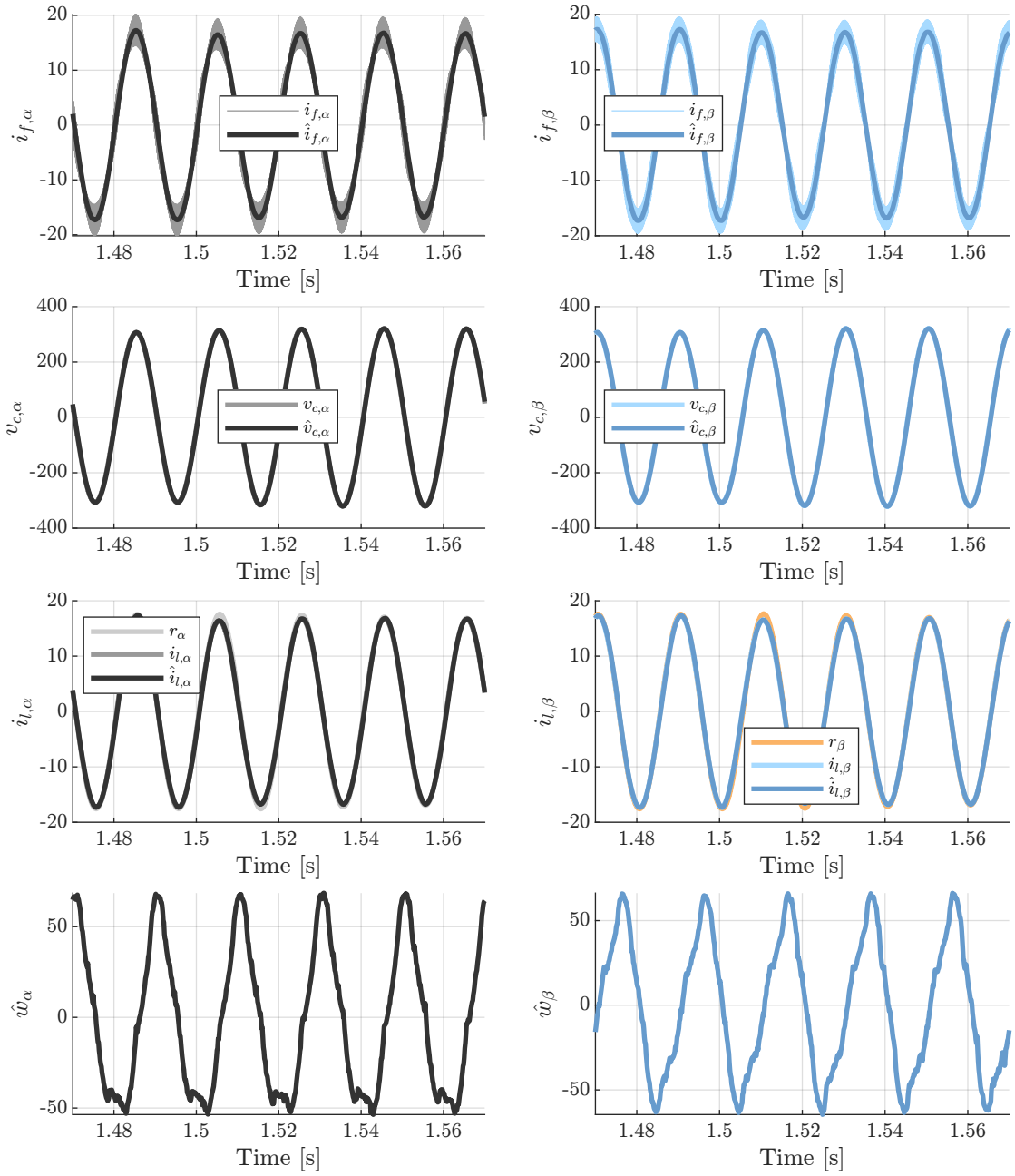

(e) Grid voltage step from 1 p.u. to 1.05 p.u.

Figure 4.20 – FPGA-based implementation of the Resonant Controller State-Feedback with Extended Sliding-Mode Observer hardware-in-the-loop validation. The hardware-in-the-loop implementation downscaled the time-constants by a factor of 100, as means of accurately representing the switched characteristic of power converters.

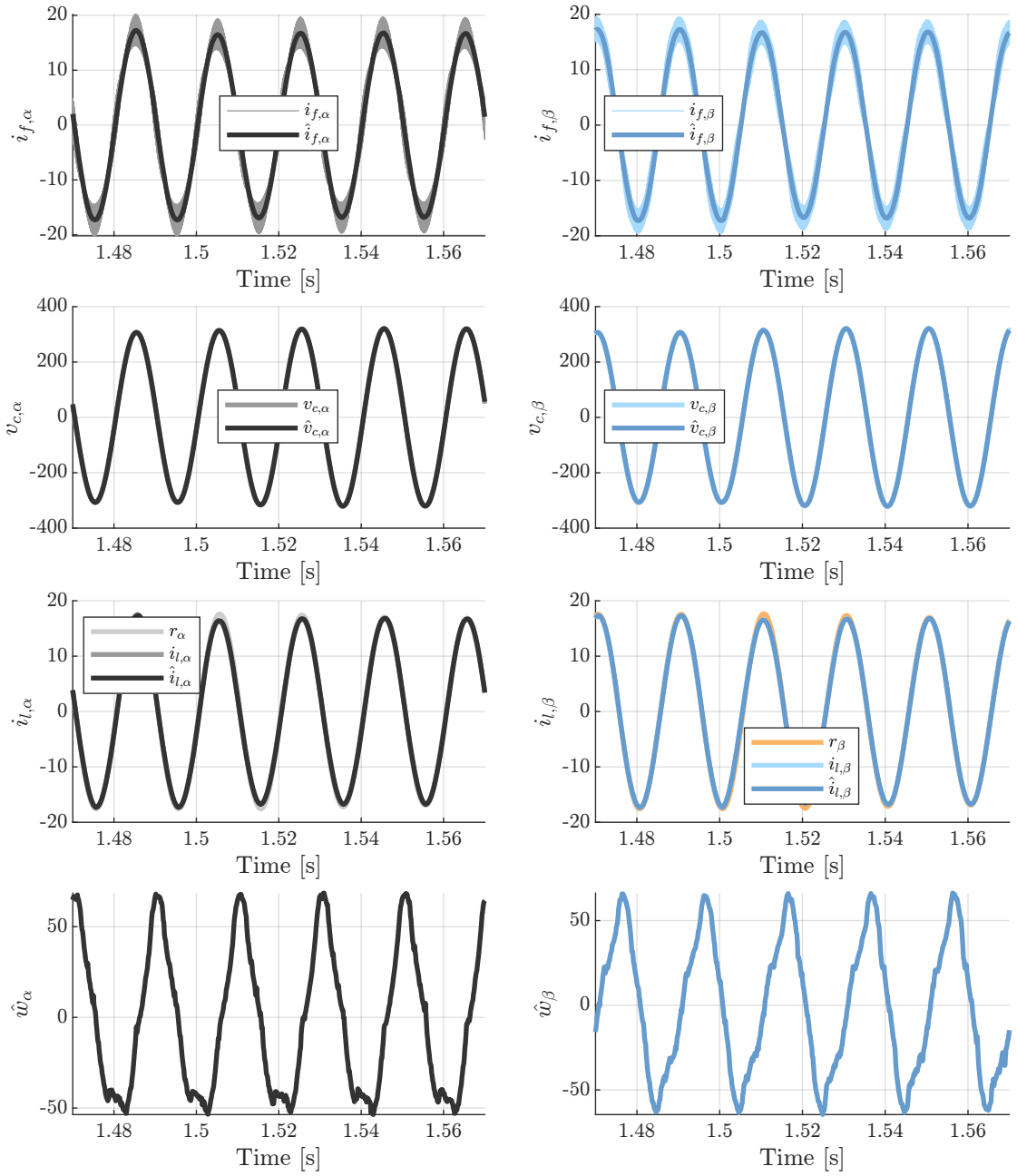

(f) Grid voltage step from 1.05 p.u. to 0.95 p.u.

Figure 4.20 – FPGA-based implementation of the Resonant Controller State-Feedback with Extended Sliding-Mode Observer hardware-in-the-loop validation. The hardware-in-the-loop implementation downscaled the time-constants by a factor of 100, as means of accurately representing the switched characteristic of power converters.

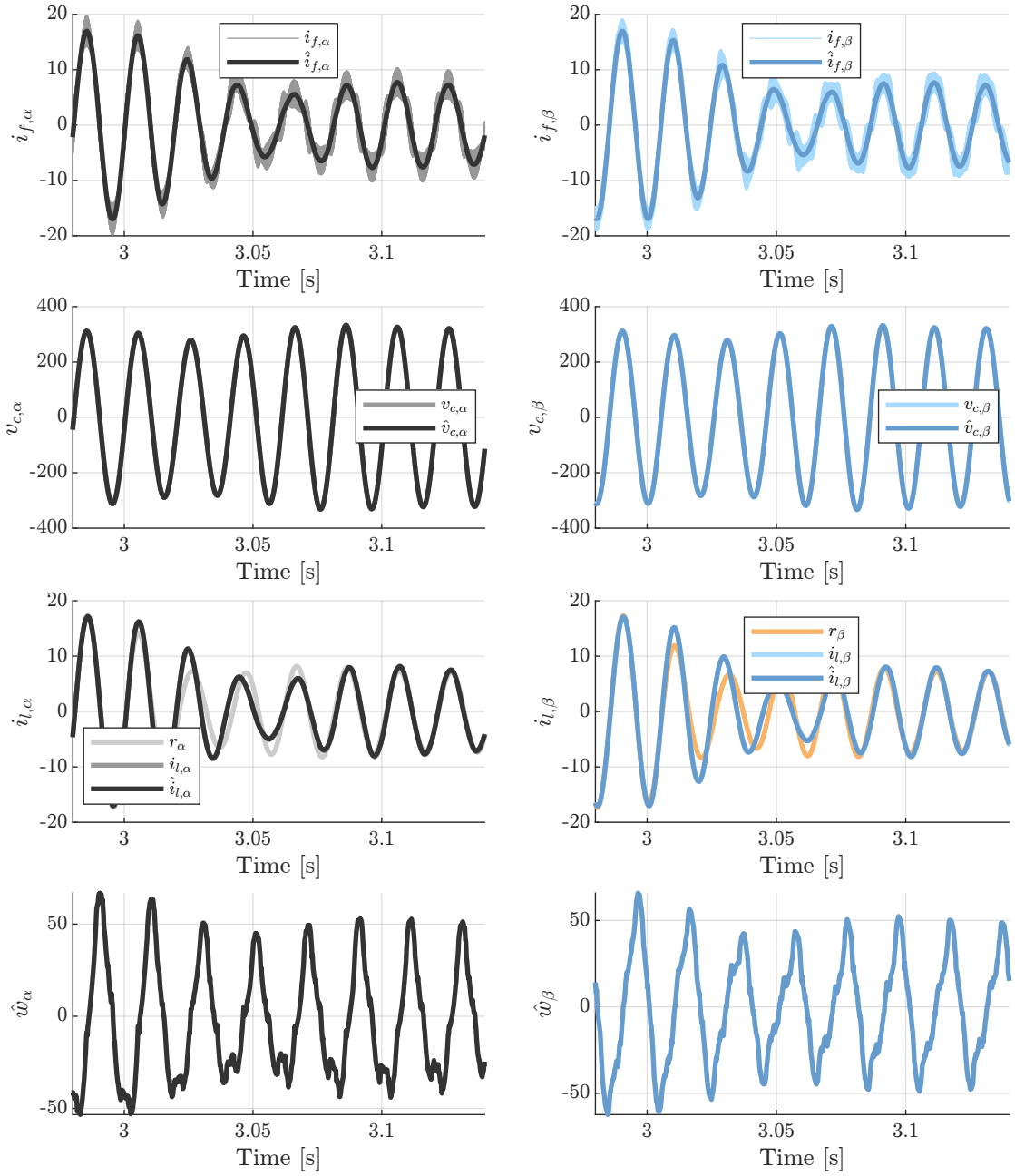

(g) Power step from 16 kW to 8 kW.

Figure 4.20 – FPGA-based implementation of the Resonant Controller State-Feedback with Extended Sliding-Mode Observer hardware-in-the-loop validation. The hardware-in-the-loop implementation downscaled the time-constants by a factor of 100, as means of accurately representing the switched characteristic of power converters.

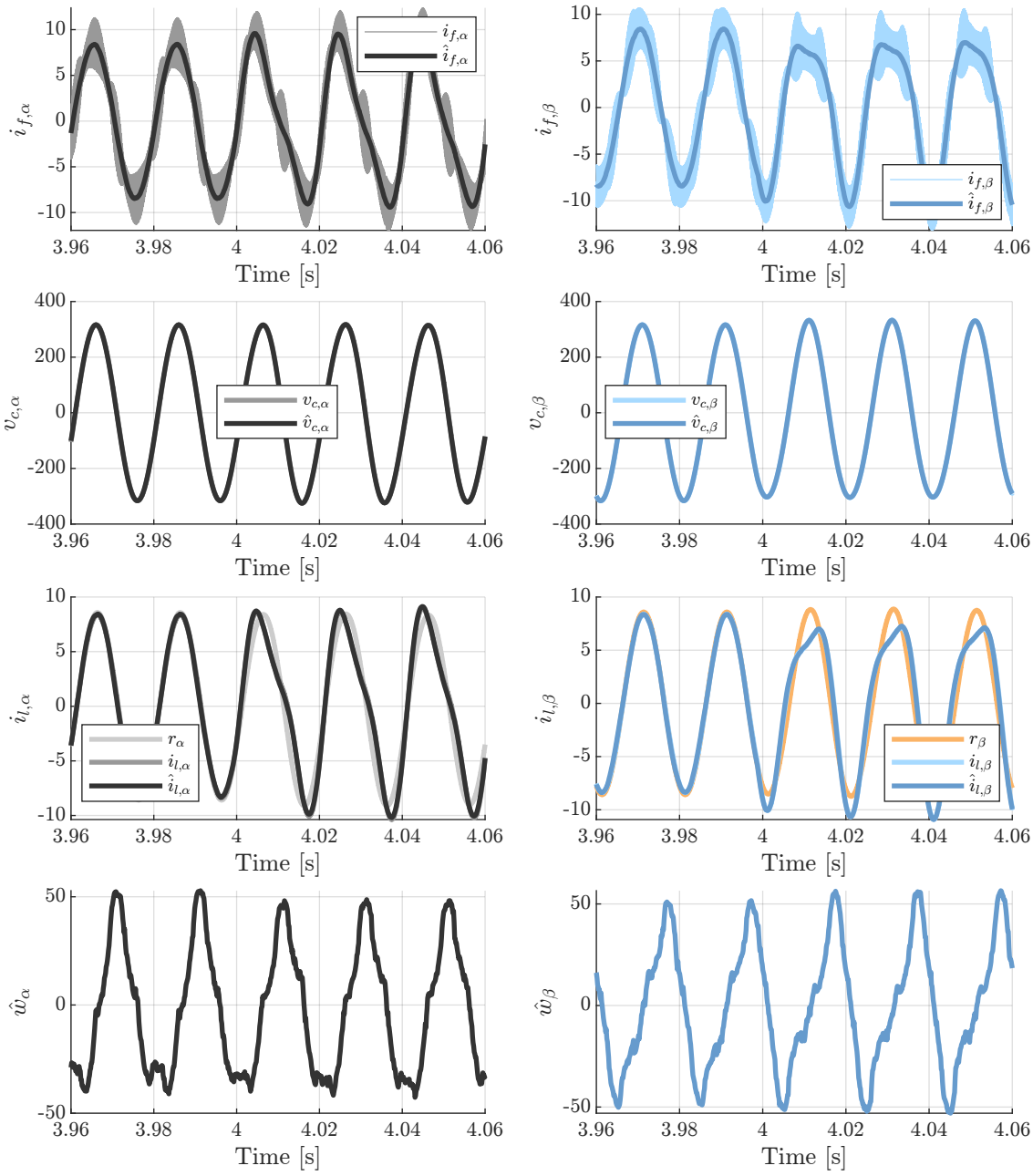

(h) 8 kW operation with 2nd harmonic injection step with 0.1 p.u. amplitude.

Figure 4.20 – FPGA-based implementation of the Resonant Controller State-Feedback with Extended Sliding-Mode Observer hardware-in-the-loop validation. The hardware-in-the-loop implementation downscaled the time-constants by a factor of 100, as means of accurately representing the switched characteristic of power converters.

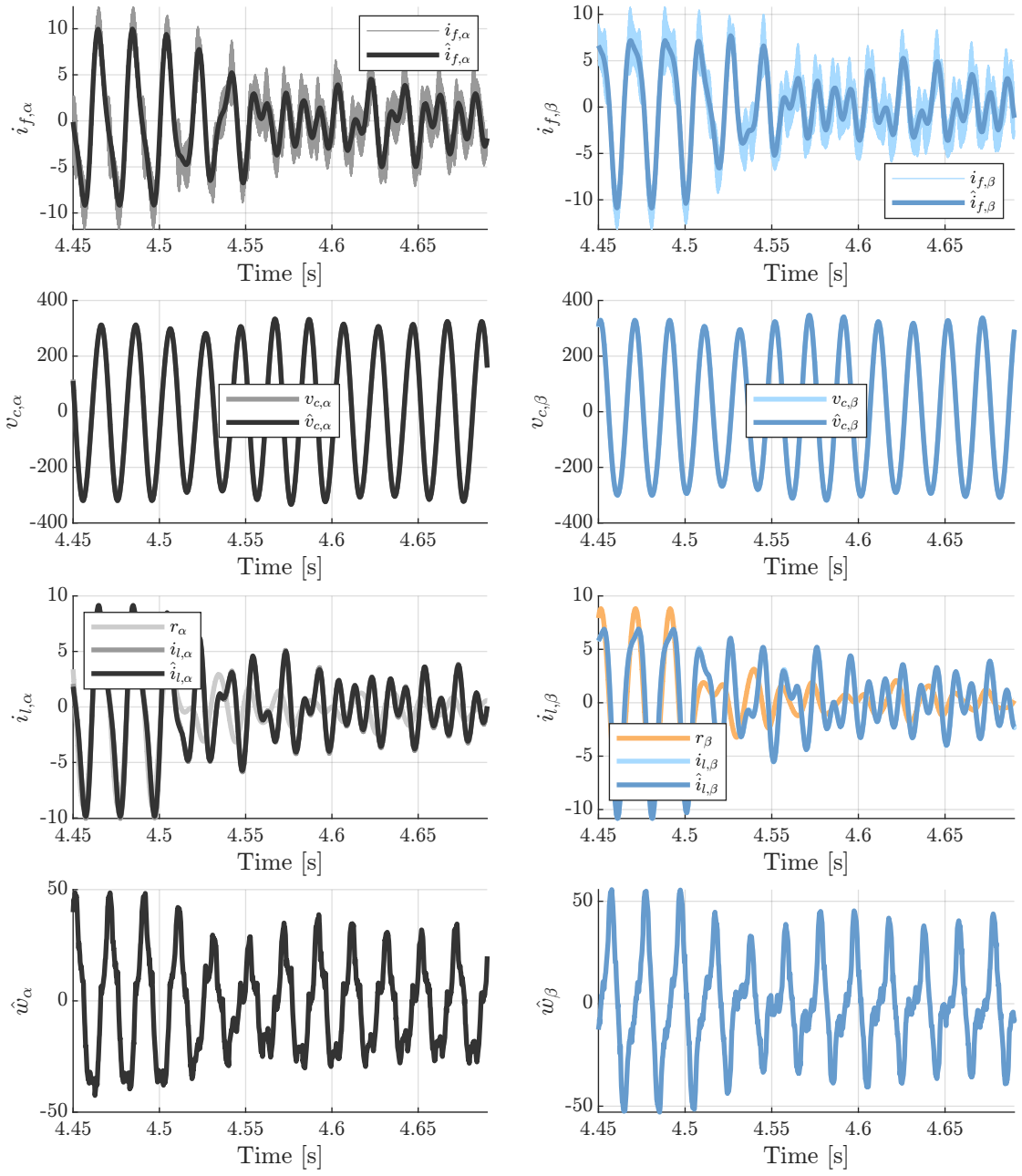

(i) Power step from 8 kW to 0 W with 2$^{\text{nd}}$ harmonic injection with 0.1 p.u. amplitude.

Figure 4.20 – FPGA-based implementation of the Resonant Controller State-Feedback with Extended Sliding-Mode Observer hardware-in-the-loop validation. The hardware-in-the-loop implementation downscaled the time-constants by a factor of 100, as means of accurately representing the switched characteristic of power converters.

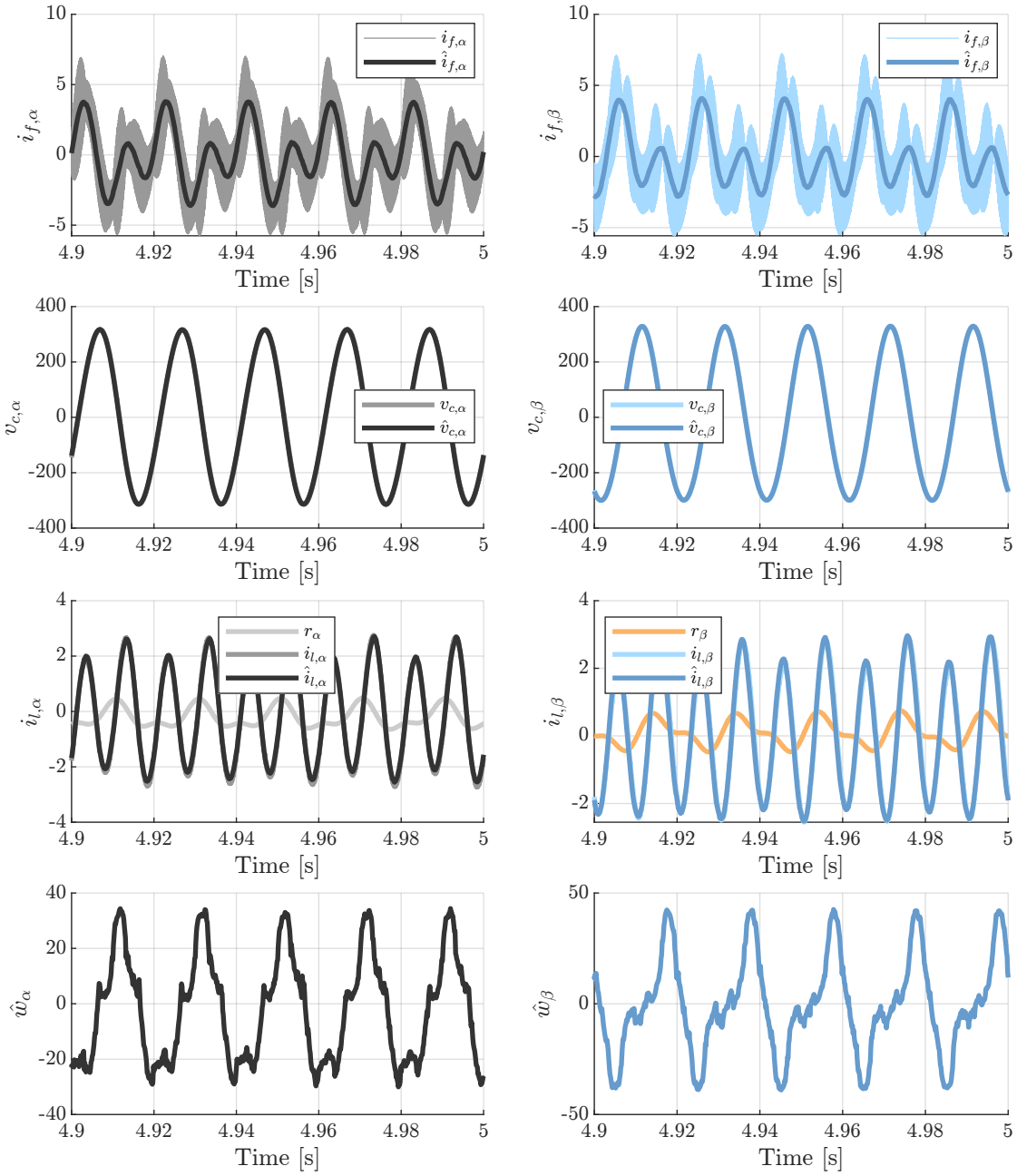

(j) 2nd harmonic injection with 0.1 p.u. amplitude.

Figure 4.20 – FPGA-based implementation of the Resonant Controller State-Feedback with Extended Sliding-Mode Observer hardware-in-the-loop validation. The hardware-in-the-loop implementation downscaled the time-constants by a factor of 100, as means of accurately representing the switched characteristic of power converters.

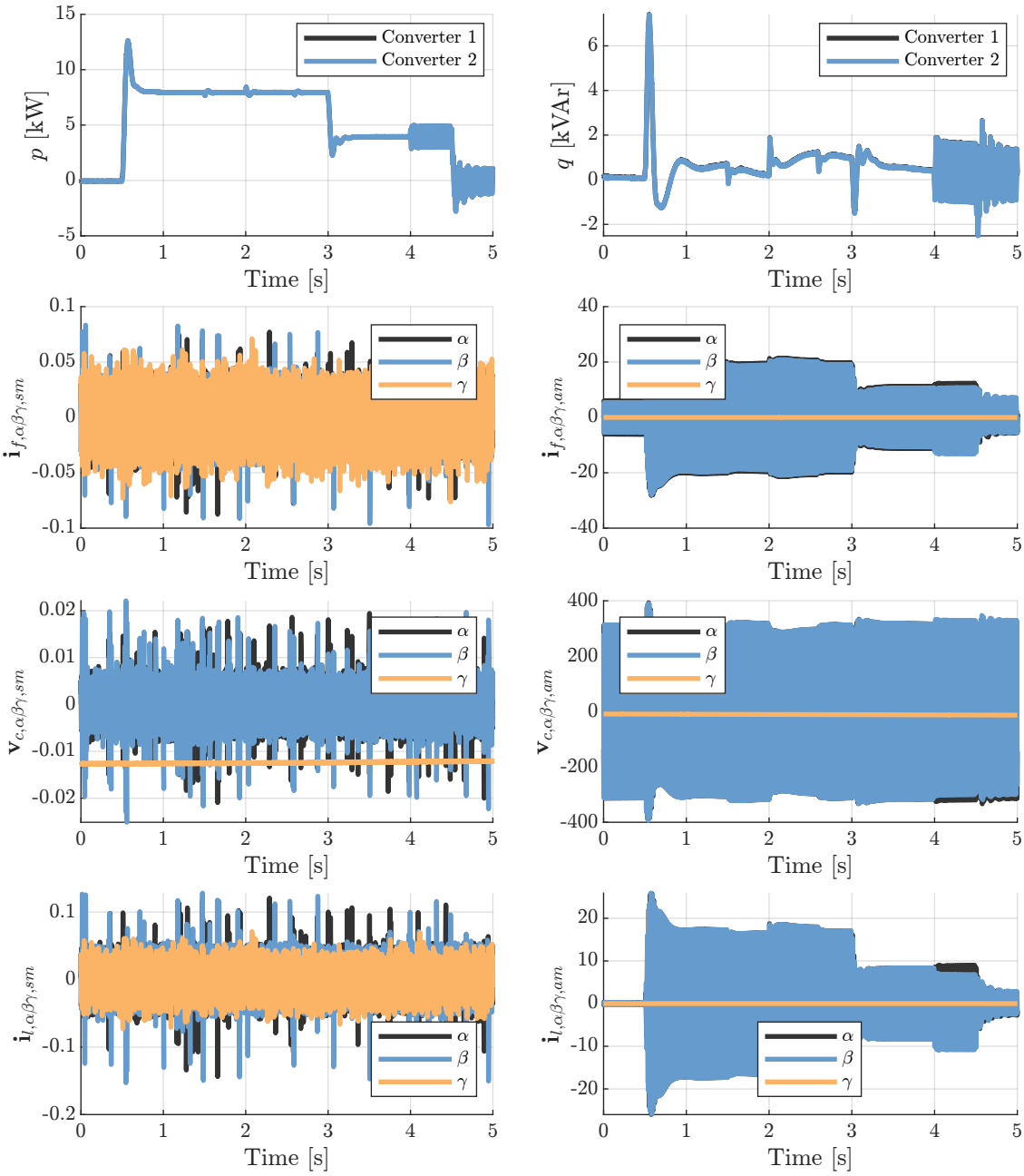

(k) Subtractive- and Additive-mode $\alpha\beta\gamma$-axis components.

Figure 4.20 – FPGA-based implementation of the Resonant Controller State-Feedback with Extended Sliding-Mode Observer hardware-in-the-loop validation. The hardware-in-the-loop implementation downscaled the time-constants by a factor of 100, as means of accurately representing the switched characteristic of power converters.

4.7 REMARKS

This chapter presented a brief review on control methods as to optimally design a controller as means to minimize medium-frequency current circulation between parallel connected power converters while looking at the passivity if the control strategy for input disturbances. From this, an optimization routine aiming to make a system passive while guaranteeing a certain behaviour at certain frequencies related to the resonant controllers, was proposed, as means to further optimize the control performance.

An in-depth analysis of the γ-axis circulating currents for paralleled converters sharing the same dc bus was presented, as means to design a controller which does not signifficantly alter the modulation common-mode voltage by creating a virtual impedance via a feedback control strategy. Since a coupling between the γ and $\alpha\beta$-axis can exist due to the parametric variations of the filter components, the virtual impedance should lower this coupling due to the smaller amplitude of the circulating currents. However, the high-frequency circulating currents still persists, as these components are uncontrollable. Hence another strategy must be employed to minimize the harmonic content, which is further discussed in Chapter 6.

In the sequence, the performance of a Sliding Mode Observer was verified to estimate non-measured states for the full state-feedback strategy. The simulations demonstrated the estimator performance for a voltage-source inverter with an LCL output filter, although this strategy should prove to be more useful for higher order filters, such as the Damped LCL, trap-LCL, due to the lack of viability to measure these states, which was proven through the experimental results. One of the limitations of the estimation performance is obtaining a more accurate disturbance estimation, as the estimator gains must be higher to accurately estimate the system states if a precise enough disturbance measurement is not fed to the estimator, which was solved by the use of the Extended Sliding Mode Observer. This is more critical for a more accurate estimation at higher frequencies, which enables a control strategy with a wider bandwidth.

The present analysis did not include the dynamics related to the dc bus, as the mapping adopted for the state feedback control turns out to be nonlinear. The dynamics of the synchronism algorithms and the dc bus dynamic are usually coupled, hence instabilities in subharmonic frequencies can be observed. However, adding the dynamics of the dc bus might also dampen the system depending on the load/source characteristic connected to the bus. This effect is more noticeable when operating in weak grid conditions. This coupling is further explored in the following chapter.

Chapter

5

Models for Stability Assessment of Power Converter Systems

The ever increasing demand for power converters to interface different energy resources with an electric grid paved the way for the insertion of distributed energy resources and energy-saving applications, while guaranteeing an appropriate operation for a wide range of conditions. Over the last few decades, the state-of-the-art evolved in a way dictated by those trends, with a special focus on the reliability of renewable power systems, which is dependent on the system stability and power quality ensured by the control strategies [7, 69, 70].

The more commonly employed control strategies can be separated into multiple-timescale control system as means of regulating the electrical quantities as means of guaranteeing an adequate system behaviour [7, 8, 11]. These control dynamics can involve electromechanical dynamics and electromagnetic transients of power networks, which may lead to instabilities and/or oscillations. Special concerns are raised on power converter dominated gris [71, 72].

The stability assessment of power converters operating under diverse grid conditions is a critical aspect in ensuring the reliable and secure performance of power systems. In the recent years, there has been an increase in demand for more faithful mathematical models representing such effects, which typically discard the eventual presence of harmonics [15] or take advantage of multiple-frequency averaging models [16] and Dynamic Phasor (DP) or Harmonic State-Space (HSS) approaches [17–19]. These approaches aim to perform and analyze the projection of the infinite-dimensional characteristic of Nonlinear Time-Periodic (NLTP) systems, which are described relating to state and input/disturbance variables expressed in terms of $L^2(\mathcal{P})$ functions with respect to a certain set $\mathcal{P}$, into a finite dimensional time-invariant space which can be complex- or real-valued depending on the adopted approach.

Furthermore, the state-of-the-art analysis are usually performed over small-signal dynamics [73–81], which hinders the identification of limit-cycles and the presence of multiple equilibrium points or a possible chaotic behaviour which can be caused by the inherent nonlinear characteristic of the control loops while significantly reducing the

complexity of the mathematical models. Concerns can also be raised over the validity of small-signal models, especially under weak-grid conditions, which present a higher degree of cross-coupling between control loops.

An accurate description of the control loops is dependent on the dynamics of the synchronism loops when considering grid-following systems. A commonly adopted approach is to employ linearized models of Phase-Locked Loops (PLLs) due to the complexity of the trigonometric functions and their description in the harmonic domain. The validity of the use of linearization is here again of concern.

Therefore, this chapter aims to demonstrate the model of nonlinear mathematical function models in the infinite-dimensional harmonic domain, which can be truncated for a finite number of harmonics, with the objective of modeling 2-D vector rotations and the division between two real-valued functions as means of obtaining a Nonlinear Time-Invariant (NLTI) model of the Park-Transformation and the Synchronous-Reference Frame Phase-Locked Loop (SRF-PLL), which serves as a base for more complex synchronism strategies [82–84]. A comprehensive analysis and modeling approach to evaluate the stability of power converters is also presented, with a specific focus on converters functioning under weak grid conditions.

The analysis begins with a thorough investigation of a single power converter, utilizing advanced analytical modeling techniques based on the Harmonic State-Space models and the functions derived in Chapter 2 obtain a complete model of the system. These models are then validated thorugh a FPGA implementation of the control strategies described in Chapter 4 and a Hardware-in-the-loop simulation as means of validating the proposed models while observing eventual instabilities and behaviours under different conditions. Additionally, the models and methodology elucidated in this work demonstrate adaptability and scalability for examining grid-forming converters. Within this framework, the grid frequency is treated as an input parameter, enabling a comprehensive exploration of the behavior exhibited by grid-forming converters.

By employing advanced modeling techniques, this chapter strives to provide valuable insights into the intricate nonlinear dynamics of power converters and the inherent coupling between active and reactive power components, as an extension of the models presented in [14]. These insights enable the development of effective strategies for decoupling the power converter system and improving system stability under varying operating conditions.

5.1 GRID CONVERTER MODEL

For this chapter, let the average model of the Voltage Source Inverter shown in Fig. 5.1 be given by

$$\begin{aligned} D_t\mathbf{x}_{dc} &= \mathbf{A}_{dc}\mathbf{x}_{dc} + \mathbf{B}_{dc}\mathbf{u}_{dc} + \mathbf{E}_{dc}\mathbf{w}_{dc}, \\ D_t\mathbf{x}_{ac} &= \mathbf{A}_{ac}\mathbf{x}_{ac} + \mathbf{B}_{ac}\mathbf{u}_{ac} + \mathbf{E}_{ac}\mathbf{w}_{ac}, \end{aligned} \tag{5.1}$$

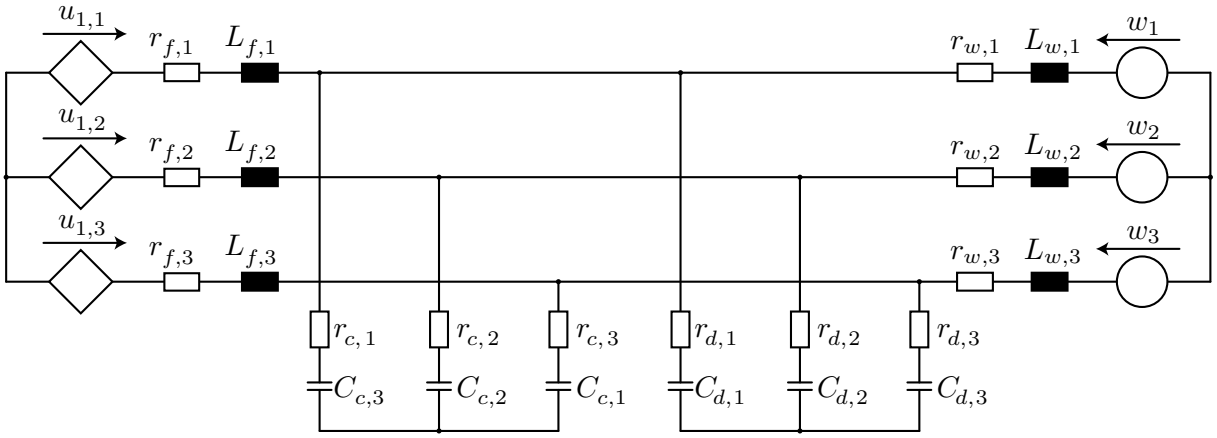

Figure 5.1 – Two-Level Voltage Source Inverter with a damped LC output filter.

where $\mathbf{A}_{dc} \in \mathbb{R}^{N_{dc}\times N_{dc}}$, $\mathbf{B}_{dc} \in \mathbb{R}^{N_{dc}\times 1}$ and $\mathbf{E}_{dc} \in \mathbb{R}^{N_{dc}\times 1}$, $\mathbf{A}_{ac} \in \mathbb{R}^{N_{ac}\times N_{ac}}$, $\mathbf{B}_{ac} \in \mathbb{R}^{N_{ac}\times 2}$ and $\mathbf{E}_{ac} \in \mathbb{R}^{N_{ac}\times 2}$, $u_{dc} := \mathbf{d}^T\mathbf{i}_f$, $\mathbf{u}_{ac} := u_{dc}\mathbf{d}$, $\mathbf{d} := (d_\alpha, d_\beta)$, $\mathbf{w} := (w_\alpha, w_\beta)$ and

$$\mathbf{x}_{ac} := (i_{f,\alpha}, v_{c,\alpha}, v_{d,\alpha}, i_{l,\alpha}, i_{f,\beta}, v_{c,\beta}, v_{d,\beta}, i_{l,\beta}) =: (\mathbf{x}_{ac,\alpha}, \mathbf{x}_{ac,\beta}).$$

Assume that

$$\mathbf{d} := \sum_{k=-n_h}^{n_h} \langle \mathbf{d} \rangle_k e^{\imath k\omega t}, \quad \mathbf{w} := \sum_{k=-n_h}^{n_h} \langle \mathbf{w} \rangle_k e^{\imath k\omega t}, \quad u_{dc} := \sum_{k=-n_h}^{n_h} \langle u_{dc} \rangle_k e^{\imath k\omega t}$$

truncated at $n_h \in \mathbb{N}$ harmonics. Let us define the state-space matrices through

$$\begin{aligned} \mathbf{A}_{dc} &:= -\frac{1}{C_{dc}R_{dc}}, \quad \mathbf{B}_{dc} := -\frac{3}{2C_{dc}}, \quad \mathbf{E}_{dc} := \frac{1}{C_{dc}}, \\ \mathbf{A}_{ac} &:= \mathbf{I}_2 \otimes \mathbf{A}_i, \quad \mathbf{B}_{ac} := \mathbf{I}_2 \otimes \mathbf{B}_i, \quad \mathbf{E}_{ac} := \mathbf{I}_2 \otimes \mathbf{E}_i, \end{aligned} \tag{5.2}$$

where the set $(\mathbf{A}_i, \mathbf{B}_i, \mathbf{E}_i)$ is defined as

$$\mathbf{A}_i = \begin{bmatrix} -\frac{r_f}{L_f} & -\frac{1}{L_f} & 0 & 0 \\ \frac{r_d(L_f - C_c r_c r_f)}{C_c L_f (r_c + r_d)} & -\frac{C_d L_f L_w r_d - C_c L_f L_w r_c + C_c C_d L_f r_c r_d^2 + C_c C_d L_w r_c r_d^2}{C_c C_d L_f L_w r_d (r_c + r_d)} & -\frac{C_c r_c - C_d r_d}{C_c C_d r_d (r_c + r_d)} & -\frac{r_d(L_w - C_c r_c r_w)}{C_c L_w (r_c + r_d)} \\ 0 & \frac{1}{C_d r_d} & -\frac{1}{C_d r_d} & 0 \\ 0 & \frac{1}{L_w} & 0 & -\frac{1}{L_w} \end{bmatrix}$$

$$\mathbf{B}_i = \begin{bmatrix} \frac{1}{2L_f} & \frac{1 r_c r_d}{2L_f(r_c + r_d)} & 0 & 0 \end{bmatrix}^T, \quad \mathbf{E}_i = \begin{bmatrix} 0 & \frac{r_c r_d}{L_w(r_c + r_d)} & 0 & -\frac{r_w}{L_w} \end{bmatrix}^T, \tag{5.3}$$

assuming that the parameters are balanced and given in Table 5.1.

We can also define the output matrices with respect to the ac voltages and currents as

$$\mathbf{C}_{v_c} = \mathbf{I}_2 \otimes [0 \quad 1 \quad 0 \quad 0], \quad \mathbf{C}_{i_l} = \mathbf{I}_2 \otimes [0 \quad 0 \quad 0 \quad 1], \tag{5.4}$$

as i_l is the current control process variable and v_c is the voltage measurement used for

Table 5.1 – Converter Parameters for Hardware-in-the-Loop Validation

Parameter	**Symbol**	**Value**
dc Bus Voltage	U_{dc}	800 V
Switching Frequency	f_s	36 kHz
Inverter Inductance	L_f	300 μH
Inverter Inductor Resistance	r_f	15 mΩ
Filter Capacitance	C_c	12 μF
Filter Capacitor Resistance	r_c	100 $\mu\Omega$
Filter Damped Capacitance	C_d	12 μF
Filter Damped Capacitor Resistance	r_d	2 Ω
Line Inductance	L_l	1 μH
Line Inductor Resistance	r_l	30 mΩ
Grid Inductance	L_w	22 mH
Grid Inductor Resistance	r_w	500 mΩ
Grid Short Circuit Ratio	SCR	approx. 1.5 (10 MW, 380 V)

Table 5.2 – Converter Parameters for Hardware-in-the-Loop Validation

Parameter	**Symbol**	**Value**
Inverter Current Feedback Gain	$k_{x,1}$	-0.0641918182373047
Capacitor Voltage Feedback Gain	$k_{x,2}$	-0.00748634338378906
Damped Capacitor Voltage Feedback Gain	$k_{x,3}$	-0.00424385070800781
Line Current Feedback Gain	$k_{x,4}$	-0.171394348144531
Control Output Feedback Gain	k_u	-1.09508514404297
Resonant Controller Gains	$k_{r,1,1}$	0.0025177001953125
	$k_{r,1,2}$	0.243587493896484

grid synchronization.

We can define a discrete-time control law as

$$\begin{aligned} \mathbf{u}_i(j) &= \mathbf{K}_x \mathbf{x}_{ac,i}(j) + \mathbf{K}_r \mathbf{x}_{r,i}(j) + k_u u_i(j-1) \\ d_i(j) &= u_i(j-1), \quad \forall i \in \{\alpha, \beta\} \end{aligned} \tag{5.5}$$

for a time instant $t = jh$, where $h = \frac{1}{2}T_s$ is the sampling-time conveniently chosen as half of the switching period and $j \in \mathbb{N}$, considering a transport delay of one sample. Note that in this case, the control variable $\mathbf{u}$ is fed back as means of minimizing the dynamics inserted by the inherent transport delay. The gains were chosen according to Table 5.2.

For continuous-time equations, a zero-order hold (ZOH) combined with the Padé approximation can be used to model the transport delay of the control variable with sufficiently small modeling error while presenting a null valued feedthrough matrix, resulting in a control variable proportional to a specific state. Thus, the complete controller model

can be described by

$$\begin{cases} D_t \mathbf{x}_c = \mathbf{A}_c \mathbf{x}_c + \mathbf{B}_x \mathbf{x}_{ac} + \mathbf{B}_{ref} \mathbf{r} \\ \mathbf{d} = \mathbf{C}_d \mathbf{x}_c \end{cases} \tag{5.6}$$

where

$$\begin{aligned} \mathbf{A}_c &:= \mathbf{I}_2 \otimes \begin{bmatrix} \mathbf{A}_r & \mathbf{0} \\ \mathbf{B}_t \mathbf{C}_r & \mathbf{A}_t + \mathbf{B}_t \mathbf{C}_t k_u \end{bmatrix}, \ \mathbf{C}_d := \mathbf{I}_2 \otimes \begin{bmatrix} \mathbf{0} & \mathbf{C}_t \end{bmatrix} \\ \mathbf{B}_x &:= \mathbf{I}_2 \otimes \begin{bmatrix} -\mathbf{B}_r \mathbf{C}_{i_l} \\ \mathbf{B}_t \mathbf{K}_x \end{bmatrix}, \ \mathbf{B}_{ref} := \mathbf{I}_2 \otimes \begin{bmatrix} \mathbf{B}_r \\ \mathbf{0} \end{bmatrix} \\ \mathbf{A}_r &:= \begin{bmatrix} 0 & \omega_r \\ -\omega_r & -2\xi_r \omega_r \end{bmatrix}, \ \mathbf{B}_r := \begin{bmatrix} 0 \\ \omega_r \end{bmatrix}, \ \mathbf{C}_r := \mathbf{K}_r, \\ \mathbf{A}_t &:= \begin{bmatrix} 0 & -\dfrac{2}{3h} \\ \dfrac{3}{h} & -\dfrac{3}{h} \end{bmatrix}, \ \mathbf{B}_t := \begin{bmatrix} \dfrac{2}{3h} \\ 0 \end{bmatrix}, \ \mathbf{C}_t := \begin{bmatrix} 0 & 1 \end{bmatrix}, \end{aligned} \tag{5.7}$$

ω_r is the resonant frequency and ξ_r is a damping factor of the resonant controller and $\mathbf{r} := (r_\alpha, r_\beta)$ is the current reference in the stationary reference frame.

5.2 PHASE-LOCKED LOOP MODEL

Let the input signal $\bar{u} \in \mathbb{C}$ be defined by

$$\bar{u} := u_\alpha + \iota u_\beta, \tag{5.8}$$

and the dq-components $\mathbf{u}_{dq} := (u_d, u_q)$ can be obtained through the transformation $\mathbf{T}_{dq} : \mathbb{R}^2 \times \mathbb{R}^3 \to \mathbb{R}^2$

$$\mathbf{T}_{dq}(\omega, t, \delta) := \begin{bmatrix} \mathbf{T}_d(\omega, t, \delta) \\ \mathbf{T}_q(\omega, t, \delta) \end{bmatrix} = \begin{bmatrix} \cos(\omega t + \delta) & \sin(\omega t + \delta) \\ -\sin(\omega t + \delta) & \cos(\omega t + \delta) \end{bmatrix} \tag{5.9}$$

or through its complex notation as

$$\bar{u}_{dq} := \bar{u} e^{-\iota(\omega t + \delta)}. \tag{5.10}$$

Hence, we can write the SRF-PLL dynamic equations according to

$$\begin{cases} \upsilon_{pll} = \dfrac{\Im\left\{\bar{u}e^{-\iota\theta_\delta}\right\}}{\Re\left\{\bar{u}e^{-\iota\theta_\delta}\right\}} \\ \dot{\mathbf{x}}_{pll} = \mathbf{A}_{pll}\mathbf{x}_{pll} + \mathbf{B}_{pll}\upsilon_{pll} \\ \dot{\delta} = \mathbf{C}_{pll}\mathbf{x}_{pll} + \mathbf{D}_{pll}\upsilon_{pll} \\ \theta_\delta = \omega_g t + \delta \\ \hat{\omega} = \dot{\delta} + \omega_g \end{cases}, \tag{5.11}$$

where ω_g is the PLL feedforward frequency, which can be fixed or adaptive as means of improving the PLL performance, and the set $\mathcal{M}_{pll} := \{\mathbf{A}_{pll}, \mathbf{B}_{pll}, \mathbf{C}_{pll}, \mathbf{D}_{pll}\}$ is the state-space model of the loop filter. The loop filter was chosen arbitrarily in a first moment, with its block diagram shown in Fig. 5.2, while considering the input normalization given by the d-axis component. A more thorough approach would be to normalize the imaginary component as in

$$\upsilon'_{pll} = \frac{\Im\left\{\bar{u}e^{-\iota\theta_\delta}\right\}}{|\bar{u}e^{-\iota\theta_\delta}|} = \frac{\Im\left\{\bar{u}e^{-\iota\theta_\delta}\right\}}{\|\mathbf{u}\|_2}, \tag{5.12}$$

solving for the normalization approach described by (5.11) when $\Re\{\bar{u}_{dq}\} \gg \Im\{\bar{u}_{dq}\}$. This is mostly true since the synchronism loop forces $\Im\{\bar{u}_{dq}\}$ to a null value, whereas $\Re\{\bar{u}_{dq}\}$ converges to $\|u\|_2$ if no disturbances in the synchronism loop are considered.

If the description of the input u belongs to a dynamic system in dq components, while leaving out harmonics of the electrical quantities, the analysis can be simplified, since u_q is not time-varying, as shown in [15]. However, if the model description for u is time-varying, the approach presented in the previous sections can be employed as means to obtain a large-signal time-invariant nonlinear model. From this, we can adopt two different approaches, which are described in the sequence.

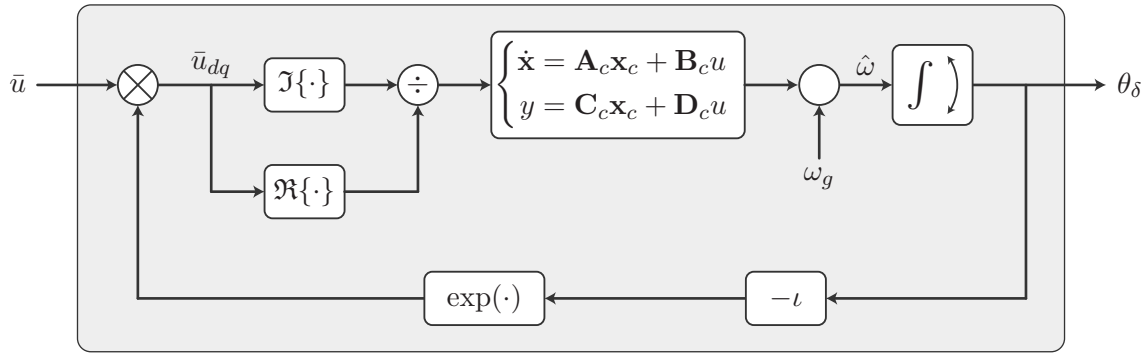

Figure 5.2 – Block Diagram of the SRF-PLL with a generic Loop Filter.

5.2.1 Discussion on Small-Signal Analysis

In a first moment, we can assume that $\|\delta\|_2$ is small enough such that the linearization for $\bar{\delta} = \delta|_{\dot{\delta}=0}$ for a certain $\bar{\delta} \in [0, 2\pi)$ is valid, hence we can write u_{dq} as

$$u_{dq} \approx \sqrt{2}\,\|\langle u\rangle_{-1:1}\|_2 \left(1, \bar{\delta} + \tilde{\delta}\right), \tag{5.13}$$

where $\tilde{\delta} = \delta - \bar{\delta}$ and the approximation for u_d is the grid or power converter ac rated voltage, and a small enough $\bar{\delta}$ which can be modelled as a disturbance. Note that if (5.13) is applied to (5.11), we have that both systems are coupled by the disturbance $\bar{\delta}$, which has no explicit formulation, i.e., the synchronism electrical quantity $\mathbf{u}$ and reference generation dynamic systems are mostly independent. Thus, equation (5.13) can be used in conjunction with the concepts of DP or HSS and the Toeplitz operator to obtain a description of the system, which is mostly valid as $\bar{\delta}$ approaches zero, corroborating the small signal analysis presented in [19, 85, 86].

However, a correct choice of $\bar{\delta}$ is necessary to define the correct point of operation, as means of coupling the outer system that defines $\mathbf{u}$ and the synchronism loop small-signal model, which is discussed in [87] as the initial angle problem. Nevertheless, such approach is inaccurate, as $\bar{\delta}$ should be the solution of the system at its fixed point. Furthermore, the existence of this fixed point is not guaranteed due to the nonlinear characteristic of said system. For example, an instability of the PLL control loop leads to a chaotic orbit (which can be periodic), as the feedback is bounded.

On a side note, the phase angle and the voltage amplitude employed for the normalization of the synchronism electrical quantity is extremely dependent on the active and reactive power processed by power converters under weak-grid conditions. Hence, this linearization is not adequate for the characterization of the fixed points as means of asserting the system's stability under weak grid conditions.

Concurrently, the frequency coupling terms given by higher order terms of the Taylor series expressed in (2.62) will lead to a synchronization deviation such that the estimation error e_δ does in fact converges to a value $\epsilon \in \mathbb{R}$ under distorted grid conditions. This effect can also be amplified by the normalisation of the PLL input, as the approximation given by (2.36) can also lead to a coupling between two distinct harmonics and $\langle\delta\rangle_0$.

5.2.2 SRF-PLL Large-Signal Model Approximation

Another alternative is to consider the nonlinear characteristic of the SRF-PLL equations in (5.11) with the feedback loop defined as

$$\upsilon_{pll} = \frac{\mathfrak{I}\left\{\bar{u}e^{-\iota(\omega t+\delta)}\right\}}{\mathfrak{R}\left\{\bar{u}e^{-\iota(\omega t+\delta)}\right\}} = \frac{u_q}{u_d} \tag{5.14}$$

As a reminder from Chapter 2, Table 2.4 shows a collection of DP functions which

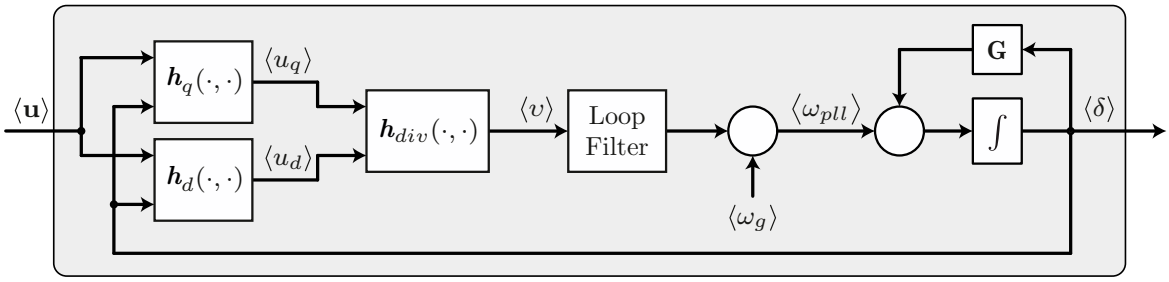

Figure 5.3 – Block diagram of the proposed SRF-PLL model with a generic loop filter base on the dynamic equations described in (5.17).

will be employed in the nonlinear model of the PLL henceforth. From (2.62), (2.64) and (2.36), we can employ the previously defined linear maps $\boldsymbol{h}_d, \boldsymbol{h}_q$ such that

$$\langle u_j \rangle = \boldsymbol{h}_j(\delta) \circ \langle \mathbf{u} \rangle \,, \quad \forall j \in \{d, q\} \tag{5.15}$$

as well as the division operator $\boldsymbol{h}_{div}$ as means of computing the normalization. Thus, the set of DPs of υ_{pll} can be written as a function of the set of dynamic phasors of the input $\langle \mathbf{u} \rangle$ and the estimated displacement angle $\langle \delta \rangle$ according to

$$\boldsymbol{h}_{pll}(\mathbf{u}, \delta) := \langle \upsilon_{pll} \rangle = \boldsymbol{h}_{div} \left(\boldsymbol{h}_q(\delta) \circ \langle \mathbf{u} \rangle \,, \boldsymbol{h}_d(\delta) \circ \langle \mathbf{u} \rangle \right). \tag{5.16}$$

Consequently, the PLL dynamic equations can be expressed as

$$\begin{cases} D_t \langle \mathbf{x}_{pll} \rangle = \left(\mathbf{I}_{N_h} \otimes \mathbf{A}_{pll} - \mathrm{diag}\left(\mathfrak{H}\right) \otimes \iota\omega \mathbf{I}_{n_{pll}} \right) \langle \mathbf{x}_{pll} \rangle \\ \qquad\qquad + \left(\mathbf{I}_{N_h} \otimes \mathbf{B}_{pll} \right) \boldsymbol{h}_{pll}(\mathbf{u}, \delta) \\ D_t \langle \delta \rangle = \left(\mathbf{I}_{N_h} \otimes \mathbf{C}_{pll} \right) \langle \mathbf{x}_{pll} \rangle + \left(\mathbf{I}_{N_h} \otimes \mathbf{D}_{pll} \right) \boldsymbol{h}_{pll}(\mathbf{u}, \delta) \\ \qquad\qquad + \langle \omega_g \rangle - \omega \hat{h}_0 - \iota\omega \mathrm{diag}\left(\mathfrak{H}\right) \langle \delta \rangle \end{cases}, \tag{5.17}$$

where $\mathfrak{H}$ is the set of harmonics considered in the analysis and $n_h := \dim(\mathfrak{H})$. A block diagram of the proposed HSS model is presented in Fig. 5.3.

A simplification can be adopted as means of reducing the complexity of the model presented in (5.17) letting $\langle \delta \rangle_j = 0, \forall j \neq 0$, while also normalizing the PLL input signal by the dc component of the d-axis signal, resulting in

$$\begin{cases} D_t \langle \mathbf{x}_{pll} \rangle_0 = \mathbf{A}_{pll} \langle \mathbf{x}_{pll} \rangle_0 + \mathbf{B}_{pll} \dfrac{\boldsymbol{g}_{q,0}(\langle \delta \rangle_0) \circ \langle \mathbf{u} \rangle}{\boldsymbol{g}_{d,0}(\langle \delta \rangle_0) \circ \langle \mathbf{u} \rangle} \\ D_t \langle \delta \rangle_0 = \mathbf{C}_{pll} \langle \mathbf{x}_{pll} \rangle_0 + \mathbf{B}_{pll} \dfrac{\boldsymbol{g}_{q,0}(\langle \delta \rangle_0) \circ \langle \mathbf{u} \rangle}{\boldsymbol{g}_{d,0}(\langle \delta \rangle_0) \circ \langle \mathbf{u} \rangle} + \langle \omega_g \rangle_0 - \omega \end{cases}, \tag{5.18}$$

which is mostly valid when employing control techniques to mitigate disturbances of the electrical quantities signals mainly caused by negative sequence components and harmonic

Table 5.3 – Parameters for Park Transformation Model Validation

t [ms]	0–160	160–480	480–800
$\langle u_\alpha \rangle_1$	50	50	50
$\langle u_\alpha \rangle_2$	0	$5e^{\iota\frac{\pi}{6}}$	$5e^{\iota\frac{\pi}{6}}$
$\langle u_\alpha \rangle_3$	0	$2.5e^{\iota\frac{\pi}{12}}$	$2.5e^{\iota\frac{\pi}{12}}$
$\langle u_\alpha \rangle_4$	0	0	$1.25e^{\iota\frac{\pi}{6}}$
$\langle u_\beta \rangle_1$	$50e^{-\iota\frac{\pi}{2}}$	$20e^{-\iota\frac{2\pi}{5}}$	$50e^{-\iota\frac{\pi}{2}}$
$\langle u_\beta \rangle_2$	0	$5e^{\iota\frac{\pi}{6}}$	$5e^{\iota\frac{\pi}{6}}$
$\langle u_\beta \rangle_3$	0	$2.5e^{\iota\frac{\pi}{12}}$	$2.5e^{\iota\frac{\pi}{12}}$
$\langle u_\beta \rangle_4$	0	0	$1.25e^{\iota\frac{\pi}{6}}$

Table 5.4 – SRF-PLL Loop Filter Parameters

Description	**Parameter**	**Value**
Feedforward Frequency	ω_g	$2\pi 50$ rad/s
Sampling Time	Δt	100 μs
PI Proportional Gain	k_p	56.2
PI Integral Gain	k_i	1784

distortions. Note that $g(\delta)$ presents a bounded behaviour for the feedback, since

$$\|g(\delta)\|_2 = \|\langle \mathbf{u}_{dq} \rangle\|_2 \, \|\langle \mathbf{u} \rangle\|_2^{-1} = 1, \quad \forall \mathbf{u} \neq \mathbf{0}, \delta \in \mathbb{R}, \tag{5.19}$$

which in turn takes into account an eventual loss-of-lock and the possibility of a re-synchronization. This poses as an advantage of truncating (2.55) at the first term, otherwise the harmonic content of δ can lead to a positive feedback, i.e, a reduction in the stability margin of the PLL control loop. This simplified model can also be employed for stability analysis of power converter systems for the investigation and identification of loss-of-lock and subharmonics, especially when operating under weak-grid conditions.

Another advantage of this procedure is that the dynamic phasor frequency was written as a system disturbance, with the assumption that $\dot{\omega}$ vanishes, hence frequency disturbances are also fed back into the dynamic system, which is useful for obtaining frequency dependent models for power system analysis. The following section presents a numerical simulation of the proposed model while employing a traditional control strategy as means of validating the proposed model and assert the dependence of the proposed model with respect to the truncation of the infinite dimensional model, which is related to the number of harmonics and terms of the Taylor series expansion.

5.2.3 Numerical Example

Assume the loop filter as a PI controller, such that

$$\mathbf{A}_{pll} = 0, \quad \mathbf{B}_{pll} = 1, \quad \mathbf{C}_{pll} = k_i, \quad \mathbf{D}_{pll} = k_p, \tag{5.20}$$

where k_p and k_i are the proportional and integral gains, respectively. Hence, equation (5.17) can be rewritten as

$$\begin{cases} D_t \langle \mathbf{x}_{pll} \rangle = -\iota\omega \mathrm{diag}\left(\mathfrak{H}\right) \langle \mathbf{x}_{pll} \rangle + \boldsymbol{h}_{pll}(\mathbf{u}, \delta) \\ D_t \langle \delta \rangle = -\iota\omega \mathrm{diag}\left(\mathfrak{H}\right) \langle \delta \rangle + k_i \langle \mathbf{x}_{pll} \rangle + k_p \boldsymbol{h}_{pll}(\mathbf{u}, \delta) + \langle \omega_g \rangle - \omega \end{cases}. \tag{5.21}$$

The truncated model has three degrees of freedom: N_h, N_{div} and N_g, related to the number of harmonics of the set $\mathfrak{H}$, the number of Taylor series terms of the normalization procedure and to the number of Taylor series terms of the 2-D rotation operation, respectively. An adequate choice of these parameters is critical due to the increased complexity related to the number of operations. Let n_h the number of harmonics such that $\mathfrak{H} = \{h \in \mathbb{Z} : -n_h \leq h \leq n_h\}$, which leads to $N_h = 2n_h + 1$. Based on this, the simulation results presented in Fig. 5.4 demonstrates the validation of the SRF-PLL with parameters defined in Table 5.4 for an arbitrary input signal with its set of dynamic phasors defined in Table 5.3. In this case, the choice of n_h was not as significant as the choice of N_{div} due to the large amplitude of the voltage unbalance during the time-interval $t \in (180, 480]$ ms, which is limited by the convergence of the inverse function Taylor series.

However, the time-interval $t \in (480, 800]$ ms demonstrates the need for a higher N_h as means of accurately expressing the d-axis components as well as the frequency estimation. Note that the amplitude of the distortions should be lower for an adequate choice of loop filter, which can lead to a lower number of components needed to accurately express these signals.

The number of terms of the rotation N_g was not significant since in this case the amplitude of the displacement angle dynamic phasor $\langle \delta \rangle_h, \forall h \neq 0$ is sufficiently small.

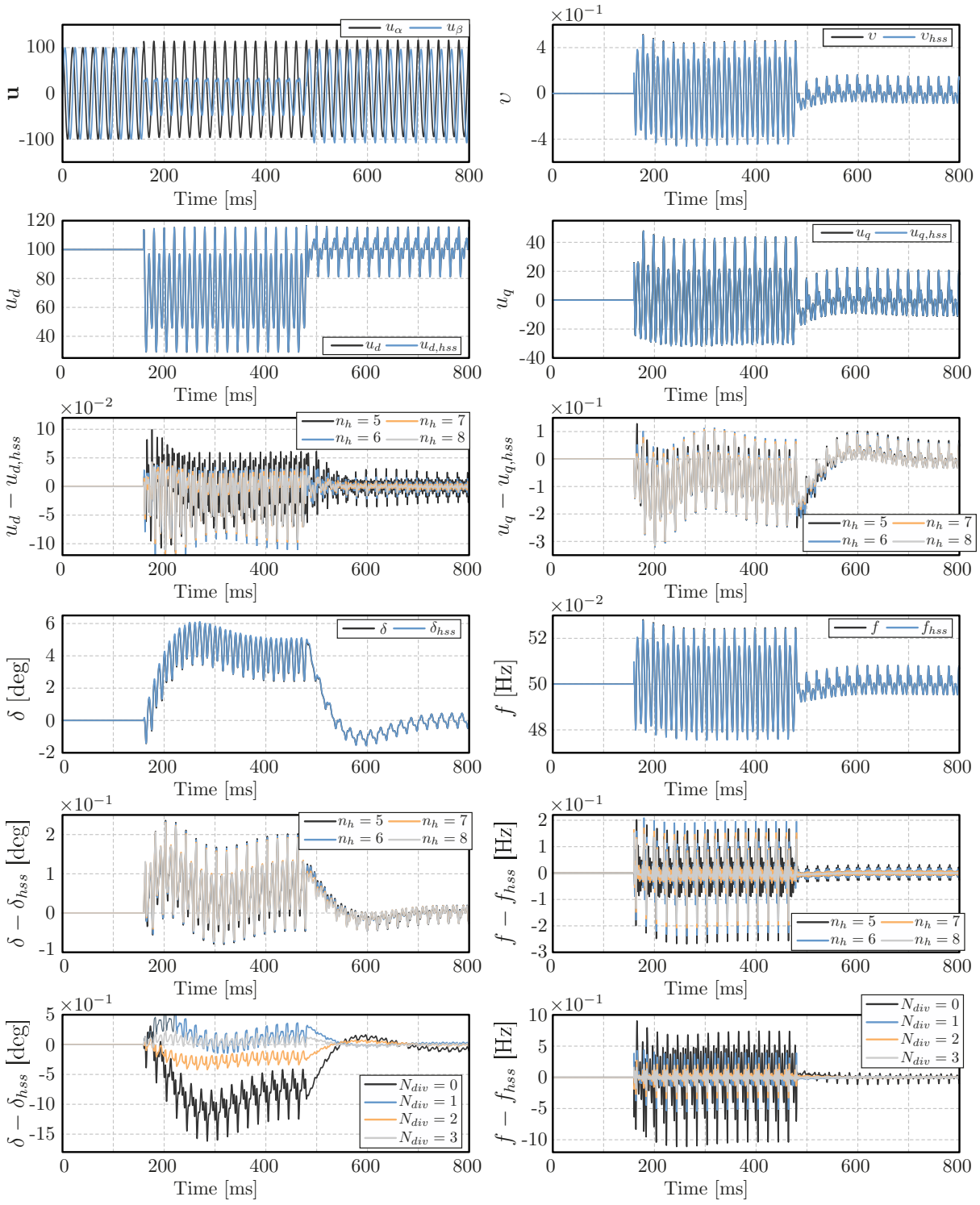

Figure 5.4 – Validation of the proposed harmonic domain-based SRF-PLL model with a PI loop filter with gains given by Table 5.4 for an arbitrary input signal $\mathbf{u}$ with its phasors amplitudes and phases given by Table 5.3. The error is defined as the absolute error between the real valued function and the projection of the approximation onto the $L^2(\mathbb{R})$ space.

5.3 CURRENT REFERENCE GENERATION

This section presents an analysis of grid-connected inverters operating with a Stationary Reference Frame ($\alpha\beta$) control strategy, incorporating resonant controllers in conjunction with a state-feedback control strategy. Additionally, the influence of the reference generation control loop is examined. Two distinct methods for generating the reference are considered:

i. Normalized Voltage Feedback: The first method involves utilizing a normalized measurement of the filter voltage to inject active power across all grid harmonic components. In this configuration, the inverter operates as an active filter, which is advantageous for the system as a whole since transmission losses for higher frequency tend to be higher especially due to skin and proximity effects. In this case, the power converters help reduce the harmonic that circulates in the grid. The normalization process can be achieved by employing the d-axis component of a SRF-PLL or other estimation techniques such as windowed RMS filtering, RDFT-based algorithms, or alternative approaches.

ii. Sinusoidal Reference: The second method employs a Phase-Locked Loop or similar method to extract the fundamental component of the synchronism signal to generate a normalized sinusoidal current reference. This approach restricts the active power injection control solely to the fundamental harmonic component.

iii. Constant Power Injection: leads to generation of current harmonics in frequencies that do not necessarily have voltage components. Thus, not desirable from the grid perspective. Therefore, not analyzed further. However, leads to minimized energy storage requirements for the converter that can be smaller and less costly.

By exploring and comparing these two reference generation methods, we can gain insights into their respective performance, efficiency, and suitability for grid-connected inverter applications.

5.3.1 Normalized Voltage Feedback

Let us define the measured voltage $\mathbf{v} \in \mathbb{R}^2$ as

$$\mathbf{v} := \mathbf{C}_v \mathbf{x}, \tag{5.22}$$

where $\mathbf{x} \in L^2(\mathbb{R}^{n_x})$ is the state vector of the converter system and $\mathbf{C}_v \in \mathbb{R}^{2\times n_x}$ is an output matrix such that

$$\mathbf{C}_v = \begin{bmatrix} \mathbf{C}_{v,\alpha} \\ \mathbf{C}_{v,\beta} \end{bmatrix}.$$

Consequently, the set of dynamic phasors of $\mathbf{v}$ can then be expressed as

$$\langle \mathbf{v} \rangle := (\mathbf{I}_\infty \otimes \mathbf{C}_v) \langle \mathbf{x} \rangle \tag{5.23}$$

such that the windowed RMS value of $\mathbf{v}$ is given by

$$\langle v_{\text{RMS}} \rangle_0 := \left(\langle \mathbf{v} \rangle^H \langle \mathbf{v} \rangle \right)^{\frac{1}{2}} = \left(\langle \mathbf{x} \rangle^H \left(\mathbf{I}_\infty \otimes \mathbf{C}_v^H \mathbf{C}_v \right) \langle \mathbf{x} \rangle \right)^{\frac{1}{2}}. \tag{5.24}$$

We can also employ an approximation by a ZOH as means of computing either the RDFT or a moving average of v_{RMS}, resulting in the dynamic system given by

$$\begin{cases} D_t x_{\text{RMS}} = \dfrac{1}{N_{\text{RMS}} h} \left(\langle \mathbf{x} \rangle^H \left(\mathbf{I}_\infty \otimes \mathbf{C}_v^H \mathbf{C}_v \right) \langle \mathbf{x} \rangle - x_{\text{RMS}} \right) \\ \quad y_{\text{RMS}} = x_{\text{RMS}}^{\frac{1}{2}}, \end{cases} \tag{5.25}$$

where N_{RMS} is the number of samples of the window and h is the sampling time. An adequate choice of N_{RMS} results in $N_{\text{RMS}} h = f_g$, where f_g is the grid frequency. It is safe to assume that the harmonics of the windowed RMS filter can be neglected as means of simplifying the analysis.

Thus, the current reference vector $\mathbf{r}$ can be defined as

$$\mathbf{r} := \frac{1}{y_{\text{RMS}}^2} \begin{bmatrix} p & q \\ -q & p \end{bmatrix} \mathbf{v} \tag{5.26}$$

by normalizing the voltage vector and the power reference (p, q) by the RMS voltage value in accordance with the Instantaneous Power Theory, assuming that $p, q \in L^2(\mathbb{R})$, where

$$p := \sum_{k=-n_h}^{n_h} \langle p \rangle_k e^{\iota k \omega t}, \quad q := \sum_{k=-n_h}^{n_h} \langle q \rangle_k e^{\iota k \omega t}, \tag{5.27}$$

Therefore, we can obtain a state-space representation of the reference generation as

$$\begin{cases} D_t x_{\text{RMS}} = \dfrac{1}{N_{\text{RMS}} h} \left(\langle \mathbf{x} \rangle^H \left(\mathbf{I}_\infty \otimes \mathbf{C}_v^H \mathbf{C}_v \right) \langle \mathbf{x} \rangle - x_{\text{RMS}} \right) \\ \quad \langle r_\alpha \rangle = \dfrac{1}{x_d^2} \left((\mathbf{\Gamma} \circ \langle p \rangle) \circ ((\mathbf{I}_{N_h} \otimes \mathbf{C}_{v,\alpha}) \langle \mathbf{x} \rangle) + (\mathbf{\Gamma} \circ \langle q \rangle) \circ ((\mathbf{I}_{N_h} \otimes \mathbf{C}_{v,\beta}) \langle \mathbf{x} \rangle) \right) \\ \quad \langle r_\beta \rangle = \dfrac{1}{x_d^2} \left(-(\mathbf{\Gamma} \circ \langle q \rangle) \circ ((\mathbf{I}_{N_h} \otimes \mathbf{C}_{v,\alpha}) \langle \mathbf{x} \rangle) + (\mathbf{\Gamma} \circ \langle p \rangle) \circ ((\mathbf{I}_{N_h} \otimes \mathbf{C}_{v,\beta}) \langle \mathbf{x} \rangle) \right) \end{cases} \tag{5.28}$$

which results in

$$\begin{cases} D_t x_{\mathrm{RMS}} = \dfrac{1}{N_{\mathrm{RMS}} h}\left(\langle \mathbf{x}\rangle^H \left(\mathbf{I}_\infty \otimes \mathbf{C}_v^H \mathbf{C}_v\right)\langle \mathbf{x}\rangle - x_{\mathrm{RMS}}\right) \\ \langle \mathbf{r}\rangle = \dfrac{1}{x_{\mathrm{RMS}}}\left(\begin{bmatrix} \langle p\rangle_0 & \langle q\rangle_0 \\ -\langle q\rangle_0 & \langle p\rangle_0 \end{bmatrix} \otimes \mathbf{C}_v\right)\langle \mathbf{x}\rangle\,, \end{cases} \tag{5.29}$$

if $\langle p\rangle_k = \langle q\rangle_k = 0, \forall k \in \mathbb{N}^*$.

If the PLL is employed for voltage estimation, then the time-variant current reference vector can be written as

$$\mathbf{r} := \frac{1}{\left(\mathbf{T}_d(\omega,t,\delta)\mathbf{v}\right)^2}\begin{bmatrix} p & q \\ -q & p \end{bmatrix}\mathbf{v} = \frac{1}{\left(\mathbf{T}_d(\omega,t,\delta)\mathbf{C}_v\mathbf{x}\right)^2}\begin{bmatrix} p & q \\ -q & p \end{bmatrix}\mathbf{C}_v\mathbf{x}. \tag{5.30}$$

However, the application of the complex rotation on a distorted voltage measurement results in a distorted d-axis component, thus we can employ a filter such as the Moving Average Filter (MAF) to improve the robustness of the voltage estimation. The state-space representation can then be approximated by

$$\begin{cases} D_t x_d = \dfrac{1}{N_{\mathrm{MAF}} h}\left(\mathbf{T}_d(\omega,t,\delta)\mathbf{C}_v\mathbf{x} - x_d\right) \\ \mathbf{r} = \dfrac{1}{x_d^2}\begin{bmatrix} p & q \\ -q & p \end{bmatrix}\mathbf{C}_v\mathbf{x}, \end{cases} \tag{5.31}$$

where N_{MAF} is the length of the Moving-Average Filter, resulting in the Harmonic-State Space description given by

$$\begin{cases} D_t\langle \mathbf{x}_{pll}\rangle = \left(\mathbf{I}_{N_h} \otimes \mathbf{A}_{pll} - \mathrm{diag}\left(\mathfrak{H}\right) \otimes \iota\omega \mathbf{I}_{n_{pll}}\right)\langle \mathbf{x}_{pll}\rangle \\ \qquad\qquad + \left(\mathbf{I}_{N_h} \otimes \mathbf{B}_{pll}\right)\boldsymbol{h}_{pll}(\mathbf{u},\delta) \\ D_t\langle \delta\rangle = \left(\mathbf{I}_{N_h} \otimes \mathbf{C}_{pll}\right)\langle \mathbf{x}_{pll}\rangle + \left(\mathbf{I}_{N_h} \otimes \mathbf{D}_{pll}\right)\boldsymbol{h}_{pll}(\mathbf{u},\delta) + \langle \omega_g\rangle - \omega\hat{h}_0 - \iota\omega \mathrm{diag}\left(\mathfrak{H}\right)\langle \delta\rangle \\ D_t\langle x_d\rangle = -\left(\dfrac{1}{N_{\mathrm{MAF}} h}\mathbf{I}_{N_h} + \iota\omega \mathrm{diag}\left(\mathfrak{H}\right)\right)\langle x_d\rangle + \dfrac{1}{N_{\mathrm{MAF}} h}\boldsymbol{h}_d(\delta) \circ \left(\left(\mathbf{I}_{N_h} \otimes \mathbf{C}_v\right)\langle \mathbf{x}\rangle\right) \\ \langle r_\alpha\rangle = \boldsymbol{h}_{div}\Big(\left(\boldsymbol{\Gamma} \circ \langle p\rangle\right) \circ \left(\left(\mathbf{I}_{N_h} \otimes \mathbf{C}_{v,\alpha}\right)\langle \mathbf{x}\rangle\right) + \left(\boldsymbol{\Gamma} \circ \langle q\rangle\right) \circ \left(\left(\mathbf{I}_{N_h} \otimes \mathbf{C}_{v,\beta}\right)\langle \mathbf{x}\rangle\right), \\ \qquad\qquad \left(\boldsymbol{\Gamma} \circ \langle x_d\rangle\right) \circ \langle x_d\rangle\Big) \\ \langle r_\beta\rangle = \boldsymbol{h}_{div}\Big(-\left(\boldsymbol{\Gamma} \circ \langle q\rangle\right) \circ \left(\left(\mathbf{I}_{N_h} \otimes \mathbf{C}_{v,\alpha}\right)\langle \mathbf{x}\rangle\right) + \left(\boldsymbol{\Gamma} \circ \langle p\rangle\right) \circ \left(\left(\mathbf{I}_{N_h} \otimes \mathbf{C}_{v,\beta}\right)\langle \mathbf{x}\rangle\right), \\ \qquad\qquad \left(\boldsymbol{\Gamma} \circ \langle x_d\rangle\right) \circ \langle x_d\rangle\Big), \end{cases} \tag{5.32}$$

which can be simplified into

$$\begin{cases} D_t \langle \mathbf{x}_{pll} \rangle = \left(\mathbf{I}_{N_h} \otimes \mathbf{A}_{pll} - \operatorname{diag}(\mathfrak{H}) \otimes \iota\omega \mathbf{I}_{n_{pll}} \right) \langle \mathbf{x}_{pll} \rangle \\ \qquad\qquad + \left(\mathbf{I}_{N_h} \otimes \mathbf{B}_{pll} \right) \boldsymbol{h}_{pll}(\mathbf{u}, \delta) \\ D_t \langle \delta \rangle = \left(\mathbf{I}_{N_h} \otimes \mathbf{C}_{pll} \right) \langle \mathbf{x}_{pll} \rangle + \left(\mathbf{I}_{N_h} \otimes \mathbf{D}_{pll} \right) \boldsymbol{h}_{pll}(\mathbf{u}, \delta) + \langle \omega_g \rangle - \omega \hat{h}_0 - \iota\omega \operatorname{diag}(\mathfrak{H}) \langle \delta \rangle \\ D_t x_d = \dfrac{1}{N_{\mathrm{MAF}} h} \left(\boldsymbol{g}_d(\langle \delta \rangle_0) \circ \left(\left(\mathbf{I}_{N_h} \otimes \mathbf{C}_v \right) \langle \mathbf{x} \rangle \right) - x_d \right) \\ \langle r_\alpha \rangle = \dfrac{1}{x_d^2} \Bigg(\left(\boldsymbol{\Gamma} \circ \langle p \rangle \right) \circ \left(\left(\mathbf{I}_{N_h} \otimes \mathbf{C}_{v,\alpha} \right) \langle \mathbf{x} \rangle \right) + \left(\boldsymbol{\Gamma} \circ \langle q \rangle \right) \circ \left(\left(\mathbf{I}_{N_h} \otimes \mathbf{C}_{v,\beta} \right) \langle \mathbf{x} \rangle \right) \Bigg) \\ \langle r_\beta \rangle = \dfrac{1}{x_d^2} \Bigg(- \left(\boldsymbol{\Gamma} \circ \langle q \rangle \right) \circ \left(\left(\mathbf{I}_{N_h} \otimes \mathbf{C}_{v,\alpha} \right) \langle \mathbf{x} \rangle \right) + \left(\boldsymbol{\Gamma} \circ \langle p \rangle \right) \circ \left(\left(\mathbf{I}_{N_h} \otimes \mathbf{C}_{v,\beta} \right) \langle \mathbf{x} \rangle \right) \Bigg) \end{cases} \tag{5.33}$$

if we assume that the d-axis component MAF is able to filter most of its harmonic content. An even further simplification can be employed with the assumption that $\langle p \rangle_k = \langle q \rangle_k = 0, \forall k \in \mathbb{N}^*$, resulting in

$$\begin{cases} D_t \langle \mathbf{x}_{pll} \rangle = \left(\mathbf{I}_{N_h} \otimes \mathbf{A}_{pll} - \operatorname{diag}(\mathfrak{H}) \otimes \iota\omega \mathbf{I}_{n_{pll}} \right) \langle \mathbf{x}_{pll} \rangle \\ \qquad\qquad + \left(\mathbf{I}_{N_h} \otimes \mathbf{B}_{pll} \right) \boldsymbol{h}_{pll}(\mathbf{u}, \delta) \\ D_t \langle \delta \rangle = \left(\mathbf{I}_{N_h} \otimes \mathbf{C}_{pll} \right) \langle \mathbf{x}_{pll} \rangle + \left(\mathbf{I}_{N_h} \otimes \mathbf{D}_{pll} \right) \boldsymbol{h}_{pll}(\mathbf{u}, \delta) + \langle \omega_g \rangle - \omega \hat{h}_0 - \iota\omega \operatorname{diag}(\mathfrak{H}) \langle \delta \rangle \\ D_t x_d = \dfrac{1}{N_{\mathrm{MAF}} h} \left(\boldsymbol{g}_d(\langle \delta \rangle_0) \circ \left(\left(\mathbf{I}_{N_h} \otimes \mathbf{C}_v \right) \langle \mathbf{x} \rangle \right) - x_d \right) \\ \langle \mathbf{r} \rangle = \dfrac{1}{x_d^2} \left(\begin{bmatrix} \langle p \rangle_0 & \langle q \rangle_0 \\ -\langle q \rangle_0 & \langle p \rangle_0 \end{bmatrix} \otimes \mathbf{C}_v \right) \langle \mathbf{x} \rangle , \end{cases} \tag{5.34}$$

This method provides the benefit of reducing the total harmonic distortion (THD) in the voltage waveform at the point of common connection (PCC), leading to a lower level of distortion and improved power quality. By minimizing harmonics in the output voltage, the system can operate with reduced energy levels. This is particularly beneficial in weak grid conditions where the line impedance is higher, as it requires a larger energy contribution from the ac voltage bus. However, this approach necessitates increased power processing capabilities from the converters. Alternatively, injecting a purely sinusoidal current allows the grid to handle harmonic frequencies, which will be explored further in the subsequent subsection.

5.3.2 Sinusoidal Current Reference

In this case, the sinusoidal reference is obtained from the SRF-PLL or similar algorithm's Voltage Controlled Oscillator (VCO). Thus, we can write the current reference

in the time-variant domain as

$$\mathbf{r} := \frac{1}{\mathbf{T}_d(\omega, t, \delta)\mathbf{C}_v\mathbf{x}} \begin{bmatrix} p & q \\ -q & p \end{bmatrix} \begin{bmatrix} \cos(\omega t + \delta) \\ \sin(\omega t + \delta) \end{bmatrix}, \tag{5.35}$$

where $p, q \in L^2(\mathbb{R})$ are the power references and $\delta \in L^2(\mathbb{R})$ is the angle estimated by the SRF-PLL algorithm.

From Chapter 2, more specifically from Equation 2.65, we can write the VCO equations in the Harmonic State-Space domain as

$$\boldsymbol{h}_{\text{vco}}(\langle\delta\rangle) := \langle\cos(\omega t + \delta)\rangle = \left(\mathbf{I}_{N_h} \otimes \begin{bmatrix} 1 & 0 \end{bmatrix}\right) \circ \boldsymbol{h}_d^H(\langle\delta\rangle) \circ \langle\hat{h}_0\rangle, \tag{5.36}$$

where $\langle\hat{h}_0\rangle_k = \delta_{k,0}$, and the orthogonal component can be obtained by

$$\langle\sin(\omega t + \delta)\rangle = \boldsymbol{h}_{\text{vco}}\left(\langle\delta\rangle - \frac{\pi}{2}\langle\hat{h}_0\rangle\right). \tag{5.37}$$

Consequently, the reference equation described in (5.35) can be written in the Harmonic State-Space domain as

$$\begin{aligned} \langle r_\alpha\rangle = \boldsymbol{h}_{div}\Bigg(& (\boldsymbol{\Gamma} \circ \langle p\rangle) \circ \boldsymbol{h}_{\text{vco}}(\langle\delta\rangle) + (\boldsymbol{\Gamma} \circ \langle q\rangle) \circ \boldsymbol{h}_{\text{vco}}\left(\langle\delta\rangle - \frac{\pi}{2}\langle\hat{h}_0\rangle\right), \\ & \boldsymbol{h}_d(\langle\delta\rangle) \circ (\mathbf{I}_{N_h} \otimes \mathbf{C}_v)\langle\mathbf{x}\rangle \Bigg) \\ \langle r_\beta\rangle = \boldsymbol{h}_{div}\Bigg(& -(\boldsymbol{\Gamma} \circ \langle q\rangle) \circ \boldsymbol{h}_{\text{vco}}(\langle\delta\rangle) + (\boldsymbol{\Gamma} \circ \langle q\rangle) \circ \boldsymbol{h}_{\text{vco}}\left(\langle\delta\rangle - \frac{\pi}{2}\langle\hat{h}_0\rangle\right), \\ & \boldsymbol{h}_d(\langle\delta\rangle) \circ (\mathbf{I}_{N_h} \otimes \mathbf{C}_v)\langle\mathbf{x}\rangle \Bigg), \end{aligned} \tag{5.38}$$

which takes into account the dynamic phasors of p, q as well as the dynamics of the PLL given by δ. Similar simplifications to (5.33) and (5.34) can also be employed to reduce the complexity of the model.

The determination of the power references (p, q) in the control strategy depends on various factors, including the chosen supervisory control approach and the characteristics of the grid. In a grid-following strategy, the parameter p is typically determined based on the control of the dc-bus voltage, ensuring its stability and desired reference value, with an additional term in case of an external active power reference. On the other hand, the parameter q is derived from the control of the ac-bus voltage, aiming to regulate and maintain the desired voltage level at the point of common connection (PCC).

In grid-forming strategies, additional considerations are taken into account, such as the frequency and ac-bus voltage dependence on the power processed by the power converters. The dynamics of this dependency can be complex, especially when considering various energy sources, machines, and loads connected to the ac-bus. However, certain

simplifications, such as the adoption of a droop characteristic, can be employed to evaluate the local stability of the system. This droop characteristic provides a relationship between the power output and the frequency or voltage deviation, allowing for the adjustment of (p, q) based on the system requirements and operating conditions.

The following sections describe a model for the power references while focusing on grid-following power converters, which will then be used for the stability assessment.

5.4 DC BUS VOLTAGE CONTROL

The proper operation of the inverter requires control of the dc bus voltage. This control can be achieved through various sources or devices connected to the dc bus. The dynamics of these voltage controllers are influenced by the inertia present in the each power interface and their capacity to be able to regulate the power injection.

For grid-forming converters, active power regulation can be utilized to control the grid frequency, considering the presence of multiple generators connected to the ac bus. The power references in this case are determined by frequency controllers, which employ specific control strategies such as direct droop control or synchronous machine emulation. On the other hand, for grid-following converters, it is assumed that the grid is sufficiently stable, and its frequency does not reach excessively high or low values. Therefore, the grid is capable of absorbing the power injected by energy sources connected to the ac and/or dc buses.

In both cases, a control strategy to regulate the dc bus voltage is usually employed. This strategy is tipically implemented via a PI controller which regulates the dc voltage or energy stored at the capacitors. We can then express the 2DOF-PI controller as

$$\begin{cases} D_t x_u = v_{dc,ref} - \mathbf{C}_{dc}\mathbf{x}_{dc} \\ \quad p = k_{i,dc} x_u - k_{p,dc}\mathbf{C}_{dc}\mathbf{x}_{dc} + \eta_{p,dc} k_{p,dc} v_{dc,ref} \end{cases} \tag{5.39}$$

where $v_{dc,ref}$ is the dc bus voltage reference and $u_{dc} := \mathbf{C}_{dc}\mathbf{x}_{dc}$. Note that $\mathbf{C}_{dc} = 1$ in this example, assuming a current (or power) source model, in accordance with the models discussed in Chapter 3.

The dynamic models of the linear systems described in (5.1) and (5.7) as well as

Table 5.5 – dc Bus Controller Parameters for Hardware-in-the-Loop Validation

Parameter	**Symbol**	**Value**
Proportional Gain	$k_{p,dc}$	-48
Integral Gain	$k_{i,dc}$	-405
Feedforward Ratio	$\eta_{p,dc}$	0.9

the previous section can be rewritten as

$$
\begin{cases}
D_t \langle \mathbf{x}_{dc} \rangle = \left(\mathbf{I}_{N_h} \otimes \mathbf{A}_{dc} - \operatorname{diag}\left(\mathbb{Z}_{-n_h}^{n_h}\right) \otimes \iota\omega \mathbf{I}_{N_{dc}}\right) \langle \mathbf{x}_{dc} \rangle + \left(\mathbf{I}_{N_h} \otimes \mathbf{E}_{dc}\right) \langle \mathbf{w}_{dc} \rangle \\
\qquad\qquad + \left(\mathbf{I}_{N_h} \otimes \mathbf{B}_{dc}\right) \begin{bmatrix} \left(\mathbf{\Gamma} \circ \left(\left(\mathbf{I}_{N_h} \otimes \mathbf{C}_{d,\alpha}\right) \langle \mathbf{x}_c \rangle\right)\right) \circ \left(\left(\mathbf{I}_{N_h} \otimes \mathbf{C}_{i_{f,\alpha}}\right) \langle \mathbf{x}_{ac} \rangle\right) \\ \left(\mathbf{\Gamma} \circ \left(\left(\mathbf{I}_{N_h} \otimes \mathbf{C}_{d,\beta}\right) \langle \mathbf{x}_c \rangle\right)\right) \circ \left(\left(\mathbf{I}_{N_h} \otimes \mathbf{C}_{i_{f,\beta}}\right) \langle \mathbf{x}_{ac} \rangle\right) \end{bmatrix} \\
D_t \langle \mathbf{x}_{ac} \rangle = \left(\mathbf{I}_{N_h} \otimes \mathbf{A}_{ac} - \operatorname{diag}\left(\mathbb{Z}_{-n_h}^{n_h}\right) \otimes \iota\omega \mathbf{I}_{N_{ac}}\right) \langle \mathbf{x}_{ac} \rangle + \left(\mathbf{I}_{N_h} \otimes \mathbf{E}_{ac}\right) \langle w_{ac} \rangle \\
\qquad\qquad + \left(\mathbf{I}_{N_h} \otimes \mathbf{B}_{ac}\right) \left(\mathbf{\Gamma} \circ \langle u_{dc} \rangle\right) \left(\mathbf{I}_{N_h} \otimes \mathbf{C}_v\right) \langle \mathbf{d} \rangle . \\
D_t \langle \mathbf{x}_c \rangle = \left(\mathbf{I}_{N_h} \otimes \mathbf{A}_c - \operatorname{diag}\left(\mathbb{Z}_{-n_h}^{n_h}\right) \otimes \iota\omega \mathbf{I}_{N_c}\right) \langle \mathbf{x}_c \rangle \\
\qquad\qquad + \left(\mathbf{I}_{N_h} \otimes \mathbf{B}_x\right) \langle \mathbf{x}_{ac} \rangle + \left(\mathbf{I}_{N_h} \otimes \mathbf{B}_{ref}\right) \langle \mathbf{r} \rangle \\
D_t \langle x_u \rangle = \langle v_{dc,ref} \rangle - \left(\mathbf{I}_{N_h} \otimes \mathbf{C}_{dc}\right) \langle \mathbf{x}_{dc} \rangle \\
D_t \langle \mathbf{x}_{pll} \rangle = -\iota\omega \operatorname{diag}\left(\mathbb{Z}_{-(n_h+1)}^{n_h+1}\right) \langle \mathbf{x}_{pll} \rangle + \boldsymbol{h}_{pll}(\left(\mathbf{I}_{N_h} \otimes \mathbf{C}_v\right) \langle \mathbf{x}_{ac} \rangle , \langle \delta \rangle) \\
D_t \langle \delta \rangle = -\iota\omega \operatorname{diag}\left(\mathbb{Z}_{-(n_h+1)}^{n_h+1}\right) \langle \delta \rangle + k_{i,pll} \langle \mathbf{x}_{pll} \rangle + k_{p,pll} \boldsymbol{h}_{pll}(\left(\mathbf{I}_{N_h} \otimes \mathbf{C}_v\right) \langle \mathbf{x}_{ac} \rangle , \langle \delta \rangle) \\
\qquad\qquad + \langle \omega_g \rangle - \omega \hat{h}_0,
\end{cases}
\tag{5.40}
$$

where the reference can be chosen according to (5.38) with

$$
\langle p \rangle = k_i \langle x_u \rangle - k_{p,dc}(\mathbf{I}_{N_{dc}} \otimes \mathbf{C}_{dc}) \langle \mathbf{x}_{dc} \rangle + \eta_{p,dc} k_{p,dc} \langle v_{dc,ref} \rangle . \tag{5.41}
$$

A bode diagram of the open-loop voltage control with respect to the error input and the dc circuit current is shown in Figure 5.5, with gains given by Table 5.5. The reactive power reference becomes less significant when the ac bus voltage amplitude remains relatively stable despite variations in active power injection. This is typically observed in strong grid conditions. However, in weak grid conditions where the ac bus voltage amplitude is more sensitive to fluctuations, a dedicated reactive power control strategy is required. The following section presents a model of a reactive power control strategy specifically designed to address the challenges associated with weak grid conditions.

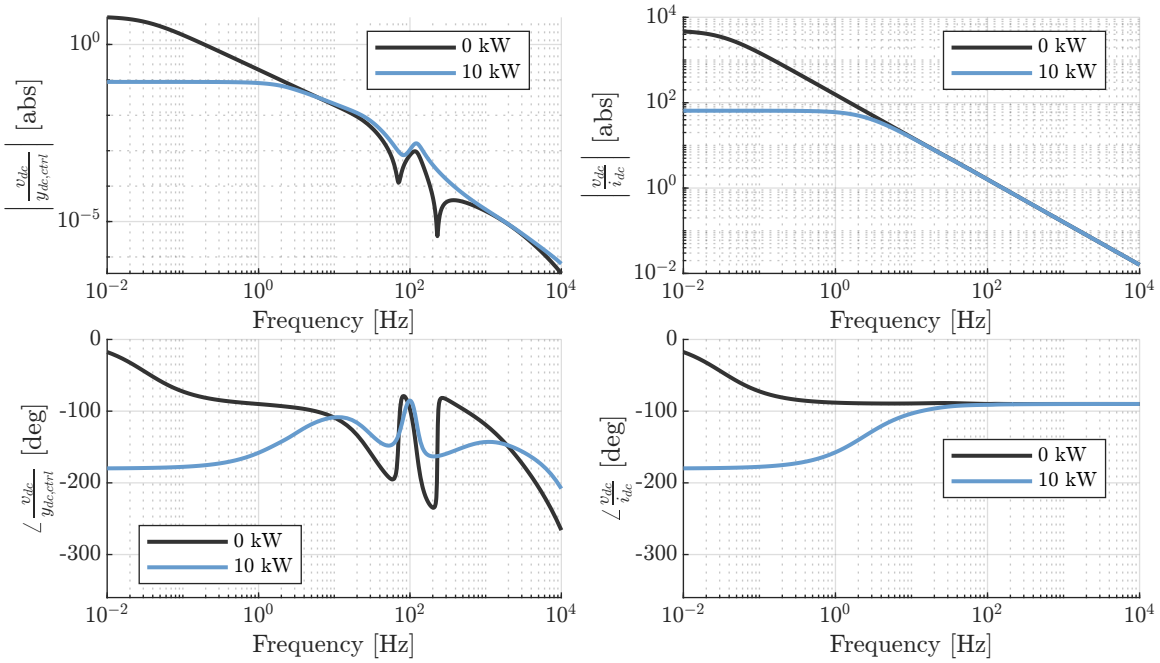

(a) Open-Loop

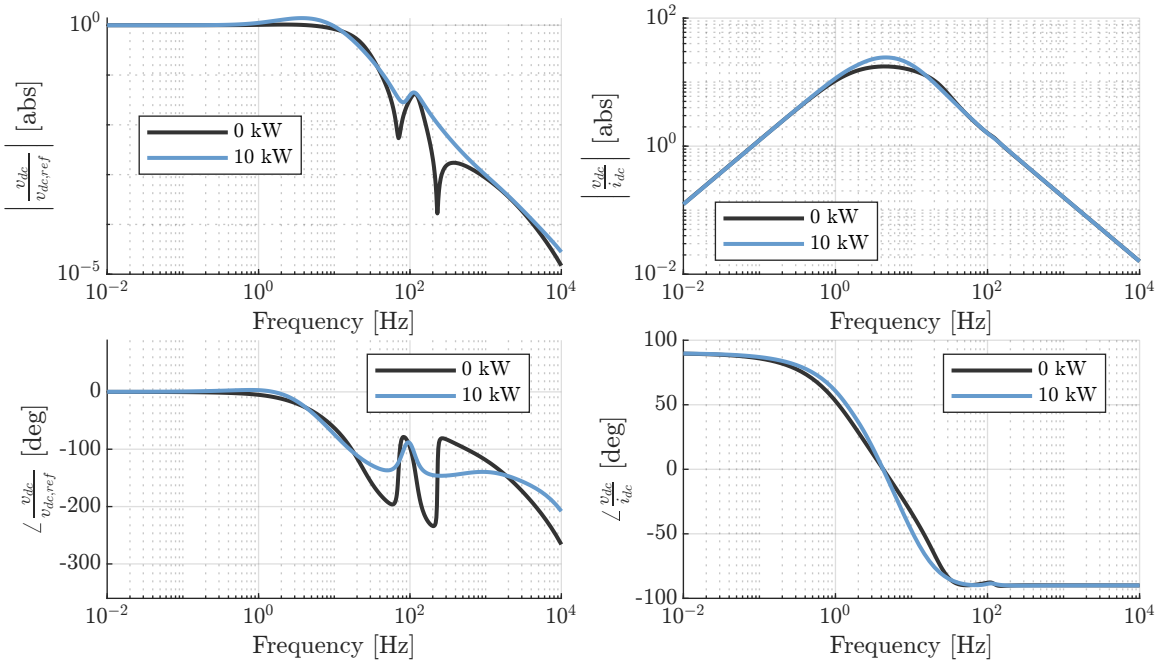

(b) Closed-Loop

Figure 5.5 – Open- and Closed-Loop Bode Diagram of the dc bus voltage v_{dc} by the (a) control signal ($y_{dc,\text{ctrl}}$) (b) voltage reference ($v_{dc,\text{ref}}$) and disturbance rejection with respect to the dc bus current source $\langle i_{dc} \rangle_0$ for the polytope vertex defined by the maximum and minimum processed power.

5.5 AC BUS VOLTAGE CONTROL

Following the reference generation, it is necessary to devise a method for generating the active and reactive power references. The Instantaneous Power Theory provides a

formulation where the instantaneous apparent power can be expressed as

$$\check{s} := \frac{3}{2}\check{w}\check{i}_w^* \tag{5.42}$$

using complex-valued phasors. Here, $\check{w} := w_\alpha + \iota w_\beta$ represents the grid voltage phasor, and $\check{i}_w := i_{w,\alpha} + \iota i_{w,\beta}$ represents the grid current phasor, assuming no γ-axis currents. Assuming that $\mathbf{i}_w$ is the control variable or compensations have been applied to account for the reactive power processed by the output filter, we can proceed with the generation of power references.

Since it is difficult to obtain an accurate estimation for $\check{w}$, the synchronization variable was chosen as the output filter capacitor voltage, resulting in a non-null angle $\bar{\delta}$ from the synchronization algorithm at the point of equilibrium. This leads to the power calculation given by

$$\check{s}_i := \frac{3}{2}\check{v}_c\check{i}_w^* = \frac{3}{2}(\check{w} + L_w D_t \check{i}_w)\check{i}_w^* \tag{5.43}$$

This in turn causes a coupling between active and reactive power, since the power injected into the system is given by

$$\check{s} = \check{s}_i - L_w \check{i}_w^* D_t \check{i}_w. \tag{5.44}$$

The voltage drop across the grid inductance can lead to a change in the voltage amplitude. This effect becomes more pronounced in weak grid conditions, where the grid inductance has significantly higher values. The power converter can operate as a reactive power compensator, operating as a sink or source of reactive power to account for these amplitude voltage variations.

We can employ the Recursive Discrete Fourier Transformation as in

$$\begin{cases} x_{q,1}(k+1) = x_{q,1}(k) + \dfrac{1}{N_{\mathrm{DFT}}}\left(\check{v}_c(k) - \check{v}_c(k - N_{\mathrm{DFT}})\right)\exp\left(\iota\dfrac{2\pi}{N_{\mathrm{DFT}}}\theta(k)\right) \\ x_{q,2}(k+1) = x_{q,2}(k) + \dfrac{1}{N_{\mathrm{MAF}}}\left(|x_{q,1}(k)|^2 - |x_{q,1}(k - N_{\mathrm{MAF}})|^2\right) \\ \theta(k+1) = \mathrm{rem}(\theta(k) + 1, N_{\mathrm{DFT}}) \\ y_q(k) = (x_{q,2}(k))^{\frac{1}{2}} \end{cases} \tag{5.45}$$

for a time instant $t = kh$ and a DFT window of N_{DFT} samples and a moving average filter with N_{DFT} samples. According to the analysis presented in Chapter 2, the dynamics of the proposed filter can be effectively approximated by a transport delay represented by

$$\tau_q := (N_{\mathrm{DFT}} + N_{\mathrm{MAF}})h, \tag{5.46}$$

granted that τ_q is much smaller then the dynamics associated with y_q. If the number of samples of the MAF is equal to the DFT window size, the dynamics of the reactive power calculation given by Equation (5.45) are expected to result in approximately two grid

Table 5.6 – ac Bus Controller Parameters for Hardware-in-the-Loop Validation

Parameter	**Symbol**	**Value**
Proportional Gain	$k_{p,q}$	20
Integral Gain	$k_{p,q}$	100
RDFT Length	N_{DFT}	1440
MAF Length	N_{MAF}	1440

cycles. This holds true since the dynamics associated with the ac bus voltage controller are much larger than two grid cycles. The system can then be approximated by

$$\begin{cases} D_t x_q = \dfrac{2}{\tau_q}\left(\displaystyle\sum_{i=\{\alpha,\beta\}} \frac{1}{2}\left\langle v_{c,i}\right\rangle^H \left\langle v_{c,i}\right\rangle - x_q\right) \\ y_q = (x_q)^{\frac{1}{2}} \end{cases} \tag{5.47}$$

in the same manner as (5.25). We can then design a 2DOF-PI controller, resulting in the following system:

$$\begin{cases} D_t \mathbf{x}_q = \begin{bmatrix} -\dfrac{2}{\tau_q} & 0 \\ -1 & 0 \end{bmatrix} \mathbf{x}_q + \begin{bmatrix} \dfrac{2}{\tau_q} \displaystyle\sum_{i=\{\alpha,\beta\}} \frac{1}{2}\left\langle v_{c,i}\right\rangle^H \left\langle v_{c,i}\right\rangle \\ v_{ac,ref} \end{bmatrix} \\ \langle q\rangle = \begin{bmatrix} -k_{p,q} & k_{i,q} \end{bmatrix} \mathbf{x}_q + k_{p,q}\eta_{p,q} v_{ac,ref}. \end{cases} \tag{5.48}$$

If the controlled system dynamic is much slower than two grid cycles, we can approximate

$$x_{q,1} \approx \sum_{i=\{\alpha,\beta\}} \frac{1}{2}\left\langle v_{c,i}\right\rangle^H \left\langle v_{c,i}\right\rangle. \tag{5.49}$$

An alternative to the proposed methodology is to employ the PLL voltage estimation in the same way as the current reference generation.

The Bode diagram in Figure 5.6 illustrates the linearized model's behavior at the polytope vertex, defined by the extremes of the processed active power, for both open-loop and closed-loop conditions with gains defined in Table 5.6. In the presence of weak grid conditions, there is a noticeable impact on the system's robustness concerning the dc bus current. Specifically, a more pronounced low-frequency resonance is observed at the operating point where higher power is being processed, as opposed to the point of operation with lower power processing.

The results from the Bode diagram highlight the sensitivity of the system's stability and resonant behavior to changes in the processed active power, especially under weak grid conditions. Understanding these characteristics is crucial for designing effective control strategies that can handle variations in active power and maintain system stability.

A reference voltage step waveform obtained from the hardware-in-the-loop imple-

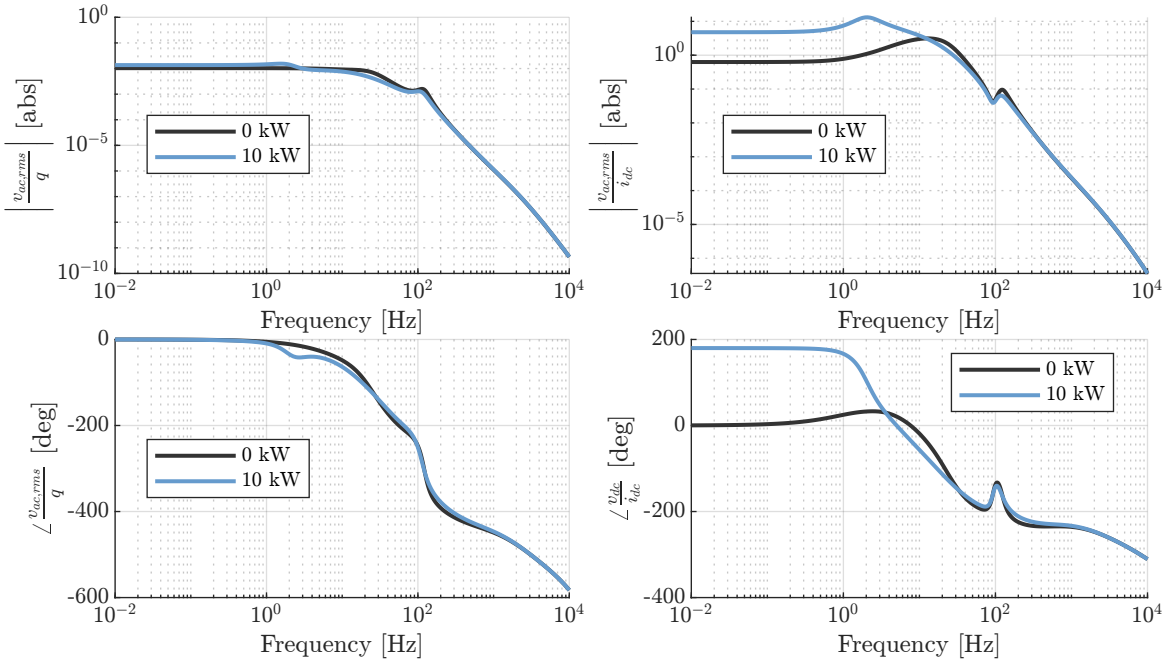

(a) Open-Loop

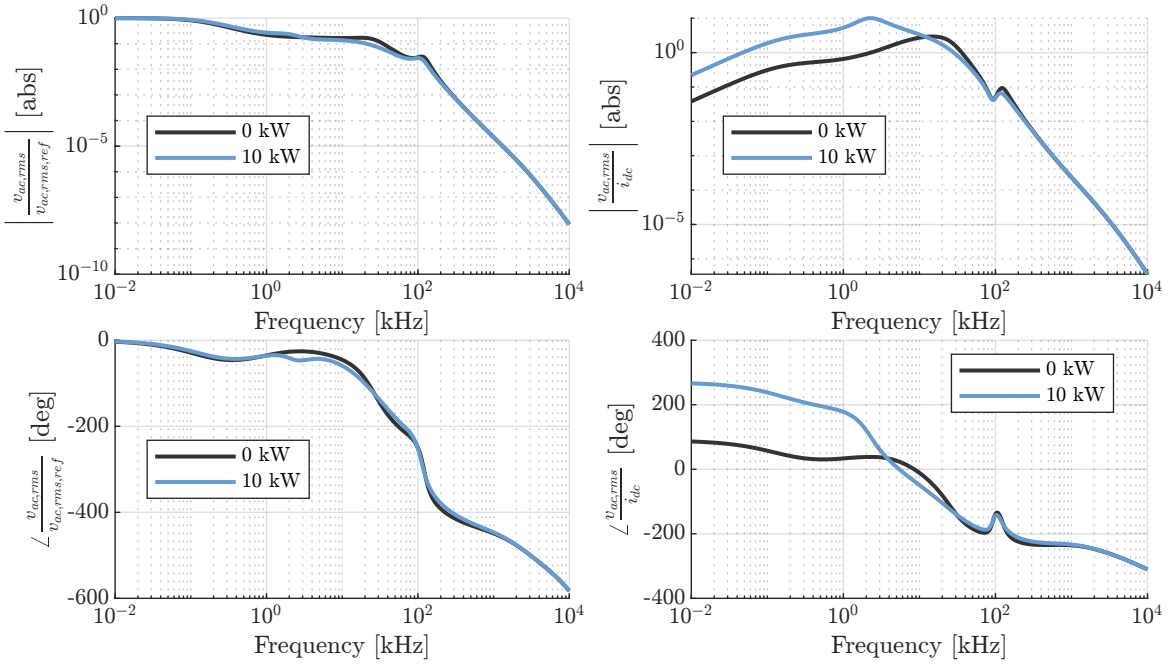

(b) Closed-Loop

Figure 5.6 – Open- and Closed-Loop Bode Diagram of the dc bus voltage $v_{ac,\text{rms}}$ by the (a) control signal ($\langle q \rangle_0$) (b) voltage reference ($v_{ac,\text{rms,ref}}$) and disturbance rejection with respect to the dc bus current source $\langle i_{dc} \rangle_0$ for the polytope vertex defined by the maximum and minimum processed power.

mentation is presented in Figure 5.7 as means of validating the control strategy for both cases. Note the underdamped behaviour of the system when the converter is processing more active power, which corroborates the previous discussion.

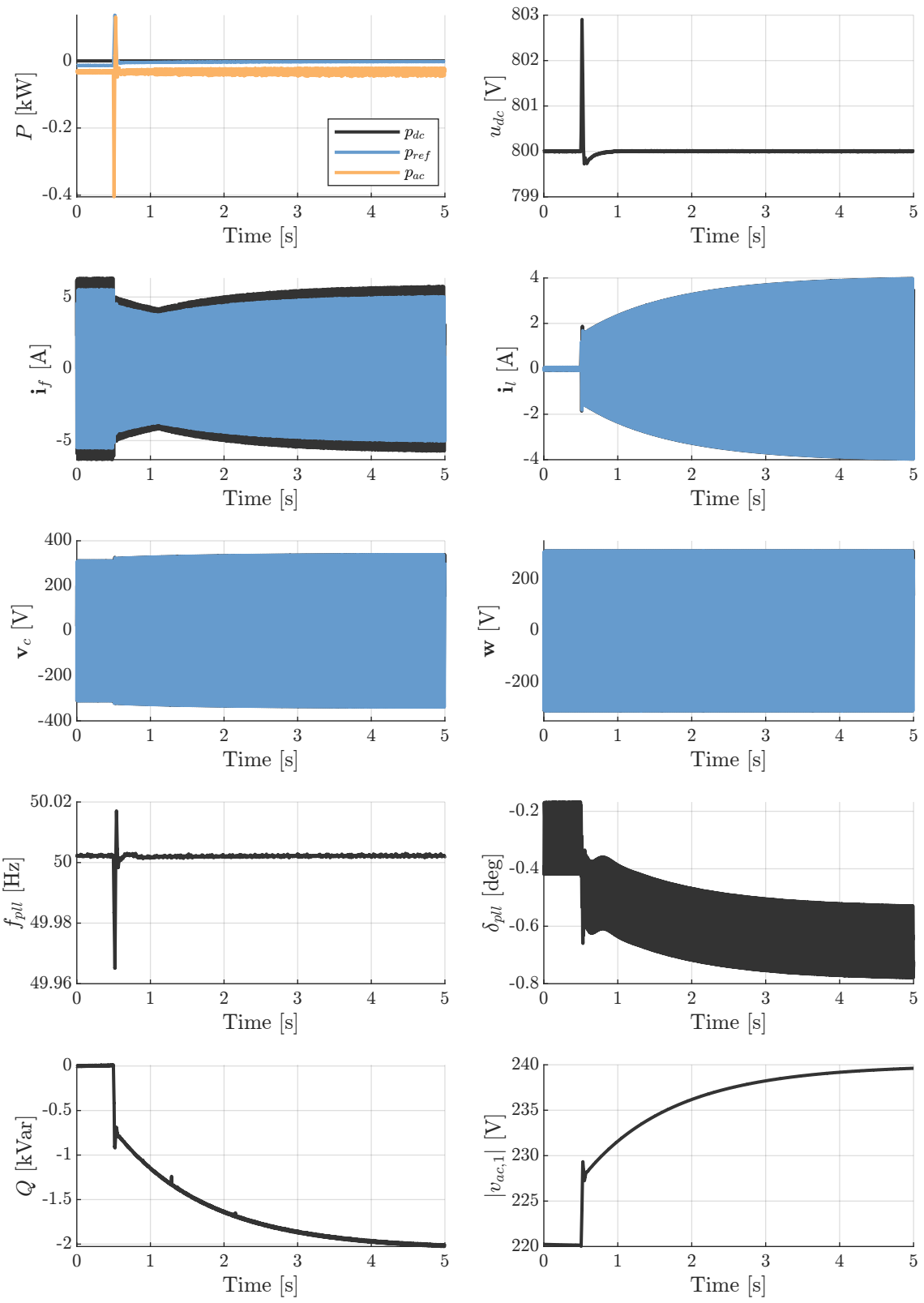

(a) 0 kW

Figure 5.7 – HIL validation of the proposed ac bus voltage control strategy.

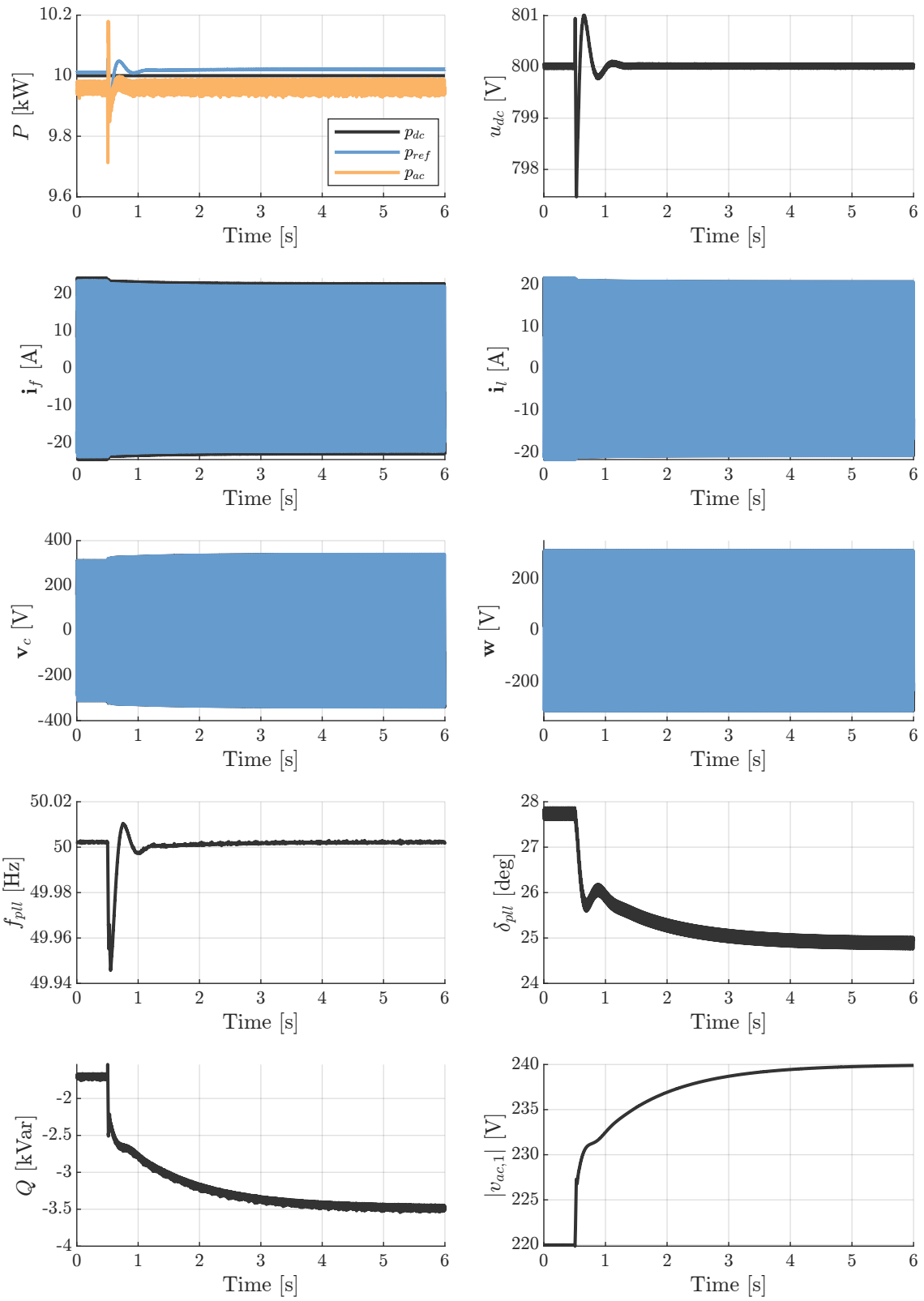

(b) 10 kW

Figure 5.7 – HIL validation of the proposed ac bus voltage control strategy.

5.6 EXPERIMENTAL VALIDATION

The current section demonstrates the behaviour of the 2LVSI connected to a weak grid with parameters given by Table 5.1. Comparisons are made with dynamic phasor models with the objective of validating the proposed models and veryfying the behaviour of the eigenvalues for different conditions.

5.6.1 DC Voltage Control and SRF-PLL

The Figure 5.8.a shows the Hardware-in-the-loop system response for multiple power steps of 1 kW up until 11 kW, and 200 W power steps from 11 kW to 11.6 kW, with some points detailed in Figure 5.8. A detailed picture of some of the power steps are also shown with the objective of demonstrating the mathematical description accuracy. Note that Figure 5.8.e shows a detailed image of the instability, which in this case is caused by the loss-of-lock of the synchronism strategy. The mathematical model is validated through a simulation employing the MATLAB's ode23tb solver to solve the differential equation, which validates the dynamic models.

In the sequence, Figure 5.9 illustrates the comparison between the Hardware-in-the-loop system response and the mathematical model for unbalances generated by disturbances on the β-axis grid voltage. This type of disturbance enables the evaluation of the coupling between different frequencies.

As the unbalance increases, so does the discrepancy between the mathematical and experimental models, attributed to the truncation of the number of harmonics and the Taylor series coefficients of the approximating functions.

The insertion of grid voltage distortions were also validated to evaluate the behaviour of the power converter mathematical model, in accordance with the validations presented in Figure 5.10. From this, we can conclude that the model is able to reproduce these types of disturbances with high enough accuracy.

An open question remains regarding the system's ability to recover from instability and the possibility of resynchronization. In Figure 5.11, a comparison of the converter resynchronization is presented, revealing significant differences between the responses. These differences arise from the saturation of the PLL normalization, where the d-axis component was saturated at 40 V to prevent positive feedback caused by signal inversion during loss-of-lock scenarios.

The observed variations in the resynchronization responses underscore the critical impact of PLL saturation on the system's stability during recovery processes. Further investigation and analysis are required to explore the system's recovery capabilities and the potential implications of the saturation effect on resynchronization behaviors.

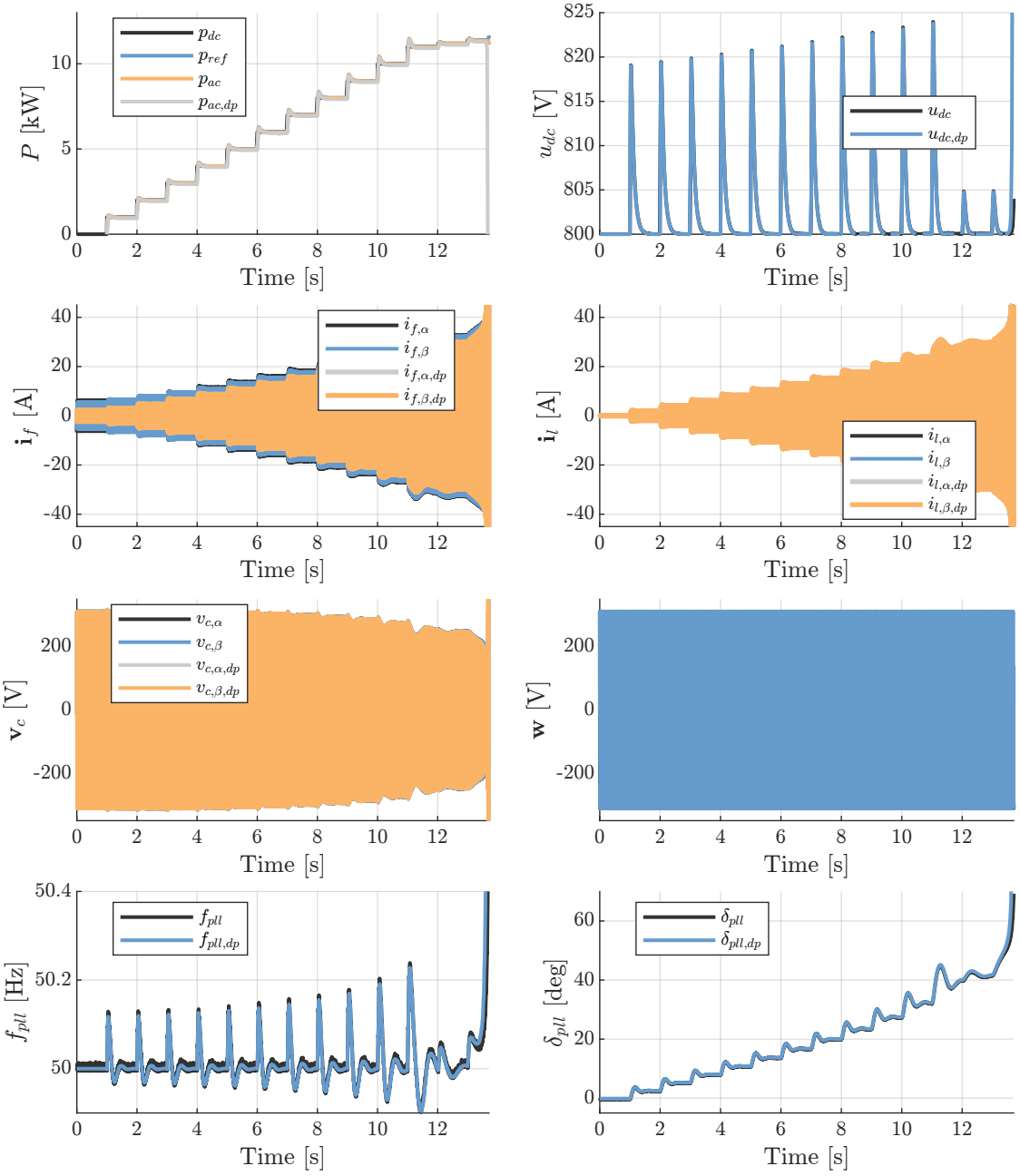

(a) 0–11.6 kW.

Figure 5.8 – Mathematical model validation via hardware-in-the-loop for multiple power steps.

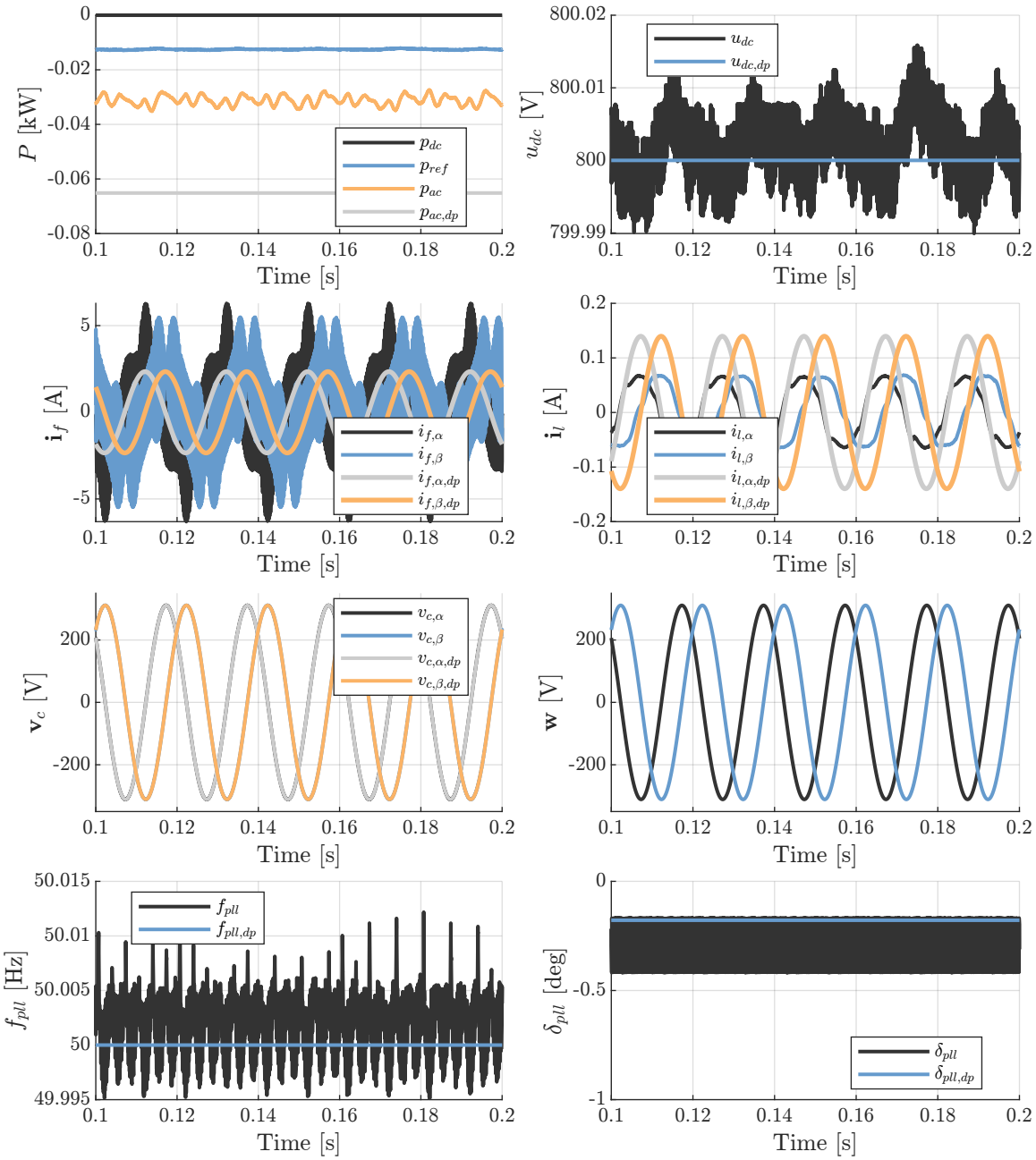

(b) 0 kW Steady State.

Figure 5.8 – Mathematical model validation via hardware-in-the-loop for multiple power steps.

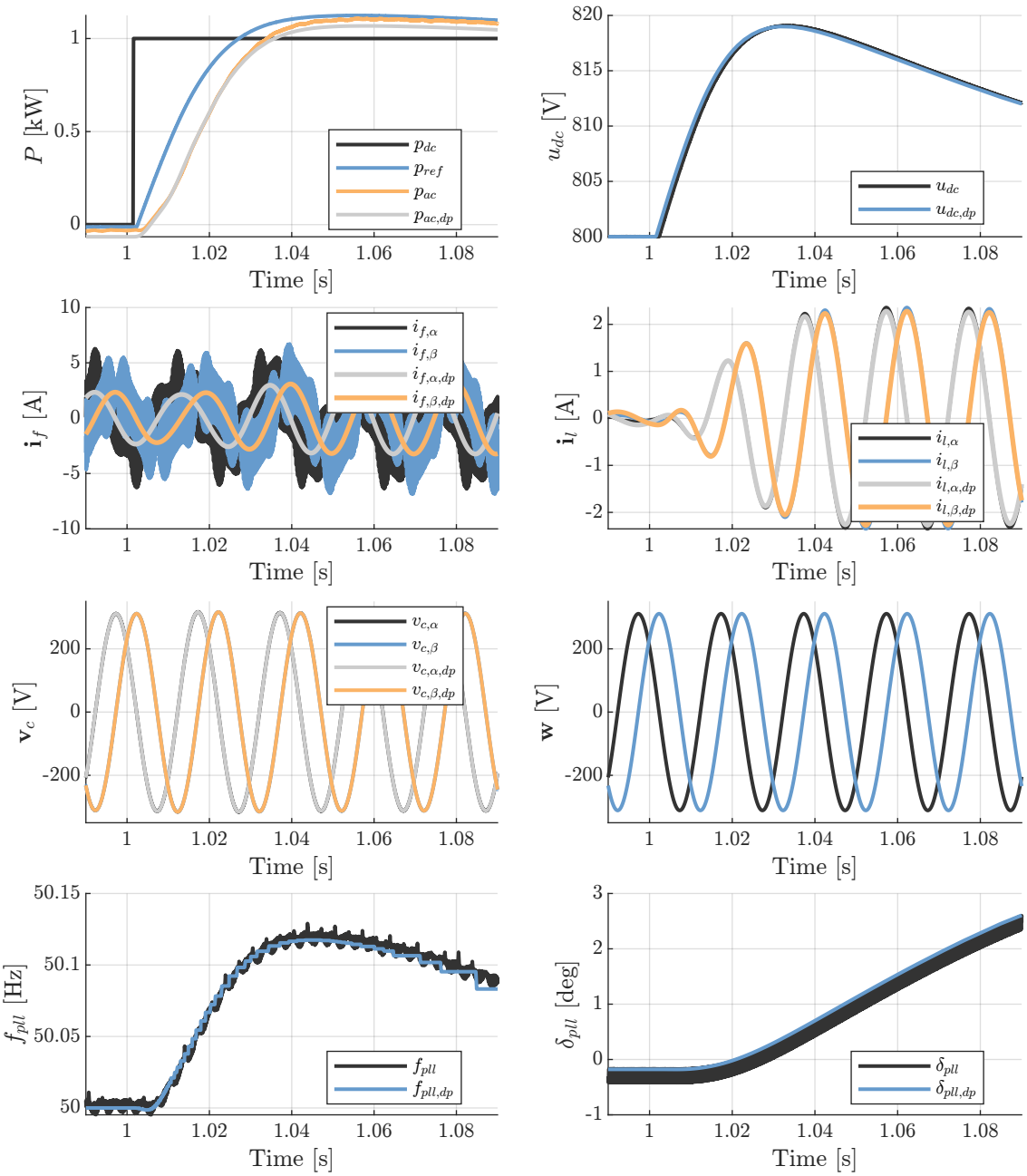

(c) 0–1 kW Power Step.

Figure 5.8 – Mathematical model validation via hardware-in-the-loop for multiple power steps.

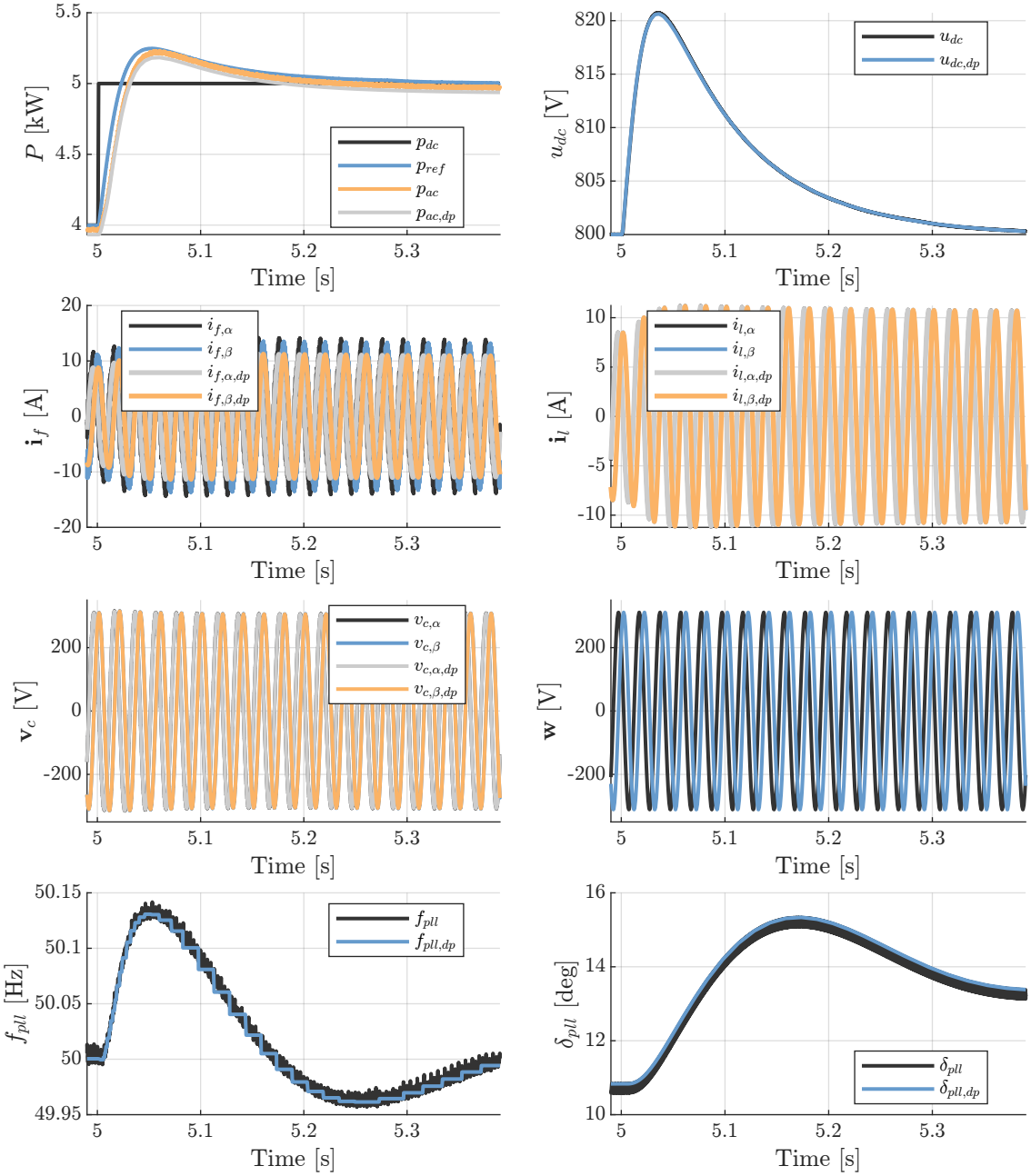

(d) 4–5 kW Power Step.

Figure 5.8 – Mathematical model validation via hardware-in-the-loop for multiple power steps.

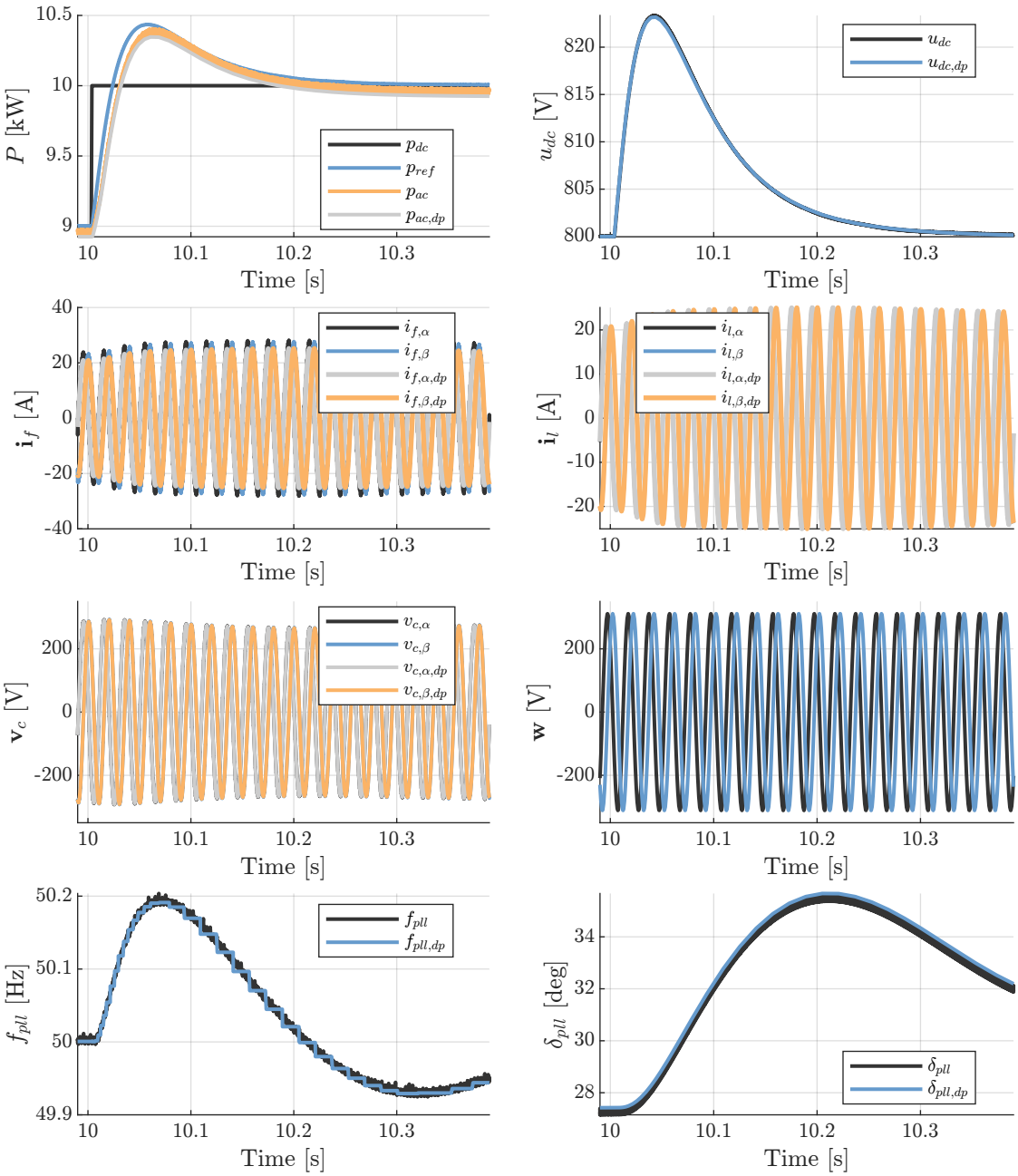

(e) 9–10 kW Power Step.

Figure 5.8 – Mathematical model validation via hardware-in-the-loop for multiple power steps.

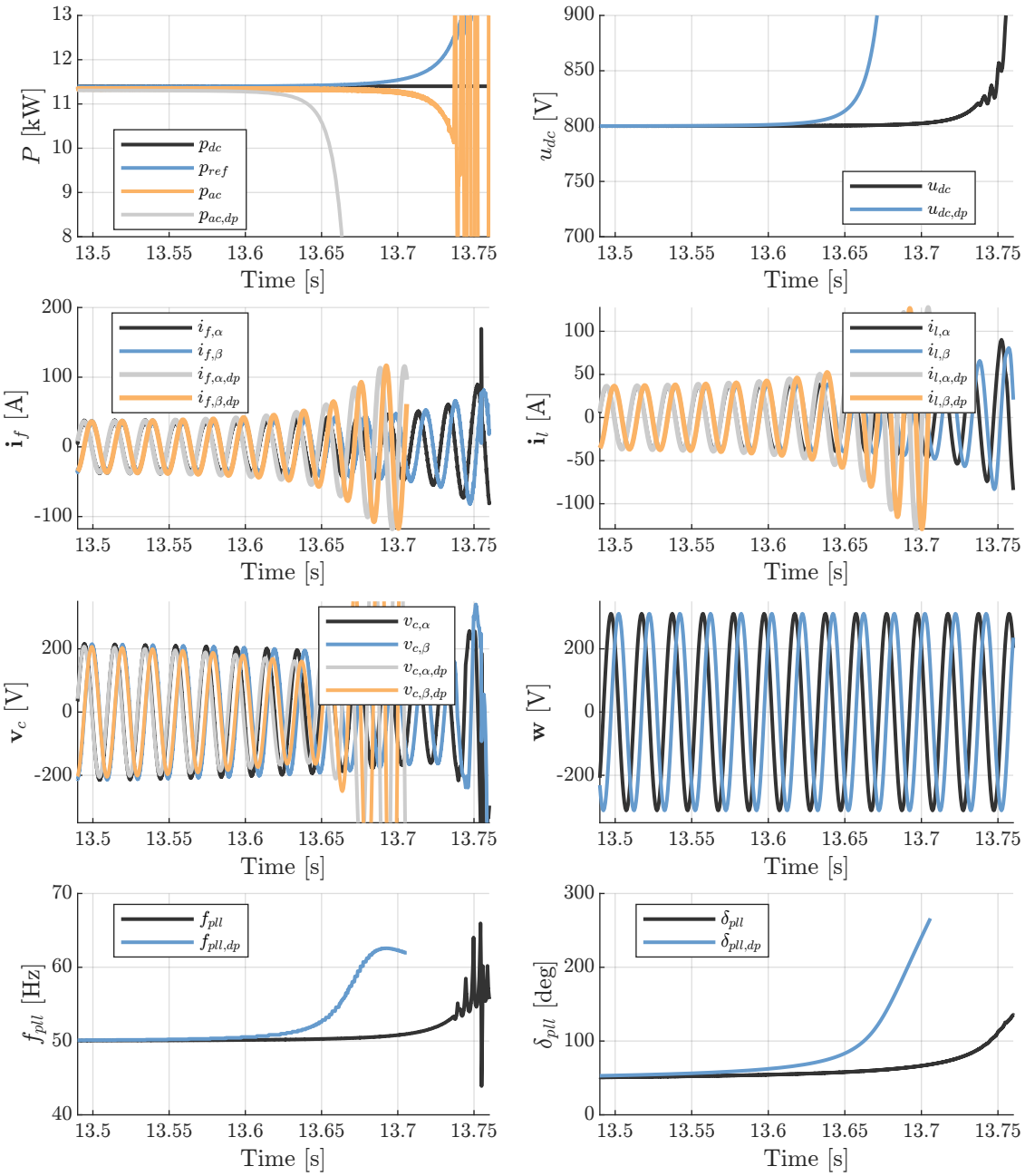

(f) 11.4–11.6 kW Power Step.

Figure 5.8 – Mathematical model validation via hardware-in-the-loop for multiple power steps.

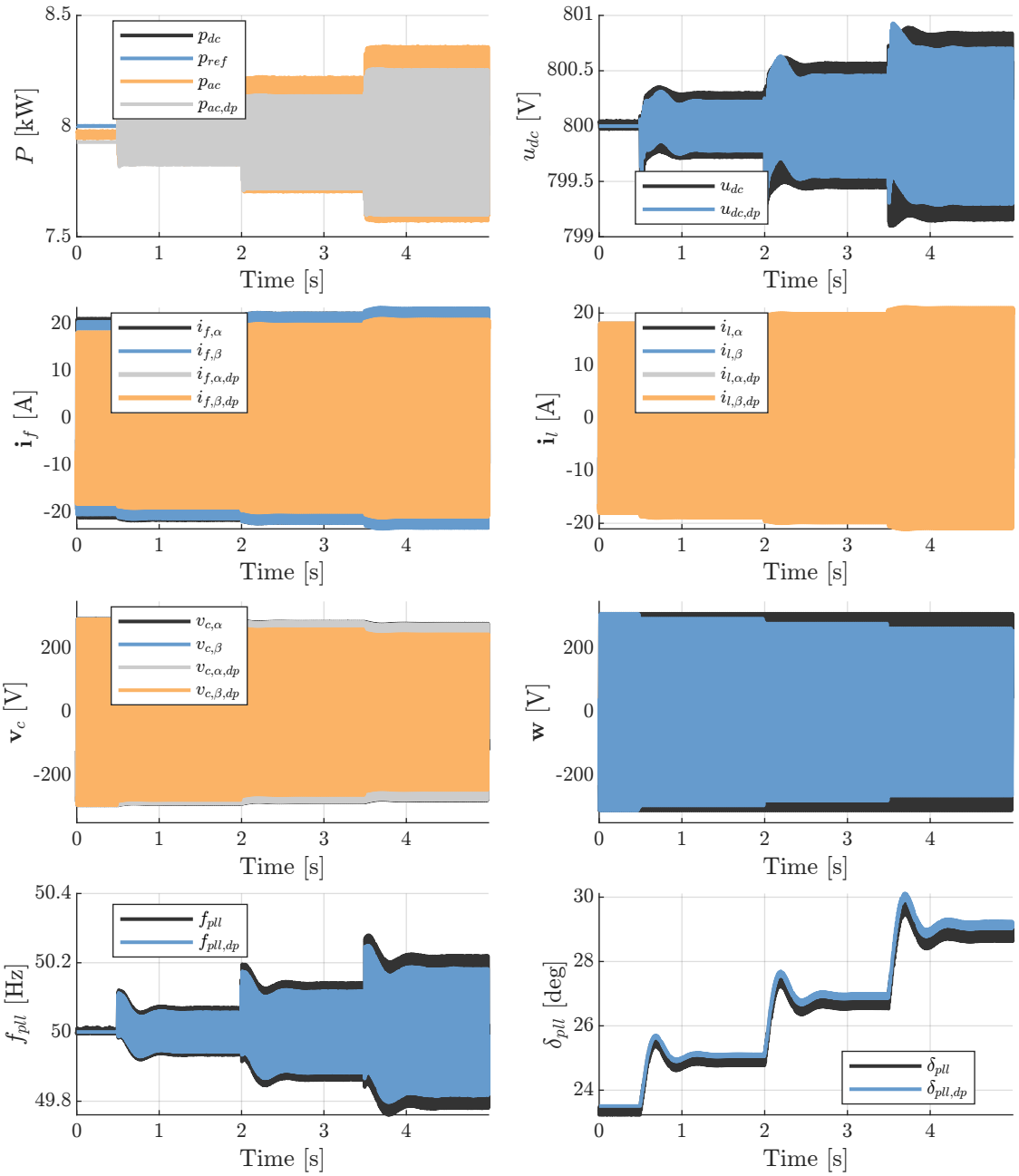

(a) β-axis voltage amplitude steps from 1 p.u. to 0.85 p.u.

Figure 5.9 – Mathematical model validation via hardware-in-the-loop for voltage unbalances.

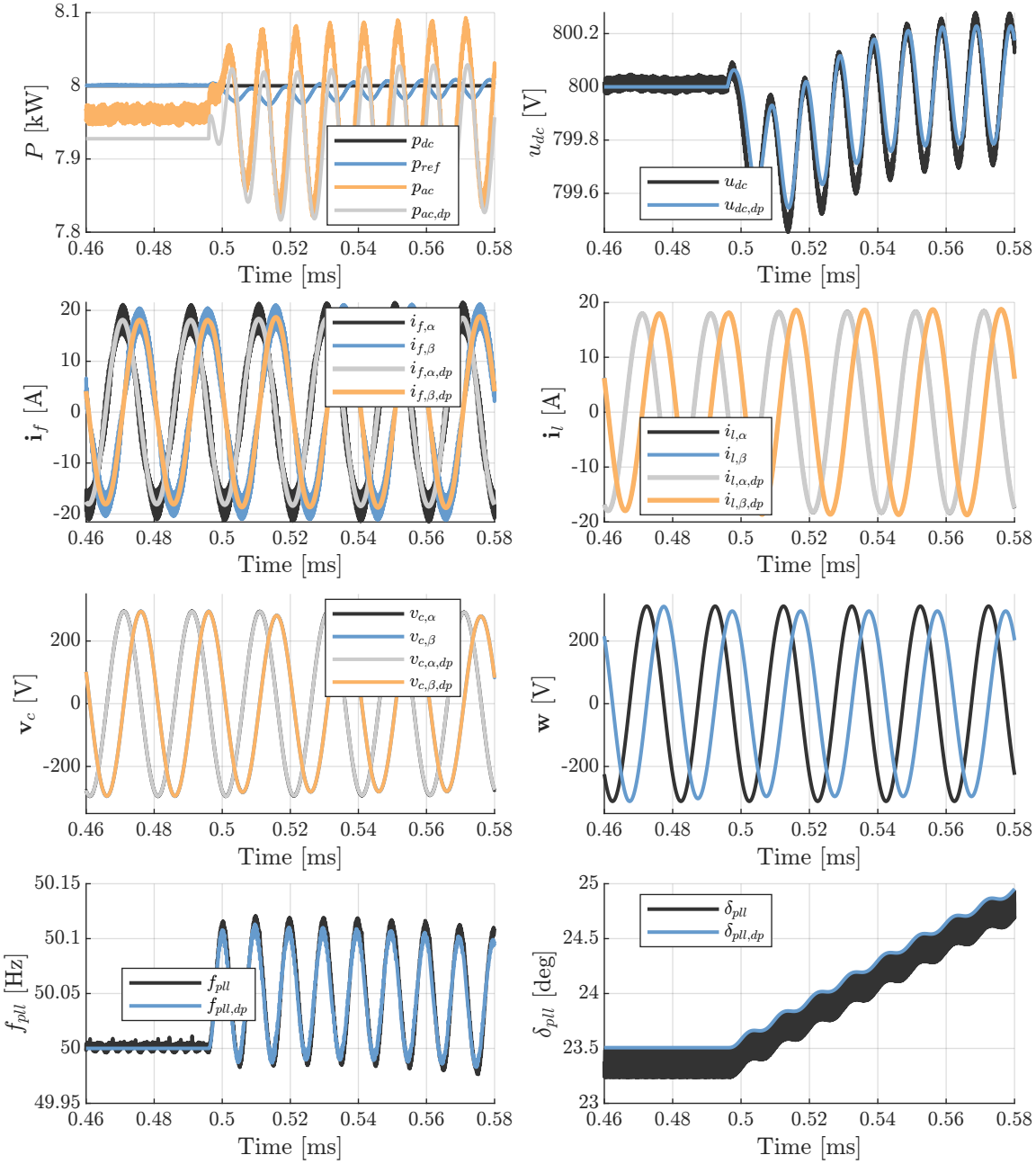

(b) β-axis voltage amplitude step from 1 p.u. to 0.95 p.u.

Figure 5.9 – Mathematical model validation via hardware-in-the-loop for voltage unbalances.

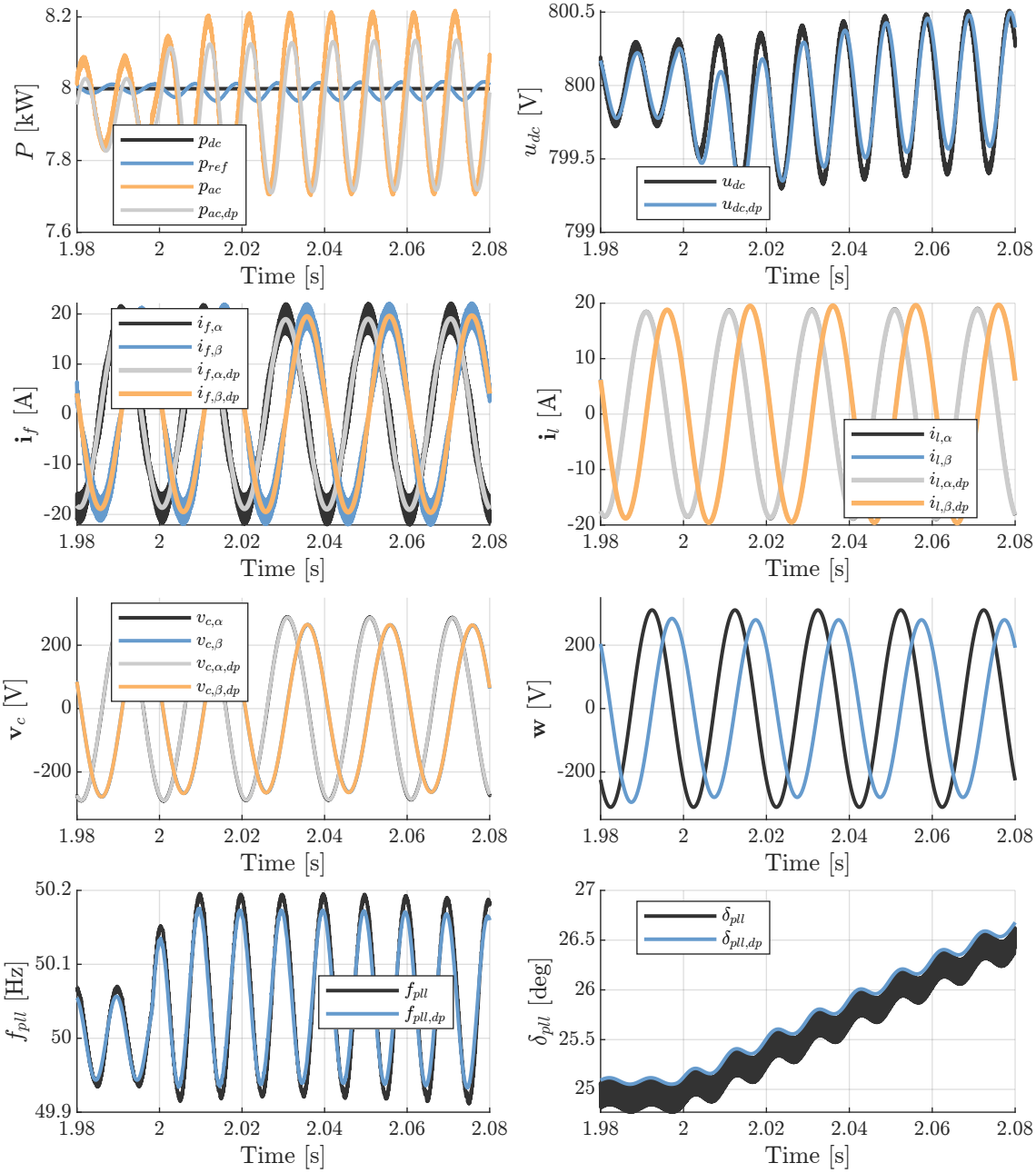

(c) β-axis voltage amplitude step from 0.95 p.u. to 0.9 p.u.

Figure 5.9 – Mathematical model validation via hardware-in-the-loop for voltage unbalances.

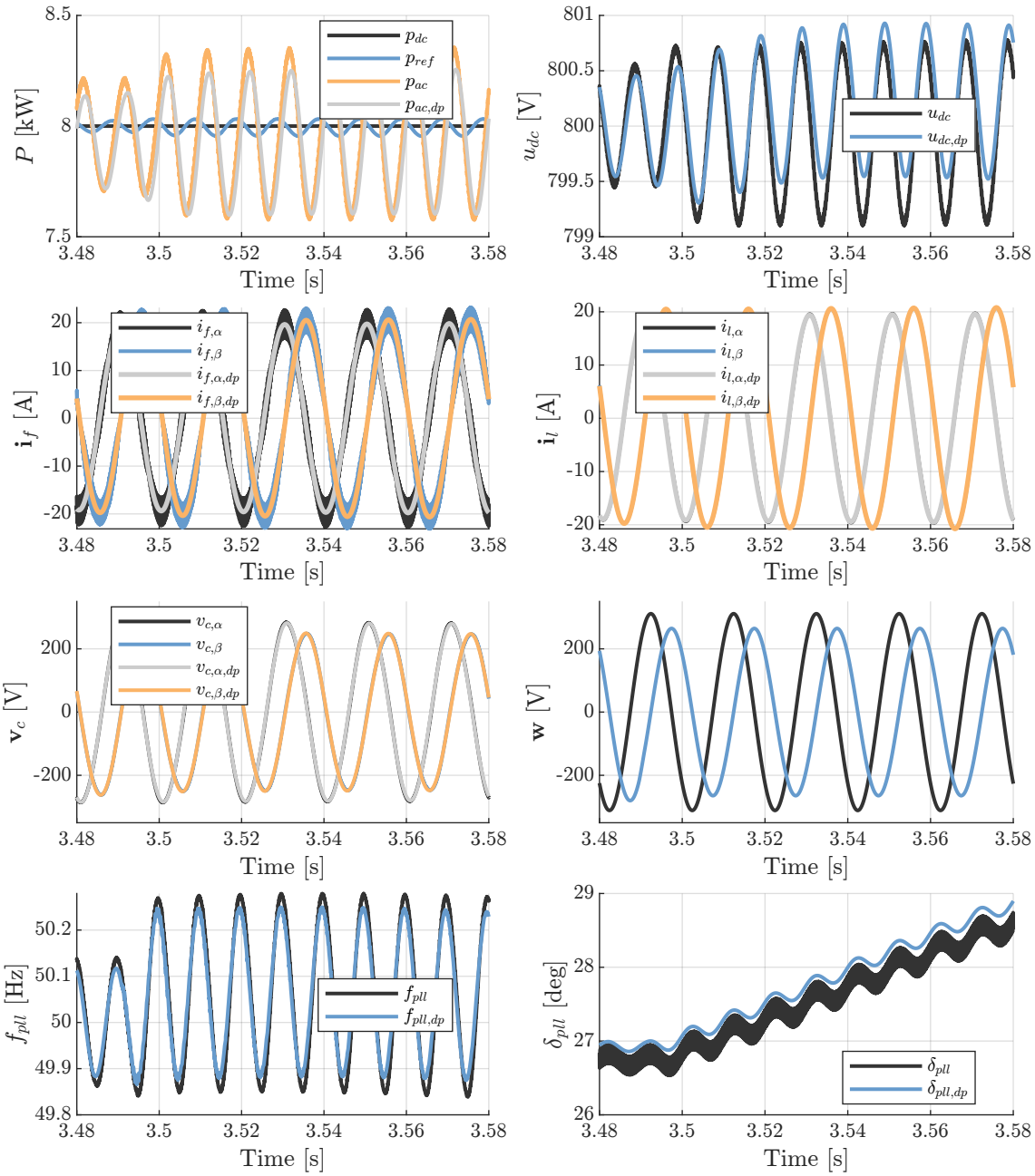

(d) β-axis voltage amplitude step from 0.9 p.u. to 0.85 p.u.

Figure 5.9 – Mathematical model validation via hardware-in-the-loop for voltage unbalances.

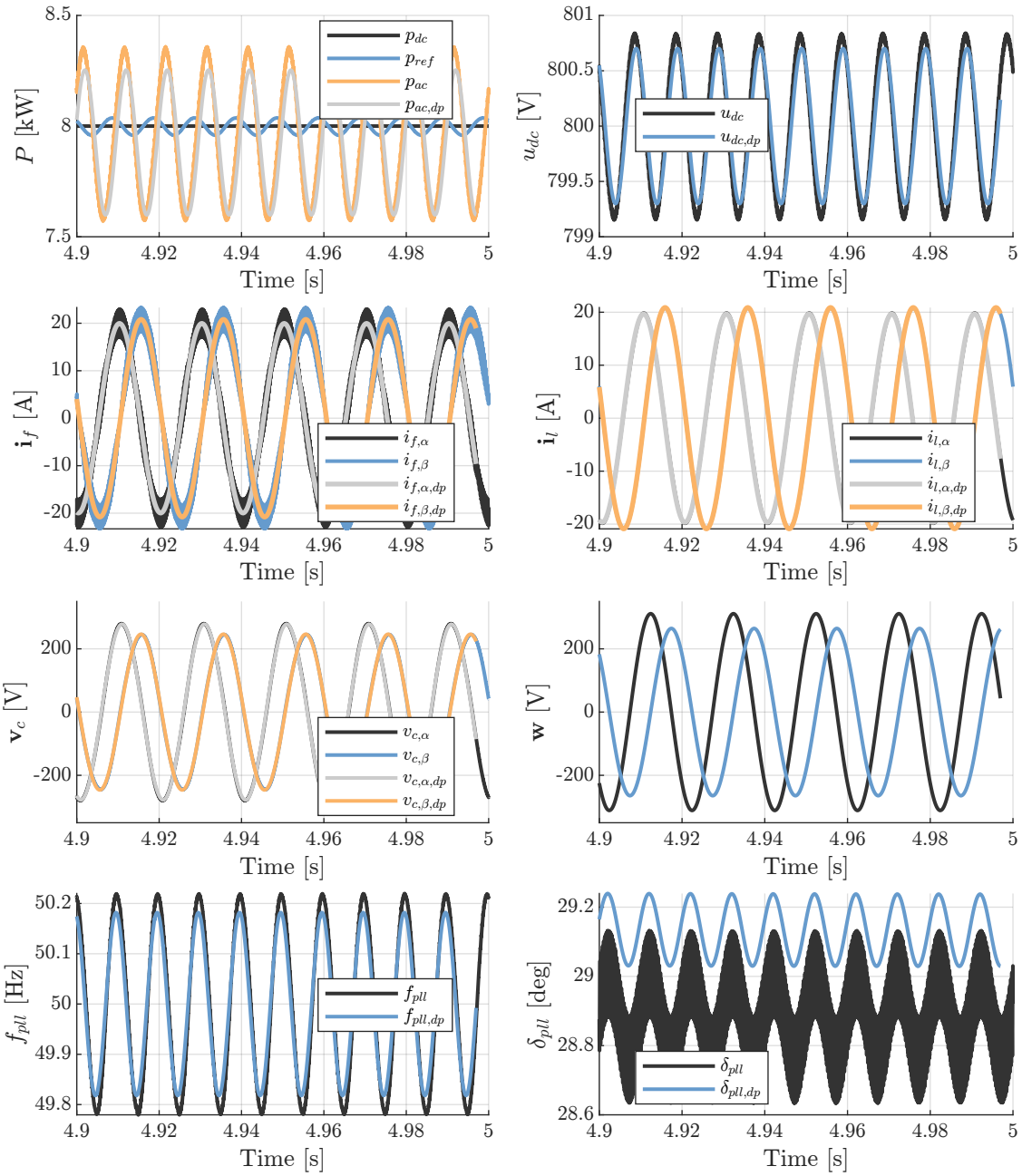

(e) Unbalanced voltage steady state.

Figure 5.9 – Mathematical model validation via hardware-in-the-loop for voltage unbalances.

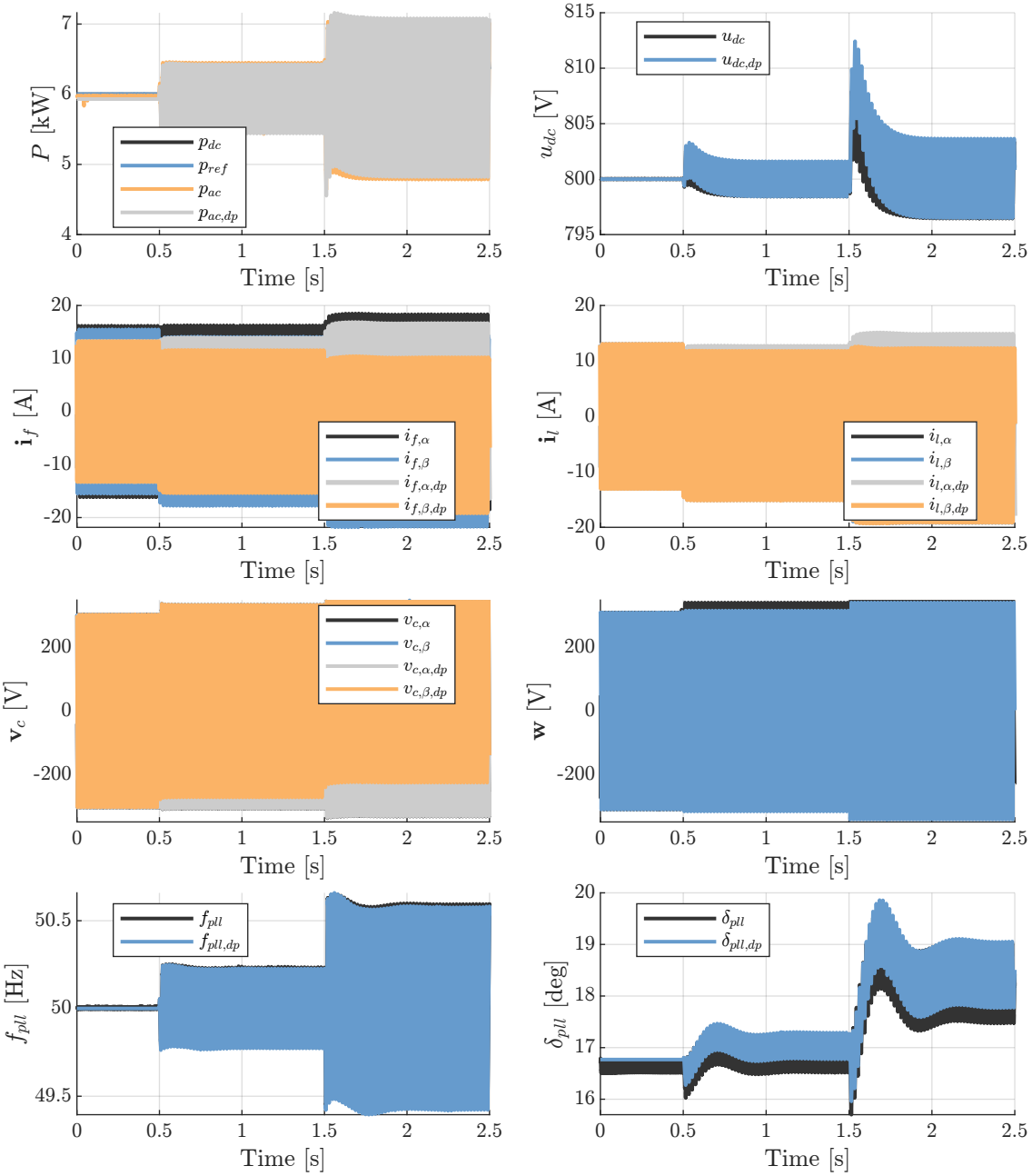

(a) Validation overview.

Figure 5.10 – Mathematical model validation via hardware-in-the-loop for grid voltage 2nd harmonic disturbances.

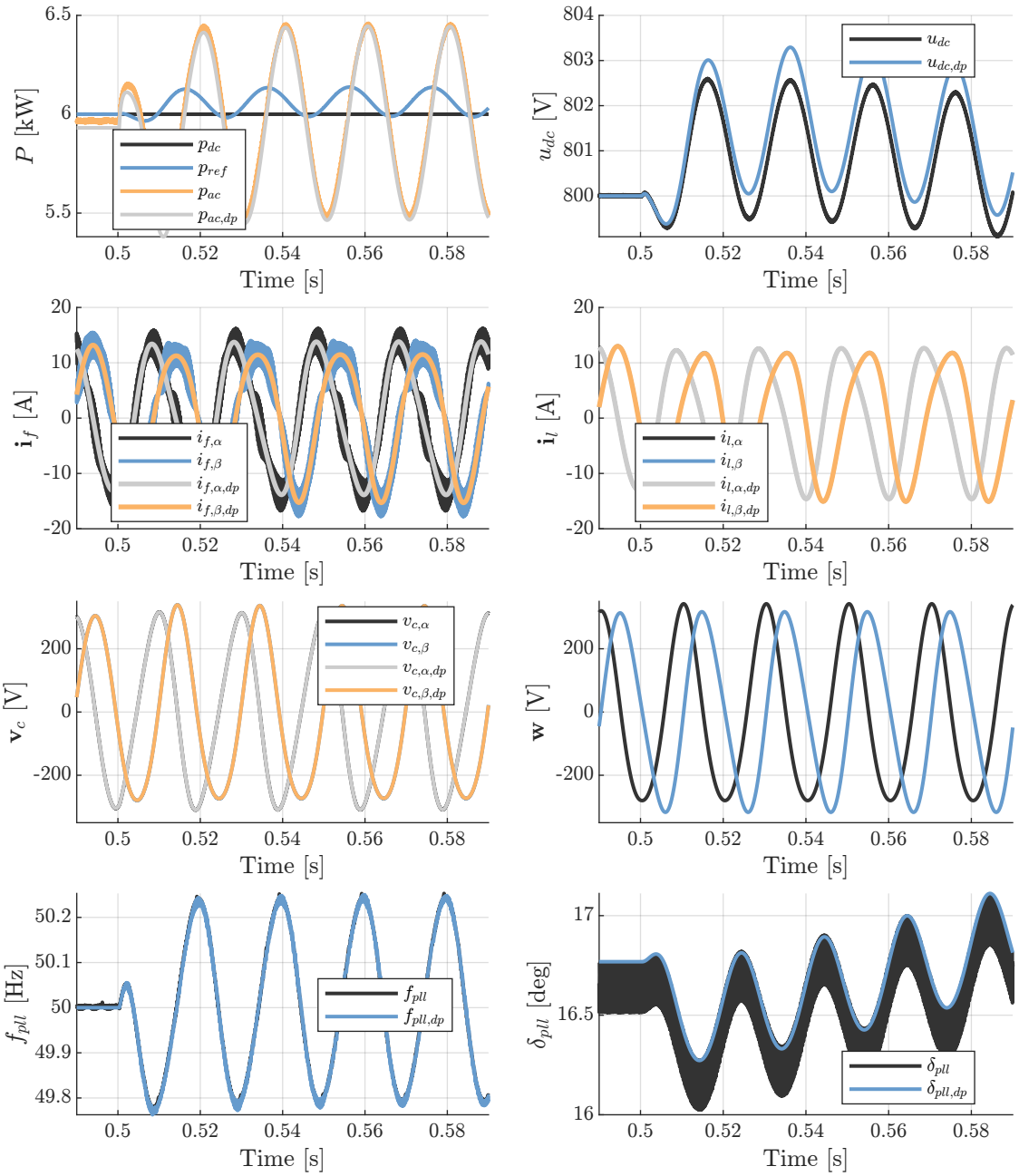

(b) Grid voltage 2nd harmonic amplitude step from 0 p.u. to 0.1 p.u.

Figure 5.10 – Mathematical model validation via hardware-in-the-loop for grid voltage 2nd harmonic disturbances.

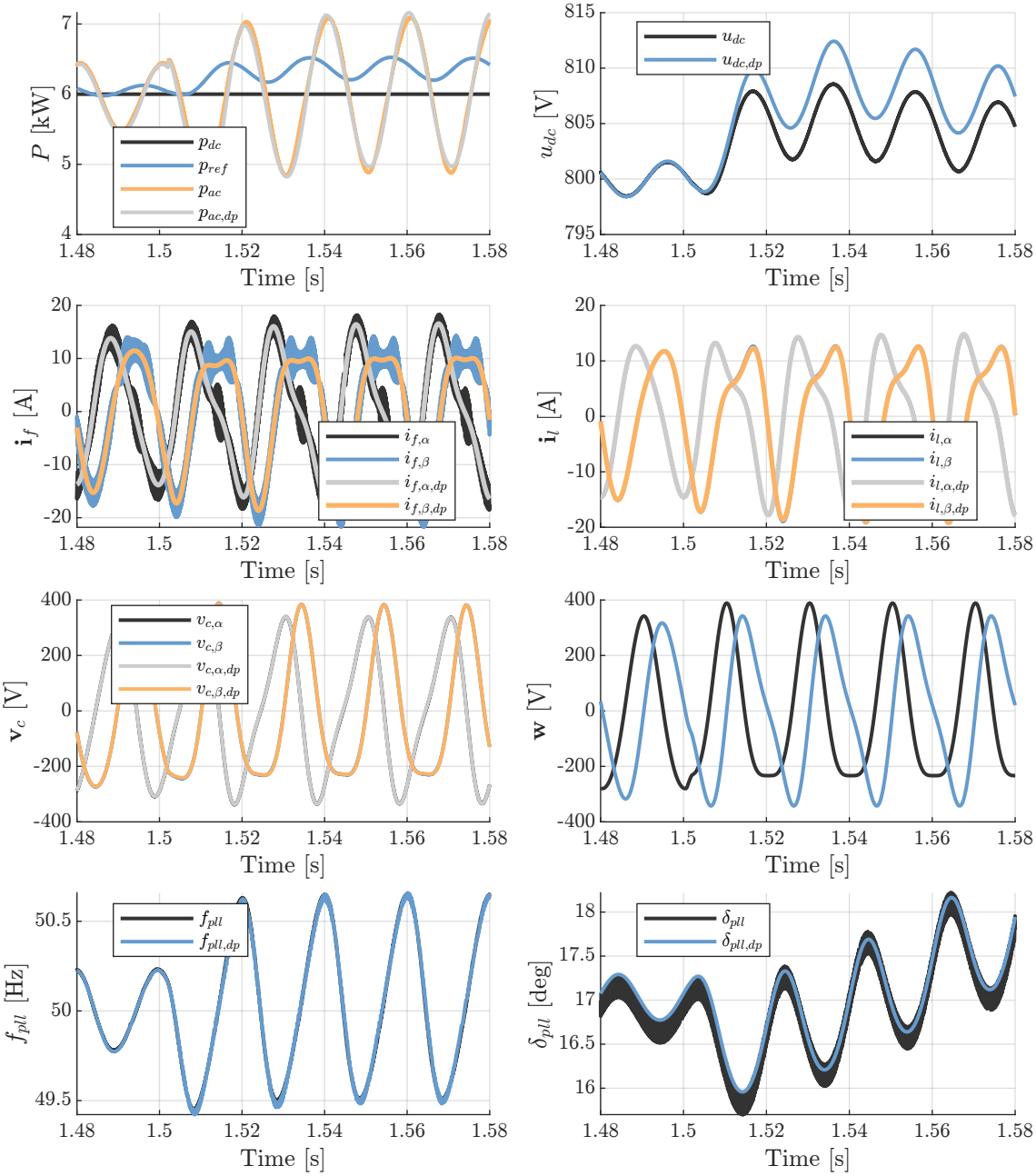

(c) Grid voltage 2nd harmonic amplitude step from 0.1 p.u. to 0.25 p.u.

Figure 5.10 – Mathematical model validation via hardware-in-the-loop for grid voltage 2nd harmonic disturbances.

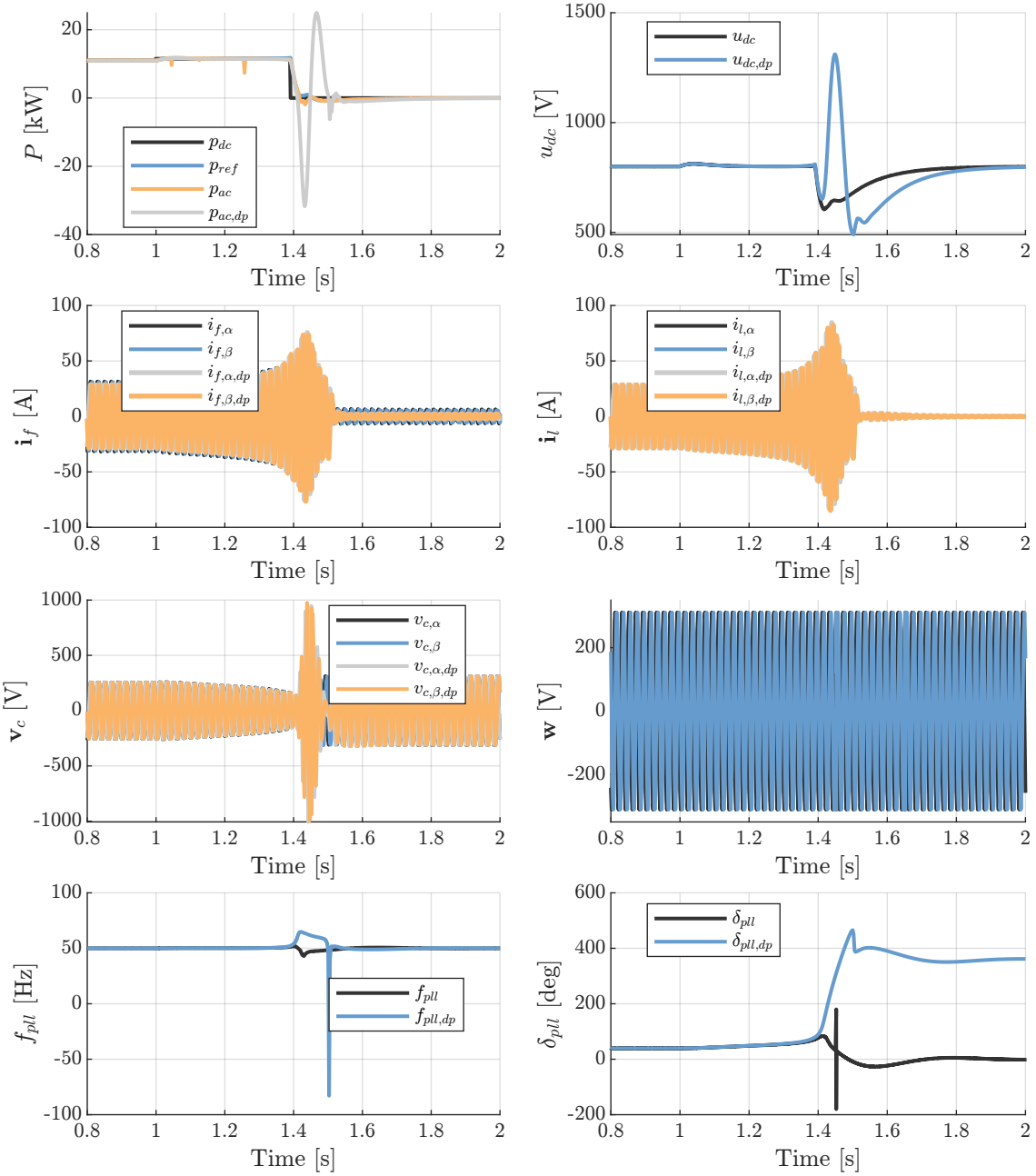

(a) Step from 11–11.5 kW and recovery.

Figure 5.11 – Mathematical model validation via hardware-in-the-loop for the recovery of an unstable point of operation.

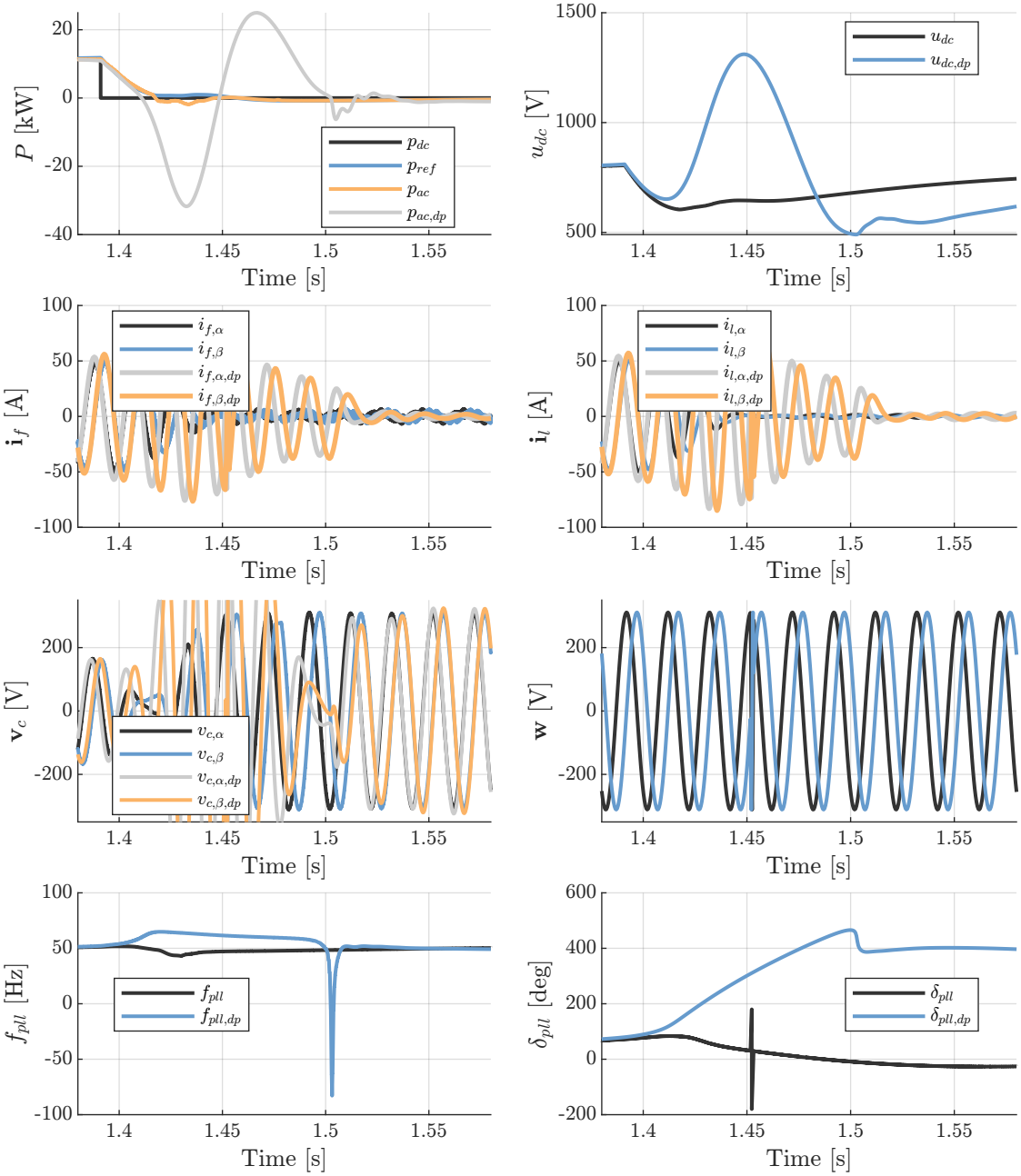

(b) Step form 11.5–0 kW.

Figure 5.11 – Mathematical model validation via hardware-in-the-loop for the recovery of an unstable point of operation.

5.6.2 DC Voltage Control and MAF-PLL

In order to address the harmonic components of the synchronism loop, we can utilize techniques like the MAF-PLL (Moving Average Filter Phase-Locked Loop) with lag compensation. This approach employs a repetitive control strategy, leveraging a moving average filter to effectively eliminate harmonics while achieving similar dynamical performance to the SRF-PLL. Thus, the PLL dynamic equations can be simplified to (5.18), as means of reducing the complexity of the analysis.

For a more accurate description of the PLL controller, the MAF-PI controller can be approximated as

$$\begin{cases} D_t \mathbf{x}_{\text{pll}} = \begin{bmatrix} 0 & 1 \\ 0 & -\dfrac{4}{N_{\text{MAF}} h} \end{bmatrix} \mathbf{x}_{\text{pll}} + \begin{bmatrix} 0 \\ 1 \end{bmatrix} \upsilon_{\text{pll}} \\ y_{\text{pll}} = \begin{bmatrix} \dfrac{4}{N_{\text{MAF}} h} k_{i,\text{pll}} & \dfrac{8}{N_{\text{MAF}} h} k_{p,\text{pll}} - k_{i,\text{pll}} \end{bmatrix} \mathbf{x}_{\text{pll}} - k_{p,\text{pll}} \upsilon_{\text{pll}}, \end{cases} \tag{5.50}$$

where h is the sampling time and N_{MAF} is the MAF buffer length. This approximation is made under the assumption that the phase-lag compensator does not provide exact compensation, with coefficients related to the sampling time and the number of samples in the controller's dynamics enabling a more accurate representation of the loss of phase given by the moving-average filter.

The dynamic model is validated in Figure 5.12 for grid voltage unbalances and in Figure 5.13 for harmonic distortions on the grid voltages. These validation figures demonstrate the accuracy of the model in capturing the behavior of the system under both unbalanced conditions and harmonic distortions in the grid voltages, enabling the use of these models in the converter stability assessment.

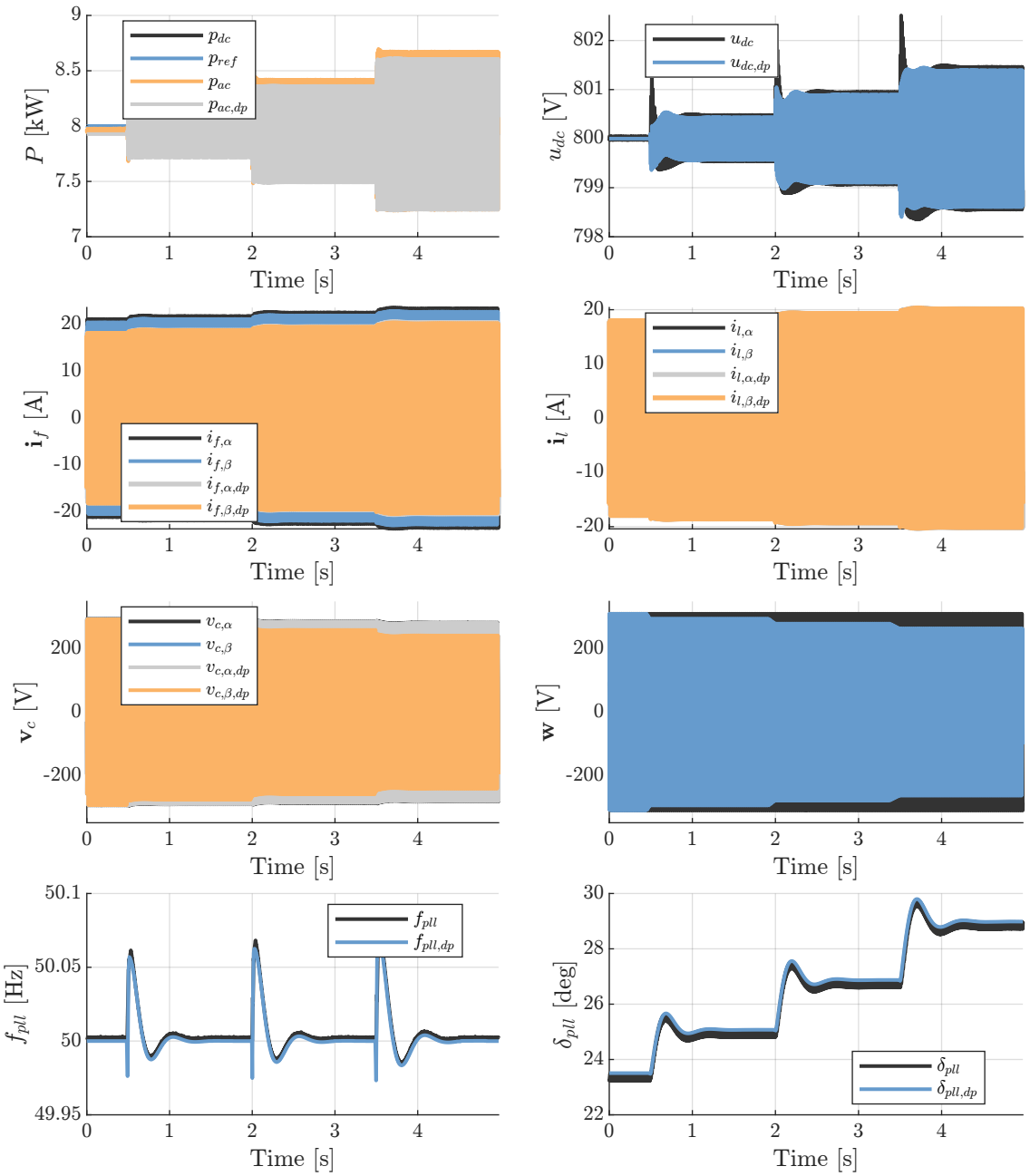

(a) β-axis voltage amplitude steps from 1 p.u. to 0.85 p.u.

Figure 5.12 – Mathematical model validation of the simplified model through hardware-in-the-loop for voltage unbalance.

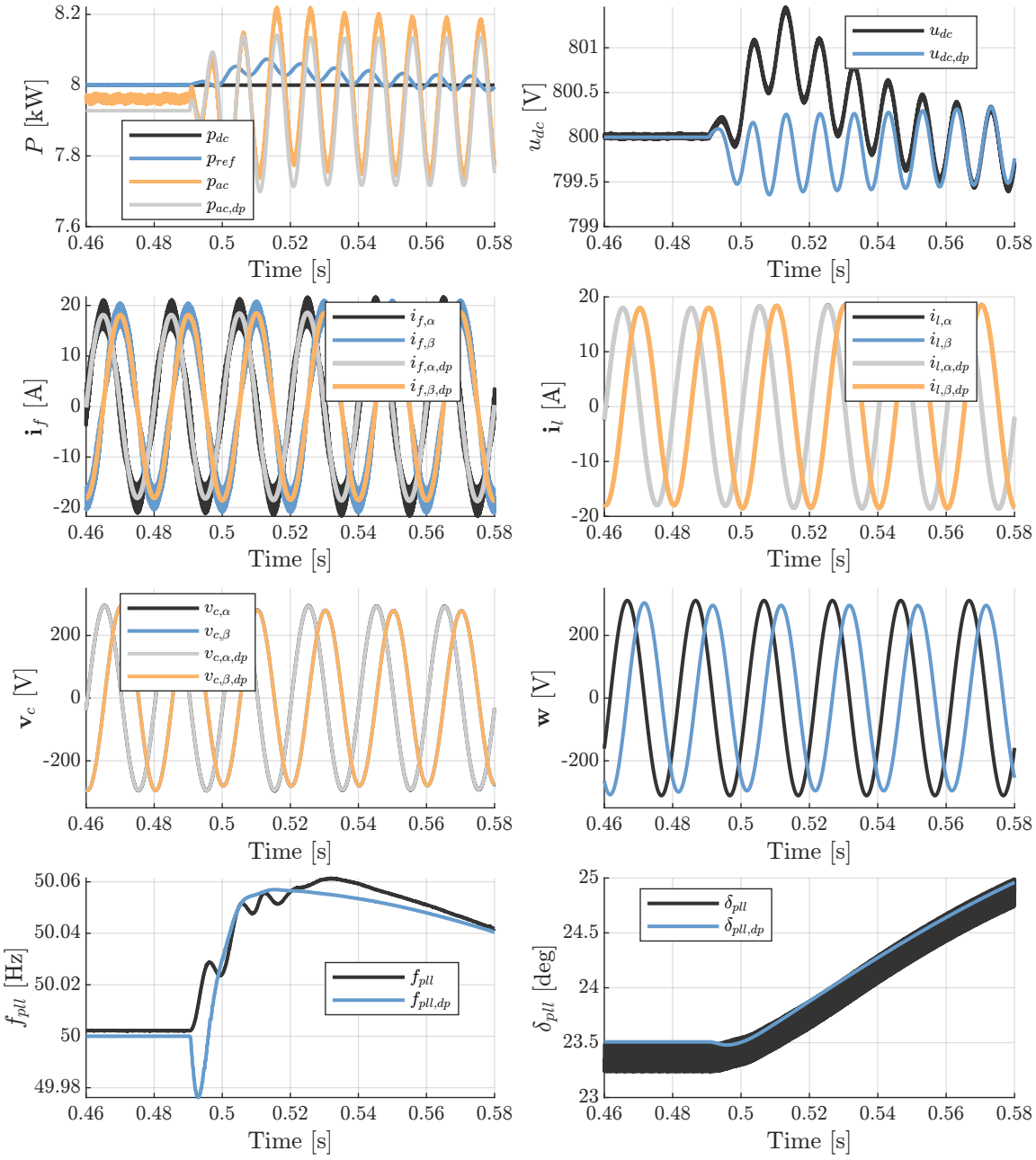

(b) β-axis voltage amplitude step from 1 p.u. to 0.95 p.u.

Figure 5.12 – Mathematical model validation of the simplified model through hardware-in-the-loop for voltage unbalance.

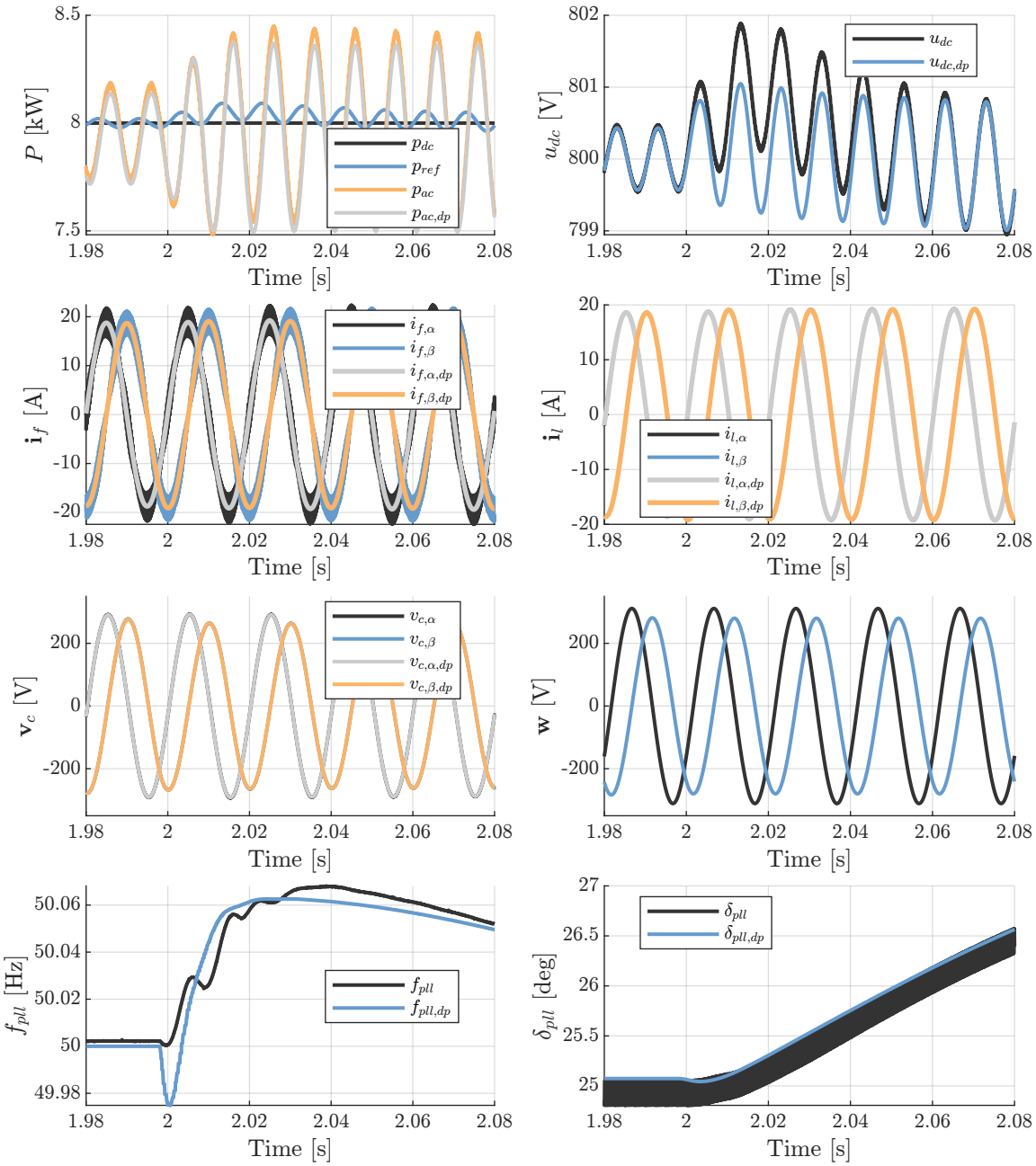

(c) β-axis voltage amplitude step from 0.95 p.u. to 0.9 p.u.

Figure 5.12 – Mathematical model validation of the simplified model through hardware-in-the-loop for voltage unbalance.

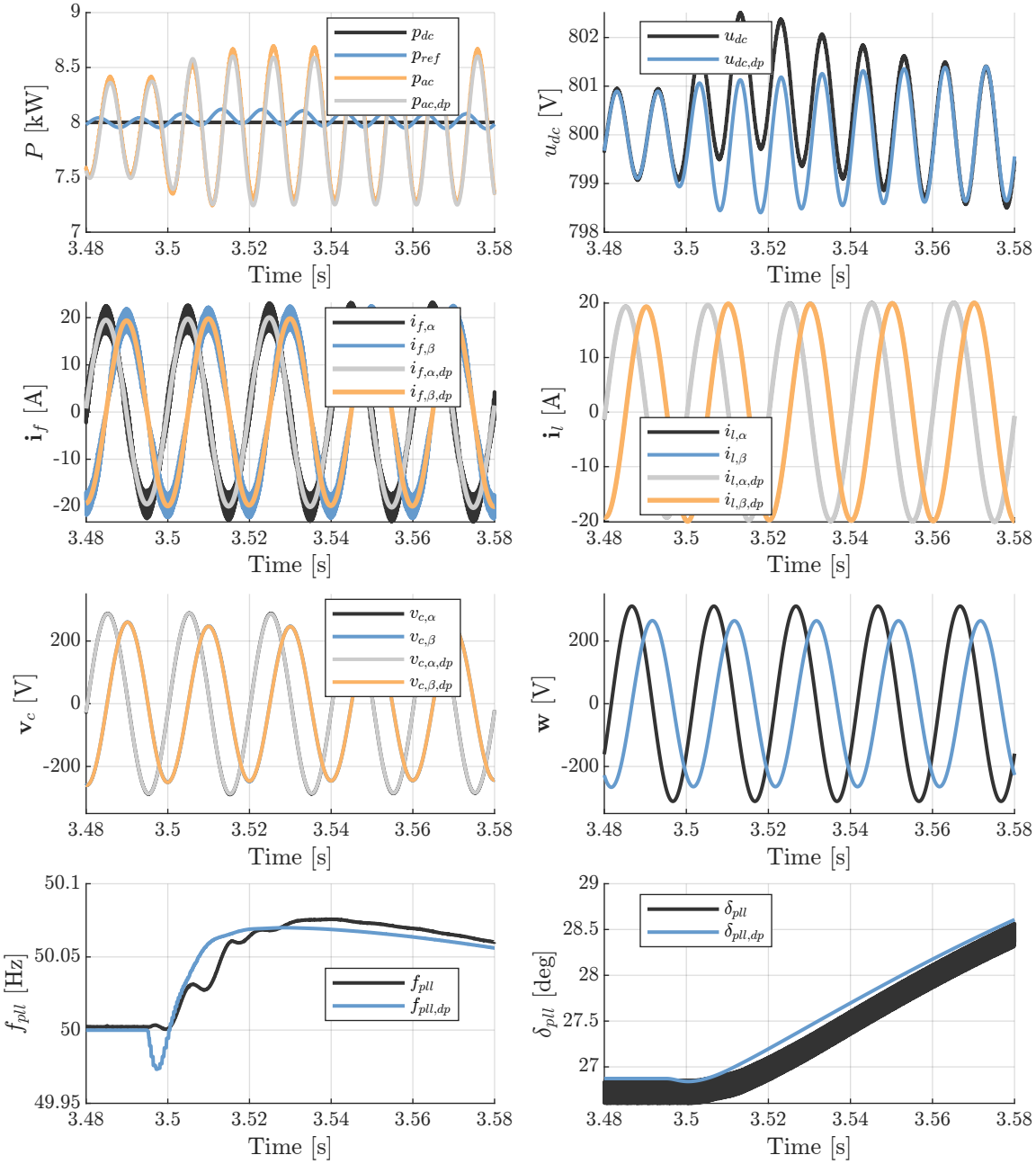

(d) β-axis voltage amplitude step from 0.9 p.u. to 0.85 p.u.

Figure 5.12 – Mathematical model validation of the simplified model through hardware-in-the-loop for voltage unbalance.

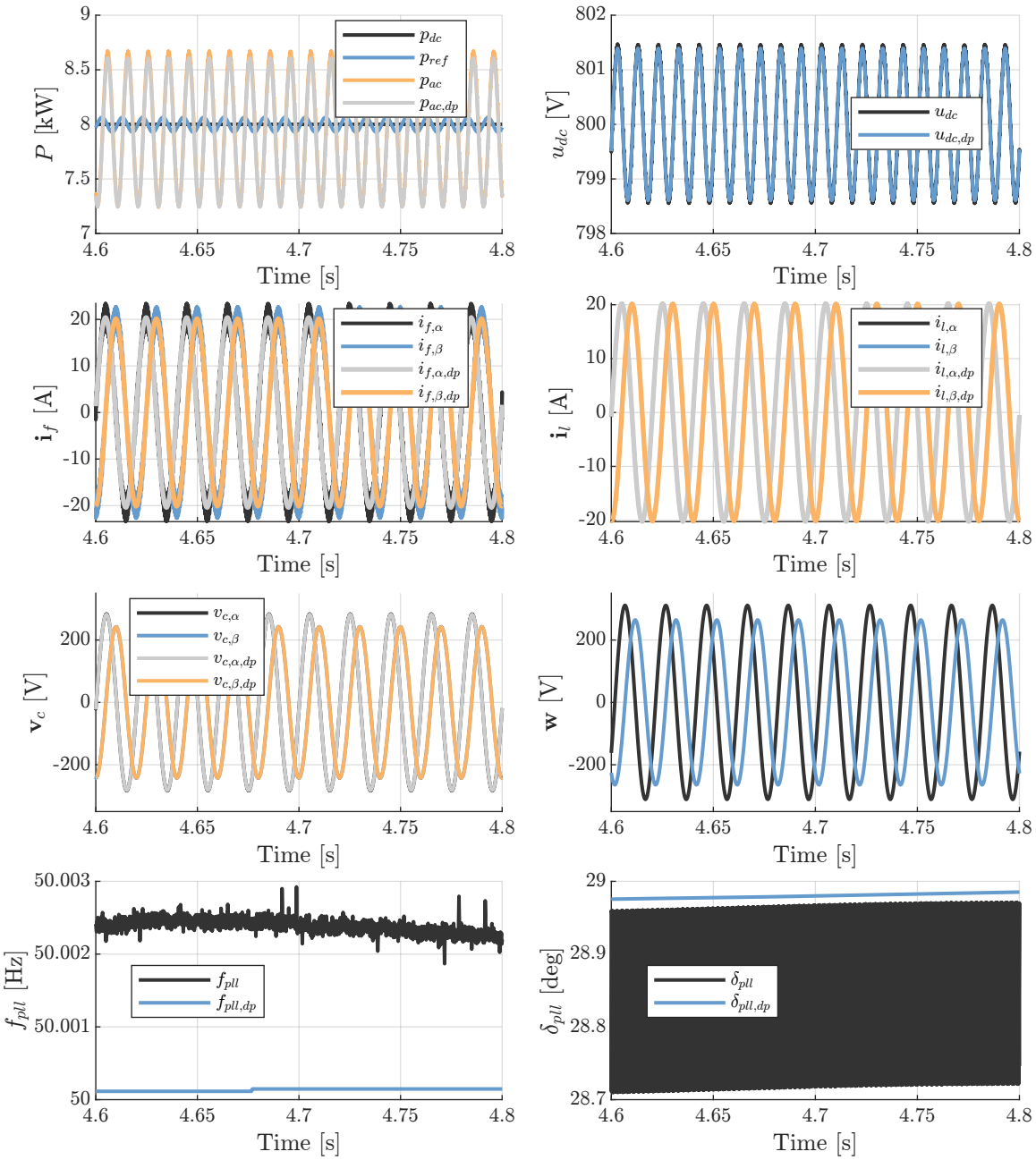

(e) Unbalanced voltage steady state.

Figure 5.12 – Mathematical model validation of the simplified model through hardware-in-the-loop for voltage unbalance.

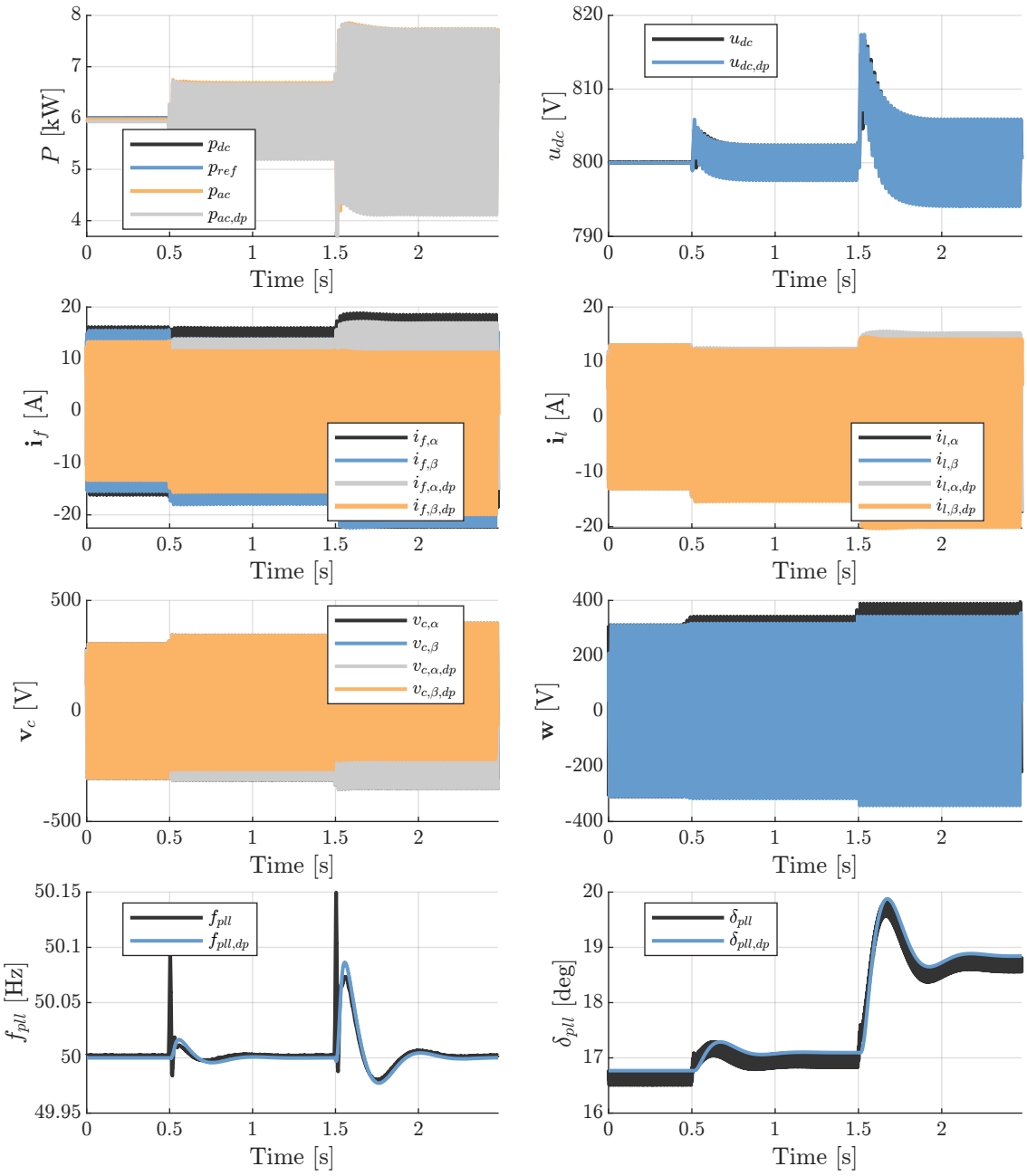

(a)

Figure 5.13 – Mathematical model validation via hardware-in-the-loop for grid voltage 2nd harmonic disturbances.

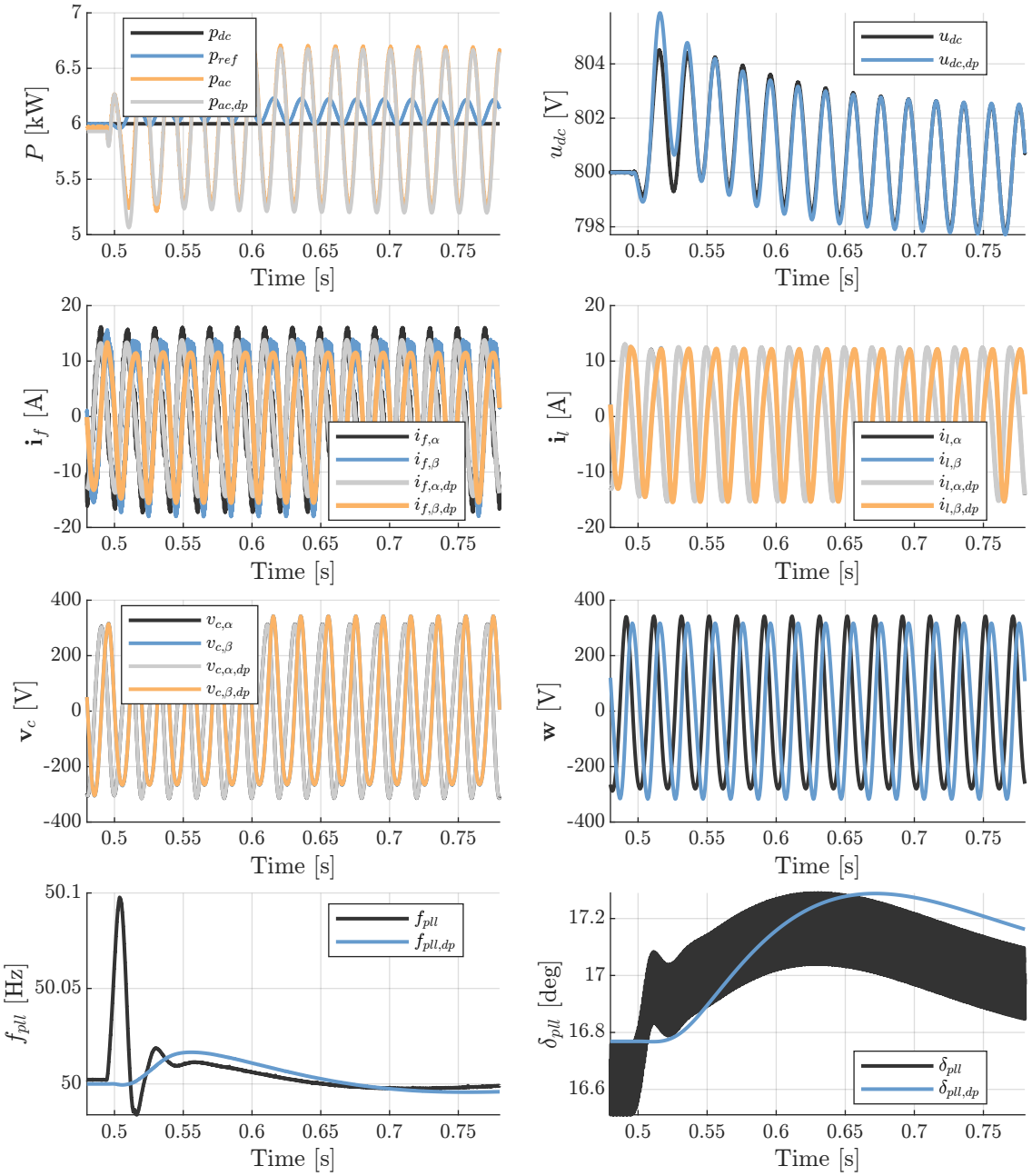

(b) Grid voltage 2nd harmonic amplitude step from 0 p.u. to 0.1 p.u.

Figure 5.13 – Mathematical model validation via hardware-in-the-loop for grid voltage 2nd harmonic disturbances.

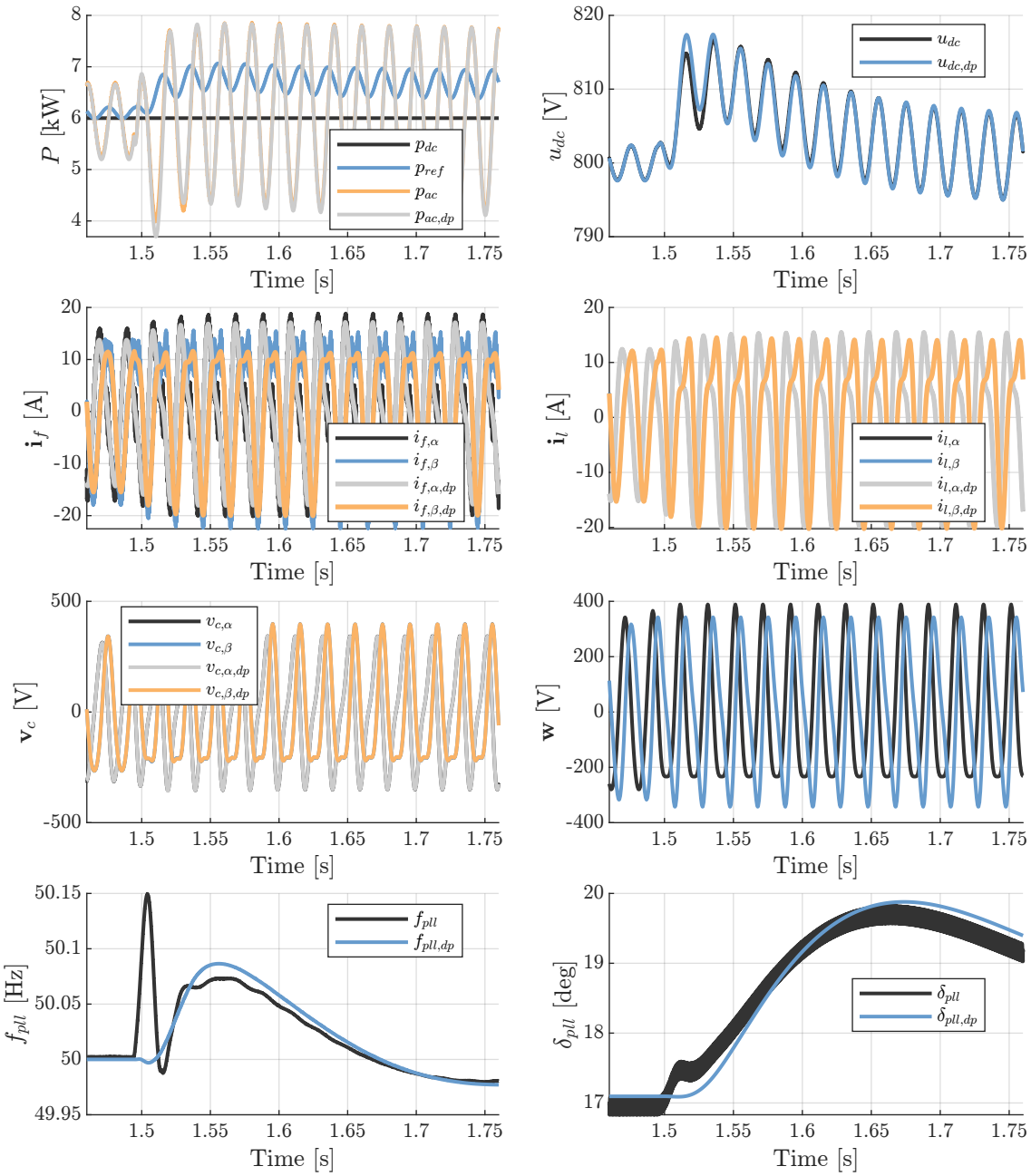

(c) Grid voltage 2nd harmonic amplitude step from 0.1 p.u. to 0.25 p.u.

Figure 5.13 – Mathematical model validation via hardware-in-the-loop for grid voltage 2nd harmonic disturbances.

5.6.3 AC Voltage Control

To handle the varying reactive power processed by the power converter and its impact on the ac bus voltage, a PI controller was implemented to regulate the RMS value of the fundamental component. This verification aims to investigate the interaction between dc and ac control loops.

The validation of the proposed model is depicted in Figure 5.14, with special focus on Figure 5.14.d, which illustrates an unstable condition in the absence of voltage control. This observation highlights the importance of considering both control loops in the stability assessment. Furthermore, it highlights the interplay between active and reactive power and their relationship with the system stability.

The mathematical models are based on the simplified PLL model due to the presence of the MAF-PLL, in accordance with model validations previously presented.

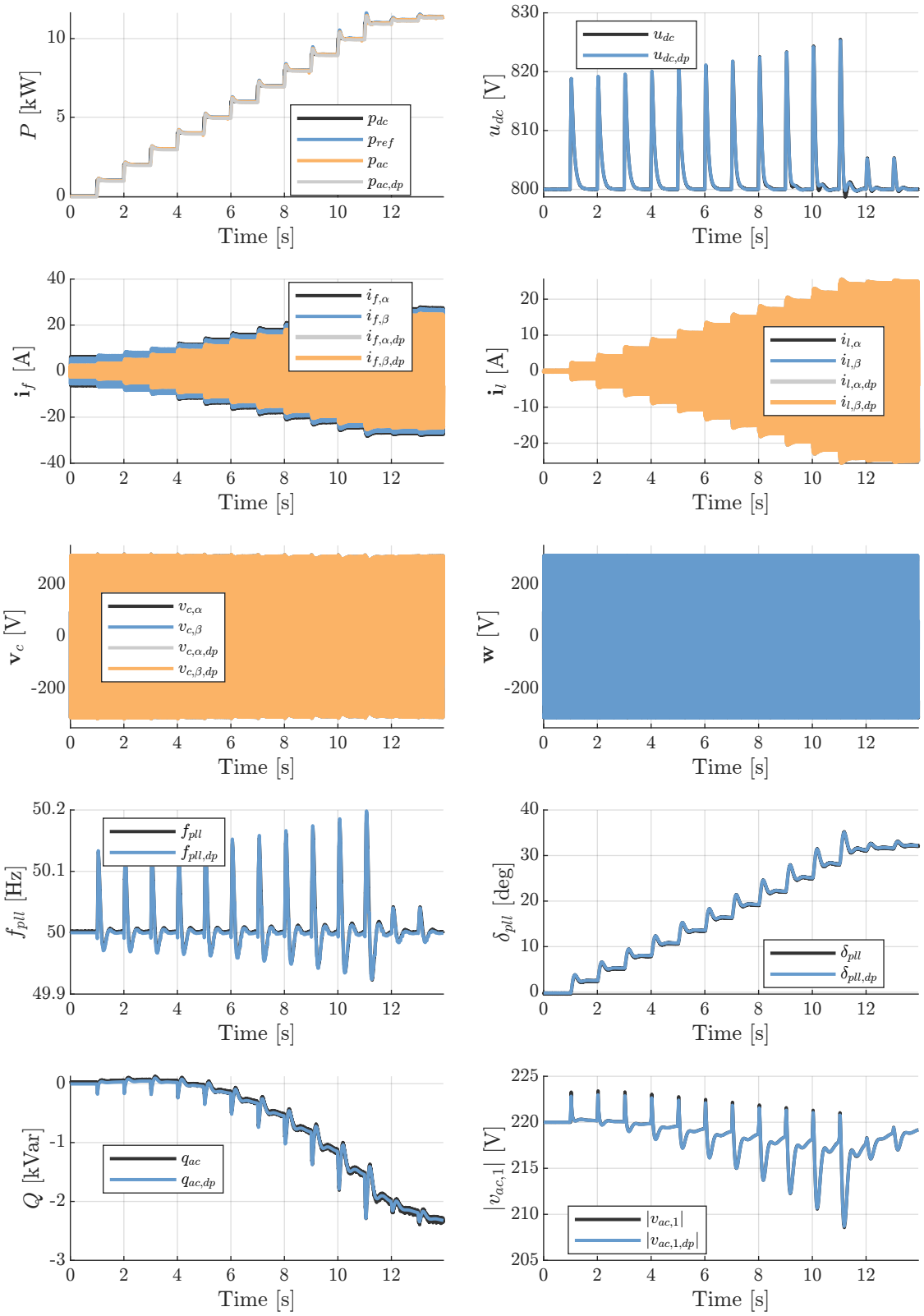

(a) 0–11.4 kW Power Step

Figure 5.14 – Mathematical model validation via hardware-in-the-loop of the grid model with ac bus voltage control.

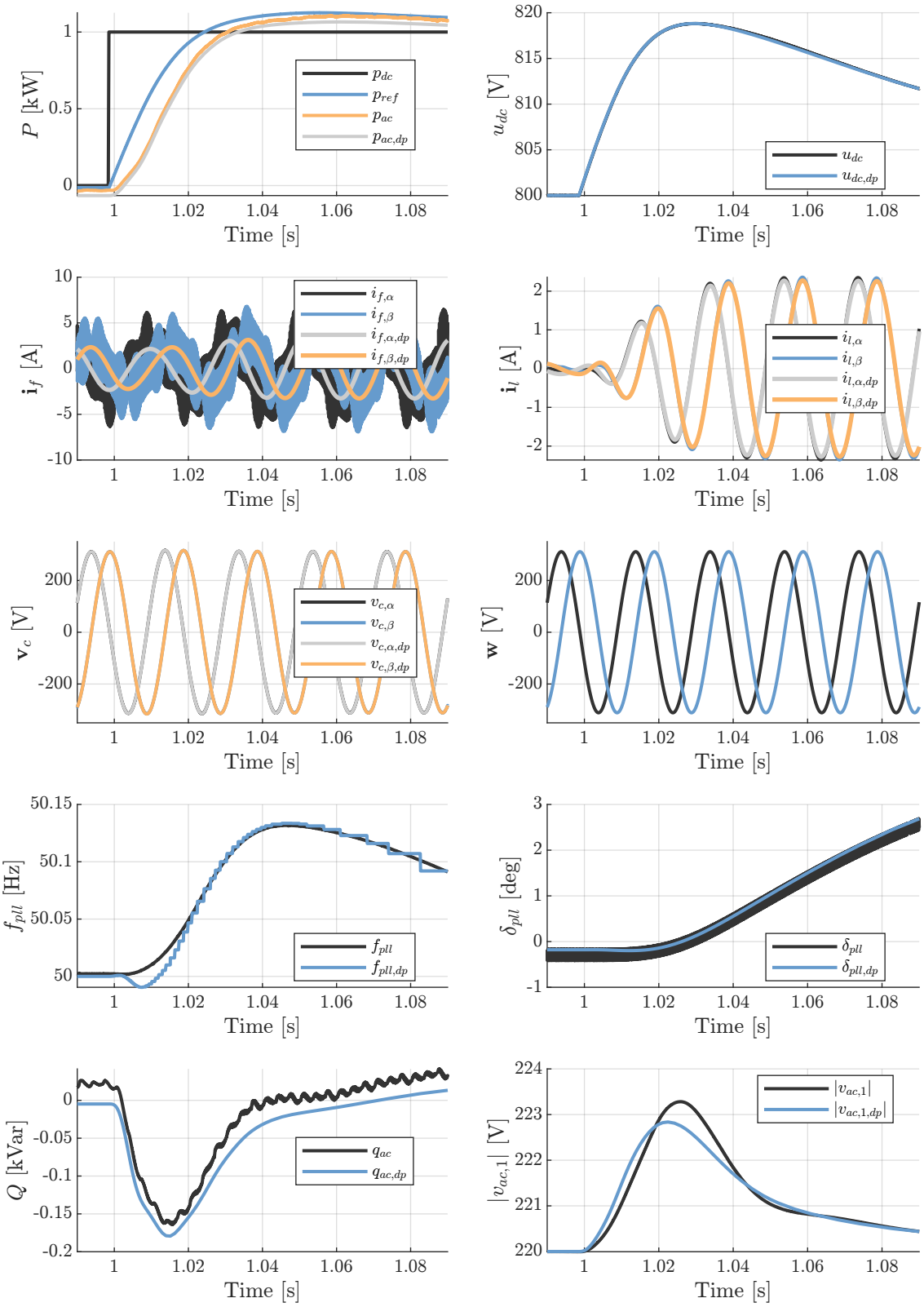

(b) 0–1 kW Power Step

Figure 5.14 – Mathematical model validation via hardware-in-the-loop of the grid model with ac bus voltage control.

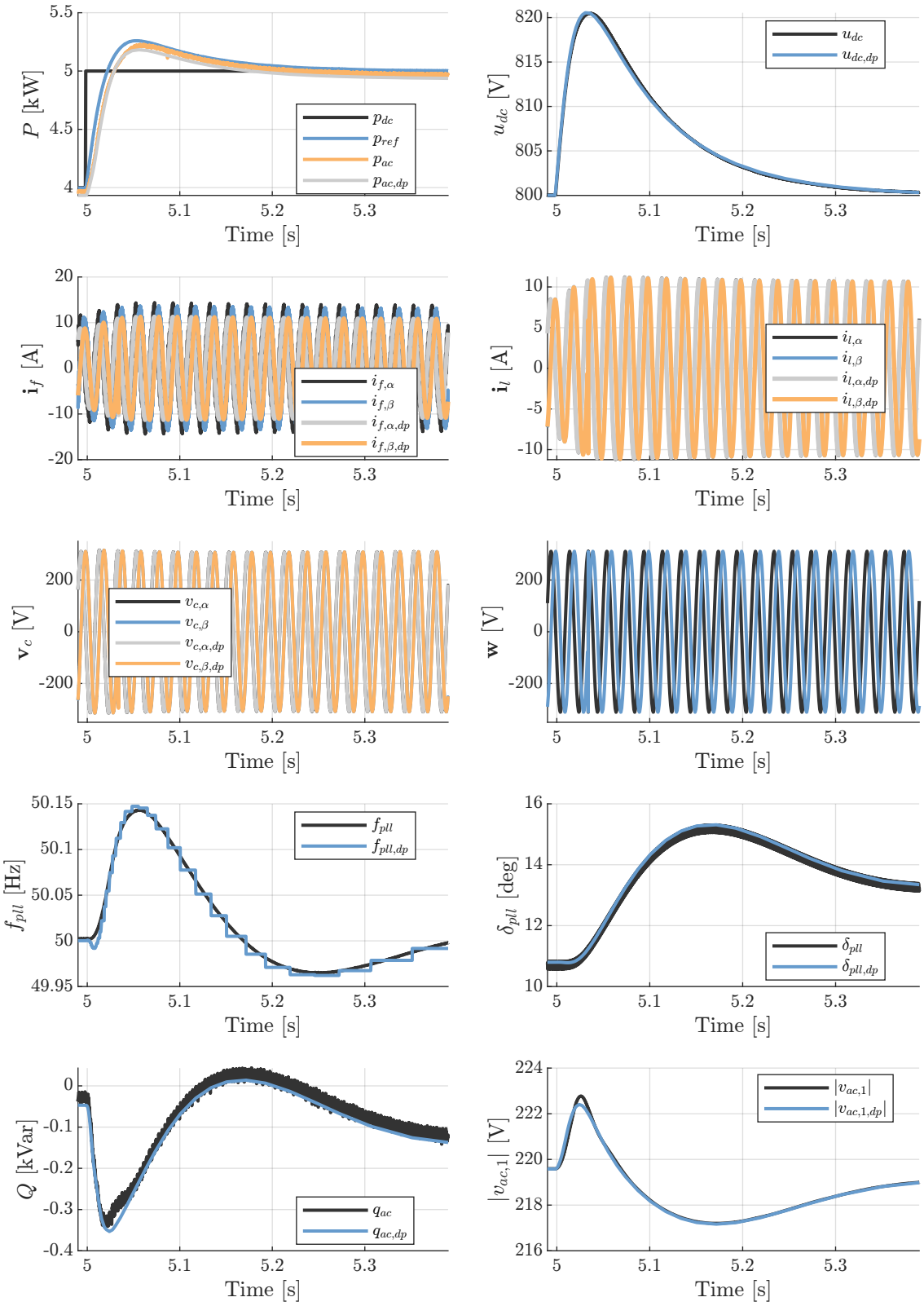

(c) 4–5 kW Power Step

Figure 5.14 – Mathematical model validation via hardware-in-the-loop of the grid model with ac bus voltage control.

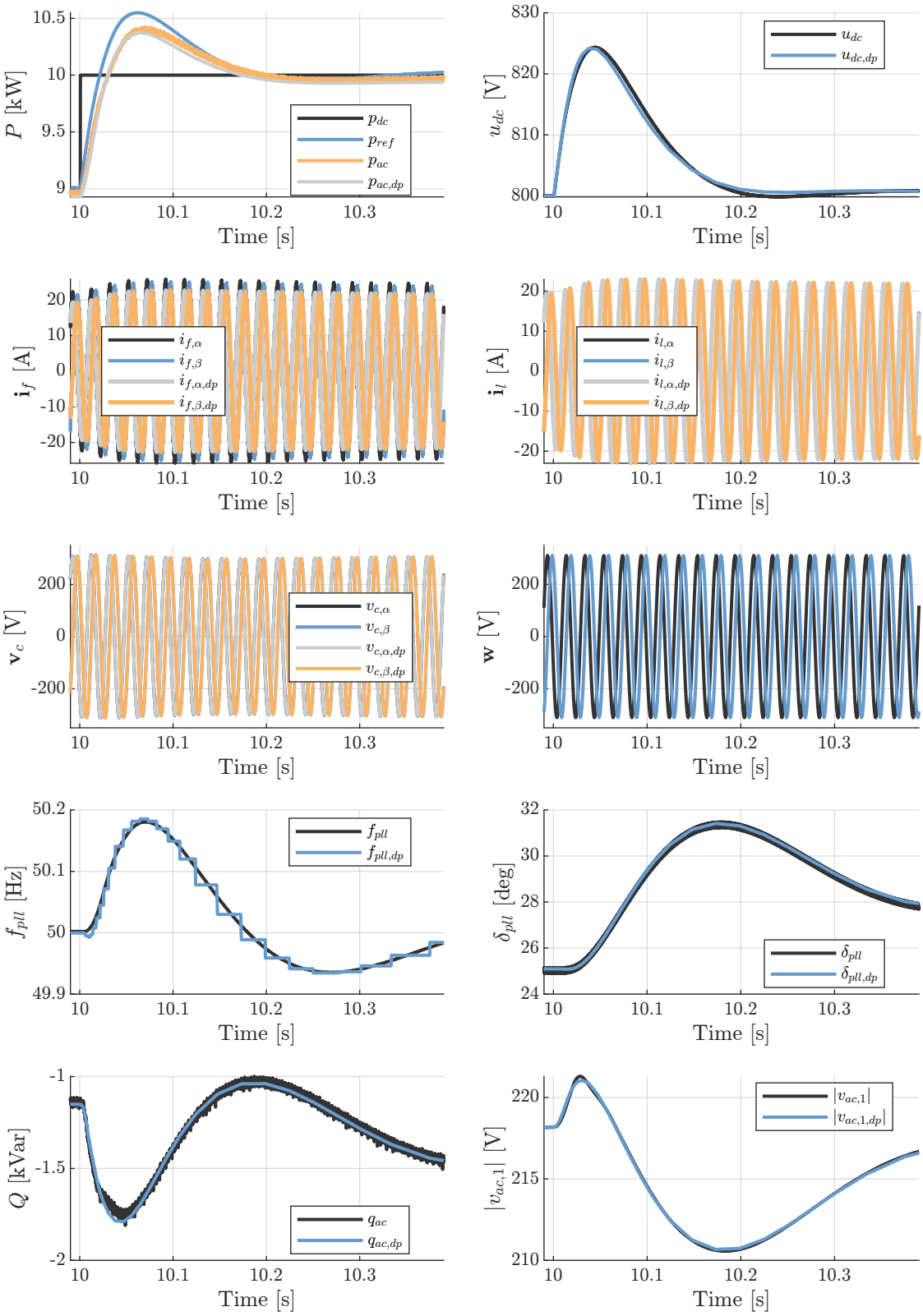

(d) 9–10 kW Power Step

Figure 5.14 – Mathematical model validation via hardware-in-the-loop of the grid model with ac bus voltage control.

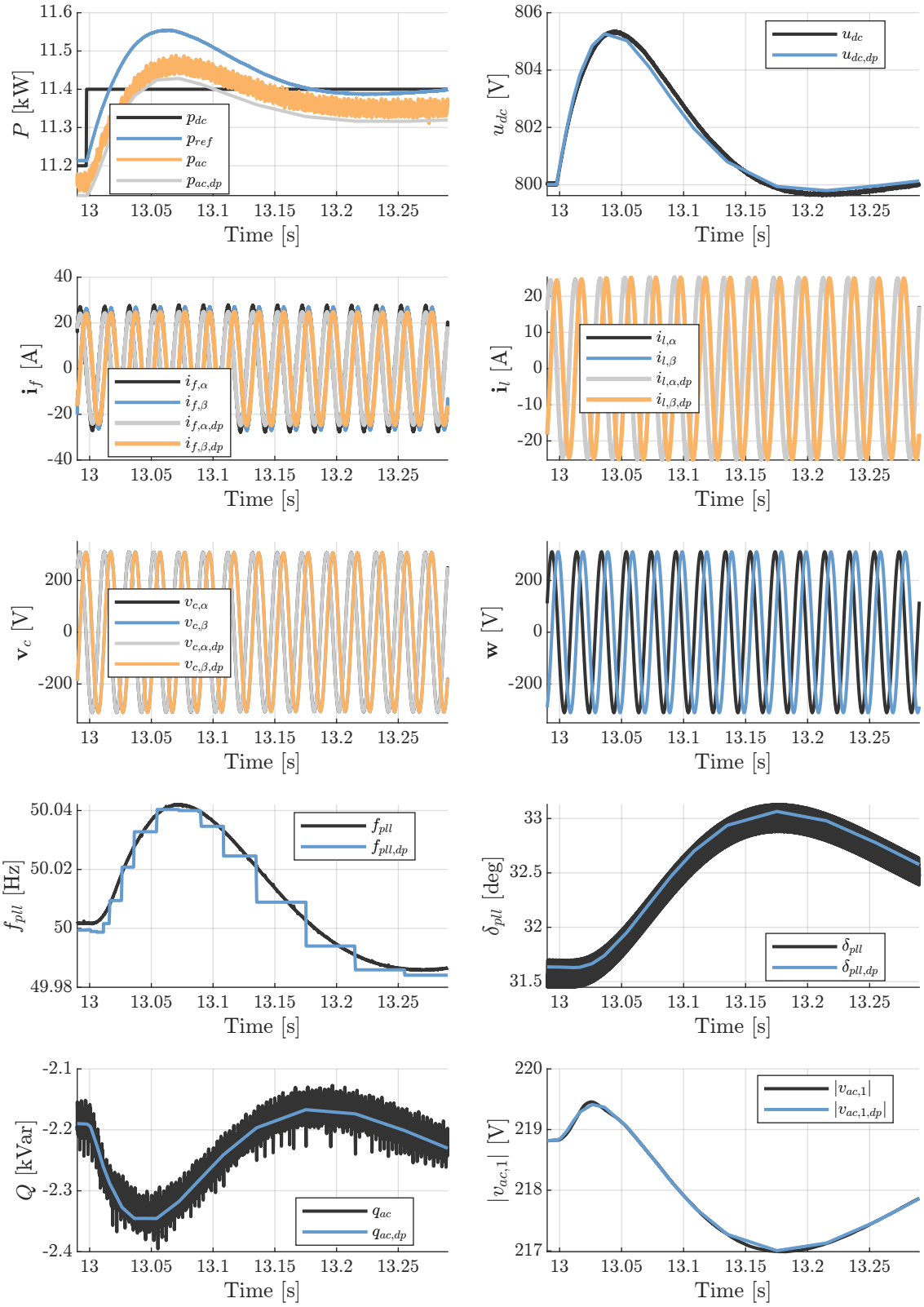

(e) 11.2–11.4 kW Power Step

Figure 5.14 – Mathematical model validation via hardware-in-the-loop of the grid model with ac bus voltage control.

5.6.4 Photovoltaic Array Comparison

A comparison between constant current source models and the PV array model described in Chapter 3 allows for a better evaluation the influence of the variable input impedance of the PV array on the model. The results presented in Figure 5.15 compare the model with a fixed input current to a rated 10 kW PV array connected to the DC bus, under conditions similar to the previously conducted tests.

The comparison shows that the PV-connected system exhibits a more damped behavior compared to the constant current source model, mainly due to the resistive characteristic of the input impedance at lower frequencies. As a result, the PV-connected system demonstrates a larger stability margin. However, the constant current model can be used as a worst-case scenario with no significant impact, providing conservative insights for stability assessment.

For a more complete model, the HSS model discussed in Figure 5.15 can also be employed as an alternative to the validated model, especially when analyzing larger power steps and/or low inertia systems.

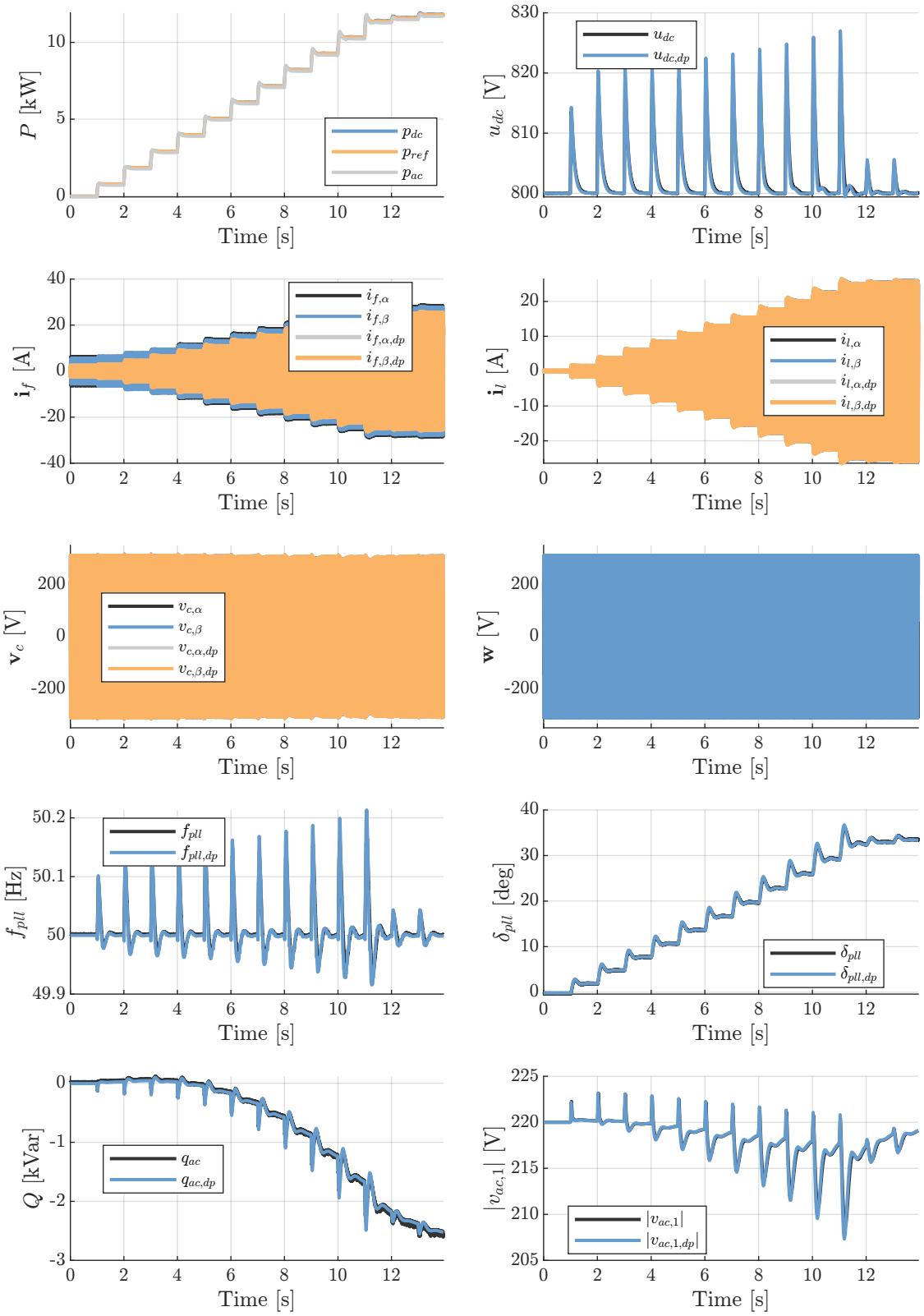

(a) 0–11.4 kW Power Step

Figure 5.15 – Comparison between mathematical model with constant power and hardware-in-the-loop implementation of PV array.

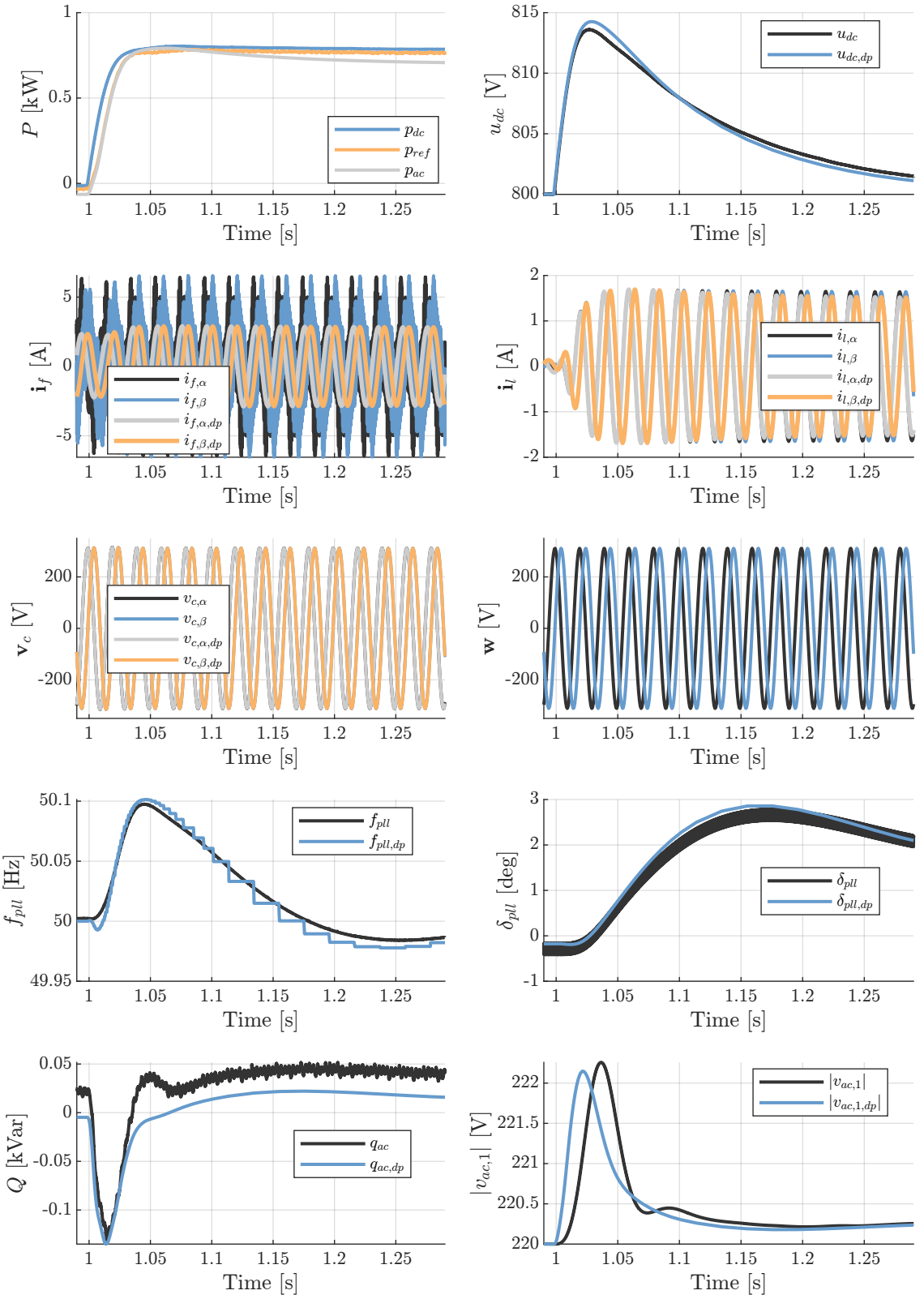

(b) 0–1 kW Power Step

Figure 5.15 – Comparison between mathematical model with constant power and hardware-in-the-loop implementation of PV array.

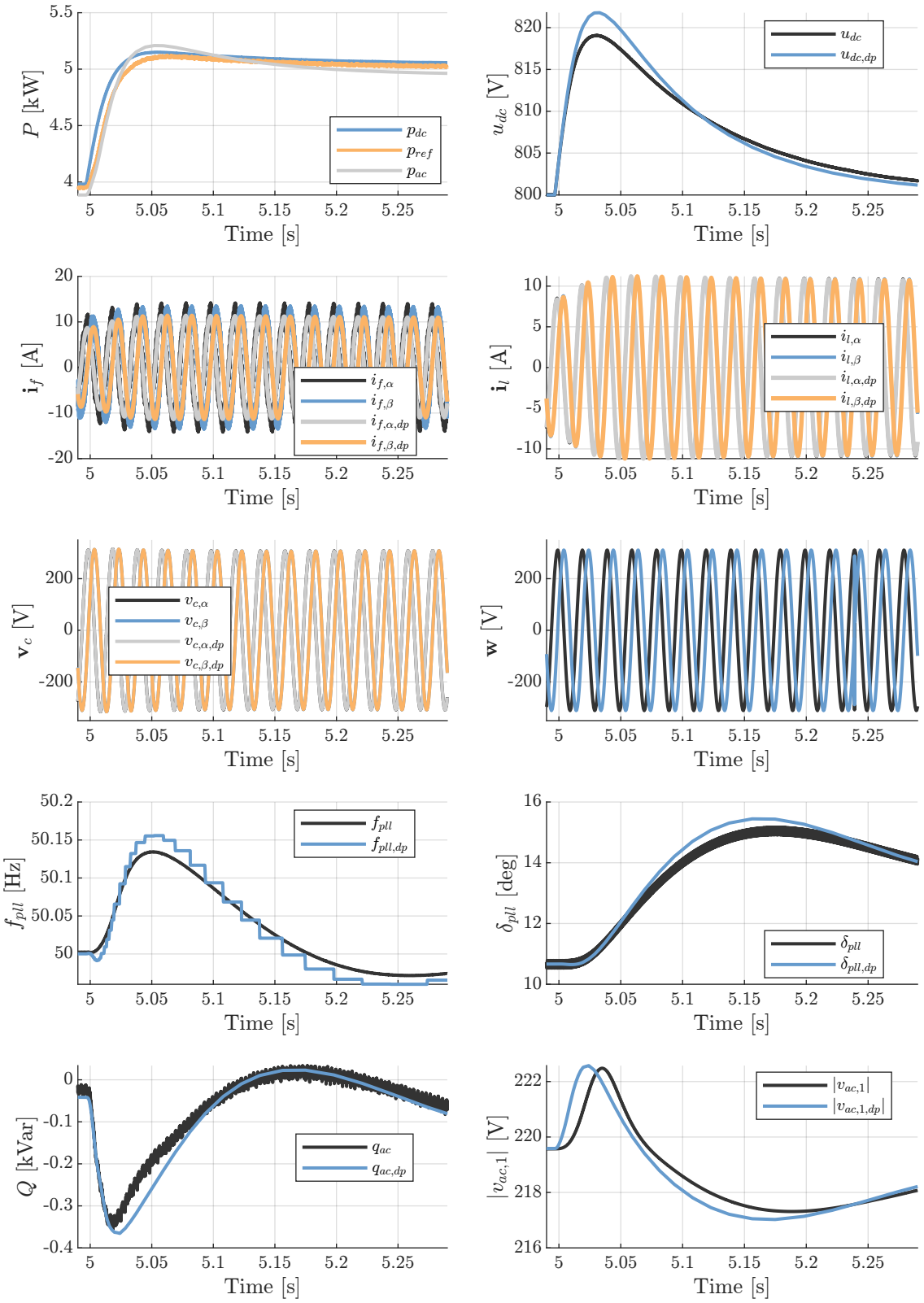

(c) 4–5 kW Power Step

Figure 5.15 – Comparison between mathematical model with constant power and hardware-in-the-loop implementation of PV array.

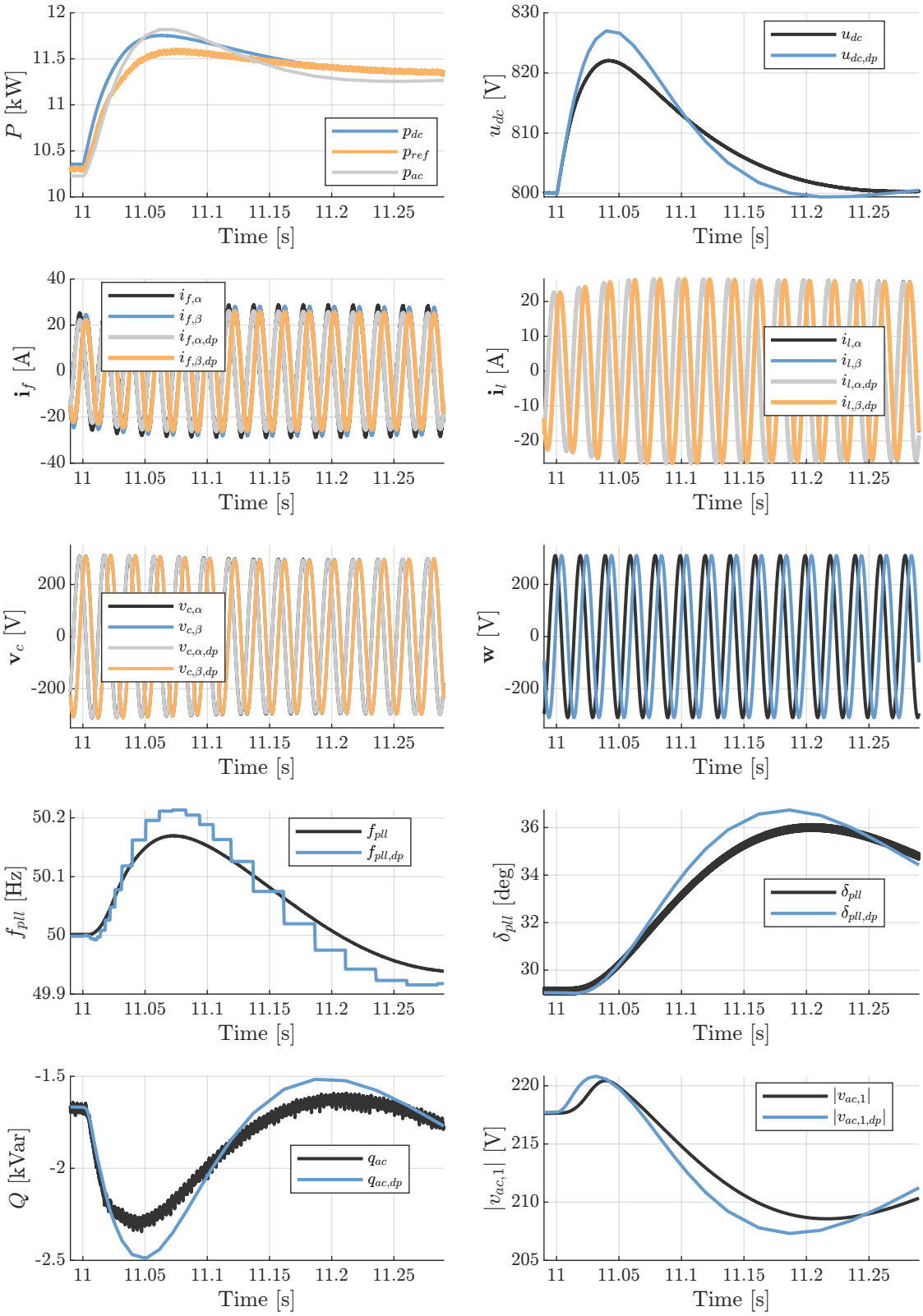

(d) 9–10 kW Power Step

Figure 5.15 – Comparison between mathematical model with constant power and hardware-in-the-loop implementation of PV array.

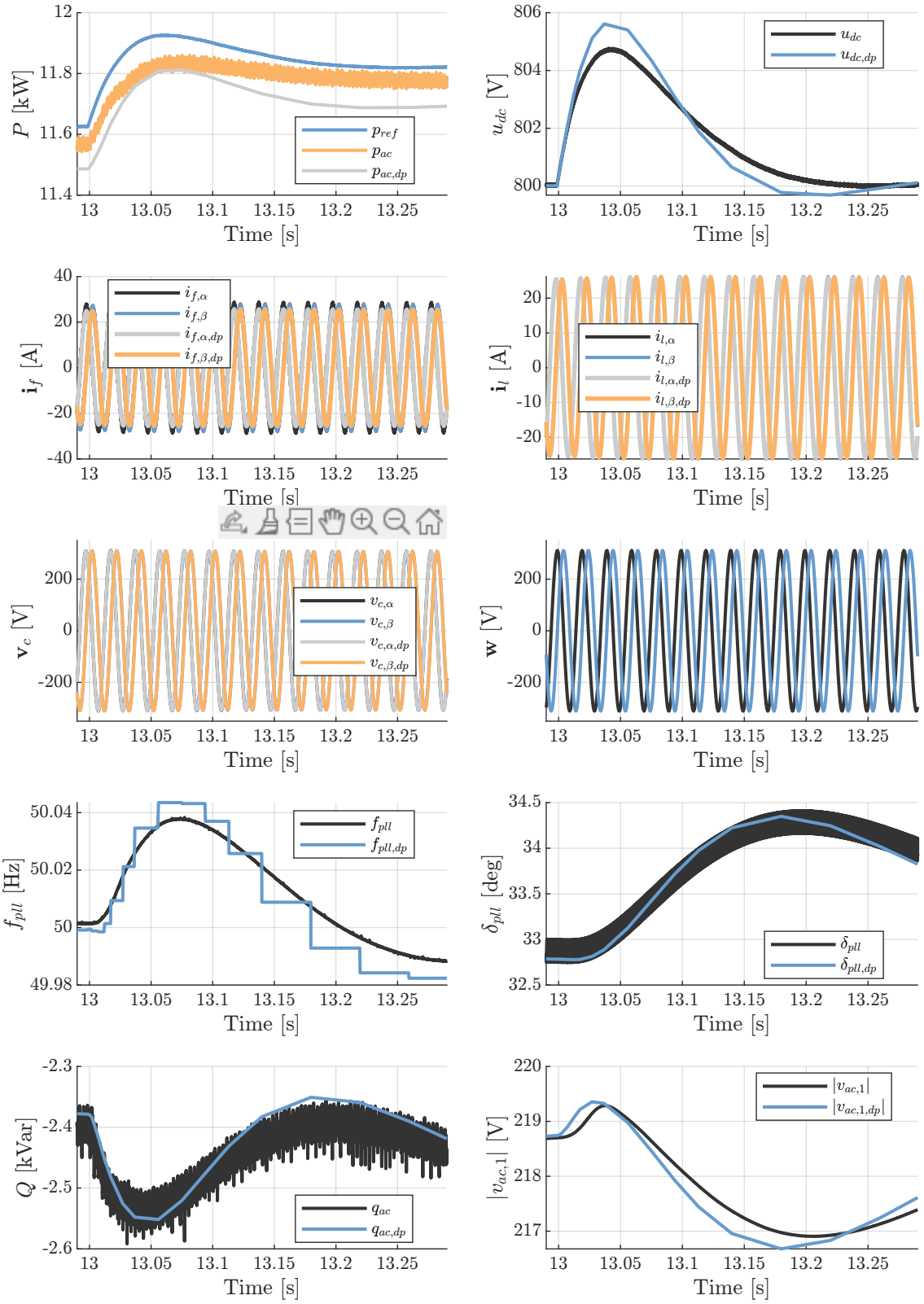

(e) 11.2–11.4 kW Power Step

Figure 5.15 – Comparison between mathematical model with constant power and hardware-in-the-loop implementation of PV array.

5.7 STABILITY ASSESSMENT

The stability assessment of the system's fixed points is a critical aspect of our analysis. To ascertain the system's stability, we employ a Newton-Raphson based recursive process, optimizing the cost function defined by the derivative functional, obtaining the fixed points through the following formulation:

$$\begin{aligned} \min_{\mathbf{x}_k} \quad & \left(\sum_{i=1}^{N_x} b_i \boldsymbol{f}(x_{i,k})^2 \right)^{\frac{1}{2}} \\ \text{s.t.} \quad & \mathbf{x}_k = \mathbf{x}_{k-1} - \mu \left(\boldsymbol{\nabla}_{\mathbf{x}\boldsymbol{f}}(\mathbf{x}_{k-1}) \right)^{-1} \boldsymbol{f}(\mathbf{x}_{k-1}) \end{aligned} \tag{5.51}$$

In this formulation, $\boldsymbol{f}(\mathbf{x}) := D_t \mathbf{x}$ represents the system dynamics, $\mu \in \mathbb{R}$ denotes the learning rate, and $\mathbf{b} \in \mathbb{R}^{N_x}$ serves as a scaling vector to normalize the contributions of each state vector component. The present analysis employs the models validated in the previous section, enabling the acquisition of valuable insights into the system's stability and performance across a range of operating conditions.

5.7.1 Complete Model

The eigenvalues computed for multiple dc power injection levels are depicted in Figure 5.16. However, the algorithm encountered numerical challenges while calculating the fixed point for the 11.4 kW level, prompting inquiries about the existence of an equilibrium point. The identified instabilities during the model simulation and hardware-in-the-loop validation suggest a chaotic behavior with a periodic orbit, where the frequency is influenced by the variation rate of δ, due to the bounded characteristic of the PLL feedback loop. Furthermore, it is discernible that eigenvalues with smaller damping coefficients tend to move closer to the origin. This observation provides an explanation for the system's tendency towards a more underdamped characteristic, which eventually approaches instability as the processed power increases.

An analysis of the eigenvalues of multiple linearizations of $\boldsymbol{f}$, linearized at each simulation step, as illustrated in Figure 5.8 and validated against experimental results, is presented in Figure 5.17. This analysis highlights the nonlinear nature of the power converter system when operating under weak grid conditions, with the effect being more pronounced for higher processed power levels.

During transitory periods, a substantial variation of the eigenvalues was also observed, and this phenomenon can potentially lead to instabilities. This observation is demonstrated in Figure 5.17.n, and it is predominantly attributed to the transitory behavior of the PLL. The dynamic response of the PLL during transients can have a significant impact on the system's stability, contributing to the observed fluctuations in eigenvalues and influencing the overall stability of the power converter system, justifying the the employment of nonlinear models in the stability assessment of power converter

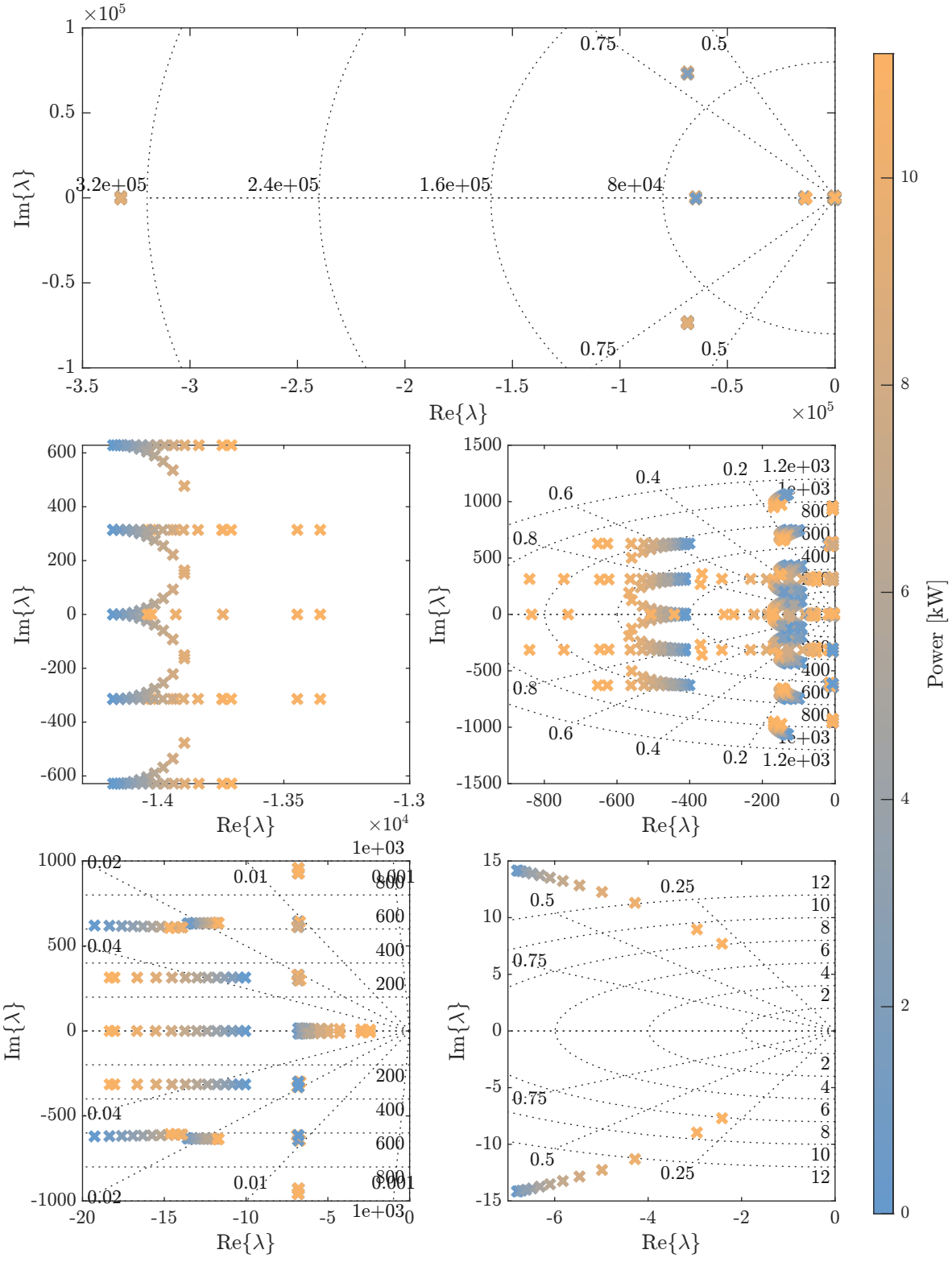

Figure 5.16 – Eigenvalues computed using the Newton-Raphson algorithm for various fixed points representing multiple DC bus injected power scenarios, with special emphasis on slower eigenvalues.

systems.

The calculation of $\boldsymbol{f}$ can be computationally intensive, especially when repeated evaluations are required. To mitigate the computational burden, a simplified model

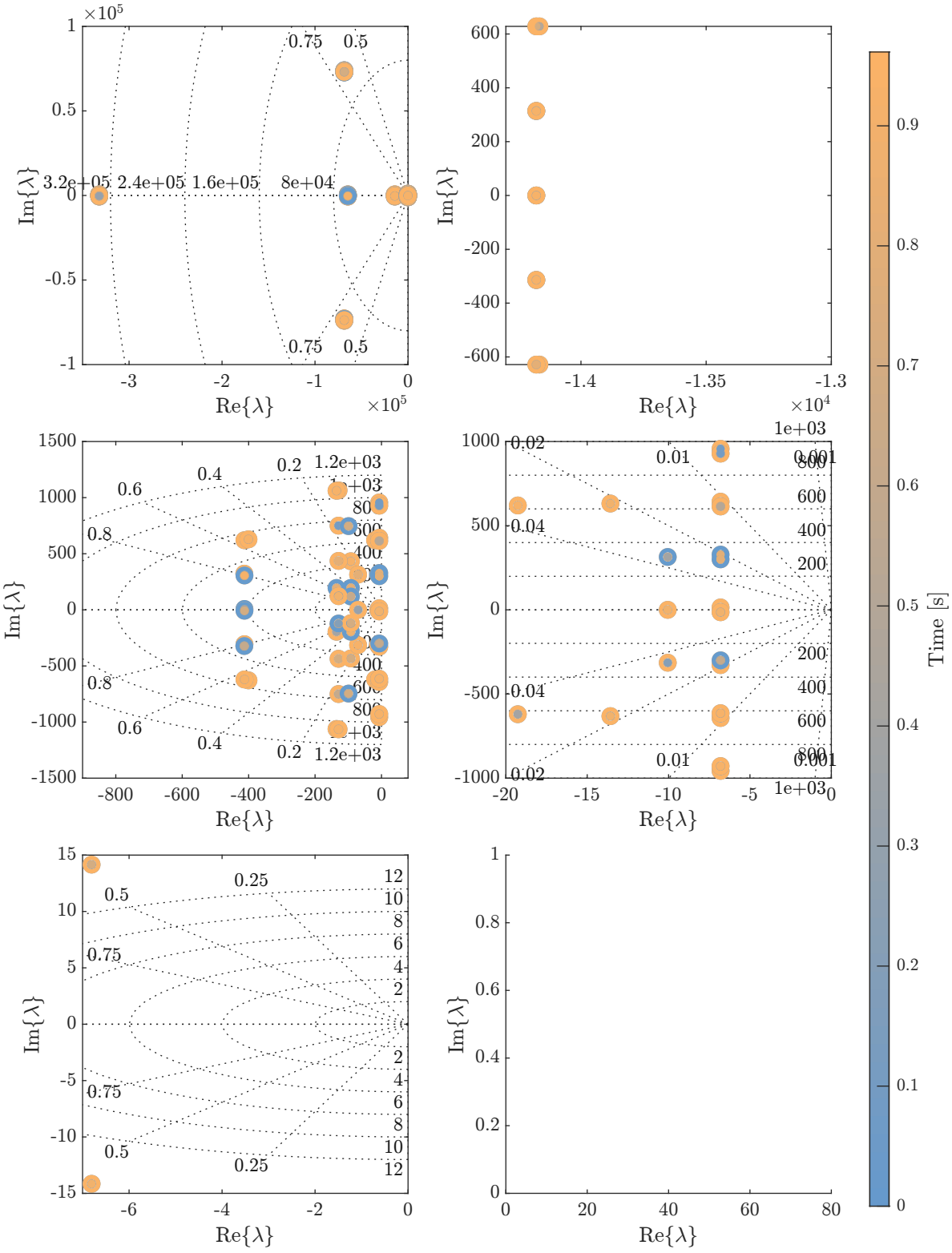

(a) 0 kW.

Figure 5.17 – Visualization of eigenvalue trajectories from the power step simulation using the complete model in MATLAB, simulated using the ode23tb solver.

incorporating a simplified PLL model, which has been validated in the previous analysis, can be utilized for assessing system stability. However, to ensure accurate stability analysis, it is essential to adopt a suitable strategy to eliminate the harmonic content of the PLL

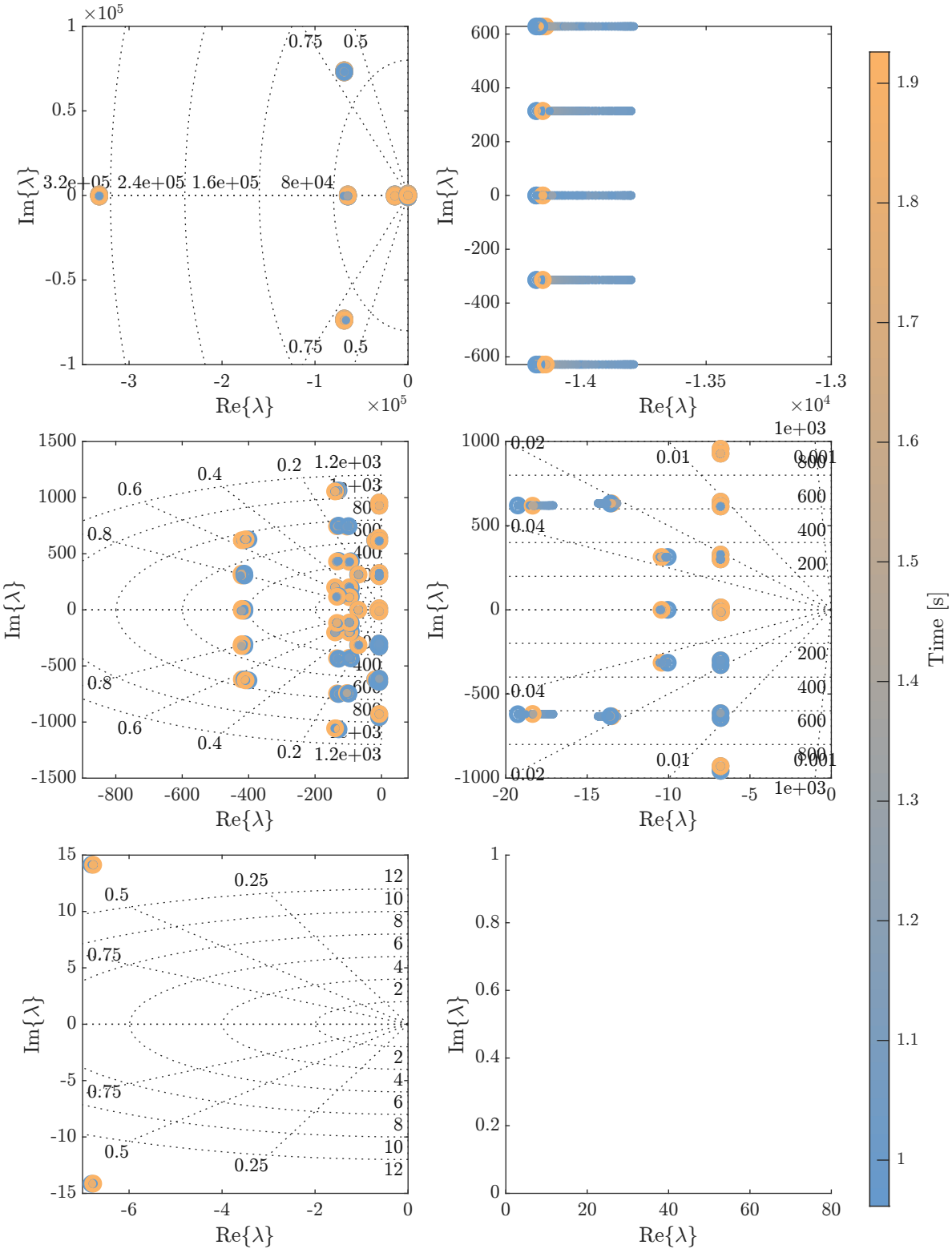

(b) 0–1 kW power step.

Figure 5.17 – Visualization of eigenvalue trajectories from the power step simulation using the complete model in MATLAB, simulated using the ode23tb solver.

state variables.

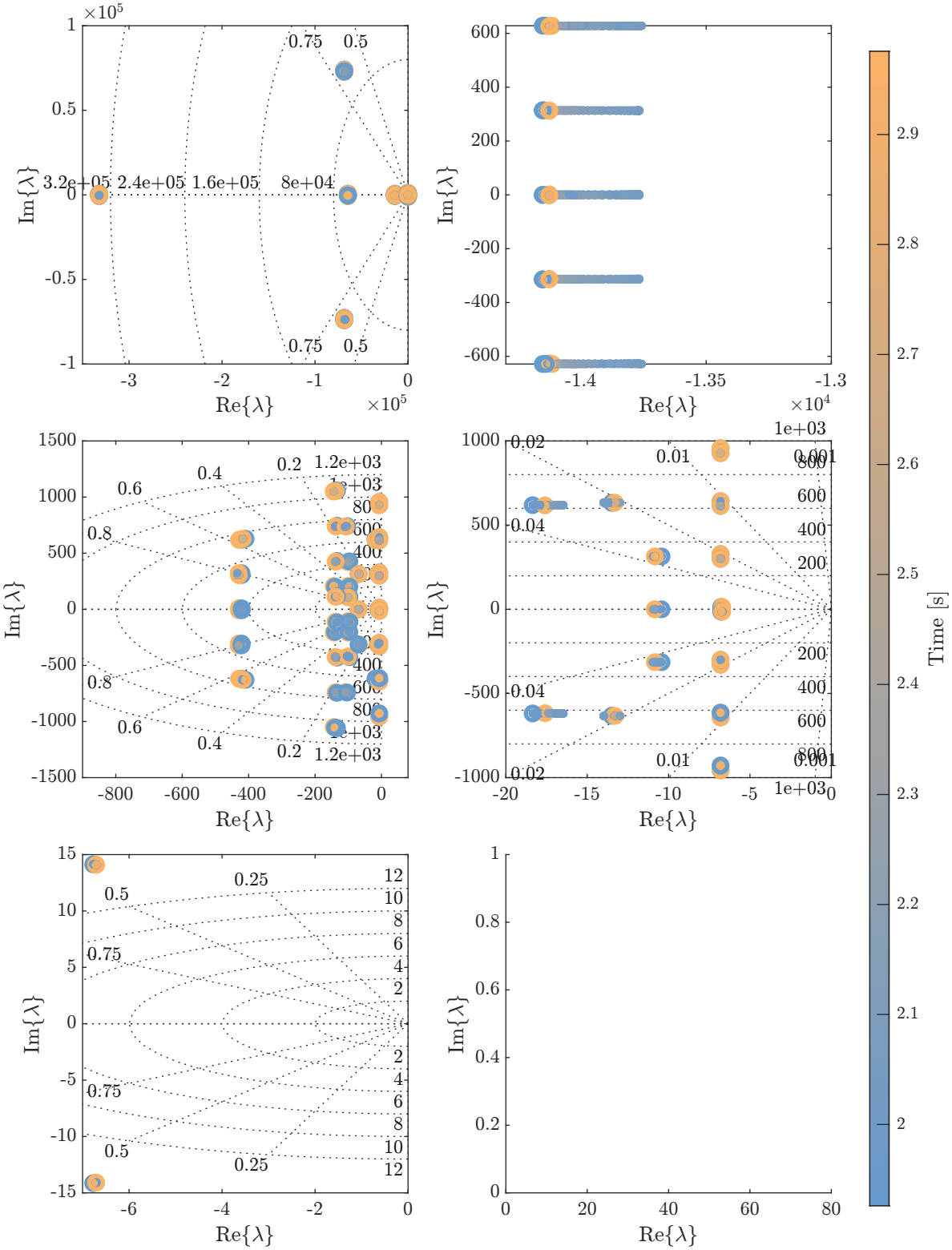

(c) 1–2 kW power step.

Figure 5.17 – Visualization of eigenvalue trajectories from the power step simulation using the complete model in MATLAB, simulated using the ode23tb solver.

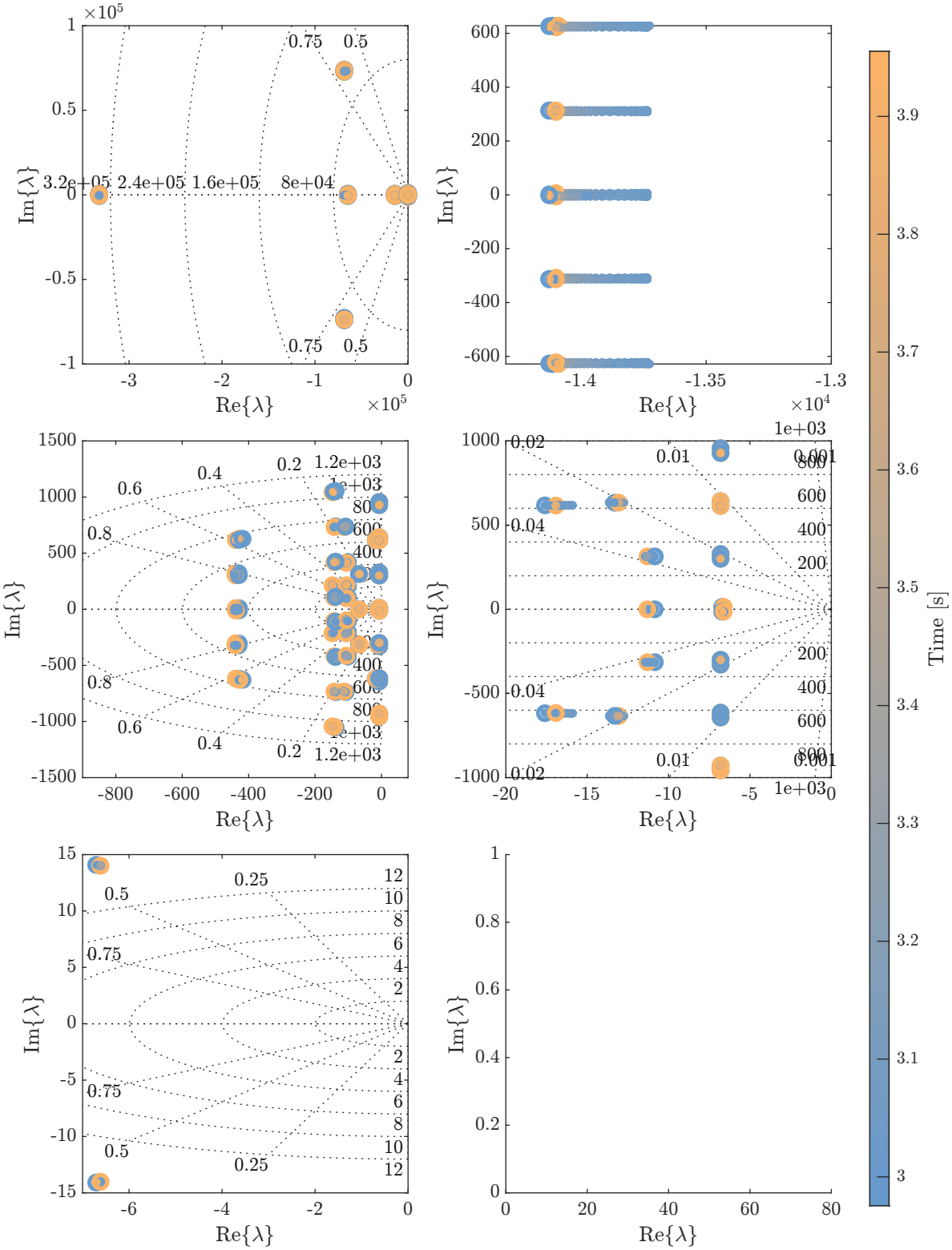

(d) 2–3 kW power step.

Figure 5.17 – Visualization of eigenvalue trajectories from the power step simulation using the complete model in MATLAB, simulated using the ode23tb solver.

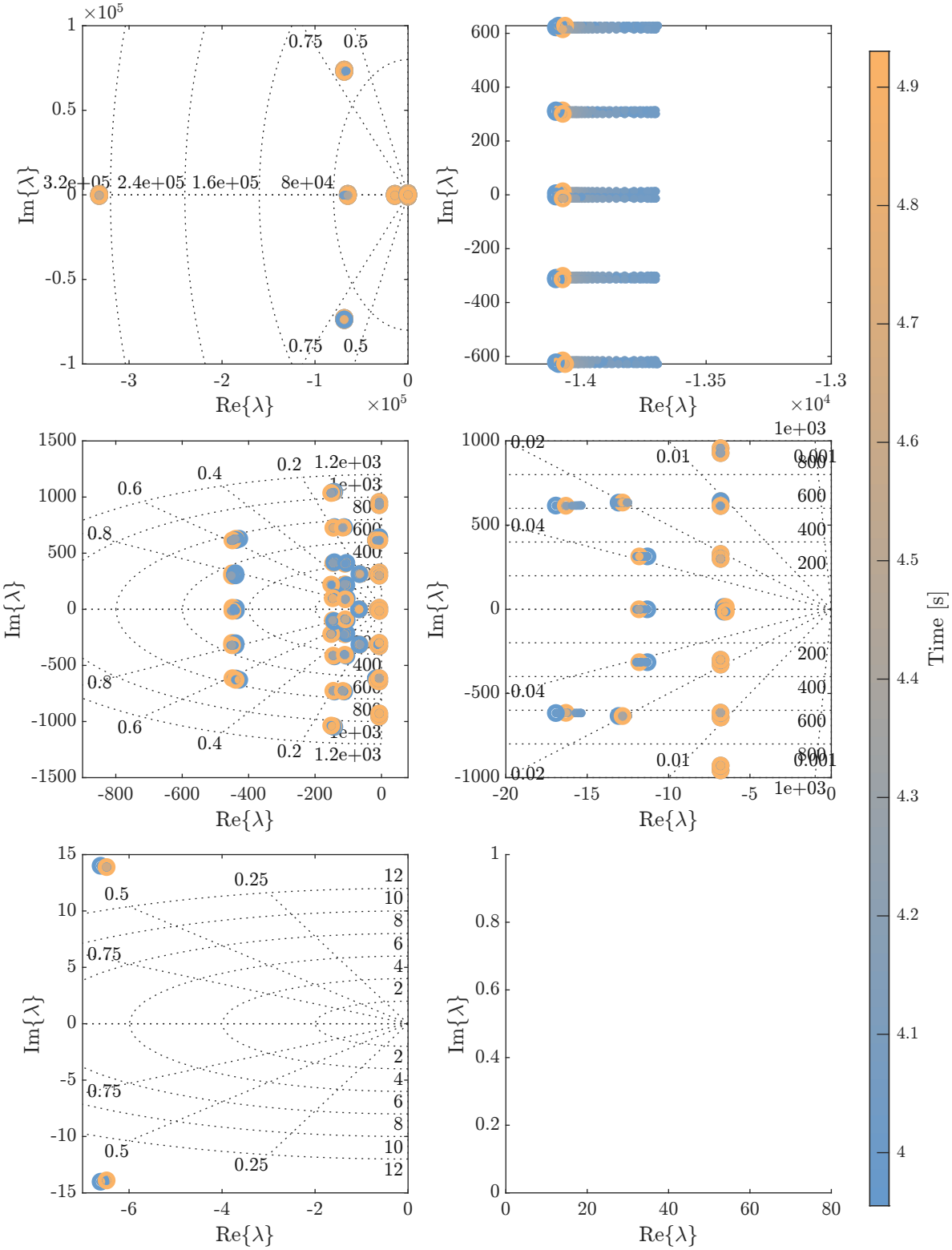

(e) 3–4 kW power step.

Figure 5.17 – Visualization of eigenvalue trajectories from the power step simulation using the complete model in MATLAB, simulated using the ode23tb solver.

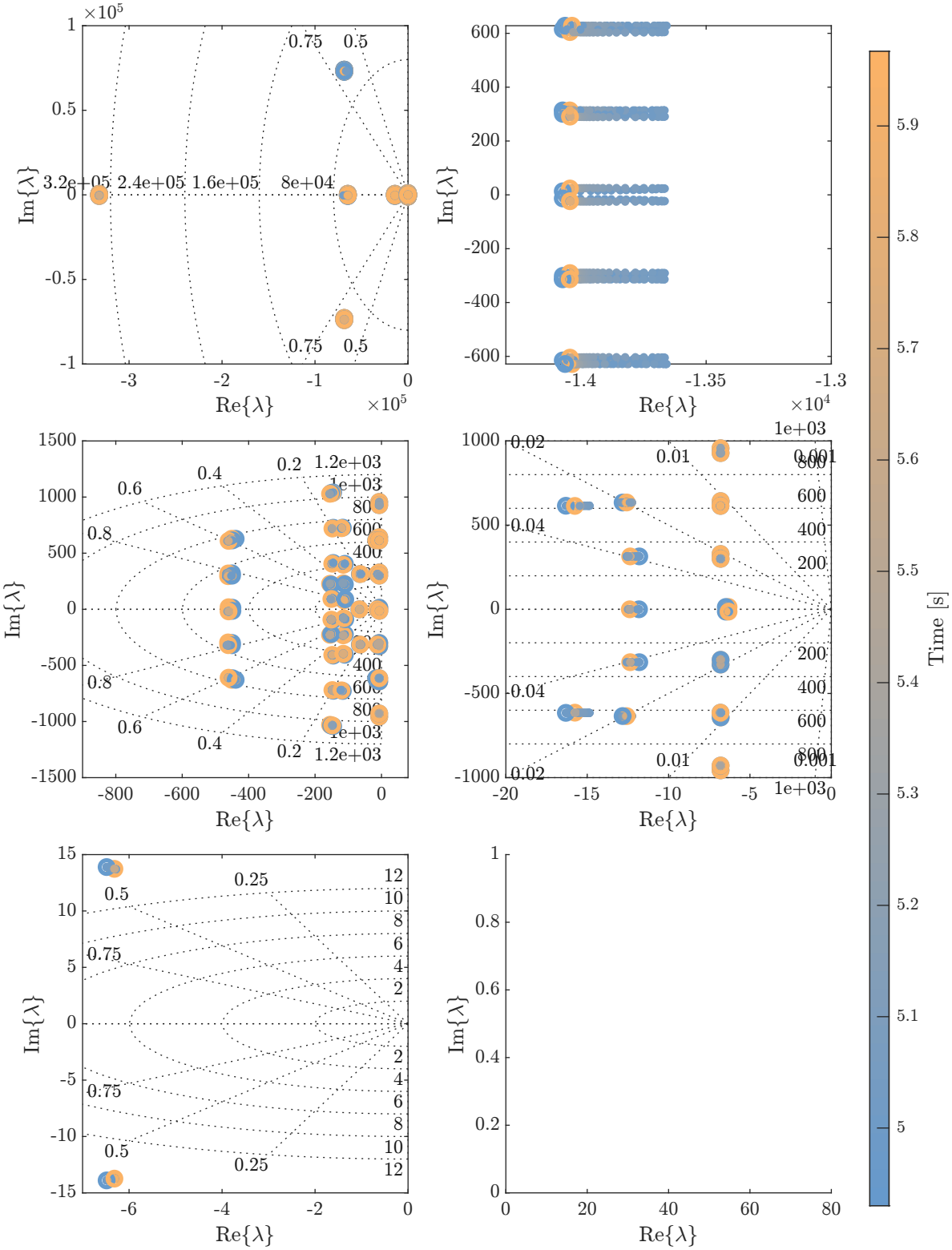

(f) 4–5 kW power step.

Figure 5.17 – Visualization of eigenvalue trajectories from the power step simulation using the complete model in MATLAB, simulated using the ode23tb solver.

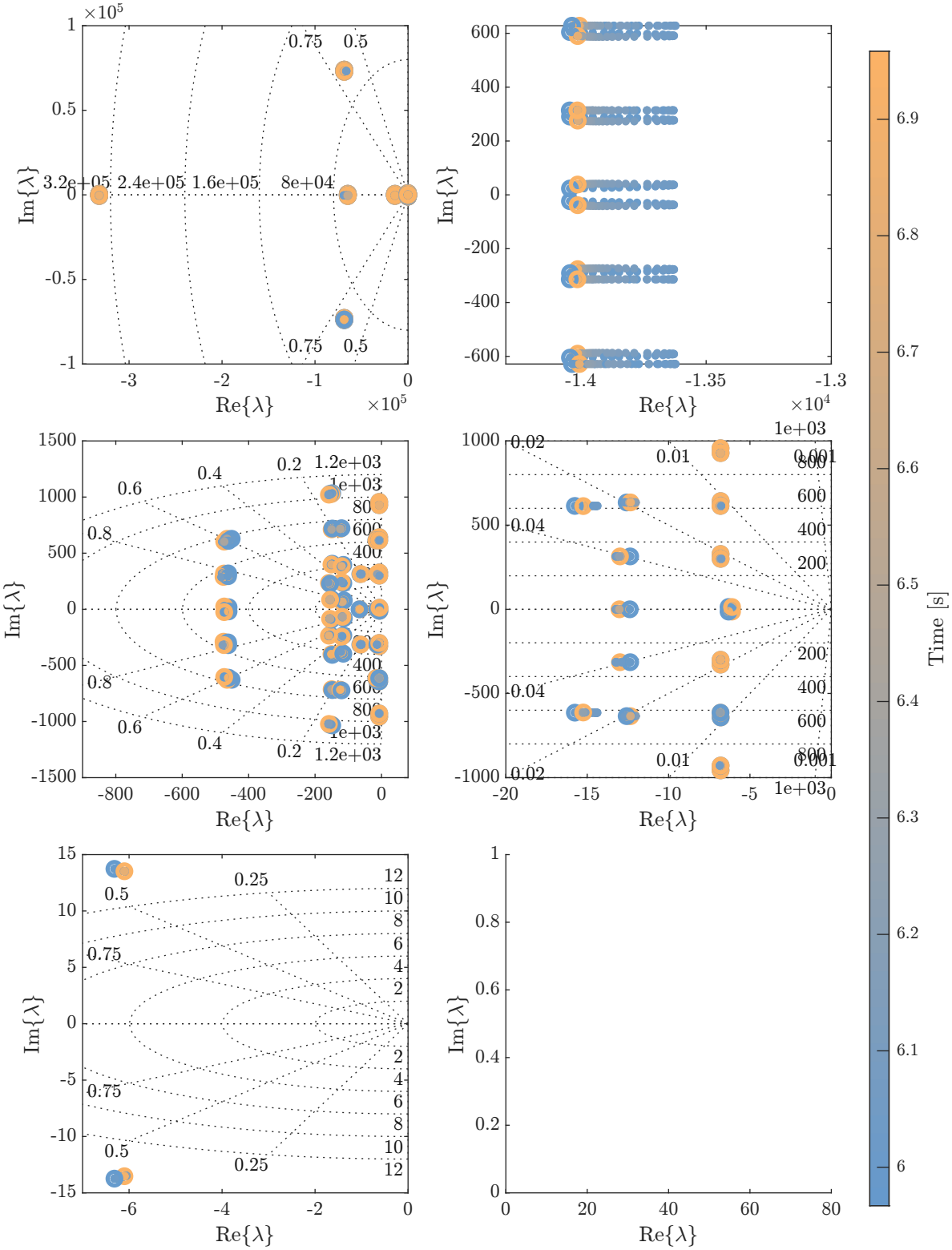

(g) 5–6 kW power step.

Figure 5.17 – Visualization of eigenvalue trajectories from the power step simulation using the complete model in MATLAB, simulated using the ode23tb solver.

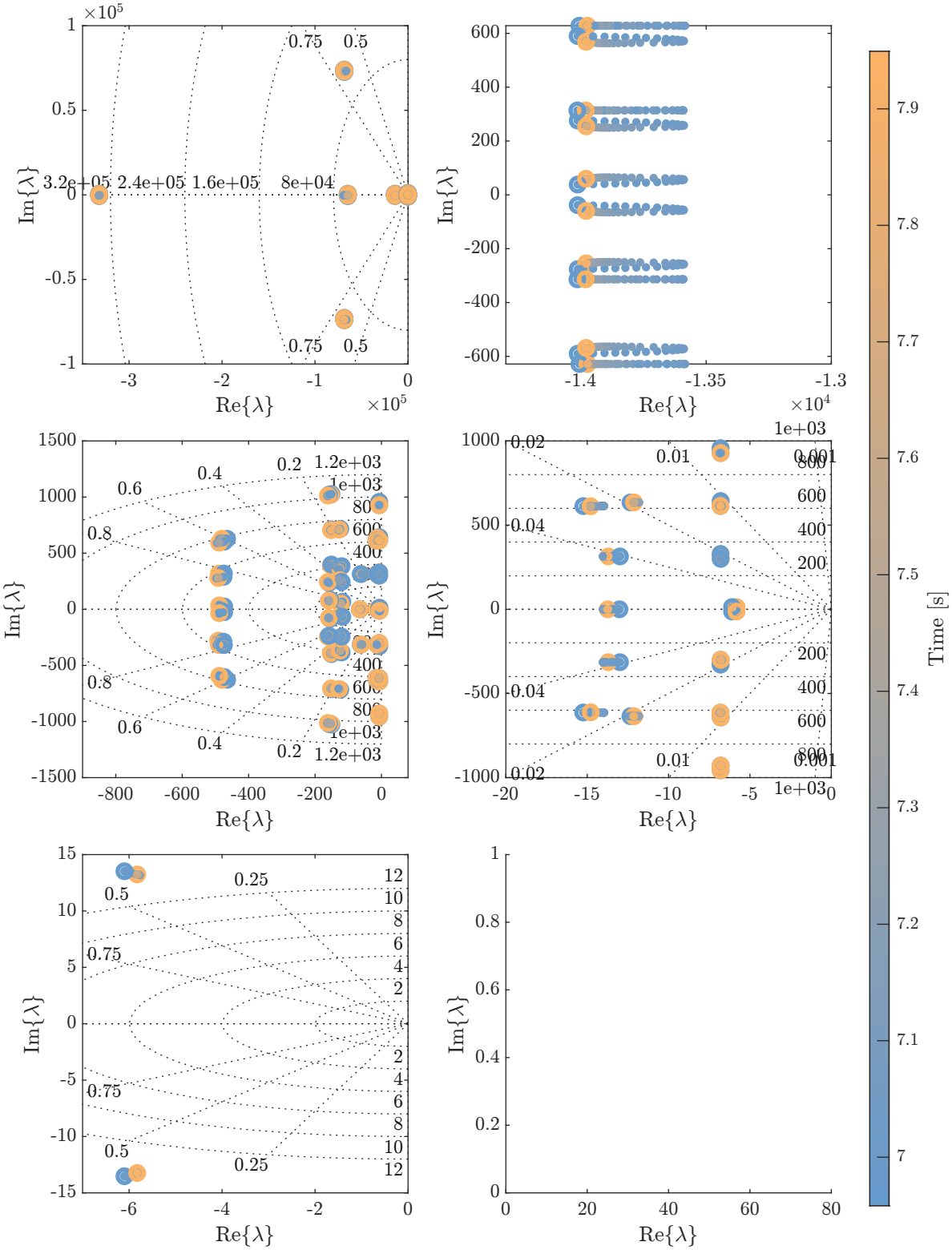

(h) 6–7 kW power step.

Figure 5.17 – Visualization of eigenvalue trajectories from the power step simulation using the complete model in MATLAB, simulated using the ode23tb solver.

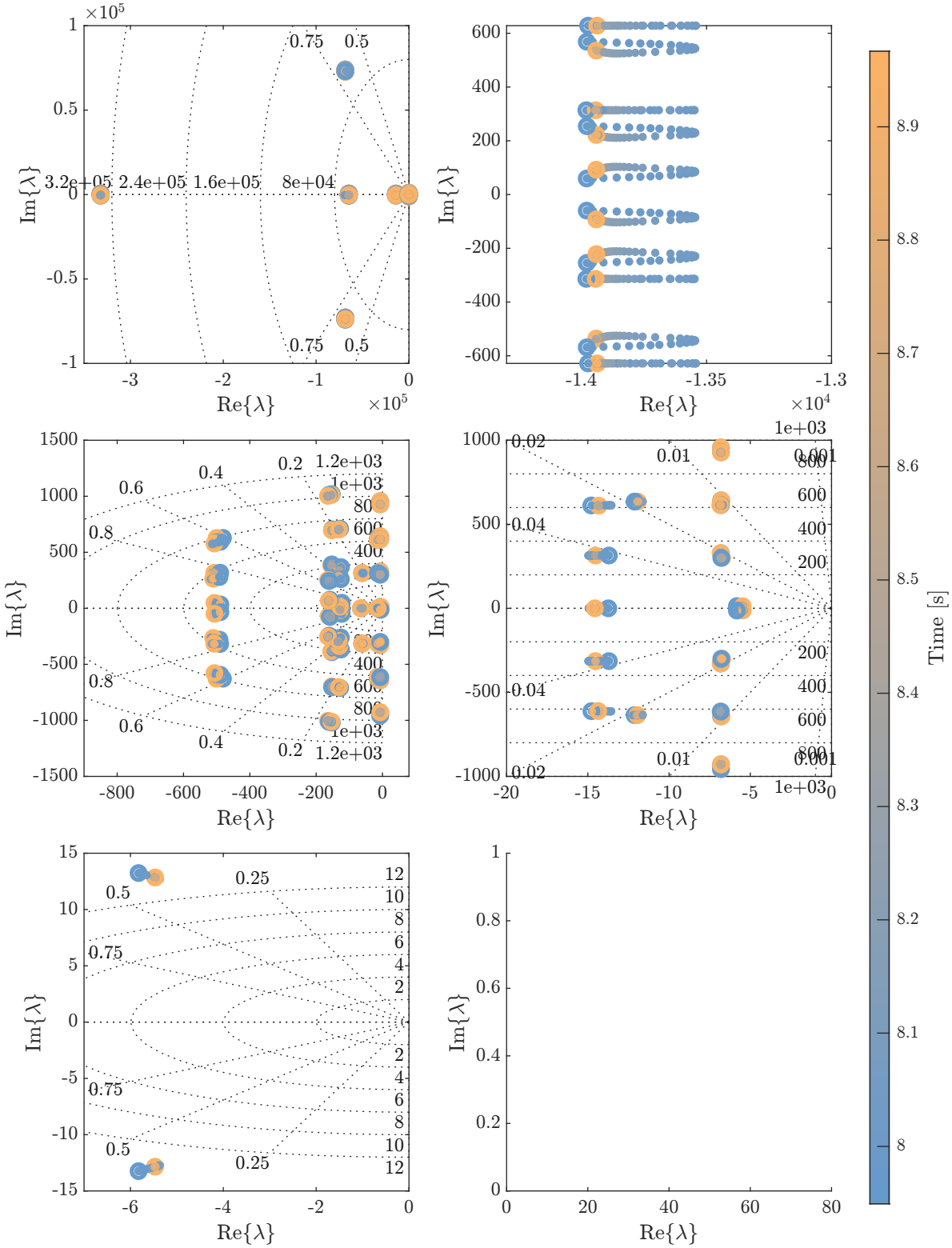

(i) 7–8 kW power step.

Figure 5.17 – Visualization of eigenvalue trajectories from the power step simulation using the complete model in MATLAB, simulated using the ode23tb solver.

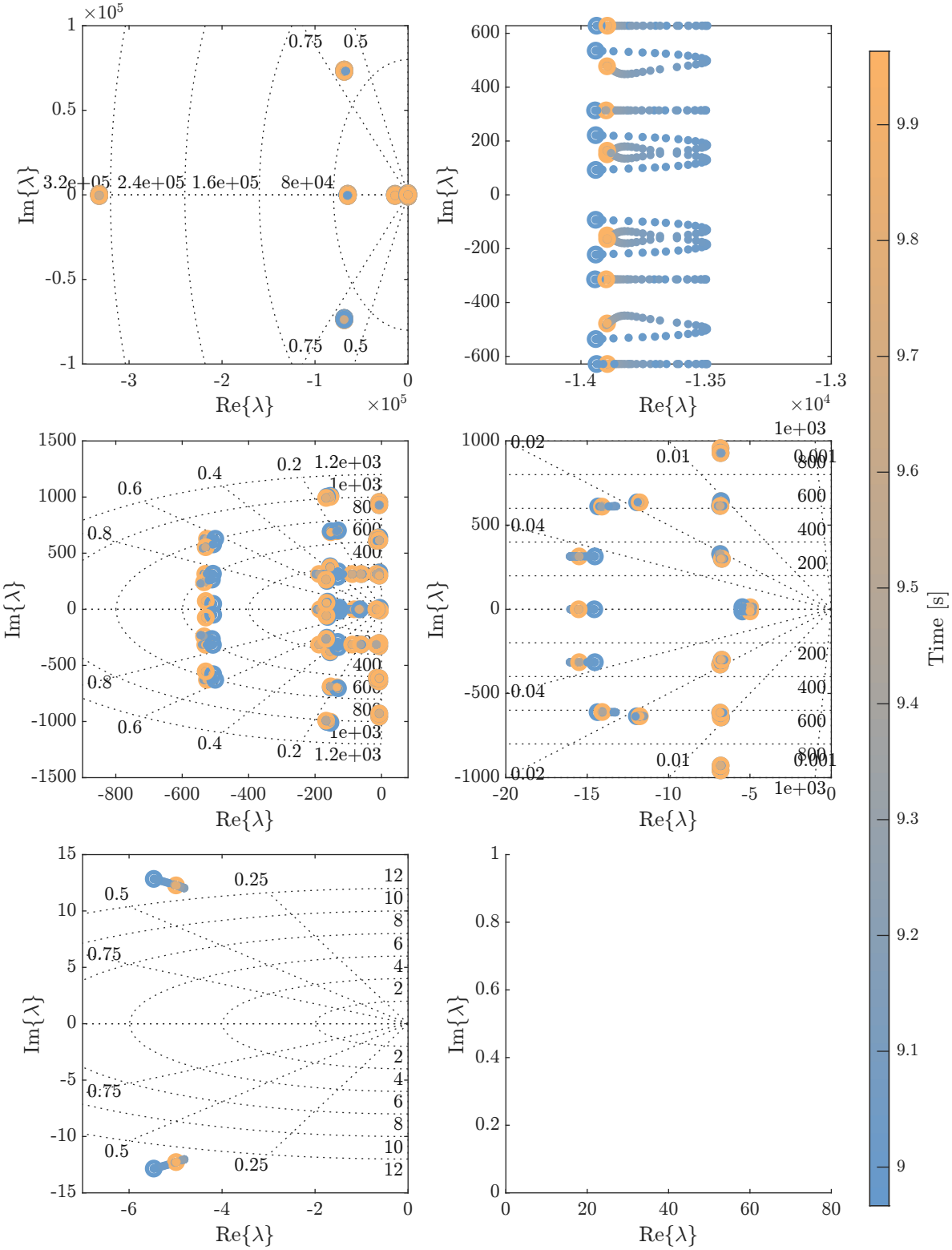

(j) 8–9 kW power step.

Figure 5.17 – Visualization of eigenvalue trajectories from the power step simulation using the complete model in MATLAB, simulated using the ode23tb solver.

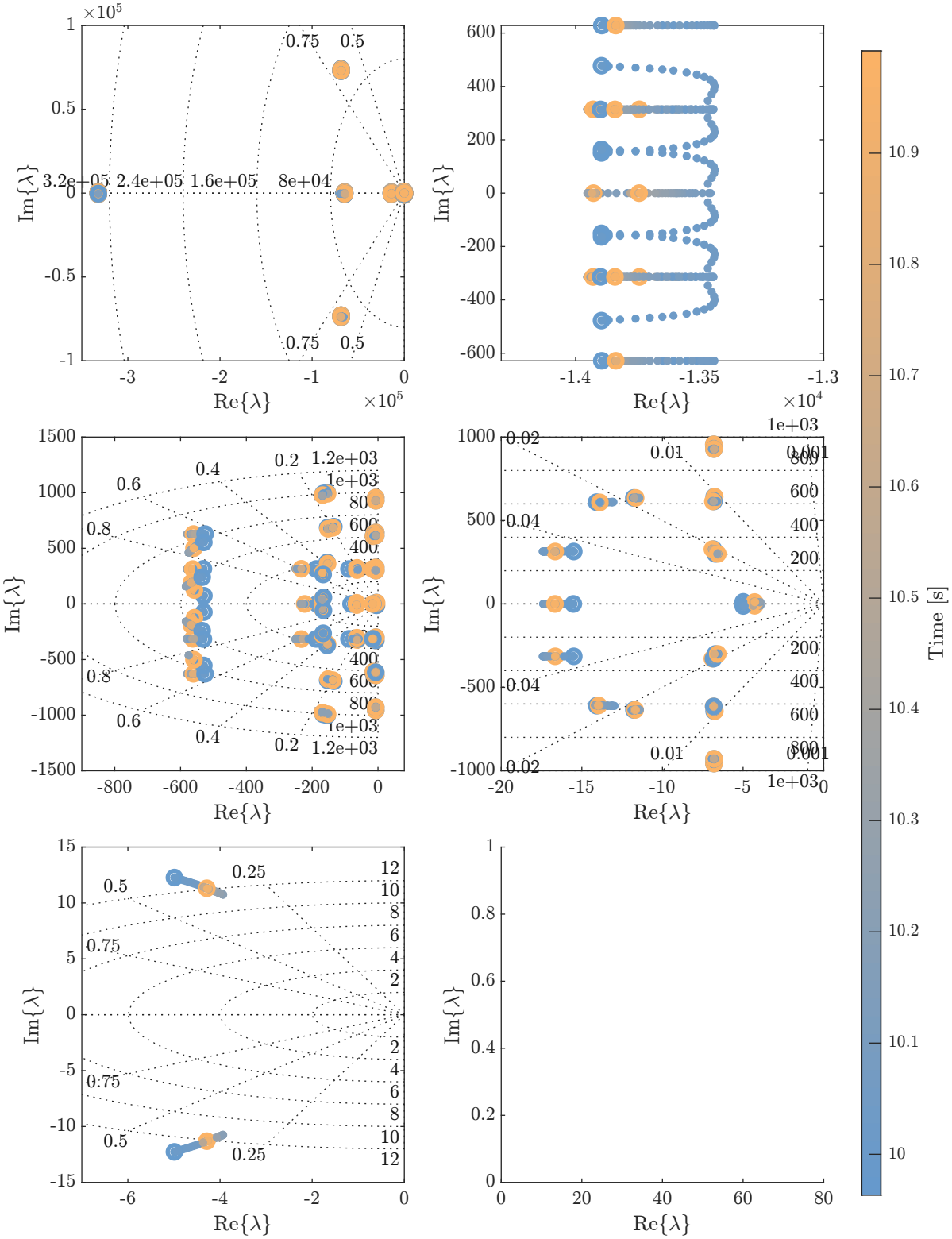

(k) 9–10 kW power step.

Figure 5.17 – Visualization of eigenvalue trajectories from the power step simulation using the complete model in MATLAB, simulated using the ode23tb solver.

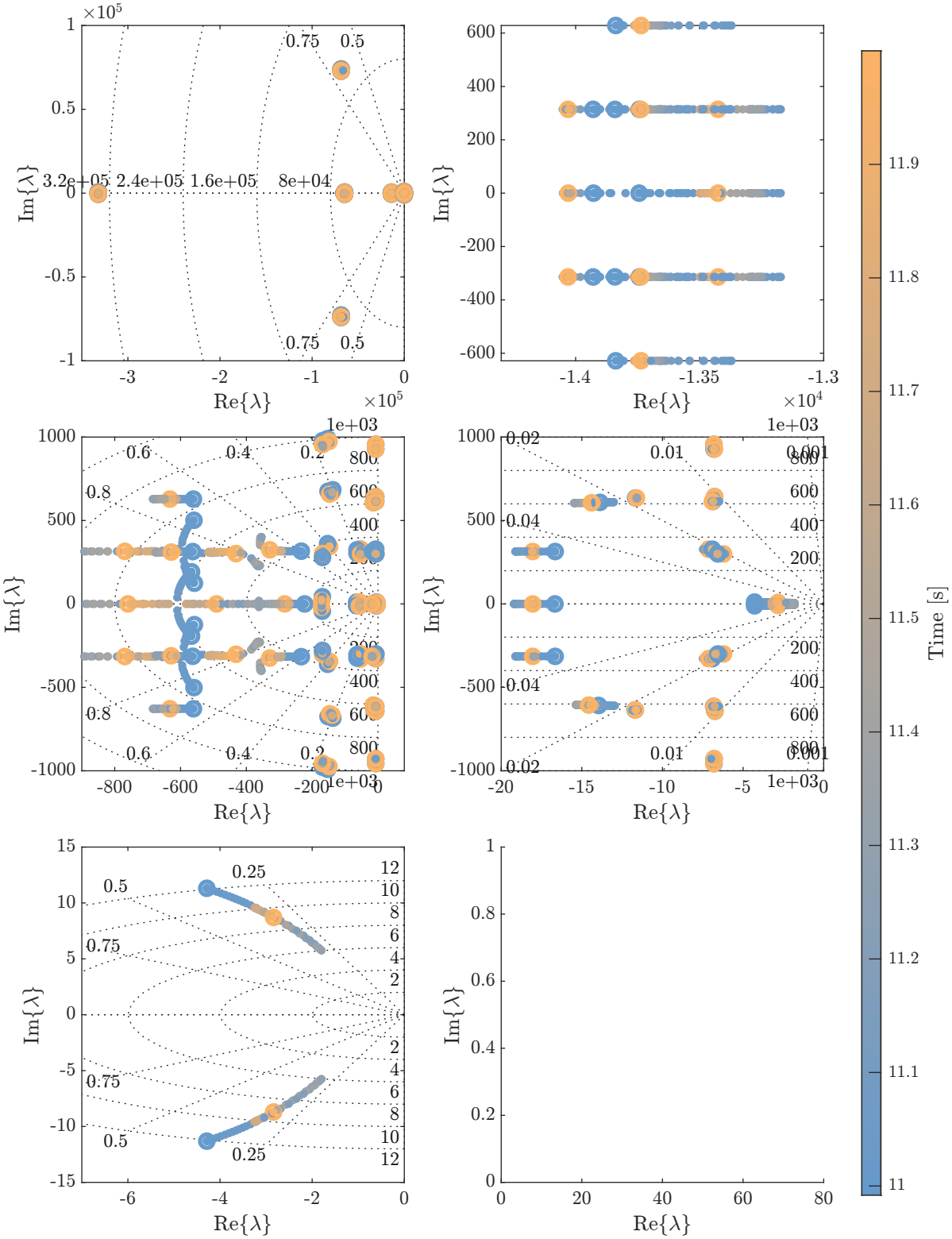

(l) 10–11 kW power step.

Figure 5.17 – Visualization of eigenvalue trajectories from the power step simulation using the complete model in MATLAB, simulated using the ode23tb solver.

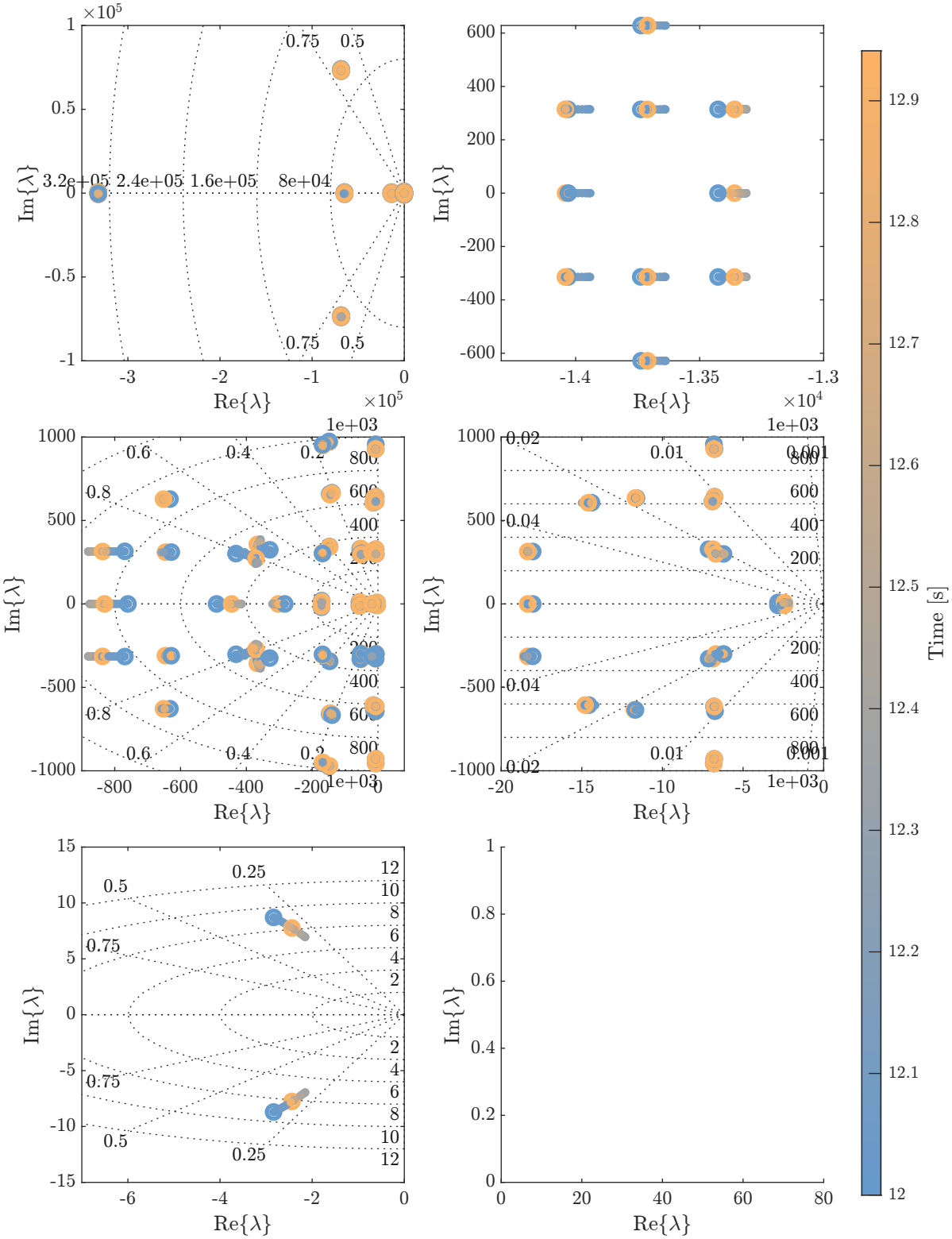

(m) 11–11.2 kW power step.

Figure 5.17 – Visualization of eigenvalue trajectories from the power step simulation using the complete model in MATLAB, simulated using the ode23tb solver.

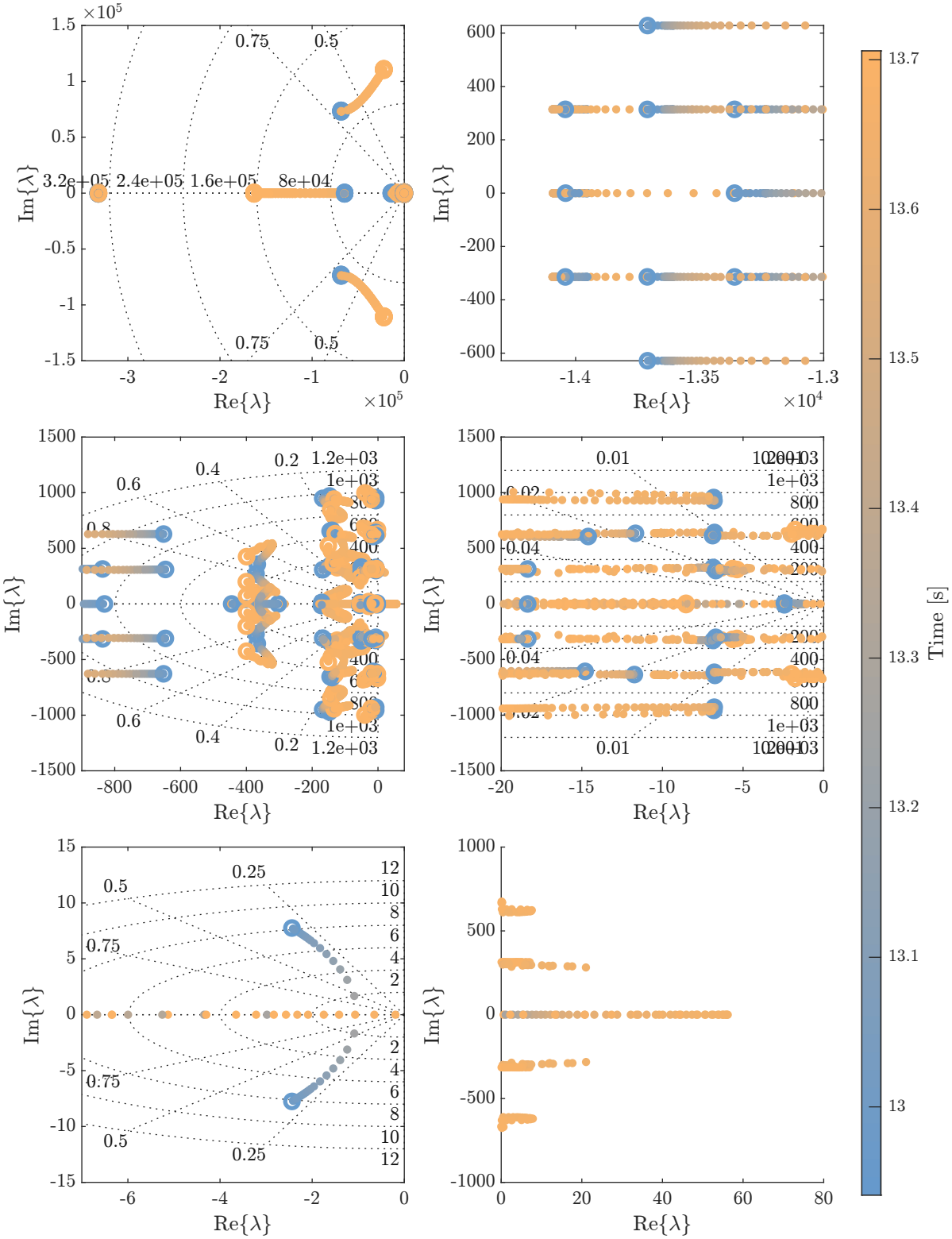

(n) 11.2–11.4 kW

Figure 5.17 – Visualization of eigenvalue trajectories from the power step simulation using the complete model in MATLAB, simulated using the ode23tb solver.

5.7.2 MAF-PLL Model

The simplified PLL model can be employed when a method to mitigate oscillations on the synchronism loop, such as the MAF-PLL, GDSC-PLL, etc. This model allows for a faster computation of stability assessments, as the simplified model reduces the computational complexity while retaining the essential dynamics of the PLL control.

In Figure 5.18, the steady-state value of the PLL angle, denoted as δ, is shown for multiple dc power levels in the absence of ac bus voltage control. Notably, for processed power exceeding 11.4 kW, the solution becomes complex due to the Harmonic State Space (HSS) characteristic, which permits complex-valued solutions. This observation suggests the absence of a point of equilibrium. This assumption is further supported by the chaotic behavior exhibited in the experimental model, indicating that these points of operation can be classified as unstable.

As a consequence, we can estimate a stability region for multiple processed reactive power, leading to the results presented in Figure 5.19. Notably, the system exhibits a higher stability margin when processing more capacitive reactive power, resulting in higher ac bus voltage levels.

The closed-loop reactive control utilizing the RDFT algorithm incorporates an inherent compensation mechanism that expands the stability region, as illustrated in Figure 5.20. However, the maximum reactive power processed by the power converter experiences saturation, which limits the stability margin concerning real-time changes in processed reactive power. Consequently, this limitation impacts the maximum admissible processed active power of the power converter system. In Figure 5.21, we demonstrate the reactive power reference generated by the ac bus voltage compensator, designed to

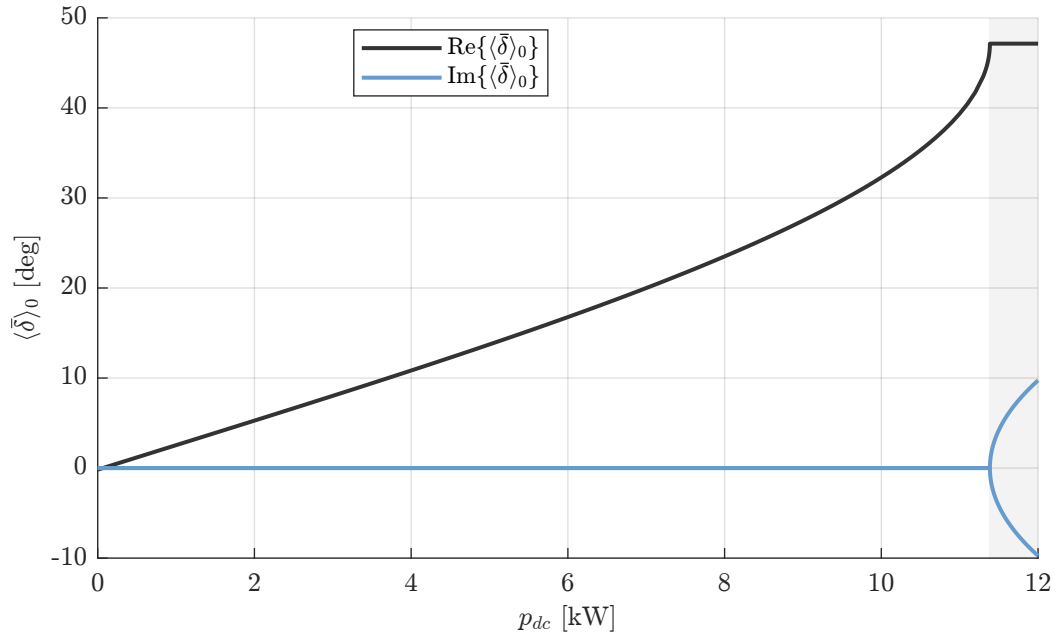

Figure 5.18 – Synchronism Angle δ at the point of equilibrium for multiple dc power processing levels without ac bus voltage control.

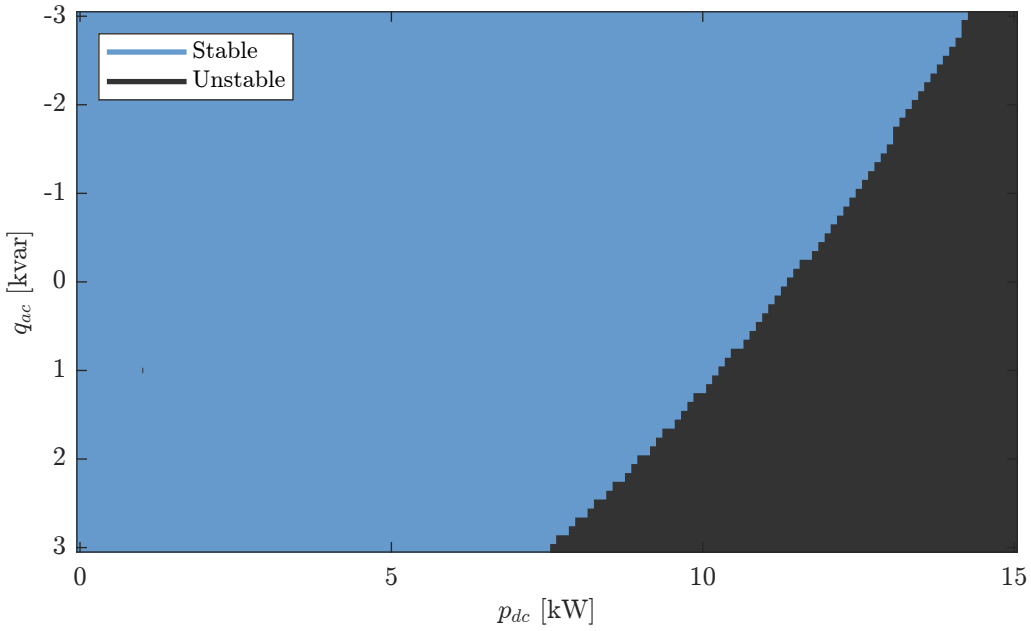

Figure 5.19 – Stability analysis of the region of operation. The computation of the points of equilibrium for the unstable region did not return a real-valued solution.

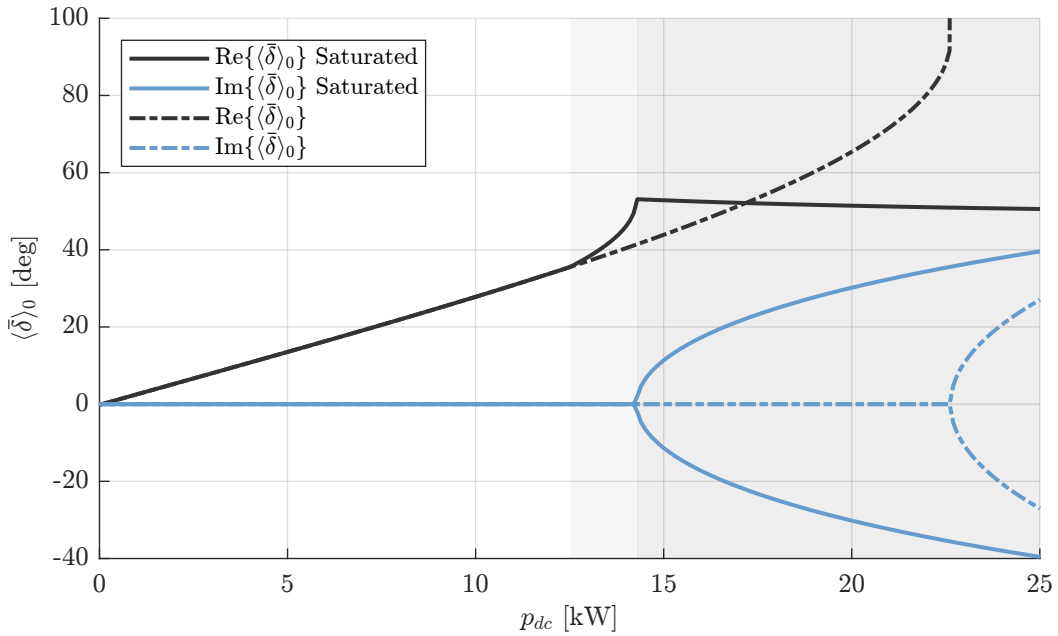

Figure 5.20 – Synchronism Angle δ at the point of equilibrium for multiple dc power processing levels with saturated and non-saturated ac bus voltage control.

maintain the voltage at the ac bus near the rated voltage. Additionally, a quadratic approximation is presented, which can be employed for open-loop compensation with the objective of decoupling the active and reactive power components. The combination of closed-loop reactive control with inherent compensation and the proposed decoupling strategy showcases the potential to enhance stability, optimize performance, and enable precise control of the active and reactive power exchange in the power converter system.

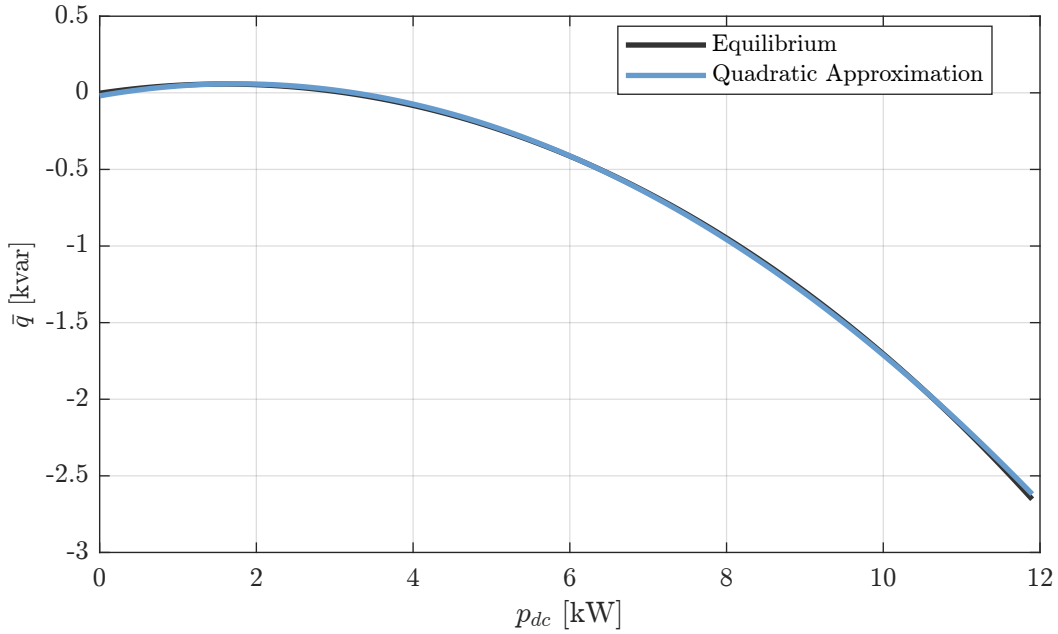

Figure 5.21 – AC power processed by the power converter with ac bus voltage control and quadratic approximation to maintain the ac bus voltage at 1.p.u.

5.7.3 Reactive Power Open-Loop Compensation

Based on the results discussed earlier, an open-loop compensation strategy can be utilized with the aim of decoupling the active and reactive power processed by the system. In particular, any curve on the stable surface depicted in Figure 5.19 has the potential to enhance the stability region of the power converter system during operation.

By employing an appropriate compensation curve, the power converter system can achieve improved stability margins and better control over the active and reactive power exchange. This decoupling strategy holds promise for optimizing system performance and ensuring reliable operation under varying operating conditions.

Thus, if we let

$$q_{\text{ref}} = \sum_{i=0}^{2} c_{q,i} p_{\text{ref}}^{i}, \tag{5.52}$$

the dynamic phasor representation can be modelled as

$$\langle q_{\text{ref}} \rangle = c_{q,0} \boldsymbol{h}_0 + c_{q,1} \langle p_{\text{ref}} \rangle + c_{q,2} \left(\boldsymbol{\Gamma} \circ \langle p_{\text{ref}} \rangle \right) \circ \langle p_{\text{ref}} \rangle , \tag{5.53}$$

with $\mathbf{c}_q$ obtained through a quadratic fitting of Figure 5.21.

Consequently, the equilibrium point of the synchronism angle is shown in Figure 5.22. A simulation of the system with the proposed compensation for multiple power steps is shown in Figure 5.23, with the eigenvalues of each simulation step presented in Figure 5.24 for the different power steps. From a direct comparison with Figure 5.17, the eigenvalues have a much smaller variation, while presenting a more damped behaviour.

The utilization of open-loop compensation, guided by the stable surface charac-

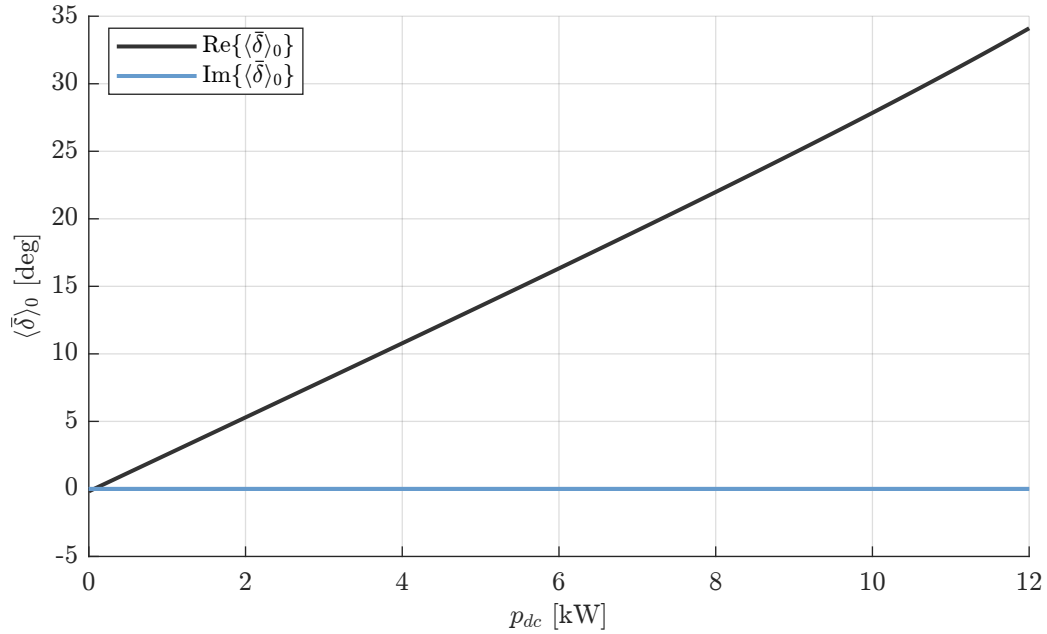

Figure 5.22 – Synchronism Angle δ at the point of equilibrium for multiple dc power processing levels without ac bus voltage control employing a reactive power open-loop compensation.

teristics from the stability assessment, is a critical step toward enhancing the system's stability and achieving robust power converter operation.

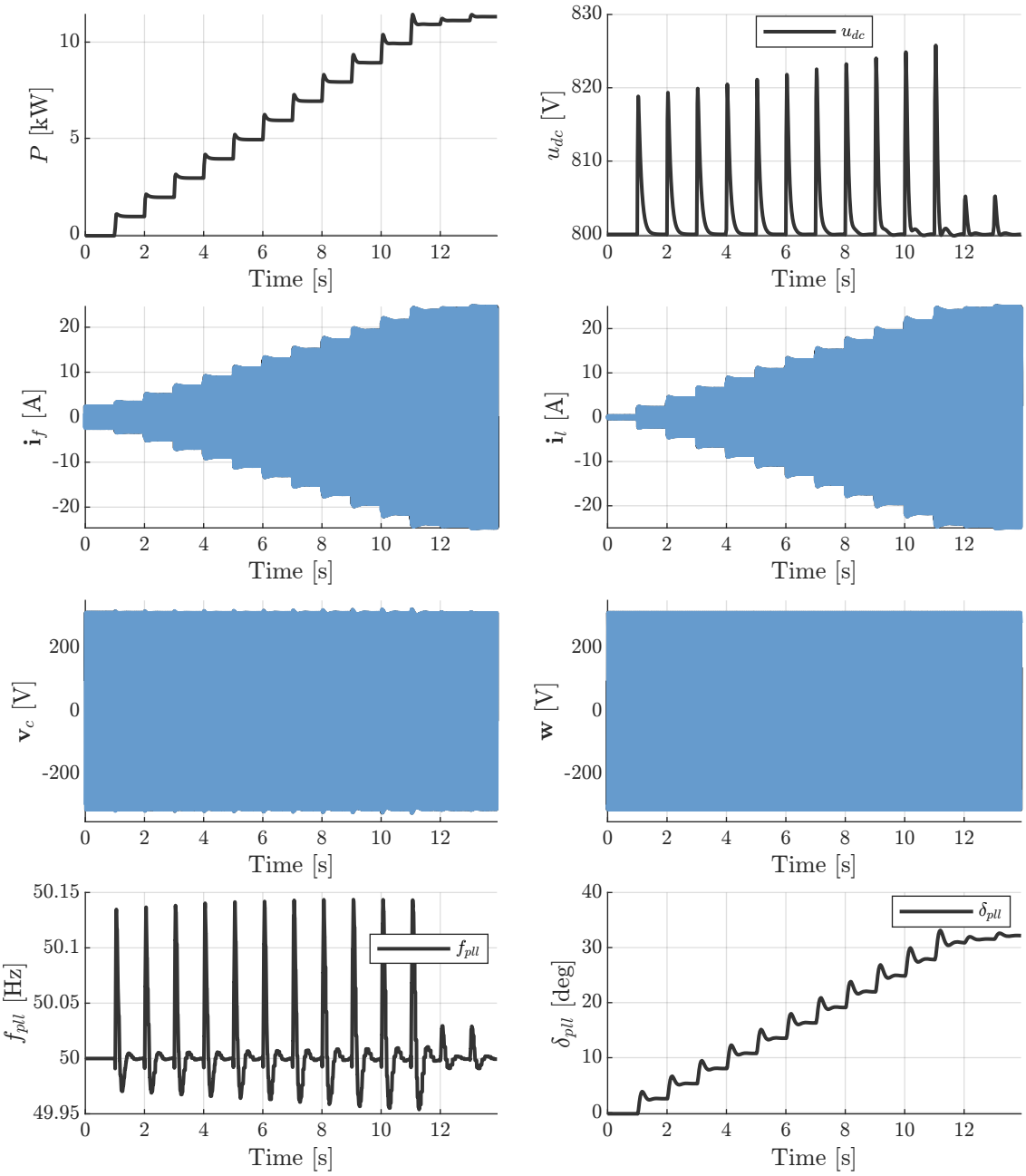

Figure 5.23 – Simulation of the Harmonic-State model for multiple power steps employing reactive power compensation.

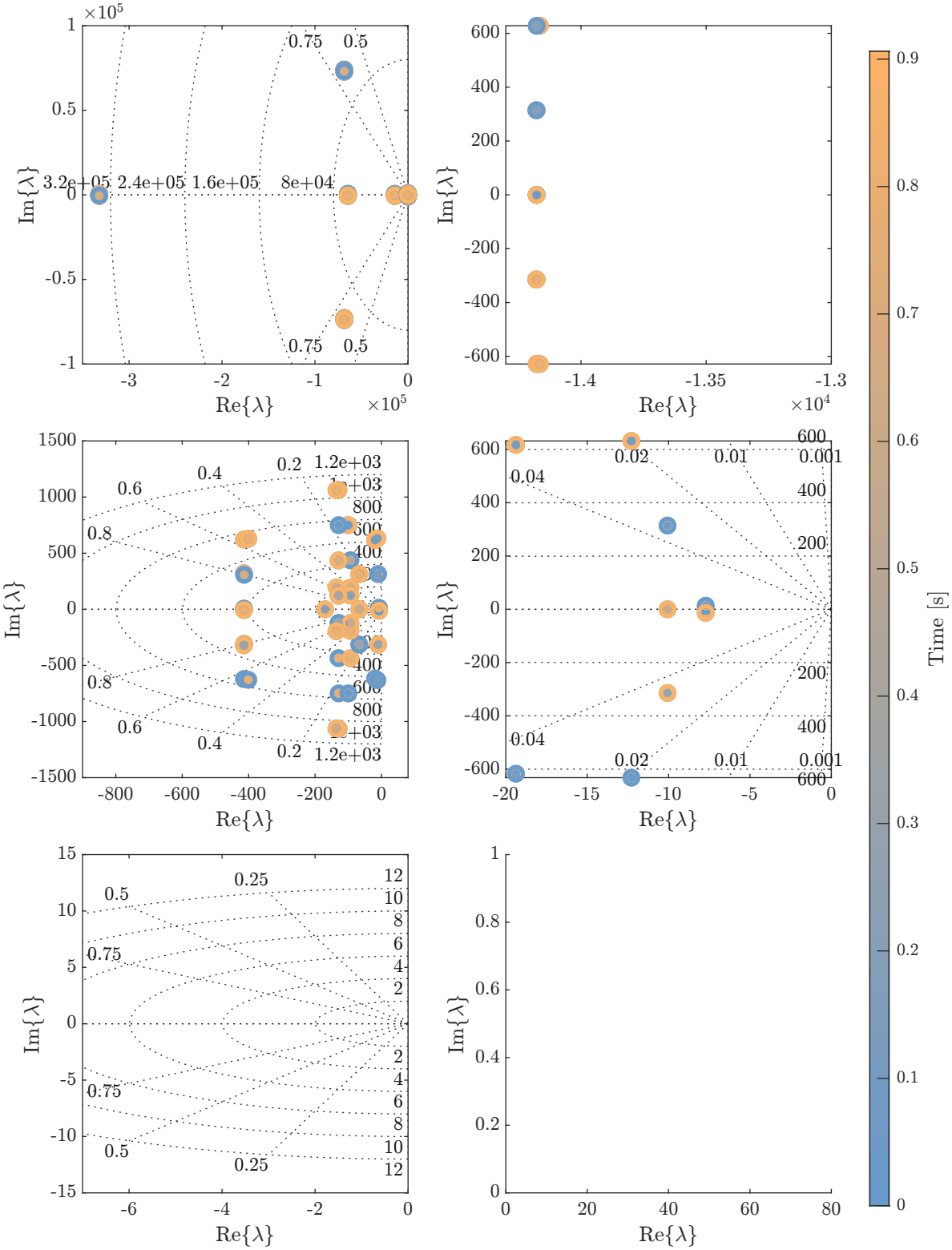

(a) 0 kW.

Figure 5.24 – Visualization of eigenvalue trajectories from the power step simulation using the complete model in MATLAB, simulated using the ode23tb solver.

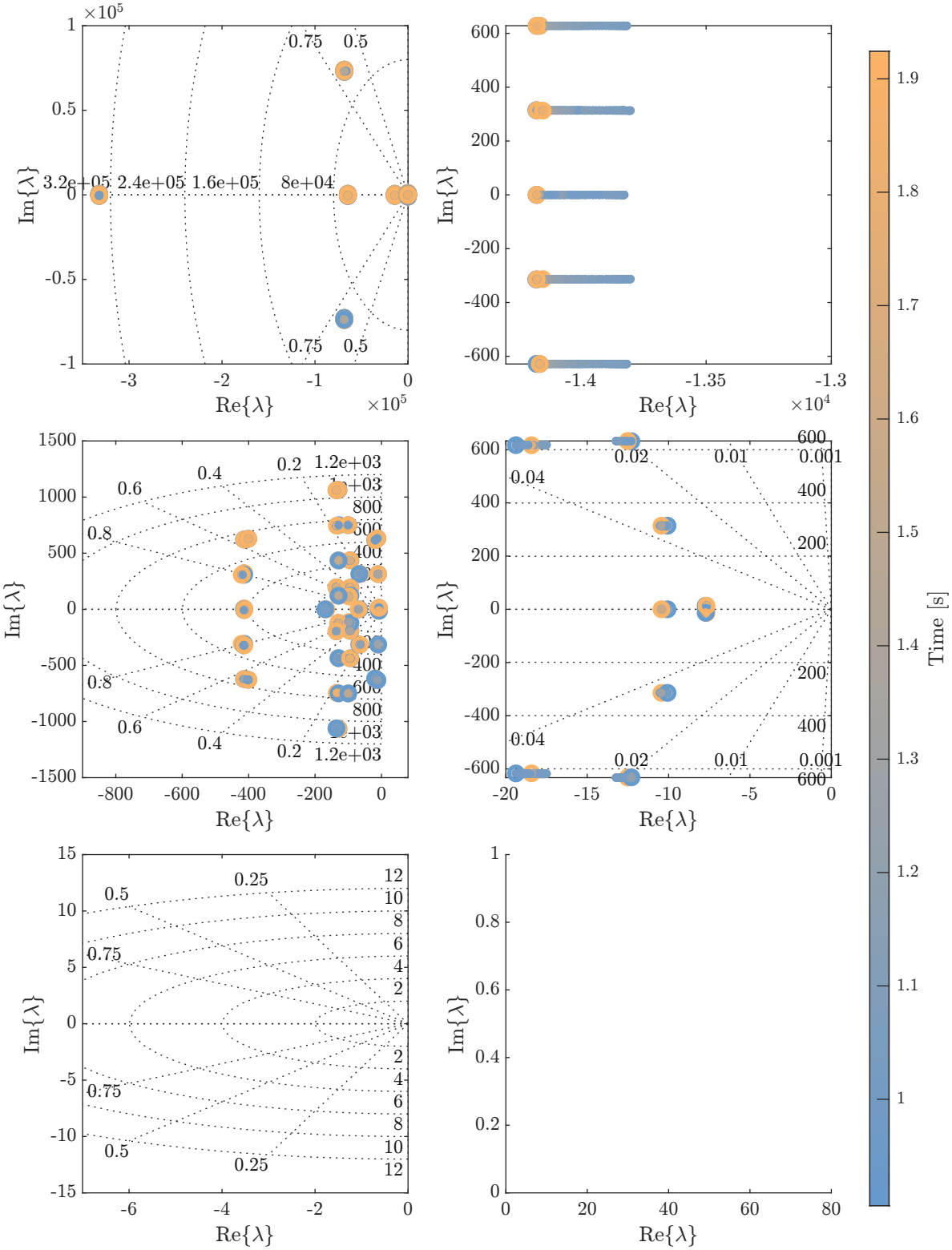

(b) 0–1 kW power step.

Figure 5.24 – Visualization of eigenvalue trajectories from the power step simulation using the complete model in MATLAB, simulated using the ode23tb solver.

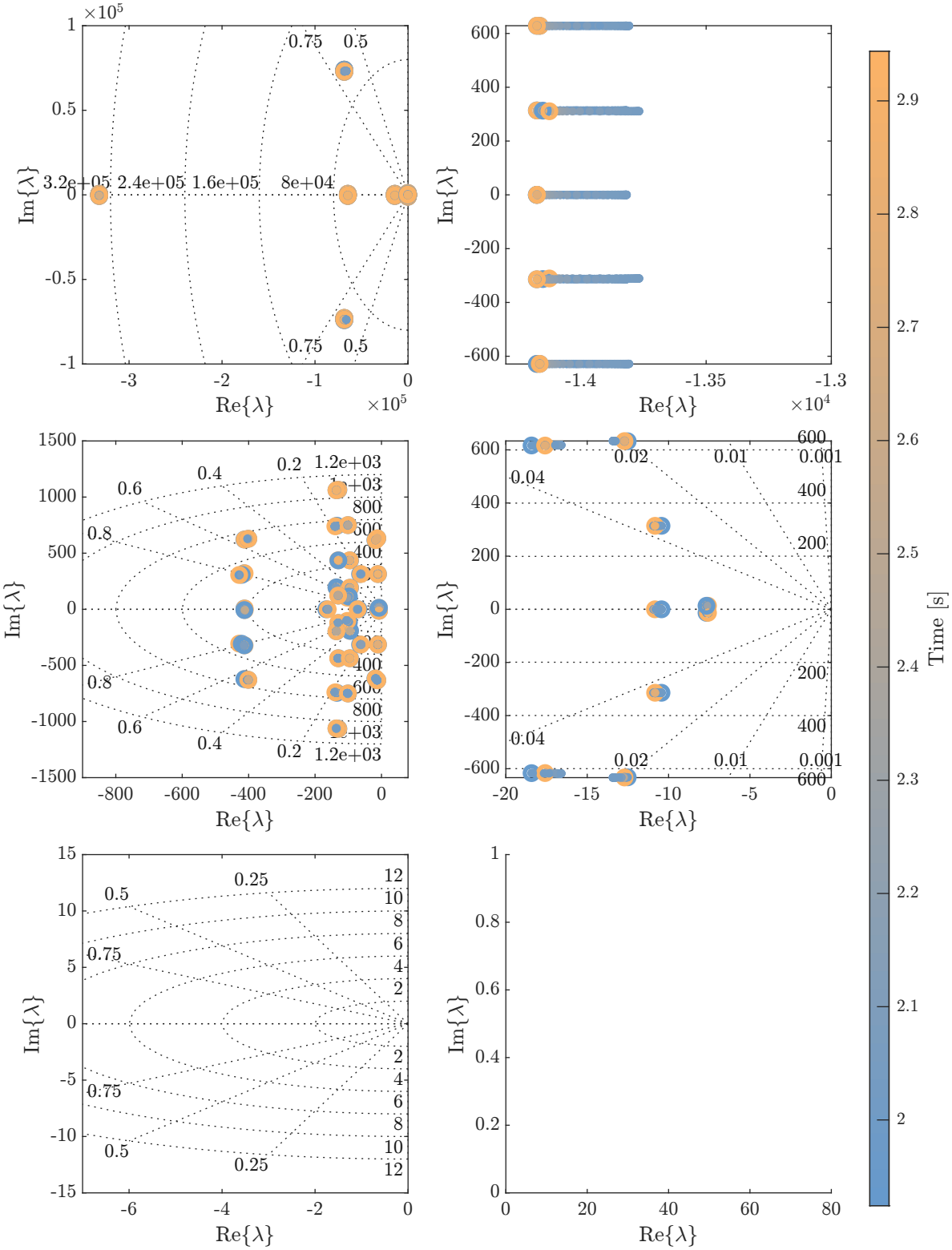

(c) 1–2 kW power step.

Figure 5.24 – Visualization of eigenvalue trajectories from the power step simulation using the complete model in MATLAB, simulated using the ode23tb solver.

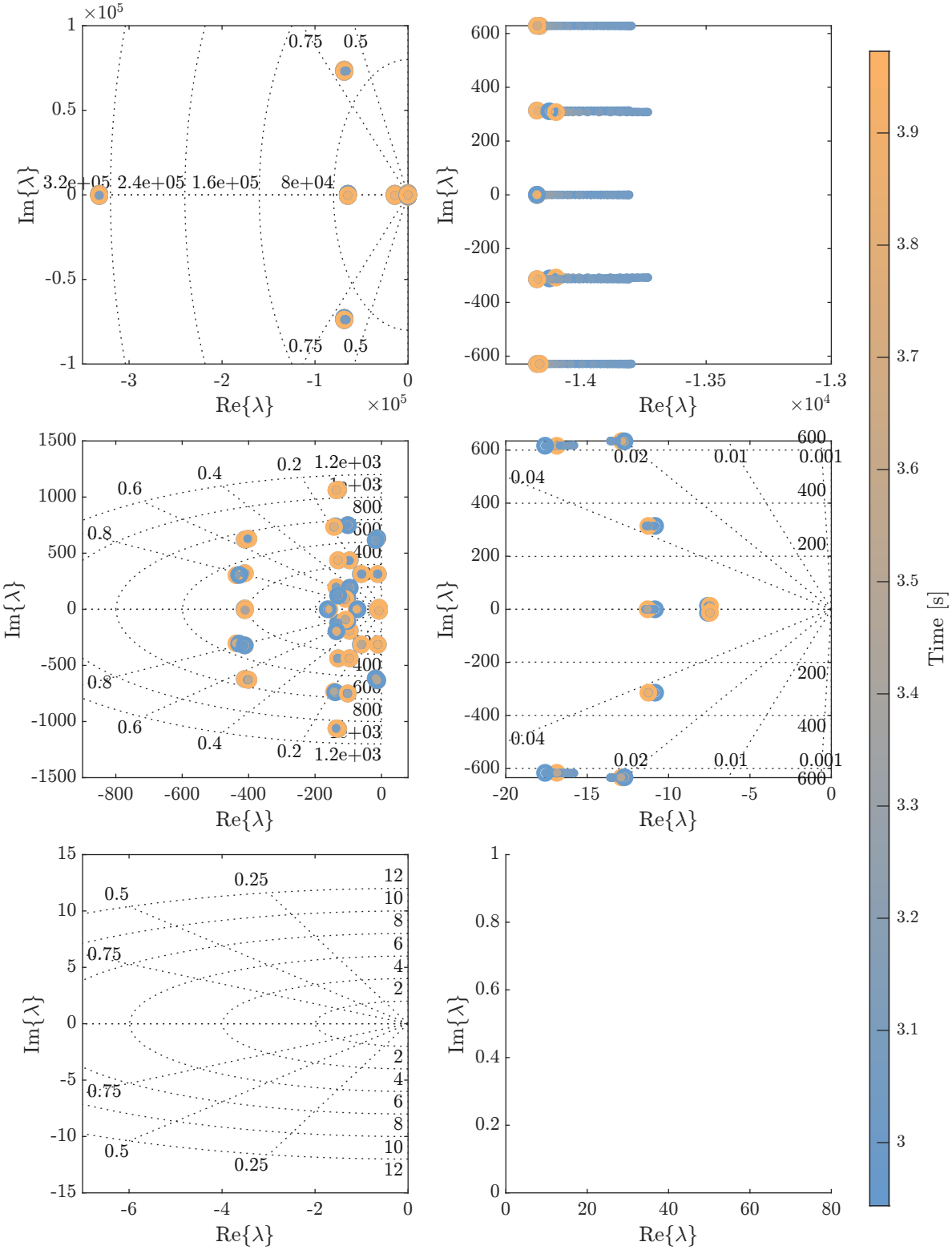

(d) 2–3 kW power step.

Figure 5.24 – Visualization of eigenvalue trajectories from the power step simulation using the complete model in MATLAB, simulated using the ode23tb solver.

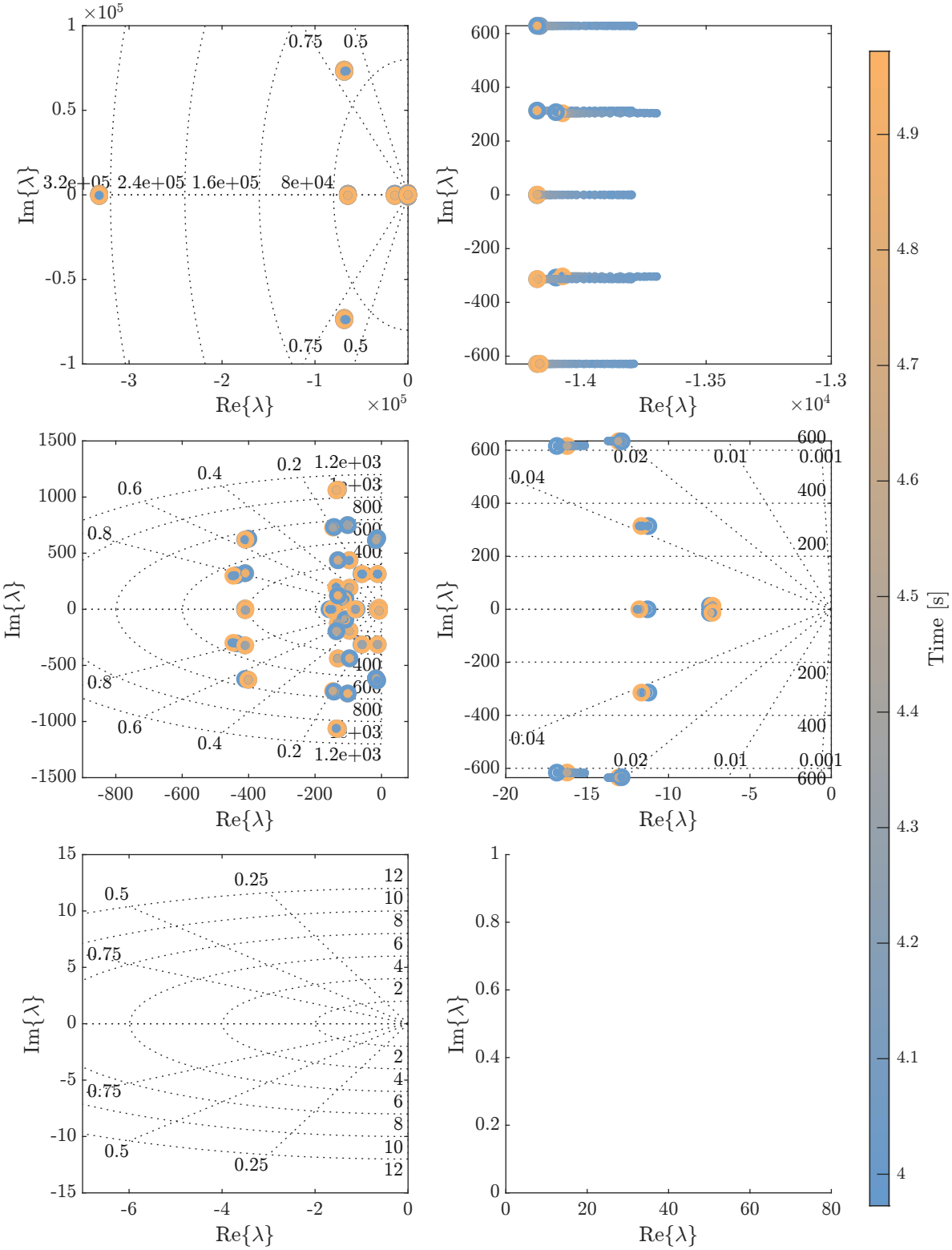

(e) 3–4 kW power step.

Figure 5.24 – Visualization of eigenvalue trajectories from the power step simulation using the complete model in MATLAB, simulated using the ode23tb solver.

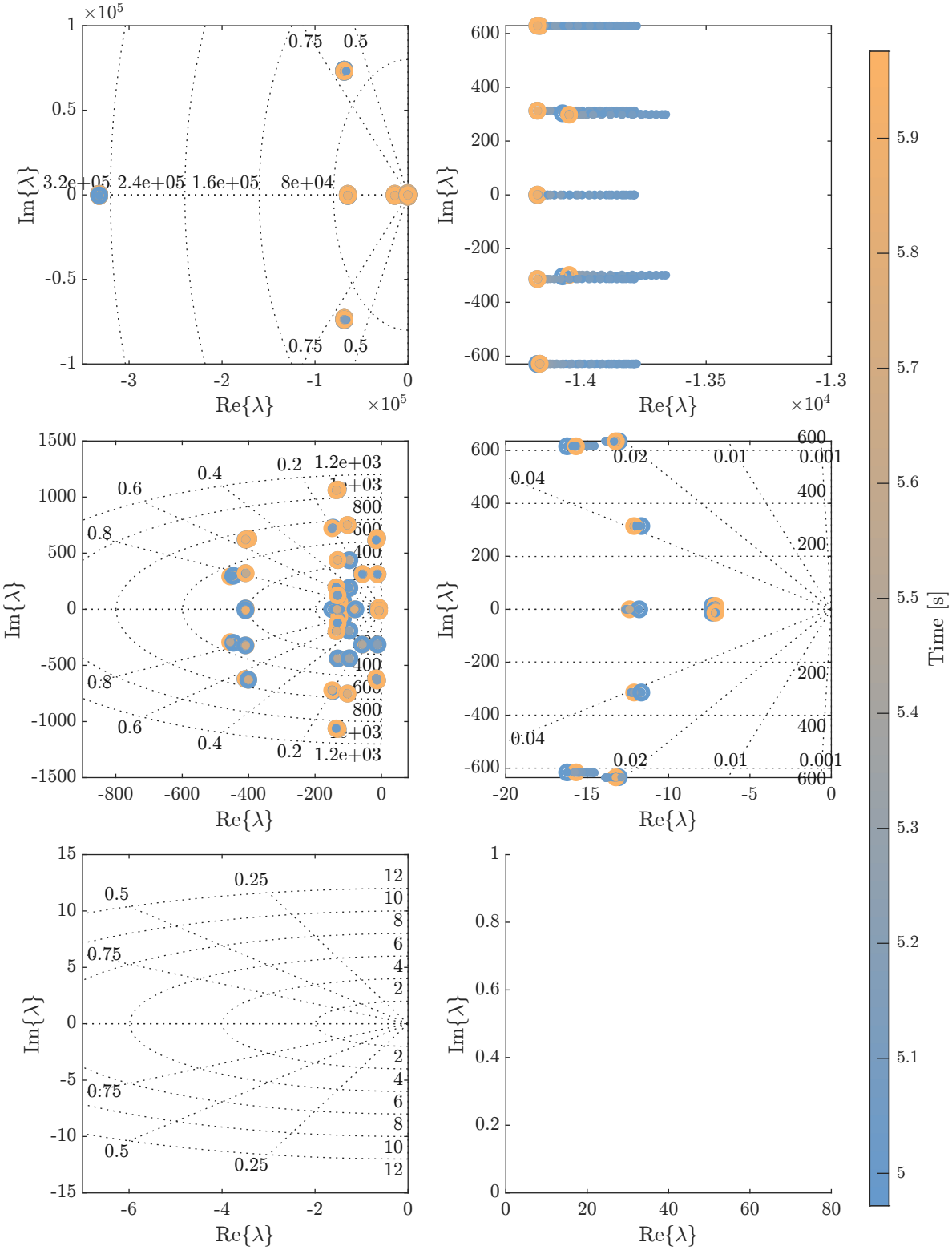

(f) 4–5 kW power step.

Figure 5.24 – Visualization of eigenvalue trajectories from the power step simulation using the complete model in MATLAB, simulated using the ode23tb solver.

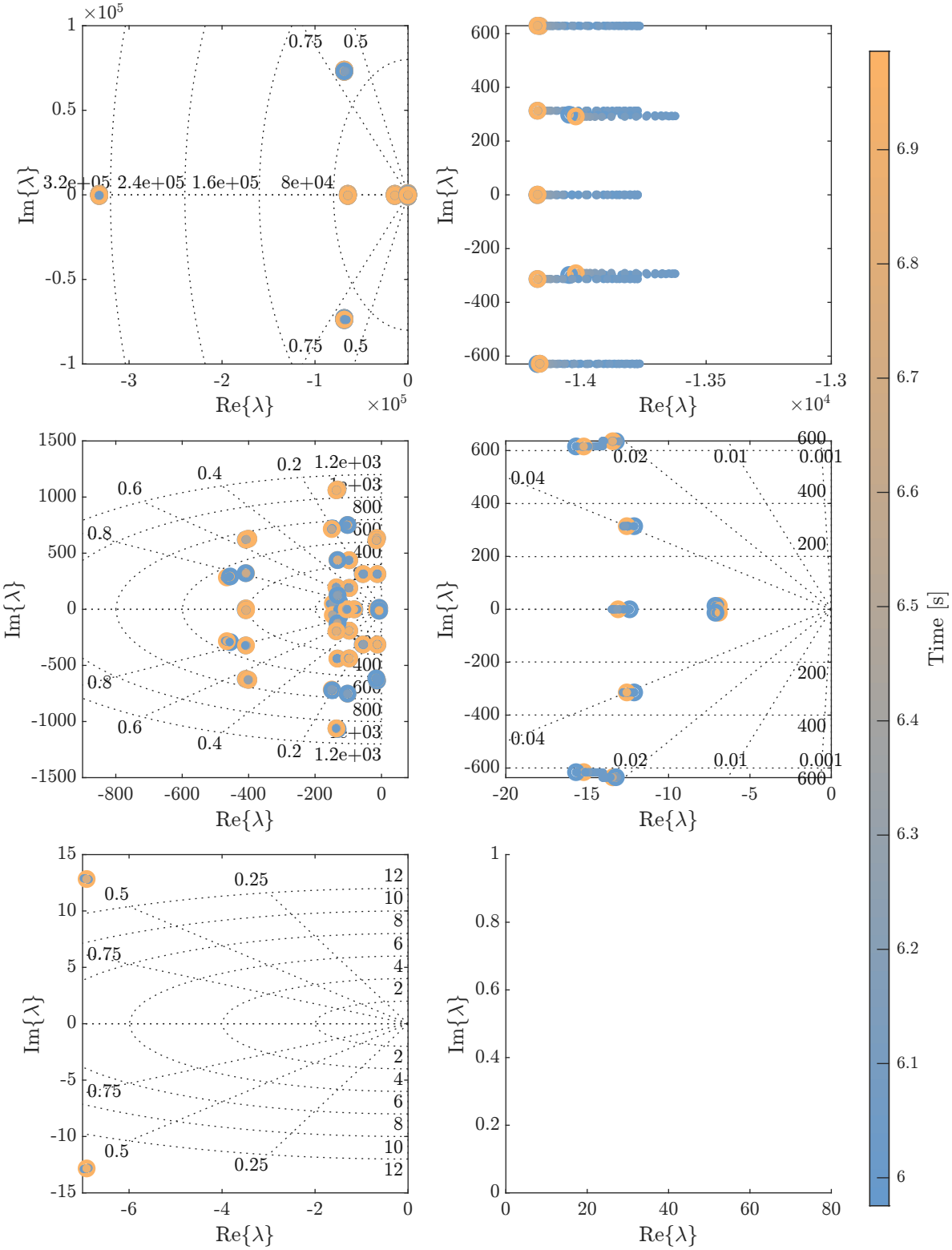

(g) 5–6 kW power step.

Figure 5.24 – Visualization of eigenvalue trajectories from the power step simulation using the complete model in MATLAB, simulated using the ode23tb solver.

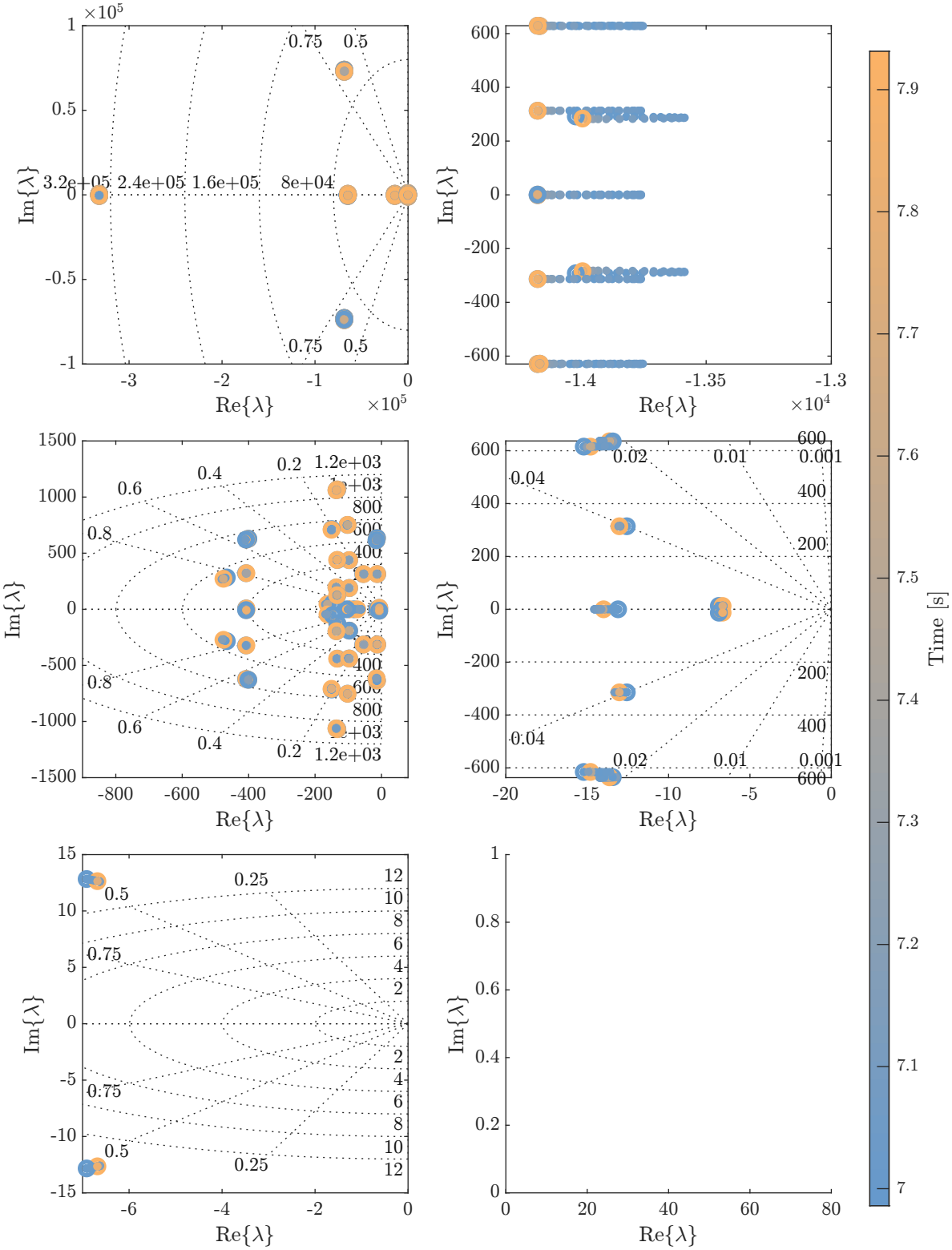

(h) 6–7 kW power step.

Figure 5.24 – Visualization of eigenvalue trajectories from the power step simulation using the complete model in MATLAB, simulated using the ode23tb solver.

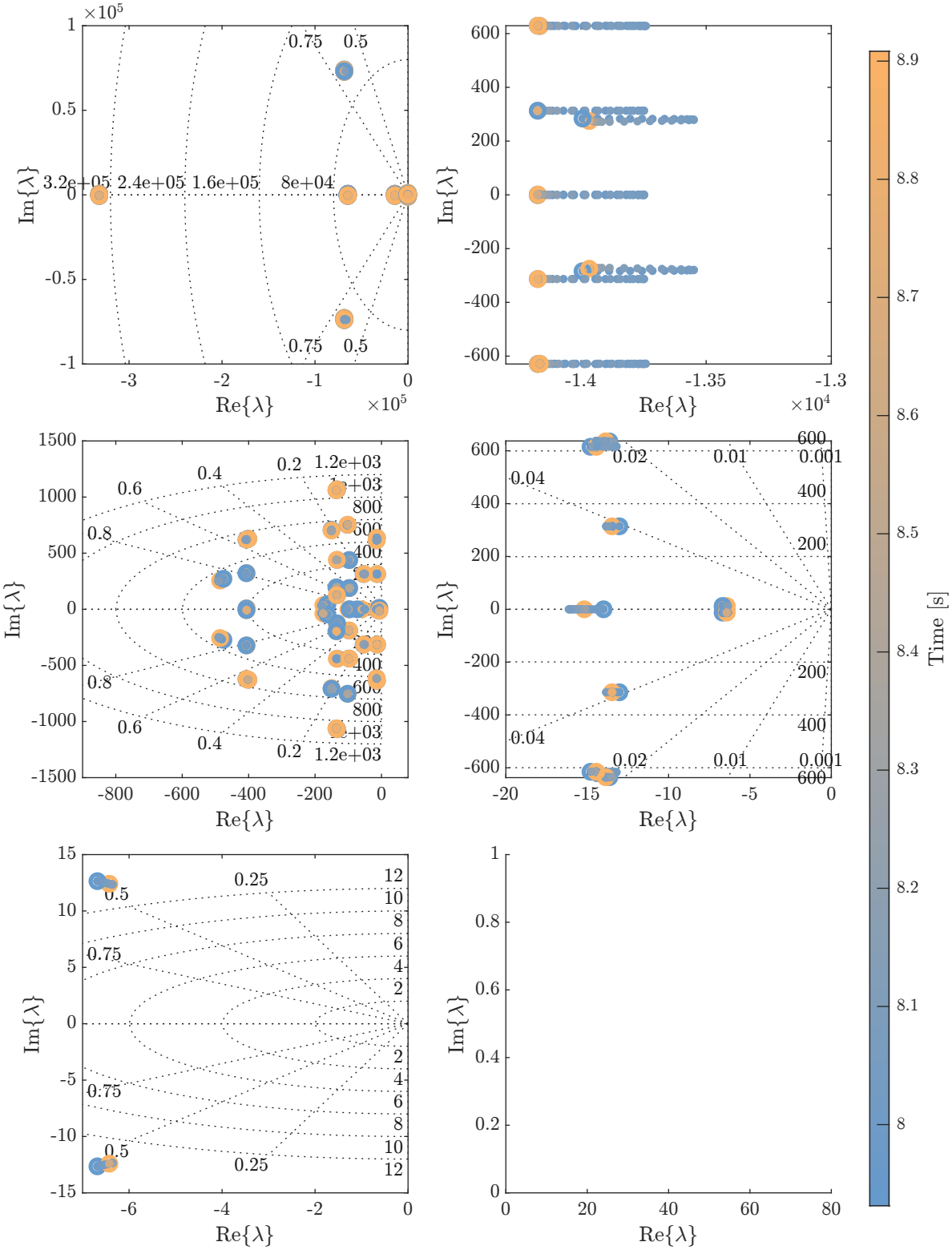

(i) 7–8 kW power step.

Figure 5.24 – Visualization of eigenvalue trajectories from the power step simulation using the complete model in MATLAB, simulated using the ode23tb solver.

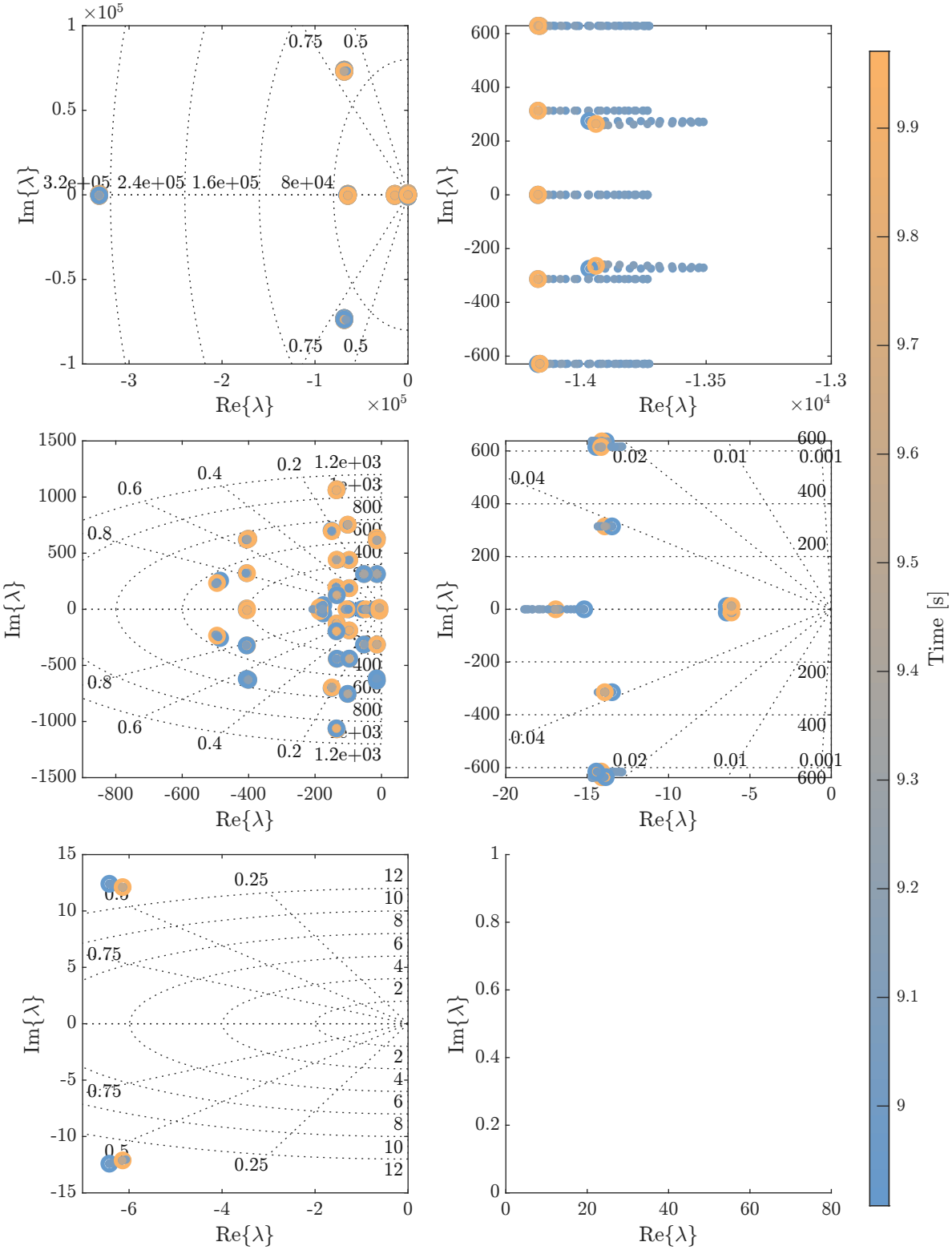

(j) 8–9 kW power step.

Figure 5.24 – Visualization of eigenvalue trajectories from the power step simulation using the complete model in MATLAB, simulated using the ode23tb solver.

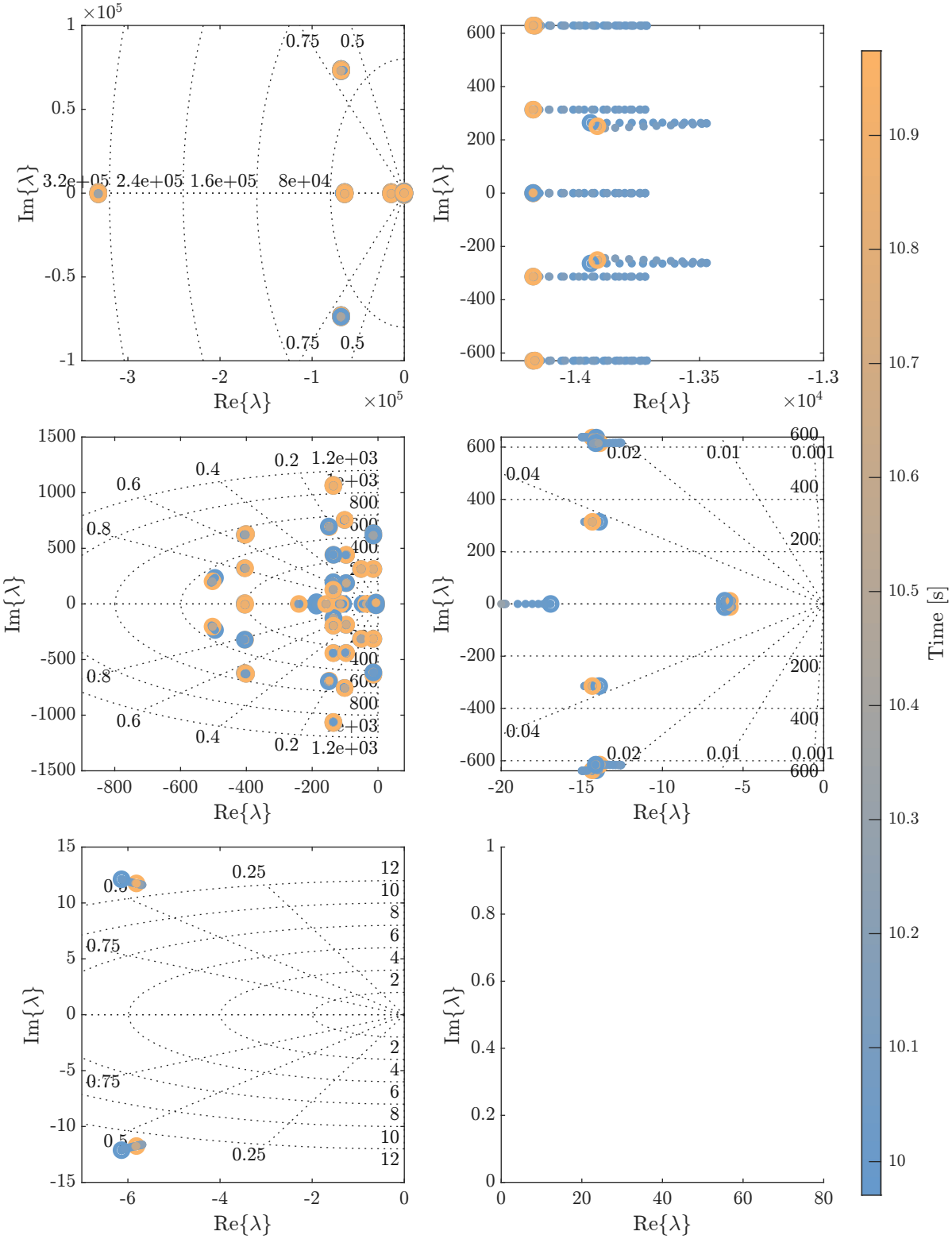

(k) 9–10 kW power step.

Figure 5.24 – Visualization of eigenvalue trajectories from the power step simulation using the complete model in MATLAB, simulated using the ode23tb solver.

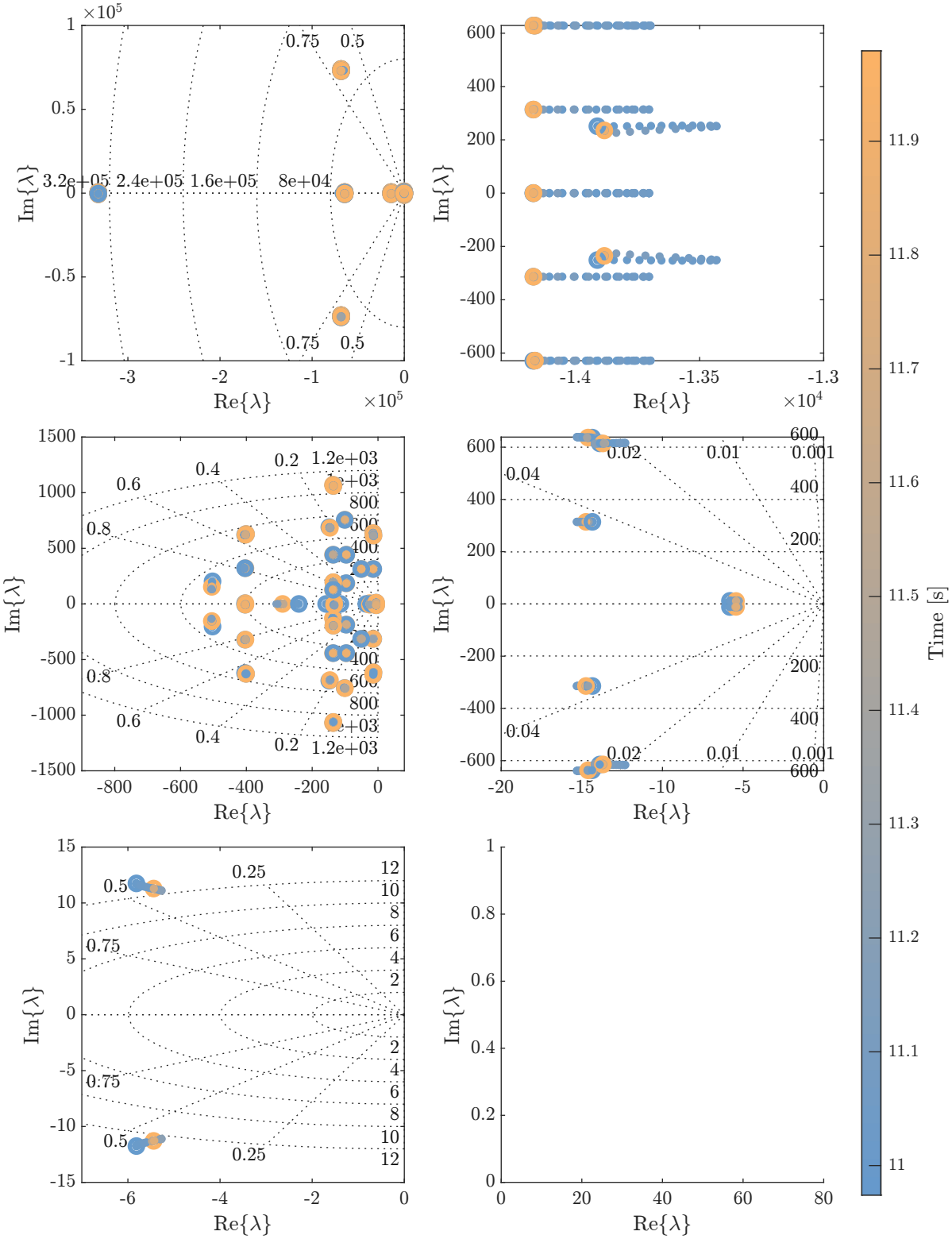

(l) 10–11 kW power step.

Figure 5.24 – Visualization of eigenvalue trajectories from the power step simulation using the complete model in MATLAB, simulated using the ode23tb solver.

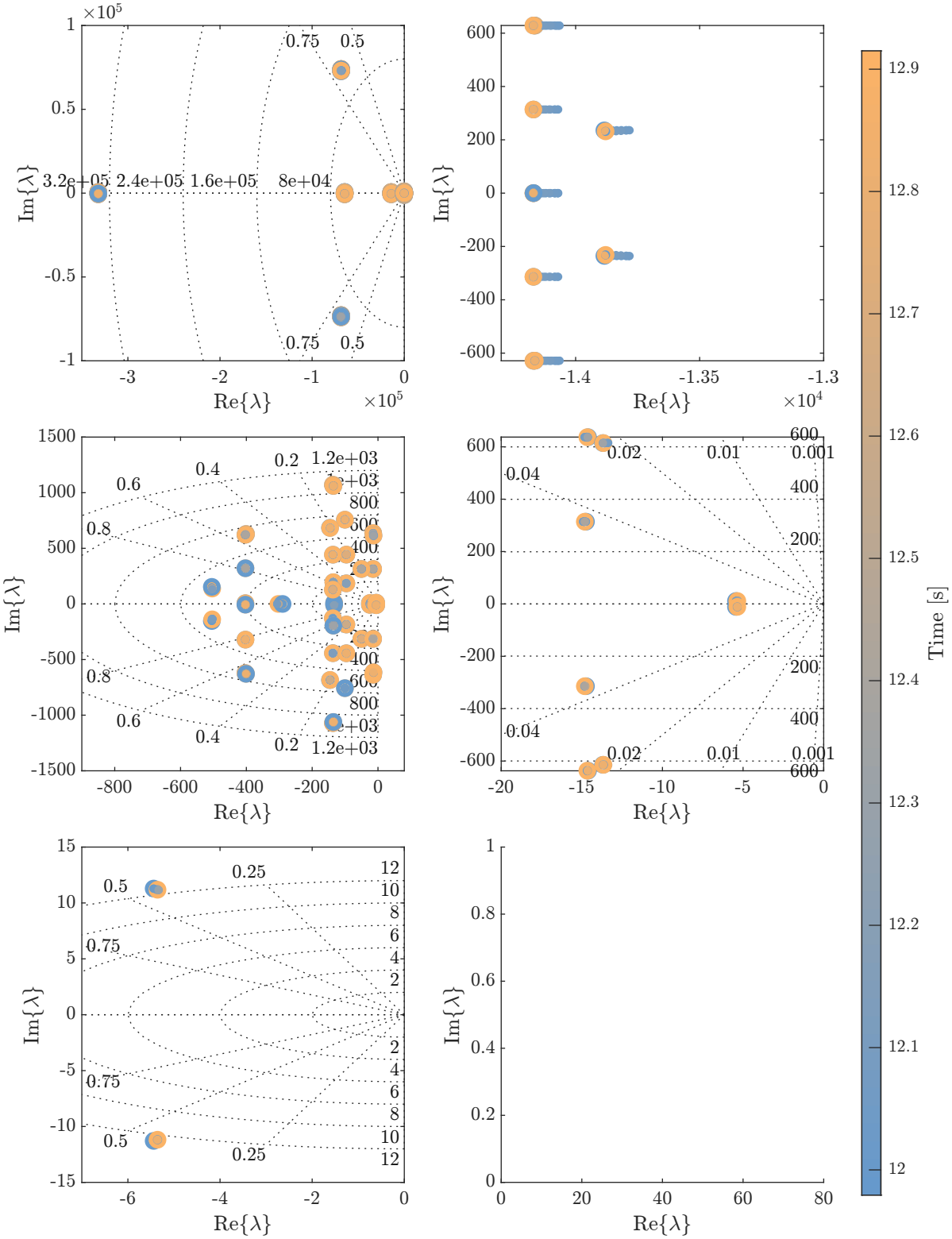

(m) 11–11.2 kW power step.

Figure 5.24 – Visualization of eigenvalue trajectories from the power step simulation using the complete model in MATLAB, simulated using the ode23tb solver.

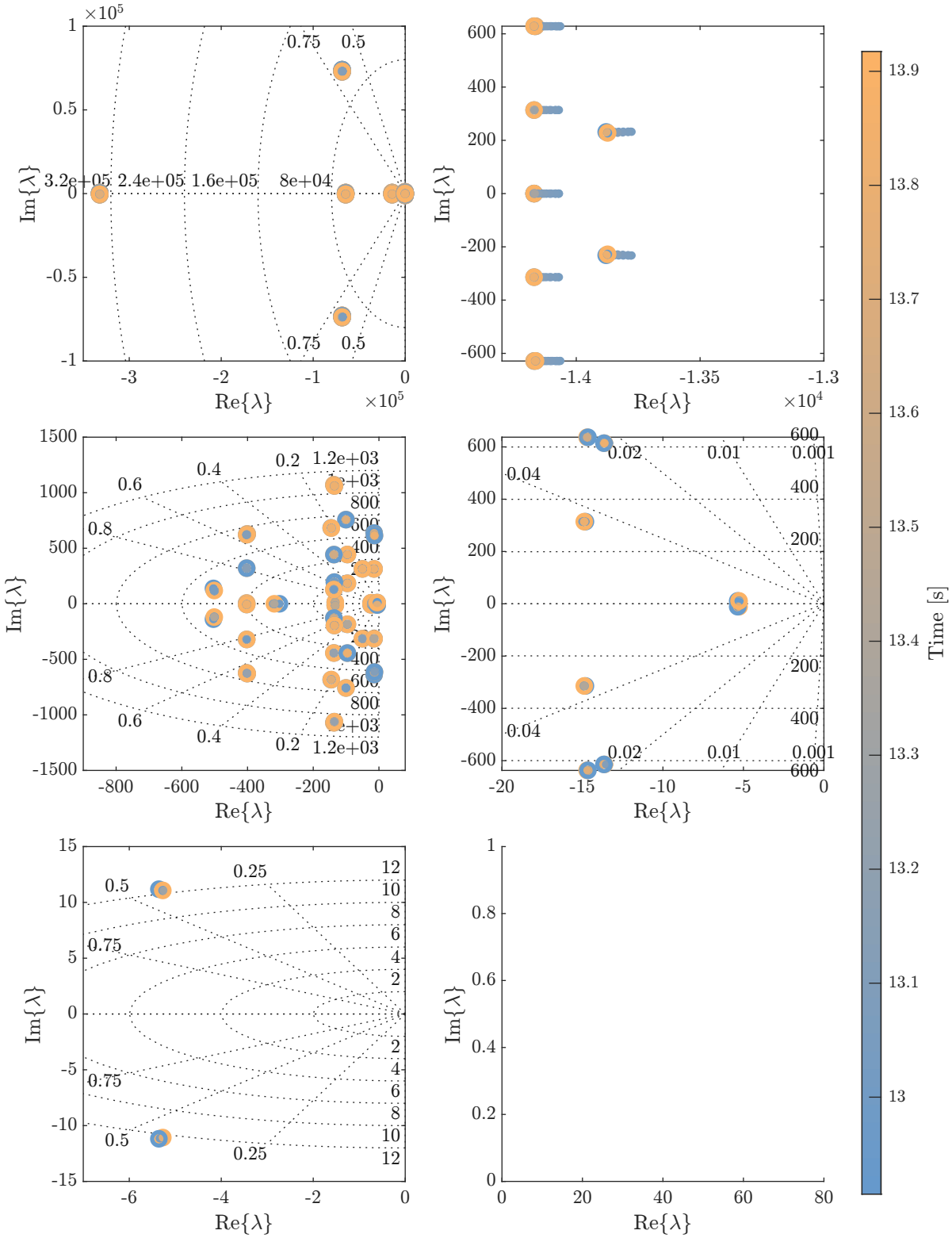

(n) 11.2–11.4 kW

Figure 5.24 – Visualization of eigenvalue trajectories from the power step simulation using the MAF-PLL model with reactive power compensation in MATLAB, simulated using the ode23tb solver.

5.8 REMARKS

The present section showcases the development of a nonlinear Harmonic State-Space model for the Synchronous Reference Frame Phase-Locked Loop (SRF-PLL). The complexity of the model varies depending on the number of harmonics considered and the number of terms in the Taylor series used to approximate the functions. Achieving higher accuracy in the model might require a larger number of terms, which may lead to longer computational times due to the challenging computation of derivative functionals involving numerous polynomial operations. Additionally, when supervisory control strategies are integrated, the overall complexity of the power converter system model can become exceedingly intricate, resulting in complex equations.

As a consequence, a primary analysis of the problem becomes imperative to validate the model's complexity and evaluate the desired behavior for multiple scenarios. Selecting an appropriate model complexity, aligned with the validations of employed models, becomes a valuable approach to assess the behavior of power converter systems while minimizing the number of simulations. Computation of fixed points and eigenvalues at these points of equilibrium can be employed to ascertain system stability. Furthermore, employing different strategies to improve system robustness and analyzing their impact and interactions with various electrical quantities within the system can provide valuable insights. This comprehensive analysis enables the exploration and optimization of the power converter system performance effectively, advancing the understanding of stability and control strategies in complex power systems.

In power converter systems operating under weak grid conditions, it has been observed that a strategy to mitigate the coupling between active and reactive power is crucial for ensuring a robust deployment of the power converters. The current chapter presented an analytical approach to this analysis, which differs from the qualitative descriptions commonly found in the current state-of-the-art literature. By employing analytical methods, a more comprehensive understanding of the problem was demonstrated while offering viable solutions to the mitigation of the exposed problems. The use of more complex models is justified in this context, considering the significant degree of nonlinearities observed in the mathematical model. A deeper insight into the intricacies of the power converter system can be obtained, allowing the development of effective strategies to address the challenges posed by weak grid conditions. This analytical approach is pivotal for designing robust and efficient power converter systems capable of maintaining stable operation under varying grid conditions.

The analysis presented in this chapter focused on a single power converter, but it is important to note that the same methodology can be extended to multiple parallel connected converters using the Lunze transformation, as described in Chapter 3. By employing this transformation, the subtractive-mode component can be suppressed, and the short circuit ratio (SCR) can be recalculated based on new base values while achieving

similar performance to the analysis demonstrated in this chapter. This approach reduces the complexity of the mathematical description, while the models and methodology presented in this thesis remain applicable for obtaining a comprehensive model of the entire system. Moreover, the models presented in this chapter hold potential for studying grid-forming converters. In this scenario, the grid frequency is modeled as an input to the system, enabling a comprehensive analysis of grid-forming converter behavior. The versatility of the models and methodology makes them suitable for investigating various converter configurations and facilitating a thorough understanding of power converter system dynamics in different grid conditions.

Chapter

6 Minimization of High-Frequency Circulating Currents

6.1 INTRODUCTION

This chapter aims to present a study on detection and minimization techniques for high-frequency circulating currents applied to paralleled connected voltage-source PWM converters, while focusing on modular solutions which can be employed without a specific communication channel between converters. In terms of reliability, these techniques should prove to be more robust, as some state-of-the-art techniques rely on communication networks with increased complexity based on the number of paralleled power converters, or useful for a reduced number of paralleled connected converters.

From the analytic analysis presented in Chapter 3, we can conclude that these high frequency currents have their origin in carrier phase-mismatches and parametric deviations, which in turn creates a coupling between additive and subtractive modes intra- and inter-converters, i.e., a coupling between α, β and γ-axis electrical quantities of each converter and their subtractive- and additive-modes while taking into account a more systemic approach, when considering the connection of similar converters. These parametric deviations are more accentuated when converters with different power ratings or different filter/converter topologies are connected in parallel, as the amplitude of the subtractive-mode γ-axis should vary.

The current state-of-the-art already presents studies on circulating currents minimization techniques for paralleled converters employing control strategies based on sliding-mode control [13] with good performance, although such strategies are heavily dependent on real-time measurements of the system electric quantities to minimize the subtractive-mode currents, which are not available for a modular solution, as a suitable operation would be reliant on very fast and low latency communication networks, capable of communicating in frequencies higher than the switching frequency, which are not attractive for high-frequency power converters. However, such techniques are proven to be adequate for centralized control strategies.

The authors in [21, 22] propose an open-loop compensation of the switching period

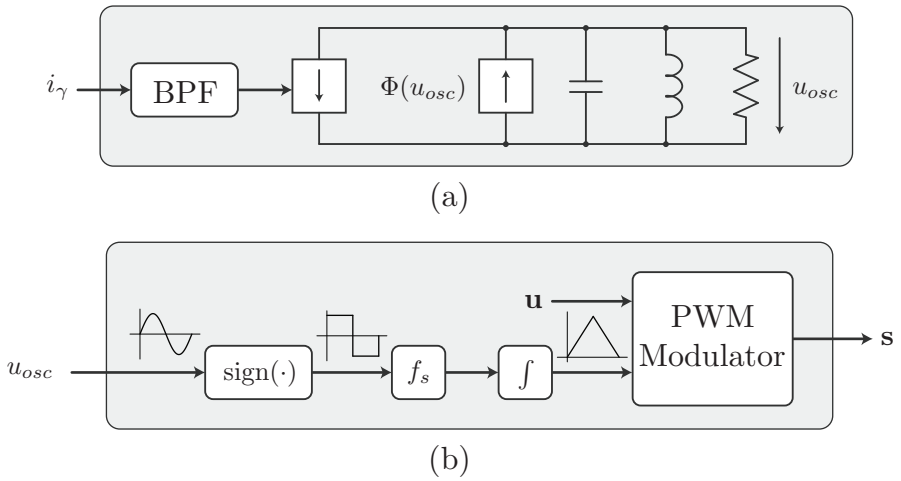

Figure 6.1 – Block diagram of the Virtual Oscillator Control for carrier generation [1] (a) Virtual oscillator circuit. (b) Nonlinear feedback of the virtual oscillator voltage.

according to the measured γ-axis current based on the mean inductance value of the subtractive-mode current path and the dc-bus voltage. In this case, a master converter must be defined, as stability is not guaranteed when there is no master converter and does not take into account parametric variations discussed in Chapter 3, thereby limiting its applicability in practical scenarios where parameter variations are inevitable.

An approach based on the Virtual Oscillator Control applied to the γ-axis circulating current is presented in [1]. In this strategy, a nonlinear oscillator is used to generate the Sinusoidal Pulse-Width Modulation (SPWM) carriers, while relying on the natural synchronization characteristic of the oscillators. The block diagram is presented in Figure 6.1. In this case, ideally the γ-axis voltage synthesized by each converter is null valued in the medium frequency-range. In this case, the circulating currents pertain to the switching frequency spectra, and the synchronization should be trivial. A concern that can be raised on its applicability for different modulation strategies is the maintenance of the passive characteristic of the γ-axis voltage when allied with a current control to raise the subtractive-mode impedance.

A more recent approach is through the use of the Global Synchronous Pulse-Width Modulation (GSPWM) [24], where the carriers are synchronized among distributed converters. In this approach, the synchronization is reliant on a low-latency communication channel, with time delays lower than 1 μs for power converters switching at a frequency of 10 kHz, as demonstrated in [24, 88, 89]. The implementation of such an approach may prove to be challenging for power converters operating at higher switching frequencies, which is a trend observed with the advancement of recent semiconductor technologies, although suitable for high-power applications. This strategy is illustrated in Figure 6.2.

In more recent advances, the synchronization is implemented via Phase-Locked Loop (PLL) and frequency decimation, with the synchronization via grid voltage, as illustrated by Figure 6.3.a, which in turn enables the communication to operate at lower

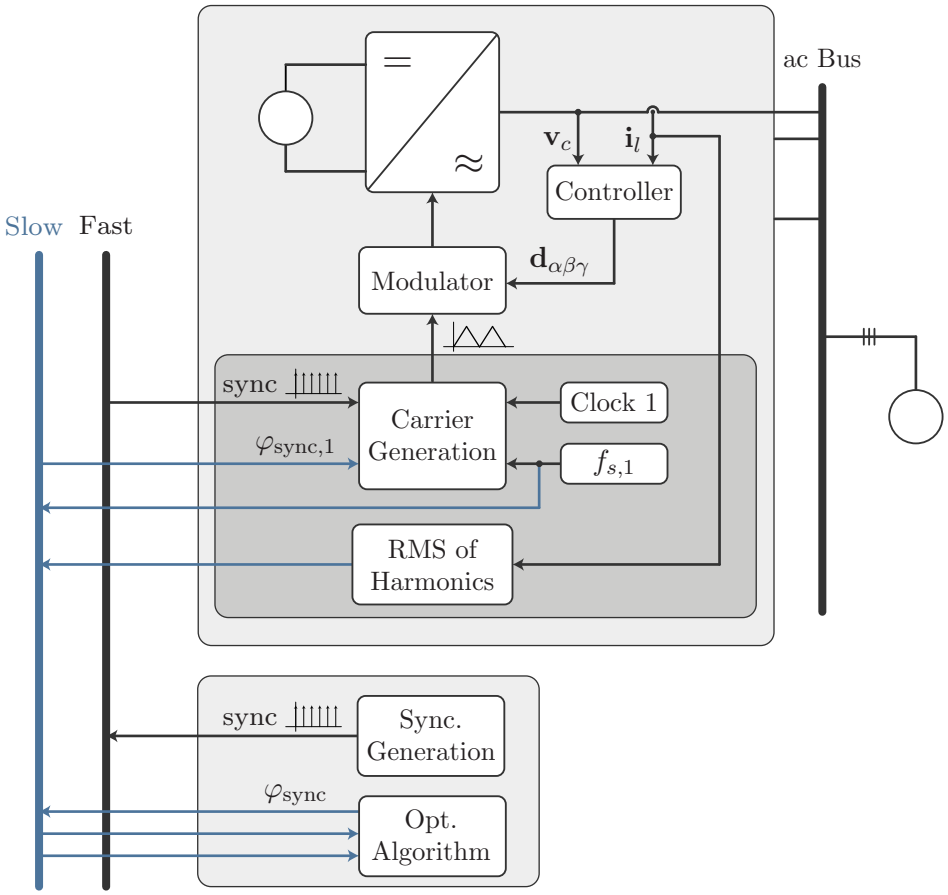

Figure 6.2 – Block Diagram of the Global Synchronous Pulse-Width Modulation [2]. The black communication bus must have a transmission delay of 1 μs to precisely synchronize the carriers, while the gray communication channel does not have a strict requirement.

speeds, but still reliant on a communication channel [2, 90] and the currents should be sampled at a high frequency. In this strategy, the phase of each modulator is fixed around an optimal value, which relies on an optimization routine with a well-defined objective function, which is performed by a central controller. This technique makes use of a Grid Angle Tracker (GAT) to track the grid angle with a limited derivative slope, limiting the switching frequency in a range, as the instantaneous grid frequency estimation from the PLL can vary abruptly, as shown in Figure 6.3.b and a Carrier Angle Tracker (CAT), which is a closed-loop control to vanish the angle difference between the modulator and the angle reference. The decoupling between carrier and grid dynamics is heavily reliant in these angle trackers.

If we define the objective function as the minimization of the additive-mode currents Total Harmonic Distortion (THD) as employed by most methods, the optimization will result in the maximization of the circulating currents. Hence by minimizing the output current THD of each conveter, proposed in [23], the strategy should be able to minimize the circulating currents. However, the execution of the optimization routines to obtain the phases of each carrier is still dependent on a communication channel.

One of the drawbacks of grid voltage synchronization is the lower robustness of the proposed strategy due to grid frequency and phase variations, which might result in instantaneous fluctuations of the switching frequency. These fluctuations might contribute to a non-monotonic behaviour of the carrier signal, which might reduce the effective resolution of the modulator and insert limit cycles. Also, if different filter topologies are taken into account, the grid voltage angle might vary with the power injection, as only L filters were considered, which in turn will be coupled to the switching frequency. Hence, subtractive-mode resonances might deviate the system behaviour from the optimal point of operation. Such discrepancies can be compensated via the optizmization routine, which in turn is reliant on the communication channel. Consequently, there is no mechanism for the converter to optimally operate without relying on the communication channel, thus distancing itself from the concept of modularity.

Therefore, the objective of this chapter is to present and illustrate two techniques that aim to achieve carrier synchronization. The first technique involves a master-slave scheme, where one converter acts as the master and others as slaves to achieve synchronization. The second technique involves a cooperative method, where multiple converters work together in a coordinated manner to achieve carrier synchronization. By exploring and comparing these two techniques, this chapter aims to provide insights into different approaches for achieving effective carrier synchronization in relevant applications.

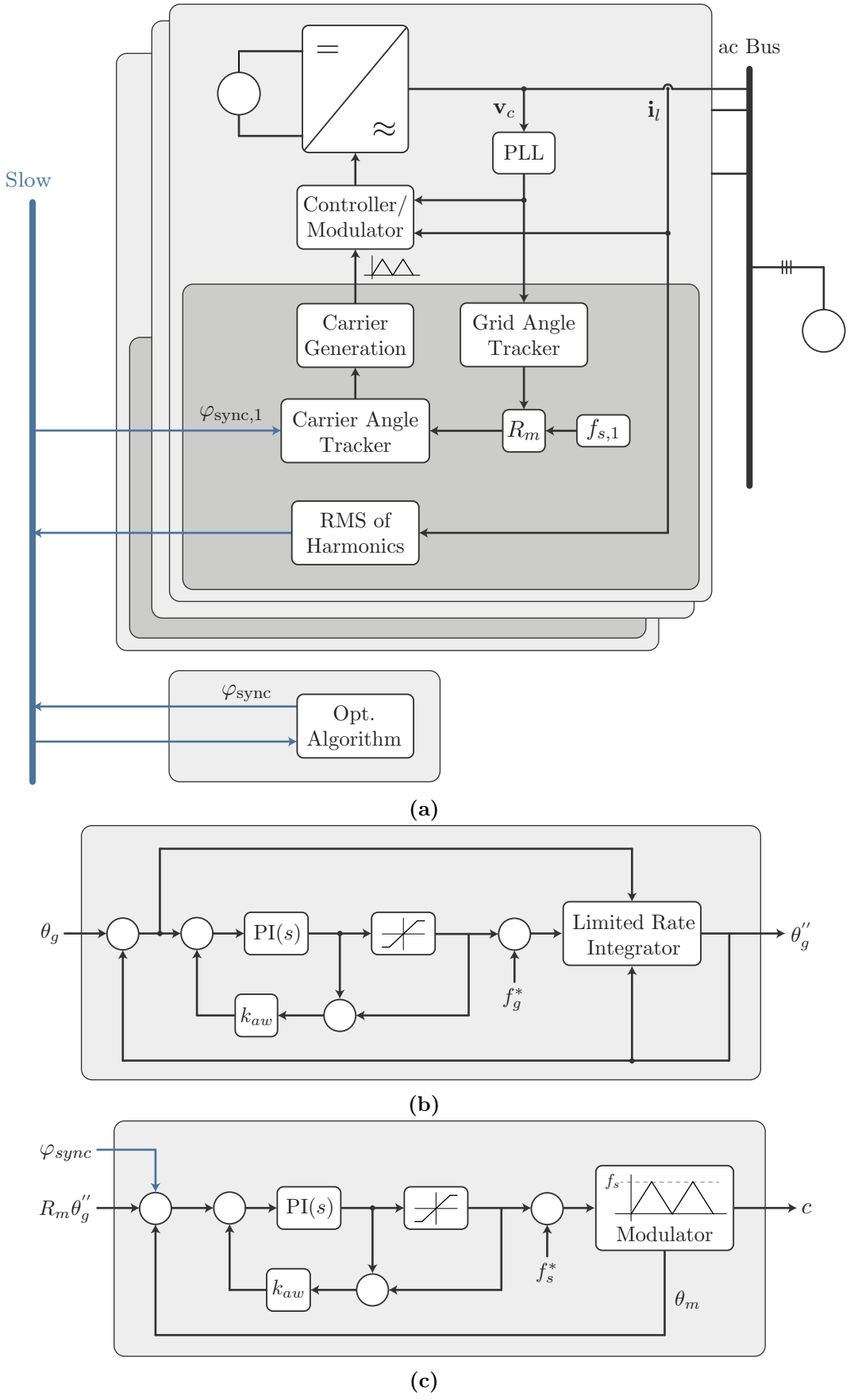

Figure 6.3 – (a) Block Diagram of the PLL-CS Global Synchronous Pulse-Width Modulation [2]. (b) Grid Angle Tracker (GAT), which limits the admissible frequency variations. (c) Carrier Angle Tracker (CAT).

6.2 BASIC CONCEPTS

Based on the discussions presented in Chapter 3 and Chapter 4, it can be inferred that there are no additive-mode currents in the γ-axis, i.e, $i_{\gamma,am}$ vanishes when multiple power converters are connected in parallel with a common dc link, as opposed to the $i_{\gamma,sm}$, which is still present. Assuming the presence of a γ-axis current controller, designed in such that the input impedance of the closed-loop system is larger in magnitude than the open-loop impedance, it can be assumed that the input impedance of each converter is sufficiently high such that there are no medium-frequency circulating currents. Consequently, the circulating currents in the γ-axis are mainly dominated by high-frequency components that are not controllable by the modulating signal in PWM-based modulation strategies. However, even if there are no γ-axis circulating currents due to the system's topological configuration, the energy of the high-frequency components will still circulate between the converters in the $\alpha\beta$ axis. This is because the additive-mode signal's L_2-norm is lower when there are phase mismatches, which forms the fundamental principle of interleaved power converters.

From inspection of the system inputs for each converter, we have that the switching function for the γ-axis for the n^{th} parallel-connected is given by

$$\mathbf{s}_n := \boldsymbol{\psi}(\mathbf{d}_n, c_n), \quad \forall\ n \in \mathbb{N}_N, \tag{6.1}$$

where $\mathbf{d}_n \in \mathbb{R}^3$ is the modulating signal vector in the $\alpha\beta\gamma$ axis, $c_n \in \mathbb{R}$, $\boldsymbol{\psi} : \mathbb{R}^3 \times \mathbb{R} \to \mathbb{R}^3$ is the modulation function and N is the number of paralleled connected converters. We can also rewrite the term in Equation 6.1 as functions of the system inputs, resulting in

$$\begin{aligned} \mathbf{d}_n &:= (\mathbf{d}_{n,\alpha\beta}, d_{n,\gamma,\text{ff}} + d_{n,\gamma,\text{ctrl}}) \\ c_n &:= \boldsymbol{\vartheta}(f_{s,n}, \varphi_n) \end{aligned} \tag{6.2}$$

where $d_{n,\gamma,\text{ff}}$ is the common-mode injection signal which is variant between different modulation schemes, $d_{n,\gamma,\text{ctrl}}$ is the control action which aims to raise the γ-axis input impedance, $f_{s,n}$ is the switching frequency, φ_n is the carrier phase of the n^{th} converter and $\boldsymbol{\vartheta} : \mathbb{R}^2 \to \mathbb{R}$ is a carrier generation operator with set frequency and phase.

6.3 LOCAL CARRIER SYNCHRONIZATION

A method for shaping the γ-axis input impedance is proposed in Chapter 4, thus we can emulate a high-impedance for a certain frequency f_{sync} through the insertion of a resonant controller given by

$$\begin{cases} x_r\left(k+1\right) = \boldsymbol{\Phi}(T, \zeta_r, \omega_{\text{sync}}) x_r\left(k\right) + \boldsymbol{\Gamma}(T, \zeta_r, \omega_{\text{sync}}) e\left(k\right) \\ y_r\left(k\right) = \mathbf{K} x_r\left(k\right) \end{cases}, \tag{6.3}$$

where

$$\begin{aligned}\mathbf{A}(\zeta,\omega) &:= \begin{bmatrix} 0 & \omega \\ -\omega & -2\zeta\omega \end{bmatrix} \quad \mathbf{B}(\zeta,\omega) := \begin{bmatrix} 0 \\ \zeta\omega \end{bmatrix} \\ \mathbf{\Phi}(h,\zeta,\omega) &:= \exp\left(\mathbf{A}(\zeta,\omega)h\right) \\ \mathbf{\Gamma}(h,\zeta,\omega) &:= \mathbf{A}(\zeta,\omega)^{-1}\left(\mathbf{\Phi}(h,\zeta,\omega) - \mathbf{I}\right)\mathbf{B}(\zeta,\omega)\end{aligned} \tag{6.4}$$

and h is chosen by the sampling time (in this case equal to half the switching period). This frequency is chosen such that f_s is an integer multiple of f_{sync} according to

$$f_s := R_s f_{\text{sync}}, \quad \forall R_s \in \mathbb{N}, \tag{6.5}$$

where R_s is the ratio between switching and synchronization frequencies. Hence the disturbance rejection by the power converters at f_{sync} should be high, thence the amplitude of the harmonic components should be small. Note that it is important to maintain a passive characteristic to avoid instabilities caused by the insertion of other converters.

The chosen frequency will be used for carrier synchronization in two different but similar methods. The first method relies on a master-slave relationship, where one power converter acts as the master and others function as slaves. The master converter provides the reference modulated signal at the controller frequency of resonance, and the slave converters synchronize their switching frequencies accordingly.

The second method, however, introduces a cooperative strategy that improves upon the limitations of the master-slave approach. This cooperative strategy enhances robustness and eliminates the need for a designated master converter. Instead, all power converters inject a synchronization signal, which is then employed for generating the carrier of each converter based on the same structure.

6.3.1 Master-Slave Synchronization Technique

Thus, let a set of N parallel connected converters sharing a common dc link, and let a single converter with the input impedance without the resonant compensator, denoted by converter 1 henceforth. The local carrier synchronization strategy uses a feed-forward voltage for the converter 1 according to

$$u_{1,\gamma,\text{ctrl}} = u_{1,\gamma,\text{mod}} + U_{\text{sync}} \cos\left(\omega_{\text{sync}} t\right), \tag{6.6}$$

fixing the reference angle in the feedforward action, such that the γ-axis current of each converter is given by

$$i_{n,\gamma,\text{sync}} \approx \frac{U_{\text{sync}}}{|Z_{in}(\omega_{\text{sync}})|} \frac{\delta_{n,1} N - 1}{N} \cos\left(\omega_{\text{sync}} t - \angle Z_{in}\left(\omega_{\text{sync}}\right)\right) \tag{6.7}$$

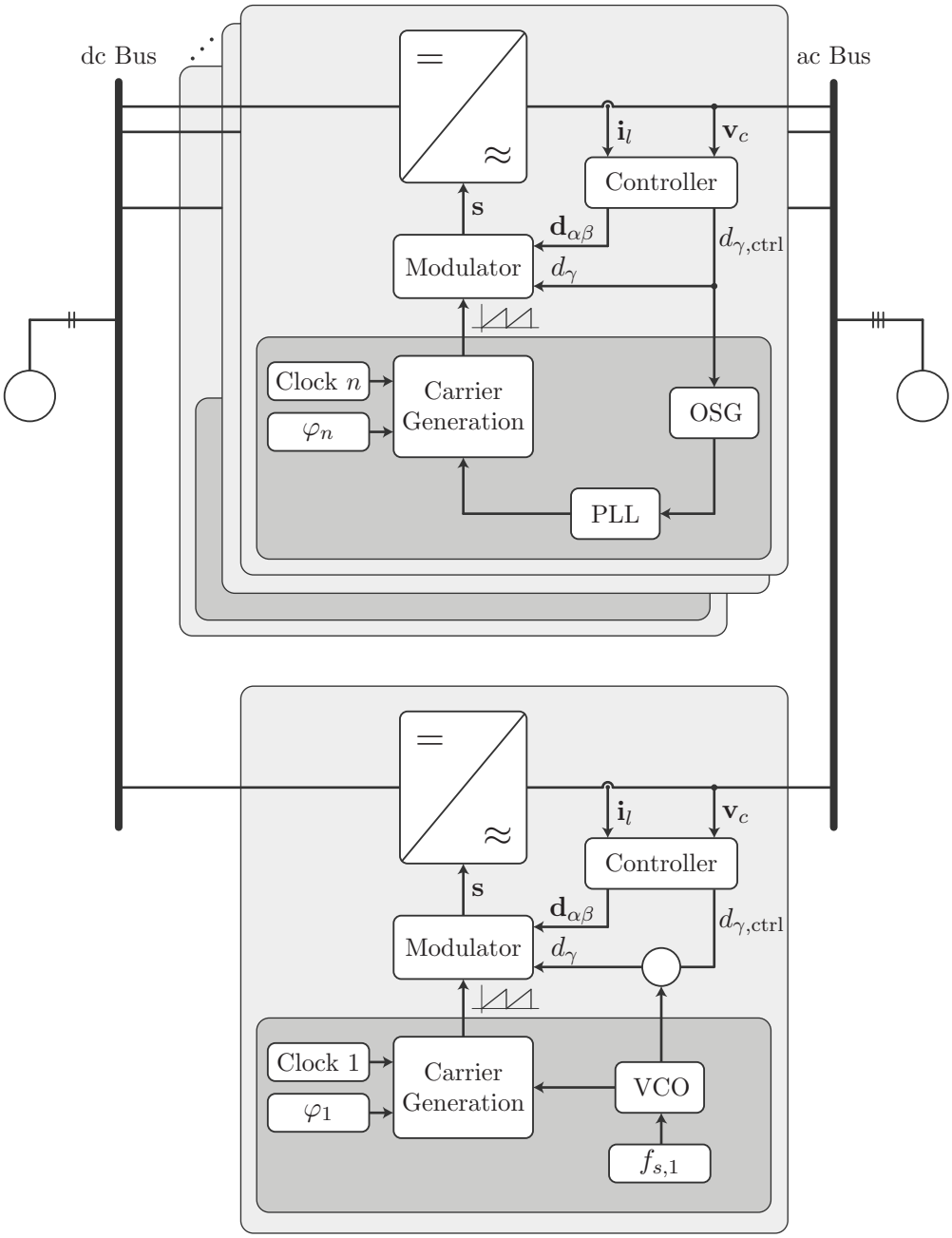

Figure 6.4 – Block Diagram of the general structure of Paralleled-Connected Three-Phase Voltage Source Inverters employing the Master-Slave Local Synchronous Pulse-Width Modulation.

assuming that $Z_{1,out}(\omega_{\text{sync}}) = -Z_{in}(\omega_{\text{sync}})$, which should be true due to the presence of a resonant controller. Thus, each converter will synthesize a γ-axis voltage which can be described by

$$u_{n,\gamma,\text{ctrl}} = \eta_n \frac{U_{\text{sync}}}{N} \cos\left(\omega_{\text{sync}} t + \theta_n\right), \tag{6.8}$$

for $\eta_n \approx 1$ and a fixed angle θ_n for each converter. These values depends on the input impedance value, the coupling between different axis and eventual mismatches due to different frequency bases.

From this, we can utilize a synchronization algorithm to obtain the phase of the

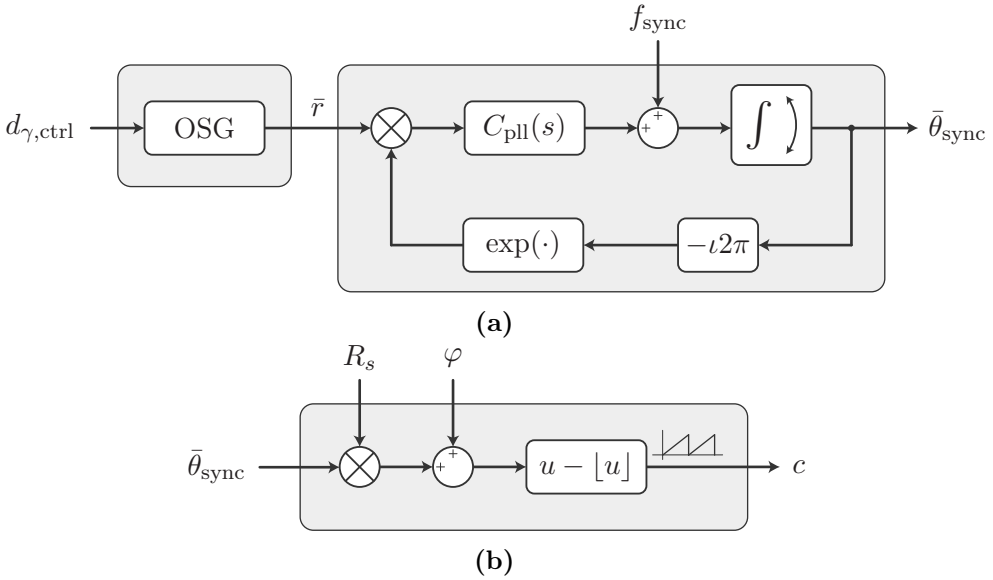

Figure 6.5 – (a) LSPWM angle tracker block diagram, employing generic a PLL controller $C_{\text{pll}}(s)$ and Orthogonal Signal Generation (OSG) unit. The Master-Slave and Cooperative strategies employ different controllers to manage their respective synchronization approaches. (b) Carrier signal generation from angle tracker.

injected sinusoidal signal. In this case, the synchronization frequency, denoted as f_{sync}, should remain constant and is only dependent on the clock frequency of converter 1. The proposed synchronism strategy is represented by the block diagram shown in Figure 6.4, with details relating to the synchronization strategy and carrier generation shown in Figure 6.5.

Considering that the γ-axis measurements are noisy, especially when the carriers are not synchronized, and due to the presence of quantization noise in the process, it is desirable to employ a synthonized filter with a low-pass characteristic for robust synchronization. Thus, a Second-Order Generalized Integrator (SOGI) structure based on equation (6.4) was employed for the Orthogonal Signal Generation (OSG) unit. The structure of the SOGI can be described as follows:

$$\begin{cases} x_{\text{osg}}\left(k+1\right) = \mathbf{\Phi}_r(h,\zeta) x_{\text{osg}}\left(k\right) + \mathbf{\Gamma}_r(h,\zeta) u_{\gamma,\text{ctrl}}\left(k\right) \\ \bar{r}\left(k\right) = \begin{bmatrix} \iota & 1 \end{bmatrix} x_{\text{osg}}\left(k\right). \end{cases} . \tag{6.9}$$

Employing the SOGI structure ensures robust synchronization by effectively filtering out noise and enables accurate phase determination of the injected sinusoidal signal, and $\bar{r}$ should present a circular trajectory. Note that the higher the filter bandwidth, the more $\bar{r}$ is coupled with the other frequency components of signal $u_{\gamma,\text{ctrl}}$. Hence, a sufficiently small ζ must be chosen to decouple both signals, and sufficiently big such that the performance is not hindered, and we can correlate the system inertia with this parameter.

We can then use a Moving Average Filter Phase-Locked Loop (MAF-PLL) to obtain an estimate of the synchronism angle to solve quantization problems. The estimated

angle obtained from the PLL can then be used to generate the carrier, which leads to a compensator given by

$$C_{\text{pll}}(z) = \left(k_{p,\text{pll}} + k_{i,\text{pll}}\frac{h}{1-z^{-1}}\right)\left(\frac{1}{N_{\text{pll}}}\frac{1-z^{-N_{\text{pll}}}}{1-z^{-1}}\right), \tag{6.10}$$

where $N_{\text{pll}} := \frac{1}{f_{\text{sync}}h}$.

This technique demonstrates high robustness against clock frequency deviations, as illustrated in Figure 6.6, with details regarding the electrical quantities before and after synchronism illustrated in Figure 6.7. However, achieving phase synchronism naturally depends on the phase of the input impedance, which is uncertain. While Chapter 4 presents a method to force the phase to a certain value, there may still be modeling errors due to parameter mismatches, which can affect the phase accuracy. To mitigate this, a local or global optimization routine can be employed to determine the phase that minimizes circulating currents for each converter. Further details regarding this optimization process will be discussed in the subsequent section.

Subsequently, we can derive two distinct implementations tailored for DSPs and FPGAs. For DSPs, the strategy based on the Carrier Angle Tracker (CAT) proposed in [2] is suitable. This approach utilizes feedback of the PWM phase and directly adjusts the frequency reference of the PWM block. The implementation is illustrated in Figure 6.3.c.

However, the strategy present strategy was conceived for a Field-Programmable Gate Array (FPGA) implementation using the Space Vector Modulation (SVM) technique. This is advantageous as it allows actuation in the modulator carrier, which is not directly accessible in a DSP. Consequently, in an FPGA implementation, the need for a closed-loop control structure for the phase difference, such as the carrier angle tracker, is eliminated. Instead, the modulator increment is directly generated by the γ-axis component Phase-Locked Loop (PLL). The angle estimation achieved through this approach is robust against variations due to the inertia introduced by the SOGI and the decoupling between synchronization and the $\alpha\beta$ axis. As a result, active stabilization strategies are not necessary.

When compared to the GSPWM with the PLL-CS method, the strategy described above exhibits higher robustness, as it is more resilient to grid variations. It ensures that the rate of change of the grid angle, $\dot{\varphi}_n$, remains sufficiently small, allowing for decoupling of the dynamic behavior between the references in the $\alpha\beta\gamma$ coordinates and the carrier. Furthermore, this strategy can be employed even in the absence of a grid for synchronization purposes.

However, one of the trade-offs is the relatively low inertia of the γ-axis compared to the grid inertia, primarily due to its low impedance. To address this limitation, a virtual inertia can be introduced through careful design of the PLL reference generation, in this case the SOGI, which assists in enhancing the synchronization performance.

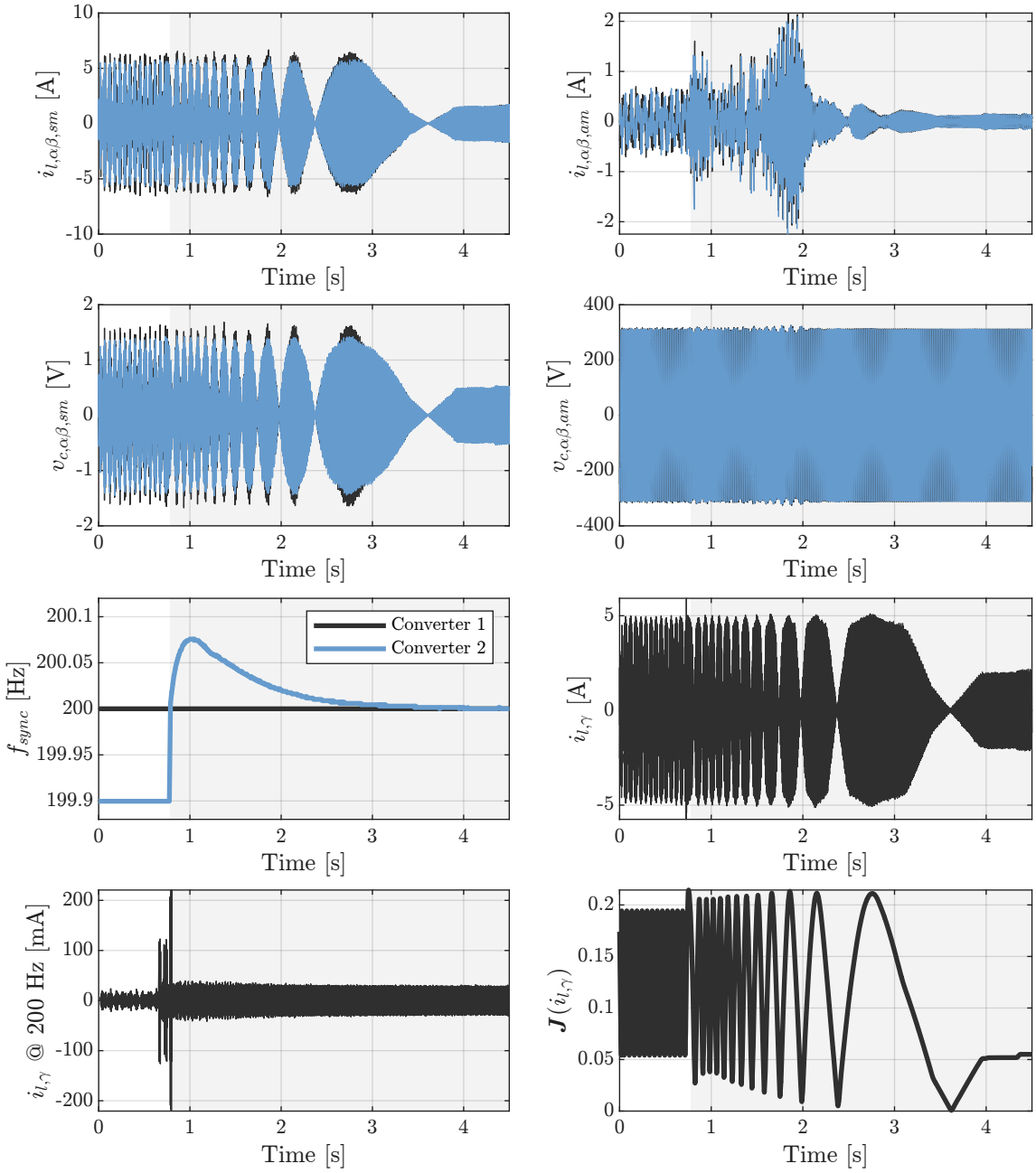

Figure 6.6 – Results of the Master-Slave Local Synchronous Pulse-Width Modulation (LSPWM) FPGA implementation, demonstrating the behaviour of the circulating currents for desynchronized carriers with different frequencies, with a 500 ppm variation on the initial switching frequency, with R_s set as 180 resulting in a switching frequency of 36 kHz.

Another drawback of the proposed strategy is the need for the determination of a master converter which will process a higher current, as demonstrated by (6.7), and the diminishing amplitude of the synchronization signal with an increase in the number of paralleled-connected power converters, as shown in (6.8), which increase the quantization noise of the synchronism loop. It is also crucial to design a fault diagnosis and action mechanism to address situations where a fault occurs with the designated master converter. The fault diagnosis system should be capable of detecting the fault condition and triggering

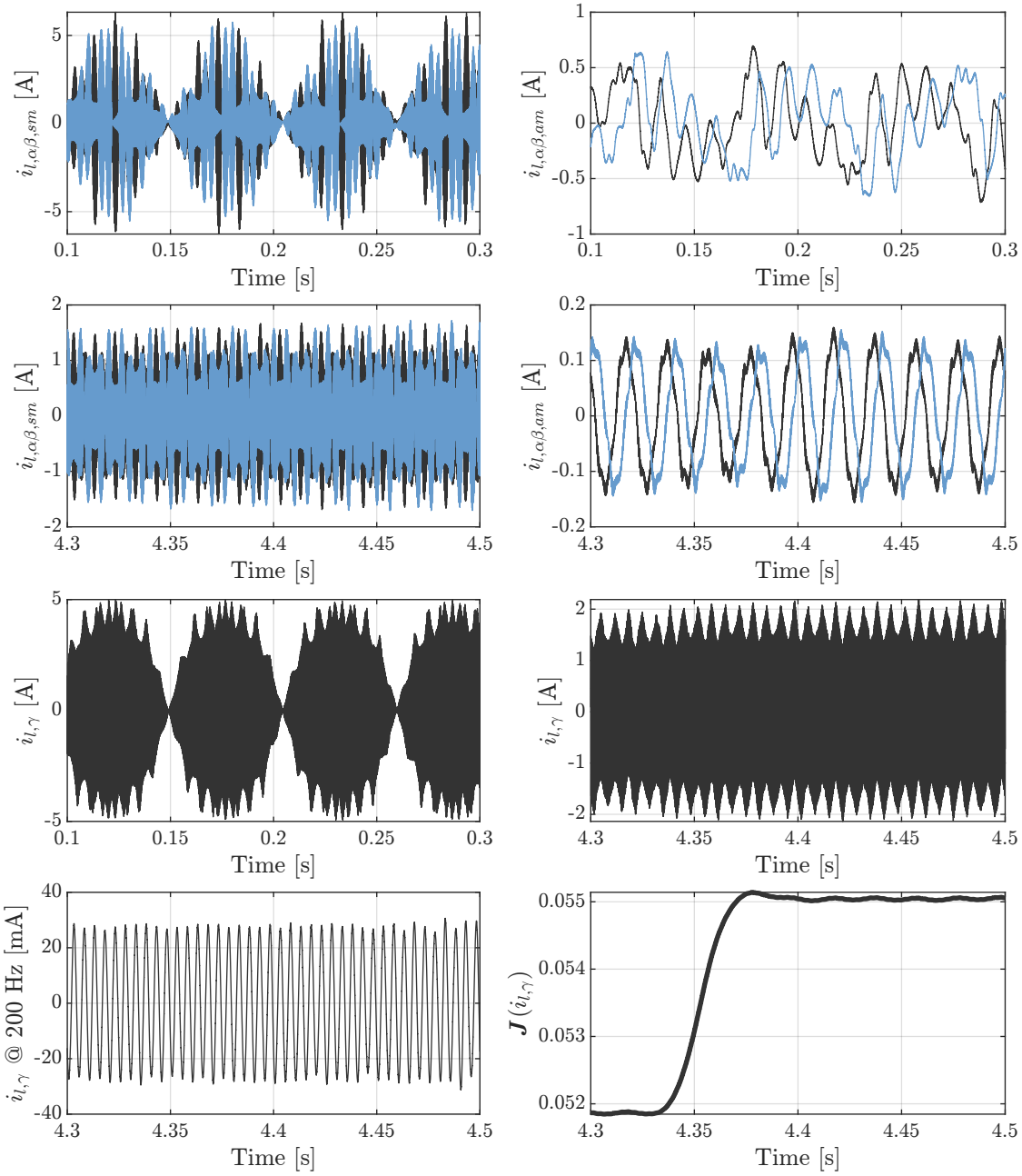

Figure 6.7 – Details on the results of the Master-Slave Local Synchronous Pulse-Width Modulation (LSPWM) FPGA implementation, demonstrating the behaviour of the circulating currents for desynchronized carriers with different frequencies, with a 500 ppm variation on the initial switching frequency.

appropriate actions to select a new master converter and ensure the continued operation of the system. In the event of a fault with the master converter, the fault diagnosis system should identify the fault and initiate a process to select a new master converter. This process typically involves evaluating the condition and performance of the available converters and choosing a suitable replacement based on predefined criteria or algorithms, which should prove to be hard to implement due to the need of a supervisory system.

The experimental results with the system emulated via HIL are presented in Fig. 6.6, with details for waveforms before and after synchronization shown in Fig. 6.7,

which demonstrates the synchronization transient dynamics, with a settling time of approximately 4 s. It is possible to lower the settling-time by sacrificing the robustness of the implementation, where $\boldsymbol{J}$ is the cost function related to the energy of the high-frequency content, to be reduced by an optimization algorithm discussed in a future section. Note the 20 mA current at the synchronization frequency of 200 Hz, which was obtained through a RDFT filter synthonized at the 4^{th} harmonic.

The subsequent subsection delves into a synchronization technique based on a cooperative synchronization method. This technique aims to address some of the limitations that were previously discussed, providing potential solutions and improvements to the synchronization process.

6.3.2 Cooperative Synchronization Technique

The Cooperative Synchronization Technique involves modifying the PLL loop controller to introduce a frequency tracking error, as the integral action of the PI controller is unstable in the configuration depicted in Figure 6.8. However, it is still desirable to maintain a low-pass characteristic to mitigate quantization noise, considering the small value of $d_{\gamma,\text{sync}}$. To achieve this, a proportional controller in combination with a Moving Average Filter (MAF) is employed, resulting in the following controller transfer function:

$$C_{\text{pll}}(z) = \frac{k_{p,\text{pll}}}{N_{\text{pll}}} \frac{1 - z^{-N_{\text{pll}}}}{1 - z^{-1}}, \tag{6.11}$$

where N_{pll} is defined as $N_{\text{pll}} = \frac{1}{f_{\text{sync}} h}$. The gain $k_{p,\text{pll}}$ should be selected in such a way that the steady-state frequency converges to a value within the range of the original synchronization frequencies.

Figure 6.9 illustrates the dynamic behavior of the synchronization process, indicating a settling time of approximately 3 seconds. Additionally, Figure 6.10 provides a detailed depiction of the behavior before and after synchronization. It is worth noting that the amplitude of the current in the γ-axis at the synchronization frequency is notably smaller compared to the Master-Slave technique for this characteristic, although the reduced amplitude can be attributed in part to the quantization noise of the γ-axis control strategy, aliasing of harmonics close to the switching frequency and the shattering of the Extended Sliding-Mode Observer (ESMO) employed in the $\alpha\beta$-axis controllers.

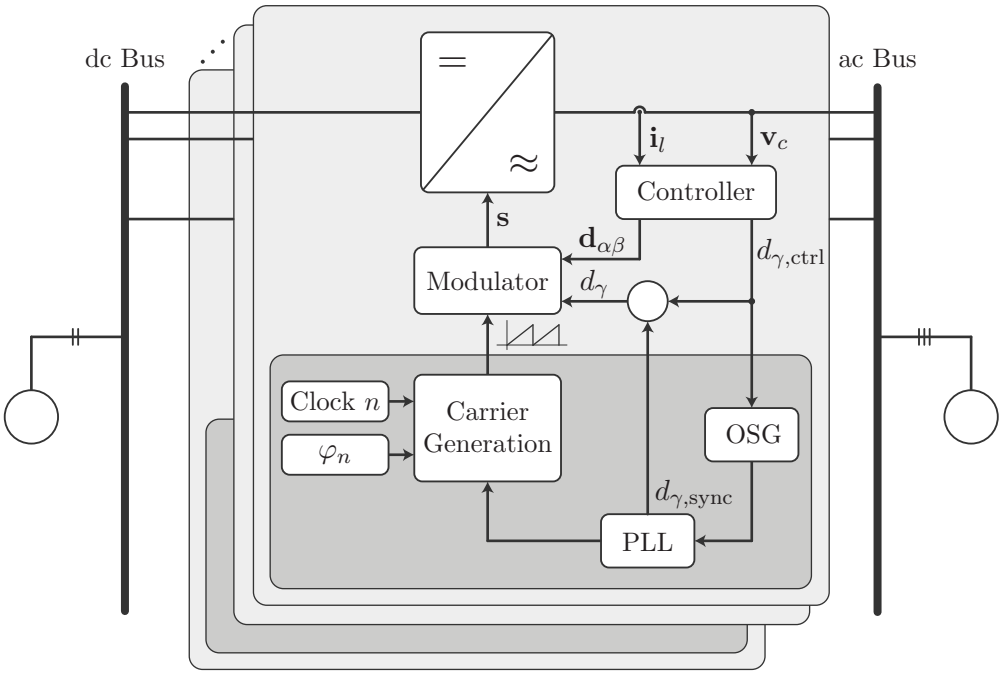

Figure 6.8 – Block Diagram of the general structure of Paralleled-Connected Three-Phase Voltage Source Inverters employing the Master-Slave Local Synchronous Pulse-Width Modulation.

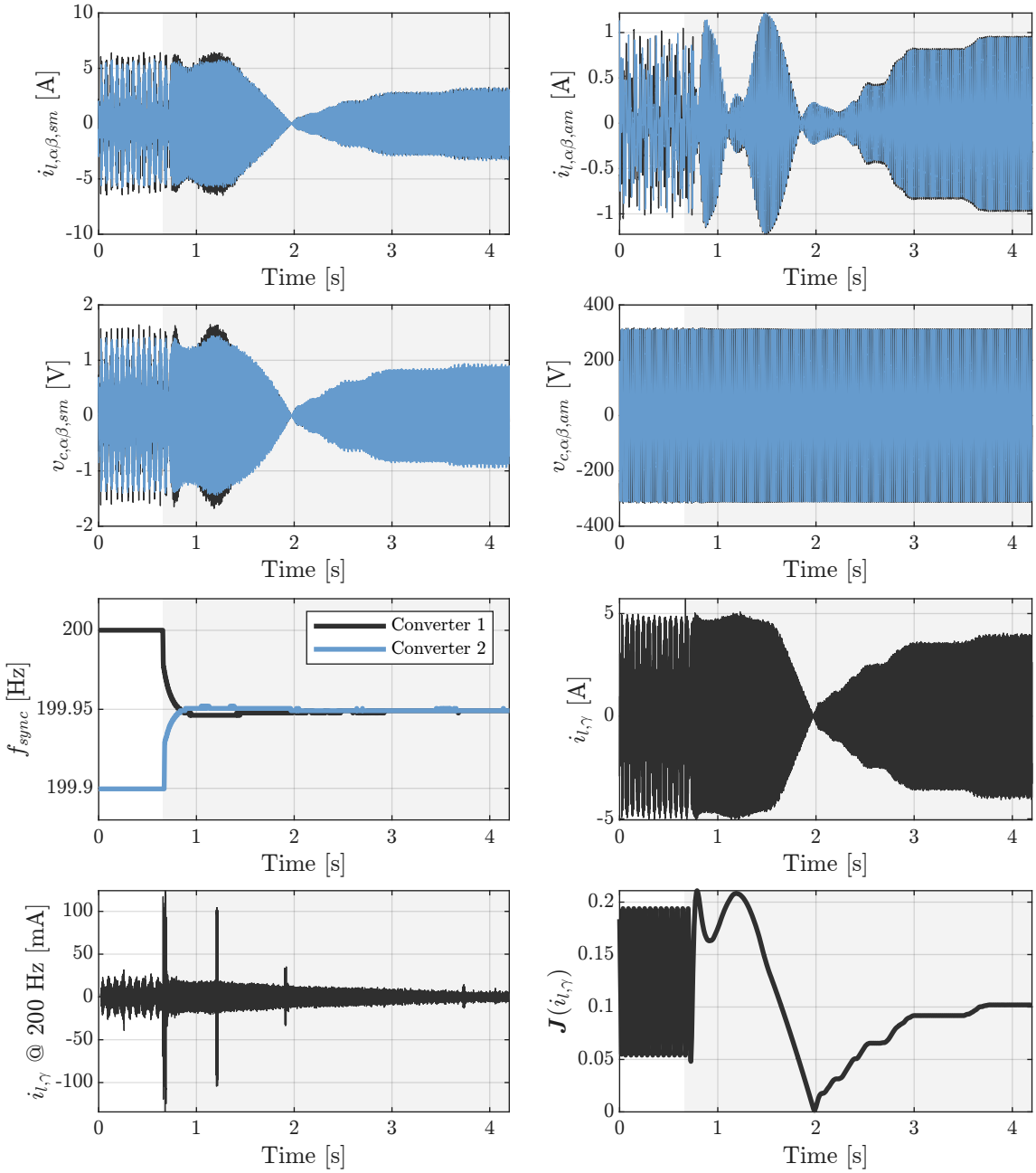

Figure 6.9 – Results of the Cooperative Local Synchronous Pulse-Width Modulation (LSPWM) FPGA implementation, demonstrating the behaviour of the circulating currents for desynchronized carriers with different frequencies, with a 500 ppm variation on the initial switching frequency, with R_s set as 180 resulting in a switching frequency of 36 kHz.

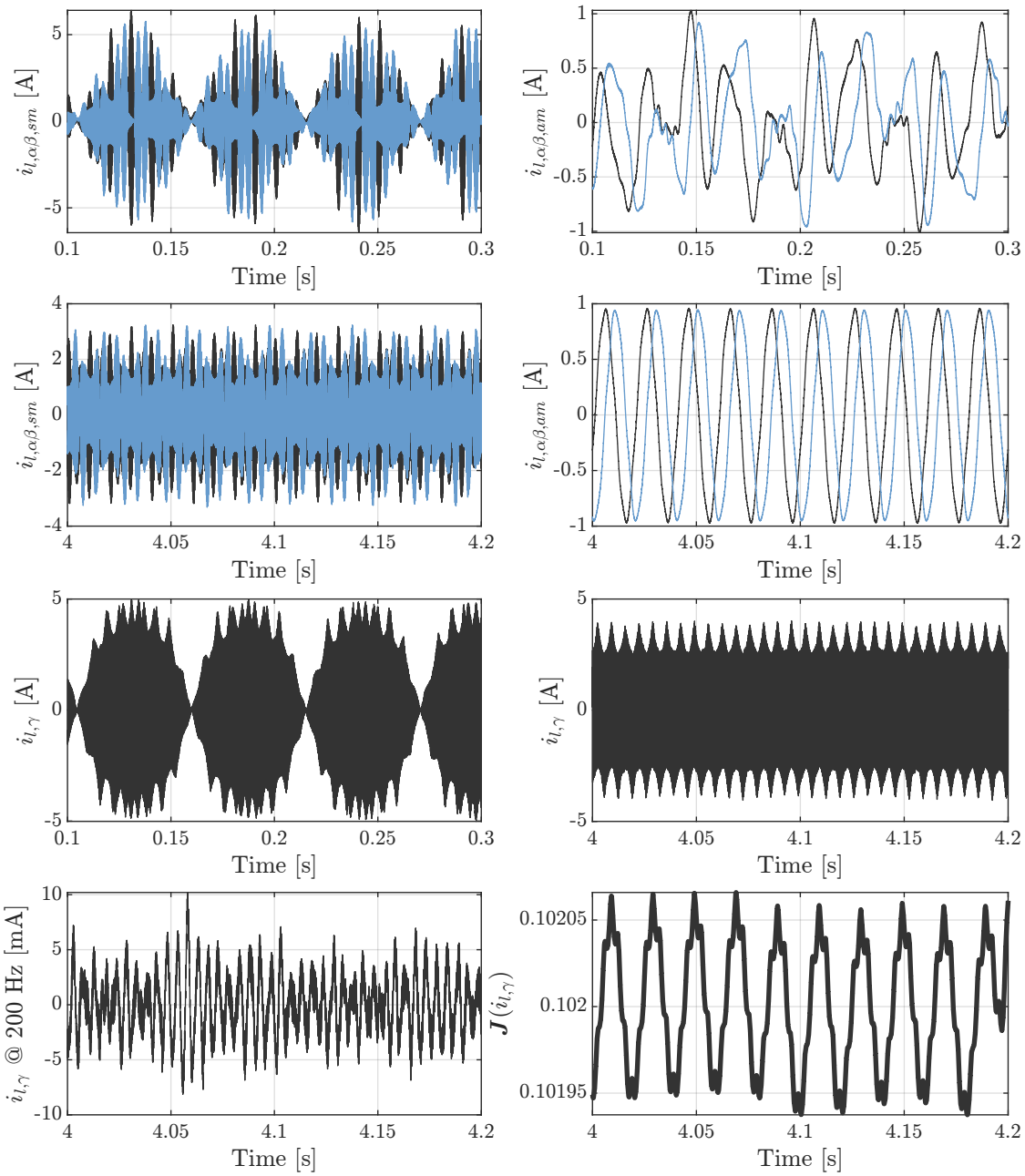

Figure 6.10 – Details on the results of the Cooperative Local Synchronous Pulse-Width Modulation (LSPWM) FPGA implementation, demonstrating the behaviour of the circulating currents for desynchronized carriers with different frequencies, with a 500 ppm variation on the initial switching frequency.

6.4 REAL-TIME CARRIER PHASE OPTIMIZATION

The previous section provided a strategy to synchronize the carriers, which is not sufficient to converge to a minimal circulating current, as shown in Figure 6.6 and Figure 6.9. This section elaborates a supervisory control to find an optimal (or suboptimal) point of operation while varying the phases of each converter's carrier with respect to the synchronized phase by employing a decentralized neural network approach. Hence, we assume that either carriers are synchronized via grid voltage (GSPWM) or the γ-axis signal injection (LSPWM) which was previoulsy discussed.

6.4.1 Cost Function Definition

We can derive multiple optimization cost functions with the objective of minimizing the harmonic distortion of the system output current or amplitude of circulating currents. The GSPWM aims to reduce the output current distortion, operating the power converters in a *quasi*-interleaving state, with a cost function given by

$$J\left(\mathbf{i}_o\right) = \sum_{k\in\mathfrak{K}} \sum_{j=1}^{3} \frac{\left|\langle i_{o,j}\rangle_k\right|}{\left|\langle i_{o,j}\rangle_1\right|}, \tag{6.12}$$

where $\mathfrak{K} \in \mathbb{N}_R^0$ is the set the harmonic components of the Fourier Transform of interest in the analysis, which in turn should consider the harmonics close to the switching frequency, or its lower computational cost

$$J\left(\mathbf{i}_o\right) = \sum_{j=1}^{3} \frac{\left\|i_{o,j}\right\|_2}{\left|\langle i_{o,j}\rangle_1\right|}, \tag{6.13}$$

which yields the same result for $\mathfrak{K} = \mathbb{N}_R$ since $x(t) \in L^2$ through the RMS filter discussed in Chapter 2. The cost function (6.12) is more convex than (6.13), as the subspace of ℓ^2 in which the evaluation of the Fourier Transform happens is more decoupled from disturbances than the whole L^2 space in which x pertains to, which also include lower-frequency disturbances, hence the choice of optimization function also depends on the application.

However, (6.12) represents the worst-case scenario for the energy of circulating currents, as this will maximize the energy of the sideband harmonics that will circulate between converters, and $-J\left(\mathbf{i}_o\right)$ is not convex, since this does not guarantee that $\boldsymbol{\varphi}$ will reach a fixed point. An alternative is to minimize the harmonic content of the output currents of each converter, according to

$$J\left(\mathbf{i}_l\right) = \sum_{n=1}^{N} \sum_{k\in\mathfrak{K}} \sum_{j=1}^{3} \frac{\left|\langle i_{l,n,j}\rangle_k\right|}{\left|\left\langle i_{l,j}^n\right\rangle_1\right|} \tag{6.14}$$

or its lower complexity form

$$J\left(\mathbf{i}_l\right) = \sum_{n=1}^{N} \sum_{j=1}^{3} \frac{\left\|i_{l,n,j}\right\|_2}{\left|\left\langle i_{l,n,j}\right\rangle_1\right|}, \tag{6.15}$$

which also presents the same characteristics and drawbacks with respect to the convexity. Equations (6.14) and (6.15) can also be separated, according to

$$J\left(\mathbf{i}_l\right) = \sum_{n=1}^{N} J_n\left(\mathbf{i}_{l,n}\right) \tag{6.16}$$

where $J_n(\cdot)$ is the cost function applied for a single converter.

The multi-dimensional characteristic of the current vector might prove as a problem, as $J_i : \mathbb{R}^3 \to \mathbb{R}$. If $J_i : \mathbb{R}^2 \to \mathbb{R}$, i.e., if the γ-axis currents dos not pertain to the domain of J_i, as is the case when there is no common-mode current path, we can use the complex-valued current vector $\bar{i}_{l,\alpha\beta}$ for the Fourier Transform.

If we assume that $i_{l,\alpha} \perp i_{l,\beta} \perp i_{l,\gamma}$ with respect to high frequency currents, we can decompose $J_i = \sum_j J_{i,j}$, with $J_{i,j} : \mathbb{R} \to \mathbb{R}, \forall j \in \{\alpha, \beta, \gamma\}$, hence the calculation must be performed for each axis. However, such assumption is not necessarily true, as the carrier signal is the same for the three synthesized inverter voltages, where the minimization of γ-axis components results in the minimization of the $\alpha\beta$ components only when the dc-buses are either directly connected or coupled in a certain way that enables the circulation of γ-axis currents.

For this thesis, the minimization of the i_γ circulating currents was the adopted strategy, since the power converters in the OPAL-RT experimental setup presented a directly connected dc-bus.

6.4.2 Band-Pass and High-Pass Filter RMS-based Cost Function

In this case, let h be the impulse responses in the time domain of a high-pass or band-pass filters. Hence, we have that

$$J(x) = \frac{\|h * x\|_2}{|\langle x\rangle_1|} \tag{6.17}$$

Both filters can be implemented analogically or digitally, each presenting its advantages. The digital filter might struggle with quantization noise especially if the high-frequency currents amplitudes are much smaller than the low- and medium-frequency ones. Also, the sampling frequency should be much higher than the switching frequency.

The analog implementation requires a higher number of Analog/Digital Converters (ADCs), although the higher numerical precision might lead to a better operation point. A nonlinear analog filter, i.e., a band-pass with a half-wave or full-wave rectifier allied with a

low-pass filter should remove the need to sample the signal with frequencies much higher than the switching frequencies. Hence, the cost function can be rewritten as

$$J(x) = \frac{\|g * \Phi(h * x)\|_2}{|\langle x \rangle_1|} \tag{6.18}$$

where

$$\Phi(\cdot) = \begin{cases} |\cdot|, & \text{if full-wave rectifier} \\ \max(0, \cdot), & \text{if half-wave rectifier} \end{cases} \tag{6.19}$$

and g is the impulse response of a low-pass filter in the time domain.

The digital implementation requires a larger sampling frequency, which can be solved via faster ADCs or through Sigma-Delta Converters.

6.4.3 Frequency Domain-based Cost Function

Let the sampling period h, the grid frequency f_w and the switching frequency f_s. The computation of the discrete fourier transform can be done with two different approaches, a real-time based calculation, with sliding-window based transformations, and a pseudo real time, where the calculation is performed for a determined time-instant. An advantage of real-time based methods over pseudo ones is that the calculations are distributed, which is optimal for parallel implementations, whereas pseudo real-time based methods generates a large computational overhead.

For real-time methods, the Sliding-Window Recursive Discrete Fourier-Transform (RDFT) of a signal $u \in \mathbb{C}$ can be calculated according to

$$\langle U(k) \rangle_n = \langle U(k-1) \rangle_n + (u(k) - u(k-W)) \exp\left(\iota \frac{2\pi}{W} \text{rem}(k, W)\right), \tag{6.20}$$

for the n^{th} harmonic, where $\text{rem}(\cdot, \cdot)$ is the remainder function, for a sliding window of W samples, which can be chosen to fit a grid period.

One of the alternatives to the DFT calculation is through a Complex Least Mean Square (CLMS) filter, with its formulation given by

$$\begin{cases} e(k) = u(k) - \mathbf{h}^H(k)\mathbf{x}(k) \\ \mathbf{h}(k+1) = \mathbf{h}(k) + \mu e(k)\mathbf{x}(k) \end{cases}, \tag{6.21}$$

where $\mathbf{x}$ is the domain, which in case of the DFT is defined as

$$\mathbf{x}(k) = \frac{1}{\sqrt{W}} \left[e^{-\iota 2\pi \frac{(W-1)k}{W}} \quad \cdots \quad e^{-\iota 2\pi \frac{k}{W}} \quad 1 \quad e^{\iota 2\pi \frac{k}{W}} \quad \cdots \quad e^{\iota 2\pi \frac{(W-1)k}{W}} \right]^T. \tag{6.22}$$

We can also use the Widely Linear Complex Least Mean Square (WL-CLMS) filter, with

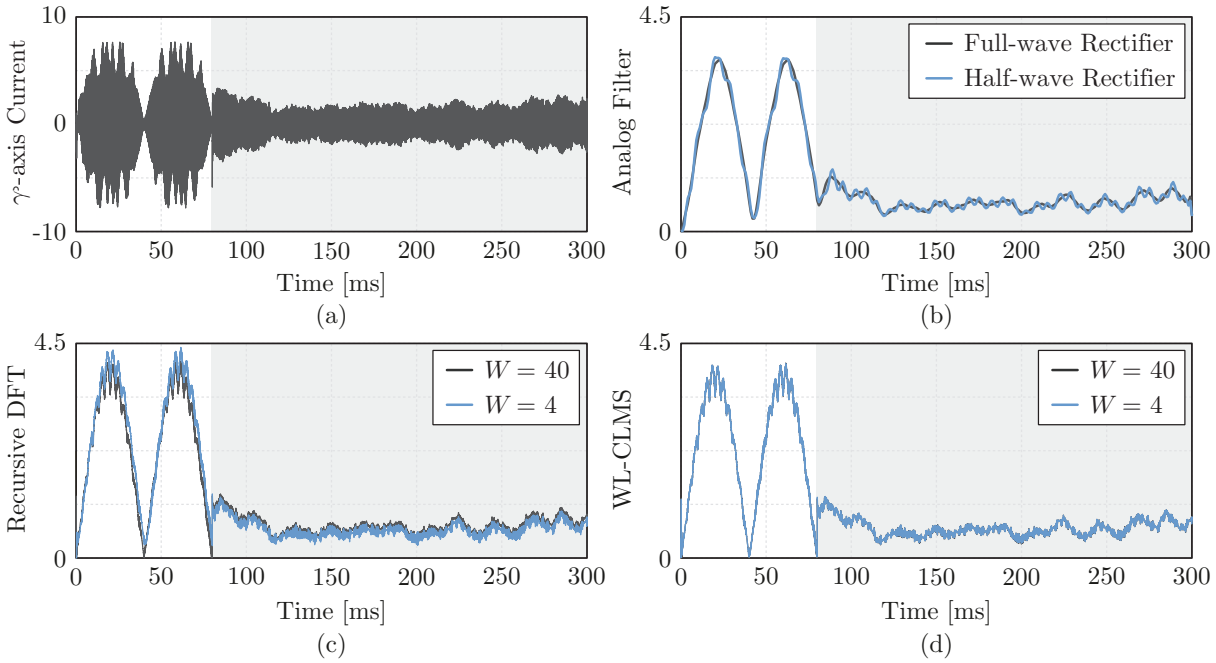

Figure 6.11 – Estimation of different methods for filtering the γ-axis circulating current switching frequency harmonics at 25 kHz. (a) Measured signal @ 1 Mhz (b) Analog filter with a butterworth low-pass filter sinthonized at 1 kHz (c) Recursive DFT (d) Widely-Linear Complex Least Mean Square filter.

its formulation given by

$$\begin{cases} e(k) = u(k) - \mathbf{h}^H(k)\mathbf{x}(k) - \mathbf{g}^T(k)\mathbf{x}^*(k) \\ \mathbf{h}(k) = \mathbf{h}(k-1) + \mu e(k)\mathbf{x}(k) \\ \mathbf{g}(k) = \mathbf{g}(k-1) + \mu e(k)\mathbf{x}^*(k) \end{cases}, \tag{6.23}$$

with its domain defined by

$$\mathbf{x}(k) = \frac{1}{\sqrt{W}} \begin{bmatrix} 1 & e^{\iota 2\pi \frac{k}{W}} & \cdots & e^{\iota 2\pi \frac{(W-1)k}{W}} \end{bmatrix}^T. \tag{6.24}$$

Since some components inside the window W vanishes for the equilibrium point, i.e., when $e \to 0$, the domain of $\mathbf{x}$ can be reduced, which might help alleviating the computational burden. A simulation of the proposed methods is presented in Figure 6.11

One of the drawbacks is the these calculations can be time and resource consuming for high frequency switched power converters. However, such algorithms serve as basis for pseudo real-time routines, as they can be executed while using a buffer of measured inputs. Another alternative is through the use of the Fast Fourier Transform (FFT), which can be computed via the FFTW [91] algorithm.

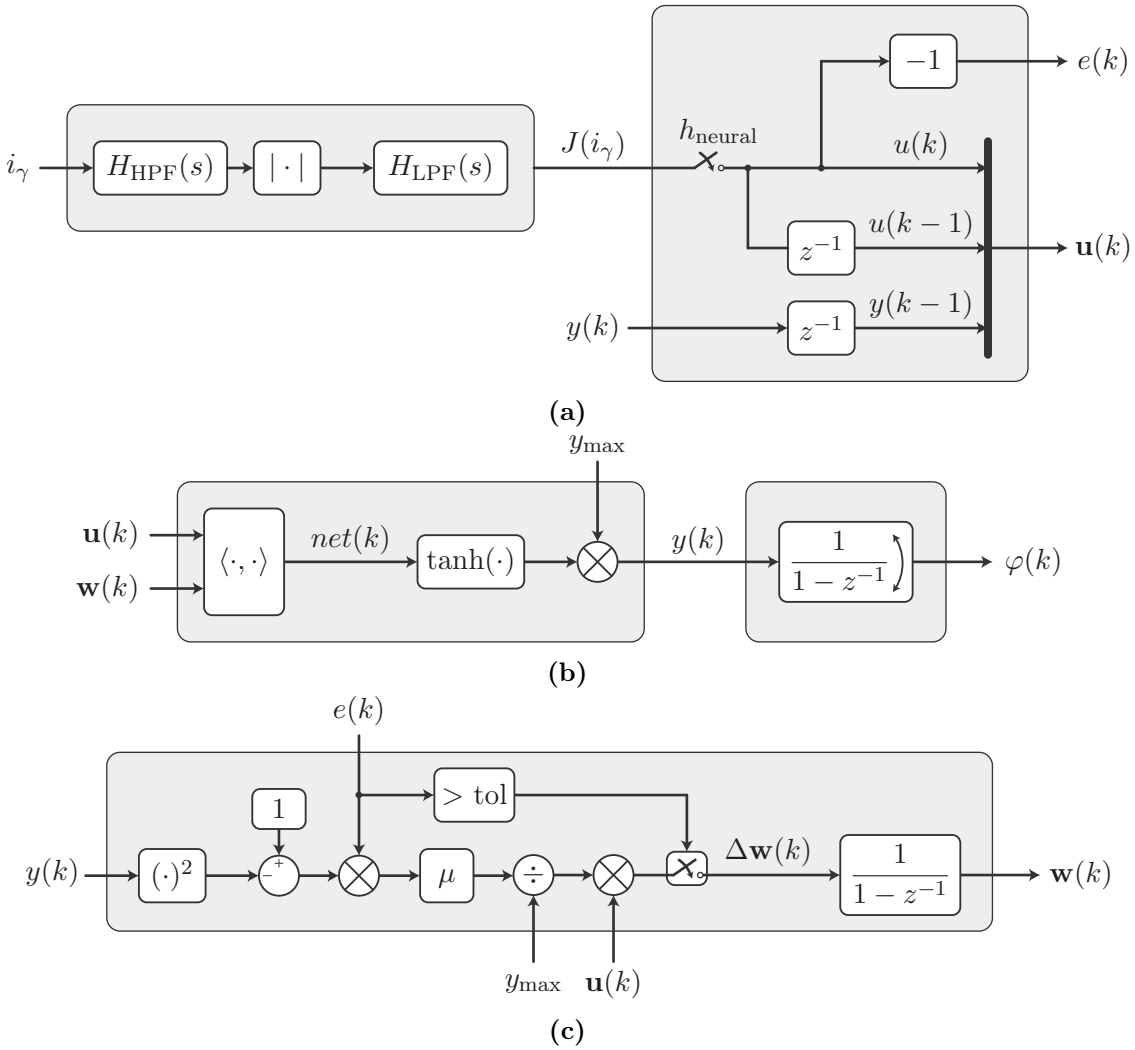

Figure 6.12 – (a) Cost Function evaluation, resulting in a normalized approximation of the γ-axis high frequency content RMS value. (b) Recurrent Neural-Network (RNN) algorithm cascaded with a wrapped integrator. (c) Back-propagation algorithm.

6.4.4 Optimization Algorithm

One drawback of executing the optimization function in a decentralized manner is the reduction in the problem's convexity. As a result, optimization algorithms may exhibit undesired behavior when applied to such problems. The lack of convexity can make the optimization process more challenging, potentially leading to suboptimal solutions or slower convergence rates. As an example, tests using the Perturbation & Observation (P&O) algorithm failed to succeed due to the coupling between the cost functions of each converter.

Therefore, an Recurrent Neural Network (RNN) composed of a single artificial neuron was implemented as means of finding the optimal phase of operation in a decentralized manner. Figure 6.12 illustrates the block diagram of the adopted structure, which can be divided into three main components. The first component is the evaluation of the cost function, which quantifies the discrepancy between the desired synchronization behavior

and the actual behavior of the system. The transfer functions of the low-pass and high-pass filters are given by

$$H_{\mathrm{HPF}} := \frac{s^2}{s^2 + 2\xi_{\mathrm{HPF}}\omega_{\mathrm{HPF}}s + \omega_{\mathrm{HPF}}^2}, \quad H_{\mathrm{LPF}} := k_{\mathrm{norm}}\frac{\omega_{\mathrm{LPF}}^2}{s^2 + 2\xi_{\mathrm{LPF}}\omega_{\mathrm{LPF}}s + \omega_{\mathrm{LPF}}^2}. \tag{6.25}$$

with chosen filter parameters in accordance with Table 6.1.

The second component is the neural network, which is responsible for capturing the nonlinear mapping between the input variables and the desired synchronization output. In the proposed structure, the output of the neural network is connected to an integrator, ensuring that the output controls the angle increment. To prevent large carrier angle variations, the activation function was chosen to limit the angle increment. In this case, the angle φ is normalized to the interval $(-1, 1)$.

The third component is the back-propagation algorithm, which is utilized to train the neural network. It adjusts the network's weights iteratively based on the calculated cost, which was set as an estimate of the γ-axis current high-frequency content RMS value. The weight update function and the wrapped integrator in Figure 6.12.b is disabled when the cost function reaches a certain value to avoid unpredicted behaviours due to quantization and the recurrent characteristic.

By integrating these three components, the system can effectively evaluate the cost function, utilize the neural network for synchronization, and refine the network's parameters in a similar manner as an adaptive controller. Details relating to Artificial Neural Networks and Adaptive Filters are further explored in Appendix B.

The experimental results of the Master-Slave Neural-Based LSPWM, utilizing the converter model running on the OPAL-RT platform, are presented in Figure 6.13. These results showcase a settling time of around 17 seconds, indicating the time required for the system to reach a stable synchronized state. For a more detailed analysis, Figure 6.14 provides waveform snapshots illustrating the behavior of the system before and after the application of the synchronization algorithm. In a similar manner, Figure 6.15 shows the experimental results for the Cooperative Neural-Based LSPWM, which presented a settling time of approximately 12 s, with a snapshot of the system before and after synchronization in Figure 6.16. These waveforms offer insights into the dynamic changes that occur in the system and highlight the effectiveness of the algorithm in achieving synchronization.

Table 6.1 – Carrier Synchronization Strategy Parameters

Parameter	Symbol	Value
High-pass filter cutoff frequency	ω_{HPF}	$2\pi \times 5000$ rad/s
High-pass filter damping factor	ξ_{HPF}	0.7
Low-pass filter cutoff frequency	ω_{LPF}	$2\pi \times 20$ rad/s
Low-pass filter damping factor	ξ_{LPF}	0.7
Neural Network Update Period	h_{neural}	200 ms
Normalization gain	k_{norm}	0.06667
Maximum Angle Increment	$y_{\max}$	0.25
Learning Rate	μ	5
Tolerance	tol	0.0005

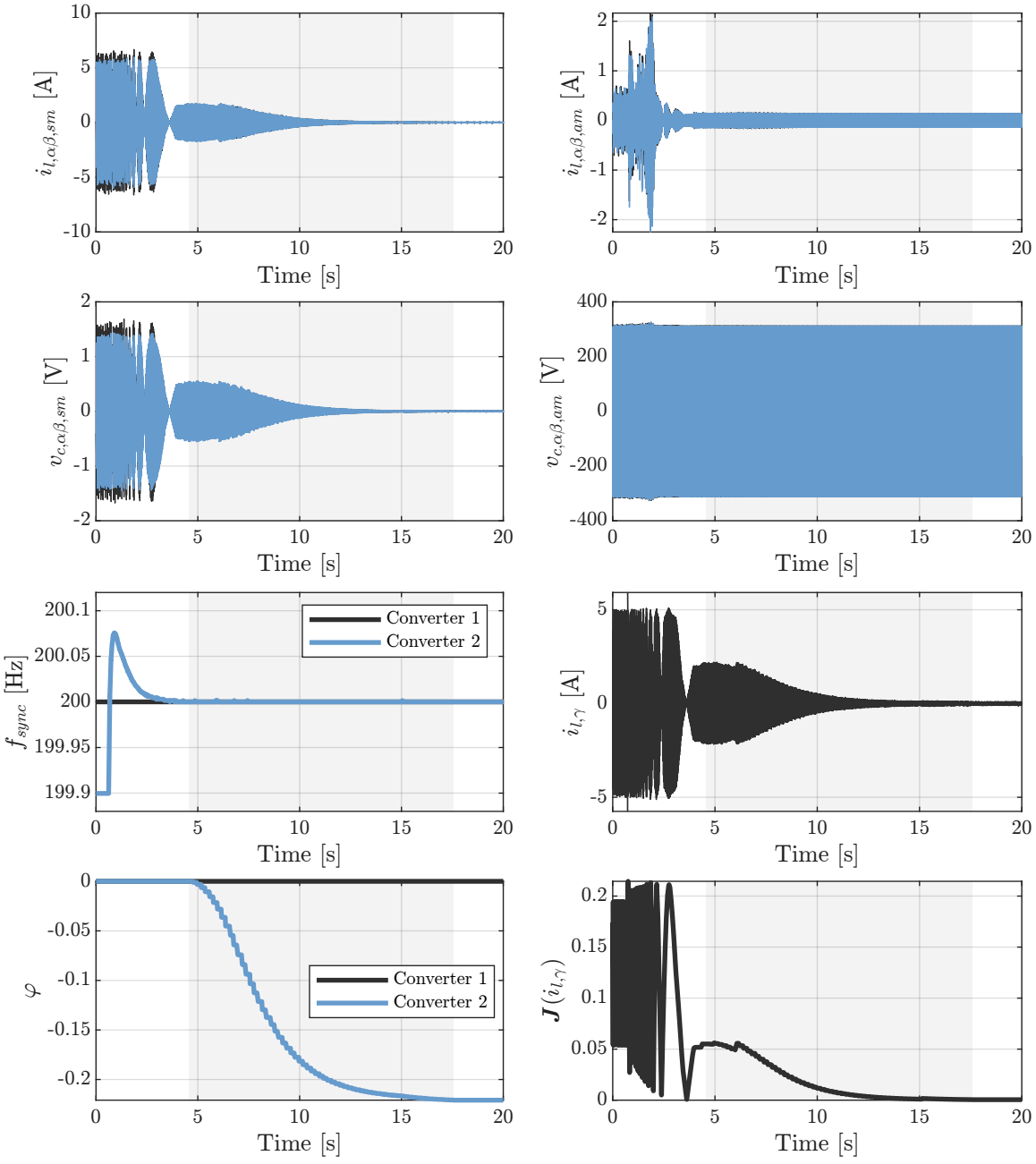

Figure 6.13 – Master-Slave Neural-Based LSPWM HIL results, with converter 1 operating as the master and converter 2 as the slave.

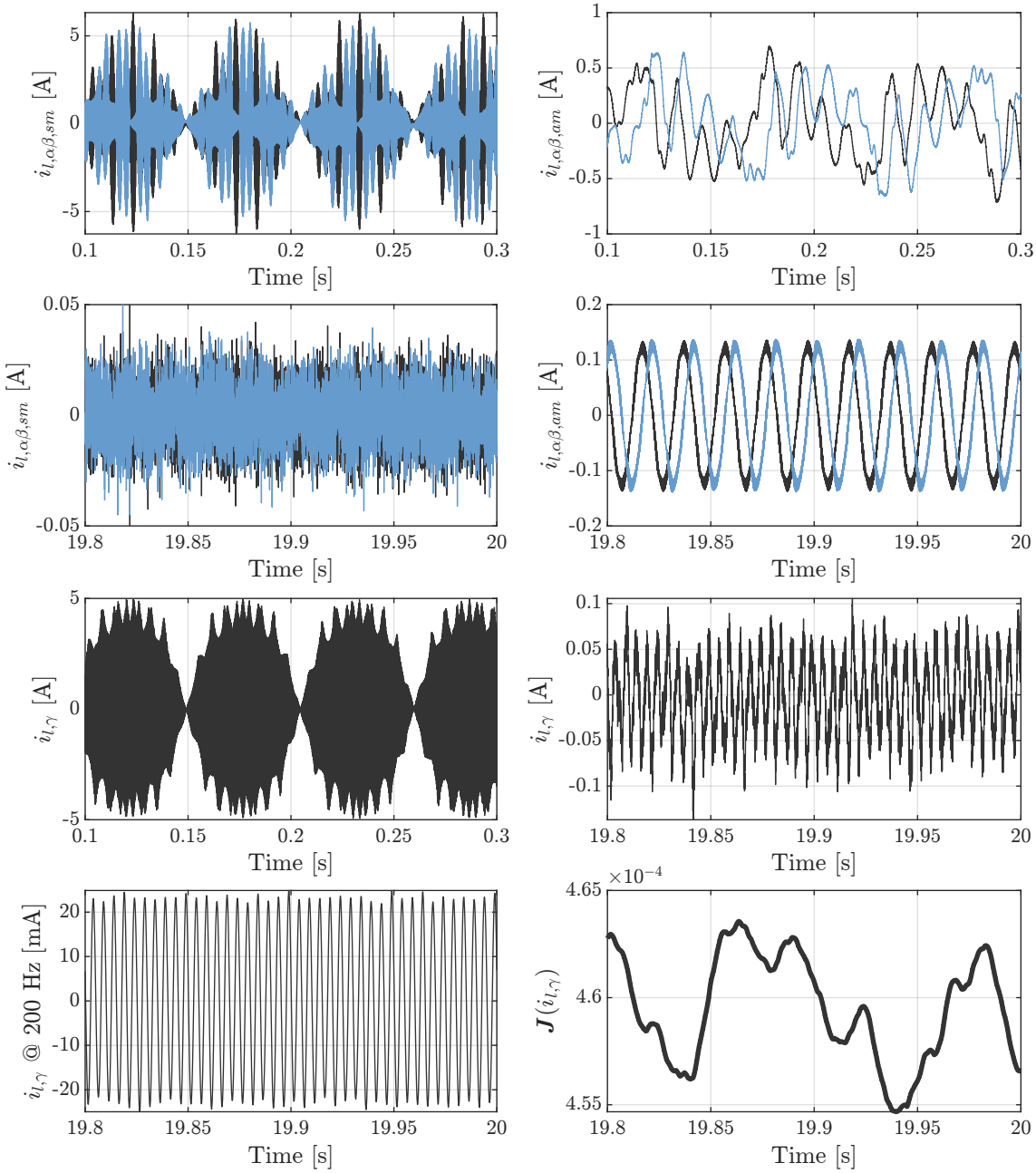

Figure 6.14 – Waveforms of the Master-Slave Neural-Based LSPWM HIL results Figure 6.13 before and after carrier synchronization.

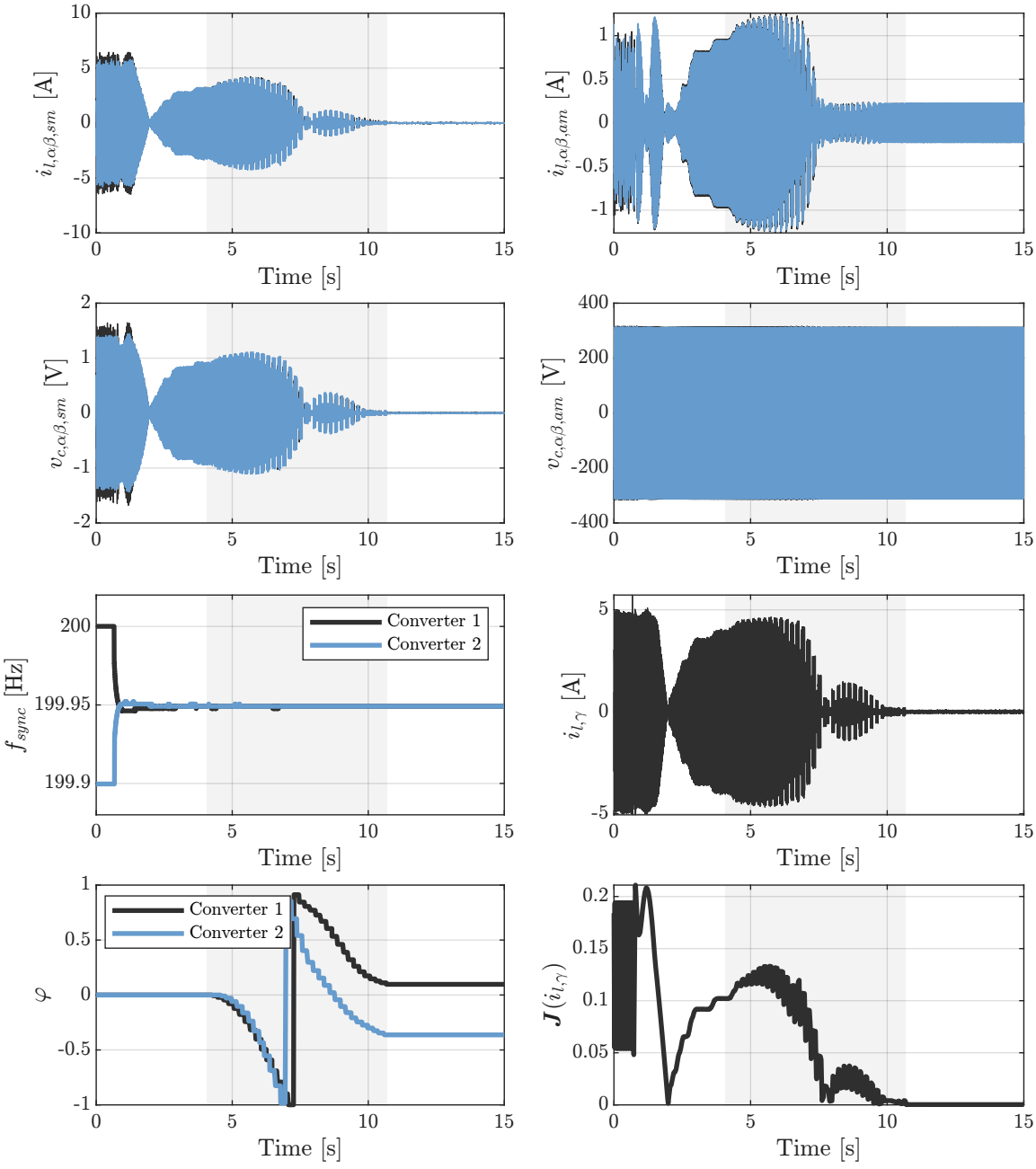

Figure 6.15 – Cooperative Neural-Based LSPWM HIL results, with converter 1 operating as the master and converter 2 as the slave.

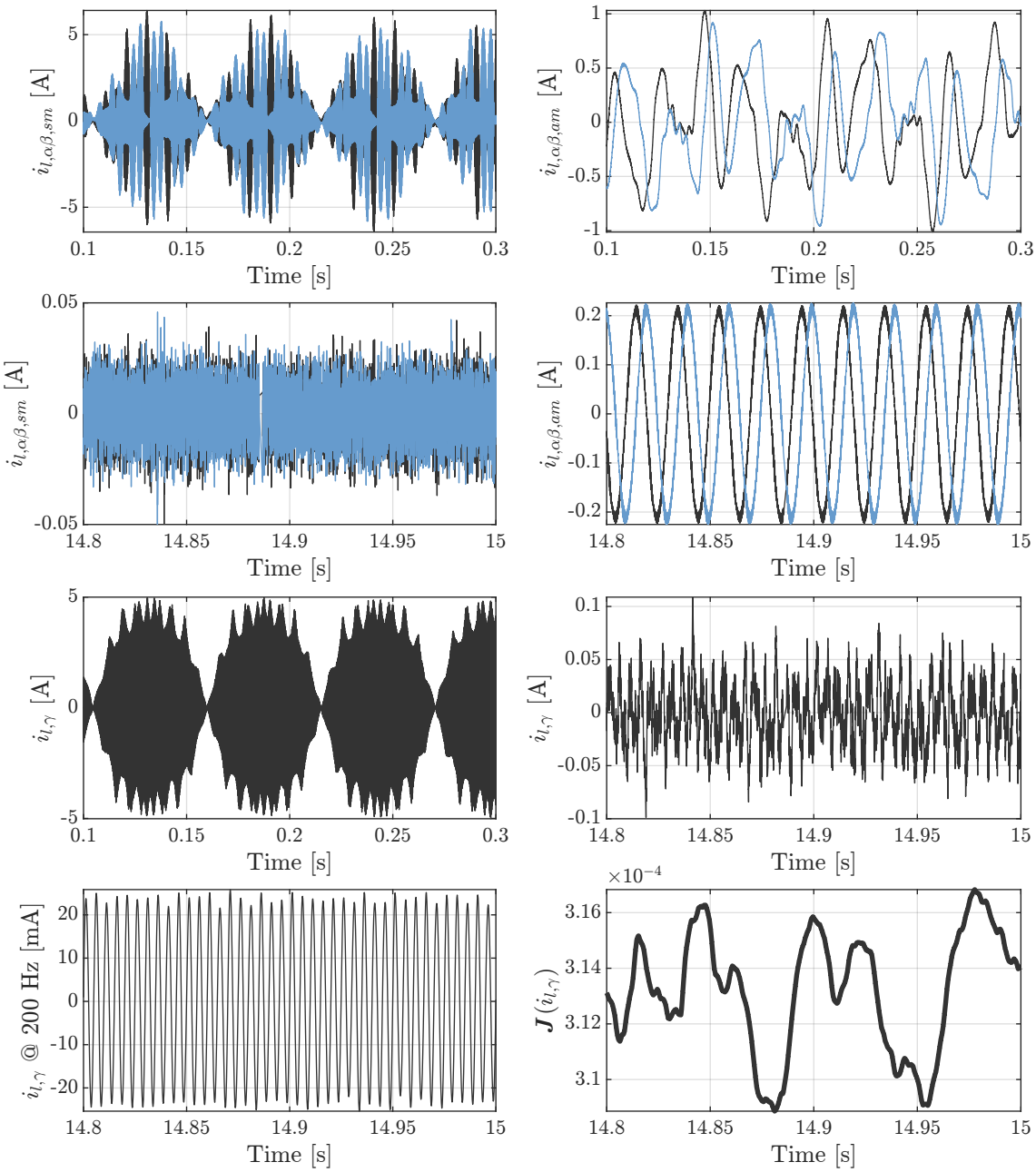

Figure 6.16 – Waveforms of the Cooperative Neural-Based LSPWM HIL results Figure 6.15 before and after carrier synchronization.

6.5 IMPLEMENTATION

The present section aims to present details related to the practical implementation of the LSPWM synchronization technique. To enhance the flexibility of the neural network phase synchronization strategy, the supervisory control responsible for executing this strategy was directly implemented in OPAL-RT via MATLAB. This choice was made to optimize the structure of the neural network, as the OPAL-RT allows for efficient optimization and customization of the neural network structure. However, it is worth noting that implementing the supervisory control in a microprocessor should also be a straightforward process, since the update period for this task is much smaller than the switching period, at around 200 ms. Therefore, this section will focus only on the FPGA algorithms.

The FPGA implementation can be separated into four main components:

- γ-axis resonant controller;
- Second-Order Generalized Integrator (SOGI);
- Moving-Average Filter Phase-Locked Loop (MAF-PLL);
- Voltage-Controlled Oscillator (VCO) for synchnization signal injection.

In certain implementations, the Voltage Controlled Oscillator (VCO) for signal injection can be directly obtained from the Phase-Locked Loop (PLL). However, in this particular case, the VCO was implemented separately.

6.5.1 γ-Axis Controller

In the γ-axis controller strategy, a Finite State-Machine (FSM) consisting of five states was implemented to manage the sequential behavior of the algorithm. The states in the FSM are as follows:

- st.Idle: In this state, the controller waits for an interruption signal from the PWM modulator;
- st.Calc: Once the interruption signal is received, the algorithm performs the resonant controller calculations based on the γ-axis current;
- st.Gain: Multiply and accumulate the controller and system states by the state-feedback gains;
- st.Updt: After the gain multiplication, the output register is updated with the cummulative sum;
- st.Wait: The system waits for the deassertion of the interruption signal before transitioning back to the idle state.

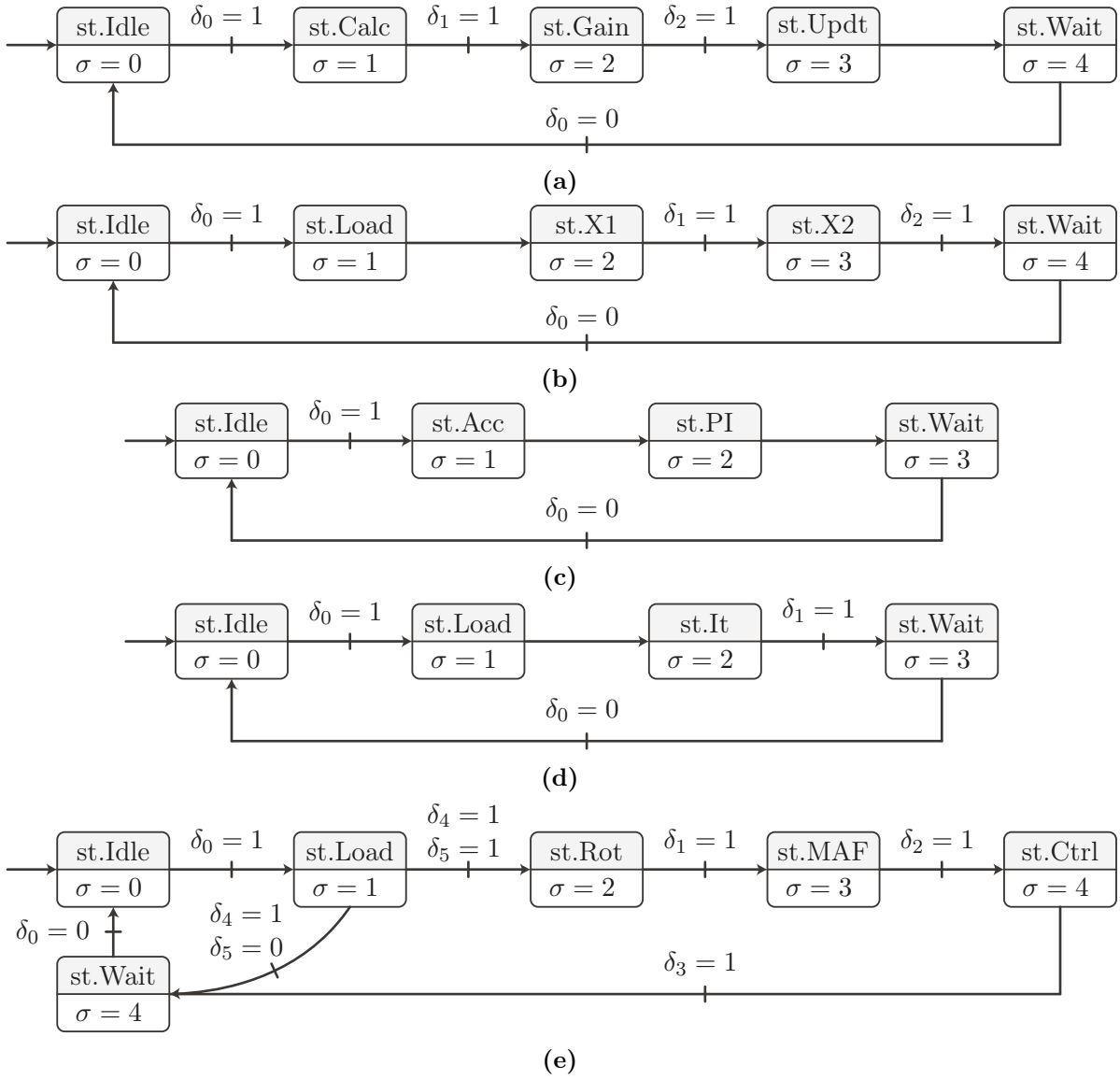

Figure 6.17 – Finite State Machines of the LSPWM FPGA implementation, where δ are the inputs related to the end of execution of each algorithm and σ are the outputs in one-hot encoding. (a) γ-axis Resonant Controller and State Feedback (b) Second Order Generalized Integrator (SOGI) (c) Phase-Locked Loop P/PI Controller (d) Iterative CORDIC Algorithm (e) Synchronization Algorithm.

Figure 6.17.a illustrates the γ-axis FSM behaviour, where σ is related to the output signal in one-hot encoding and δ are the inputs related to the algorithm's start and the end of separate algorithm execution. Note that the controller start is decoupled from the execution of the LSPWM algorithm, as the higher input impedance in also crucial in ensuring the proper functioning of the paralleled-connected converters.

For the resonant converter implementation, as well as the state-feedback gain vector multiplication, a multiply and accumulate algorithm was implemented, where the matrix constants are loaded from a memory shared with a NIOS II processor.

6.5.2 Second-Order Generalized Integrator

The structure of the Second-Order Generalized Integrator (SOGI) closely resembles that of the resonant controller, with minor distinctions related to the chosen damping factor.

The Finite State Machine (FSM) encompasses the following states:

- st.Idle: In this state, the SOGI remains inactive, awaiting an interruption signal from the synchronization algorithm.
- st.Load: Upon receiving the interruption signal, the input register receives a scaled γ-axis duty cycle.
- st.X1: The first state value of the resonant controller is computed using a multiply and accumulate algorithm.
- st.X2: The second state value of the resonant controller is determined similarly to the first state.
- st.Wait: The output register for the orthogonal components is updated, the flag indicating the end of the algorithm is set, and the FSM waits for the start signal to be deasserted.

The FSM's behavior diagram is depicted in Figure 6.17.b. To optimize resource utilization, the multiplier input is multiplexed, resulting in a total execution time of eight clock cycles.

Please note that you need to provide the link to the actual image for me to include it in the response.

6.5.3 Moving-Average Filter Phase-Locked Loop

The MAF-PLL structure was implemented using a moving average filter with a length of $N_{\mathrm{MAF}} = (hf_g)^{-1}$, where f_g represents the grid frequency. This implementation aimed to reduce disturbances in the estimated synchronism frequency and mitigate quantization noise resulting from the limited number of quantization levels in the control action.

A controllable P/PI controller was employed utilizing a sequential approach, with the integral action enabled/disabled by a NIOS II processor flag. The FSM governing the controller's behavior consists of the following states:

- st.Idle: The controller waits for an interruption signal from the synchronization algorithm FSM.
- st.Acc: The PI controller's state is updated based on the accumulation of errors.
- st.PI: The output register is updated by multiplying the input, states, and gains.

- st.Wait: The controller waits for the interruption signal to be deasserted.

This FSM is illustrated in Figure 6.17.c.

The VCO (Voltage Controlled Oscillator) in the system was implemented using a recursive Fixed-Point Coordinate Rotation Digital Computer (CORDIC) algorithm with 17 iterations. This algorithm was chosen for its efficient computation of trigonometric functions, making it well-suited for angle rotation operations in the VCO and its reduced resource usage while in its recursive form.

The CORDIC algorithm n^{th} iteration can be written as

$$\begin{cases} x_n = x_{n-1} - d_{n-1} y_{n-1} 2^{n-1} \\ y_n = x_{n-1} + d_{n-1} y_{n-1} 2^{n-1} \\ z_n = z_{n-1} - d_{n-1} \theta_{n-1} \end{cases}, \tag{6.26}$$

where

$$d_n := \operatorname{sign}(z_n), \quad \theta_n := \tan 2^{n-1}$$

when operating in rotating mode. Through this iterative process, the algorithm converges to the following approximation:

$$(\bar{x}, \bar{y}, \bar{z}) = k_{\text{CORDIC}} (x_0 \cos z_0 - y_0 \sin z_0, y_0 \cos z_0 + x_0 \sin z_0, 0), \tag{6.27}$$

where

$$k_{\text{CORDIC}} := \prod_{i=0}^{n} (1 + \tan^2 \theta_i)^{\frac{1}{2}}.$$

Here, $\bar{x}$, $\bar{y}$, and $\bar{z}$ represent the final values obtained after a finite number of iterations. Additionally, by defining $w_n \in \mathbb{C}$ as $w_n = x_n + y_n$ for all $n \in \mathbb{N}$, we can express the fixed point as

$$\bar{w} = w_0 \exp(\iota z_0), \tag{6.28}$$

which can be used directly in the dq-transformation of the SRF-PLL.

The FSM controlling the CORDIC algorithm presents the following states:

- st.Idle: In this state, the CORDIC algorithm waits for an interruption signal from the synchronization algorithm. This signal serves as a trigger to start the computation process;

- st.Load: Once the interruption signal is received, the CORDIC inputs (x, y) are loaded with the outputs from the Second-Order Generalized Integrator (SOGI) module. Additionally, the axis z is initialized with the angle given by the integrator output of the PLL corresponding to the first quadrant. This step sets the initial values and prepares the algorithm for further computations.

- st.It: This state represents the iteration phase of the algorithm. The algorithm proceeds with a series of iterations, each step refining the approximation of the desired angle rotation. The number of iterations is determined by an internal counter that increments until the specified number of iterations is reached;

- st.Wait: Once the desired number of iterations is completed, the output register captures the final (x, y) values. These values undergo an appropriate rotation adjustment based on the quadrant identification, ensuring accurate representation of the VCO's output signal.

The FSM behaviour is illustrated by Figure 6.17.d. It is important to emphasize that the VCO's output directly corresponds to the dq-axis components of the SRF-PLL (Synchronous Reference Frame Phase-Locked Loop). As a result, a separate algorithm is required to generate the synchronization signal.

A separate Finite State Machine (FSM) was implemented to control the behavior of the synchronization algorithm. The FSM's states are defined as follows:

- st.Idle: In this state, the synchronization algorithm waits for an interruption signal from the PWM modulator. It remains idle until the interruption is received, indicating the need to perform synchronization.

- st.Load: Upon receiving the interruption signal, the FSM output signal triggers the start of the Second-Order Generalized Integrator (SOGI) module. The FSM then waits for the completion of the SOGI operation At this stage, the FSM behavior branches into two possible actions based on an enable flag generated by the NIOS II supervisory. This flag determines whether the algorithm is enabled or disabled.

- st.Rot: If the algorithm is enabled, the FSM transitions to this state. Here, the CORDIC algorithm is initiated with inputs generated by the SOGI, facilitating the necessary angle rotation calculations.

- st.MAF: The FSM proceeds to this state, where the output signal from the CORDIC algorithm's q-axis is processed through a Moving Average Filter (MAF). This filtering step helps to smooth out the signal and reduce noise or fluctuations.

- st.Ctrl: In this state, the FSM executes the PI Controller algorithm. This algorithm updates the angle increment of the Phase-Locked Loop (PLL) integrator, enabling fine adjustments and ensuring accurate synchronization.

- st.Wait: The FSM enters this state and waits for the deassertion of the start signal, indicating the completion of the synchronization process.

The FSM behaviour is shown in Figure 6.17.e.

Table 6.2 – Resource Utilization by Entity after Analysis and Synthesis: LSPWM and Space Vector Modulation FPGA Implementation.

Hierarchy Node	Comb. ALUTs	Dedicated Regs.	Block Memory Bits	DSP Blocks
Synch PLL	703	552	6480	6
γ-Control	240	174	0	2
Fast-SVM	308	148	0	2

Table 6.3 – Resource Utilization by Entity after Analysis and Synthesis: LSPWM Carrier Generation

Hierarchy Node	Comb. ALUTs	Dedicated Regs.	Block Memory Bits	DSP Blocks
MAF Memory	44	28	6480	0
PLL CORDIC	193	83	0	0
PI Controller	22	22	0	2
SOGI	85	172	0	1
Sync CORDIC	186	83	0	0
Others	173	164	0	3

The resource utilization for the implementation in a Cyclone V 5CSEMA4U23C6 FPGA is presented in the Analysis and Synthesis compilation report, as shown in Table 6.2. It is important to note that these values were obtained from the final compilation report for two control strategies implemented in the same FPGA, where the optimization was set to Performance. This optimization choice was made to address the congestion issues experienced by the buses connected to the supervisory processor. In addition, the resource utilization specifically for the carrier generation, which encompasses the MAF-PLL and the CORDIC-based VCOs, is outlined in Table 6.3. This breakdown provides a detailed understanding of the resource allocation for these crucial components of the implementation. These tables offer valuable insights into the utilization of FPGA resources, enabling a comprehensive assessment of the implementation's efficiency and highlighting any potential limitations or areas of improvement.

6.6 REMARKS

This chapter presented a review on methods for the minimization of high-frequency circulating currents. The minimization of these currents can minimize the swithing devices current RMS values, as well as ohmic losses in the magnetic devices, as these currents are limited mainly by the inductance values of the inductors employed in the output filters.

Two different strategies, one based on a master-slave and one based on a cooperative architecture were presented, with a decentralized optimization method based on a neural-network as means of finding an optimal carrier phase which minimized the energy of the circulating currents. The strategies here proposed were validated via a FPGA

implementation, with the power converters emulated through hardware-in-the-loop.

Comments were also provided with respect to the FPGA implementation strategy, mostly related to the Finite-State Machines of each Hierarchy Node and the CORDIC algorithm implemented in rotation mode to solve vector rotations and trigonometric functions.

Chapter

7 Final Considerations

This work presented a study on issues related to the control of power converter systems. In a first moment, the three-phase power converters were modelled with the assumption of balanced parameters, and a rule to model three-phase converters from theirs single-phase counterpart based on the Clarke-Lunze Transform was employed. Different models were obtained as a new framework to analyze parametric variations and the coupling of additive and subtractive modes inter- and intra-converters. A study on possible dc circuits was also presented, with the objective of analyzing the interconnection between dc-ac systems. An indirect matrix converter multifrequency model was also obtained, completing the analysis for ac-ac power converter systems.

From the analysis and simulations of paralleled converter systems, a non-passive behaviour was observed, although the analysis of a single converter resulted in a passive system. This happened when the frequency of the power converter filters approach the switching frequency. The subtractive mode resonance, which is related to the disturbance's dynamics, mainly by the interactions between filters can serve as basis for the design of passive damping structures. If left out when designing output filters, the loss on passive components might be underestimated, and can result in catastrophic effects.

The study on minimization of medium-frequency circulating currents resulted in the proposal of a controller to maintain a passive behaviour of the control-loop. However, the coupling between the $\alpha\beta$ components and the γ-axis synthesized voltage by means of zero-axis harmonic injection might need a higher disturbance rejection for certain frequencies, especially when the paralleled converters process different energy levels. Hence the utilization of resonant controllers was also verified and a design procedure was proposed, with the passivity dependent on the controller damping. The proposed procedure was compared to other procedures, such as LQR and robust control. A Extended Sliding Mode Observer was then employed as means of reducing the number of sensors required for the full state-feedback control strategy, resulting in additional complexity to the control implementation. A multiresonant control strategy together with the observer were implemented in a FPGA, and validated in Hardware-in-the-loop to verify the system

behaviour when operating with parallel-connected converters.

The operation of power converters, and effects such as loss-of-lock of the synchronism algorithms and coupling between different control loops motivated the study of modeling the dynamics of the dc bus and synchronism strategies into the model, leaded to the obtention of a complete closed loop model which represented the whole system. This lead to the obtention of the control loops and disturbance rejection bode diagrams, and enabled the computation of the global stability, or at least the local stability when ignoring effects by assuming a stiff grid. The obtained models can be further expanded for grid-forming power converter systems, by assuming a certain dynamic which governs the grid voltage amplitude and frequency.

A strategy for carrier synchronization was also proposed, as means to reduce the high-frequency circulating currents. However, it was detected that although the synchronism solves issues related to small switching frequency deviations due to parametric variations of clock crystals, the system still needed an optimization method to actuate in the phase of the carriers. The current state-of-the-art on this topic is still reliant on a communication channel to perform the optimization routine, hence it was detected that these strategies still have room for improvement, as means to improve the modularity and reliability of power converter systems, thus the neural-network based method presented promising results with respect to the possibility of operating without a specific communication channel. This can be further expanded for different converter topologies.

Bibliography

1 HU, J.; MA, H. Synchronization of the carrier wave of parallel three-phase inverters with virtual oscillator control. *IEEE Transactions on Power Electronics*, v. 32, n. 10, p. 7998–8007, 2017.

2 XU, T. et al. A closed-loop global synchronous pwm method for immunizing parameters uncertainty in distributed parallel-connected vsis. In: *2019 IEEE Energy Conversion Congress and Exposition (ECCE)*. [S.l.: s.n.], 2019. p. 6219–6223.

3 KOLAR, J. W. et al. Pwm converter power density barriers. In: *2007 Power Conversion Conference - Nagoya*. [S.l.: s.n.], 2007. p. P–9–P–29.

4 HELDWEIN, M. L.; KOLAR, J. W. Impact of emc filters on the power density of modern three-phase pwm converters. *IEEE Transactions on Power Electronics*, v. 24, n. 6, p. 1577–1588, 2009.

5 KAWABATA, T.; HIGASHINO, S. Parallel operation of voltage source inverters. *IEEE Transactions on Industry Applications*, v. 24, n. 2, p. 281–287, 1988.

6 CHANDORKAR, M.; DIVAN, D.; ADAPA, R. Control of parallel connected inverters in standalone ac supply systems. *IEEE Transactions on Industry Applications*, v. 29, n. 1, p. 136–143, 1993.

7 OLIVARES, D. E. et al. Trends in microgrid control. *IEEE Transactions on Smart Grid*, v. 5, n. 4, p. 1905–1919, 2014.

8 GUERRERO, J. M. et al. Advanced control architectures for intelligent microgrids—part i: Decentralized and hierarchical control. *IEEE Transactions on Industrial Electronics*, v. 60, n. 4, p. 1254–1262, 2013.

9 HAN, Y. et al. Review of active and reactive power sharing strategies in hierarchical controlled microgrids. *IEEE Transactions on Power Electronics*, v. 32, n. 3, p. 2427–2451, 2017.

10 SUN, Y.-z. et al. Review on frequency control of power systems with wind power penetration. In: *2010 International Conference on Power System Technology*. [S.l.: s.n.], 2010. p. 1–8.

11 EID, B. M. et al. Control methods and objectives for electronically coupled distributed energy resources in microgrids: A review. *IEEE Systems Journal*, v. 10, n. 2, p. 446–458, 2016.

12 MIDDLEBROOK, R.; VORPERIAN, V.; LINDAL, J. The n extra element theorem. *IEEE Transactions on Circuits and Systems I: Fundamental Theory and Applications*, v. 45, n. 9, p. 919–935, 1998.

13 MAZUMDER, S. K. *Nonlinear Analysis and Control of Standalone, Parallel DC-DC, and Parallel Multi-Phase PWM Converters*. PhD. Dissertation — Virginia Polytechnic Institute and State University, 2001.

14 CESAR, E. L. *Modelagem e análise da dinâmica de microrredes de distribuição de energia elétrica*. PhD. Dissertation — Federal University of Santa Catarina, 2017.

15 LENZ, E. et al. Two-parameter stability analysis of resistive droop control applied to parallel-connected voltage-source inverters. *IEEE Journal of Emerging and Selected Topics in Power Electronics*, v. 8, n. 4, p. 3318–3332, 2020.

16 CALISKAN, V.; VERGHESE, O.; STANKOVIC, A. Multifrequency averaging of dc/dc converters. *IEEE Transactions on Power Electronics*, v. 14, n. 1, p. 124–133, 1999.

17 ORMROD, J. E. *Harmonic state space modelling of voltage source converters*. Master's Thesis — University of Canterbury, 2013.

18 BLAABJERG, F. et al. Overview of control and grid synchronization for distributed power generation systems. *IEEE Transactions on Industrial Electronics*, v. 53, n. 5, p. 1398–1409, 2006.

19 KWON, J. B. et al. Harmonic instability analysis of a single-phase grid-connected converter using a harmonic state-space modeling method. *IEEE Transactions on Industry Applications*, v. 52, n. 5, p. 4188–4200, 2016.

20 BORUP, U.; BLAABJERG, F.; ENJETI, P. Sharing of nonlinear load in parallel-connected three-phase converters. *IEEE Transactions on Industry Applications*, v. 37, n. 6, p. 1817–1823, 2001.

21 JIANG, W. et al. Suppression of high-frequency circulating current caused by asynchronous carriers for parallel three-phase grid-connected converters. *IEEE Transactions on Industrial Electronics*, v. 65, n. 2, p. 1031–1040, 2018.

22 JIANG, W. et al. Suppression of zero sequence circulating current for parallel three-phase grid-connected converters using hybrid modulation strategy. *IEEE Transactions on Industrial Electronics*, v. 65, n. 4, p. 3017–3026, 2018.

23 XU, T. et al. A closed-loop gspwm method for attenuating circulating leakage current in pv station. In: *2019 10th International Conference on Power Electronics and ECCE Asia (ICPE 2019 - ECCE Asia)*. [S.l.: s.n.], 2019. p. 1353–1358.

24 XU, T.; GAO, F. Global synchronous pulse width modulation of distributed inverters. *IEEE Transactions on Power Electronics*, v. 31, n. 9, p. 6237–6253, 2016.

25 LUNZE, J. *Feedback Control of Large Scale Systems*. Prentice-Hall, 1992. (Ellis Horwood Series in Mechanical Engineering). ISBN 9780133183535. Available at: <https://books.google.com.br/books?id=U91SAAAAMAAJ>.

26 SOUSA, G. J. M. d. *Sistemas de controle para a operação eficiente de conversores modulares multiníveis em acionamentos elétricos*. PhD. Dissertation — INEP/UFSC, 2022.

27 YANG, T. *Development of dynamic phasors for the modelling of aircraft electrical power systems*. PhD. Dissertation — University of Nottingham, 2013.

28 GUSTAVSEN, B.; SEMLYEN, A. Rational approximation of frequency domain responses by vector fitting. *IEEE Transactions on Power Delivery*, v. 14, n. 3, p. 1052–1061, 1999.

29 BERTOLDI, B. *Systematic procedures for the design of passive components applied to a high performance three-phase rectifier*. Master's Thesis — Federal University of Santa Catarina, 2021.

30 FINAMOR, G. A. et al. Solar photovoltaic static conversion system applied to a smart microgrid. In: *2017 IEEE 8th International Symposium on Power Electronics for Distributed Generation Systems (PEDG)*. [S.l.: s.n.], 2017. p. 1–6.

31 WANG, H. et al. Design for reliability in power electronics in renewable energy systems 2013; status and future. In: *4th International Conference on Power Engineering, Energy and Electrical Drives*. [S.l.: s.n.], 2013. p. 1846–1851. ISSN 2155-5516.

32 FRIEDLI, T.; KOLAR, J. W. Comprehensive comparison of three-phase ac-ac matrix converter and voltage dc-link back-to-back converter systems. In: *The 2010 International Power Electronics Conference - ECCE ASIA* -. [S.l.: s.n.], 2010. p. 2789–2798.

33 JAPPE, T. K. *Conversores Matriciais Indiretos Alimentados em Corrente*. PhD. Dissertation — INEP/UFSC, 2015.

34 SCHAFMEISTER, F. *Indirekte Sparse Matrix Konverter*. PhD. Dissertation — ETH Zurich, 2008.

35 SCHONBERGER, J. et al. An ultra sparse matrix converter with a novel active clamp circuit. In: *2007 Power Conversion Conference - Nagoya*. [S.l.: s.n.], 2007. p. 784–791.

36 GRABOVSKI, E. F. C.; JAPPE, T. K.; MUSSA, S. A. Fpga-based space vector modulation of an indirect matrix converter. *Brazilian Journal of Power Electronics*, v. 24, n. 1, p. 47–49, 2019.

37 ZHANG, K. et al. Direct repetitive control of spwm inverter for ups purpose. *IEEE Transactions on Power Electronics*, v. 18, n. 3, p. 784–792, 2003.

38 MATTAVELLI, P.; MARAFAO, F. Repetitive-based control for selective harmonic compensation in active power filters. *IEEE Transactions on Industrial Electronics*, v. 51, n. 5, p. 1018–1024, 2004.

39 ESCOBAR, G. et al. Repetitive-based controller for a ups inverter to compensate unbalance and harmonic distortion. *IEEE Transactions on Industrial Electronics*, v. 54, n. 1, p. 504–510, 2007.

40 ZHANG, M. et al. Circulating harmonic current elimination of a cps-pwm-based modular multilevel converter with a plug-in repetitive controller. *IEEE Transactions on Power Electronics*, v. 29, n. 4, p. 2083–2097, 2014.

41 HORNIK, T.; ZHONG, Q.-C. A current-control strategy for voltage-source inverters in microgrids based on h^{∞} and repetitive control. *IEEE Transactions on Power Electronics*, v. 26, n. 3, p. 943–952, 2011.

42 XIONG, Y.; YE, Y. Physical interpretations of grid voltage full feedforward for grid-tied inverter. *IEEE Transactions on Circuits and Systems II: Express Briefs*, v. 66, n. 2, p. 267–271, 2019.

43 CAO, Y. et al. Adrc-based current control for grid-tied inverters: Design, analysis, and verification. *IEEE Transactions on Industrial Electronics*, v. 67, n. 10, p. 8428–8437, 2020.

44 KHAJEH, K. G. et al. A full-feedforward harmonic mitigation scheme in multi-parallel grid-tied inverters. In: *2020 IEEE International Conference on Power Electronics, Drives and Energy Systems (PEDES)*. [S.l.: s.n.], 2020. p. 1–6.

45 YAN, Q. et al. An improved grid-voltage feedforward strategy for high-power three-phase grid-connected inverters based on the simplified repetitive predictor. *IEEE Transactions on Power Electronics*, v. 31, n. 5, p. 3880–3897, 2016.

46 LIU, J. et al. Disturbance observer-based adaptive current control with self-learning ability to improve the grid-injected current for *lcl* -filtered grid-connected inverter. *IEEE Access*, v. 7, p. 105376–105390, 2019.

47 FUKUDA, S.; YODA, T. A novel current-tracking method for active filters based on a sinusoidal internal model [for pwm invertors]. *IEEE Transactions on Industry Applications*, v. 37, n. 3, p. 888–895, 2001.

48 FUKUDA, S.; IMAMURA, R. Application of a sinusoidal internal model to current control of three-phase utility-interface converters. *IEEE Transactions on Industrial Electronics*, v. 52, n. 2, p. 420–426, 2005.

49 LISERRE, M.; TEODORESCU, R.; BLAABJERG, F. Multiple harmonics control for three-phase grid converter systems with the use of pi-res current controller in a rotating frame. *IEEE Transactions on Power Electronics*, v. 21, n. 3, p. 836–841, 2006.

50 ZHANG, R. et al. A grid simulator with control of single-phase power converters in d-q rotating frame. In: *2002 IEEE 33rd Annual IEEE Power Electronics Specialists Conference. Proceedings (Cat. No.02CH37289)*. [S.l.: s.n.], 2002. v. 3, p. 1431–1436 vol.3.

51 MATTAVELLI, P. A closed-loop selective harmonic compensation for active filters. *IEEE Transactions on Industry Applications*, v. 37, n. 1, p. 81–89, 2001.

52 PEREIRA, L. F. A. et al. Multiple resonant controllers for uninterruptible power supplies-a systematic robust control design approach. *IEEE Transactions on Industrial Electronics*, v. 61, n. 3, p. 1528–1538, 2014.

53 HUERTA, F. et al. Frequency-adaptive multiresonant lqg state-feedback current controller for lcl-filtered vscs under distorted grid voltages. *IEEE Transactions on Industrial Electronics*, v. 65, n. 11, p. 8433–8444, 2018.

54 BONAN, G. et al. Robust control design of multiple resonant controllers for sinusoidal tracking and harmonic rejection in uninterruptible power supplies. In: *2010 IEEE International Symposium on Industrial Electronics*. [S.l.: s.n.], 2010. p. 303–308.

55 ZHAO, W.; CHEN, G. Comparison of active and passive damping methods for application in high power active power filter with lcl-filter. In: *2009 International Conference on Sustainable Power Generation and Supply*. [S.l.: s.n.], 2009. p. 1–6.

56 KALSI, K. et al. Sliding-mode observers for systems with unknown inputs: A high-gain approach. *Automatica*, v. 46, n. 2, p. 347–353, 2010. ISSN 0005-1098. Available at: <https://www.sciencedirect.com/science/article/pii/S000510980900524X>.

57 ANGELIS, G. Z. *System analysis, modelling and control with polytopic linear models*. PhD. Dissertation — Eindhoven University of Technology, 2001.

58 ANGELIS, G. *System Analysis, Modelling and Control with Polytopic Linear Models*. Technische Universiteit Eindhoven, 2001. ISBN 9789038626727. Available at: <https://books.google.com.br/books?id=F0EROAAACAAJ>.

59 ASTROM, K. J.; MURRAY, R. M. *Feedback Systems: An Introduction for Scientists and Engineers*. USA: Princeton University Press, 2008. ISBN 0691135762.

60 Boyd, S. et al. *Linear Matrix Inequalities in System and Control Theory*. [S.l.]: SIAM studies in applied mathematics: 15, 1994.

61 ROTONDO, D.; NEJJARI, F.; PUIG, V. Robust state-feedback control of uncertain lpv systems: An lmi-based approach. *Journal of the Franklin Institute*, v. 351, n. 5, p. 2781–2803, 2014. ISSN 0016-0032. Available at: <https://www.sciencedirect.com/science/article/pii/S0016003214000337>.

62 WANG, X.; BLAABJERG, F.; LOH, P. C. Passivity-based stability analysis and damping injection for multiparalleled vscs with lcl filters. *IEEE Transactions on Power Electronics*, v. 32, n. 11, p. 8922–8935, 2017.

63 PUERTO-FLORES, D. del et al. Passivity-based control by series/parallel damping of single-phase pwm voltage source converter. *IEEE Transactions on Control Systems Technology*, v. 22, n. 4, p. 1310–1322, 2014.

64 BAI, H.; WANG, X.; BLAABJERG, F. Passivity enhancement in renewable energy source based power plant with paralleled grid-connected vsis. *IEEE Transactions on Industry Applications*, v. 53, n. 4, p. 3793–3802, 2017.

65 KHALIL, H. *Nonlinear Systems*. Prentice Hall, 2002. (Pearson Education). ISBN 9780130673893. Available at: <https://books.google.com.br/books?id=t_d1QgAACAAJ>.

66 FéLIX, J. P. i. *Modulation and Control of Three-Phase PWM Multilevel Converters"*. PhD. Dissertation — Universitat Politécnica de Catalunya, 2002.

67 DRAKUNOV, S.; UTKIN, V. Sliding mode observers. tutorial. In: *Proceedings of 1995 34th IEEE Conference on Decision and Control*. [S.l.: s.n.], 1995. v. 4, p. 3376–3378 vol.4.

68 MOCCELINI, M. A. *Real-time simulation of power electronics systems and hardware-in-the-loop applications*. Master's Thesis — Federal University of Santa Catarina, 2018.

69 BLAABJERG, F. et al. Distributed power-generation systems and protection. *Proceedings of the IEEE*, v. 105, n. 7, p. 1311–1331, 2017.

70 WANG, X.; BLAABJERG, F. Harmonic stability in power electronic-based power systems: Concept, modeling, and analysis. *IEEE Transactions on Smart Grid*, v. 10, n. 3, p. 2858–2870, 2019.

71 HARNEFORS, L. et al. Passivity-based stability assessment of grid-connected vscs—an overview. *IEEE Journal of Emerging and Selected Topics in Power Electronics*, v. 4, n. 1, p. 116–125, 2016.

72 MOLLERSTEDT, E.; BERNHARDSSON, B. Out of control because of harmonics-an analysis of the harmonic response of an inverter locomotive. *IEEE Control Systems Magazine*, v. 20, n. 4, p. 70–81, 2000.

73 ZHOU, J. Z. et al. Impact of short-circuit ratio and phase-locked-loop parameters on the small-signal behavior of a vsc-hvdc converter. *IEEE Transactions on Power Delivery*, v. 29, n. 5, p. 2287–2296, 2014.

74 WANG, X.; HARNEFORS, L.; BLAABJERG, F. Unified impedance model of grid-connected voltage-source converters. *IEEE Transactions on Power Electronics*, v. 33, n. 2, p. 1775–1787, 2018.

75 DONG, D. et al. Analysis of phase-locked loop low-frequency stability in three-phase grid-connected power converters considering impedance interactions. *IEEE Transactions on Industrial Electronics*, v. 62, n. 1, p. 310–321, 2015.

76 LI, M. et al. The control strategy for the grid-connected inverter through impedance reshaping in q-axis and its stability analysis under a weak grid. *IEEE Journal of Emerging and Selected Topics in Power Electronics*, v. 9, n. 3, p. 3229–3242, 2021.

77 WU, J. et al. Full feedforward control strategy with pre-filter of lcl grid-connected inverter in weak grid. In: *2022 10th International Conference on Smart Grid and Clean Energy Technologies (ICSGCE)*. [S.l.: s.n.], 2022. p. 59–64.

78 SUUL, J. A. et al. Extended stability range of weak grids with voltage source converters through impedance-conditioned grid synchronization. In: *11th IET International Conference on AC and DC Power Transmission*. [S.l.: s.n.], 2015. p. 1–10.

79 YANG, L. et al. Control scheme and performance analysis of dual-frequency single-phase grid-connected inverter interfaced with weak and distorted grids. *IEEE Access*, v. 8, p. 178639–178650, 2020.

80 YOON, S.-J.; KIM, K.-H. Harmonic suppression and stability enhancement of a voltage sensorless current controller for a grid-connected inverter under weak grid. *IEEE Access*, v. 10, p. 38575–38589, 2022.

81 CHEN, X. et al. Impedance-phased dynamic control method for grid-connected inverters in a weak grid. *IEEE Transactions on Power Electronics*, v. 32, n. 1, p. 274–283, 2017.

82 RODRIGUEZ, P. et al. Double synchronous reference frame pll for power converters control. In: *2005 IEEE 36th Power Electronics Specialists Conference*. [S.l.: s.n.], 2005. p. 1415–1421.

83 LIU, B. et al. A three-phase pll algorithm based on signal reforming under distorted grid conditions. *IEEE Transactions on Power Electronics*, v. 30, n. 9, p. 5272–5283, 2015.

84 GOLESTAN, S.; GUERRERO, J. M.; VASQUEZ, J. C. Three-phase plls: A review of recent advances. *IEEE Transactions on Power Electronics*, v. 32, n. 3, p. 1894–1907, 2017.

85 KWON, J. B. et al. Precise model analysis for 3-phase high power converter using the harmonic state space modeling. In: *2015 9th International Conference on Power Electronics and ECCE Asia (ICPE-ECCE Asia)*. [S.l.: s.n.], 2015. p. 2628–2635.

86 KWON, J. et al. Harmonic instability analysis of single-phase grid connected converter using harmonic state space (hss) modeling method. In: *2015 IEEE Energy Conversion Congress and Exposition (ECCE)*. [S.l.: s.n.], 2015. p. 2421–2428.

87 LIAO, Y.; WANG, X. Small-signal modeling of ac power electronic systems: Critical review and unified modeling. *IEEE Open Journal of Power Electronics*, p. 1–1, 2021.

88 XU, T.; GAO, F.; ZHOU, L. Practical implementation of global synchronous pulse width modulation with time delay compensation and distributed calculation capabilities. In: *2016 IEEE Energy Conversion Congress and Exposition (ECCE)*. [S.l.: s.n.], 2016. p. 1–6.

89 XU, T. et al. Performance analysis of global synchronous pulsewidth modulation for distributed inverters. In: *2015 IEEE Energy Conversion Congress and Exposition (ECCE)*. [S.l.: s.n.], 2015. p. 6475–6482.

90 XU, T. et al. A carrier synchronization method for global synchronous pulsewidth modulation application using phase-locked loop. *IEEE Transactions on Power Electronics*, v. 34, n. 11, p. 10720–10732, 2019.

91 FRIGO, M.; JOHNSON, S. G. The design and implementation of FFTW3. *Proceedings of the IEEE*, v. 93, n. 2, p. 216–231, 2005. Special issue on "Program Generation, Optimization, and Platform Adaptation".

92 GUERRERO, J. M. et al. Hierarchical control of droop-controlled ac and dc microgrids—a general approach toward standardization. *IEEE Transactions on Industrial Electronics*, v. 58, n. 1, p. 158–172, 2011.

93 ROCABERT, J. et al. Control of power converters in ac microgrids. *IEEE Transactions on Power Electronics*, v. 27, n. 11, p. 4734–4749, 2012.

94 ZHONG, Q.-C. et al. Self-synchronized synchronverters: Inverters without a dedicated synchronization unit. *IEEE Transactions on Power Electronics*, v. 29, n. 2, p. 617–630, 2014.

95 CHUNG, S.-K. A phase tracking system for three phase utility interface inverters. *IEEE Transactions on Power Electronics*, v. 15, n. 3, p. 431–438, 2000.

96 GOLESTAN, S.; GUERRERO, J. M.; VASQUEZ, J. C. Is using a complex control gain in three-phase flls reasonable? *IEEE Transactions on Industrial Electronics*, v. 67, n. 3, p. 2480–2484, 2020.

97 GOLESTAN, S. et al. A study on three-phase flls. *IEEE Transactions on Power Electronics*, v. 34, n. 1, p. 213–224, 2019.

98 FALLAH, M. et al. Novel structure for unbalance, reactive power and harmonic compensation based on vff-rls and sogi-fll in three phase four wire power system. In: *2015 IEEE Energy Conversion Congress and Exposition (ECCE)*. [S.l.: s.n.], 2015. p. 6254–6260.

99 HE, X.; GENG, H.; YANG, G. A generalized design framework of notch filter based frequency-locked loop for three-phase grid voltage. *IEEE Transactions on Industrial Electronics*, v. 65, n. 9, p. 7072–7084, 2018.

100 PRADHAN, A.; ROUTRAY, A.; BASAK, A. Power system frequency estimation using least mean square technique. *IEEE Transactions on Power Delivery*, v. 20, n. 3, p. 1812–1816, 2005.

101 ROUTRAY, A.; PRADHAN, A.; RAO, K. A novel kalman filter for frequency estimation of distorted signals in power systems. *IEEE Transactions on Instrumentation and Measurement*, v. 51, n. 3, p. 469–479, 2002.

102 YANG, J.-Z.; LIU, C.-W. A precise calculation of power system frequency and phasor. *IEEE Transactions on Power Delivery*, v. 15, n. 2, p. 494–499, 2000.

103 XIA, Y.; MANDIC, D. P. A full mean square analysis of clms for second-order noncircular inputs. *IEEE Transactions on Signal Processing*, v. 65, n. 21, p. 5578–5590, 2017.

104 XIA, Y.; MANDIC, D. P. Widely linear adaptive frequency estimation of unbalanced three-phase power systems. *IEEE Transactions on Instrumentation and Measurement*, v. 61, n. 1, p. 74–83, 2012.

105 XIA, Y. et al. Widely linear adaptive frequency estimation for unbalanced three-phase power systems with multiple noisy measurements. In: *2017 22nd International Conference on Digital Signal Processing (DSP)*. [S.l.: s.n.], 2017. p. 1–5.

106 GRABOVSKI, E. F. C.; HELDWEIN, M. L.; MUSSA, S. A. Three-phase adaptive frequency estimator with a delayed signal cancellation pre-filter under heavily distorted

grid conditions. In: *2019 IEEE 15th Brazilian Power Electronics Conference and 5th IEEE Southern Power Electronics Conference (COBEP/SPEC)*. [S.l.: s.n.], 2019. p. 1–6.

107 BATISTA, Y. N. et al. Variable-structure generalized delayed signal cancellation pll to improve convergence time. *IEEE Transactions on Industrial Electronics*, v. 62, n. 11, p. 7146–7150, 2015.

108 GOLESTAN, S.; GUERRERO, J. M.; VASQUEZ, J. C. Hybrid adaptive/nonadaptive delayed signal cancellation-based phase-locked loop. *IEEE Transactions on Industrial Electronics*, v. 64, n. 1, p. 470–479, 2017.

109 NEVES, F. A. S. et al. A generalized delayed signal cancellation method for detecting fundamental-frequency positive-sequence three-phase signals. *IEEE Transactions on Power Delivery*, v. 25, n. 3, p. 1816–1825, 2010.

110 GOLESTAN, S. et al. An efficient implementation of generalized delayed signal cancellation pll. *IEEE Transactions on Power Electronics*, v. 31, n. 2, p. 1085–1094, 2016.

111 NASCIMENTO, P. S. B. et al. Fpga implementation of the generalized delayed signal cancelation—phase locked loop method for detecting harmonic sequence components in three-phase signals. *IEEE Transactions on Industrial Electronics*, v. 60, n. 2, p. 645–658, 2013.

112 HAYKIN, S. *Adaptive filter theory*. 4th. ed. Upper Saddle River, NJ: Prentice Hall, 2002.

113 MANDIC, D.; GOH, V. *Complex Valued Nonlinear Adaptive Filters*. [S.l.]: John Wiley & Sons, Ltd, 2009. ISBN 9780470742624.

APPENDIX

A Frequency Estimation Algorithms

From Chapter 4, we have that a precise, reliable frequency and fast estimation is extremelly useful for tuning resonant controllers, as to decouple the controller parameter tuning and the power converters' dynamics. However, the importance of this estimaiton goes beyond this, as some control methods, such as droop [7, 14, 92, 93] and virtual synchronous machines [94], are also extremelly reliant on precise frequency estimations as to correctly control the power injection of a power converter. Also, fault detection and operation limits are also strictly regulated, requiring a satisfying dynamic performance of such algorithms. In this sense, the insertion of power converters units on the electric grid is reliant on the performance of synchronization algorithms as to ensure a safe and stable operation of the interface between source and grid, while respecting the grid codes.

Currently, the most employed methods in power electronics are tipically associated with Phase-Locked Loops (PLLs) [75, 83, 84, 95] and Frequency-Locked Loops [96–99]. While PLLs are necessary to ensure a correct synchronization of the electric quantities synthesized by power converters and the grid, due to a small phase estimation error, FLLs are usually responsible for an accurate estimation of the grid frequency.

Other approaches, such as employing Least Mean Square (LMS) adaptive filters [100], Kalman filters [101] and Fourier-transform based algorithms [102] have been proposed in the state-of-the-art and present faster dynamics if compared to traditional methods. However, such methods are optimally employed in balanced/non-distorted grid conditions, and may present low numerical stability and/or extremelly complex implementation. Methods based on low-order linear adaptive filters are usually susceptible to deterministic disturbances, such as grid harmonics, as they assume a white noise in their conception.

This section aims to present a review on adaptive filters based on the LMS algorithm for grid frequency estimation and some techniques to improve robustness for deterministic disturbances and quantization noise. Some of the concepts on the formulation of linear adaptive filters are discussed in Appendix B.

A.1 WIDELY-LINEAR FREQUENCY ESTIMATOR

A solution to non-circular second-order noise is presented in [103, 104] through the use of a the Complex LMS (CLMS) and the Augmented Linear CLMS (ACLMS). The

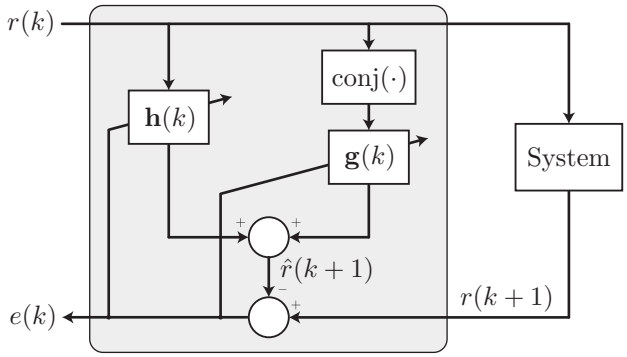

Figure A.1 – Block diagram of the Augmented Complex Least Mean Square (ACLMS) filter for system identification. The CLMS algorithm can be obtained by vanishing $\mathbf{g}$.

estimator is called Strictly Linear Estimator (SLE) if employing a CLMS filter and Widely Linear Estimator (WLE) if employing the ACLMS filter.

The algorithm for the ACLMS is given by

$$\begin{cases} e(k) = r(k) - \mathbf{h}^H(k)\mathbf{x}(k) - \mathbf{g}^T(k)\mathbf{x}^*(k) \\ \mathbf{h}(k+1) = \mathbf{h}(k) + \mu e(k)\mathbf{x}(k) \\ \mathbf{g}(k+1) = \mathbf{g}(k) + \mu e(k)\mathbf{x}^*(k) \end{cases}, \tag{A.1}$$

and the CLMS algorithm can be obtained by vanishing $\mathbf{g}$. Hence the first order ACLMS and CLMS can be obtained by taking

$$\mathbf{x}(k) := r(k-1), \tag{A.2}$$

hence the domain of the CLMS is defined by $\{r\}$ and the domain of the ACLMS defined by $\{r, r^*\}$, which in turn justifies the second-order noise-rejection of the latter. A block diagram of the ACLMS is presented in Figure A.1.

We can define the complex input r as

$$r(k) := \frac{2}{3}\left[1 \quad \exp\left(-\iota\frac{2}{3}\pi\right) \quad \exp\left(\iota\frac{2}{3}\pi\right)\right]\vec{r}_{abc}(k) \tag{A.3}$$

the image of projection of the $\alpha\beta$ plane spannign over $\mathbb{C}$, representing a certain electrical quantity.

From [104], we have that the estimated frequency, which is based in the estimated parameters $\mathbf{h}$ and $\mathbf{g}$, is equal to

$$\Omega(k) = \tan^{-1}\left(\frac{\sqrt{\Im\{\mathbf{h}(k)\}^2 - |\mathbf{g}(k)|^2}}{\Re\{\mathbf{h}(k)\}}\right). \tag{A.4}$$

We can also perform the algorithm for a window of W samples by using the

Augmented Complex Total Least Squares (ACTLS) [105]. Hence let us define the window vector as

$$\bar{\mathbf{r}}(k) = (r(k), \ldots, r(k-W+1)) \tag{A.5}$$

such that

$$\bar{\mathbf{r}}(k+1) \approx \bar{\mathbf{r}}(k)h(k) + \bar{\mathbf{r}}(k)g(k).$$

We can define an augmented data matrix $\bar{\mathbf{R}}(k)$ as

$$\bar{\mathbf{R}}(k) = [\bar{\mathbf{r}}(k), \bar{\mathbf{r}}^*(k), \bar{\mathbf{r}}(k+1)]^H \tag{A.6}$$

and an augmented weigth vector as

$$\mathbf{w}(k) = [h(k), g(k), -1]^T. \tag{A.7}$$

In this case, we can write the update equations as

$$\begin{cases} \mathbf{e}(k) = \bar{\mathbf{R}}^H(k)\mathbf{w}(k) \\ \mathbf{w}(k+1) = \mathbf{w}(k) + \mu \dfrac{\mathbf{w}(k)\mathbf{e}^H(k) - \|\mathbf{w}(k)\|^2 \bar{\mathbf{R}}(k)}{\left(\|\mathbf{w}(k)\|^2\right)^2} \end{cases} \tag{A.8}$$

However, the experimental results presented in [105] are not sufficient to justify the algorithm's increased complexity for a large window, if compared to [106], which is discussed in the next section.

A.2 WIDELY-LINEAR ADAPTIVE FREQUENCY ESTIMATOR WITH A DELAYED-SIGNAL CANCELLATION PRE-FILTER

A.2.1 Delayed-Signal Cancellation Pre Filter

Other adaptive solutions based on PLLs and DSC filters have been proposed in the state-of-the-art [107–111], although the inherent imprecision of the PLL frequency estimation and the slow dynamic of the loop filter hinders the settling-time of such strategies. Hence, a solution to filter deterministic noise can be proposed through the use of a Delayed-Signal Cancellation (DSC) pre-filter stage to eliminate frequency components multiples of the fundamental frequency, pre-conditioning the electrical quantities to improve the adaptive estimator's disturbance rejection. A block diagram of the proposed implementation is illustrated in Figure A.2.

A drawback lies in the settling time and the implementation complexity of such filters, which demand for a large amount of memory.

Hence let the input voltage r defined by (A.3). The signal can then be rewritten in

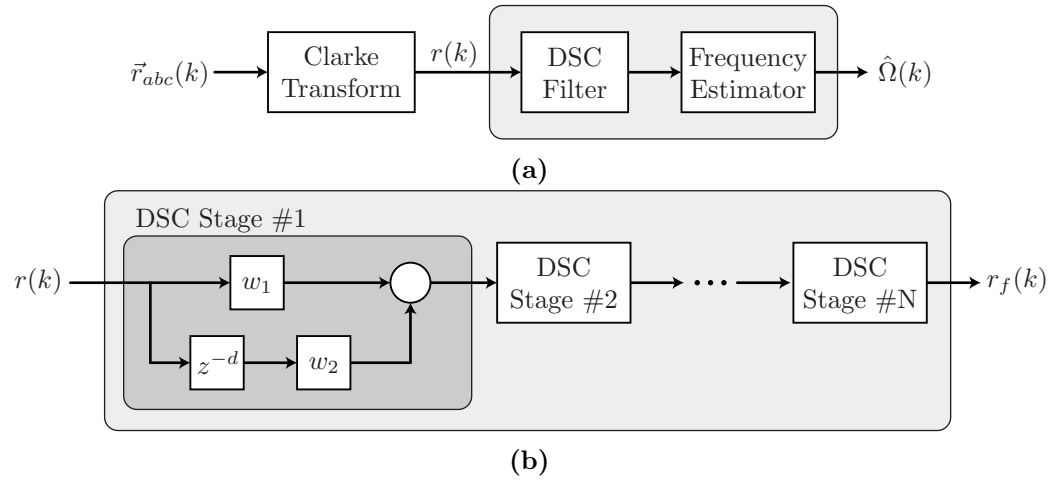

Figure A.2 – (a) Block diagram of the proposed frequency estimator based on the Delayed-Signal Cancellation filter and the Widely (or Strictly) Linear Estimator. (b) Block diagram of a DSC filter with N stages.

terms of its Fourier series according to

$$r(k) = \sum_{n\in\mathcal{N}} r_n(k) = \sum_{n\in\mathcal{N}} R_n(k)\exp\left(\iota\Omega_r k\right), \tag{A.9}$$

with h as the sampling time, $\Omega = 2\pi f_r h = 2\pi/N$ as the discrete angular frequency of the fundamental component of r, N as the number of samples per period. Also, let $n \in \mathcal{N}$ be the set of harmonics, with $\mathcal{N} \cap \mathbb{Z}^+$ as the positive sequence harmonics and $\mathcal{N} \cap \mathbb{Z}^-$ as the negative sequence harmonics, and let $R_n \in \mathbb{R}$ be the amplitude of the n^{th} harmonic component.

Hence, the signal r delayed by d samples can be written as

$$r(k-d) = \sum_{n\in\mathcal{N}} R_n\exp\left(-\iota\Omega_r d\right)\exp\left(\iota\Omega_r k\right) \tag{A.10}$$

with a generic delay $\{d \in \mathbb{N} : d < N\}$. The objective of the DSC filter project is to find a linear combination between the vector r and its delayed counterpart as to selective cancel an harmonic $n_s \in \mathcal{N}$, resulting in

$$r_f(k) = w_1 r(k) + w_2 r(k-d) = \sum_{n\neq n_s \pm \frac{N}{d}}, \tag{A.11}$$

with complex-valued constants w_1, w_2 that solve for

$$\begin{cases} w_1(\Omega_s, n_s, d) = \dfrac{1}{1-\exp\left(\iota(n_s-1)\Omega_s d\right)} \\ w_2(\Omega_s, n_s, d) = w_1(\Omega_s, n_s, d)\exp\left(\iota n_s \Omega_s d\right) \end{cases}, \tag{A.12}$$

for a certain rated frequency Ω_s. However, if the signal frequency and the rated frequency

are different, the cancellation is hindered, and the trajectory of the filtered signal r_f is not necessarily circular. Hence the frequency estimation algorithm must be able to reject noncircular second-order noise, i.e, eventual unbalances and or harmonic components, as to provide an accurate estimation.

A.2.2 Experimental Results

Most of the harmonic content of r can be filtered through the use of multiple DSC stages. However, the insertion of each stage results in an increase in the settling time, which is directly tied to the number of samples used in the delay structure.

The experimental results were separated into steady-state and dynamic behaviour as to analyze both numerical precision and dynamic response of the proposed algorithm under different grid disturbances. The algorithm was implemented with the DSC filter operating at a 100 kHz frequency to provide a high resolution for the delay choice.

The algorithm was fully implemented in an Altera Cyclone V 5CSEMA4U23C6N FPGA. A 16-bit reference source was implemented using an Opal-RT OP5700 real-time simulator connected to the FPGA. The DSC-filter sampling frequency was chosen as 160 kHz as to improve the filtering capabilities for higher order frequencies and to reduce quantization noise in the subsequent structures. However, the filtered signal was downsampled to 10 kHz for the execution of the WLE, as the higher the sampling frequency, the smaller is the rotation of the electric quantity r in the $\mathbb{C}$ plane. The DSC pre-filter delay and harmonics for each stage are shown in Table A.1, and were chosen to filter the most common grid harmonics while minimizing the number of operations required, as w_1 is fixed at 0.5, which represent a right shift operation. A Moving Average Filter with 16 samples was used before the downsampling to avoid aliasing and improve the resolution of the filtered signal.

The experimental results were obtained using the SignalTap II Logic Analyzer directly from the FPGA, as other methods would mask the precision and numerical stability, which is also present in most estimation algorithms.

Table A.1 – Delayed Signal Cancellation (DSC) Time Delays

Pre-filter Stage	Delay	Filtered Harmonics	w_1	w_2
1	$N/2$	$2 \pm 2n$	0.5	$0.5\exp(\iota\pi)$
2	$N/6$	$3 \pm 6n$	0.5	$0.5\exp\left(\iota\frac{\pi}{2}\right)$
3	$N/6$	$5 \pm 6n$	0.5	$0.5\exp\left(\iota\frac{\pi}{4}\right)$
4	$N/12$	$7 \pm 12n$	0.5	$0.5\exp\left(\iota\frac{\pi}{8}\right)$
5	$N/24$	$13 \pm 24n$	0.5	$0.5\exp\left(\iota\frac{\pi}{16}\right)$

All the signals were acquired with a 16-bit numerical accuracy with one signal bit, and the learning rate for all cases was fixed in 0.0625, and the voltage vector rated frequency was defined as 50 Hz. A trade-off between numerical precision and dynamic behaviour was observed, as a higher learning rate leads to a faster although less precise behaviour. However, if the learning-rate is chosen to be too small, the numerical precision of the update equation is hindered, as the error update equation has less bits to perform the update.

A.2.2.1 Steady-State Frequency Estimation

The estimation precision for a pure sinusoidal grid condition operating with the rated DSC frequency of 50 Hz is shown in Figure A.3a, with a maximum estimation error of 0.008% and an estimation bias of 0.004%, mostly due to quantization errors. The dynamic of a frequency step from 50 Hz to 55 Hz is illustrated in Figure A.4a, demonstrating a settling time of approximately 20 ms.

A.2.2.2 Unbalanced conditions at non-rated frequency

In this case, the three-phase vector amplitude was set to (1.0, 0.6, 0.4) p.u. with phase displacements of $-15°$ in phase b and $+12°$ in phase c, describing an ellipsoidal trajectory in $\alpha\beta$ coordinates. The filtered signal trajectory presented an eccentricity of 0.98634 due to the frequency mismatch of the pre-filter, which demonstrates the need of a WLE approach. The estimation in this case was more precise, with a maximum estimation error of 0.0055%, as shown in Figure A.3b, due to the lower amplitude of the three-phase vector has a similar effect of a slower having a smaller learning rate and fewer quantization levels.

A.2.2.3 Short-circuit at non-rated Frequency

Similarly to the previous case, the three-phase vector amplitude was set to (1.0, 0.6, 0), with a maximum frequency estimation error of 0.0055%, as shown in Figure A.3c. The filtered signal also demonstrated an ellipsoidal trajectory with an eccentricity of 0.98948. This condition demonstrates the algorithm behaviour under a grid short-circuit. It is worth noting that the algorithm cannot operate with two short-circuited phases.

The dynamic behaviour of a frequency step from 50 Hz to 55 Hz is shown in Figure A.4b, which in this case is slower than the balanced case due to the smaller signal amplitude.

A.2.3 Distorted grid conditions

A (0.75, 0.75, 0.75) p.u. signal contaminated with the following grid harmonics: 2% 2^{nd}, 5% 3^{rd}, 1% 4^{th}, 30% 5^{th}, 20% 7^{th}, 10% 11^{th}, 5% 13^{th} and 2% 17^{th}, aiming to emulate a heavily distorted grid condition. The steady-state frequency estimation is shown

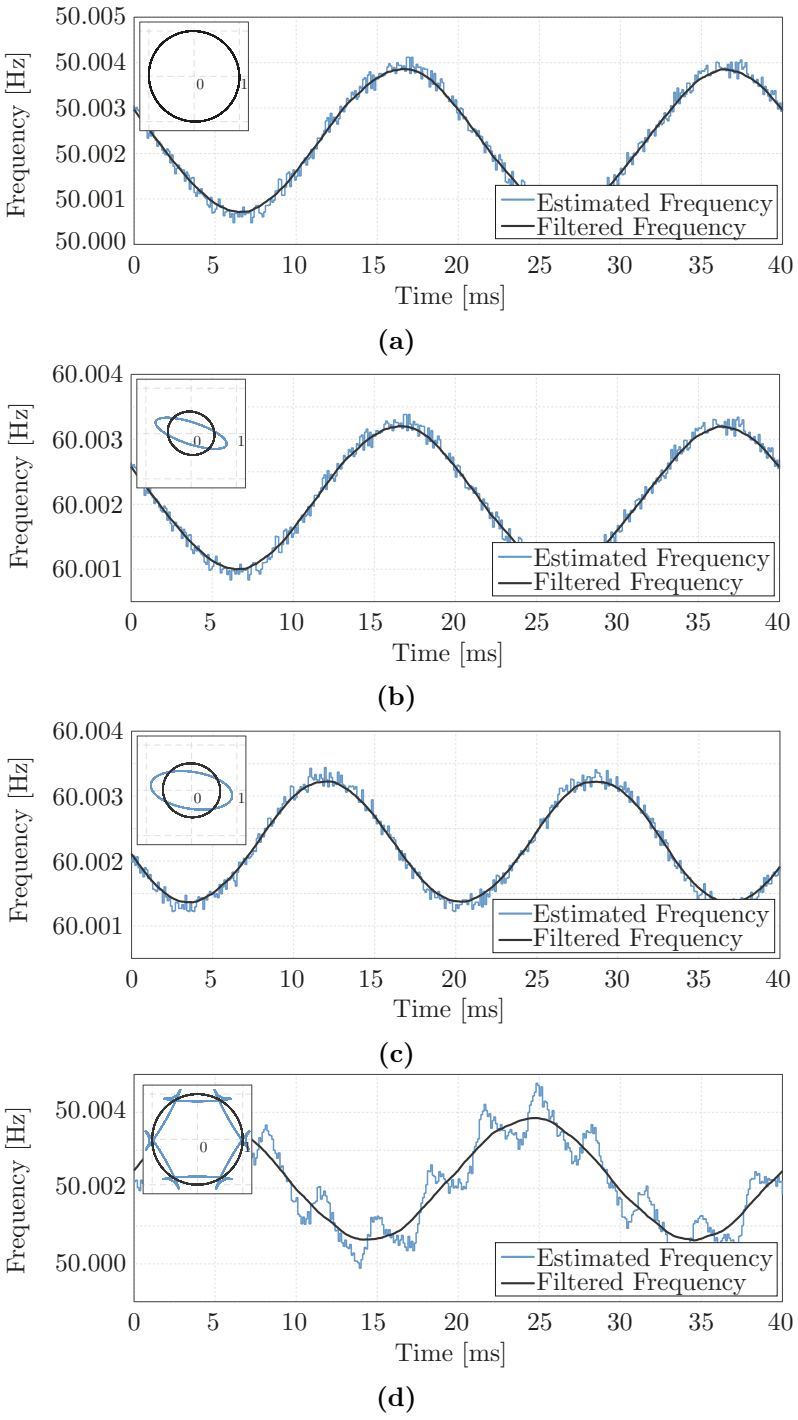

Figure A.3 – Steady-state estimated frequency for four different conditions: (a) a circular trajectory signal operating at rated frequency (50 Hz). (b) an unbalanced signal with three-phase amplitude vector given by (1.0, 0.6, 0.4) p.u operating at non-rated frequency (60 Hz). (c) a short-circuit operation with three-phase amplitude vector given by (1.0, 0.6, 0.0) operating at non-rated frequency (60 Hz). (d) a distorted signal of amplitude vector (0.75, 0.75, 0.75) contaminated with 2% 2^{nd}, 5% 3^{rd}, 1% 4^{th}, 30% 5^{th}, 20% 7^{th}, 10% 11^{th}, 5% 13^{th} and 2% 17^{th} harmonics operating at rated frequency (50 Hz).

in Figure A.3d, with a maximum error of approximately 0.008%, and the dynamic of a change from non-distorted to distorted can be seen in Figure A.4c, with a maximum

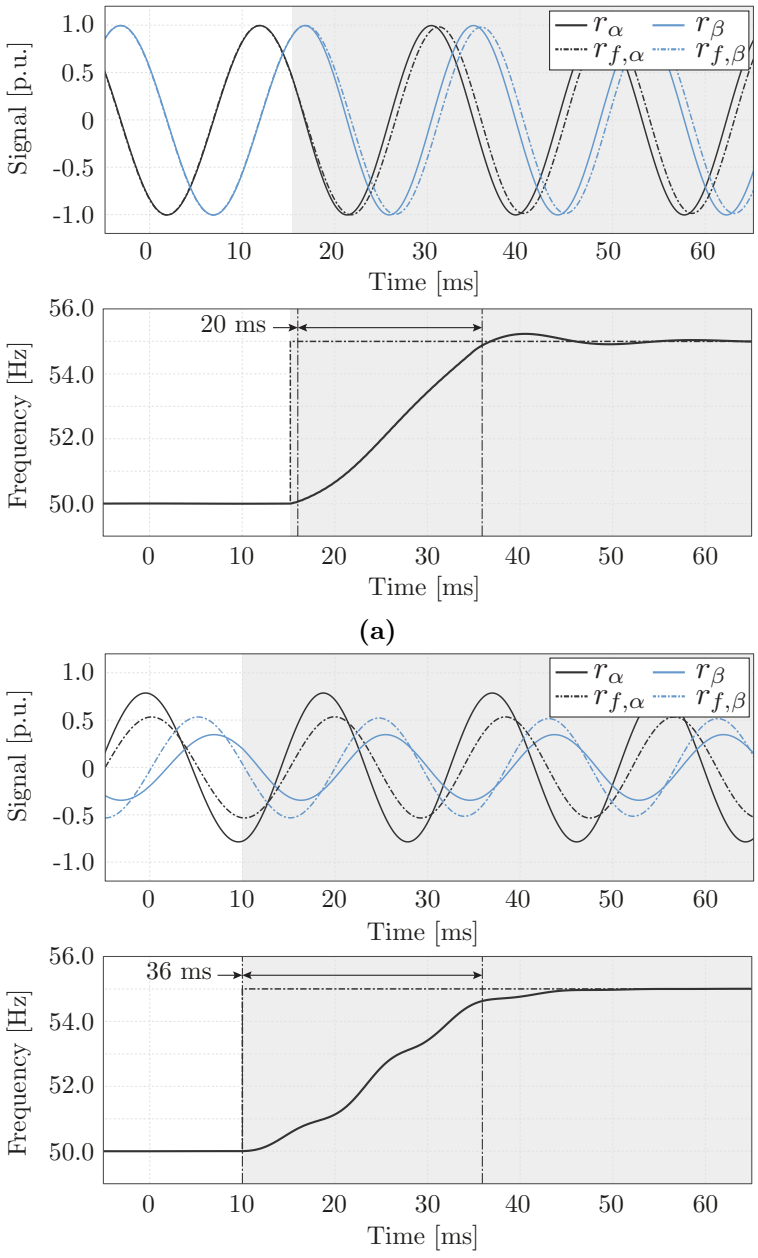

Figure A.4 – Dynamic behaviour of the estimated frequency for three different conditions: (a) a circular trajectory signal operating at rated frequency (50 Hz) to 55 Hz. (b) a short-circuit operation with three-phase amplitude vector given by (1.0, 0.6, 0.0) operating at rated frequency (50 Hz) to 55 Hz.

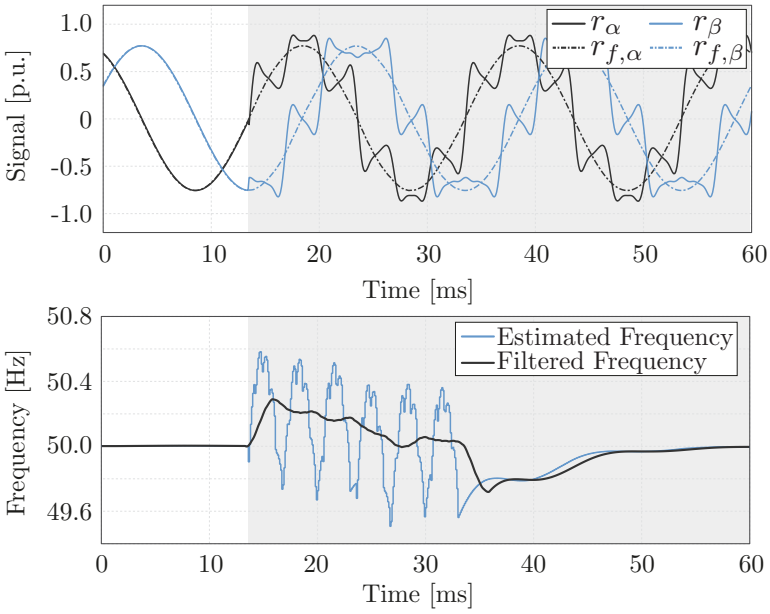

(c)

Figure A.4 – Dynamic behaviour of the estimated frequency for three different conditions: (c) from a circular trajectory signal of amplitude vector (0.75, 0.75, 0.75) to a distorted condition with 2% 2^{nd}, 5% 3^{rd}, 1% 4^{th}, 30% 5^{th}, 20% 7^{th}, 10% 11^{th}, 5% 13^{th} and 2% 17^{th} harmonics operating at rated frequency (50 Hz).

averaged frequency deviation of approximately 0.3 Hz during the transient reponse.

One of the drawbacks of this strategy is its poor performance under heavily distorted grid when the grid frequency deviates from the DSC rated frequency. However, the structure can be cascaded, and a second estimation stage can be employed, by varying the delay length of each DSC according to the frequency estimated by the first stage.

A.3 WIDELY-LINEAR ADAPTIVE FREQUENCY ESTIMATOR WITH AN ADAPTIVE DELAYED-SIGNAL CANCELLATION PRE-FILTER

The strategy proposed in the previous section can also be employed as a frequency estimator for a second DSC filter stage, according to the block diagram shown in Figure A.5. A third frequency estimation change did not present a significant advantage to the algorithm.

On a first moment, the agorithm was implemented using a SLE instead of a WLE, due to its lower complexity, as to validate the need for a WLE when the grid frequency is different than the rated frequency.

The algorithm was implemented using an Altera Cyclone V 5CSEMA4U23C6N. The grid voltage references were generated using a TI TMS320F28335 communicating with the FPGA via SPI to emulate a voltage phasor with 11-bits, where the MSB is the bit signal. It is important to notice that the implementation of the previous algorithm was reviewed to minimize numerical imprecisions of the calculations, thus a better performance for a final implementation is expected. The results were obtained through the SignalTap II

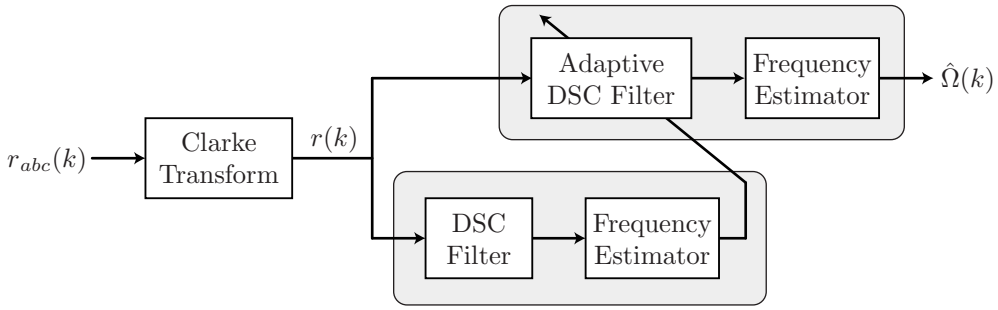

Figure A.5 – Block diagram of the Widely-Linear Adaptive Frequency Estimator with an Adaptive Delayed-Signal Cancellation Pre-Filter with two frequency estimation stages.

Logic Analyzer, aiming to minimize external noise and perturbations to the measurements which might dirtort the results.

The first stage DSC's rated frequency was chosen as 50 Hz. The DSCs sampling rate was chosen as 100 kHz, while the SLE sampling rate is equal to 10 kHz. The steady-state estimated frequencies of each estimator is presented in Figure A.6 for 50 Hz and 55 Hz. The input r was contaminated with 7.4% 2^{nd} harmonic, 14.7% 3^{rd} harmonic, 29.4% 5^{th} harmonic, 3.7% 7^{th}, 11^{th} and 13^{th} harmonics and an unbalance of $\mathfrak{I}\{r\} = 0.7\mathfrak{R}\{u\}$. The performance of the first DSC stage is sufficient to filter the input signal without the need for a second stage at the rated frequency. However, the adaptive estimator does not present an adequate behaviour at the 55 Hz frequency, and CLMS estimator is not designed to reject harmonics, hence the first estimation is not sufficiently accurate.

The phase plane of the input signal r and the filtered signal r_f of the first and second stages is presented in Figure A.7 for two different grid frequencies. The dynamic response is presented in Figure A.8. However, the settling time can be improved by improving the numerical precision, and the final result is expected to be closer to the non-adaptive algorithm.

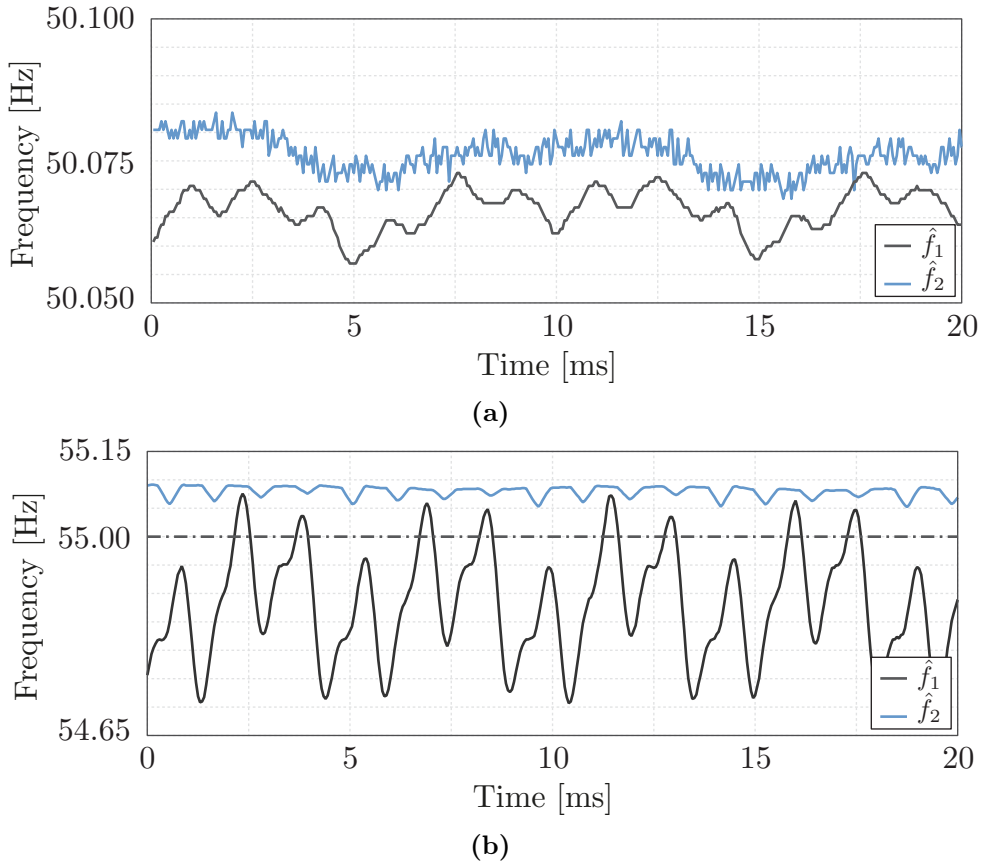

Figure A.6 – Steady state behaviour of the Widely-Linear Adaptive Frequency Estimator with an Adaptive Delayed-Signal Cancellation Pre-Filter for (a) Rated Frequency of 50 Hz (b) Non-rated frequency of 55 Hz.

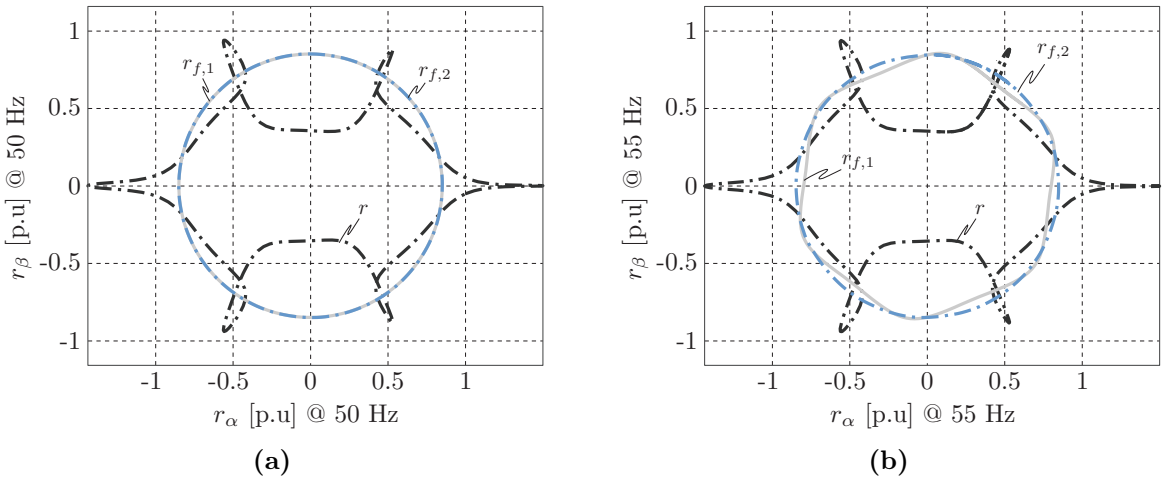

Figure A.7 – Block diagram of the Widely-Linear Adaptive Frequency Estimator with an Adaptive Delayed-Signal Cancellation Pre-Filter with two frequency estimation stages for (a) Rated Frequency of 50 Hz (b) Non-rated frequency of 55 Hz.

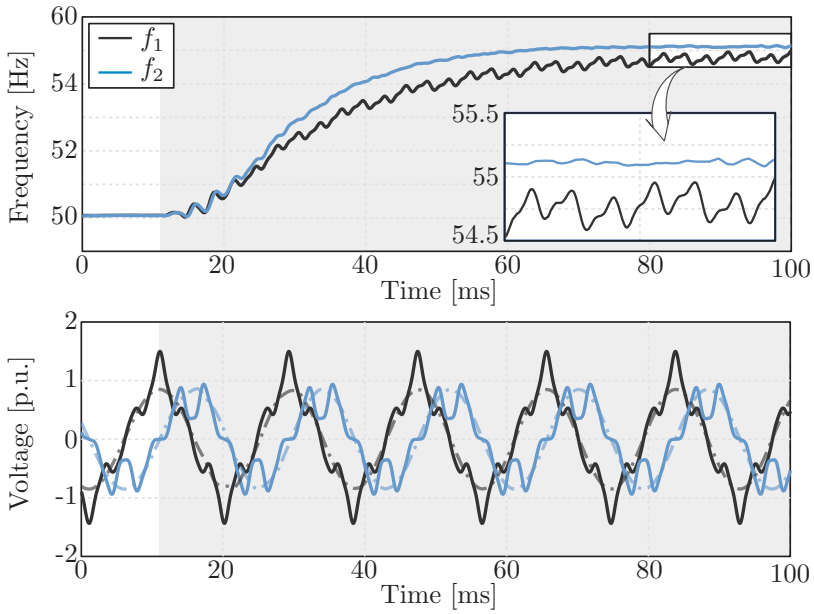

Figure A.8 – Step response of the Widely-Linear Adaptive Frequency Estimator with an Adaptive Delayed-Signal Cancellation Pre-Filter for a frequency step from 50 Hz to 55 Hz.

A.4 REMARKS

This appendix presented a study on frequency estimators based on the Complex Least Mean Square filter. The low order of the system identification poses as a problem, since the samples are correlated, and the process does not correspond to an AR(1), which is one of the premisses. This non-null correlation matrix creates a bias in the system identification, which translates into a frequency estimation error.

One solution for the harmonic compensation is through the use of a window of measurements, such as the ACTLS, although the probabilistic gradient does not follow an optimal trajectory, hence the settling time is hindered. Another solution is to perform the estimation for a window, considering an autoregressive model of higher order. For a more adequate filtering, the process should be modelled as an AR(N), where N is the last pronounced harmonic which contaminates the input signal. However, the complexity and performance of the algorithm would be hindered. Hence an evaluation of this strategy might result in a better disturbance rejection. Another solution is to model the frequency estimator as an autoregressive Volterra process, however questions on the filter order might rise. Another difficulty is related to the stability, as the input vector might surpass the maximum value for the algorithm converge, which in turn would lead to stability issues.

The substitution of the ACLMS in the proposed algorithms by the ACTLS with a small window might solve problems related to quantization, as the formulation for exogenous disturbances is contemplated in the problem formulation, which also should lower the requirements for the sampling frequency of the DSC algorithm, and consequently the buffer size.

The experimental results presented in this appendix were implemented in an FPGA. The execution of the DSC usually generates a large computattional overhead due to the number of calculations and the high sampling frequency for a better filter resolution. However, the adaptive algorithms might have a more adequate DSP implementation, since the sampling frequency requirements are much lower.

APPENDIX

B Adaptive Filtering Framework and Neural Networks

B.1 THE Z-TRANSFORM

The **two-sided z-transform** of $u(k)$ is defined as

$$U(z) = \mathcal{Z}\{u(k)\} := \sum_{k=-\infty}^{\infty} u(k)z^{-k}, \tag{B.1}$$

which is equivalent to the Laureant series, thus creating a **z-transform pair** defined by

$$u(k) \Leftrightarrow U(z), \tag{B.2}$$

with properties given by:

- $a(u_1(k) + u_2(k)) \Leftrightarrow aU_1(k) + aU_2(k)$ (Superposition)
- $u(k - k_0) \Leftrightarrow z^{-k_0}U(z)$ (Time-shifting)
- $\sum_{n=-\infty}^{\infty} u_1(n)u_2(k - n) \Leftrightarrow U_1(z)U_2(z)$ (Convolution).

B.2 LINEAR TIME-INVARIANT FILTERS

Let a time sequence denoted by $y(k)$ denoted by the set of samples $\{y(0), y(1), \ldots\}$, which is the output of a discrete-time system with an impulse response $w(k)$ with input $u(k)$. Thus, the output sequence can be described as the convolution of u and w, as in

$$u(k) = \sum_{n=-\infty}^{\infty} w(n)u(k - n). \tag{B.3}$$

Hence, the z-transform of the output y is given by

$$Y(z) = W(z)U(z), \tag{B.4}$$

and the z-transformation of the inpulse response w(k) results in

$$W(z) = \frac{Y(z)}{U(z)}. \tag{B.5}$$

From (B.5) and [112], it is possible to assume that

$$\exists a_k, b_k : \sum_{n=0}^{N} a_k y(k-n) = \sum_{n=0}^{N} b_k u(k-n) \; \forall k = 0, ...N, \tag{B.6}$$

which enables the representation of the impulse response in term of constants a_k and b_k, as in

$$W(z) = \frac{\sum\limits_{n=0}^{N} a_n z^{-n}}{\sum\limits_{n=0}^{N} b_n z^{-n}} \tag{B.7}$$

and its factored form

$$W(z) = \frac{a_0}{b_0} \frac{\prod\limits_{n=0}^{N} \left(1 - c_n z^{-1}\right)}{\prod\limits_{n=0}^{N} \left(1 - d_n z^{-1}\right)}. \tag{B.8}$$

From (B.8), we may distinguish between two types of linear time-invariant systems:

B.2.1 Finite-duration Impulse Response (FIR)

A filter is classified as a **FIR filter** *iff* the set of constants $\{d_n = 0, \; \forall n \in \mathbb{N}\}$. All the poles of $W(z)$ lie in the origin, and the impulse response $w(k)$ has a finite duration.

B.2.2 Infinite-duration Impulse Response (IIR)

A filter is classified as an **IIR filter** *iff* $W(z)$ has at least one polse which is not cancelled by a zeros, resulting in the sequence $w(k)$ having an infinite duration. A special case lies in $\{c_n = 0, \; \forall n \in \mathbb{N}\}$, where $W(z)$ is said to be an **all-pole filter**.

A system with impulse response $w(k)$ is said to be causal *iff*

$$w := \left\{w(k) = 0, \; \forall n \in \mathbb{Z}^-\right\}.$$

From a linear time-invariant point of view, the system is Bounded Input Bounded Output (BIBO) stable *iff* $\sum_{k=-\infty}^{\infty} \|w(k)\| < \infty$, i.e, $w(k)$ is absolutely summable. This translates into some requirements for $W(z)$, as the region of convergence must lie outside the outermost poles of $W(z)$ and must include the unit circle in the z-plane.

B.2.3 ARMA Process

From a linear point of view, a discrete-time system can be described through an union of Autoregressive (AR) model and Moving Average (MA) models, resulting in a Autoregressive Moving Average (ARMA) Model.

B.2.3.1 Autoregressive Process

A process is said to be autoregressive if its output is a linear combination of its previous output, as described in

$$\mathrm{AR}(p) \rightarrow y(k) = \sum_{n=1}^{p} a_n y(k-n), \tag{B.9}$$

where p is the order of the autoregressive process. From the previous analysis, this process consists in an all-pole filter with p zeros.

Example. Three-Phase Voltage Vector as an AR(1) Process Let a complex-valued voltage phasor v in $\alpha\beta$ coordinates be given by applying the Clarke Transformation on a three-phase voltage vector $\vec{v}_{abc}$, as in

$$v = \begin{bmatrix} 1 & e^{-\iota\frac{2}{3}\pi} & e^{\iota\frac{2}{3}\pi} \end{bmatrix} \boldsymbol{v}_{abc}. \tag{B.10}$$

For a purely sinusoidal three-phase voltage vector containing only the positive sequence component, the voltage time-varying phasor can be expressed as

$$v(k) = V e^{\iota 2\pi f_v k h}, \tag{B.11}$$

where V is the voltage amplitude, f_v is the voltage frequency and h is the sampling period. Thus, the voltage in the next time-step can be described as

$$v(k+1) = V e^{\iota 2\pi f_v (k+1) h} = e^{\iota 2\pi f_v h} v(k), \tag{B.12}$$

demonstrating the autoregressive behaviour the complex-valued voltage phasor.

B.2.3.2 Moving Average Process

A process is said to be moving-average if its output is a linear combination of the input samples, as in

$$\mathrm{MA}(q) \rightarrow y(k) = \sum_{n=0}^{q-1} b_n x(k-n), \tag{B.13}$$

where q is the order of the moving-average process. From inspection, this process results in a FIR filter.

An ARMA(p, q) process is the combination of an AR(p) and a MA(q) process, This model is used to describe the dynamics of feedback systems while resulting in a IIR filter, and can be described as

$$\mathrm{ARMA}(p,q) \rightarrow y(k) = a_0 + \sum_{n=1}^{p} a_n y(k-n) + \sum_{n=0}^{q-1} b_n x(k-n) \tag{B.14}$$

B.3 A GENERAL FRAMEWORK FOR LINEAR ADAPTIVE FILTERS

This section presents a framework which can be used for linear adaptive filters, which serves as a basis for nonlinear adaptive filters. The analysis here presented is based on [113].

Gradient descent algorithms can approximately track the weights of a certain process with impulse response weights $\mathbf{w}(n)$. Thus, a general expression for the weight update is given by

$$\hat{\mathbf{w}}(k+1) = \hat{\mathbf{w}}(k) + \eta\mathbf{\Gamma}(k)\left(y(k) - \mathbf{u}^T(k)\mathbf{w}(k)\right) \tag{B.15}$$

To asses how far an adaptive algorithm is from the optimal solution, an error vector and a sample input matrix can be defined as

$$\begin{aligned} \tilde{\mathbf{w}}(k) &= \mathbf{w}(k) - \hat{\mathbf{w}}(k), \\ \mathbf{\Sigma}(k) &= \mathbf{\Gamma}(\mathbf{k})\mathbf{u}^T(k) \end{aligned} \tag{B.16}$$

respectively. From this, we have that the new weight error equation

$$\tilde{\mathbf{w}}(k+1) = \left(\mathbf{I} - \eta\mathbf{\Sigma}(k)\right)\tilde{\mathbf{w}}(k) - \eta\mathbf{\Gamma}(k)\nu(k) + \Delta\mathbf{w}(k+1) \tag{B.17}$$

From (B.17), the **Least Mean Square** (LMS) algorithm follows the probabilistic gradient, given as

$$\mathbf{\Sigma}(k) = E\left\{\mathbf{u}^T(k)\mathbf{u}(k)\right\}, \tag{B.18}$$

the **Recursive Least Squares** (RLS) algorithm aims to minimize a weighted linear least square cost function, resulting in

$$\begin{aligned} \mathbf{\Sigma}(k) =& P(k)\mathbf{u}^T(k)\mathbf{u}(k) \\ P(k) =& \frac{1}{1-\eta}\left(P(k-1) - \eta\frac{P(k-1)\mathbf{u}(k)\mathbf{u}^T(k)P(k-1)}{1-\eta+\eta\mathbf{u}^T(k)P(k-1)\mathbf{u}(k)}\right), \end{aligned} \tag{B.19}$$

and the Kalman filter results in

$$\begin{aligned} \mathbf{\Sigma}(k) =& \frac{P(k-1)\mathbf{u}(k)\mathbf{u}^T(k)}{R+\eta\mathbf{u}^T(n)P(n-1)\mathbf{u}(n)} \\ P(k) =& P(k-1) + \eta Q - \frac{P(k-1)\mathbf{u}(k)\mathbf{u}^T(k)P(k-1)}{R+\eta\mathbf{u}^T(k)P(k-1)\mathbf{u}(k)}. \end{aligned} \tag{B.20}$$

B.4 DISCRETE-TIME NONLINEAR MODELS

From the basic linear processes discussed in the last section, nonlinear models can be obtained through the use of many different techniques, such as Polynomial filters, which are based on the Volterra series, and through modifications of ARMA processes, which

are widely used as building blocks for Artificial Neural Networks.

B.4.1 Polynomial Nonlinear Models

In this approach, the nonlinearity is localized at the front end of the process. Considering the input discrete time series $u(k)$, we may combine these samples, defining a set of **Discrete Volterra kernels** as follows:

- W_0: *zero-order (dc) term*
- $W_1\left[u(k)\right] = \sum_i w_i u(i)$: *first-order (linear) term*
- $W_2\left[u(k)\right] = \sum_i \sum_j w_{ij} u(i)u(j)$: *second-order (quadratic) term*
- $W_3\left[u(k)\right] = \sum_i \sum_j \sum_m w_{ijm} u(i)u(j)u(m)$: *third-order (cubic) term*
- and so on...

The polynomial approach can be used for stability analysis of polynomial systems, and in nonlinear adaptive filters. Such approach might prove interesting for the grid autoregressive model under distorted grid conditions. A frequency estimation algorithm is currently being developed based on Volterra filters. A drawback is an inability to represent discontinuous systems due to the series truncation.

B.4.2 Nonlinear Models

The Artificial Neural Networks in this study are mainly composed by *neurons*, which are based on nonlinear versions of ARMA processes, as to distribute the nonlinearities throughout the network. In this sense, these neurons are based on slight modifications of the linear processes discussed in the previous section. In this paper, the **Nonlinear Moving-Average (NAR)** and the **Nonlinear Autoregressive Moving-Average (NARMA)** processes are further discussed as basis for the Artificial Neural Networks. The nonlinearity introduced into the linear process is henceforth called **activation function**, which is a memoryless nonlinearity inserted into the model.

B.4.2.1 Nonlinear Moving-Average Process

The NMA(q) can be described by

$$\mathrm{NMA}(q) \rightarrow y(k) = \sum_{n=0}^{q-1} \Phi\left(b_n x(k-n)\right), \tag{B.21}$$

where $\Phi(\cdot)$ is the activation function. This process behaves as a FIR filter with finite duration due to the absence of a feedback.

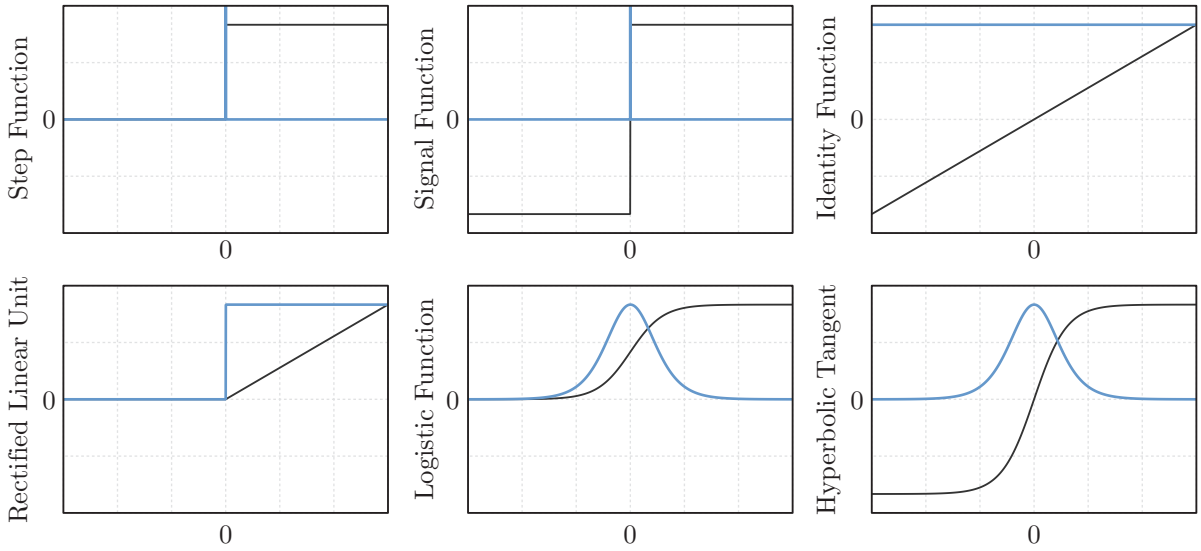

Figure B.1 – Examples of activation functions for neural networks.

B.4.2.2 Nonlinear Autoregressive Moving-Average Process

As opposed to the previous process, the NARMA(p, q) process can be described as

$$\text{NARMA}(p,q) \rightarrow y(k) = \Phi\left(\sum_{n=0}^{q-1} b_n x(k-n) + \sum_{n=1}^{p} a_n y(k-n)\right), \tag{B.22}$$

where $\Phi(\cdot)$ is the activation function. Unlike the previous process, the NARMA process behaves as an IIR filter.

The NARMA(p, q) based neurons are employed in *Recurrent Neural Networks* (RNNs).

B.4.3 Activation Function

The activation function serves as means to insert nonlinearities, which are usually of the saturation type, into the model. There is a wide variety of functions that can be chosen, each with its own advantages and disadvantages, with some functions exemplified in Figure B.1.

Usually, these nonlinearities are of the discontinuous type, although any nonlinear function can be employed according to the process behaviour, hence the process of choosing an activation process can be quite complex.

B.5 ARTIFICIAL NEURAL NETWORKS

The Artificial Neural Network models are made up of the interconnection of a large number of nonlinear processign unit, referred to as **neurons**. The internal structure of these neurons are based on the NARMA models presented in the last section.

From a signal-processing perspective, interest in ANNs is motivated by the following important properties [112]:

- *Nonlinearity*: Attributed to the nonlinear nature of the activation functions distributed along the neurons;
- *Weak Statistical Assumptions*: An ANN relies on the availability of training data for its design, as to capture the statistical characteristics of the environment in which it operates, provided that the training data are large enough as to be "representative" of the environment;
- *Learning*: An ANN has a built-in capability to learn from its environment.

B.5.1 Models of a Neuron

A generic neuron model can be illustrated by Figure B.2. The model consists in a linear combiner, consisting of a set of *synaptic weights* (adjustable parameters) and a *nonlinear unit*, described by the activation function. An external **bias** is also employed as to alter the activation function behaviour.

The neuron models ban be classified into four basic types, depending on the behaviour of the activation function:

- **Linear Model**: In this model, the activation function has a linear behaviour, demonstrated by Figure B.1.c. This form operates as a linear adaptive filter.
- **McCulloch–Pits Model**: In this second model, the activation function behaves as a Heavyside function, illustrated by Figure B.1.a and Figure B.1.b.
- **Piecewise Linear Model**: This third model is a union of the two previous models. An example is the Rectified Linear Unit (ReLU), illustrated by Figure B.1.d.
- **Sigmoidal Model**: This last model is so called because the activation functions demonstrates an S-shaped characteristic. In this sense, the activation function $\Phi(\cdot)$ may be written as

$$\Phi(u) = \begin{cases} 1, & u \to \infty \\ 0.5 & u = 0 \\ 0, & u \to \infty \end{cases} \tag{B.23}$$

A common choice of sigmoidal function is the *logistic function* shown in Figure B.1.e, defined by

$$\Phi(u) = \frac{1}{1 + e^{-\mu u}}, \tag{B.24}$$

where μ is a slope parameter. The derivative with respect to its input is given by

$$\frac{\partial}{\partial u}\Phi(u) = \mu\Phi(u)(1 - \Phi(u)), \tag{B.25}$$

with maximum slope equal to 0.25μ.

B.5.2 Multilayer Perceptron

The **Multilayer Perceptron** (MLP) is an ANN that consists of an *input layer* of source nodes, one or more *hidden layers* of computational nodes and an output layer also made of computational nodes. Two features can be inferred from this structure:

- A multilayer perceptron is a *feedforward network* if there is no feedback in the network (NMA model). Otherwise, it is called a *recurrent neural network* (RNN) if the neurons are modelled as NARMA processes.
- The network is said to be *fully connected* if each node in one layer is connected to every other node in the adjacent layer. Alternatively, the network is called *partially connected* if not every neuron is connected.

In this sense, the design of a multilayer perceptron depends on three different parameters:

1. Number of hidden layers;
2. Number of neurons in each layer;
3. The synaptic weights that interconnect the neurons in the different layers.

Issues 1 and 2 relate to the *neural (model) complexity*, which is said to be the weakest link in the present knowledge on how to design MLPs [112]. Issue 3 can be solved through the *back-propagation algorithm*, optimization routines or a combination of both methods.

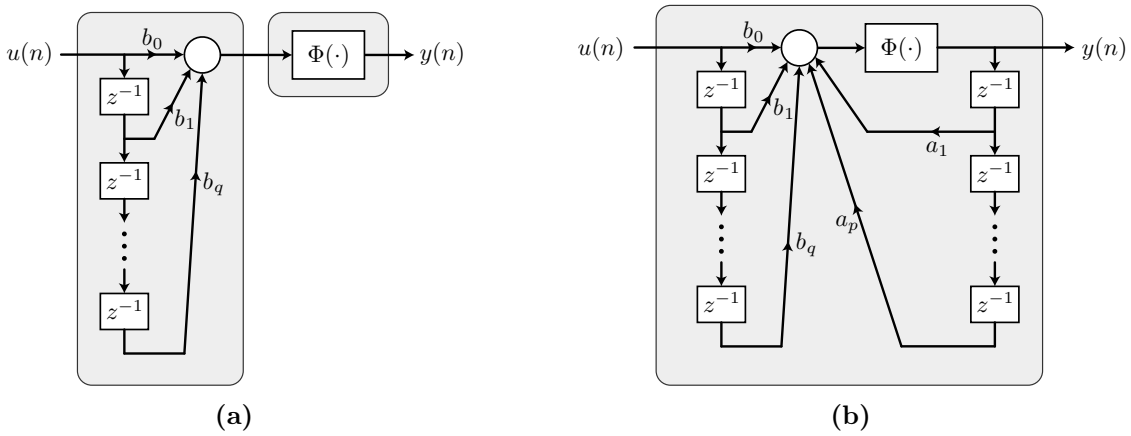

Figure B.2 – Block diagram of the (a) NMA perceptron model (b) NARMA perceptron model.

B.5.3 Back-Propagation Algorithm

Consider a feedforward network, where the output of a single neuron be given by

$$y(k) = \Phi\left(\mathbf{u}(k)^T\mathbf{w}(k)\right) = \Phi\left(net(k)\right) \tag{B.26}$$

where $\mathbf{u}(n)$ is a vector of input samples and $\mathbf{w}(n)$ is the weight vector of the synaptic part. Also, assume that $\Phi(\cdot)$ is differentiable and let the desired response be given by $d(n)$. Thus, the error signal can be given by

$$e(k) = d(k) - y(k) = d(k) - \Phi\left(\mathbf{u}^T(k)\mathbf{w}(k)\right) \tag{B.27}$$

From the adaptive filter theory, the weight vector at the following sampled time can be written as

$$\mathbf{w}(k+1) = \mathbf{w}(k) - \mu\nabla_{\mathbf{w}(k)}J(k), \tag{B.28}$$

where $J(k)$ is a cost function and μ is the learning rate. Using the ideas of the LMS, the cost function can be written as

$$J(k) = \frac{1}{2}E\left\{e(k)^Te(k)\right\} = \frac{1}{2}e^2(k) \tag{B.29}$$

and the gradient can be computed from

$$\nabla_{\mathbf{w}(k)}J(k) = \frac{\partial}{\partial\mathbf{w}(k)}J(k) = -e(k)\dot{\Phi}\left(\mathbf{u}^T\mathbf{w}(k)\right)\mathbf{u}(k), \tag{B.30}$$

with $\dot{\Phi}$ as the derivative of the activation function, granted that the chosen function is differentiable. From this, the weight update equation bvecomes

$$\mathbf{w}(k+1) = \mathbf{w}(k) + \mu\dot{\Phi}\left(net(k)\right)e(k)\mathbf{u}(k). \tag{B.31}$$

From this, we can infer that the filter is BIBO stable if $\Phi(\cdot)$ is bounded, as the output range is limited. Also, if the activation function is of the saturation type, its derivative vanishes for large inputs, causing the weights not to be updated.

From (B.31), the following procedure can be adopted for multi-layer training of feedforward networks, according to Figure B.3:

1. Receive new observation (or input) vector $\mathbf{u}(n)$
2. **Feedforward**: for each unit g_l in each layer $[1..L]$ compute g_l based on units f_m from the previous layer
$$g_j = \Phi(x_{j,bias} + \sum_m x_{lm}f_m) \tag{B.32}$$
3. Compute prediction and prediction error $y - d$

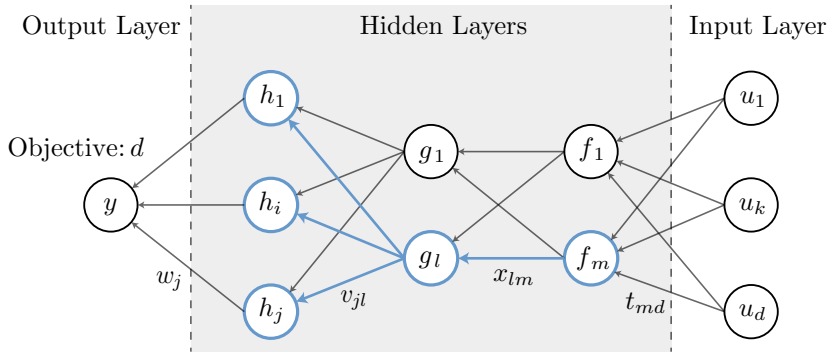

Figure B.3 – Back-propagation algorithm for training neural networks.

4. **Back-propagate error**: for each unit g_l in each layer $[L..1]$

   a. Compute error on g_l

$$\frac{\partial}{\partial g_l} E = \sum_i \dot{\Phi}(h_i) v_{il} \frac{\partial}{\partial h_i} E \tag{B.33}$$

   b. For each x_{lm} that affects g_l compute error on x_{lm}

$$\frac{\partial}{\partial x_{lm}} E = \sum_m \dot{\Phi}(g_l) f_m \frac{\partial}{\partial g_m} E \tag{B.34}$$

   and update the weight

$$x_{lm} = x_{lm} - \eta \frac{\partial}{\partial x_{lm}} E. \tag{B.35}$$

A few modifications on the back-propagation algorithms must be performed for RNNs.

One of the advantages of the algorithm is the possibility of real-time training and the lower training time consumption if compared to optimization routines. A disadvantage is the need to know the desired response d, which for power electronics applications sometimes is not trivial.

B.5.4 Nonlinear Optimization

The optimization objective lies in finding a set of weights $\mathbf{w}_i$ for $i = [1..N]$ neurons, according to

$$\begin{aligned} \min_{\mathbf{w}_i} \quad & J(\mathbf{w}_i) \\ \text{s.t.} \quad & \Gamma(\mathbf{w}_i) > 0, \end{aligned} \tag{B.36}$$

where $J(n)$ is a cost function, combined with a nonlinear solver. The difficulty lies in the fact that the problem domain is not convex, and the presence of many local minima might prove a challenge for the operation of the neural network. However, nonlinear optimization solvers, such as genetic algorithm, can be employed if the cost function is well-defined, especially for bounded problems.

B.6 CURRENT ESTIMATOR FOR A POWER FACTOR CORRECTION RECTIFIER

Consider the boost rectifier shown in Figure B.4. The objective of this Artificial Neural Network is to provide an estimate for the boost inductor current, which can be used as a state estimator for sate-feedback control or used for current feedback.

In a first moment, a RNN was trained as to provide a current estimate using the rectifier input voltage v_r and the output voltage v_{dc} as the network input. However, one of the main challenges is the ANN initial transitory behaviour, hence the current i_g was also used as an input to the RNN. It is worth noting that a more thorough study should be made as to verify the use of an ANN for current sensorless control. The output (or grid-side) current is easier to measure, as it presents a lower signal-to-noise (SNR) ratio.

The RNN was conceived with a single hidden layer with 10 neurons. It is worth noting that the time for training was of approximately 6 hours using the MATLAB back-propagation algorithm. The optimization routine described in the previous application may be employed for a more refined result, which was deemed not necessary in this case. The block diagram of the proposed control strategy is shown in Figure B.5.

The boost current and estimated current are shown in Figure B.5, and it is possible to notice that the estimate struggles with the initial transitory and with the high-frequecy transitions that occur as the current reaches zero. A solution would be to train with a sinusoidal waveform and take the absolute value of the estimate, however the estimation during the Discontinuous Conduction Mode is hindered. Also, problems related to the initial transitory might be solved during the capacitor pre-charge stage, solving instability issues observed during simulations. Future works might show a comparison between the proposed current estimator and other estimation techniques, such as the Luenberger observer and the Sliding Mode observer.

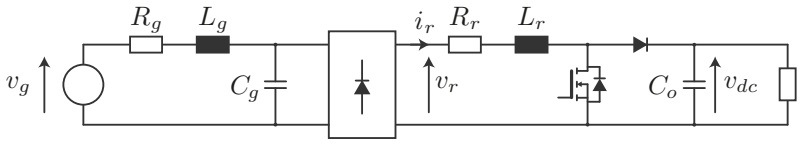

Figure B.4 – Boost PFC converter with an LCL filter.

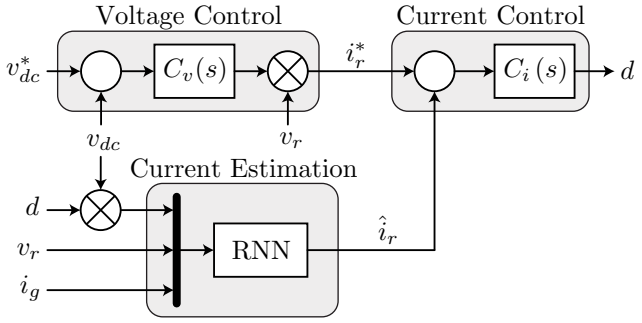

Figure B.5 – Block diagram of the proposed boost PFC rectifier control strategy employing a Recurrent Neural Network current estimator

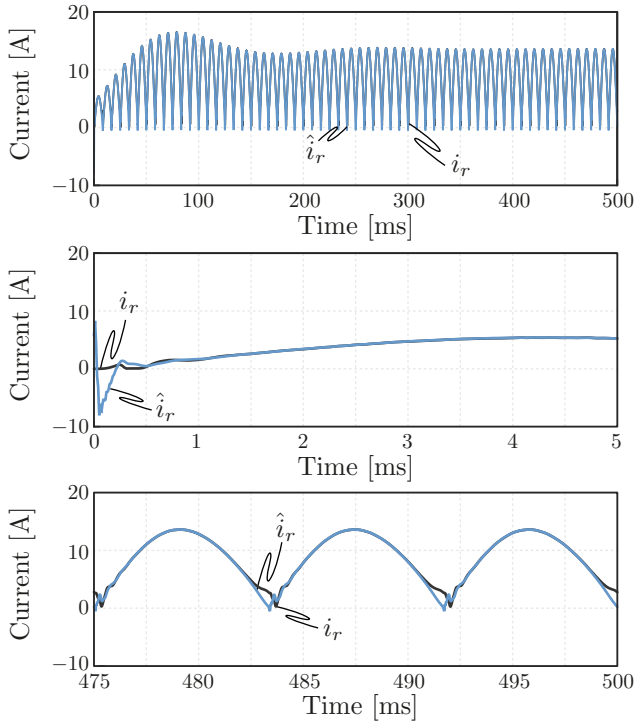

Figure B.6 – Boost PFC converter operating in closed-loop using a Recurrent Neural Network current estimator.

From the simulation results presented in Figure B.6, the estimation of the boost inductor current is feasible with RNNs when measuring the output current, and a more thorough study is necessary as to solve transitory problems for a current sensorless control.